

Lecture Notes in Mechanical Engineering

J. S. Rao
V. Arun Kumar
Soumendu Jana *Editors*

Proceedings of the 6th National Symposium on Rotor Dynamics

NSRD 2019

 Springer

Lecture Notes in Mechanical Engineering

Series Editors

Francisco Cavas-Martínez, Departamento de Estructuras, Universidad Politécnica de Cartagena, Cartagena, Murcia, Spain

Fakher Chaari, National School of Engineers, University of Sfax, Sfax, Tunisia

Francesco Gherardini, Dipartimento di Ingegneria, Università di Modena e Reggio Emilia, Modena, Italy

Mohamed Haddar, National School of Engineers of Sfax (ENIS), Sfax, Tunisia

Vitalii Ivanov, Department of Manufacturing Engineering Machine and Tools, Sumy State University, Sumy, Ukraine

Young W. Kwon, Department of Manufacturing Engineering and Aerospace Engineering, Graduate School of Engineering and Applied Science, Monterey, CA, USA

Justyna Trojanowska, Poznan University of Technology, Poznan, Poland

Lecture Notes in Mechanical Engineering (LNME) publishes the latest developments in Mechanical Engineering—quickly, informally and with high quality. Original research reported in proceedings and post-proceedings represents the core of LNME. Volumes published in LNME embrace all aspects, subfields and new challenges of mechanical engineering. Topics in the series include:

- Engineering Design
- Machinery and Machine Elements
- Mechanical Structures and Stress Analysis
- Automotive Engineering
- Engine Technology
- Aerospace Technology and Astronautics
- Nanotechnology and Microengineering
- Control, Robotics, Mechatronics
- MEMS
- Theoretical and Applied Mechanics
- Dynamical Systems, Control
- Fluid Mechanics
- Engineering Thermodynamics, Heat and Mass Transfer
- Manufacturing
- Precision Engineering, Instrumentation, Measurement
- Materials Engineering
- Tribology and Surface Technology

To submit a proposal or request further information, please contact the Springer Editor of your location:

China: Dr. Mengchu Huang at mengchu.huang@springer.com

India: Priya Vyas at priya.vyas@springer.com

Rest of Asia, Australia, New Zealand: Swati Meherishi at swati.meherishi@springer.com

All other countries: Dr. Leontina Di Cecco at Leontina.dicecco@springer.com

To submit a proposal for a monograph, please check our Springer Tracts in Mechanical Engineering at <http://www.springer.com/series/11693> or contact Leontina.dicecco@springer.com

Indexed by SCOPUS. The books of the series are submitted for indexing to Web of Science.

More information about this series at <http://www.springer.com/series/11236>

J. S. Rao · V. Arun Kumar · Soumendu Jana
Editors

Proceedings of the 6th National Symposium on Rotor Dynamics

NSRD 2019

 Springer

Editors

J. S. Rao
The Vibration Institute of India
Bengaluru, Karnataka, India

V. Arun Kumar
Department of Mechanical Engineering
Dr. Ambedkar Institute of Technology
Bengaluru, Karnataka, India

Soumendu Jana
Propulsion division
National Aerospace Laboratories
Bengaluru, Karnataka, India

ISSN 2195-4356

ISSN 2195-4364 (electronic)

Lecture Notes in Mechanical Engineering

ISBN 978-981-15-5700-2

ISBN 978-981-15-5701-9 (eBook)

<https://doi.org/10.1007/978-981-15-5701-9>

© Springer Nature Singapore Pte Ltd. 2021

This work is subject to copyright. All rights are reserved by the Publisher, whether the whole or part of the material is concerned, specifically the rights of translation, reprinting, reuse of illustrations, recitation, broadcasting, reproduction on microfilms or in any other physical way, and transmission or information storage and retrieval, electronic adaptation, computer software, or by similar or dissimilar methodology now known or hereafter developed.

The use of general descriptive names, registered names, trademarks, service marks, etc. in this publication does not imply, even in the absence of a specific statement, that such names are exempt from the relevant protective laws and regulations and therefore free for general use.

The publisher, the authors and the editors are safe to assume that the advice and information in this book are believed to be true and accurate at the date of publication. Neither the publisher nor the authors or the editors give a warranty, expressed or implied, with respect to the material contained herein or for any errors or omissions that may have been made. The publisher remains neutral with regard to jurisdictional claims in published maps and institutional affiliations.

This Springer imprint is published by the registered company Springer Nature Singapore Pte Ltd. The registered company address is: 152 Beach Road, #21-01/04 Gateway East, Singapore 189721, Singapore

Proceeding of NSRD-2019

Dedicated to

Prof. J. S. Rao



Prof. J. S. Rao in a career spanning for almost 60 years has made phenomenal contribution to the fields of engineering in general and rotor dynamics & vibration in particular. A world renowned academician in the area of mechanical engineering has established many professional bodies for the advancement of engineering and technology. Students, academicians, researchers and engineering practitioners have been immensely benefitted with his association.

Organizing Committee

Patron

Mr. Jitendra J. Jadhav, Director, CSIR-NAL

Scientific Advisory Committee

Prof. J. S. Rao, President, Vibration Institute of India
Mr. M. Z. Siddique, Director, GTRE, Bengaluru
Dr. T. R. Rajanna, CD, AERDC, HAL, Bengaluru
Prof. K. Gupta, IIT Delhi
Prof. S. Y. Kulkarni, VC, REVA University, Bengaluru
Prof. C. W. Lim, City University, Hong Kong
Prof. C. Nataraj, Villanova University
Prof. R. Rzadkowski, Polish Academy of Sciences
Prof. Nalinaksh S. Vyas, IIT Kanpur
Prof. J. K. Sinha, The University of Manchester
Prof. A. Seshadri Sekhar, IIT Madras
Dr. Rama Rao, BARC, Mumbai
Prof. Rajiv Tiwari, IIT Guwahati
Prof. A. K. Darpe, IIT Delhi
Prof. A. R. Mohanty, IIT Kharagpur
Prof. V. Arun Kumar, Dr. AIT, Bengaluru
Prof. J. Srinivas, NIT, Rourkela
Prof. Mayank Tiwari, IIT Patna
Dr. Soumendu Jana, CSIR-NAL, Bengaluru
Dr. V. S. Ganesh Kumar, NSTL
Mr. S. P. Suresh Kumar, GTRE
Dr. Bhaskar Sarma, SRDS

Mr. P. P. George, CPEG/LPSC, Trivandrum
r. B. K. Sreedhar, IGCAR, Kalpakkam

Chairman

Mr. Manjunath P., Head, Propulsion

Co-chairman

Dr. J. S. Mathur, Head, KTMD

Convenor

Dr. Soumendu Jana, Sr. Pr. Scientist, PR, CSIR-NAL

Members of the Local Organizing Committee

C. Rajashekar
H. S. Muralidhara
K. M. Pillai
V. P. S. Naidu
M. T. Shobhavathy
R. Prathanayaka
Venkat Iyengar S.
Sathiyamoorthy K.
Dileepkumar B. Alone
Giridhara Babu Y.
R. Senthil Kumaran
Satish Kumar S.
Balaji Sankar
Raghavendra V. M.
M. Radhakrishna
J. Meghanathan
K. Satishkumar
Shailaja Menon N.
Rajasekar A. S.
Vinodkumar Vyas
Thennavarajan S.

Sharath P. P.
Steve Mithran
Sangeetha A. L.
Sandeep N.
Abin George
Vivek E. K.
R. Agilan
R. Jagadeesha
Satish Kumar M.
Lakshmikanthaiah H. B.
Ganesh Rao
Sadanand Kulkarni
Veera Sesa Kumar
Vinod kumar N.
Venu G.
Brijeshkumar J. Shah
Santhosh Kumar S.
Rajesh Emandi
Manikandan L. P.
Jayaprakash C.
Narendra Sharma

Organized by

Propulsion Division, CSIR-National Aerospace Laboratories, Bengaluru-560017.
In association with Vibration Institute of India.



Foreword



It is with deep satisfaction that I write this foreword to the Proceedings of the Sixth National Symposium on Rotor Dynamics (NSRD-2019) held during 2–3 July, 2019 at CSIR-National Aerospace Laboratories, Bengaluru, India. Rotor dynamics is a key and challenging aspect of engineering applications involving machineries with rotating parts. The prominent researchers in the field of rotor dynamics and related areas from India regularly organize this symposium, biennially. It was a great pleasure to host the Sixth National Symposium fully dedicated on this subject, at CSIR-NAL, Bengaluru.

I feel proud to state that there has been overwhelming response from students, research scholars, academicians, scientists and Industry from all over the country in the form of research papers to this conference. The invited lectures given by eminent persons with decades of rich experience provided valuable insights on the

subject for all the participants of this symposium. The proceedings of this symposium published by Springer will serve as an excellent reference book for the researchers and students.

A handwritten signature in black ink, appearing to read 'Jitendra J. Jadhav', is written over a light gray rectangular background.

September 2019

Jitendra J. Jadhav
Director
CSIR-National Aerospace Laboratories
Bengaluru, Karnataka, India

Preface

Rotor Dynamics is the key element in design and maintenance of all rotating machinery, which forms the backbone of infrastructure in our country. It is important that we discuss this subject at national level to bring the desired awareness on the advances in this field to the Government and industry by the rotor dynamics community of the country. In view of this, the first National Symposium on Rotor Dynamics (NSRD-2003) was held at Indian Institute of Technology, Guwahati in December 2003. Subsequently, four more symposiums were organized at IIT, Madras (December 2011), Dr. Ambedkar Institute of Technology, Bengaluru (January 2014), NIT, Rourkela (December 2015) and IIT, Patna (December 2017). The sixth symposium is being organized at CSIR-National Aerospace Laboratories, Bengaluru on 2nd and 3rd July 2019 the *Centenary Year of Jeffcott Rotor Model (1919)*.

The theme of the symposium is Rotor Dynamics and application of related techniques to solve industrial problems. Major topics included are:

- Analytical, computational and experimental methods
- Nonlinear and parametric effects on rotor
- Misalignment, rotor-bow, crack, rub-impact analyses
- Bearings, dampers and seals
- Vibration control using active and semi active methods
- Condition monitoring, diagnostics and prognostics of rotors
- Bladed disc systems
- Micro rotors and developments
- Any other relevant issues related to rotor dynamics
- Rotor dynamics of turbomachinery and IC engines

This symposium focuses on latest trends in rotor dynamics and various challenges encountered in the design of rotating machineries through several invited talks by experts and peers in the field of rotor dynamics from across the globe. The symposium also offers a good platform to researchers from academia and industry to present their work through contributed papers. The technical programme consists of plenary session, invited lectures and contributed paper presentations. The

symposium starts with a keynote speech followed by a plenary talk. There will be 8 invited talks from academia and R&D institutions, 10 sessions for paper presentation and four technical presentations from sponsors.

We would like to acknowledge the financial support provided by Government agencies (DST, DAE-BRNS) and industries (PROSIG, COMSOL, ANSYS, NUMECA, DYNASPEDE, AIMIL, Cubic Transmission, CTTC). We wish to thank all the authors, reviewers, sponsors, invited speakers, members of the Scientific Advisory Board and the Local Organizing Committee. We are grateful to Mr. Jitendra J. Jadhav, Director CSIR-NAL and Prof. J. S. Rao, President, Vibration Institute of India for their encouragement and support at various stages. We sincerely thank Mr. Sadanand S. Kulkarni, Mr. Brijeshkumar J. Shah, Mr. Senthil Kumaran R., Mr. L. P. Manikandan, Mr. Satish Kumar S. and Mr. Sandip N. for their help in bringing out this Souvenir in time.

Bengaluru, India

J. S. Rao
V. Arun Kumar
Soumendu Jana

Contents

Analytical, Computational and Experimental Methods

Stability Improvement for Upgraded Four-Stage Centrifugal Compressor Rotor-Bearing System	3
Vignesh Selvam, Roman Kochurov, Evgen Kashtanov, Leonid Moroz, and Abdul Nassar	
3D Finite Element Rotor Dynamic Analysis of Turbine Test Rig Rotor-Shaft Systems	17
Nanjundaiah Vinod Kumar, Rajeevalochanam Prathapanayaka, Revanna Jai Maruthi, and Shashidhar Swaroop	
Evaluation of Dynamic Characteristics of a VMC Spindle System Through Modal and Harmonic Response. Part 1: Spindle Supported by Angular Contact Ball Bearings	29
Gireesha R. Chalageri, Siddappa I. Bekinal, and Mrityunjay Doddamani	
Evaluation of Dynamic Characteristics of a VMC Spindle System Through Modal and Harmonic Response—Part 2: Spindle Supported by Hybrid Bearing Set	39
Gireesha R. Chalageri, Siddappa I. Bekinal, and Mrityunjay Doddamani	
Dynamic Analysis of Three-Dimensional Composite Tube Shafts	51
Pavani Udatha, A. S. Sekhar, and R. Velmurugan	
Analysis of Rotor Supported in Double-Layer Porous Journal Bearing with Gyroscopic Effects	65
C. Shravan Kumar, K. Jegadeesan, and T. V. V. L. N. Rao	
Rotordynamic Analysis and Redesign of High-Pressure Turbine Test Rig	77
C. Veera Sesa Kumar, E. K. Vivek, and S. Vignesh	

Thermo-Mechanical Analysis of a Rotor-Bearing System Having a Functionally Graded Shaft with Transverse Breathing Cracks	93
Debabrata Gayen, Rajiv Tiwari, and Debabrata Chakraborty	
A Coupled Field, Circuit and Rotor Model of a BCW Induction Machine	105
Gaurav Kumar, Karuna Kalita, Kari Tammi, and Seamus Garvey	
Dynamic Modeling and Analysis of Propeller Shaft Supported on Rolling Element Bearings	117
Devendra Singh and J. Srinivas	
Rotordynamic Analysis of High-Speed Rotor Used in Cryogenic Turboexpander Using Transfer Matrix Method	129
Debanshu S. Khamari, Partha Sarathi Kar, Shantashree Jena, Jitesh Kumar, and Suraj K. Behera	
Clustering in Pareto Front: Application on an Aero Engine Rotor-Bearing System for Improved Design	141
K. Joseph Shibu, K. Shankar, Ch. Kanna Babu, and Girish K. Degaonkar	
Sensitivity Analysis for Unbalance Identification of Rotor Systems	155
Dinesh Kumar Pasi, Manoj Chouksey, and Amit Kumar Gupta	
Sommerfeld Effect Attenuation Using Switched-Stiffness Method of a Non-ideal Internally Damped Shaft–Disk System with Constant Eccentricity	165
Abhishek Kumar Jha and Sovan Sundar Dasgupta	
Rotor Dynamic Analysis of Rotor Assembly of a Small Liquid Metal Pump	177
Ashish Kumar, Y. V. Nagaraja Bhat, B. K. Sreedhar, S. I. Sundar Raj, S. Murugan, and P. Selvaraj	
Bearings, Dampers and Seals	
Rotor Dynamics of Turbine–Generator Shaft with Dampers During Subsynchronous Resonance Generated by Series Capacitors	191
P. Manikandan and Faheem Ahmed Khan	
Active Control of Bridge Configured Self-bearing Motor, a Numerical Study	203
Gaurav Kumar, Karuna Kalita, and Kari Tammi	
Stability Analysis of Partial Slip Texture Journal Bearing	217
T. V. V. L. N. Rao, Ahmad Majdi Abdul Rani, Norani Muti Mohamed, Hamdan Haji Ya, Mokhtar Awang, and Fakhruddin Mohd Hashim	

Experimental Study of Temperature Effect on Labyrinth Seal Leakage and Vibration Characteristics of Rotor 227
 Vivek V. Shet, A. S. Sekhar, and B. V. S. S. S. Prasad

Study of Static Performance Characteristics of Offset-Pressure Dam Bearing Considering Turbulent and Adiabatic Thermal Effects 237
 Sivakumar Dakshinamurthi and Suresh Nagesh

Computational Fluid Dynamics Study of Oil Lubrication in Ball and Roller Bearings 253
 Vijay Tijare, Shanmukha Nagaraj, Mehul Pandya, and Jun Wang

Feasibility Studies on Newly Conceptualized Inter-shaft Squeeze Film Damper (ISSFD) Rings for Vibration Attenuation 267
 H. M. Shivaprasad, G. Giridhara, Ajit Kumar, Praveenkumar Kamanat, and V. Arun Kumar

Characterization of a Squeeze Film Damper for Aircraft Engine Applications 279
 Praveen Thirumalasetty, Kishore Vetcha, Mahesh Sivakumar, Tod R. Steen, and Anthony M. Metz

Stability of Parametrically Excited Active Magnetic Bearing Rotor System Due to Moving Base 293
 Tukesh Soni, J. K. Dutt, and A. S. Das

Experimental Investigation on the Effect of Housing Profile and Its Relative Position on the Performance of Semi-Active Journal Bearing 307
 Raghu Yogaraju, L. Ravikumar, G. Saravanakumar, and V. Arun Kumar

Some Fundamental Issues in Foil Bearings 317
 P. Samanta, N. C. Murmu, and M. M. Khonsari

Condition Monitoring, Diagnostics and Prognostics of Rotors

Study of Turbocharger Fully Floating Hydrodynamic Bearing Oil Whirl Behavior—Test and Prediction 329
 Lokesh Chandrasekaran, Praveen Kumar Selvaraj, Prasanth R. Vengala, and Subramani D. Arthanarisamy

Rolling Element Bearing Fault Diagnosis by Different Data Fusion Techniques 341
 Sandaram Buchaiah and Piyush Shakya

Diagnosability Index and Its Application to Bearing Fault Diagnosis . . . 351
 Ankush C. Jahagirdar and K. K. Gupta

Gearbox Health Condition Monitoring Using DWT Features 361
 Setti Suresh and V. P. S. Naidu

Gas Turbine Engine Fan Blade Flutter Detection Using Casing Vibration Signals by Application of Recurrence Plots and Recurrence Quantification Analysis	375
A. N. Viswanatha Rao, V. P. S. Naidu, and Soumendu Jana	
Condition Monitoring of Rolling Contact Bearing by Vibration Signature Analysis	391
Kashinath Munde and Ganesh Kondhalkar	
Misalignment, Rotor-Bow, Crack, Rub-Imapct	
Dynamic Response Analysis of an Unbalanced and Misaligned Rotor Supported on Active Magnetic Bearings and Touchdown Bearings	407
Prabhat Kumar and Rajiv Tiwari	
Finite Element Modeling and Analysis of Coupled Rotor System Integrated with AMB in the Presence of Parallel and Angular Misalignments	419
R. Siva Srinivas, Rajiv Tiwari, and Ch. Kanna Babu	
Detection of Fatigue Crack in the Shaft Using Time-Frequency Analysis	433
Sagi Rathna Prasad and A. S. Sekhar	
Coupling Misalignment Detection and Condition Monitoring of a Rotor Assembly Using FEA-Based Reduced-Order Modeling Methods	445
Anil Kumar, Dinesh Kumar, and Ravindra Masal	
Vibration Control Using Active and Semi Active Methods	
Vibration Reduction in Indigenous Wankel Rotary Combustion Engine with Structured Layer Damping	461
Sadanand Kulkarni, S. Satish Kumar, S. Santhosh Kumar, Umesh Kumar Sinha, Brijeshkumar Shah, K. Satish Kumar, A. J. Steve Mithran, and K. Monickavasagom Pillai	
Characteristic Parameters Estimation of Active Magnetic Bearings for Varying Controlling Parameters	469
Sampath Kumar Kuppa and Mohit Lal	
Characterization of Digital Power Amplifier-Based Active Magnetic Bearings	481
Pravina R. Mali, Balaji Sankar, Gurunayk Nayak, Soumendu Jana, and A. S. Sekhar	

Nonlinear, Parametric Effects on Rotor

Effect of Sinusoidal and Non-sinusoidal Periodic Forces on the Stability of Gas Foil Bearing 495

Kamal Kumar Basumatary, Sashindra K. Kakoty, and Manash Pratim Ghosh

Modal Response of a 4-DOF Cantilever Rotor System with 2 Bearing Support Under Rotor Rub Impact with Unbalance 509

Aman K Srivastava, Mayank Tiwari, and Akhilendra Singh

Dynamic Response Analysis of Rotating Shaft-Bearing System with an Open Crack 519

S. Bala Murugan, R. K. Behera, and P. K. Parida

Rotordynamic Design Studies of Medium Thrust Class Twin Spool Engine 531

R. Siva Srinivas, S. E. Muthu, and Girish K. Degaonkar

Rotor Structural Dynamics

Improving Structural Integrity of a Centrifugal Compressor Impeller by Blading Optimization 545

E. K. Vivek, Lakshya Kumar, R. Senthil Kumaran, and C. Veera Sesha Kumar

3D Finite Element Vibrational Analysis of T385 Turbine Rotor BLISK Using SAFE Diagram 555

Revanna Jai Maruthi, Rajeevalochanam Prathapanayaka, and Nanjundaiah Vinod Kumar

Dynamic Analysis of Thermo-Mechanically Loaded Functionally Graded Disks by an Iterative Variational Method 569

Priyambada Nayak and Kashinath Saha

Stationary and Rotating Frame Instrumentation for Large Scale Rotating Rig 579

N. Poornima, R. Senthil Kumaran, and Kishor Kumar

Performance of Bolted Joint Modelling Using Master Element 595

G. Vamsi Krishna, C. Viswanath, and Ashok Kumar Pandey

About the Editors

J. S. Rao is an AICTE-INAE Distinguished Visiting Professor associated to BMS College of Engineering, Bangalore, and Reva University, Bangalore, President of The Vibration Institute of India (TVII) and the Chief Editor of Journal of Vibration Engineering and Technology. He was the Ex-Chief Science Officer with Altair Engineering (India), Bangalore, and was a Professor at IIT Delhi and Kharagpur as well as at several universities in England, France, Canada, USA, Germany, Taiwan and Australia. He is a founding father of IFToMM, a member of its executive council and Chairman of its Rotor Dynamics Committee and Permanent Commission on Conferences and has received numerous honors and awards. He authored over 400 research publications and 12 textbooks.

V. Arun Kumar is a Professor in the Department of Mechanical Engineering, Dr. Ambedkar Institute of Technology, Bangalore, and a technical consultant for a number of private companies. He pursued M.Sc. in Engineering from Madras University and Ph.D. from IIT Madras. Prior to joining Dr. Ambedkar Institute of Technology, he was the Head of the Propulsion division in CSIR-National Aerospace Laboratory. He has authored over a hundred research publications and holds 15 patents.

Soumendu Jana is a Scientist in CSIR-National Aerospace Laboratories, Bangalore, where his work focuses on rotor dynamics, vibrations, passive and active magnetic bearings, vibration control, external dampers and aero-engine health management. He has done his Ph.D. from IIT Kharagpur and postdoctoral work in the University of Wales, UK. He has authored numerous research papers and technical reports and holds 2 patents.

Analytical, Computational and Experimental Methods

Stability Improvement for Upgraded Four-Stage Centrifugal Compressor Rotor-Bearing System



Vignesh Selvam, Roman Kochurov, Evgen Kashtanov, Leonid Moroz, and Abdul Nassar

Abstract As the plant capacity is increased, the equipment in the plant also needs to be upgraded. Replacing with a new machine is not always the right economical decision when alternative options for upgrading and retrofitting the existing machine exist. Upgrading the machine not only increases the performance thus reducing the power consumption, but it also increases the system reliability, reducing the downtime and thus helping the plant operate more efficiently. The compressor used for this work was in operation, and due to prolonged operation, the impellers had degraded primarily due to fouling caused by process contaminants. This multi-stage centrifugal compressor was subsequently upgraded to increase the inlet volume flow rate by 20% with the objective of retaining the same casing and rotor shaft. The redesigned compressor stages has better performance with reduced power consumption. The redesigned four-stage centrifugal compressor operating at design speed of ~8856 rpm may be prone to instabilities caused by aerodynamic cross-coupling and hydrodynamic bearing modification. The authors in the present study are exploring any instabilities in the rotor-bearing system that may be caused due to the upgrade of the compressor for higher volume flow rate. To meet the new operational requirements, the bearings were redesigned. The stability analysis was performed considering the destabilizing effects of the aerodynamic excitations, based on which modifications

R. Kochurov · L. Moroz

SoftInWay Inc, 1500 District Ave, Burlington, MA 01803, USA
e-mail: r.kochurov@softinway.com

L. Moroz

e-mail: l.moroz@softinway.com

V. Selvam (✉) · A. Nassar

SoftInWay Turbomachinery Solutions Private Limited, Cunningham Road, Bangalore, KA 560052, India
e-mail: vickyflyer@gmail.com

A. Nassar

e-mail: abdul.nassar@softinway-india.com

E. Kashtanov

SoftInWay Switzerland GmbH, Baarerstrasse 2, Zug 6300, Switzerland
e-mail: evgen.kashtanov@softinwayswitzerland.ch

© Springer Nature Singapore Pte Ltd. 2021

J. S. Rao et al. (eds.), *Proceedings of the 6th National Symposium on Rotor Dynamics*, Lecture Notes in Mechanical Engineering,
https://doi.org/10.1007/978-981-15-5701-9_1

were performed on the design to stabilize the multi-stage centrifugal compressor and to conform to satisfy the API Level I stability criteria. The modifications performed on the rotor/bearing system resulted in reduced vibration amplitudes for the required level of rotor unbalance conditions. These modifications also significantly eliminated the instability that was initially observed, and the redesigned compressor not only met the requirements for the change in operating conditions but also fully complied with API 617 standards.

Keywords Destabilizing forces · Rotor-bearing stability · Bearing sensitivity study · API · Retrofit

List of the Most Important Symbols

API	American Petroleum Institute
ISO	International Organization of Standardization
FEM	Finite element method
FDM	Finite difference method
CS	Critical speed
FB	Front bearing
RB	Rear bearing
AF	Amplification factor
MOFT	Minimum oil film thickness
L	Axial length
D	Journal diameter
L/D	Length-to-diametric ratio
n_o	Operating speed
x amp	x -direction amplitude
y amp	y -direction amplitude
m	Preload ($1 - C_b/C_p$)
γ	Offset
α_{LE}	Orientation angle
$d\phi_1$	Axial groove
P	Load
H_{min}	Minimum oil film thickness
N_{fr}	Power loss
Fr	Friction factor
ΔT	Temperature rise
C_b	Bearing clearance
C_p	Pad clearance

1 Introduction

With increase in plant capacity, there is a need to upgrade different equipment's used in the process. Centrifugal compressors are one of such components which can be upgraded by redesigning the flow path while retaining most of the major parts like casing and rotor therefore keeping costs relatively low. When the compressor system is retrofit/upgraded for increasing the volume flow rate or pressure, there arises additional challenges in terms of meeting the reliability of the system as per the API standards. In the present work, a four-stage centrifugal compressor was retrofitted by redesigning the impellers for an increased volume flow rate [1]. The aerodynamic efficiency of the compressor has been improved and is reported in [1]. In addition to improving the specific power consumption of the compressor, the mechanical losses also need to be reduced. As the compressor was redesigned to meet the requirement of increased inlet volume flow rate, the power consumption also increased, thus necessitating to perform studies on the rotor-bearing system. The rotordynamics studies were performed using AxSTREAM RotorDynamics™ at first for the existing bearing. As the rotor was found to be unstable with the existing bearings, it was decided that the bearings had to be redesigned. A sensitivity study is required not only to reduce the mechanical losses in the bearings, but also to make ensure that the designed system meets the API standards. To obtain an optimized bearing, some of the parameters that are considered are power loss due to bearing, bearing stability, and unbalance responses [2–6]. Recent studies with bearing optimization are performed using sensitivity analysis based on DOE method [2, 3]. Since the retrofitted multi-stage centrifugal compressor rotor is to be used, there is little scope for modifications in the rotor and all studies are focused mainly on the bearing design [1]. To reduce frictional losses and power losses, the minimum film thickness needs to be increased [6] without increasing the oil film temperature and the separation margin of the critical speed should also be satisfied per the API standards. The present study first focuses on the existing elliptical bearing that was optimized to avoid high temperatures at the bearings and instability in the rotor-bearing system. Since the requirements were not satisfied even with the optimized elliptical bearings, tilting pad bearings were considered as the next alternative and optimized. To study the influence of different parameters on bearing stability, a sensitivity study was performed based on a set of variables. The sensitivity analysis was performed manually without considering an optimization algorithm.

2 Rotordynamics Analysis of Baseline Rotor-Bearing System

The rotor geometry in Fig. 1 was modeled (in AxSTREAM RotorDynamics™) as beam elements with 47 nodes and impellers as lumped mass-inertia elements (four degrees of freedom; two displacements and rotations in the lateral plane). The existing

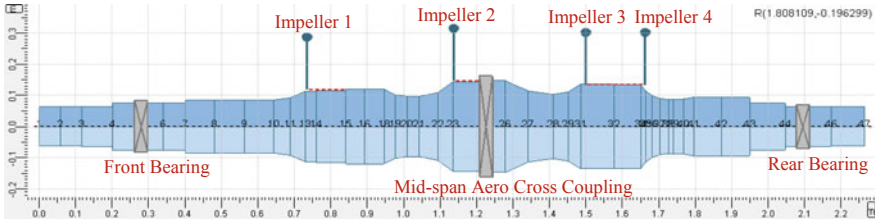


Fig. 1 Rotordynamics FE model

elliptical bearing was independently analyzed using AxSTREAM Bearing™ which is based on FDM and uses Elrod and Adams model [2, 3] with a successive over-relaxation (SOR) algorithm. The front and rear bearing journals have diameters of 149 mm and 126 mm, respectively, with preload of 0.34, length of 80 mm and 68 mm, respectively, and vertical clearance of 0.11175 mm and 0.0945 mm, respectively. The bearing gravitation loads are 4107 N and 4067 N for the front and rear bearings, respectively. The lubricant used is ISO 32 with temperature-dependent properties. These bearings were designed to operate up to 15 °C temperature rise. The inlet oil temperature is 50 °C, and the design bulk oil discharge temperature is 65 °C. Since the strength of the Babbitt material reduces at elevated temperatures, the maximum temperature should not exceed 85 °C. The results of the hydrodynamic and mechanical characteristics for the rated speed and other rotational speeds as applicable were also calculated and are presented in Table 3.

2.1 Synchronous Unbalance Response Analysis of Baseline Design

From the rotordynamics analysis, it was observed that the first three undamped critical speeds of the machine supported by flexible bearings are within the operating speed range. The accurate prediction of unbalance response for the rotor-bearing system is difficult as the unbalance mass (distribution) along the rotor is usually unknown [7]. In order to excite a mode shape, a certain set of unbalance masses was attached to the rotor and the unbalance response was calculated in the operating regime. In this study, at 0.5586 kg mm of unbalance, the first bending mode on bearing stiffness x -axis direction was excited as calculated according to API 617/684 requirements [8] and applied at station 13 (see Fig. 2: Case 1). The second bending mode on bearing stiffness x -axis direction was excited and applied at station 24 as shown in (see Fig. 2: Case 2). Similarly, the first conical mode on bearing stiffness x -axis direction was excited by two equal unbalance masses that were applied at stations 1 and 47 as shifted 180° out of phase (see Fig. 2: Case 3). The conical mode is caused in the system due to lower bearing stiffness present in the y -axis direction.

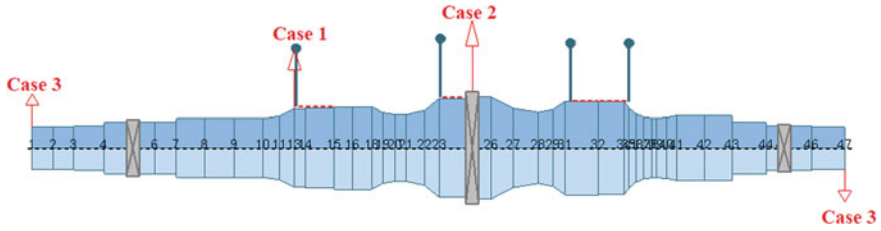


Fig. 2 Unbalances to excite mode shape cases

The damped unbalance responses were evaluated for speeds starting from 0 to 13,367 rpm in steps of 300 rpm using corresponding speed-dependent bearing coefficients. The rated speed was 8856 rpm. For the maximum amplitudes of the major elliptical whirling orbits, upper limit constraints were mentioned and the unbalance was calculated for the first case at the front and rear bearing locations ($1.26 \mu\text{m}$ and $1.39 \mu\text{m}$, respectively) and shaft mid-span location ($1.14 \mu\text{m}$). For the second unbalance case, the response amplitude at the front and rear bearing locations (1.72 and $2.06 \mu\text{m}$) and shaft mid-span location ($2.52 \mu\text{m}$) was calculated. Similarly, the third unbalance case response amplitude at the front and rear bearing locations ($4.66 \mu\text{m}$ and $4.25 \mu\text{m}$, respectively) and shaft mid-span locations ($0.48 \mu\text{m}$) was calculated. Baseline unbalance results are presented in Fig. 3b, and their corresponding undamped critical speed mode shapes (eigenvectors) are shown in Fig. 3a.

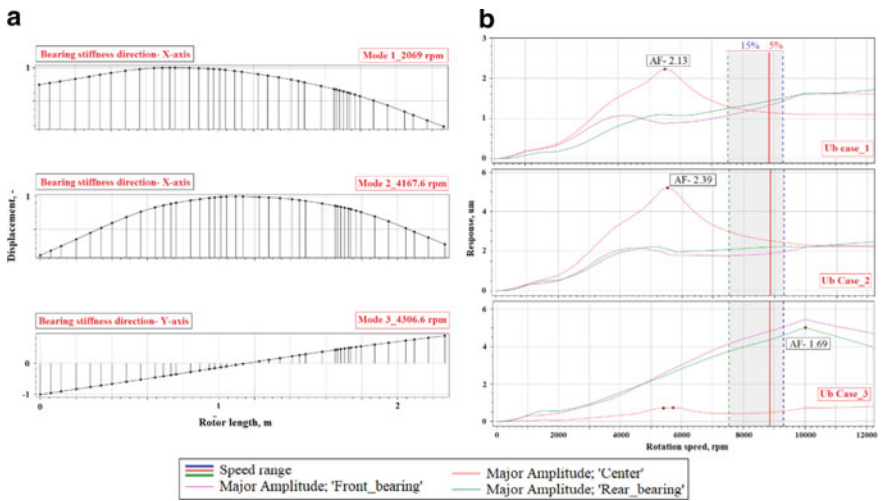


Fig. 3 a Undamped critical speed mode shapes and b frequency response amplitude (peak-to-peak, μm) for initial existing rotor-bearing system

2.2 Stability Analysis of Baseline Design

A necessary condition for the rotor-bearing system is to be stable within the operational speed range which is mentioned in the last paragraph. Indeed, an unstable system would generate high level of vibrations which may severely damage the equipment. If sufficient damping is available to counter the destabilizing forces generated by seals and aerodynamic cross-coupling, the rotor may become stable even though there exist some instabilities in the rotor-bearing system. The cumulative summation of cross-couplings values on each stage is calculated and added at the rotor mid-span for between bearing rotors like the current one [8]. However, if damping is insufficient, the instability in a rotor will cause the rotor-bearing system to be unstable [9]. The stability of the rotor-bearing system is checked by using the “logarithmic decrement” (defined as the natural log of the ratio of two successive vibration amplitudes) stability criterion of API 684 [8]. As a design criterion, it is desirable to have a log decrement greater than or equal to $+0.1$ [8] for a stable behavior to exist. The stability results are listed in Table 4 for the first four forward and backward whirl modes. The results show that the second mode is at 61.34 Hz with a log decrement of -0.43 resulting in an unstable rotor. This requires some modification in the existing design which is described in the following section. The first, third and fourth modes are very stable thus satisfying the API requirements.

The mode shapes (eigenvectors) for the second mode are illustrated in Fig. 4.

3 Bearing Sensitivity Study

To overcome the vibration and reliability challenges, the rotor-bearing system needs to be modified such that the system becomes stable. Additionally, it is also desired to reduce the power losses so that the overall system efficiency can be improved. It was decided to perform a sensitivity study by varying selected geometrical parameters of the bearing without any changes to the rotor [2, 3]. The main design variables used for the sensitivity analysis are L/D ratio (bearing axial length to journal diameter), pad offset factor, pad preload factor, orientation angle, angular groove extent and bearing radial clearance. The pad axial length to journal diameter ratio has an effect

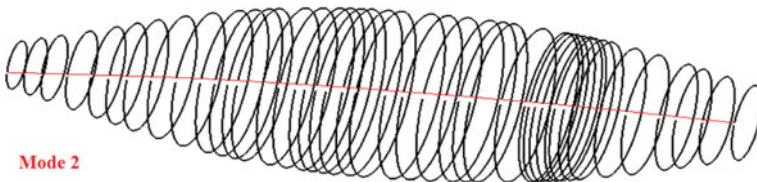


Fig. 4 3D mode shapes for initial existing rotor-bearing system design, second damped natural frequencies at 8856 rpm

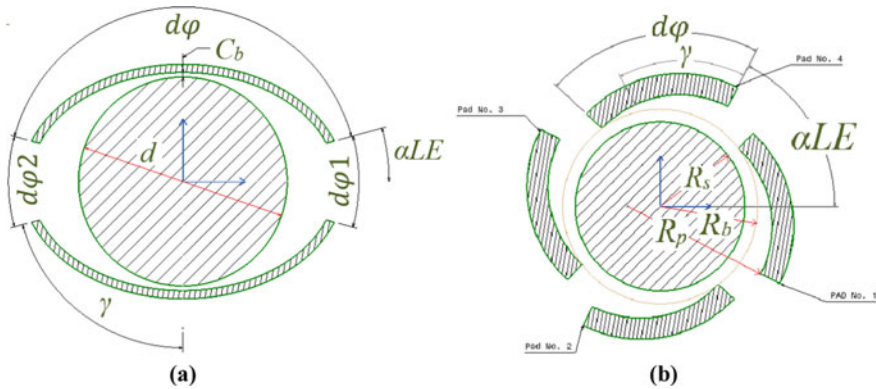


Fig. 5 Bearing schemes: **a** elliptical and **b** tilting pad bearings

on fluid-induced instability as well as on load capacity. When the ratio is increased, the load carrying capacity increases [10, 11]. With increasing bearing pad offset factor, the pad pivot position moves from the center of the pad toward the trailing edge. It is a common practice in the industry to provide journal pads with preload. The relationship between the two clearances C_b and C_p , namely bearing radial clearance and bearing pad clearance, is defined as preload. C_p is the difference of the radius of curvature of the pad, r_p , and journal radius, r_s . The preload factor can be expressed as [12].

$$m = ((1 - C_b)/C_p)$$

where C_p and C_b can be computed as:

$$C_p = r_p - r_s; \quad C_b = r_b - r_s$$

The sensitivity analysis was performed using the following objective functions—minimum film thickness, maximum oil film temperature rise, power loss, friction factor, etc. Two different bearings were used in the present study: one elliptical bearing and the other a tilting pad bearing as shown in Fig. 5. The variables for sensitivity analysis are listed in Tables 1 and 2.

3.1 Results of Bearing Design Sensitivity Study

The sensitivity analysis ranges for the selected design variables and the corresponding operating characteristics are shown in Tables 1 and 2 for each bearing type. The value of m is taken as ranging from 0.25 to 0.6 [5]. The load and bearing temperature increases as the ellipticity ratio increases. However, it is observed here that the

Table 1 Ranges for the design variables of the elliptical bearings

Parameters		Lower limit	Upper limit	Lower limit	Upper limit
Bearing length, mm	L	74.5	96.85	63	81.9
Length to diameter ratio	L/D	0.5	0.65	0.5	0.65
Bearing clearance, mm	C_b	0.11175	0.2682	0.0945	0.2268
Preload	m	0.34	0.56	0.34	0.56
Offset	γ	0.5	0.5	0.5	0.5
Orientation, °	αLE	9	25	9	25
Axial groove, °	$d\phi 1$	45	50	45	50

Table 2 Ranges for the design variables of the tilting pad bearings

Parameters		Front bearing		Rear bearing	
		Lower limit	Upper limit	Lower limit	Upper limit
Bearing length, mm	L	80	149	68	126
Length to diameter ratio	L/D	0.54	1	0.54	1
Bearing clearance, mm	C_b	0.0745	0.149	0.063	0.126
Preload	m	0.2857	0.375	0.2857	0.375
Offset	γ	0.55	0.65	0.55	0.65

maximum averaged oil film temperature is 58.54 °C which is lower than the acceptable limit of 650 °C. The effects of the two clearances in the elliptical bearing on its steady-state characteristics are shown in Fig. 6a–c. Figure 6 shows the results for a 149 mm diameter front bearing. The main controlling influence on the power loss is the bearing. When the clearance increases, it leads to a reduction in the power loss as shown in Fig. 6a. An increase in bearing clearance also tends to decrease maximum temperature, Fig. 6c. Minimum film thickness increases with increasing clearance (see Fig. 6b), the effect being a function of the actual values of journal load and

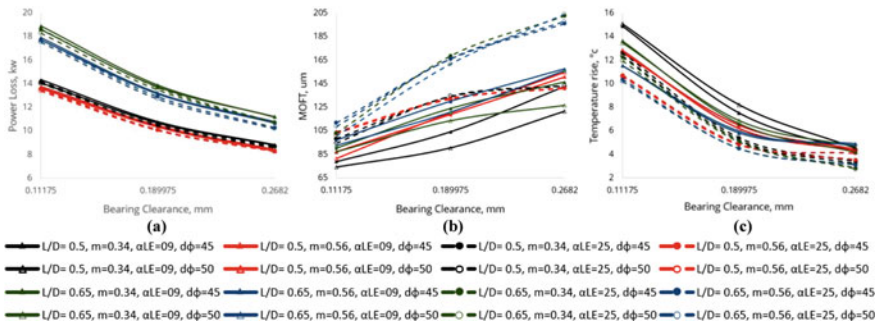


Fig. 6 Results of **a** power loss [kW], **b** minimum oil film thickness [μm], **c** temperature rise [$^{\circ}\text{C}$] versus bearing clearances for redesigned elliptical front bearing

operating speed. Therefore, an increase in the bearing clearance will also produce an increase in the maximum MOFT. This is due to the formation of a large supporting oil wedge which is mandatory for stable hydrodynamic lubrication [4]. Similarly, with minimum clearance, there is more friction which results in more power loss. Whereas the maximum clearance has better results of reduction in power loss, but it can cause instability if the clearances are too large.

The effects of the tilting pad bearing on its steady-state characteristics are shown in Fig. 7a–c. Results show when the clearance increases, it leads to a reduction in the power loss. Decreasing the L/D ratios also leads to a reduction in the power loss (Fig. 7a). An increase in bearing clearance tends to decrease the maximum temperature, and there is a minimum influence for different L/D ratios as shown in Fig. 7c. Minimum film thickness increases with increasing clearance (see Fig. 7b), the effects being a function of the actual values of journal load and operating speed. The redesigned elliptical front and rear bearings have diameters of 149 mm and 126 mm, with a preload of 0.56 and 0.34, length of 74.5 mm and 63 mm, respectively, and clearance of 0.19 mm and 0.2268 mm, respectively. The newly designed tilting pad front and rear bearings have diameters of 149 mm and 126 mm, with a preload of 0.375, length of 111.75 mm and 95 mm, respectively, and clearance of 0.149 mm and 0.126 mm, respectively.

The redesign of elliptical bearing increases the front and rear bearing minimum oil film thickness (MOFT) by 45% and 34%, respectively. Power losses are reduced by 70% for both bearings. In addition, temperature rises are also reduced by 84% compared to the original elliptical bearings which is quite significant. The newly designed tilting pad bearing decreases the front bearing MOFT by 18% and increases the rear bearing MOFT by 5%. Despite decreasing the corresponding minimum oil film thickness value also, there are enough load carrying capacity present in the present retrofitted system. Power losses are reduced by 24 and 28% at the front and rear bearings, respectively. In addition, temperature rises are significantly reduced: about 85% compared to the original elliptical bearings. The undamped critical speeds

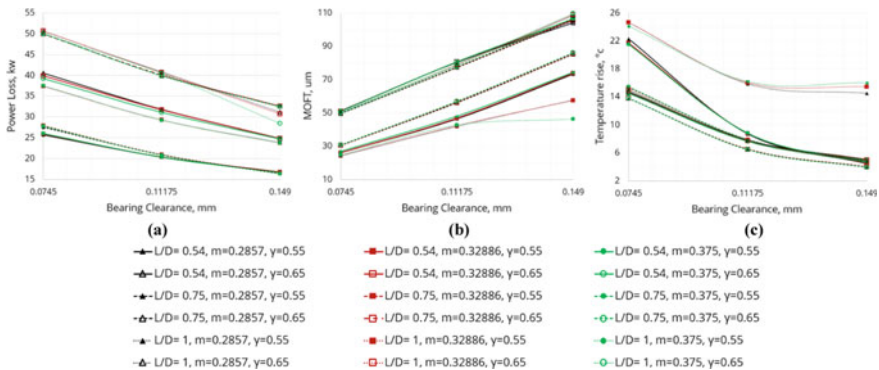


Fig. 7 Results of **a** power loss [kW], **b** minimum oil film thickness [μm], **c** temperature rise [$^{\circ}\text{C}$] versus bearing clearances for tilting pad front bearing

Table 3 Bearing sensitivity analysis results

Parameters		Initial existing design		Redesigned elliptical design		Tilting pad bearing	
		Lower limit	Upper limit	Lower limit	Upper limit	Lower limit	Upper limit
MOFT	H_{min} (μm)	90.76	72.24	131.79	96.92	74.30	75.72
Power loss	Nfr (kW)	32.26	19.37	10.08	5.45	24.68	13.92
Friction loss	Fr, –	0.113	0.081	0.035	0.023	0.086	0.058
Temp rise	ΔT , $^{\circ}\text{C}$	27.93	28.82	4.84	4.16	4.56	4.01
1st UCS, X-axis	rpm	2069		1769		4154	
2nd UCS, X-axis	rpm	4167		3580		10,468	
3rd UCS, Y-axis	rpm	4306		3651		–	

in the operating range are improved with these bearings. Some of the undamped critical speeds exist in the original and redesigned bearings, due to their axisymmetric stiffness and damping characteristics. For the redesigned elliptical bearing case, the first undamped critical speed decreases from 2069 to 1769 rpm, and the second undamped critical speed decreases from 4167.6 to 3580.4 rpm. These are suppressed by the new tilting pad design where the first mode frequency changes from 1769 to 4154.6 rpm. The second and third mode frequencies move away from the 8856 rpm operating speed range (-15 to $+5\%$ of rated speed). Bearing performance characteristics such as the maximum averaged oil film temperature across the film thickness T_{max} , minimum oil film thickness H_{min} , power loss Nfr, friction coefficient Fr and undamped critical speeds for the selected bearing model can be seen in Table 3.

The impact of the bearings on the vibrational behavior of the rotor system also becomes more important. For rotors operating below the first critical speed, the bearing stiffness can play a large part in determining the vibration levels resulting from critical speed, balance, or aerodynamic cross-coupled forces.

Bearing stability analysis results are presented in Fig. 8a. It shows the results of shaft center motion trajectories as a result of perturbation in dimensionless coordinates for the initial bearing for an unbalanced rotor mass. At the rotating speed of $N_{op} = 8856$ rpm, the shaft follows an elliptical trajectory within the limit cycle with a violent whirling motion making contact with the bearing surface, which may result in a failure of the rotor-bearing system. Based on the initial existing bearing instability and thermal conditions, the redesign of bearing was carried out to get better performance and improve the bearing stability.

Figure 8b shows the results of the redesigned elliptical bearing for an unbalanced rotor mass. At $N_{op} = 8856$ rpm, the shaft follows an elliptical orbital path with a decreasing radius. The results show that the shaft features are acceptable and within

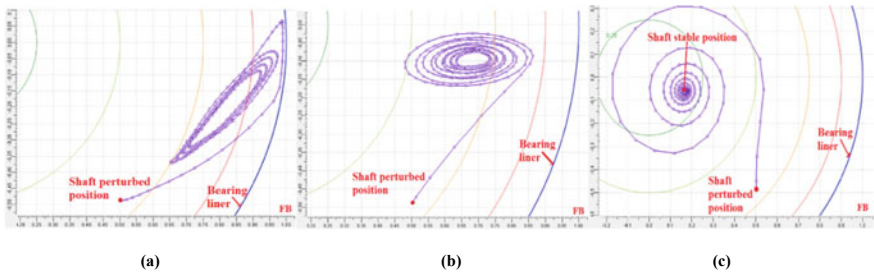


Fig. 8 Bearing stability for front bearings **a** initial existing elliptical, **b** redesigned elliptical and **c** tilting pad bearing

stable limits. However, these conditions do not satisfy the API recommendations as discussed in the following section. This is why the new tilting pad design was carried out to meet these requirements. Finally, Fig. 8c shows the results of the new tilting pad bearing for an unbalanced rotor mass. At $Nop = 8856$ rpm, the shaft follows a circular orbital path with a decreasing radius. The results show that the shaft is more stable than the previous bearing design. This condition satisfies the API requirements for the rotor-bearing system.

3.2 Synchronous Unbalance Response Analysis

The same unbalance criteria which were previously described in the original design configurations were used. The redesigned elliptical bearings improve the unbalance response amplitudes at both bearings and reduce the amplitudes at the shaft center. This amplitude reduction can reduce the chances of developing a hard rub which could set off the sensitive second mode as previously described in the stability analysis of the original rotor-bearing system. In the redesigned elliptical bearings, increased amount of unbalance response (vibrations) did not cause any of the two bearings peak-to-peak (p-p) amplitudes to exceed 75% of the minimum design diametral running clearances throughout the machine. Unbalance results for the redesigned model are presented in Fig. 9a.

The new tilting pad rotor-bearing system follows the same unbalance criteria used previously. Figure 2 describes the unbalance cases and their locations. The “worst case” unbalance condition consists of a $63 \mu\text{m}$ diametral running clearance. The new bearings improve the unbalance response amplitudes at both bearings and reduce them at the shaft center, as shown in Fig. 9. With the new tilting pad bearings, the increased amount of unbalance response did not cause either bearings peak-to-peak (p-p) amplitude to exceed 75% of the minimum design diametral running clearances throughout the machine.

The unbalance response amplitude results of the tilting pad rotor-bearing system are compared with the redesigned elliptical rotor-bearing system. The front bearing

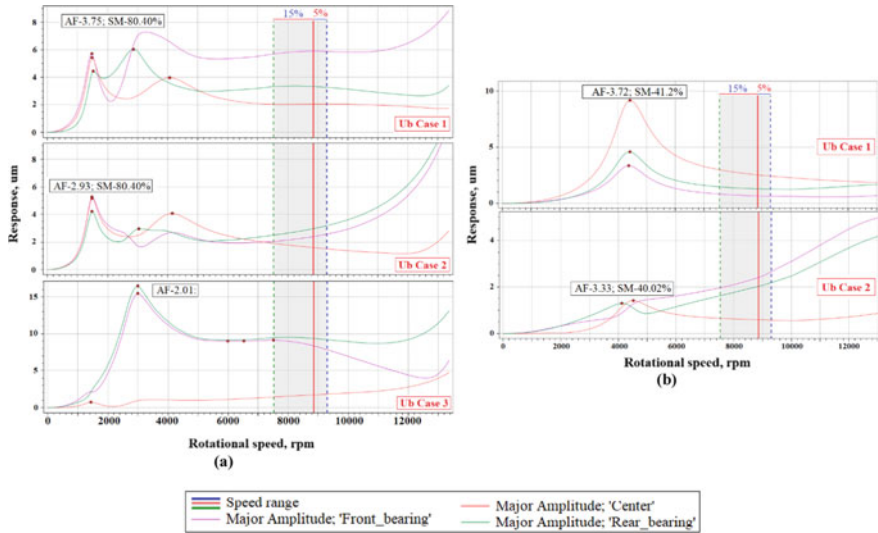


Fig. 9 Frequency response amplitude (peak-to-peak, μm) for **a** redesigned elliptical rotor/bearing system, **b** tilting pad rotor/bearing system

response amplitude is decreased by 2.6%. In addition, the amplitude response increases by 1.5% at the shaft center and reduces by 3.1% at the rear bearing location. This increase at the shaft center location represents a change from 0 to 10 μm p-p. This is acceptable considering that the new tilting pad bearing has a diametric clearance of 63 μm . The new tilting pad model unbalance results are presented in Fig. 9b.

3.3 Stability Analysis

The stability analysis was performed considering the destabilizing effects of the aerodynamic excitations, based on which modifications were applied to the design in order to stabilize the multi-stage centrifugal compressor and to conform to the API Level I stability criteria. The stability results are listed in Table 4 for the first four whirl modes. Particularly noted are the low values of the “log decrements” for the modes with frequencies near the targeted operating speed of 8856 rpm. Results reveal that the redesigned elliptical bearings of the second, third and fourth modes are very stable. The first mode is at 29.66 Hz with a log decrement of +0.02 is only marginally stable. The second mode is at 102.27 Hz with a log decrement of +0.97. In addition, the third mode is at 52.32 Hz with a log decrement of +1.99. Finally, the fourth mode is at 255.75 Hz with a log decrement of +3.43. In the redesigned elliptical bearings, the rotor stability condition is slightly improved compared to the original elliptical bearings. The second mode log decrement increases from -0.43

Table 4 Logarithmic decrement comparison results

Stability				
Parameters	Mode number	Damped natural frequency, Hz	Log. dec., -	Stability condition
Initial existing bearing	1	87.22	1.88	Very stable
	2	61.34	-0.43	Unstable
	3	90.83	0.68	Stable
	4	143.81	4.94	Very stable
Redesigned elliptical bearing	1	29.66	0.02	Marginally stable
	2	102.27	0.97	Stable
	3	52.32	1.99	Very stable
	4	255.75	3.43	Very stable
Tilting pad bearing	1	238.22	1.58	Very stable
	2	438.96	3.11	Very stable
	3	80.95	0.15	Stable
	4	81.72	0.45	Stable

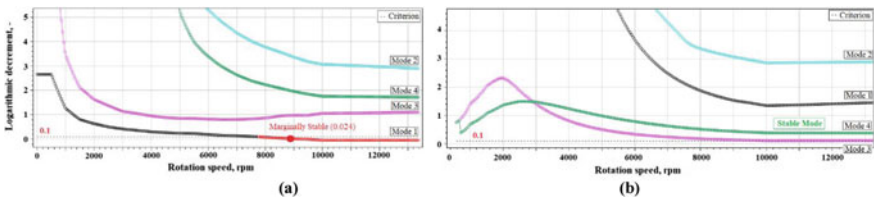


Fig. 10 Logarithmic decrement for **a** redesigned elliptical and **b** tilting pad rotor-bearing system

to +0.97. However, these redesigned log decrements are still lower than the desired 0.1 threshold.

In the new “tilting pad” bearings, the rotor stability condition is very much improved compared to the redesigned elliptical bearing configurations. The first mode log decrement increases from +0.02 to +1.58. Finally, these new tilting pad bearings log decrements satisfy the API recommendations. Comparison of log decrements for the redesigned elliptical bearing and new tilting pad bearing is shown in Fig. 10.

4 Conclusions

The analysis results have indicated that the redesigned elliptical bearing improves the rotor stability condition, compared to that with the original elliptical bearings. However, the redesigned log decrements are still lower than desired as per the API

recommendations. To increase the value of log decrements and improve stability, the whirl frequency needs to be shifted further away from the operating speed. For this, the tilting pad bearing were designed considering the results of the redesigned elliptical bearings. From the systematic studies done by this approach, we have obtained an improved bearing that could reduce the possibility of rotor rubbing with the bearing when there are excessive vibration amplitudes. The tilting pad bearings designed here significantly improved the rotor-bearing system unbalance response amplitudes, compared to the response with the original bearings and the redesigned elliptical bearings. The worst case unbalance condition considers a 63 μm diametrical clearance. With the redesigned bearings, this amount of unbalance did not cause the front bearing peak-to-peak (p-p) amplitude to exceed its 75% diametric clearance safety limit. These modifications also significantly eliminated the instability that was initially observed, and the redesigned compressor met not only the changed operating requirements but also satisfied API 617/684 standards.

References

1. Chen C, Moroz L, Sherbina A, Ketelaar D (2015) Retrofit and re-design of a four-stage centrifugal compressor. Internal report. SoftInWay Consulting Project with Sulzer Turbo Services, Rotterdam B.V
2. Moroz L, Romanenko L, Kochurov R, Kashtanov E (2018) Hydrodynamic journal bearings optimization considering rotor dynamics restrictions. In: Proceedings of ASME turbo expo 2018, Oslo
3. Moroz L, Romanenko L, Kochurov R, Kashtanov E, Nassar A (2017) Hydrodynamic journal bearing optimization based on multidisciplinary analysis of the rotor-bearing system for the induction motor. In: 9th international conference on electrical rotating machines and drives, ELROMA 2017
4. http://www.substech.com/dokuwiki/doku.php?id=oil_clearance_and_engine_bearings. Last accessed on 30 July 2019
5. Davidson TR, Salamone DJ, Gunter EJ (1992) Rotor bearing and shaft dynamics redesign of a double-overhung turboexpander for reliability improvement. In: Turbomachinery and pump symposia, pp 35–56
6. API, 684 (2005) API recommended practice. American Petroleum Institute, Washington
7. Hashimoto H, Matsumoto K (2001) Improvement of operating characteristics of high-speed hydrodynamic journal bearings by optimum design: part I—formulation of methodology and its application to elliptical bearing design. *J Tribol* 123
8. Ma MT, Taylor CM (1996) An experimental investigation of thermal effects in circular and elliptical plain journal bearings. *Tribol Int* 2
9. Jones GJ, Martin FA (1979) Geometry effects in tilting-pad journal bearings. *ASLE Trans* 22
10. Barrett LE, Gunier EJ, Allaire PE (1978) Optimum bearing and support damping for unbalance response and stability of rotating machinery. *J Eng Power* 100
11. Saruhan H (2006) Optimum design of rotor-bearing system stability performance comparing an evolutionary algorithm versus a conventional method. *Int J Mech Sci* 48
12. Saruhan H, Rouch KE, Roso CA (2004) Design optimization of tilting-pad journal bearing using a genetic algorithm. *Int J Rotating Mach* 10(4):301–307

3D Finite Element Rotor Dynamic Analysis of Turbine Test Rig Rotor-Shaft Systems



Nanjundaiah Vinod Kumar , Rajeevalochanam Prathapanayaka ,
Revanna Jai Maruthi , and Shashidhar Swaroop 

Abstract Design of a 385 kW turbine (T385 turbine) to drive the compressor of 1 kN small gas turbine engine is carried out in Propulsion Division, CSIR-NAL. Aero-thermodynamic performance evaluation of designed turbine stage was planned through experimental testing in VTTR, Propulsion Division, CSIR-NAL. The turbine speed is 50,500 rpm at the engine design point, and the equivalent design speed in test rig conditions is 30,000 rpm. Since performance evaluation at higher speeds consists of high-speed rotating components constituting a complex dynamic system, it is of prime importance to consider rotor dynamic characteristics to operate the turbine safely. Test section is designed for the T385 turbine rotor BLISK considering rotor-shaft system with bearings. The dynamic behavior of test rig rotor systems was evaluated for vibration reliability. This paper presents the 3D FE rotor dynamic analysis of T385 turbine rotor-shaft system. The stiffness of bearing supporting structure is evaluated along the direction of stress field using FEA. T385 turbine rig rotor system is modeled in FEA using lumped mass method. All the masses of rotor shaft system with inertias are considered in the analysis. The Campbell and response plots are plotted using frequencies and mode shapes to predict the critical speeds and unbalance response, respectively. The critical speeds from Campbell diagram indicates that rotor system is safe to operate in the test rig. The maximum amplitude due to unbalance is within the limits of clearance at the operating conditions. The predicted natural frequencies of T385 rotor system from modal analysis are compared with impact hammer test and frequencies are matching well with analysis.

N. Vinod Kumar (✉) · R. Prathapanayaka · R. Jai Maruthi · S. Swaroop
Propulsion Division, CSIR-National Aerospace Laboratories, Bengaluru, Karnataka 560017, India
e-mail: nvkumar@nal.res.in

R. Prathapanayaka
e-mail: prathap@nal.res.in

R. Jai Maruthi
e-mail: jaimarutinayaka@gmail.com

S. Swaroop
e-mail: swaroop.s1992@gmail.com

Keywords Gas turbine · T385 turbine rotor · Rotor dynamics · Vibration · FEA · Critical frequencies · Critical speed · Campbell diagram

Nomenclature

N	Speed
F_n	Frequency
ω_n	Rotational velocity
C_g	Center of gravity
M_I	Polar moment of inertia
K	Stiffness
M	Mass
RHS	Running speed harmonics
NPF	Nozzle passing frequencies
FEA	Finite element analysis

1 Introduction

Rotor dynamic analysis of a rotor system includes evaluation of dynamic characteristics and resonance of structural systems. The dynamic characteristics include mode shapes, frequencies, system behavior, and external excitations. Resonance condition occurs when natural frequency of the system coincides with external excitations leading to release of high strain energy to give rise to higher amplitude. The resonance condition leads to catastrophic failure at critical speeds. Rotor dynamic analysis will help the designer in prediction of resonance condition, to keep critical speeds sufficiently away from the operating speed range. The evaluation of instability of rotor system and unbalance response is also of critically important in overall design criterion. Many methods are available for numerical approximation of rotor-shaft system. The simplest and suitable method which is used for large-scale models with complex system is FEM. Gas turbine rotating systems are very critical systems due to the range of operating power and speed. Turbines are most crucial among all the rotating components as they are subjected to high speeds and temperatures; hence, dynamic characteristics evaluation of turbine rotor-shaft system is very much necessary using rotor dynamic analysis.

Swanson et al. [1] presented practical understanding of terminology and behavior based on visualizing how a shaft vibrates, and examining issues that affect vibration. It also helps to understand machinery vibrations and all the theoretical concepts beyond rotor-shaft vibration which can be used as further knowledge for developing a stable rotor-shaft model. Filho et al. [2] performed a full rotor dynamic analysis of investigated single-spool gas turbine with dynamic behavior. The rotor-shaft with

Fig. 1 T385 turbine rotor
BLISK



two bearings is considered with stiffness and damping dynamic properties. C class formulation by FE model is used to study critical speeds and unbalance response to avoid overall vibrational problems. Srikrishnanivas [3] submitted a thesis related to rotor dynamics of gas turbine engine. In his study, RM12 Jet engine rotor model was evaluated using ANSYS and Dyrobes which helped in understanding simulation and post processing techniques for rotor dynamics. Borovkov and Artamonov [4] analyzed natural frequencies of the gas turbine unit rotor with varying bearings stiffness. Transient process by finite element modeling and natural frequencies of full-scale gas turbine turbo compressors models were analyzed.

Aero-thermodynamic and mechanical design of a single-stage axial turbine stage has been carried out for 1 kN small gas turbine engine in Propulsion Division, CSIR-NAL. From the engine design configuration extract, it is envisaged that the single-stage axial gas turbine operating close to 50,500 rpm and at an elevated temperature would meet the power requirement of mixed flow compressor of 385 kW [5]. The photograph of turbine rotor hardware is shown in Fig. 1. This paper presents the detailed rotor dynamic analysis and harmonic response due to unbalance of turbine rotating system which is designed to test the turbine stage using FEA. The stiffness of bearing supporting structure is evaluated along the direction of stress field using FEA. Impact hammer test is conducted to verify the rotor dynamic analysis results.

2 Methodology

2.1 T385 Turbine Rotor BLISK

Design and development of gas turbine engine is being carried out in the propulsion division, CSIR-NAL. T385 turbine rotor with 50 blades shown in Fig. 1 is an integrated bladed disk (BLISK) made of nickel-based alloy weighs around 1.65 kg. Aerodynamic performance evaluation of T385 turbine through experimental testing was planned to verify the design at versatile turbine test rig (VTTR), Propulsion Division, CSIR-NAL. The turbine speed is 50,500 rpm at the engine design point, and

the equivalent design speed in test rig conditions is 30,000 rpm based on simulated parameters.

2.2 Versatile Turbine Test Rig (VTTR) Facility

Aerodynamic performance evaluation of T385 turbine through experimental testing was planned at versatile turbine test rig (VTTR), Propulsion Division, CSIR-NAL. Versatile Turbine Test Rig (VTTR) facility has been established in Propulsion Division, CSIR-NAL to evaluate the turbines performance through testing of small gas turbine engines. Photograph of VTTR is shown in Fig. 2. Power absorption capacity of the VTTR facility is 500 kW up to 50,000 rpm (constant power absorption from 14,000 to 50,000 rpm). VTTR facility specifications are as follows:

Specifications of the VTTR facility

- Max air mass flow: 9 kg/s
- Max turbine inlet pressure: 10 kg/cm²
- Max inlet temperature: 700 K
- Turbine tip diameter: 305 mm and variable
- Max speed: 50,000 rpm
- Max power absorbing: 500 kW from 14,000 rpm
- Dynamometer: Eddy current type (bi-directional)
- Stages: Single and multi-stage
- Type of testing: Hot and cold air.



Fig. 2 Photograph of VTTR

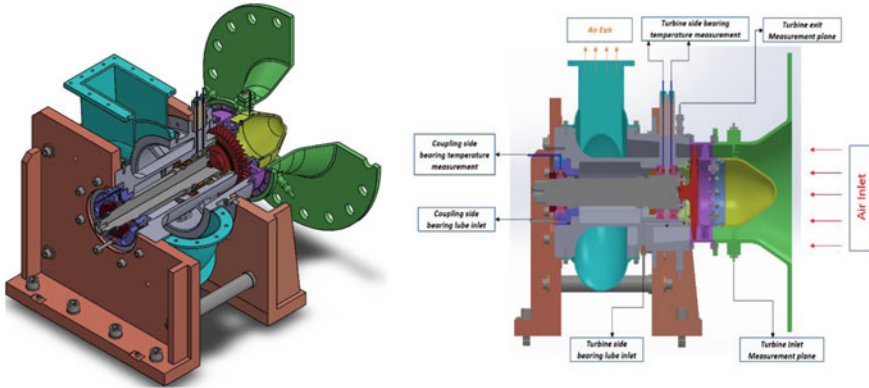


Fig. 3 T385 turbine test section

2.3 T385 Turbine Test Section

To evaluate the aerodynamic performance of the T385 turbine, a suitable test section is designed by adopting the turbine rotor. This test section is designed by keeping inlet and exit compressed air systems to match the VTTR facility. Figure 3 shows the test section designed to test T385 turbine. The test section consists of an inlet adapter to connect between the existing 10-in. pipe line and the stator inlet, a volute casing for exhaust, a bearing housing to support the rotating system, and two vertical stands which support the overall test section. Apart from aerodynamic measurements, provisions are made to measure the bearing temperatures and fixing of bearing lubrication pipelines and accelerometers.

2.4 Turbine Rotor System

The rotor system is designed based on the interface required to mount turbine at one end and geared coupling for power transmission on other end as shown in Fig. 4. It is supported by two angular contact bearings at turbine end and cylindrical roller bearing at coupling end.

At the turbine end, an angular contact ball bearing is chosen to resist axial thrust load. To improve stiffness of the rotor bearing support structure and to eliminate preloading of the bearing by a spring, it is suggested to use a pair of bearings in back-back arrangement. The bearing material is chosen with metal rolling elements and cage made out of PEEK.

SKF cylindrical roller bearing is chosen at coupling end based on the load and speed rating. This roller bearing, which can permit 2 mm axial relative displacement between inner and outer rings, acts as floating bearing when the casing expands/contracts with respect to the rotor.

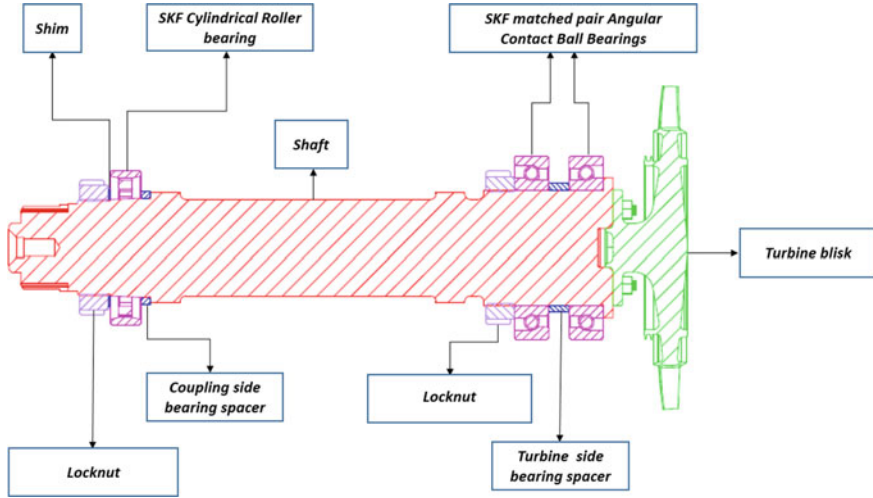


Fig. 4 T385 turbine rotor-shaft model

2.5 Bearing and Structural Stiffness

The bearing stiffness data over a range of radial loads and bearing clearances for the given operating conditions is obtained by consulting with M/s SKF Bearings, Bangalore. For ball bearing, stiffness value of 753 MN/m corresponding to minimum preload is considered to be on the conservative side. In case of roller bearing, the measured clearance during assembly is 5 μm and corresponding stiffness value for this is 104 MN/m and same taken for analysis.

The structural stiffness is computed by taking deformations along the direction of respective stress field. The slope of the line shown in Fig. 5a, b gives the structural stiffness at ball bearing and cylindrical roller bearing planes, respectively.

The stiffness of both bearing and supported structure is considered in rotor dynamic analysis. The rotor dynamic analysis of T385 rotor-shaft system is

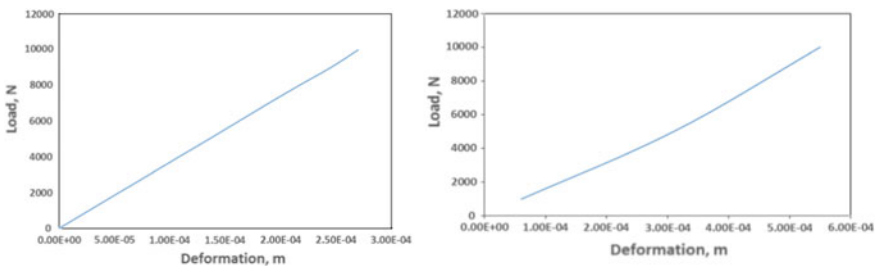


Fig. 5 a Structure stiffness at ball bearing plane. b Structure stiffness at roller bearing plane



Fig. 6 T385 turbine rotor-shaft model with supported component locations

performed using ANSYS by considering centrifugal loads, stiffness, center of gravity and masses of supported components with lumped mass system.

3 Finite Element Analysis

3.1 Defining the Model

The finite element analysis is performed using lumped mass model. The shaft material EN-24 is assigned to T385 turbine shaft model. Mass moment of inertia, center of gravity, and mass of supported components are defined as shown in Fig. 6. The bearings and structural stiffness are assigned at the bearing planes.

3.2 Meshing

In the present work, both hexahedron and tetrahedron elements are used to mesh the rotor system. The optimum mesh quality is ascertained to rotor system by taking Jacobian and aspect ratios close to unity. The grid size of rotor system is 46,092 nodes and 15,357 elements, and representation is shown in Fig. 7.



Fig. 7 Meshing of T385 turbine rotor-shaft model

4 Results and Discussion

The T385 turbine shaft system for test rig conditions is designed to operate up to 30,000 rpm. The rotor dynamic analysis is performed considering a speed range from 0 to 50,000 rpm. Spin softening is considered in the analysis to get proper forward and backward whirls. The frequencies for different centrifugal loads and different mode shapes are extracted from the analysis in undamped condition. Obtained frequencies from analysis are plotted in Campbell diagram.

Figure 8 shows the Campbell diagram of the T385 turbine shaft system. The diagram indicates that the first critical speed is 40,000 rpm which is excited from first-order (rotor unbalance) excitation. First critical is away from maximum operating speed of 30,000 rpm. Critical speeds may also get excited due to higher-order excitation as shown in Fig. 8, which needs to be crossed with higher acceleration. The aerodynamic test points falling at this speed have to be shifted away from this region with sufficient margin. Critical speeds which are excited due to higher-order excitations (3X, 4X, 5X, ... etc.) need to be carefully crossed as these critical speeds will not have much energy to affect the rotating system. Critical speeds due to backward whirl are also present, which may occur in rare instance will be considered during testing.

The Campbell plot indicates that the fourth bending mode at the coupling side is getting excited from external excitations as shown in Fig. 9. The first six modes are extracted in FEA to get Campbell diagram, and first few modes are very dangerous since they have more strain energy stored in their system. The rotor system is vibrating in a forward whirl and backward whirl due to gyroscopic effect. The gyroscopic effect

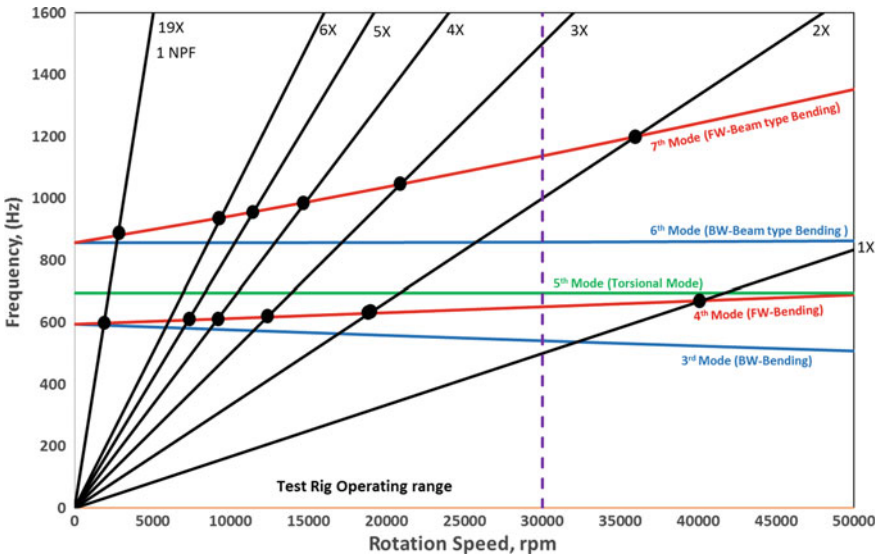


Fig. 8 Campbell diagram for T385 turbine rotor-shaft system

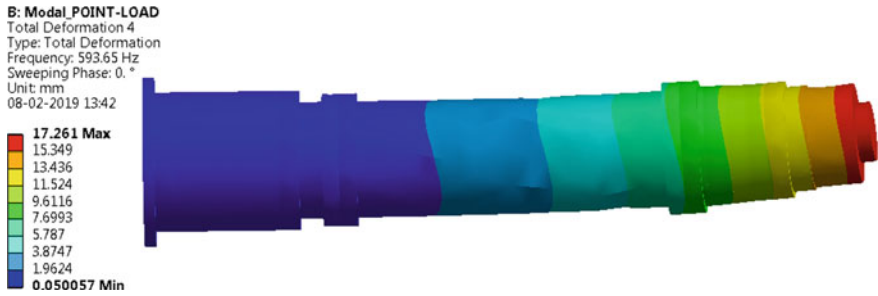


Fig. 9 Fourth mode shape (forward whirl) bending at coupling side

is proportional to the rotor speed and the polar mass moment of inertia, which in turn proportional to the mass and square of the area. The rotor is whirling in forward direction due to gyroscopic stiffening, and rotor is whirling backward direction due to gyroscopic softening. The modes with forward whirl have predominant in rising higher deflections to reach resonant condition.

The harmonic response of rig rotor systems is carried out to find out the response of the system in the critical region by considering rotor unbalanced mass for balancing grade of G 2.5. In this analysis, the damping is neglected as the damping provided by the ball bearings is negligible. It is observed that the maximum amplitude of vibration is 31 μm at rotor speed of 675 Hz (40,500 rpm) as shown in Fig. 10. The computed maximum amplitude is checked at all the critical clearance sealing locations and found that all are within the limits of clearance at the operating conditions.

Impact Hammer Test

Impact hammer test is carried out by considering assembled rotor system to the test section at the Versatile Turbine Test Rig, CSIR-NAL. Accelerometer is mounted on

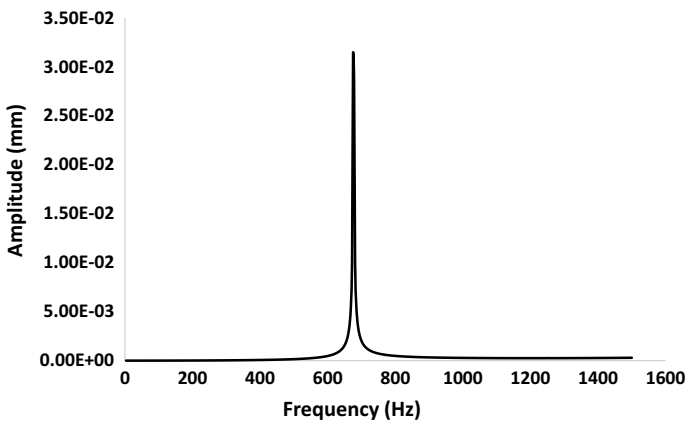


Fig. 10 Response at coupling side

Table 1 Frequency comparison b/w FEA and impact hammer test

FEA F_n (Hz)	593	705	878
Test 1 (Hz)	581	731	893
Test 2 (Hz)	575	725	881

the critical region of test section based on mode shapes resulted from FE analysis. Dytran-make Impulse hammer with aluminum tip is used to give impact on the test section at different locations. A six-channel OROS DAQ is used to record the readings from accelerometer. The acquired data are processed using OROS NV GATE software to get the natural frequencies. The results are compared with frequencies obtained from rotor dynamics to evaluate critical. The frequencies at zero rotor rpm from rotor dynamic analysis are 593, 705 and 878 Hz which are shown in Fig. 8. The impact hammer test results and analysis have been listed in Table 1. From Table 1, it is very clear that impact hammer test results are quite close to analysis which confirms the analysis.

5 Conclusion

3D FE rotor dynamic analysis of T385 turbine rig rotor-shaft system has been carried out. The Campbell plot from 3D FE rotor dynamic analysis shows that there are no critical speeds in the operating range from first-order excitation (1X). There is a critical speed around 18,837 rpm due to second-order excitation (2X) and care should be taken while running in test rig to cross this critical speed. There are critical speeds which are excited due to higher-order excitations (3X, 4X, 5X and 1NPF), and these critical speeds may not cause major effect on the rotor system. The harmonic response due to unbalance is carried out using 3D FEA. The maximum amplitude due to unbalance is within the limits of clearance at the operating conditions. The predicted natural frequencies of T385 rotor system from modal analysis are compared with impact hammer test and frequencies are matching well with analysis.

Acknowledgements Authors acknowledge CSIR support for this project. Authors would like to thank Director, CSIR-NAL, Head and Joint Head, of Propulsion Division. Authors also thank Propulsion Division colleagues for their support in carrying out this work.

References

1. Swanson E, Powell CD, Weissman S (2005) A practical review of rotating machinery critical speeds and modes. Sound Vib
2. Filho GC, Menezes JC, de Castro Monteiro JF, Corra JA (2009) Rotor-bearing analysis of a single spool gas turbine by using the finite element method. In: Proceedings of COBEM, Gramado, 15–20 Nov 2009

3. Srikrishnanivas D (2012) Rotor dynamic analysis of RM12 jet engine rotor using ANSYS. ISRN: BTH-AMT-EX-2012/D-10-SE
4. Borovkov AI, Artamonov IA (2004) 3D finite element modeling and vibration analysis of gas turbine structural elements. St. Petersburg State Polytechnical University, Russia
5. Rajeevalochanam P, Agnimitra Sunkara SN, Mayandi B, Ganesh BB, Chappati VSK, Kumar K (2016) Design of highly loaded turbine stage for small gas turbine engine. In: ASME turbo expo 2016, South Korea

Evaluation of Dynamic Characteristics of a VMC Spindle System Through Modal and Harmonic Response. Part 1: Spindle Supported by Angular Contact Ball Bearings



Gireesha R. Chalageri, Siddappa I. Bekinal, and Mrityunjay Doddamani

Abstract Machine spindle dynamic characteristics are precisely related to the operation and stability of the machining process. The finite element analysis (FEA) has been used to find out the dynamic behavior of spindle-bearing system. The unbalance response of the vertical machining center (VMC) spindle system at the cutting tool due to thrust force is calculated to study the dynamic properties. In this paper, Ansys Workbench rotordynamic and harmonic response have been used to make the dynamic investigation of VMC spindle and estimate the final values. Results show that the obtained critical speeds are nowhere near to the spindle operating speed range; hence, the resonance would not occur, and at operating speed, the maximum unbalance response is within an acceptable limit. The effect of rotordynamic and harmonic response on same VMC spindle system supported by hybrid bearing set is analyzed in Part 2 as an extension of this work.

Keywords Rotor dynamics · Machine spindle · Bearings · Ansys workbench · Critical speed

G. R. Chalageri (✉)

School of Mechanical Engineering, KLE Technological University, Hubballi, Karnataka 580031, India

e-mail: giri2884@gmail.com

S. I. Bekinal

Department of Mechanical and Manufacturing Engineering, Manipal Institute of Technology, Manipal, Udupi, Karnataka 576104, India

e-mail: sibekinal@rediffmail.com

M. Doddamani

Department of Mechanical Engineering, National Institute of Technology, Surathkal, Mangalore, Karnataka 575025, India

e-mail: mrd7819@gmail.com

© Springer Nature Singapore Pte Ltd. 2021

J. S. Rao et al. (eds.), *Proceedings of the 6th National Symposium on Rotor Dynamics*, Lecture Notes in Mechanical Engineering,

https://doi.org/10.1007/978-981-15-5701-9_3

1 Introduction

Rotor dynamics deals with studies of lateral and torsional vibrations of rotating shafts, with the objective of predicting the spindle/rotor vibrations and vibration level under a satisfactory limit [1]. Delgado et al. analyzed the preload effect on stiffness and frequency response function using Ansys and Spindle Pro FEA tools, and it is shown that bearing preload has the greatest influence on dynamic response [2]. Static and dynamic performance of the high-speed electric spindle is investigated for different spindle span using Ansys tool [3]. The analysis of rotor is carried out to investigate the dynamic behaviors of grinding spindle using FE program Ansys Parametric Design Language (APDL) [4]. Tlalolini et al. developed a system to measure the dynamic and quasi-static characters of machine tool spindle, and classical tap test measurement is used to compare the obtained FRF results [5]. Spindle dynamic characteristics are studied under different bearing preload conditions, and it is found that vibrational frequency of spindle increases as bearing preload increases [6]. An analytical approach is developed to evaluate the critical speeds of multi-section rotor assembly with varying external loads, and the results obtained by varying rotor dimensional aspects are compared with APDL program results [7]. Unbalanced forces cause the backward whirl modes which are dependent on asymmetry of stiffness values at the rotor support. Direct stiffness asymmetry has greater influence on backward mode, while cross-coupled stiffness is having negligible effect on backward mode resonance. Further, peak amplitude of backward mode resonance decreases by increasing the direct damping [8]. A 5 degrees of freedom analysis model proposed and validated for precision grinding machine tool spindle for dynamic characteristics with varying loading and geometrical features of spindle-bearing arrangements [9]. Higher rotational speed of milling spindle affects the machining stability and causes dynamic instability in micro-milling of titanium alloy TiAl4V. Additional degrees of freedom contribute gradual improvement in the stability limits of milling spindle [10].

The present paper focuses on rotor-dynamic analysis for studying the modal and harmonic response of the VMC spindle system. Campbell diagrams are obtained for different preload conditions, and determining critical speed is helpful in analyzing the spindle vibrational characteristics. Harmonic response of spindle has been done by incorporating calculated unbalance mass at the cutting tool. In this work, Ansys Workbench rotordynamic and harmonic response tools have been implemented to analyze and evaluate the dynamic results.

2 Methodology

In this paper, a Botliboi DTC-50 spindle system of CNC drill tap machine as shown in Fig. 1 is analyzed for rotordynamic characteristics. The pulley belt system connected to the shaft along with a 3.7 kW motor to operate spindle at up to 9000 rpm speed. In the present model, bearings, cutting tool, spindle shaft, and tool holder were included.

Fig. 1 Schematic model of the VMC drilling spindle

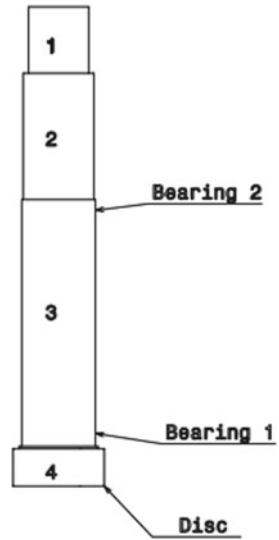


Table 1 Spindle element’s geometry

Element numbers	1	2	3	4
Diameter (<i>D</i>) in mm	45	53	55	68
Length (<i>L</i>) in mm	50	95	185	30

All spindle components are represented as separate assembly parts with bearings and disk along with distributed mass and elasticity.

Table 1 represents the mechanical and geometrical properties of spindle element. Three masses are considered in the analysis; one is the cutting tool and tool holder component as rigid disk element 1 and remaining two are bearing masses at bearing locations 1 and bearing location 2. The stiffness values of each bearing with varying preload are given in Table 2. A representation of the spindle’s numerical model is as shown in Fig. 1. In the present work, SKF 7011 CB/P4A type of angular contact spindle bearings is used. The numbers of rolling elements in these bearings are 26 with ball diameter as 6.74 mm. Each angular contact bearing is having a mass of 0.42 kg. The mass of the disk 1 is considered as 2 kg which includes mass of tool

Table 2 Bearing stiffness values [11]

Preload types	Preload force in N	Stiffness in N/m	
		Bearing 1	Bearing 2
Class A	46	38×10^6	38×10^6
Class B	92	50×10^6	50×10^6
Class C	275	80×10^6	80×10^6

holder and cutting tool. Case carbonized alloy steel (15Ni2Cr1Mo15) is used as spindle material with modulus of elasticity as $2.5 \times 10^5 \text{ N/mm}^2$.

The spindle unit was preloaded using the clearances created by different set of spacers as low, medium, and high as shown in Table 2.

Three-dimensional FE model of the spindle-bearing system is being modeled with the Ansys Workbench program with necessary boundary conditions as shown in Fig. 2. Shear effect is nullified by constraining element motion along y-axis path and rotation about y-axis; hence, twist motion and displacement of the spindle about y-axis would not occur. The spindle FE model is meshed using hexadent second-order meshing option as shown in Fig. 3. Rotordynamic analysis of spindle is performed to determine natural frequencies, mode shapes, critical speeds, and Campbell value.

Fig. 2 Schematic FE model of the VMC drilling spindle

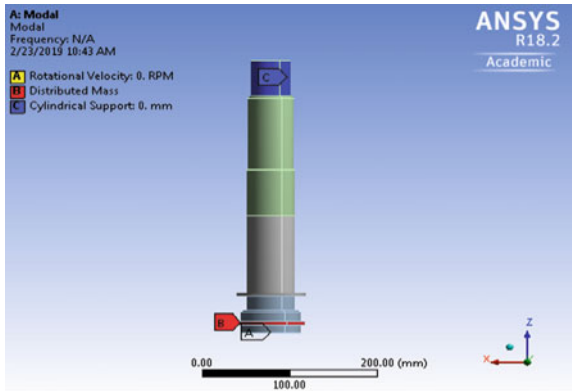


Fig. 3 FE meshed model of VMC drilling spindle



3 Results

The numerical analysis carried out at different speeds ranges from initial 0 to 60,000 rpm. Table 3 shows the expected spindle-bearing assembly (at operating speed of 9000 rpm) frequencies obtained from rotordynamic module of Ansys Workbench. The mode shapes at first four natural frequencies of all preload classes are shown in Figs. 4, 5 and 6. Also, Fig. 7 shows the Campbell diagrams attained by the numerical model constructed in Ansys rotordynamic tool.

Table 3 Bearing stiffness values at 9000 rpm

Natural frequencies	Rotordynamic model (Hz)		
	Preload class A	Preload class B	Preload class C
1	490.98	551.29	671.45
2	1083.2	1083.2	1083.2
3	1597	1636.9	1733.8
4	3951.7	3956.8	3969.2

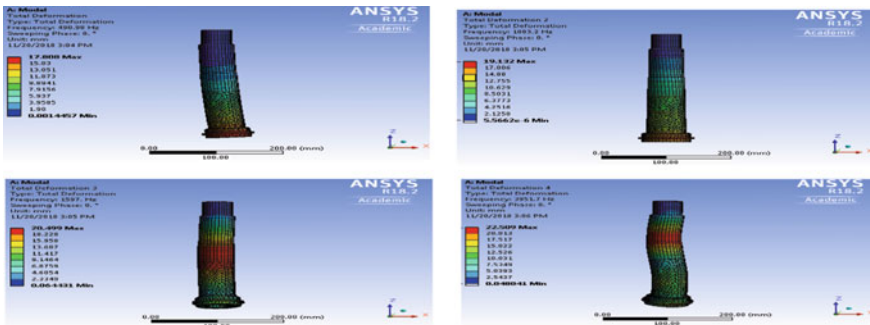


Fig. 4 Mode shapes for preload class A

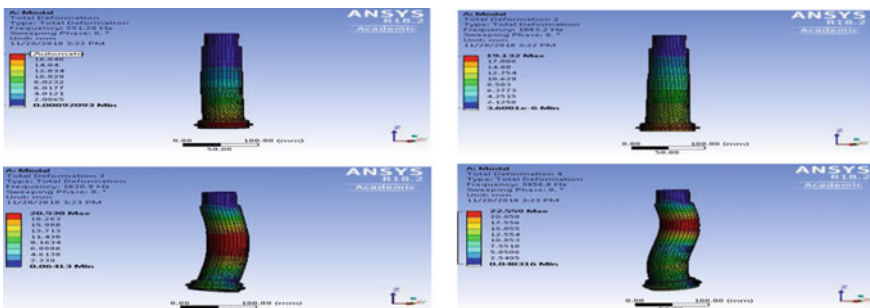


Fig. 5 Mode shapes for preload class B

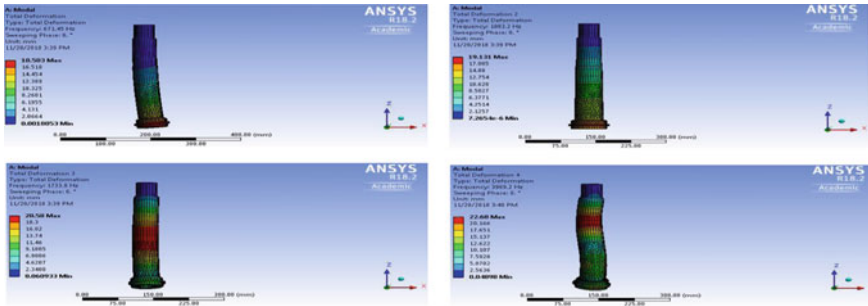


Fig. 6 Mode shapes for preload class C

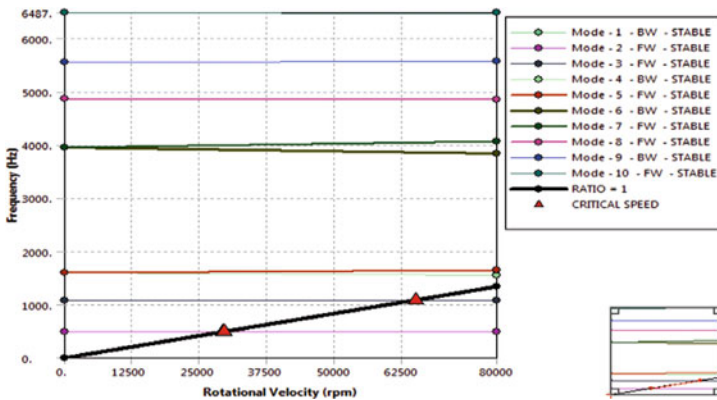


Fig. 7 Campbell diagram of preload class A

The natural frequencies of three conditions were found out and analyzed. Mode shapes are observed for careful examination of deformation. The type of mode with the corresponding frequency has been tabulated. These characteristics prove to be very helpful in the design of the machine spindle for dynamic conditions. In all the three cases, preload of bearings and corresponding stiffness increases with all the modal frequencies except in second mode which remained the same due to 180° in-phase or out-phase motion.

Structural displacement when excited at natural frequencies is illustrated by the configuration or the pattern of mode shapes. From the mode shapes deflection pattern, it is clear that mode 1 and mode 3 are bending modes in opposite vertical direction. In mode 2, all displacements are either in-phase or 180° out of phase. Mode 4 is complex nature in which every position can have a different phase angle. The mode shapes in all three preload conditions are nearly the same, and in all first four modes, deformation pattern and value are in close agreement (Figs. 8 and 9).

The critical speeds are obtained by referring the Campbell diagrams plotted as frequency versus speed. The obtained speeds are in terms of radian per second in

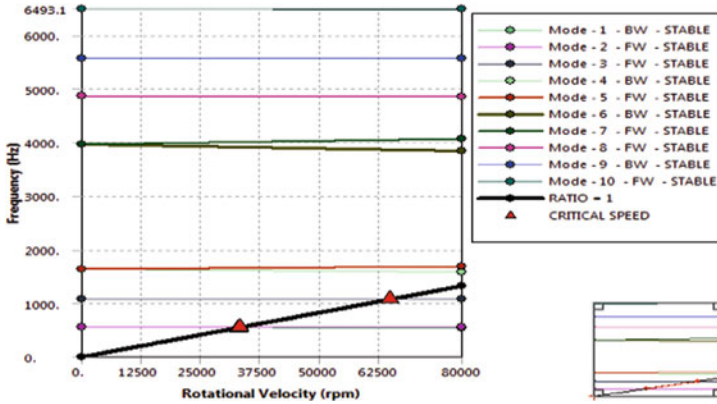


Fig. 8 Campbell diagram of preload class B

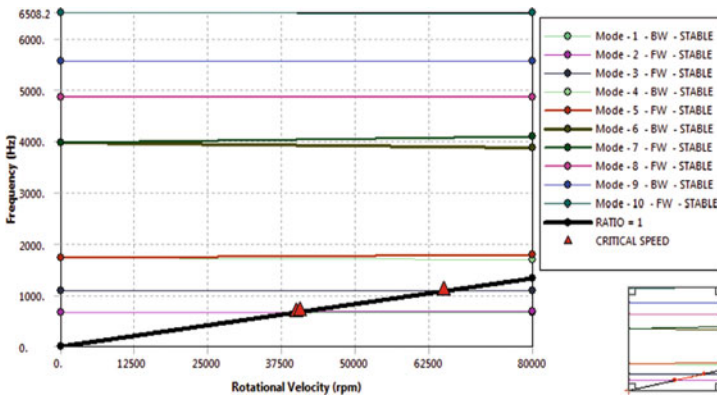


Fig. 9 Campbell diagram of preload class C

Ansys Workbench program. The critical speeds (rpm) correspond to preload force or classes are given in Table 4. Since the critical speeds in all the cases are much higher than the operating speed, i.e., 9000 rpm the system is stable.

Frequencies determined by rotordynamic analysis were validated through harmonic response analysis of spindle by adding the unbalanced thrust force. Since maximum drill bit used in the present VMC is 12 mm and maximum cutting speed is 30 m/min, thrust force of 3492 N is calculated using power and force requirements of drilling [12]. The response function of frequency shown in Figs. 10, 11 and 12

Table 4 Critical speeds of vertical machining system

Speed No.	Critical speed (rpm)		
	Preload class A	Preload class B	Preload class C
1	29,301	32,883	40,000

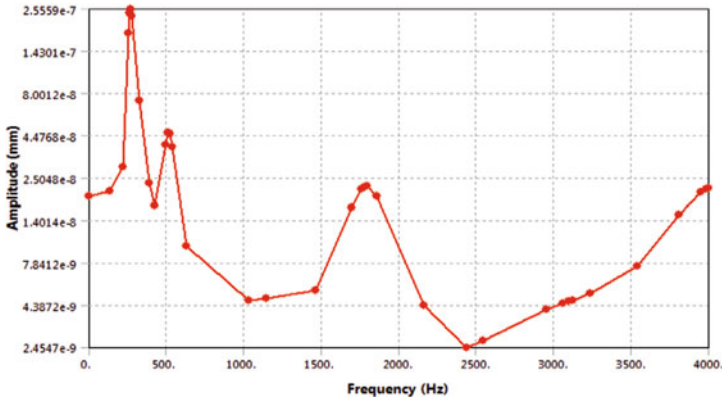


Fig. 10 Frequency versus amplitude unbalance response of preload class A

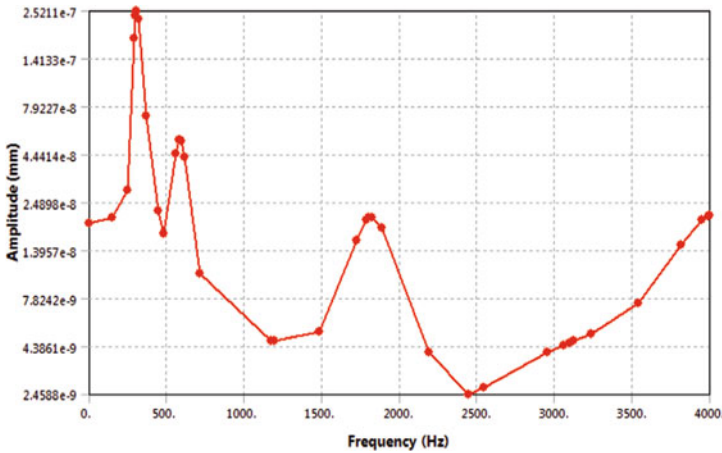


Fig. 11 Frequency versus amplitude unbalance response of preload class B

was measured at cutting tool for different preload conditions, which gives harmonic frequency vibration modes. From the frequency response function analysis, it is clear that peak amplitude decreases with increase in the preload and corresponding decrease in the harmonic frequency modes.

The nodal solutions of harmonic responses have been obtained using the Ansys Workbench FE harmonic response model. Figure 13 compares the modal frequencies and harmonic frequencies of VMC spindle with different bearing preload classes. Results show that the modal and harmonic frequencies are in good agreement and maximum difference is less than 6%. These frequencies are dependent on preload and bearing stiffness values. Generally, increase in preload value increases the frequencies in both modal and harmonic environments. The variation in frequency modes for both the models is less than 3% except second mode where the variation is nearly

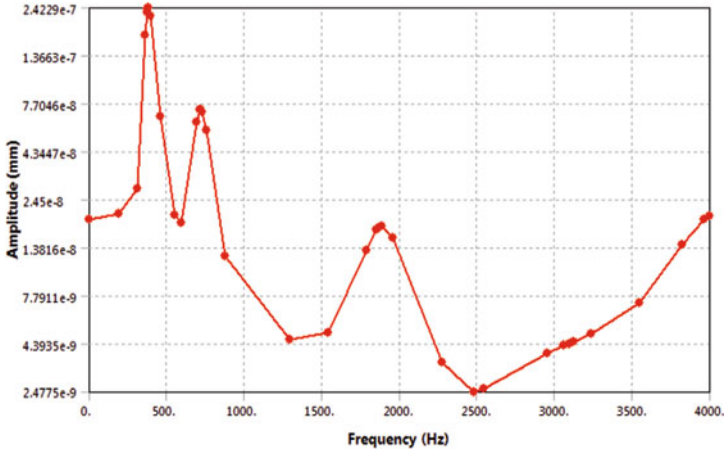


Fig. 12 Frequency versus amplitude unbalance response of preload class C

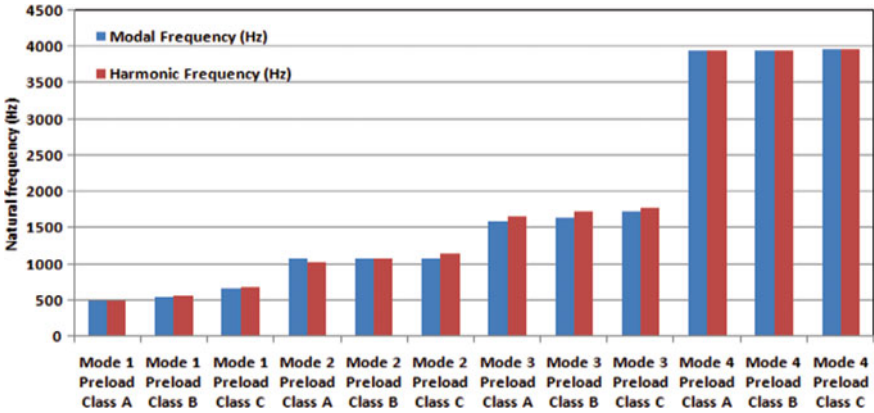


Fig. 13 Comparison of modal and harmonic frequencies of spindle with different bearing preload classes

6%. The harmonic frequency values are slightly higher due to the consideration of thrust force acting on cutting tool.

4 Conclusions

A drill tap VMC spindle system with defined geometrical and mechanical properties is analyzed for dynamic characteristics and results are evaluated. The mode shapes of the spindle at operating speeds, the Campbell diagrams, critical speeds are obtained. Based on the study, the following conclusions are drawn.

- Basically, the dynamic behavior of spindle is influenced by preload force and corresponding stiffness of the bearings.
- The spindle vibrates at lower frequencies in Preload Class A, and spindle vibrating frequencies increase gradually as preload increases to Class B and Class C.
- The critical speeds of spindle increase with increase in preload of bearings, and these coinciding speeds are still far away from the working speed range of the spindle; thus, the spindle resonance would not occur.

References

1. Nelson FC (2003) A brief history of early rotor dynamics. *J Sound Vib* 37:8–11
2. Delgado AS, Ozturk E, Sims N (2013) Analysis of non-linear machine tool dynamic behavior. In: *The manufacturing engineering society international conference, MESIC*
3. Zhang X-Y, Wang M, Zan T, Hu J-Z (2011) The static and dynamic analysis of high-speed electric spindle based on ANSYS. Beijing University of Technology, Beijing. 978-0-7695-4455-7/11. IEEE
4. Jauhari K, Widodo A, Haryanto I (2015) Evaluation of dynamic behavior a machine tool spindle system through modal and unbalance response analysis. *World Acad Sci Eng Technol Int J Ind Manuf Eng* 9(2)
5. Tlalolini D, Ritou M, Rabréau C, Le Loch S, Furet B (2018) Modeling and characterization of an electromagnetic system for the estimation of frequency response function of spindle. *Mech Syst Signal Process* 104:294–304
6. Alfares MA, Elsharkawy AA (2003) Effects of axial preloading of angular contact ball bearings on the dynamics of a grinding machine spindle system. *J Mater Process Technol* 136:48–59
7. Jagannath K (2012) Evaluation of critical speed of generator rotor with external load. *Int J Eng Res Dev* 1:11–16
8. Greenhill M, Guillermo CA (1995) Critical speed resulting from unbalance excitation of backward whirl modes. *ASME Des Eng Tech Conf* 3:991–10000
9. Aini R, Rahnejat H, Gohar R (1990) A five degrees of freedom analysis of vibrations in precision spindles. *Int J Mach Tools Manuf* 30:1–18
10. Rinku KM, Salil SK, Ramesh KS (2018) Multiple degree of freedom rotordynamics based stability modeling in high-speed micromilling of Ti-6Al-4V. *Procedia Manuf* 26:607–616
11. <http://www.skf.com/in/products/bearings-units-housings/super-precision-bearings/angular-contact-ballbearings/acbb-skf-high-and-super-precision/index.html?designation=7011%20CB->. Accessed on 24 Nov 2018
12. CMTI (2017) Machine tool design handbook. TMH

Evaluation of Dynamic Characteristics of a VMC Spindle System Through Modal and Harmonic Response—Part 2: Spindle Supported by Hybrid Bearing Set



Gireesha R. Chalageri, Siddappa I. Bekinal, and Mrityunjay Doddamani

Abstract This paper extends the proposed dynamic analysis of spindle with conventional bearings of Part 1 and demonstrates feasibility of hybrid bearing set (HBS) usage in machine tool spindles. HBS consists of permanent magnet bearing (PMB) and conventional angular contact bearing (ACB). The rotordynamic and unbalance response of vertical machining center (VMC) spindle supported by HBS is presented. Harmonic responses are also determined using Ansys Workbench finite element tool. Results show that the system is stable at obtained frequencies, critical speeds are higher than the spindle operating speed range, and the maximum unbalance response is within acceptable limit. The comparison between the results of ACB and HBS has verified that the HBS can effectively be used in machine tool spindles with higher critical speeds and maximum amplitudes generating due to cutting forces.

Keywords Rotordynamics · VMC spindle · Hybrid magnetic bearings · Frequency response

1 Introduction

Forces due to friction and heat are unnecessary in machine spindle. In order to reduce impact of friction and heat on the system, the integration of magnetic bearings with

G. R. Chalageri (✉)

School of Mechanical Engineering, KLE Technological University, Hubballi 580031, Karnataka, India

e-mail: giri2884@gmail.com

S. I. Bekinal

Department of Mechanical and Manufacturing Engineering, Manipal Academy of Higher Education, Manipal 576104, India

e-mail: sibekinal@rediffmail.com

M. Doddamani

Department of Mechanical Engineering, National Institute of Technology, Surathkal, Mangalore 575025, Karnataka, India

e-mail: mrd7819@gmail.com

© Springer Nature Singapore Pte Ltd. 2021

J. S. Rao et al. (eds.), *Proceedings of the 6th National Symposium*

on *Rotor Dynamics*, Lecture Notes in Mechanical Engineering,

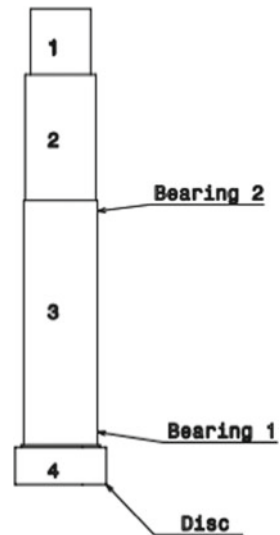
https://doi.org/10.1007/978-981-15-5701-9_4

conventional is feasible solution [1]. Prince Owusu-Ansah et al. analyzed flywheel supported by hybrid magnetic bearing (HMB) which balances levitation and gravitation force by providing a way of resolving difficulties associated with flywheel energy storage [2]. Vector approach with Coulombian model is used to develop a mathematical model for axially, radially and perpendicularly magnetized PMB to estimate the force and stiffness [3–6]. The fundamental of rotor-bearing system dynamics is provided for simple to complex systems using basic principles and modeling in [7]. FEA applied to 3D HMB models is presented for various conditions of air gap, flux density distribution, and force current characteristics [8]. Ansys FEA tool is used to solve set of two symmetrical axial PMBs and one permanent magnet. The air gap length and axial dimensions between magnetic rings are varied to study the effect of stiffness and restoring force of bearings [9]. Bekinal et al. achieved complete passive levitation of the rotor at the speed around 40,000 rpm. The rotor is supported by a permanent magnet bearing and discrete bump foil bearing for the axial and radial supports, respectively [10]. The main objective of this paper is to analyze the rotor supported by HBS for rotor dynamic characteristics using FEA.

2 Methodology

In this paper, a Batliboi DTC-50 VMC spindle system of CNC drill tap machine tool as shown in Fig. 1 is analyzed for rotordynamic characteristics. The spindle is designed to operate at 9,000 rpm with a 3.7 kW motor connected to the shaft. Spindle is supported by HBS, i.e., SKF angular contact B7011 bearing on one end and PMB on other end. In line with Earnshaw's theorem, it can be expected that

Fig. 1 Schematic model of the VMC drilling spindle



the axial stiffness of a radial magnetic bearing to be negative and twice of its radial stiffness [11].

The dimensional properties of VMC spindle element are given in Table 1. Tool holder and cutting tool are considered as rigid disk mass elements. Two bearing masses are considered at locations of bearings 1 and 2. The stiffnesses of angular bearings and PMBs with different preloads are given in Table 2. Figure 1 shows the schematic numerical model of VMC spindle. SKF 7011 CB/P4A type of angular contact spindle bearings is used along with PMBs in the present study. The numbers of rolling elements in these bearings are 26 with ball diameter as 6.74 mm. Each ACB is having a mass of 0.42 kg. The distributed mass of 2 kg is added to disk which includes mass of drilling tool and tool holder [12]. The modulus of elasticity for spindle material case carbonized alloy steel (15Ni₂Cr₁Mo₁₅) is taken as 2.5×10^5 N/mm². Different sets of spacers are used to create the clearances in spindle and angular contact ball-bearing unit to achieve the class A, class B and class C preload forces.

Figure 2 shows the three-dimensional FEA model of the spindle-bearing system modeled in the Ansys Workbench program with necessary boundary conditions. Axial and tangential motions are constrained at top element 1 of the spindle in order to facilitate cylindrical support condition by nullifying the shear effect, also radial direction kept free for rotation about y-axis. Figure 3 shows the second order hexa dent type meshing option used to mesh the drilling spindle FEA model. Rotordynamic response analysis of spindle is performed to determine natural frequencies, mode shapes, critical speeds, and Campbell value.

Table 1 Spindle element’s geometry

Element numbers	1	2	3	4
Diameter (D) in mm	45	53	55	68
Length (L) in mm	50	95	185	30

Table 2 Bearing stiffness values

Permanent magnetic bearing [13]	Angular contact bearing [14]		
Radial stiffness = 1×10^5 N/m	Preload types	Preload force in N	Stiffness in N/m
	Class A	46	38×10^6
Axial stiffness = -2×10^5 N/m	Class B	92	50×10^6
	Class C	275	80×10^6

Fig. 2 Schematic model of the drilling spindle

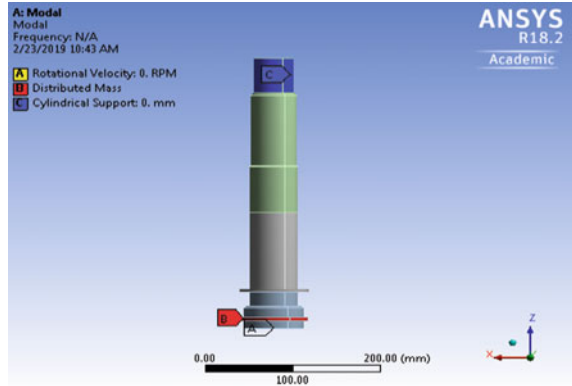


Fig. 3 Hex-dominant FEA model of drilling spindle



3 Results

The numerical analysis is carried out at different speeds ranging from initial 0 to 80,000 rpm. Initially, natural frequencies for angular contact bearings at location 2 and PMB at 1, i.e., near the cutting tool at operating speed of 9000 rpm, are obtained and results are shown in Table 3. Later, the bearing locations are interchanged as ACB at 1 and PMB at 2, i.e., near the motor belt transmission, and frequencies are

Table 3 Dynamic parameters of HBS at 9000 rpm when bearing 1 as PMB

Natural frequencies	Rotordynamic model (Hz)		
	Preload class A	Preload class B	Preload class C
1	255.93	276.02	314.07
2	1083.2	1083.2	1083.2
3	1592.4	1630.1	1720.3
4	3939	3940	3942.7

obtained using same procedure as shown in Table 4. The mode shapes at first four natural frequencies of ACBs of all preload classes and PMB are shown in Figs. 4, 5, 6, 7, 8 and 9.

The natural frequencies of all the conditions were found out and analyzed. Natural frequencies increase as preload increases in both the cases. Higher frequencies are observed when PMB is away from cutting tool, due to less experiencing of chattered vibrations as well as cylindrical support at the element 4 near PMB. Lower frequencies are observed when PMB is nearer the cutting tool as more chattered vibrations from drilling operations experienced near the tool.

Deformation patterns of spindle unit are studied through careful examination of mode shapes. The type of mode with the resultant frequency has been compiled. These features of modes prove to be very useful in the design of the machine spindle for dynamic situations. In all the three cases, as preload of bearings and corresponding stiffness increases, all the modal frequencies increase except second mode which remained same due to 180° in-phase or out-phase motion.

Structural displacement when excited at natural frequencies is illustrated by the configuration or the pattern of mode shapes. From the mode shape deflection pattern, it is clear that modes 1 and 3 are bending modes in opposite vertical direction. In mode 2, all displacements are either in phase or 180° out of phase. Mode 4 is complex nature in which every position can have a different phase angle. The mode shapes in all conditions are nearly same, and in all first four modes, deformation pattern and value are in close agreement.

Table 4 Dynamic parameters of HBS at 9000 rpm when bearing 2 as PMB

Natural frequencies	Rotordynamic model (Hz)		
	Preload class A	Preload class B	Preload class C
1	449.56	507.23	626.51
2	1083.2	1083.2	1083.2
3	1470.5	1471.5	1474.3
4	3948.7	3952.8	3963.2

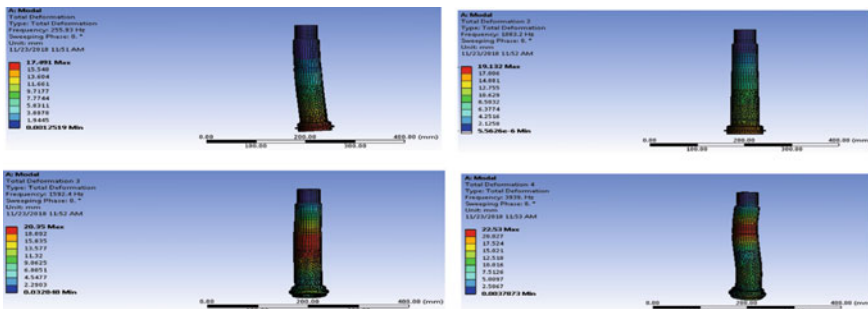


Fig. 4 Mode shapes for preload class A when bearing 1 as PMB

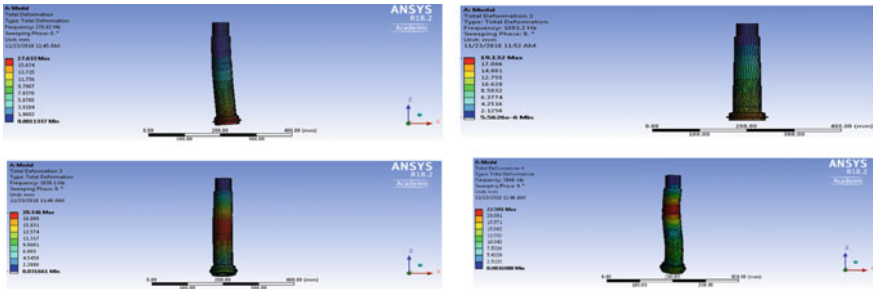


Fig. 5 Mode shape for preload class B when bearing 1 as PMB

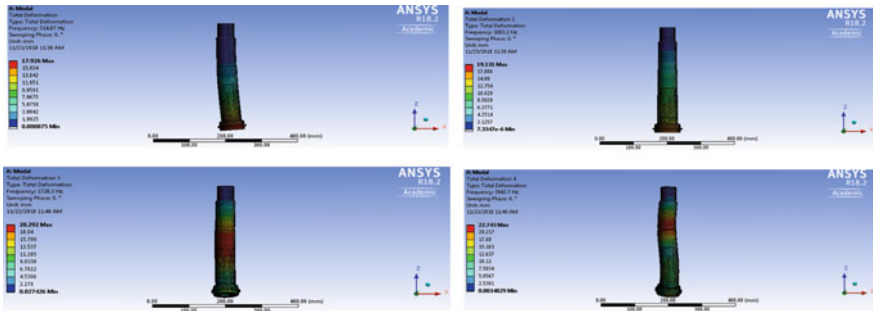


Fig. 6 Mode shape for preload class C when bearing 1 as PMB

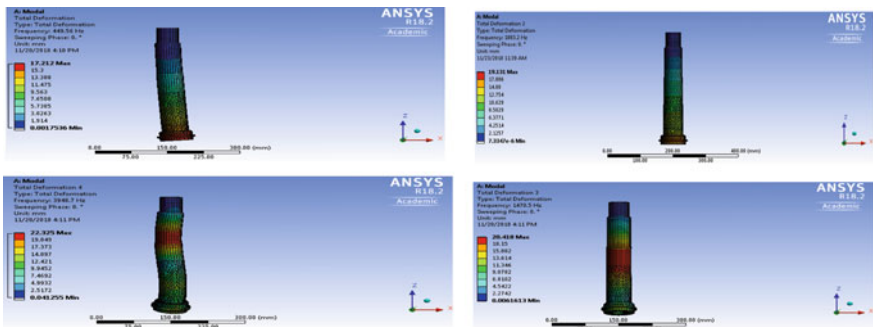


Fig. 7 Mode shape for preload class A when bearing 2 as PMB

The Campbell diagrams for angular contact bearings at different preload classes and PMB at top and bottom locations are shown in Figs. 10, 11, 12, 13, 14 and 15. The critical speeds are obtained by referring the Campbell diagrams plotted as frequency versus speed. The critical speeds (rpm) of corresponding spindle-bearing combinations are given in Table 5. As the critical speeds in all the combinations

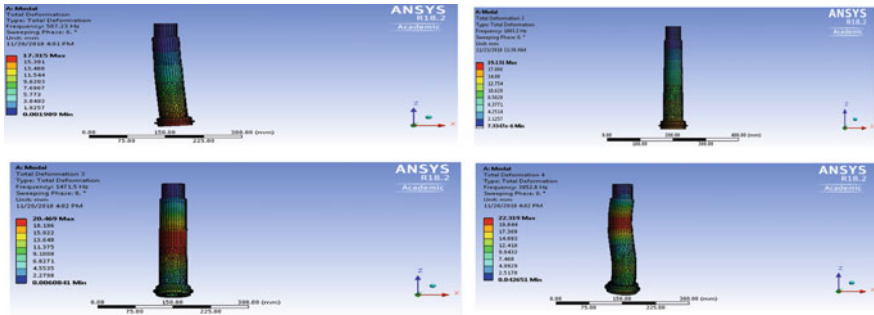


Fig. 8 Mode shape for preload class B when bearing 2 as PMB

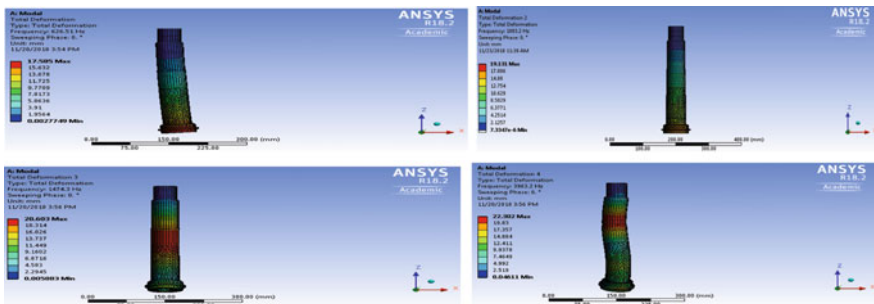


Fig. 9 Mode shape for preload class C when bearing 2 as PMB

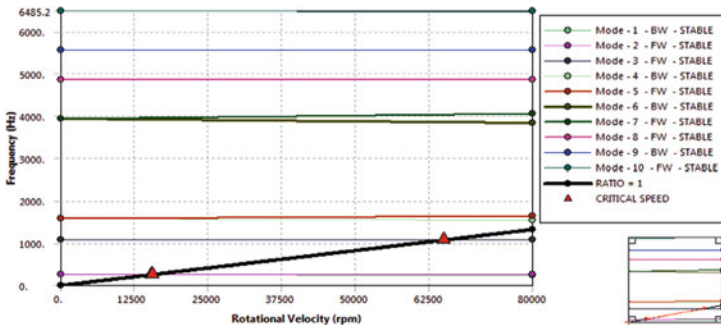


Fig. 10 Campbell diagram for preload class A when bearing 1 as PMB

of bearings are much higher than the operating speed, i.e., 9000 rpm, the system is stable.

Harmonic response analysis is performed to validate the rotordynamic frequencies of spindle by considering the thrust force. Considering the maximum drill bit used in the present VMC as 12 mm and maximum cutting speed as 30 m/min, thrust

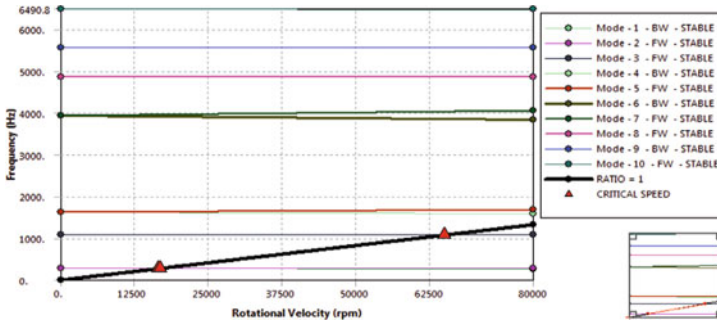


Fig. 11 Campbell diagram for preload class B when bearing 1 as PMB

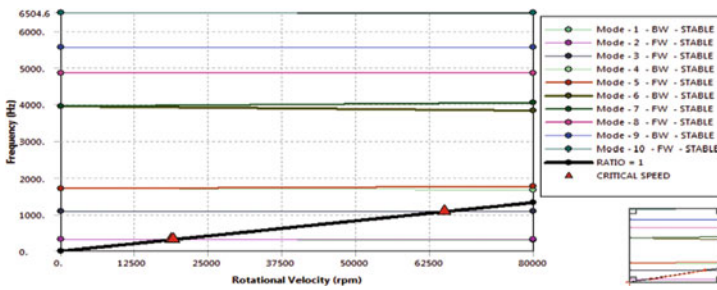


Fig. 12 Campbell diagram for preload class C when bearing 1 as PMB

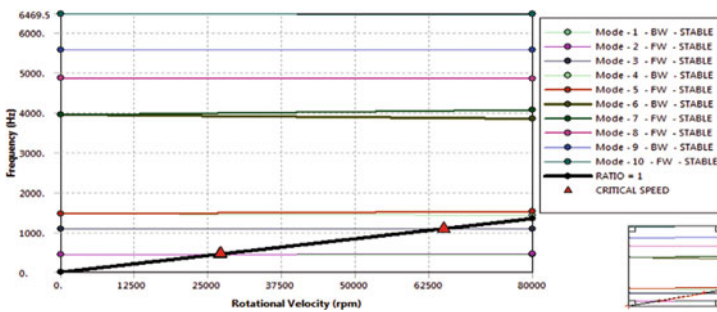


Fig. 13 Campbell diagram for preload class A when bearing 2 as PMB

force of 3492 N is calculated using power and force requirements of drilling [15]. The calculated unbalance mass is applied as center mass of the cutting tool in the harmonic response. For different spindle-bearing combinations, the response function of frequency is measured as shown in Figs. 16, 17, 18, 19, 20 and 21. From analysis, it is observed that peak amplitudes are high when PMB is used near the cutting tool, i.e., as bearing 1, and peak amplitudes are low when PMB is used away from the cutting tool, i.e., as bearing 2.

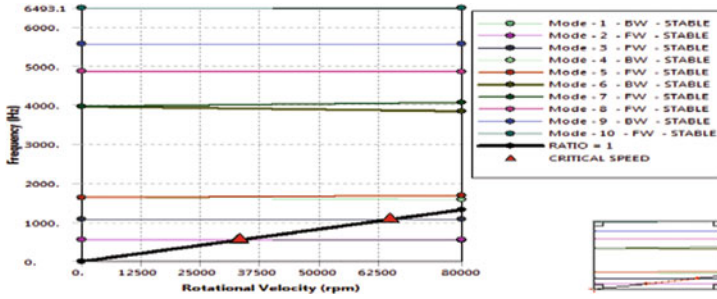


Fig. 14 Campbell diagram for preload class B when bearing 2 as PMB

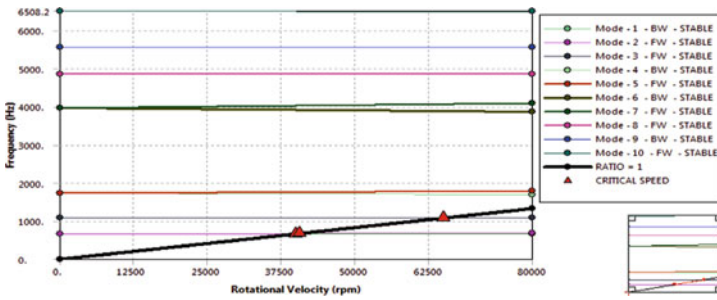


Fig. 15 Campbell diagram for preload class C when bearing 2 as PMB

Table 5 Critical speeds of vertical machining spindle system

Spindle-bearing combinations	First critical speed (rpm)		
	Preload class A	Preload class B	Preload class C
Bearing 1—PMB and bearing 2—ACB	15,510	16,691	18,928
Bearing 1—ACB and bearing 2—PMB	26,998	30,444	37,560
Both the bearings as ACBs	29,301	32,883	40,000

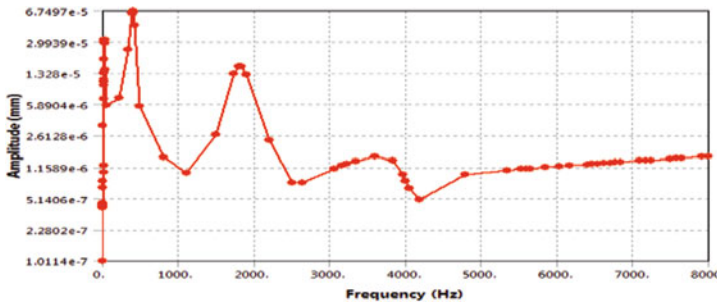


Fig. 16 Frequency versus amplitude unbalance response of preload class A when bearing 1 as PMB

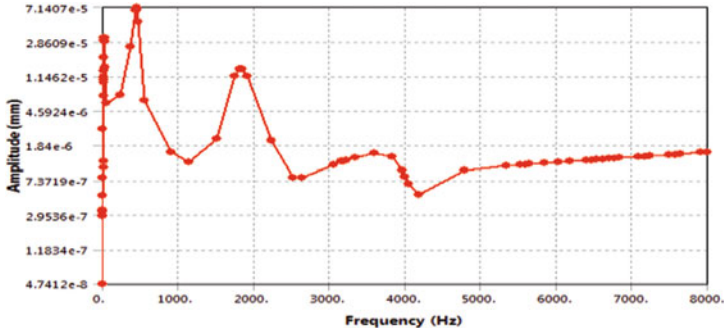


Fig. 17 Frequency versus amplitude unbalance response of preload class B when bearing 1 as PMB

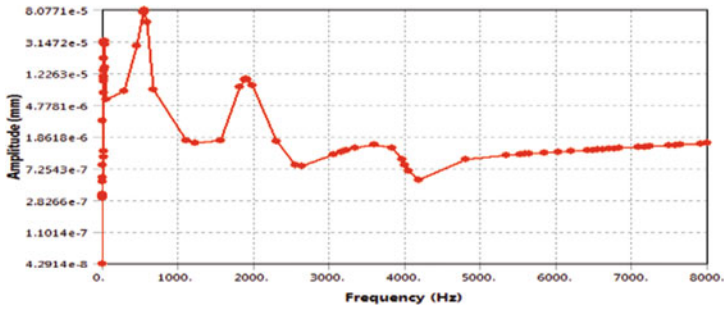


Fig. 18 Frequency versus amplitude unbalance response of preload class C when bearing 1 as PMB

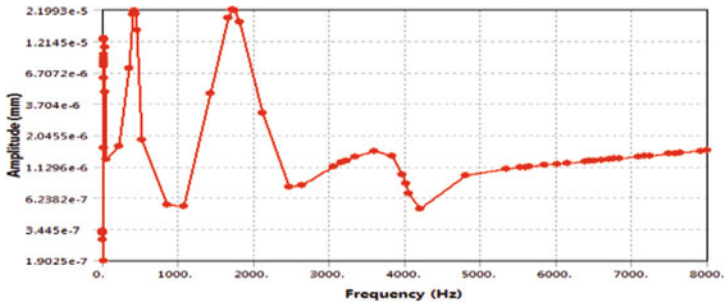


Fig. 19 Frequency versus amplitude unbalance response of preload class A when bearing 2 as PMB

The comparison of harmonic values for different bearing conditions is shown in Fig. 22. The harmonic response frequencies are very low when PMB is used at location 1, and these values are very close when both the bearings are ACBs and bearing 2 as PMB and bearing 1 as ACB.

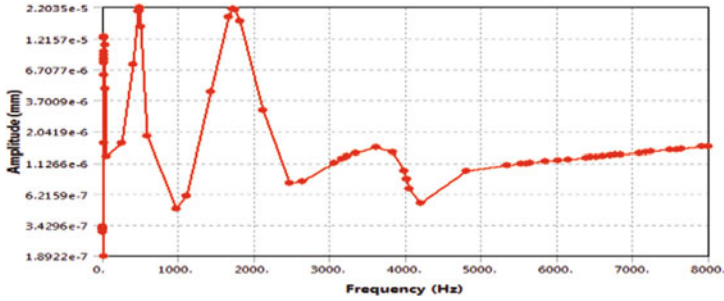


Fig. 20 Frequency versus amplitude unbalance response of preload class B when bearing 2 as PMB

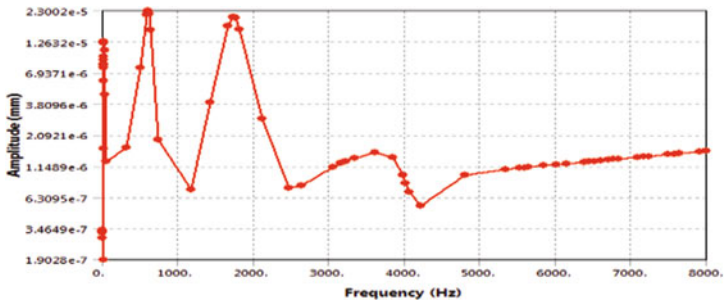


Fig. 21 Frequency versus amplitude unbalance response of preload class C when bearing 2 as PMB

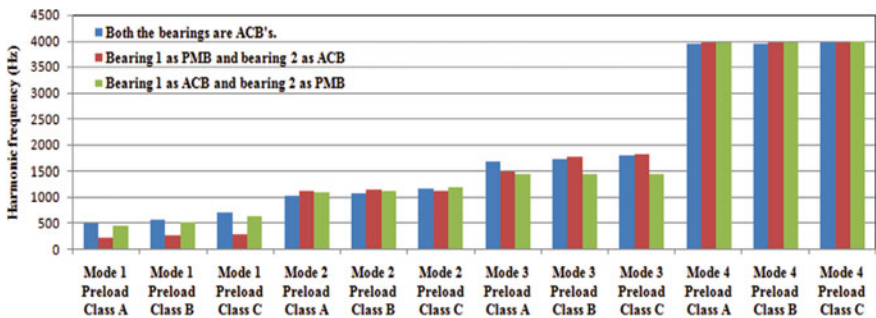


Fig. 22 Comparison of harmonic frequencies of spindle with different spindle-bearing conditions

4 Conclusions

A drill tap VMC spindle system with defined mechanical and geometrical properties supported by HBS is analyzed, and results are evaluated in Ansys Workbench rotor-dynamic module based on finite element method. Based on the study, the following results are drawn.

- The spindle critical speeds with HBS are very close to conventional angular contact bearings when PMB is used away from cutting tool.
- The difference between rotordynamic frequencies and harmonic frequency response modes is negligible when PMB is used away from cutting tool, i.e., at location 2.
- It is observed that the presented concept of hybrid bearing set can be used to support VMC spindles with higher critical speeds.

References

1. Fillion G, Ruel J, Dubois M (2013) Reduced-friction passive magnetic bearing: innovative design and novel characterization technique. *Machines* 1(3):98–115 (2013)
2. Prince O-A, Hu Y, Wu H (2016) Design and Analysis of a Flywheel Supported by Hybrid Magnetic Bearing. *Res J Appl Sci Eng Technol* 12:1–8
3. Bekinal SI, Anil TR, Jana S (2012) Analysis of axially magnetized permanent magnet bearing characteristics. *Prog Electromag Res B* 44:327–343
4. Bekinal SI, Anil TR, Jana S (2013) Analysis of radial magnetized permanent magnet bearing characteristics for five degrees of freedom. *Prog Electro Res B* 52:307–326
5. Bekinal SI, Doddamani M, Jana S (2017) Optimization of axially magnetized stack structured permanent magnet thrust bearing using three-dimensional mathematical model. *J Tribol* 139(3):031101
6. Bekinal SI, Doddamani M, Vanarotti M, Jana S (2018) Generalized optimization procedure for rotational magnetized direction permanent magnet thrust bearing configuration. In: *Proceedings of the Institution of Mechanical Engineers, Part C: Journal of Mechanical Engineering Science*, 0954406218786976
7. Chen WC, Gunter EJ (2007) *Introduction to dynamics of rotor-bearing systems*, Trafford, Victoria, pp 1–469
8. Yanliang X, Yueqin D, Xiuhe W, Yu K (2006) Analysis of hybrid magnetic bearing with a permanent magnet in the rotor by FEM. *IEEE Trans Magn* 42(4):1363–1366
9. Man F et al (2011) Analysis of structure and mechanics feature of axial permanent magnet bearings based on ANSYS. In: *Proceedings of international conference on consumer electronics, communications and networks (CECNet)*, Xian Ning, pp 94–97
10. Bekinal SI, Anil TR, Kulkarni SS et al (2015) Hybrid permanent magnet and foil bearing system for complete passive levitation of rotor. In: *10th International conference on vibration engineering and technology of machinery*, University of Manchester, UK, pp 939–949, 9–11 Sept 2015. *Mechanisms and Machine Science* 23, Springer International Publishing, Switzerland
11. Earnshaw S (1842) On the nature of the molecular forces which regulate the constitution of the luminiferous ether. *Trans Camb Philol Soc* 7:97–112
12. Khairul J, Achmad W, Ismoyo H (2015) Evaluation of dynamic behavior a machine tool spindle system through modal and unbalance response analysis. *World Academy of Science, Engineering and Technology. Int J Ind Manuf Eng* 9(2)
13. Bekinal SI, Jana S (2016) Generalized 3D Mathematical models for force and stiffness in axially, radially and perpendicularly polarized passive magnetic bearings with ‘n’ number of ring pairs. *ASME J Tribol* 138(31105):1–9
14. <http://www.skf.com/in/products/bearings-units-housings/super-precision-bearings/angular-contact-ballbearings/acbb-skf-high-and-super-precision/index.html?designation=7011%20CB>. Accessed on 24 Nov 2018
15. CMTI (2017) *Machine tool design handbook*. TMH

Dynamic Analysis of Three-Dimensional Composite Tube Shafts



Pavani Udatha, A. S. Sekhar , and R. Velmurugan 

Abstract Three-dimensional (3D) composites have good delamination resistance along with high specific stiffness and high specific strength. Composite tube shafts are modeled with different reinforcement architecture such as multi-axial, stitched, knitted, braided, orthogonal woven, interlock and z-pinned. The in-plane elastic properties at different fiber volume fractions of these composites are obtained from the literature. 3D composite tube shafts are modeled with length: 1 m, internal radius: 25 mm and thickness: 4 mm using modified equivalent modulus beam theory formulation. Modal analysis is carried out, and bending natural frequencies are calculated for different 3D composite tube shafts with E-glass, carbon and kevlar fibers and epoxy as matrix materials. The natural frequency reduces with through thickness reinforcement for orthogonal, knitted, z-pinned and stitched composites. Braided composites tube shafts have higher natural frequencies compared to that of other types.

Keywords Bending natural · 3D composites tube shafts · Modified EMBT formulation

P. Udatha (✉) · A. S. Sekhar
Machine Design Section, Department of Mechanical Engineering, Indian Institute of Technology Madras, Chennai 600036, India
e-mail: pavaniudatha@gmail.com

A. S. Sekhar
e-mail: as_sekhar@iitm.ac.in

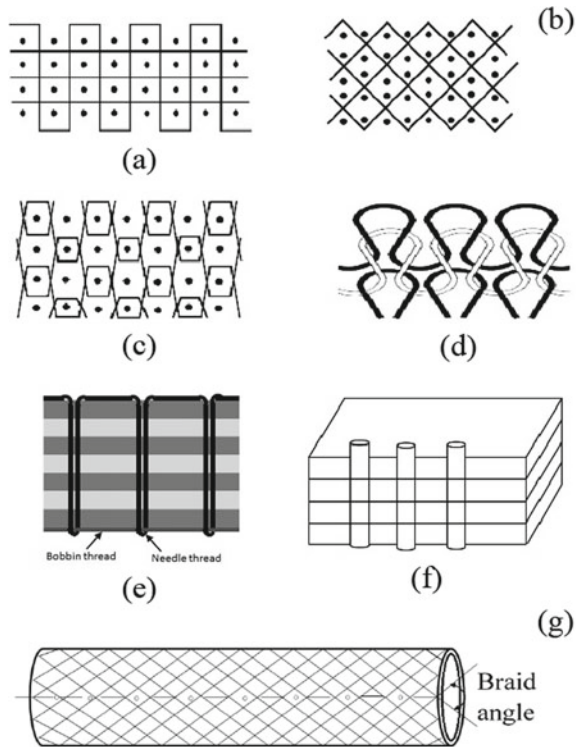
R. Velmurugan
Department of Aerospace Engineering, Indian Institute of Technology Madras, Chennai 600036, India
e-mail: ramanv@iitm.ac.in

P. Udatha
Rajiv Gandhi University of Knowledge Technologies, Nuzvid, Andhra Pradesh 521201, India

1 Introduction

Composites are becoming more efficient materials for present automobile, infrastructure and aerospace industries due to their special features such as high specific stiffness, high specific strength and corrosion resistance. In literature, many studies are carried out on composite tube shafts of UD composite, laminate, etc., for dynamic analysis. On the other side, research on 3D composites is available; however, dynamics of 3D composites tube shafts are not explored in detail. 3D composites are designed by reinforcing the fiber along the thickness direction. The different applications of 3D woven, braided, stitched and knitted composites are explained by Mouritz et al. [1]. Different braided preform structures, techniques and applications of 3D braided composites are studied by Bilisik [2]. 3D composites are classified into mainly orthogonal, braided, knitted and z-pinned based on type of reinforcement architecture as shown in Fig. 1. Gereke and Cherif [3] studied the different numerical models developed for 3D composites. They have observed that 3D composites have high resistance to impact and delamination, and reduction in the in-plane properties compared to 2D composites. A comparative study is carried out on in-plane elastic properties of 3D orthogonal woven, z-pinned and stitched composites [4]. They have observed that the in-plane properties are not much influenced by fiber volume fraction

Fig. 1 Different types of 3D composites. **a** orthogonal, **b** through thickness interlock, **c** layer-to-layer interlock, **d** knitted, **e** stitched, **f** z-pinned and **g** braided tube shaft [1]



and diameter of the fiber. Huang et al. [5] reviewed the recent developments in the mechanical properties, manufacturing processes and applications of layer-to-layer orthogonal, layer-to-layer angle, through thickness orthogonal and through thickness angle woven composites. The different reinforcing techniques and microstructural damages for tufting, z-pinning and stitching are explained by Gnaba et al. [6]. Mohamed and Boganovich [7] did a comparative study on different reinforcement architecture and machines used for preparing 3D non-crimp and 3D interlock weave composites. Microstructure, manufacturing techniques and mechanical properties of z-pinned polymer composites are studied by Mouritz [8]. The z-pinning improves impact damage tolerance, inter-laminar fracture toughness, through thickness properties and bearing strength and reduces the strength, in-plane elastic modulus and fatigue life of the laminate. Steeve and Fleck [9] did numerical and experimental studies for elastic properties of z-pinned composites. They have observed that the addition of pins reduces the in-plane compressive and tensile strength by 30 and 27%, respectively. The decrease in the in-plane properties stiffness is due to formation of voids and misalignment of fiber during the insertion of pins. It is concluded from the literature that 3D composites have advantages over laminates such as high delamination resistance, high through thickness properties, fatigue strength, impact resistance and possibility of complex shapes with reduction in the in-plane properties.

Dynamic analyses of composite tube shafts are performed using layerwise boundary theory (LBT) and equivalent modulus beam theory (EMBT) [10]. EMBT is derived from Timoshenko beam theory with shear deformation and LBT developed from shell theory without considering shear deformation along the thickness direction. EMBT formulation has less mathematical complexity compared to LBT. Modified EMBT is developed by adding bending normal coupling, bending twisting and shear bending coupling to EMBT formulation [11]. The bending natural frequencies for GFRP and CFRP unidirectional composite tube shafts are calculated at different stacking sequences. Gurban [12] observed that improved dynamic performance and reduction in the circumferential deformation of metal and composite hybrid tube shafts. Modal analysis for GFRP, CFRP, GFRP and CFRP hybrid composite tube shafts is performed using ANSYS and compared with the experimental studies [13]. Udatha et al. [14] observed that the addition of CNT to GFRP and CFRP hybrid tube shafts enhances bending natural frequencies. Dynamic analysis of composite tube shafts is performed for UD, laminate and hybrid composite, but the studies on 3D composites are limited. The present study is to obtain the bending natural frequencies for 3D composite tube shafts with different reinforcement architecture.

2 Modified EMBT Formulation

Theoretical formulations for performing dynamic analysis of composite tube shaft are LBT and EMBT by neglecting the deformations along the thickness direction. Modified EMBT is achieved with the addition of coupling effects such as shear normal, bending twisting and normal bending to EMBT formulation. The input elastic

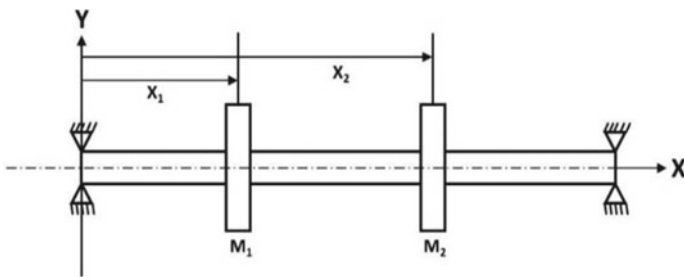


Fig. 2 Coordinate system of rotor [11]

properties for the modal analysis are Poisson's ratio, longitudinal, transverse and shear moduli. A tube shaft with disks M_1 and M_2 is considered with simply supported boundary condition as shown in Fig. 2. The dimensions of the shaft: length ' l ' is 1 m and inner and outer radius ' r_i ' is 25 mm and ' r_o ' is 29 mm. The displacements of the shaft are v , w along Y , Z axes respectively. α and β are the bending slopes in XZ and XY planes respectively, φ is the angle of twist, and whirl velocity is Ω . The strain energy of the shaft is due to axial strain, transverse deformation and torsional deformation. The potential energy of the shaft is given by

$$U = \frac{1}{2} \int_0^l \left\{ C_B \left[\left(\frac{\partial \alpha}{\partial x} \right)^2 + \left(\frac{\partial \beta}{\partial x} \right)^2 \right] + C_S \left[\left(\frac{\partial w}{\partial x} - \alpha \right)^2 + \left(\frac{\partial v}{\partial x} - \beta \right)^2 \right] + C_T \left(\frac{\partial \varphi}{\partial x} \right)^2 \right\} dx \quad (1)$$

Here, C_B , C_S and C_T are bending, shear and torsional stiffness coefficients of the tube shaft, respectively [11]. The thickness of 3D composite is divided into sections. Each section has thickness of 1 mm. The sections are equivalent to layers in the lamina by neglecting the fiber along the thickness direction. The stiffness coefficients are calculated using the in-plane stiffness properties of the 3D composite at each section. The kinetic energy of the shaft is due to mass of the shaft, mass of the disks and gyroscopic effect of the rotor and disks. The kinetic energy of the rotor system is given by:

$$T = \frac{1}{2} \int_0^l \left\{ \rho A [(\dot{w})^2 + (\dot{v})^2] + \rho I [(\dot{\alpha})^2 + (\dot{\beta})^2] + \rho I_P (\dot{\varphi})^2 + 2\rho I_P \omega \dot{\alpha} \dot{\beta} \right\} dx \\ + \frac{1}{2} \sum_{i=1}^{ND} \left\{ M_{Di} [(\dot{w}(x_i))^2 + (\dot{v}(x_i))^2] + I_{Di} [(\dot{\alpha}(x_i))^2 + (\dot{\beta}(x_i))^2] \right. \\ \left. + 2I_{Di} \omega \dot{\alpha}(x_i) \dot{\beta}(x_i) \right\} \quad (2)$$

Here, A is area, I and I_p are lateral and polar area moments of inertia, and ρ is the effective density of shaft. The number of disk is ND , and mass, lateral and

polar mass moments of inertia of the i th disk are M_{Di} , I_{DTi} and I_{Dpi} , respectively. Equation of motion for the rotor system is derived using Lagrangian equation and formulation is coded in MATLAB R2014a [14]. In the present study, only tube shaft is considered without disks mounted on it. The bending natural frequencies for different 3D composite tube shafts for a given geometry are calculated.

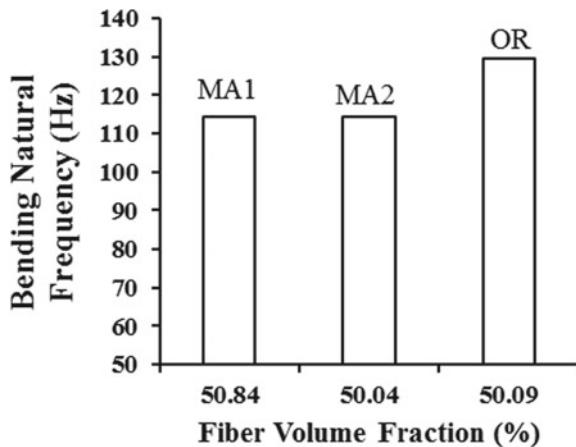
3 Results and Discussion

3D composite tube shafts have advantages over 2D composites tube shafts such as high delamination resistance and improved through thickness direction properties. The dynamic analysis of different 3D composite tube shafts is performed using modified EMBT formulation and presented below:

3.1 Multi-axial Composite Tube Shafts

Labanieh et al. [15] found the in-plane and through thickness properties of 3D multi-axial (MA) and 3D orthogonal composites from experiments. The 3D composites are made of glass fiber along in-plane direction and kevlar fiber along the through thickness direction. It is observed that 3D MA composites have more inter-laminar strength compared to 3D orthogonal composite. The stacking sequences of multi-axial and orthogonal composites are MA 1: $[90/0/45/0/-45/90]_s$, MA 2: $[90/0/45/-45/0/90]_s$ and OR (O3): $[90/0/0/90]_s$ [15]. The natural frequencies of the composites tube shafts modeled from these materials are shown in Fig. 3. From this figure, it can be observed that the natural frequency of 3D orthogonal composite is higher than MA composite for the same volume fraction. This is due to the degradation of in-plane

Fig. 3 Bending natural frequency of MA (MA1, MA2) and orthotropic (OR) composite tube shafts



properties along length direction. Comparing MA1 and MA2, it is observed that the change in the bias layer position is not much affecting the natural frequency.

3.2 Stitched Composite Tube Shafts

Stitched and unstitched composite tube shafts are modeled with four-layered (thickness 3 mm) unstitched UD and MA composites with 3 mm stitch length (US1, US2) and four-layered stitched UD and MA composite with 3 mm stitch length (S1, S4) and 5 mm stitch length (S2, S5) and eight layered (thickness 6 mm) UD composite with 5 mm stitch length (S3, S6). The UD and MA laminates with stacking sequence $[90/450/-45]_{2s}$ with glass/epoxy composites with kevlar fiber along thickness direction and elastic properties are calculated from an analytical micromechanical model based on representative volume element (RVE) [16]. The bending natural frequencies of stitched (S7) and unstitched (US3) carbon/epoxy composites tube shafts using the elastic properties derived from modal analysis experiments and finite element method [17]. The natural frequencies of unstitched and stitched composite tube shafts with fiber volume fraction are presented in Fig. 4. The fiber volume fraction decreases with stitching, and this is due to the formation of voids during stitching. The in-plane properties are reduced due to the formation of voids and results in lower bending natural frequency for UD stitched composites compared to that of UD unstitched composites. The increase in the stitch length improves the natural frequency for UD stitched and deteriorates for MA stitched composites by comparing S1, S2 and S4, S5 from Fig. 4. This is due to increase in the stitch length decreases the fiber content along the thickness direction and improved elastic properties for UD composite compared to MA composite. By comparing S2, S3 and S5, S6, the change in the thickness

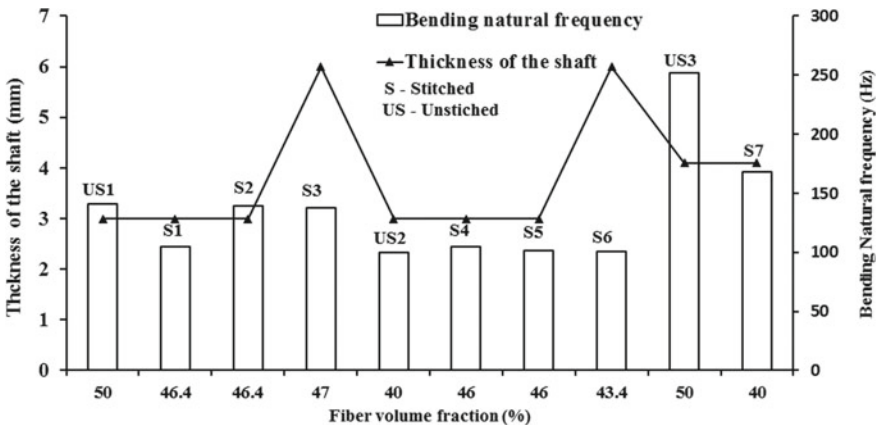
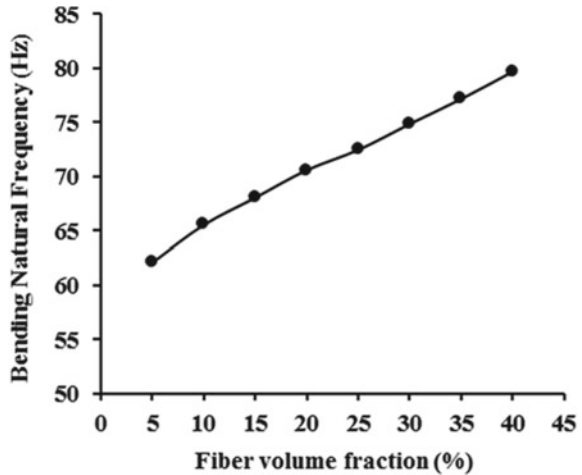


Fig. 4 Variation of bending natural frequency of stitched and unstitched composite tube shafts with fiber volume fraction and thicknesses of the shaft

Fig. 5 Variation of bending natural frequency of glass/epoxy warp knitted composites tube shafts with fiber volume fraction



of laminate is not much affecting the natural frequency for stitched UD composites shafts compared to the reduction for stitched MA composites shafts. This is due to the increase in the thickness increases the fiber content along the length direction and improved elastic properties for UD composite compared to MA composite.

3.3 Knitted Composite Tube Shafts

Huang and Ramakrishna [18] reviewed different micromechanical models for the calculation of strength and stiffness of knitted composites. Hamada et al. [19] developed micromechanical model for knitted composites, and the variation of the elastic and strength properties with increased volume fraction from 5 to 40% for glass/epoxy warp knitted composites is presented. These properties are used in the present study. The variation of natural frequencies of knitted composite tube shafts with fiber volume fraction is presented in Fig. 5. It shows that the increase in the fiber content increases the natural frequency. This is due to improvement in in-plane stiffness properties with fiber content. The natural frequency is increased by 28.3% by increasing the fiber volume fraction from 5 to 40%.

3.4 Braided Composite Tube Shafts

3D and 2D braiding technique gives tube-like structure as shown in Fig. 1g. Jiang et al. [20] presented the relation between the elastic properties of 3D braided carbon/epoxy composites with braid angle at 45% fiber volume fraction using helix geometry model and finite multiphase element method. The variation of bending natural frequency

for 3D braided carbon/epoxy tube shafts with braid angle is presented in Fig. 6. It shows the increase in braid angle decreases the natural frequency up to 35°, and then, the value is more or less constant. Composite tube shafts are modeled with four-step 3D AS4 carbon/epoxy braided composites using the elastic properties from multi-unit cell method [21]. The bending natural frequencies for four-step 3D braided carbon/epoxy composites are calculated and presented in Fig. 7. It shows that the natural frequency is decreasing from 201 to 88 Hz with increase in braid angle from 10° to 50°. It is concluded that 3D braided and four-step 3D braided composites have

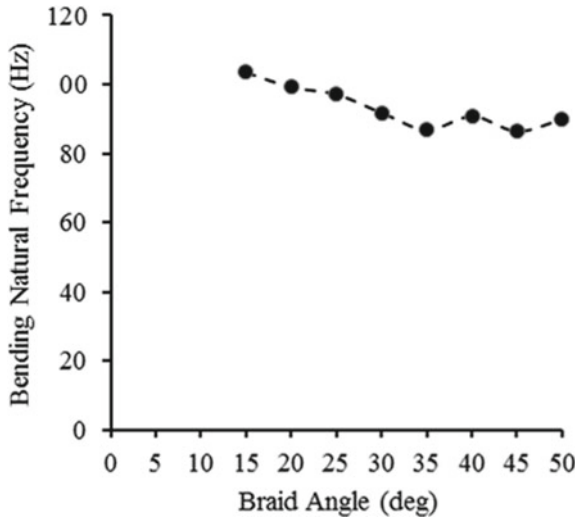


Fig. 6 Effect of braid angle on bending natural frequency for 3D braided carbon/epoxy composite tube shafts at 45% fiber volume fraction

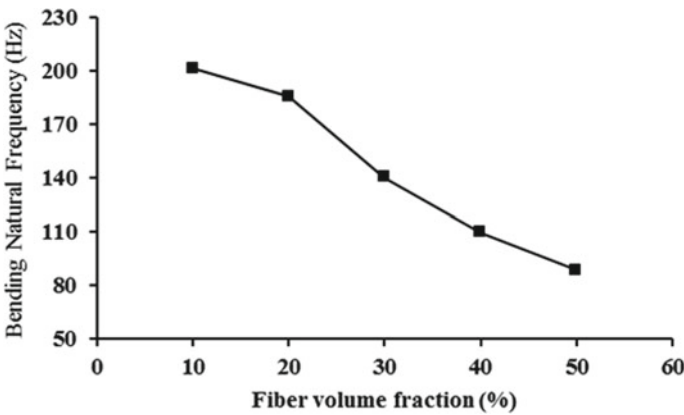


Fig. 7 Variation of bending natural frequency of four-step 3D braided composites tube shafts with fiber volume fraction

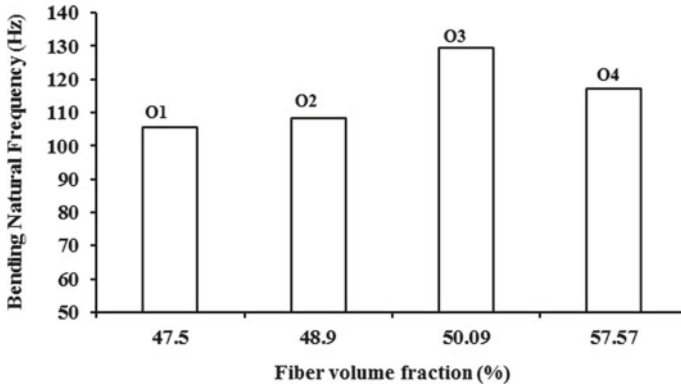


Fig. 8 Variation of bending natural frequency of 3D orthogonal glass/epoxy woven composites tube shafts with fiber volume fraction

increase in natural frequency with decrease braid angle. The increase in the braid angle leads to more inclination of the axis of the shaft with increase in the braid angle as shown in Fig. 1g and results in the reduction in the stiffness along the length direction. The reduction in stiffness reduced the natural frequency.

3.5 Orthogonal Woven Composite Tube Shafts

The 3D orthogonal woven E-glass/epoxy composite tube shafts are modeled at fiber volume fractions 47.5% (O1), 48.9% (O2) [22] and 57.7% (O4) [23] with glass fiber along the third direction, 50.07% (O3) [15] with kevlar fiber along the third direction. The bending natural frequencies of the composite tube shafts are presented in Fig. 8, which shows that the increase in the fiber content increases the natural frequency. The natural frequency is further increased with kevlar fiber instead of glass fiber reinforcement along the thickness direction with glass fiber in the in-plane direction. This can be observed by comparing O3 with O1, O2 and O4.

3.6 Interlock Composite Tube Shafts

Naik et al. [24] developed an analytical model based on two-level discretization of representative unit cell for 3D interlock composites. They have predicted the elastic and strength properties with one fiber and two fibers reinforcement along the thickness direction for layer-to-layer angle interlock woven (LLAW-1, LLAW-2), through thickness angle interlock woven (TTAW-1, TTAW-2), layer-to-layer orthogonal woven (LLOW-1, LLOW-2) and through thickness orthogonal woven (TTAW-1, TTAW-2) carbon/epoxy composites. The natural frequencies are calculated for 3D

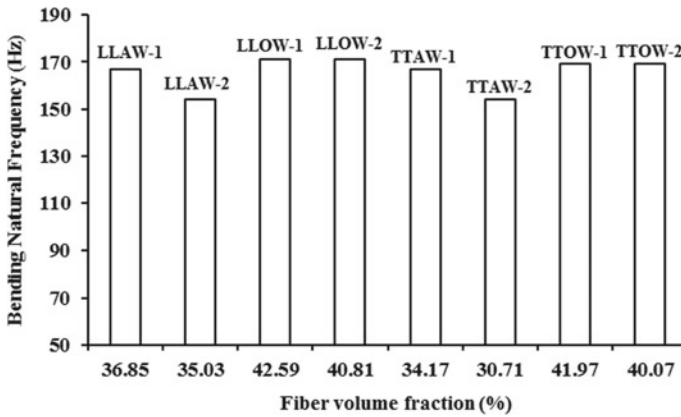


Fig. 9 Variation of bending natural frequency of 3D interlock woven composite tube shafts with fiber volume fraction

interlock and orthogonal woven carbon/epoxy composite tube shafts and presented in Fig. 9. The orthogonal woven composites have higher natural frequency and higher fiber content compared to angle woven composites for both layer-to-layer (LL) and through thickness (TT). By increasing the reinforcement from one fiber to two fibers along the thickness direction, natural frequency decreased for angle woven in comparison with LLAW-1, 2 and TTAW-1, 2. And the effect is negligible for orthogonal woven by comparing LLOW-1, 2 and TTOW-1, 2. This is due to increase in the void content and reduction in the fiber content for angle woven composite compared to orthogonal woven composite.

3.7 *z*-Pinned Composite Tube Shafts

Grassi et al. [25] predicted the in-plane stiffness properties of *z*-pinned carbon/epoxy composites with different stacking sequence UD $[0]_4$, angle-ply $[\pm 45]_s$, cross-ply $[0/90]_s$ and quasi-isotropic $[+45, 90, -45, 0]_s$. The addition 2% of *z*-pins increases the through thickness modulus by 22–35% with reduction in the in-plane properties. The natural frequencies of the *z*-pinned carbon/epoxy composite tube shafts without and with pins are presented in Fig. 10. The increasing order natural frequency of composite tube shafts is UD, cross-ply, quasi-isotropic and angle-ply laminates for both stitched and unstitched composite tube shafts. The natural frequencies decrease from 3 to 5% with addition of pins. This is due to the formation of dislocation of fiber while inserting the pins and reduction in the in-plane properties.

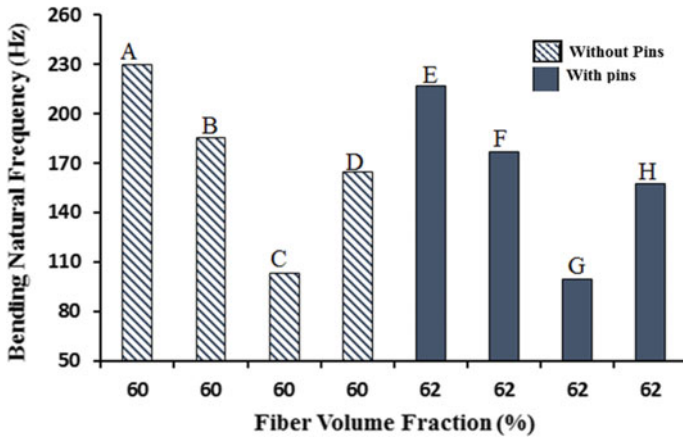


Fig. 10 Bending natural frequency of UD (A, E), cross-ply (B, F), angle-ply (C, G) and quasi-isotropic (D, H) composites tube shafts with and without z-pins

4 Conclusions

Dynamic analyses of 3D composite tube shafts are performed using modified EMBT formulation. The bending natural frequencies of stitched, knitted, braided, orthogonal woven, interlock and z-pinned are calculated using the in-plane properties from the literature. The decreasing order of the natural frequency range is braided, knitted, z-pinned, 3D orthotropic and layer-to-layer interlock composites for the same geometry. The range of natural frequencies of 3D braided composite tube shafts is higher compared to the other 3D configurations. This is due to orienting the more fiber along the length direction results improved properties compared to the other types. For braided composites, the natural frequencies are higher at lower braid angle. The lessening in the natural frequency observed for orthogonal, knitted, z-pinned and stitched composites to without reinforcement (UD and 2D composites). This is due to formation of voids and dislocation of in-plane fibers during reinforcement along the thickness direction. UD and 2D composite tube shafts experience delamination and cause failure of tube shafts while transmitting torque. 3D composite tube shafts are having higher delamination resistance. From the present study, braided composites with lower braid angle can be one explored for optimum selection for power transmission. However, further study has to be carried out on dynamic analysis of 3D composites by taking through thickness properties into consideration and comparison of 3D composites with 2D composites

References

1. Mouritz AP, Bannister MK, Falzon PJ, Leong KH (1999) Review of applications for advanced three-dimensional fibre textile composites. *Compos A Appl Sci Manuf* 30(12):1445–1461
2. Bilisik K (2012) Multiaxis three-dimensional weaving for composites: a review. *Text Res J* 82(7):725–743. <https://doi.org/10.1177/0040517511435013>
3. Gereke T, Cherif C (2019) A review of numerical models for 3D woven composite reinforcements. *Compos Struct* 209:60–66
4. Mouritz AP, Cox BN (2010) A mechanistic interpretation of the comparative in-plane mechanical properties of 3D woven, stitched and pinned composites. *Compos A Appl Sci Manuf* 41(6):709–728
5. Huang T, Wan Y, Wang G (2017) A review of the mechanical properties of a 3D Woven composite and its applications. *Polym-Plast Technol Eng.* <https://doi.org/10.1080/03602559.2017.134485>
6. Gnaba I, Legrand X, Wang P, Soulat D (2018) Through-the-thickness reinforcement for composite structures: a review. *J Indus Textil* 1–26. <https://doi.org/10.1177/1528083718772299>
7. Mohamed M, Bogdanovich AE (2009) Comparative analysis of different 3D weaving processes, machines and products. In: *Proceedings of 17th international conference on composite materials (ICCM-17)*, Edinburgh, CD edition
8. Mouritz AP (2007) Review of z-pinned composite laminates. *Compos A Appl Sci Manuf* 38(12):2383–2397
9. Steeves CA, Fleck NA (2006) In-plane properties of composite laminates with through-thickness pin reinforcement. *Int J Solids Struct* 43(10):3197–3212
10. Singh SP, Gupta K (1994) Free damped flexural vibration analysis of composite cylindrical tubes using beam and shell theories. *J Sound Vib* 172(2):171–190
11. Gubran HBH, Gupta K (2005) The effect of stacking sequence and coupling mechanisms on the natural frequencies of composite shafts. *J Sound Vib* 282:231–248
12. Gubran HBH (2005) Dynamics of hybrid shafts. *Mech Res Commun* 32:368–374
13. Alwan V, Gupta A, Sekhar AS, Velmurugan R (2010) Dynamic analysis of shafts of composite materials. *J Reinf Plast Compos* 29(22):3364–3379
14. Udatha P, Sekhar AS, Velmurugan R, The effect of CNT to enhance the dynamic properties of hybrid composite tube shafts. *Mech Adv Mater Struct.* <https://doi.org/10.1080/15376494.2018.1534172>
15. Labanieh AR, Liu Y, Vasiukov D, Soulat D, Panier S (2017) Influence of off-axis in-plane yarns on the mechanical properties of 3D composites. *Compos A Appl Sci Manuf* 98:45–57
16. Chun HC, Kim HW, Byun JH (2006) Effects of through-the-thickness stitches on the elastic behavior of multi-axial warp knit fabric composites. *Compos Struct* 74(4):484–494
17. Li N, Tahar NB, Aboura Z, Khellil K (2016) A dynamic analysis approach for identifying the elastic properties of unstitched and stitched composite plates. *Compos Struct* 152:959–968
18. Huang ZM, Ramakrishna S (2000) Micromechanical modeling approaches for the stiffness and strength of knitted fabric composites: a review and comparative study. *Compos A Appl Sci Manuf* 31:479–501
19. Hamada H, Ramakrishna S, Huang ZM (1999) 3-D textile reinforcements in composite materials—knitted fabric composites. Woodhead Publishing Ltd
20. Jiang L, Zeng T, Yan S, Fang D (2013) Predicting mechanical properties of 3D braided composites using a helix geometry model. *Compos Struct* 100:511–516
21. Mahmood S, Sadegh S (2012) A new analytical model for calculation of stiffness of three-dimensional four-directional braided composites. *Composite Structures*
22. Lomov SV, Bogdanovich AE, Ivanov DS, Mungalov D, Karahan M, Verpoest I (2009) A comparative study of tensile properties of non-crimp 3D orthogonal weave and multi-layer plain weave E-glass composites. Part 1: Materials, methods and principal results. *Compos Part A: Appl Sci Manuf* 40(8):1134–1143

23. Tan P, Tong L, Steven GP (2001) Mechanical behavior for 3-D orthogonal woven E-Glass/epoxy composites. *J Reinf Plast Compos* 20(4):274–303
24. Naik NK, Durga Prasad S, Thuruthimattam JB, Stress and failure analysis of 3D orthogonal interlock woven composites. *J Reinf Plast Compos* 20(17):1485–1523
25. Grassi M, Zhang M, Meo M (2002) Prediction of stiffness and stresses in z-fibre reinforced composite laminates. *Compos Part A: Appl Sci Manuf* 33(12):1653–1664

Analysis of Rotor Supported in Double-Layer Porous Journal Bearing with Gyroscopic Effects



C. Shravankumar , K. Jegadeesan, and T. V. V. L. N. Rao 

Abstract In this paper, a numerical analysis on the dynamics of a multi-degree of freedom shaft–rotor, supported on bearings, is presented. The system is a shaft with multiple rotor discs attached to it and supported on double-layer porous journal bearings. The system is modelled using finite element methods. Euler-Bernoulli beam element theory is used for modelling the shaft. The discs are considered as rigid. The support bearings are modelled based on linear spring elements for stiffness and linear damping elements for viscous damping coefficients. The rotor dynamic model of the system is analysed by incorporating the gyroscopic effects due to the precession of the offset discs and the bearing stiffness and damping anisotropy. The fluid flow in double-layer porous film is analysed using Brinkman equations to consider lubricant additives influences. The pressure gradients with respect to linearized perturbation of displacements and velocities under dynamic conditions are derived using Reynolds modified equation for Ocvirk (short) bearing. The dynamic linear and cross-coupled coefficients (stiffness and damping) dependent on speed are calculated using dynamic pressure gradients for the double-layer porous journal bearings. The system is represented in reduced order state-space form, and eigen value problem is solved to calculate its whirl frequencies. The rotor system critical speeds are obtained by plotting the Campbell diagram. This paper provides the basis for rotor system design with support bearings, representative of a multi-stage centrifugal pump. The design helps to identify and prevent rotor vibrations.

Keywords Shaft–rotor-bearing system · Dynamic coefficients · Campbell diagram · Critical speeds

C. Shravankumar (✉) · K. Jegadeesan · T. V. V. L. N. Rao
Department of Mechanical Engineering, SRM Institute of Science and Technology,
Kattankulathur 603203, India
e-mail: shravanc@srmist.edu.in

© Springer Nature Singapore Pte Ltd. 2021
J. S. Rao et al. (eds.), *Proceedings of the 6th National Symposium on Rotor Dynamics*, Lecture Notes in Mechanical Engineering,
https://doi.org/10.1007/978-981-15-5701-9_6

Nomenclature

C	Damping
c_{ij}, C_{ij}	Damping coefficients, Ns/m; $C_{ij}, c_{ij}C^3/\eta R^3 L$; for $i = x, y$
C_{ijl}, C_{ijh}	Nondimensional damping coefficients of double-layer porous and homogeneous layer
C	Radial clearance, m
E	Young's modulus of the shaft material
g	Gyroscopic moment
h, H	Film thickness, m; $H = h/C$
I_a	Shaft area moment of inertia
I_d	Mass moment of inertia of disc
I_{pd}	Polar mass moment of inertia of disc
I_p	Shaft polar mass moment of inertia
k	Stiffness
k_i	Permeability of layer in porous regions, m^2 ; $K_i = k_i/h^2$; for $i = 1, 2$
k_{ij}, K_{ij}	Stiffness coefficients evaluated at equilibrium position, N/m; $K_{ij} = k_{ij}C^3/\eta\omega R^3 L$; for $i = x, y$
K_{ijl}, K_{ijh}	Nondimensional stiffness coefficients of double-layer porous and homogeneous layer
l	Length of the shaft element
l'	Shaft length
M	Moments
m_d	Mass of discs
r	Shaft radius
R	Journal radius, m
w	Static load capacity, N; $W = wC^2/\eta\omega R^3 L$
W_l, W_h	Double porous and homogeneous layer nondimensional load capacity
Y, x	Vertical and horizontal coordinates, m; $Y = y/C, X = x/C$
\dot{Y}, \dot{X}	Journal centre velocity (nondimensional) in y and x direction
ρ_s	Density of shaft material
ε	Journal bearing eccentricity ratio
γ_i	Porous layer thickness ratio; $\gamma_i = i/h$; for $i = 1, 2$
η	Fluid dynamic viscosity, Ns/m ²
μ	Mass of the shaft per unit length
θ	Coordinate from maximum film thickness
Θ	Coordinate from load line
ϕ	Attitude angle
ω	Shaft spin frequency

Subscripts

s Shaft

Superscript

e Element

1 Introduction

Turbomachinery system often consists of several offset mounted rotors on a shaft, which in turn is supported on bearings. During run-up and run-down, the system has to cross through critical speeds. Hence, rotor dynamic analysis of such systems becomes a preliminary design requirement.

Ruhl and Booker [1] developed a finite element analysis of a turbo rotor system. The system has distributed mass and stiffness parameters. Consistent matrices are employed for the finite element model. Free and forced vibration rotor system responses are obtained. A shaft supported on hydrodynamic bearings is investigated by Kim and Lee [2]. The finite element model consists of five elements of equal length. Rao et al. [3] performed rotor dynamic analysis of a synchronous generator consisting of flywheels, armature, core, fan and a rotor shaft using ANSYS environment. The bearing oil film is modelled with spring as well as damping coefficients. The mass unbalance of the rotor system is modelled in accordance with ISO1940 standards. Modal analysis and rotor unbalance calculations are performed. Rotor orbit whirl plots and Campbell diagram for the rotor system are presented. Shrivankumar and Tiwari [4] presented a comparative analysis of the effects of gyroscopic moments on a cantilever rotor system, using different numerical methods. The gyroscopic effect on simple rotor systems is discussed. Hsu [5] performed experimental and numerical studies on a turbomolecular rotor pump. The system is a flexible rotor-bearing system with discrete discs and bearings. The mass and stiffness properties are distributed. Gyroscopic moments due to disc precession are considered. He et al. [6] analysed the natural frequencies, critical speeds and unbalance responses for a multi-stage centrifugal pump. It is observed that the support stiffness has a large influence on the critical speed of rigid modes, while having less influence on the critical speeds of the flexible modes.

Lund and Thomsen [7] and Rao [8] presented calculation methodology of stiffness and damping coefficients using linearized perturbation method. Lin and Hwang [9] evaluated porous bearings stability. The hydrodynamic journal bearings performance considering the lubricant additive effects is studied using porous and couple stress media models [10, 11], respectively. Rao et al. [12] evaluated improvement in static

characteristics of a double-layer porous bearing. Rao et al. [13] presented static and stability coefficients of double-layer porous (or layers of surface film topped with porous film) to the conventional journal bearing. Stability characteristics of porous layered journal bearings are enhanced by lubricant additives properties.

2 Finite Element Modelling

A flexible shaft-bearing system (multi-degree of freedom) with rigid discs modelled using finite element method is presented. A schematic diagram of the shaft-rotor-bearing system, along with finite element discretization is shown in Fig. 1.

The primary assumptions for modelling include a flexible shaft, rigid discs and flexible bearing supports. The shaft-rotor geometry is axisymmetric. The properties considered for the shaft include distributed mass and stiffness. The disc properties are concentrated mass, diametric moment of inertia and polar moment of inertia. Four degrees of freedom (DoFs) are considered for the model, two translational DoFs along the two transverse directions and two rotational DoFs about the same. Gyroscopic effects due to shaft and disc mass are considered. No effects of unbalance mass or misalignment between shaft and bearings are considered. Four rigid discs are mounted along the length of the shaft, and it is assumed for simplicity that centres of gravity of the rigid discs coincide with that of the elastic shaft. Figure 2a shows the beam element. The shaft element is a two-node beam element with four degrees of freedom at each node.

There are two linear displacements u_x and u_y (along the X and Y axes) and two rotational displacements θ_y and θ_x (about the X and Y axes). The elements have isotropy, and they are also symmetric about the Z axis. Because of the symmetry of the shaft elements, the same mass matrices and same stiffness matrices result in the two transverse planes XZ and YZ . The rigid disc element is shown in Fig. 2b.

The Brinkman equations are used to model fluid flow in the double porous region. These dynamic coefficients correspond to a double-layer porous hydrodynamic journal bearing (Fig. 3). The stiffness and damping coefficients are represented using linear spring and damping elements in Fig. 3b-c.

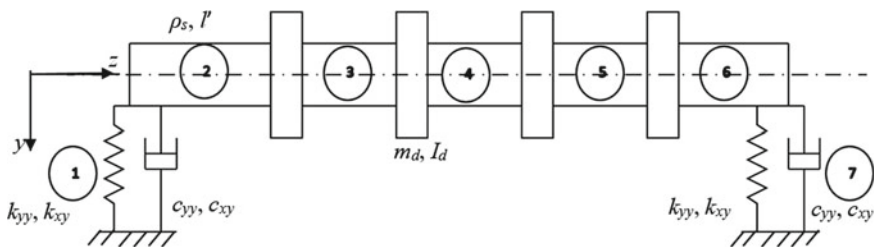


Fig. 1 Rotor system model and discretization into finite elements in yz transverse plane

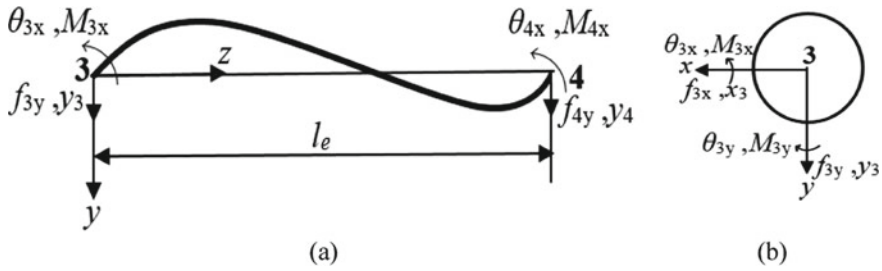


Fig. 2 Conventions (positive) for nodal displacements, rotations, forces and moments. **a** beam element and **b** rigid disc element

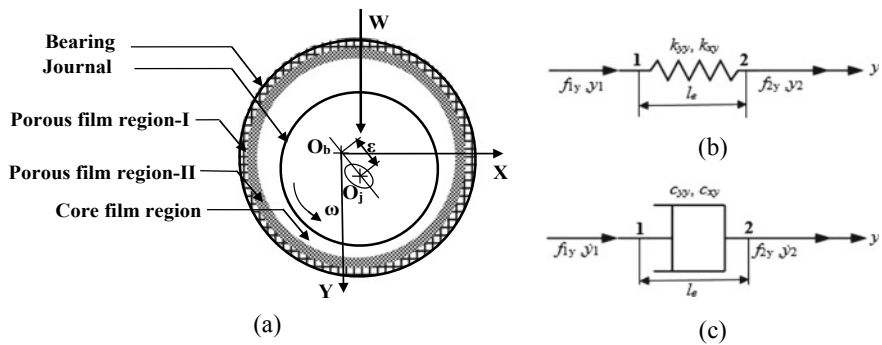


Fig. 3 **a** Double-layer porous journal bearing, **b** Linear spring element with positive conventions for nodal displacements and forces and **c** Linear damping element with positive conventions for nodal velocities and forces

2.1 Shaft Model

Euler-Bernoulli theory of bending is used for modelling the shaft finite element. Mass and stiffness properties of the shaft element are considered, and its internal damping is neglected. Also, the gyroscopic moments due to the rotation of elemental shaft masses about the bearing centre lines are considered. The equations of motion for the shaft element are in Eq. (1).

$$[m_s^e]\{\ddot{u}_s^e\} + [g_s^e]\{\dot{u}_s^e\} + [k_s^e]\{u_s^e\} = \{f_s^e\}. \tag{1}$$

$[m_s^e]$ is the elemental mass matrix, obtained as the summation of the mass matrices corresponding to translation as well as rotation motion, $[g_s^e]$ is the elemental gyroscopic matrix, $[k_s^e]$ is the elemental stiffness matrix, displacement vector is $\{u_s^e\} = [x^i \ y^i \ \theta_y^i \ \theta_x^i \ x^{i+1} \ y^{i+1} \ \theta_y^{i+1} \ \theta_x^{i+1}]$, subscripts i and $i + 1$ are the position of the two nodes along Z axis, and $\{f_s^e\}$ is the force vector.

2.2 Rigid Disc Model

The discs are modelled as point masses. Also, gyroscopic moments in two transverse planes exist due to the offset position of these discs on the shaft, which results in a change of angular momentum and therefore gyroscopic moment. Any external forces acting on the discs, such as due to unbalance, are also considered.

$$[m_d^e]\{\ddot{u}_d^e\} + [g_d^e]\{\dot{u}_d^e\} = \{f_d^e\}. \quad (2)$$

$[m_d^e]$ is the elemental mass matrix, $[g_d^e]$ is the elemental gyroscopic matrix for the rigid disc, and $\{f_d^e\}$ is the elemental force vector acting on a disc. Displacement vector is $\{u_d^e\} = [x^j \ y^j \ \theta_y^j \ \theta_x^j]^T$.

2.3 Double-Layer Porous Journal Bearing Model

The double-layer porous journal bearings are modelled using a total of eight dynamic coefficients which are used at each shaft end to model the fluid film bearings. Using the principle of superposition

$$f_x = k_{xx}x + k_{xy}y + c_{xx}\dot{x} + c_{xy}\dot{y}, \quad f_y = k_{yx}x + k_{yy}y + c_{yx}\dot{x} + c_{yy}\dot{y} \quad (3)$$

The load capacity coefficient ratio (C_w) and eight dynamic coefficients for double-layer porous journal bearing [12, 13] are obtained from the stiffness coefficient ratio (C_k) and damping coefficient ratio (C_c) as

$$C_w = w_{ijl}/w_{ijh} = \Delta_s/\Delta_p, \quad C_k = k_{ijl}/k_{ijh} = \Delta_s/\Delta_p, \\ C_c = c_{ijl}/c_{ijh} = 1/\Delta_p \quad (4)$$

The journal eccentricity ratio is obtained from Newton–Raphson iterative procedure for the given bearing parameters and operating conditions.

2.4 Boundary Conditions and Assembly

The system shown (Fig. 1) is discretized into seven numbers of elements with four degrees of freedom at each node. This gives the size of the assembled matrices are 28×28 . Then, the fixed boundary conditions are considered at one end of the spring and damper elements which represent the two journal bearings. With the application of these boundary conditions, the size of the assembled matrices reduces to 24×24 . In matrix form, the assembled system equations of motion are represented as in

Eq. (5).

$$[M]\{\ddot{U}\} + [G]\{\dot{U}\} + [C]\{\dot{U}\} + [K]\{U\} = \{F\}.. \quad (5)$$

$[M]$, $[G]$, $[C]$ and $[K]$ are the assembled mass, gyroscopic, damping and stiffness matrices of the rotor-bearing system.

2.5 Rotor Dynamic Analysis

Equation (5) is solved as an eigen value problem to obtain the whirl frequencies. The homogenous equation of Eq. (5) is reduced into first-order differential equations of size $2n$ times. This is called as state-space reduction and is given in Eq. (6). The eigen values and eigen vectors of Eq. (6) are calculated using QZ algorithm or Cholesky factorization in MATLAB environment.

$$\begin{Bmatrix} \dot{u} \\ \dot{v} \end{Bmatrix} = \begin{bmatrix} [0] & [I] \\ -[[M^{-1}][K]] & -[[M^{-1}][C + \omega G]] \end{bmatrix} \begin{Bmatrix} u \\ v \end{Bmatrix}. \quad (6)$$

The eigen values obtained are complex quantities, because of the viscous damping. These eigen values can be used to identify the damped critical speeds of the rotor system.

3 Results and Discussion

In this section, numerical simulation is carried out to obtain the following: the dynamic coefficients of the bearing as a function of the rotor spin frequency; whirl frequencies of the system. Table 1 gives the various geometric and material properties of the shaft–discs–bearings, required to carry out the numerical analysis.

The bearing stiffness and damping with spin speed of the rotor are shown in Fig. 4a–b. It can be observed from Fig. 4b, the stiffness coefficient k_{yx} (cross-coupled) is negative for the entire speed range.

Figure 5 shows the Campbell diagram for the rotor-bearing system under study. The natural frequencies in the Campbell diagram are split into two: a slow one where the whirl is opposed to the spin, and a fast one where their directions are the same. The split in the natural frequencies indicates the forward whirl and reverse whirl. In this system, this split is due to the gyroscopic effect as well the asymmetric nature of the bearing stiffness coefficients in the two transverse directions. Each rotor mode consists of forward precession and reverse precession. The $1 \times$ straight line in Fig. 6 represents the synchronous frequency, which is representative of any mass unbalance exciting the rotor.

Table 1 Geometric and material properties of the rotor system with double porous layer bearing

Symbol	Value	Symbol	Value
l'	1.5 m	L/D	0.5
r	12.5 mm	K_1	10^{-4}
ρ_s	7810 kg/m ³	K_2	10^{-5}
I_p	0.0048 kg m ²	γ_1	0.08
I_a	3.067×10^{-7} m ⁴	γ_2	0.02
E	2×10^{11} N/m ²	η	0.02 Pas
m_d	10 kg	R	0.025 m
r_d	60 mm	C	0.025 mm
I_d	0.009 kg m ²	ω	10–300 rad/s
I_{pd}	0.018 kg m ²		

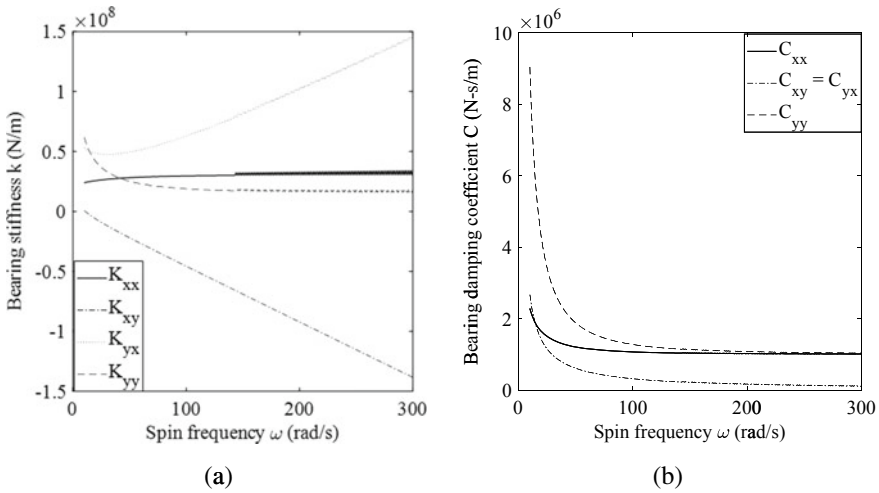


Fig. 4 **a** Bearing stiffness coefficients versus spin speed and **b** Bearing damping coefficients versus spin speed

The critical speeds of the rotor system for synchronous whirl condition are given by $\nu = \omega$. These critical speeds can be used in the design of the rotor to decide the operating speed range as well as the vibration prone spin speeds. Figure 7 shows variation of system damping with spin frequency for rotors supported on double-layer porous journal bearings. The negative real part of the lowest eigenvalues is plotted versus spin frequency. The rotor system on double porous bearings (Fig. 7a–b) is stable over the entire spin frequency range.

Fig. 5 Campbell diagram in the operating speed range of 10–300 rad/s

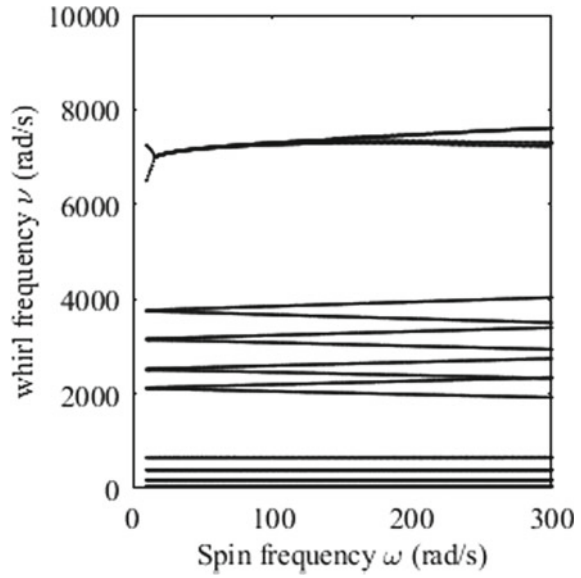
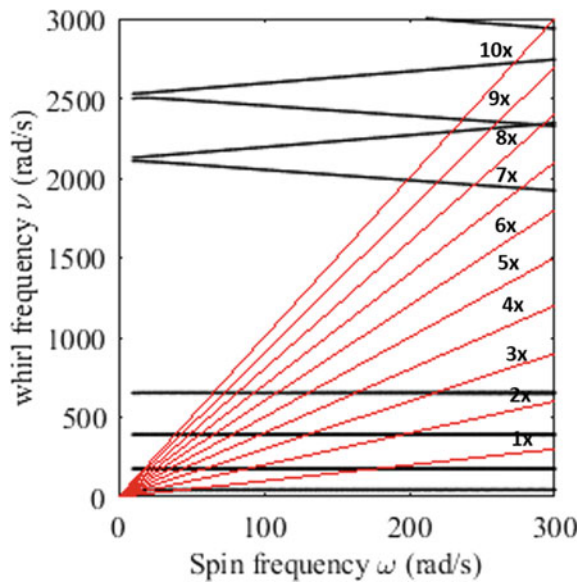


Fig. 6 Intersection of forward and reverse precession modes with order lines ranging from 1x to 10x for calculation of critical speeds



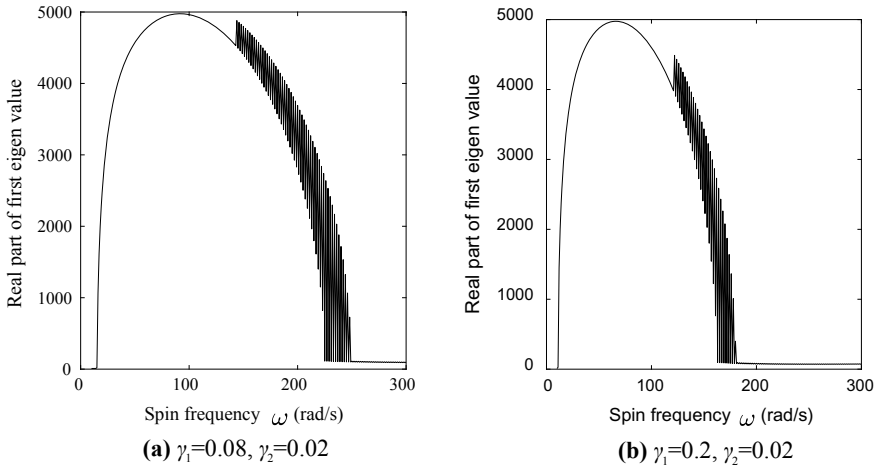


Fig. 7 Variation of system damping with spin frequency. **a** $\gamma_1 = 0.08$, $\gamma_2 = 0.02$. **b** $\gamma_1 = 0.2$, $\gamma_2 = 0.02$

4 Conclusions

This study presents finite element method modelling of dynamics of a shaft–rotor system, with multiple rotor discs and supported on double-layer porous journal bearings. The whirl frequencies and system damping are evaluated for a lubricant film double porous layer with porous layer II (low permeability) over porous layer I (bearing surface adsorbent high permeability layer). The whirl frequencies obtained for various spin speeds using speed dependent eight dynamic coefficients of double porous layer journal bearing are plotted as a Campbell diagram. The design of a rotor system of a multi-stage centrifugal pump with support bearings helps to identify the operating speed range as well as prevent the rotor vibration spin speeds.

Acknowledgements The authors appreciate the support of SRM Institute of Science and Technology.

References

1. Ruhl RL, Booker JF (1972) A finite element model for distributed parameter turborotor systems. *J Eng Indu* 94:126–132
2. Kim YD, Lee CW (1986) Finite element analysis of rotor bearing systems using a modal transformation matrix. *J Sound Vib* 111:441–456
3. Rao JS, Gupta V, Khullar P, Srinivas D (2015) Prediction of rotor dynamic behavior of synchronous generators. In: *Proceedings of the 9th IFTOMM International Conference on Rotor Dynamics, Mechanisms and Machine Science*, vol 21, pp 1797–1807

4. Shrivankumar C, Tiwari R (2011) Gyroscopic effects on a cantilever rotor system—a comparative analysis. National Symposium on Rotor Dynamics. NSRD-2011 Indian Institute of Technology Madras
5. Hsu C (2015) Experimental and performance analysis of a turbomolecular pump rotor system. Vacuum 1–14
6. He H, Zhang B, Pan G, Zhao G (2016) Rotor dynamics of multistage centrifugal pump. In: Proceedings of the 24th International conference on nuclear engineering. ICONE24-60929:1–8
7. Lund JW, Thomsen KK (1978) A calculation method and data for the dynamic coefficients of oil-lubricated journal bearings. Topics in Fluid Film Bearing and Rotor Bearing System Design and Optimization. ASME, New York, pp 1–28
8. Rao JS (2009) Rotor dynamics. New Age International (P) Limited, New Delhi
9. Lin J-R, Hwang C-C (1994) Linear stability analysis of finite porous journal bearings—use of the Brinkman-extended Darcy model. Int J Mech Sci 36:645–658
10. Li W-L, Chu H-M (2004) Modified Reynolds equation for couple stress fluids—a porous media model. Acta Mech 171:189–202
11. Elsharkawy AA (2005) Effects of lubricant additives on the performance of hydrodynamically lubricated journal bearings. Tribol Lett 18:63–73
12. Rao TVVLN, Rani AMA, Nagarajan T, Hashim FM (2013) Analysis of journal bearing with double-layer porous lubricant film: influence of surface porous layer configuration. Tribol Trans 56:841–847
13. Rao TVVLN, Rani AMA, Awang M, Nagarajan T, Hashim FM (2016) Stability analysis of double porous and surface porous layer journal bearing. Tribol Mater Surf Interf 10:19–25

Rotordynamic Analysis and Redesign of High-Pressure Turbine Test Rig



C. Veera Sesa Kumar, E. K. Vivek, and S. Vignesh

Abstract The high-speed test rigs pose several operational problems originating from rotordynamics, bearings, lubrication and thermal gradients. When the critical speeds exist within the design speed, it is possible to accelerate the rotor through resonant speed zones in many applications. However, in very few cases, the resonance crossovers pose serious problems resulting from operational schedules and demand major modifications to rotor-bearing system. The design modifications, driven by rotordynamic considerations, carried out for an existing high-speed test rig with serious operability issues are presented in this paper. During operation, one of the bearings supporting the rotor has failed twice causing significant damages. On both occasions, the bearing failure took place when the rotor was approaching the first critical speed. Considering the difficulty experienced to pass the first critical speed quickly, the rotor-bearing system of the rig is completely redesigned with safe separation margin away from the design speed. Designer's challenges arising from overall layout, manufacturing, imported hardware, assembly and operation are highlighted while addressing the problem. The turbine stage could be tested successfully up to its design speed after implementing all design modifications.

Keywords High speed test rig · Rotor dynamics · Critical speeds and bearing preload

C. Veera Sesa Kumar (✉) · E. K. Vivek · S. Vignesh
Propulsion Division, National Aerospace Laboratories, Bangalore 560017, India
e-mail: seshakumarch@nal.res.in

E. K. Vivek
e-mail: vivekek@nal.res.in

S. Vignesh
e-mail: vickyflyer@gmail.com

1 Introduction

The component level performance testing of turbomachinery plays a vital role in any gas turbine engine development. The turbine and compressor stages need to be tested experimentally to obtain their characteristics at the design and off-design operating conditions. It is essential to test turbomachinery components not only for their aerodynamic performance but also to confirm their structural integrity. The performance testing of turbomachinery needs setting-up of experimental test facilities comprising high-speed rotating rigs, high end instrumentation, data acquisition systems and analysis software. The high-speed test rig under consideration was designed and developed to evaluate the performance of high pressure turbine (HPT) stage of a small gas turbine engine. Versatile turbine test rig established at Propulsion Division, CSIR-National Aerospace Laboratories, is identified as an appropriate facility to test this high-pressure turbine stage. A suitable test section is designed and developed with appropriate adaptations to the rig. The test section comprised of the turbine stage to be tested, rotor-bearing system, bearing housing, casing and the support structure. The rotor-bearing system of the test section is the most critical element of the test rig and is vulnerable for failure. The turbine drive shaft was designed to be supported by a pair of angular contact ball bearings. The rotor-bearing system of existing test section had two flexural critical speeds within the design speed of 31,000 rpm.

During testing, one of the bearings supporting the rotor has failed twice causing significant damages. As the bearing failure took place when the rotor was approaching the first critical speed on both occasions, it is proposed to redesign rotor-bearing system of existing turbine test section. This activity had two major objectives. The first objective was to redesign the rotor-bearing system without any critical speed up to 115% of the design speed. The second objective was to make the bearing preload insensitive to varying operating conditions such as cold/warm/hot air testing. Literature available on high-speed rotors of turbo pumps, machine spindles and gas turbine engines [1–6] presents rotordynamic analysis results and experimental validation. But, there is hardly any literature that presents design solutions to a trouble-stricken rotating machinery. This paper presents various solutions offered to overcome serious operability issues for a high-speed test rig. The description of existing test section, observations from failures and the details of proposed changes are presented in the following sections.

2 Layout of the Existing Test Section

The layout of the versatile turbine test rig is shown in Fig. 1. The rig comprises a high-pressure compressed air line, an inline combustor, the test section where the test article is mounted and the gearbox-eddy current dynamometer system. The test section layout was designed considering adaptability of the turbine rotor to the test rig.

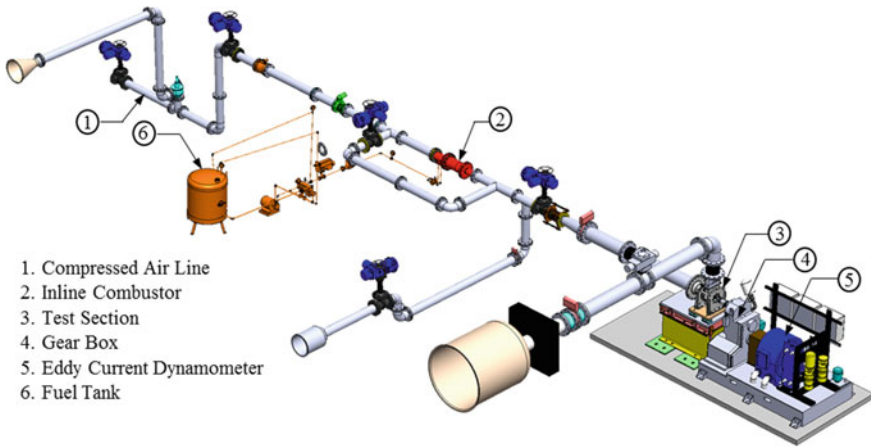


Fig. 1 Layout of the turbine test rig

The cross-sectional view of the test section for HP turbine stage is shown in Fig. 2. The nozzle guide vane (NGV) is mounted to the test section with simulated attachment conditions of the engine. The rotor is configured as an overhang arrangement to allow uninterrupted supply of air at the upstream end. In order to reduce the turbine rotor overhang, a special sleeve is introduced on the shaft to permit the bearing to be placed closer to the rotor.

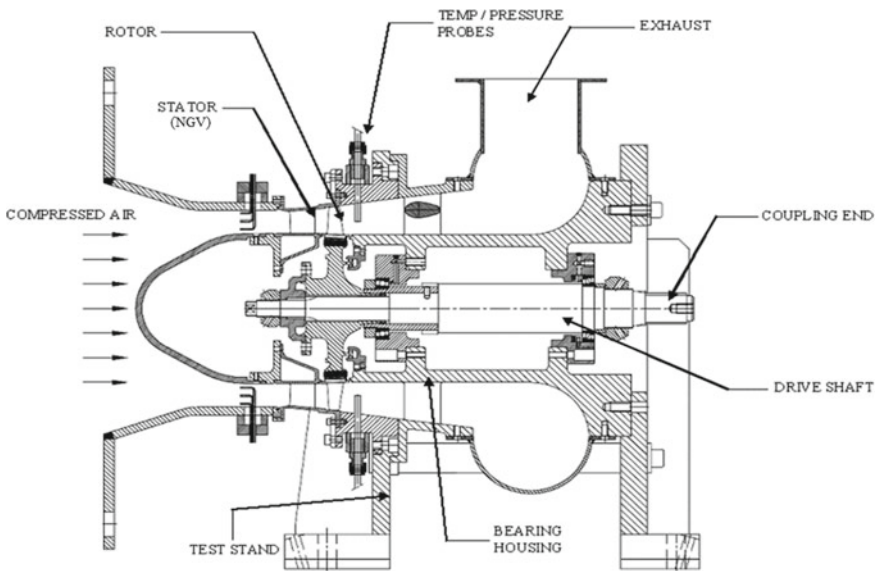


Fig. 2 Cross-sectional view of the turbine test section

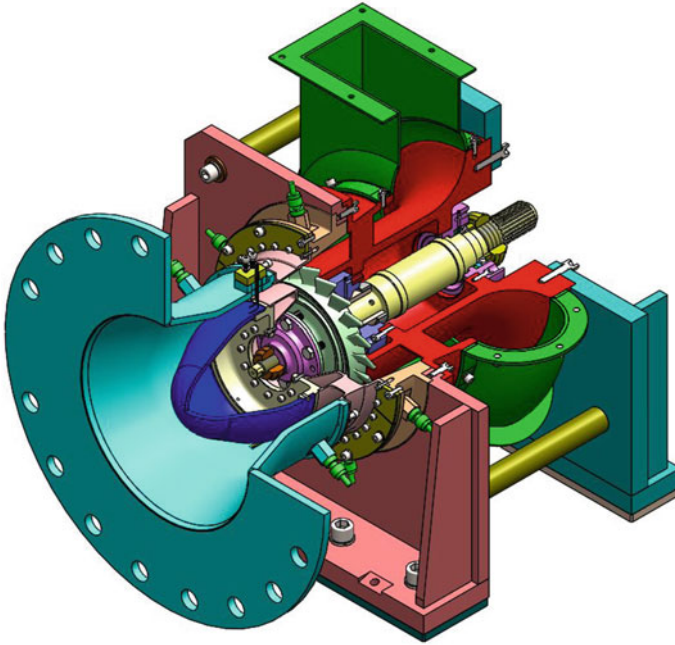


Fig. 3 Turbine test section

The shaft is supported by a pair of angular contact ball bearings with ceramic rolling elements in back-to-back configuration. The bearing with 40 mm bore size was chosen at the turbine end to meet thrust load requirement of 1 kN at test speed of 30,765 rpm. At the coupling end, slightly larger bearing with 45 mm bore size is chosen to support the radial load. This bearing is configured as non-locating bearing and is preloaded as recommended by the bearing manufacturer. Oil–air lubrication arrangement is provided to lubricate the bearings. 3D CAD model of the test section is shown in Fig. 3. Variation of eigen frequencies due to gyroscopic effect with respect to the rotational speed is presented in Campbell diagram and is shown in Fig. 4. The first and second bending critical speeds resulting from rotor unbalance excitation are identified at 21,250 and 26,500 rpm.

3 The Test Rig Failures

3.1 *First Failure*

During test runs, the coupling end bearing was failed when the rotor was approaching 20,000 rpm. However, the bearing at the turbine end was found to be good. From the

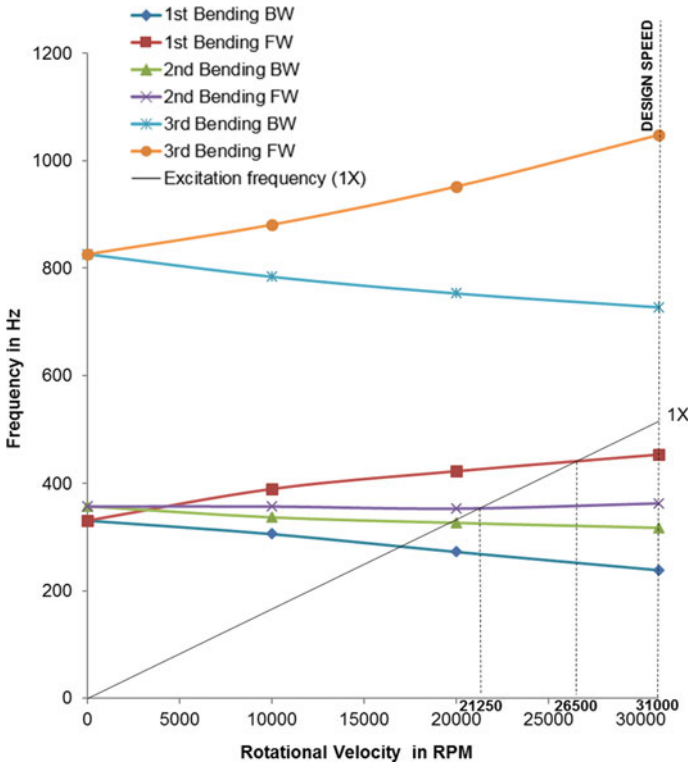


Fig. 4 Campbell plot for existing system

rotordynamic analysis, the first bending critical speed influenced by coupling mass resulting from rotor unbalance excitation ($1\times$) is predicted at 21,250 rpm. Effect of heavy coupling mass (4 kg), its response at the critical speed, loss of bearing preload due to cold air testing and the rotor misalignment were suspected to be the reasons for failure. This test was conducted using cold air at approximately 25 °C. The turbine stage downstream temperature of the air was dropped below -35 °C. Considerable contraction of casing relative to the shaft could result in loss of bearing preload. Hence, it was decided to carry out only warm air testing to avoid uncertainty to bearing preload and lubricant properties.

3.2 Second Failure

After incorporating all corrections suggested by the failure investigation committee, the rig was again assembled, and testing was resumed. The rig was run at incremental speeds as suggested by the bearing manufacturer. The coupling end bearing was again failed when the rotor was approaching 20,000 rpm. The bearing components were

studied by the supplier to investigate the probable cause of the failure. The path pattern present on the outer ring was throughout and moderate. However, the path pattern on the inner ring was predominant over half of the circumference race way, and remaining part was clean. Further, slight run over was observed on the raceway in the axial direction. From these observations through visual inspection, it is apparent that the probable failure causes are improper misalignment and excessive preload.

4 Redesign of the Test Section

The test section is redesigned based on findings from both failures. Since the bearing failure took place when the rotor was approaching the first critical speed on both occasions, the primary objective was to redesign the rotor-bearing system without any critical speed up to 115% of the design speed. Further, the bearing preload needs to be insensitive to varying operating conditions such as cold/warm/hot air testing. This redesign necessitated significant changes in size and type of bearings, rotor drive shaft and driving end of the coupling. The bearing sizing is finalized first, in order to shift the critical speeds to higher levels with desired separation margin. Other problems related to preload are addressed in bearing selection and arrangement.

The mass model of the HP turbine test section rotor-bearing system, as shown in Fig. 5, is studied to explore parameters that can be varied in order to push its natural speeds. The turbine rotor and the coupling are configured as overhang masses. The natural frequency of an overhang shaft subjected to a point mass depends on stiffness of the overhung shaft and the overhung mass. The stiffness of the shaft is again a function of shaft diameter, overhang length and Young's modulus of the material. These parameters have been varied in the order of their merit within permissible limits to increase the critical speed beyond the design speed.

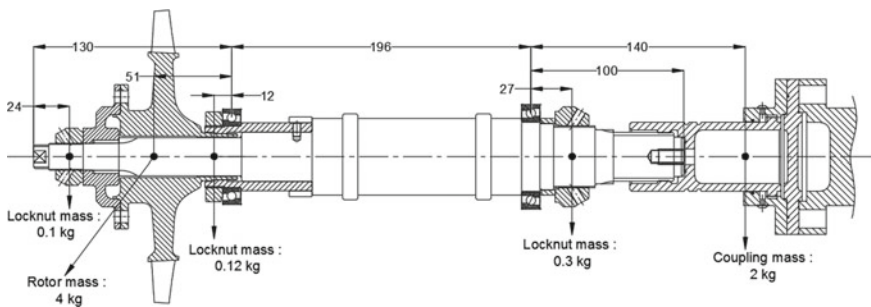


Fig. 5 Existing rotor model

4.1 Coupling Side Modifications

- Increasing shaft stiffness by reduction in overhang length:** The shaft overhang is the most sensitive parameter as the stiffness is inversely proportional to cube of the overhang length. Hence, in the first attempt, the shaft is shortened to reduce the coupling overhang length. In the existing design, overhang length between bearing plane to shaft end is 100 mm and the coupling c.g. location is another 40 mm away from shaft end as shown in Fig. 6a. The reduction in overhang is achieved by removing the bearing spacer and changing the series of locknut. Further, excessive length near the spline meant to accommodate spline cutter radius has been removed and is proposed to cut the spline using spark erosion process. With all these modifications, the overhang length is brought down from 100 to 55 mm as shown in Fig. 6b. With the shortened shaft, a preliminary rotordynamic analysis was carried out to study the effect. The coupling side critical speed has been increased from 21,000 to 29,000 rpm. Though there is significant upward shift, the new critical speed has approached to the close vicinity of the design speed of 31,000 rpm, making it much more unsafe at full speed.
- Increasing shaft stiffness with higher area moment of inertia:** In order to push the critical speed further, other option left was to increase the stiffness of the overhang shaft by increasing its diameter. Hence, the diameter of the shaft is increased from $\text{Ø}45$ to $\text{Ø}50$ mm at coupling end bearing location. Locknut is changed accordingly. Suitably, the size of the drive spline is increased from 1.2"

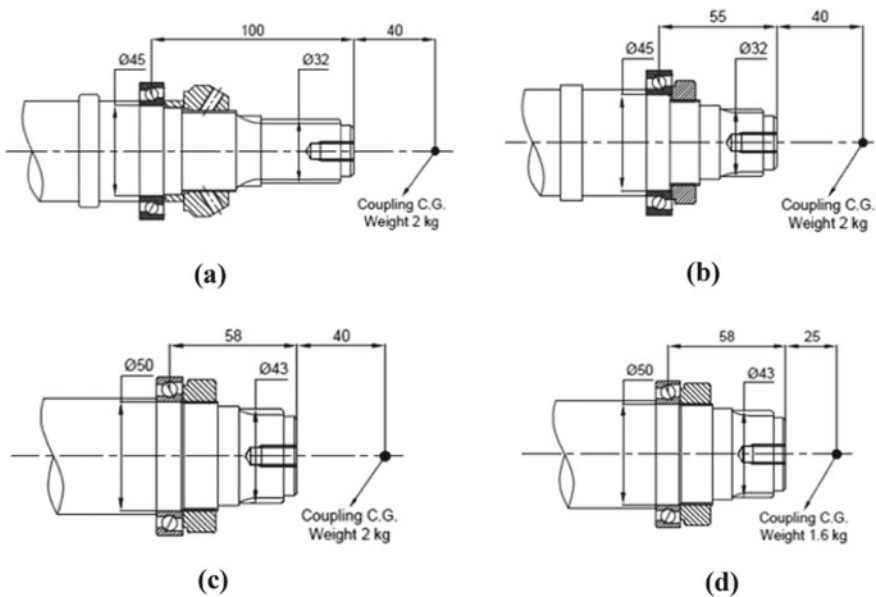


Fig. 6 Coupling side shaft end modifications

pitch diameter to 1.625" pitch diameter, conforming to spline standard AS972A as shown in Fig. 6c. Increase in shaft spline size requires increase in gear coupling size, resulting in heavier coupling. Since the coupling mass is a sensitive parameter for critical speed, undesirable increase in coupling weight would offset the benefit of increasing shaft stiffness by increasing its diameter. So, there is a need to keep the coupling weight unchanged in spite of increase in its size. The existing high-speed coupling which is an imported one has been studied in detail, and several possibilities have been identified to optimize its weight.

The rotordynamic analysis was carried out again with modified shaft end as shown in Fig. 6c. The coupling mass of 2 kg is assumed to remain same. The coupling side critical speed has been increased from 29,000 to 33,500 rpm. Though there is significant upward shift, the separation margin is not enough considering uncertainties in the stiffness values of bearings and the support structure.

- Increasing shaft stiffness by reduction in coupling c.g. overhang:** Increase in shaft diameter as described above requires a new coupling in which all the components (hub, flange and adaptor) need to be properly optimized without compromising minimum safety factors. Since the new coupling has to be developed as a customized one, the possibility of reducing coupling c.g. overhang (40 mm from the shaft end) is also explored in order to enhance the separation margin further. From the transmission layout, it is understood that, the input shaft of gear box is located deep inside from the gear box face. Hence, a lengthy coupling hub was desired at the gear box side to facilitate the assembly. But, the same hub length on the turbine side (by symmetry) was unnecessarily long. The space between shaft end to coupling adaptor plate is used to fill oil for spline lubrication. Reduction of this axial length to a permissible extent is seen as a potential parameter to improve separation margin.

Optimization of coupling for weight as well as c.g. location is quite challenging task. The existing high-speed coupling, imported from USA, is shown in Fig. 7.

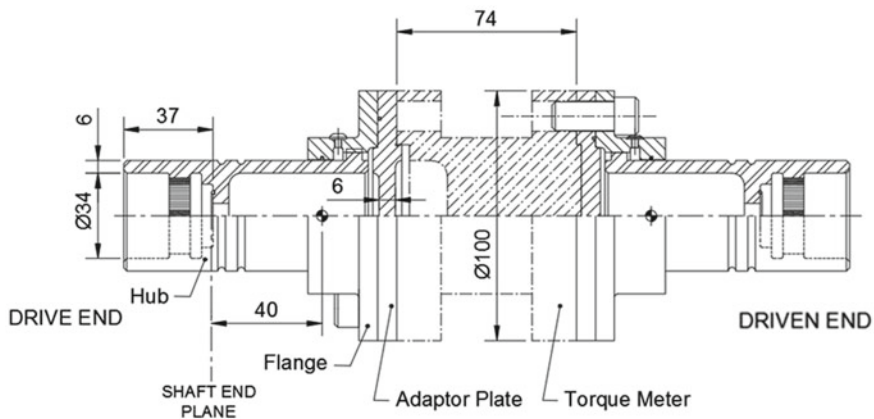


Fig. 7 Existing coupling

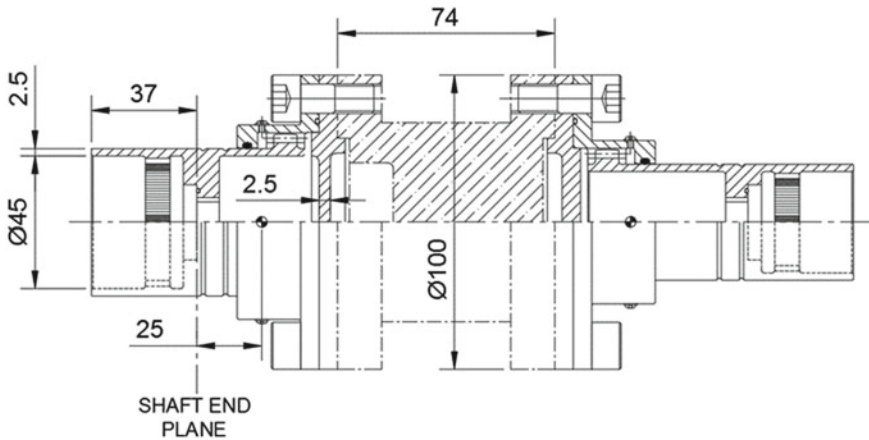


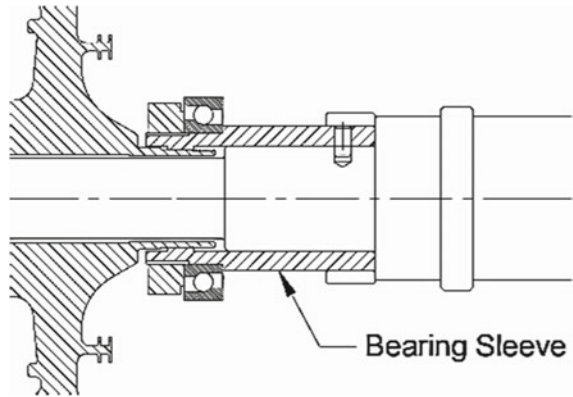
Fig. 8 Modified coupling

Purchase of another coupling from the foreign sources involves huge cost and lead time. Hence, a local coupling manufacturer was approached to supply a coupling with proposed modifications. Larger coupling hub and flange are designed at turbine end to suit increased shaft diameter. In order to control the weight of the coupling, the thicknesses of hub, flange and adaptor plates are reduced from 6 to 2.5 mm based on design calculations. Since the adapter plates act as mere oil isolators and do not take part in torque transmission, its material is changed from steel to titanium. Though the objective of this optimization was to retain the larger coupling weight at 2 kg, the modifications discussed above yielded 20% additional reduction over the target weight. Reduction in oil chamber length brought down the coupling overhang from 40 to 25 mm as shown in Fig. 6d. The modified coupling drawing is shown in Fig. 8. Rotordynamic analysis with all these coupling modifications indicated critical speed around 48,000 rpm with the stiffness data provided by bearing manufacturer.

4.2 Turbine Side Modifications

- Increasing shaft stiffness by reduction in turbine rotor c.g. overhang:** The critical speed, influenced by turbine rotor mass, at 27,500 rpm is also considered very critical. Hence, the rotor system is changed on the turbine side as well. The turbine rotor stub sleeve at the bore location posed several complications to keep the rotor close to the bearing plane. In the present configuration, a special sleeve as shown in Fig. 9 is introduced on the shaft to permit the bearing to be placed closer to the rotor. In order to increase the critical speed beyond the design speed, only option left was to modify the test article itself by truncating the turbine rotor stub sleeve. When the sleeve is trimmed, the diameter of the collar available for bearing

Fig. 9 Existing bearing arrangement



abutment is lower than the bore size of existing bearing which forced the bearing size to be reduced from 40 to 30 mm. Further, the flange thickness of the coupling sleeve was reduced to bring down the overhang mass. The locknut which was used in the earlier setup has been eliminated with anti-rotation fastener. All these design changes resulted in significant reduction in turbine rotor c.g. overhang from 51 to 34 mm. Rotordynamic analysis for the modified configuration indicated critical speed around 42,000 rpm.

4.3 Changes in Bearing Type and Arrangement

The critical speeds of the modified rotor system have been successfully shifted away from the design speed with sufficient separation margin. The primary objective of this redesign has been met by reducing overhang distances, increasing shaft/bearing sizes and reducing overhang masses. Secondary objective is to make the bearing preload insensitive to varying operating conditions such as cold/warm/hot air testing. This issue is addressed by changing bearing type. A cylindrical roller bearing with 50 mm bore diameter is chosen at coupling end with desired load and speed rating to eliminate uncertainties in bearing preload in case of relative thermal expansion. This roller bearing, which can permit up to 2 mm axial relative displacement between inner and outer rings, acts as floating bearing when the casing expands/contracts with respect to the rotor. The rolling element and the cage for this bearing are made of ceramic and PEEK, respectively. Modified shaft end at coupling side with cylindrical roller bearing is shown in Fig. 10.

At the turbine end, a pair of angular contact ball bearings is chosen to resist axial thrust load. To improve the stiffness of the rotor-bearing support and to eliminate preloading of the bearing by a spring, it is suggested to use a pair of bearings in back-to-back arrangement. The material for rolling elements and the cage for the ball bearings has been a serious concern from earlier failures. Hence, this bearing

Fig. 10 Bearing arrangement at coupling end

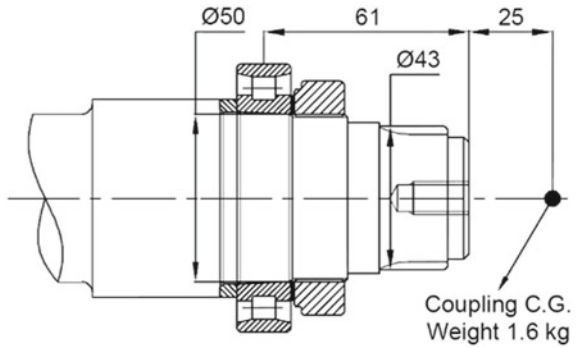
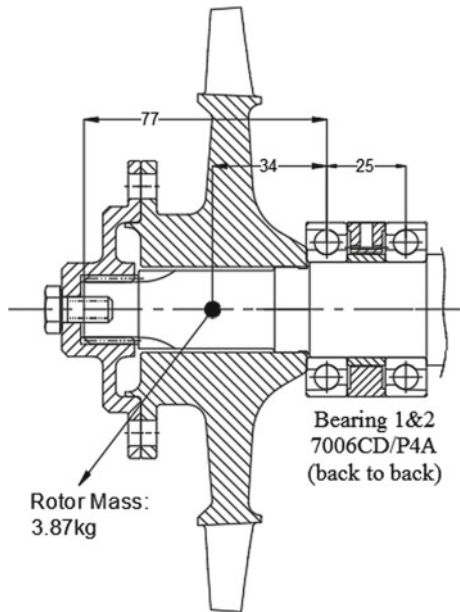


Fig. 11 Bearing arrangement at the turbine end



is chosen with metal rolling elements and cage made out of PEEK. The bearing arrangement at the turbine end is shown in Fig. 11.

5 Rotordynamic Analysis

The rotordynamic analysis was carried out for the modified rotor. The shaft was axially constrained at turbine end bearing plane. The coupling overhang distance beyond the shaft end is simulated with coupling stiffness having no mass. Modal analysis was carried out from 0 to 50,000 rpm with an increment of 10,000 rpm.

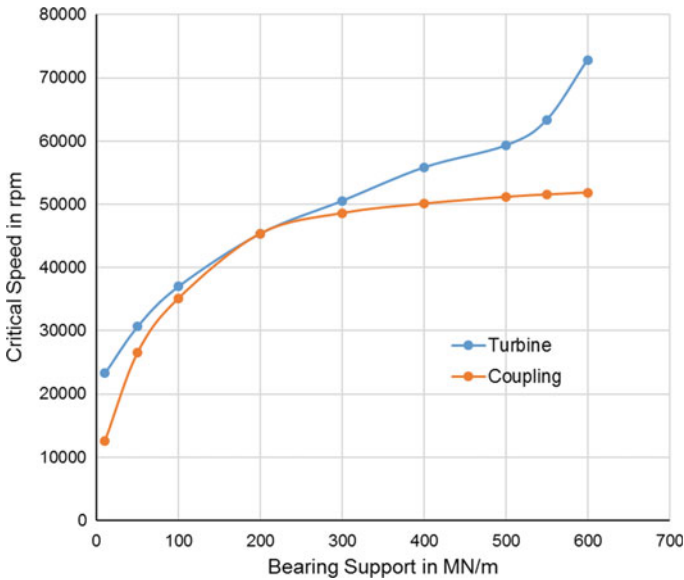


Fig. 12 Critical speed map

The stiffness of the bearings is a function of bearing preload which is in turn varies with rotor speed, external loads and thermal gradients in the system. Hence, the critical speed map is derived for first two modes over a stiffness range up to 600 MN/m and is shown in Fig. 12. The bearing stiffness data over a range of operating speed for the given operating conditions is obtained from bearing supplier. At static condition, the preload in both angular contact ball bearings will be same. But during operation, under the influence of external thrust load, the variation of load in both bearings results in considerably different stiffness. The stiffness of both angular contact ball bearings at design speed is estimated to be 160 and 50 MN/m, whereas the stiffness of cylindrical roller bearing is estimated to be 300 MN/m. Six modes were extracted at each speed increment. The orbit plots of flexural modes at 440, 761 and 1025 Hz are shown in Fig. 13. The Campbell diagram depicting the critical speeds at the intersection of natural frequencies and the synchronous excitation is shown in Fig. 14. The bending critical speeds influenced by turbine rotor and coupling masses are predicted at 42,600 and 48,400 rpm, respectively. Separation margin of 37% and 56% is achieved for the first and second critical speeds.

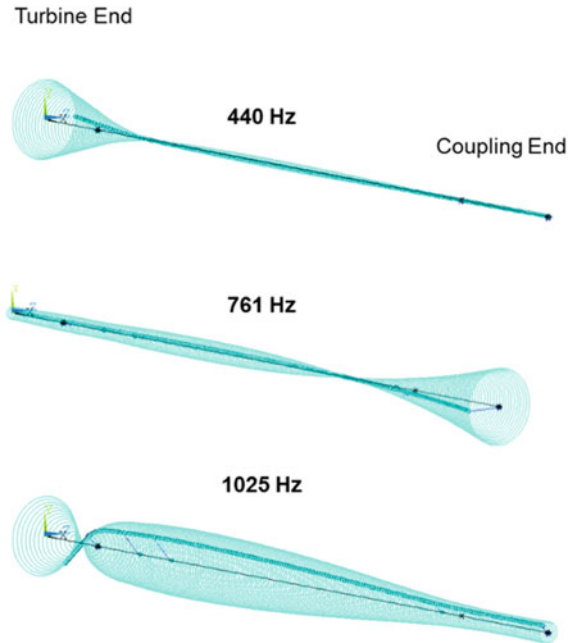


Fig. 13 Orbit plots

6 Testing

The rotor components were manufactured maintaining desired tolerances. Turbine rotor assembly was balanced G 2.5 balance grade. New bearings were assembled with utmost care using special tools. The turbine drive shaft is aligned with the gearbox to recommended values. Actual stiffness of the bearing supports achieved after complete test section assembly is assessed using hammer test, and the results were found to be in good agreement. These results are tabulated in Table 1. The rig was instrumented to measure and record vibrations, bearing temperatures and rotor speed continuously as shown in Fig. 15. The rig was run at speeds ranging from 50 to 100% of design speed, and complete turbine stage characteristics were generated.

7 Conclusions

The rotor-bearing system of high-pressure turbine test section has been modified to push the critical speeds beyond the design speed of 31,000 rpm by several changes in design. Modifications included reduction of overhang distances, changes in shaft diameters at both bearing ends and reductions in overhang masses involving major

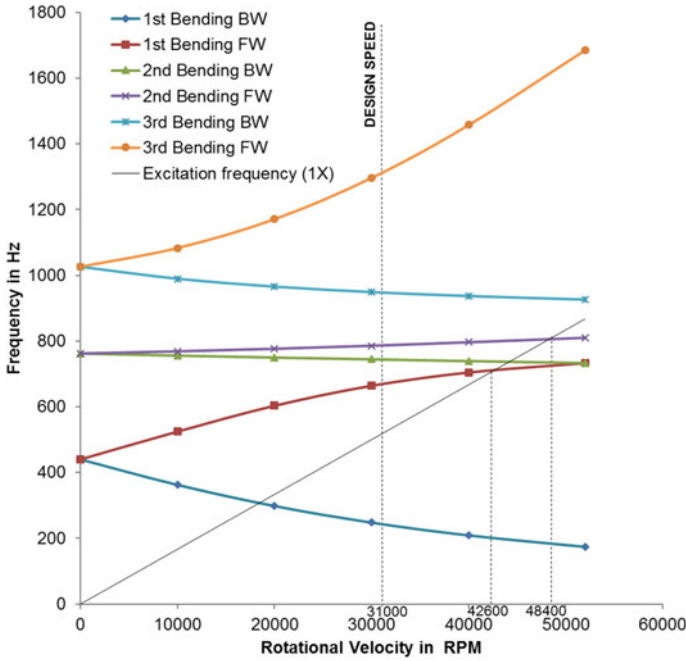


Fig. 14 Campbell diagram

Table 1 Comparison of impact hammer test results and rotordynamic analysis

Results	1st Frequency (Hz)	2nd Frequency (Hz)	3rd Frequency (Hz)
Rotordynamic analysis	440	761	1025
Impact hammer test	445	865	1130

changes in coupling and turbine rotor. The modified rotor is configured with a cylindrical roller bearing at the coupling end and a pair of angular contact ball bearings at the turbine end. With all these modifications, the first and second bending critical speeds have been pushed to 42,600 and 48,400 rpm, respectively. The turbine stage characteristics were generated up to 100% corrected speed. The modifications implemented in the rotor-bearing system helped the turbine stage to be tested up to its full speed meeting all objectives.




Fig. 15 Test section after instrumentation

References

1. Moroz L, Romanenko L, Kochurov R, Kashtanov E (2017) Prediction of structural supports influence on rotating machinery dynamics. In: Proceedings of ASME Turbo Expo 2017: Turbomachinery Technical Conference and Exposition GT2017, 26–30 June 2017
2. Jeon SM, Kwak HD, Yoon SH, Kim J (2008) Rotordynamic analysis of a turbopump with the casing structural flexibility. *J Propuls Power* 24(3)
3. Taplak H, Parlak M (2012) Evaluation of gas turbine rotor dynamic analysis using the finite element method. *Measurement* 45:1089–1097
4. Hong D-K, Choi J-H, Woo B-C et al (2013) Rotordynamic analysis and experimental validation of a high speed induction motor made by copper die casting process. *J Mech Sci Technol* 27(10):3035–3041
5. HadiJalali M, Ghayour M, Ziaei-Rad S, Shahriari B (2014) Dynamic analysis of a high speed rotor-bearing system. *Measurement* 53:1–9
6. Jauhari K, Widodo A, Haryanto I (2015) Evaluation of dynamic behavior a machine tool spindle system through modal and unbalance response analysis. *Int J Ind Manuf Eng* 9(2)

Thermo-Mechanical Analysis of a Rotor-Bearing System Having a Functionally Graded Shaft with Transverse Breathing Cracks



Debabrata Gayen , Rajiv Tiwari, and Debabrata Chakraborty

Abstract *Purpose:* The dynamic behavior of two-cracked functionally graded (FG) shaft system under thermal environment has been carried out. The finite element (FE)-based formulation is used to model metal-ceramic FG (SS/ZrO₂) shaft using Timoshenko beam theory (TBT). Power law of material gradation is used to derive effective thermo-elastic properties of radially graded FG shaft. *Methods:* The governing system equations of motion are formulated using Hamilton's principle. The local flexibility coefficients (LFCs) are derived as functions of material gradient, temperature, size and orientation of crack, for the cracked FG circular cross-sectional FG shaft, using linear elastic fracture mechanics, Castigliano's theorem and energy method. *Results:* Numerical simulations are performed to analyze the effects of geometric, material and temperature gradient parameters on the natural frequencies of the cracked FG shaft system. *Conclusion:* LFCs are functions of material gradient and temperature besides crack size. Even though the reduction in eigenfrequencies is decided by crack parameters, material gradient and temperature, however, the reduction in eigenfrequencies is greatly influenced by gradient index and the index may be selected properly to design FG shafts for high-temperature applications.

Keywords Material gradient index · FG shaft · Multiple cracks · LFC · Temperature · Dynamic response

D. Gayen (✉) · R. Tiwari · D. Chakraborty
Department of Mechanical Engineering, Indian Institute of Technology Guwahati, Guwahati
781039, Assam, India
e-mail: d.gayen@iitg.ac.in

R. Tiwari
e-mail: rtiwari@iitg.ac.in

D. Chakraborty
e-mail: chakra@iitg.ac.in

Nomenclature

Symbol

b	Crack half-width
E	Young's modulus
I_p^s and I_d^s	Polar and diametric mass moment of inertia
L_c/L	Crack location
P_1, P_2, P_5 and P_6	Shear forces
P_3, P_4, P_7 and P_8	Bending moments
R	Radius of the shaft
V	Volume fraction
v and w	Translational displacements
T	Temperature
M, G and K	Mass, gyroscopic and stiffness matrix
K	Thermal conductivity
k	Material gradient index
L	Total length
L_c	Crack distance

Greek Letter

ν	Poisson's ratio
θ	Crack orientation angle
ρ	Mass density
Ω	Spin speed of rotor
α	Depth of crack
α/R	Crack size
β and Γ	Rotational displacements
ω	Whirling frequency

Subscripts

c and m	Ceramic and metal
V and H	Vertical and horizontal
t	Translational
r	Rotational

Superscripts

s, b and d	Shaft, bearing and disc
c	Crack
uc	Uncrack

1 Introduction

In the improvement of structural performance, FG materials (FGMs) are used as multifunctional and high-performance materials in which thermo-elastic properties graded are followed by material gradation laws. FGMs offer numerous superior properties over laminated composite materials and are used mainly to reduce interlaminar stresses and delamination problem. Historically, the concept of gradation was first proposed [1] in 1972, for composites and polymeric materials. However, the work [1] was limited impact. FGMs were first introduced [2] in 1980s in Japan. Then, FGMs are rapidly becoming well known and widely used in aerospace, automotive, biomedical and so on. A lot of researches were reported on the behavior of FG structural systems with great interest during the last few years. Some of the important works in the directions are presented here. Thermo-mechanical responses of structure made of FG materials are studied by Reddy and Chin [3]. By using TBT, Piovan and Sampaio [4] developed a composite rotating nonlinear FG beam model accounting for arbitrary axial deformations. Gayen and Roy [5] carried out vibration and stability of a shaft made of FGMs and reported effect of gradient index on dynamic responses. Boukhalfa [6] studied dynamic responses of a spinning shaft made of FGMs using TBT.

Transverse cracks in structural members such as shaft and rotor lead dangerously to failure associated with economic loss and more importantly human life. The first studies on cracked rotors were started in the 1970s. Thereafter, several researchers reported the review works of cracked shaft and rotors [7]. Papadopoulos and Dimarogonas [8] derived local flexibility matrix and studied the coupled vibration for a shaft made of homogeneous materials. Jun et al. [9] carried out vibration characteristics of a cracked rotor based on fracture mechanics approach. Sinou and Lees [10] carried out dynamic response for a shaft using an alternate frequency/time domain approach. Coupled vibration responses [11] were reported for a breathing cracked shaft using nonlinear FE method. However, appearances of more than one crack in shafts create complication of obtaining the dynamic characteristics. Sekhar [12] carried out the eigenfrequencies and instability of a rotor system with two cracks. Vibration responses were reported by Darpe et al. [13] for a simple Jeffcott rotor with two cracks.

Crack in FG structure has vital role due to their safe performance for high demands in various engineering sectors. Yang and Chen [14] studied free vibration and buckling analysis of cracked FG Euler–Bernoulli beams. Aydin [15] reported free vibration of FG beams considering multiple edge cracks with different end conditions. Gayen et al. [16] modeled an FG shaft based on Euler–Bernoulli beam theory and studied the free vibration of the FG shaft system. Based on the FE analysis and considering TBT, a cracked FG shaft modeled and carried out the dynamic responses by Gayen et al. [17–19].

Therefore, the present study aims in analyzing the thermo-mechanical behavior of a multi-cracked rotor system with a shaft made of FGMs, using FE method. Numerical results are performed at determining the eigenfrequencies to understand the importance of shaft’s slenderness, number, size, location and orientation of crack, material gradient and temperature on the vibration responses of cracked FG shaft.

2 Thermo-Elastic Material Model

The effective thermo-elastic materials properties C [20] for the FG shaft are obtained as

$$C(T) = C_0(C_{-1}T^{-1} + 1 + C_1T + C_2T^2 + C_3T^3) \tag{1}$$

where C_0, C_{-1}, C_1, C_2 and C_3 are temperature coefficients for each constituent materials.

For a shaft made of FGMs, the following power law of material gradation, C [3], as functions of y and temperature (T) is obtained

$$C(y, T) = C_m(T) + \{C_c(T) - C_m(T)\}V_c(y) \tag{2}$$

where

$$V_c(y) = \left\{ \frac{(y - R_m)}{(R_c - R_m)} \right\}^k, V_m(y) = 1 - V_c(y), \\ R_c \leq y \leq R_m, \quad 0 \leq k \leq \infty \tag{3}$$

Now, for radially graded FG shaft, temperature profile is obtained, using steady-state one-dimensional heat conduction equation as

$$d/dy[yK(y)dT/dy] = 0 \tag{4}$$

In solving Eq. (4) for a solid shaft, for temperature distribution at the center ($y = R_i = 0$), the solution becomes singular. This singularity could be handled by considering the inner radius $R_i = \varepsilon \simeq 0$. However, the solution depends upon the proper choice of ε and needs a good amount of study to assure convergence.

Therefore, a conservative approach is used to compute the eigenfrequencies considering uniform temperature ($T = T_0$, at any y) even though the actual temperature distribution will not be uniform. But the results could safely be used for the actual case where the temperature gradient exists.

3 Modeling of FG Shaft System Based on FE Method

Using TBT, an FG shaft is modeled considering two-noded beam element with four degrees of freedom at each node. Figure 1a–d presents a rotor-disk-bearing system interconnecting the components such as cracked FG shaft, rigid disk and bearings.

3.1 Cracked Shaft Element Made of FGM

Using Paris’s equations [21] and Castigliano’s theorem, the cross-coupled and direct LFCs are calculated with the expressions of stress intensity factors (SIFs). The additional displacement u_i^c due to crack is

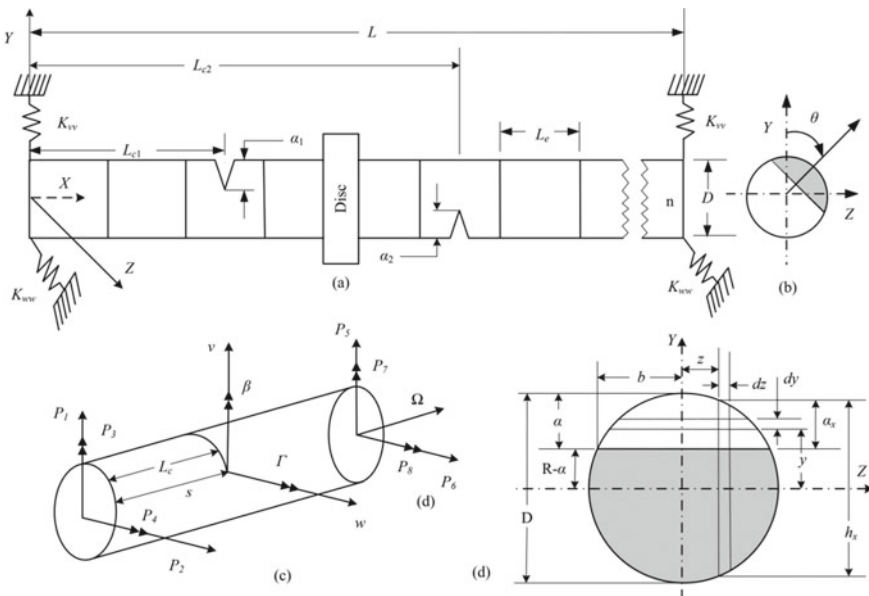


Fig. 1 Cracked FG rotor system: **a** FE discretization, **b** crack orientation, **c** general loads, **d** cross section of cracked geometry

$$u_i^c = \frac{\partial}{\partial P_i} \int_0^{\alpha_x} \frac{1}{E(y, T)} \left[\left(\sum_{i=1}^4 K_{Ii} \right)^2 + \left(\sum_{i=1}^4 K_{IIi} \right)^2 + \{1 + \nu(y, T)\} \left(\sum_{i=1}^4 K_{IIIi} \right)^2 \right] dy \quad (5)$$

where K_I , K_{II} and K_{III} are SIFs for modes I, II, and III, respectively, and $i = 1, 2, 3$ and 4 are load indices.

Referring Fig. 1d, the LFCs for fully open crack $\theta = 180^\circ$ are obtained

$$C_{ij}^c = \frac{\partial u_i^c}{\partial P_j} = \frac{\partial^2}{\partial P_i \partial P_j} \int_{-b}^b \int_0^{\alpha_x} \frac{1}{E(y, T)} \left[\left(\sum_{i=1}^4 K_{Ii} \right)^2 + \left(\sum_{i=1}^4 K_{IIi} \right)^2 + \{1 + \nu(y, T)\} \left(\sum_{i=1}^4 K_{IIIi} \right)^2 \right] dy dz \quad (6)$$

In Eq. (6), numerical integrations are performed to derive local flexibility matrix $[C^c(y, T)]$ and corresponding \mathbf{K}^c (cracked stiffness matrix) are derived following the works of Gayen et al. [17, 18].

The stiffness variation during the crack opening and closure, i.e., the breathing effect of the cracked rotor, is given following the work [10] as

$$\mathbf{K}(t) = \mathbf{K}^{uc} - f(t)\mathbf{K}^c \text{ with } f(t) = (1 - \cos \Omega t)/2 \quad (7)$$

where $f(t)$ is crack opening and closure function.

The equations of motion of the cracked shaft element are given as

$$(\mathbf{M}_t^s + \mathbf{M}_r^s) \ddot{\mathbf{p}}^s(t) - \Omega \mathbf{G}^s \dot{\mathbf{p}}^s(t) + \mathbf{K}^s \mathbf{p}^s(t) = \mathbf{f}^s(t) \quad (8)$$

where the elementary matrices are given in the works [17, 18].

3.2 System Equations of Motion and Solution

The resultant system equations of motion including the shaft, rigid disk and bearing are given

$$(\mathbf{M}_t^s + \mathbf{M}_r^s + \mathbf{M}_t^d + \mathbf{M}_r^d) \ddot{\mathbf{p}} + (\mathbf{C}^b - \Omega \mathbf{G}^s - \Omega \mathbf{G}^d) \dot{\mathbf{p}} + (\mathbf{K}^s + \mathbf{K}^b) \mathbf{p} = \{\mathbf{F}^s(t) + \mathbf{F}^d(t) + \mathbf{F}^b(t)\} \quad (9)$$

For the analysis of natural whirling speeds of the rotor-bearing system with FG shaft, the force term can be omitted. Then, the final system equations of motion are given

$$\mathbf{M}\ddot{\mathbf{p}} + \mathbf{C}\dot{\mathbf{p}} + \mathbf{K}\mathbf{p} = \{0\} \tag{10}$$

For Eq. (10), the eigenvalue solution is $\lambda_n(\Omega) = \xi_n(\Omega) \pm i\omega_n(\Omega)$, logarithmic decrement is $\delta_n = -2\pi\xi_n/\omega_n$ and stability threshold speed is obtained for $\delta_n = 0$.

4 Results and Discussion

Here, a cracked FG shaft with diameter $D = 0.1$ m and temperature-dependent material properties of the constituents of the FG (SS/ZrO₂) are considered same as in [20]. Density for SS and ZrO₂ is 8166 and 5700 kg/m³, respectively. The shaft is discretized with 25 finite elements; simply supported (S–S) and flexible end condition is considered for dynamics of shafts. A disk is located at midspan of the shaft with weight 1.406 kg, I_p^s and I_d^s 0.002 and 0.0135 kg-m², respectively.

Due to lack of appropriate results for dynamic characteristics of FG shafts, the present crack formulation has been validated in two steps. First, computed natural frequencies are compared with classical solution and results. Table 1 shows an excellent agreement with the closed-form solutions, thereby validating the FE formulation of homogeneous beam and developed code.

Second, dimensionless natural frequencies are computed for the first crack size $\alpha_1/R = 0.2$, first crack location $L_{c1}/L = 0.35$ and $L/D = 8$, varying the second crack size α_2/R and location L_{c2}/L . The computed results are listed in Table 2. The dimension and material properties are used same as in Sekhar [12]. Table 2 shows a good agreement which has been attained, thus validating the multiple cracks formulation.

Table 1 Evaluation of fundamental frequency (in Hz) for a homogeneous beam

Boundary condition	Without disk			Single disk		
	Classical	Present/FEA	% Error	Classical	Present/FEA	% Error
Fixed–free	7.258	7.259	–0.014	5.301	5.430	–2.434
Fixed–fixed	45.846	46.189	–0.748	36.931	36.811	0.325
S–S	20.376	20.375	0.005	16.797	16.908	–0.661

Table 2 Variation of fundamental frequencies with α_2/R and L_{c2}/L

$\frac{L_{c2}}{L}$	$\alpha_2/R = 0.4$			$\alpha_2/R = 0.6$			$\alpha_2/R = 0.8$		
	Present	Sekhar [12]	% Error	Present	Sekhar [12]	% Error	Present	Sekhar [12]	% Error
0.15	0.979	0.978	-0.102	0.957	0.960	0.312	0.915	0.926	1.187
0.25	0.968	0.966	-0.207	0.928	0.936	0.854	0.859	0.865	0.693
0.45	0.956	0.952	-0.420	0.899	0.900	0.111	0.810	0.817	0.856
0.85	0.989	0.984	-0.508	0.982	0.975	-0.717	0.969	0.958	-1.148

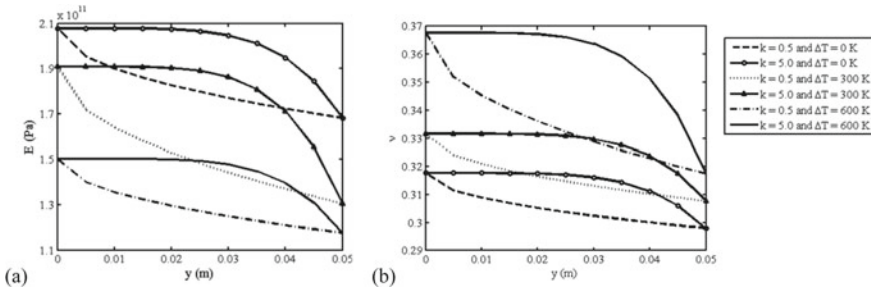


Fig. 2 Variation of **a** Young's modulus and **b** Poisson's ratio, as functions of y , k and ΔT

4.1 Material Properties Variation for an FG Shaft

The variations of temperature-dependent properties E and ν along the radial distance of the FG (SS/ZrO₂) shaft for different values of k are shown in Fig. 2a, b, following power law distribution and using Eq. (2).

4.2 LFCs Variation

Using Eq. (6) along with Eq. (2) and uniform temperature distribution (i.e., $T = T_0$ at all y), LFCs are obtained as non-dimensional quantities such as $\bar{C}_{11} = C_{11}/\pi E_{ss} R$, $\bar{C}_{22} = C_{22}/\pi E_{ss} R$, $\bar{C}_{33} = C_{33}/\pi E_{ss} R^3$, $\bar{C}_{34} = C_{34}/\pi E_{ss} R^3$ and $\bar{C}_{44} = C_{44}/\pi E_{ss} R^3$. Figure 3a shows the variation of \bar{C}_{11} as functions of α/R and k for $\Delta T = 0$ K and $\theta = 180^\circ$. It has been seen that the LFC increases in magnitude as k decreases due to the decrease in the metallic content. Figure 3b shows the variation of \bar{C}_{11} as a function of ΔT and θ for $k = 5.0$ and $\alpha/R = 0.8$. With the increase in ΔT , it has been seen that the LFC increases as material becomes softer. It is also noticed that the magnitude of LFC increases as the crack gradually opens. Similar kinds of trends are observed for other LFCs.

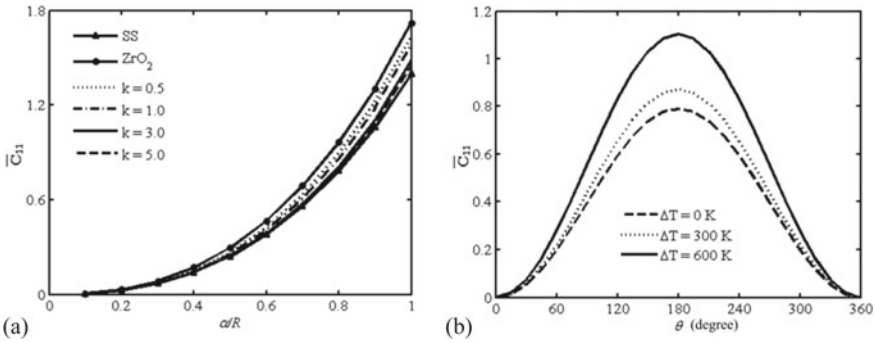


Fig. 3 Variation of \bar{C}_{11} : **a** α/R for different k and **b** θ for different ΔT

Table 3 Frequency parameters ϖ_n of FG shaft for $\alpha/R = 0.6$ and $L_c/L = 0.5$

Modes	$k = 0.5$			$k = 3.0$		
	$\Delta T = 0$ K	$\Delta T = 300$ K	$\Delta T = 600$ K	$\Delta T = 0$ K	$\Delta T = 300$ K	$\Delta T = 600$ K
1st	2.6237	2.5105	2.4153	2.5945	2.5287	2.4018
3rd	6.3202	6.0231	5.7956	6.2273	6.0352	5.7300
5th	8.4184	8.0313	7.7270	8.3027	8.0590	7.6515

4.3 Importance of ΔT and k on Natural Frequencies

A non-spinning simply supported cracked shaft made of FGM ($L/D = 12.5$, $L_c/L = 0.5$, $k = 3.0$ and $\alpha/R = 0.6$) is considered and dimensionless natural frequencies ϖ_n ($\varpi_n^4 = \rho_{SS}AL^4\omega^2/E_{SS}I$) is computed for different values of ΔT . Computed results are listed in Table 3 and show that for a certain α/R , ϖ_n decreases with the increase in ΔT . Table 3 also shows the reduction in ϖ_n with ΔT which is more for lower value of k .

4.4 Influence of Material Gradient Index on Whirling Frequencies

Here, the FG shaft ($L/D = 12.5$) is supported by isotropic undamped bearings with stiffness coefficients $K_{vv}^b = K_{ww}^b = 1.7513 \times 10^7$ N/m and $K_{vw}^b = K_{wv}^b = 0$ for obtaining the whirling frequencies of the cracked rotor systems. Figures 4a, b show the variation of whirling frequencies ω with Ω of the uncracked FG shaft with $\Delta T = 0$ K for different magnitudes of k . From Fig. 4a, b, it is seen that with the increase in Ω , forward whirling (FW) frequencies increase while decrease the backward whirling (BW) frequencies. It is also observed that with the increase in

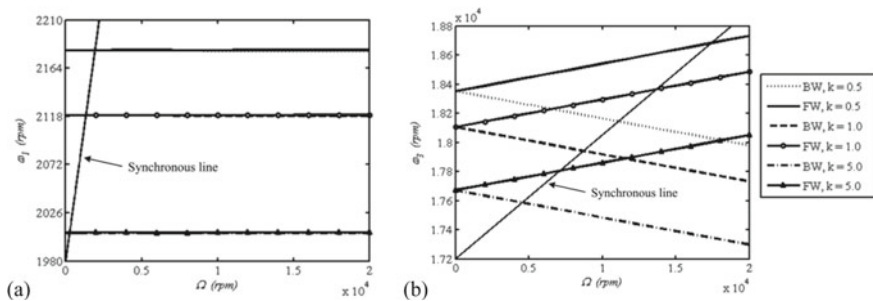


Fig. 4 Campbell diagram for an uncracked shaft system with k : **a** first mode and **b** second mode

k , FW and BW frequencies decreases. Therefore, for an FG shaft system, whirling frequencies are kept within a desired limit by choosing an appropriate k .

4.5 Influences of θ and ΔT on Whirling Frequencies

The fundamental frequencies associated with the plane of vertical ω_{1V} and horizontal ω_{1H} are computed for two-cracked FG shaft with $\alpha_1/R = \alpha_2/R = 0.8$, $L_{c1}/L = 0.34$, $L_{c2}/L = 0.5$ and $\theta_1 = 180^\circ$, while θ_2 is varied and the influences of ΔT on the natural frequencies are carried out for $L/D = 12.5$ and $k = 5.0$. The results are presented in Fig. 5a, b which show that with the increase in ΔT , % reduction in $\omega_{1V,1H}$ decreases, and for $\theta_1 = \theta_2 = 180^\circ$, maximum reduction occurs. It is also seen that for lower magnitudes of ΔT , % reduction in $\omega_{1V,1H}$ will be higher even though the difference is not significant.

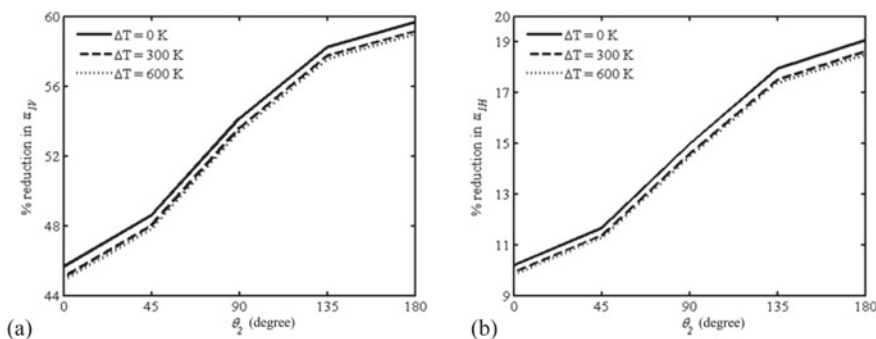


Fig. 5 Percentage reduction of ω for FG cracked shaft system with θ_2 and ΔT : **a** ω_{1V} and **b** ω_{1H}

5 Conclusions

The present work studies the eigenfrequencies analysis of a functionally graded shaft with two cracks, considering thermo-elastic material properties gradation followed by power law of material gradation law. The LFCs are evaluated using linear elastic fracture mechanics and energy method. The validations are performed in various steps using developed FE code in MATLAB, and using this developed code, the importance of size of cracks, material gradient and temperature on the computation of LFCs and eigenfrequencies is discussed. It is observed that in the case of two cracks of different depths, the larger crack has the more significant effect on the eigenfrequencies. The natural whirling frequencies decrease with increase in material gradient and temperature. However, reductions in FW and BW frequencies are greatly influenced by material gradient index. Hence, the material index could be chosen properly to design shafts made of FGMs for high-temperature applications. The present FE formulations and determination of LFCs may be helpful to the design of FG shafts following other material gradation laws such as exponential and sigmoidal.

References

1. Bever MB, Duwez PE (1972) Invited review gradients in composite materials. *Mater Sci Eng* 10:1–8
2. Koizumi M (1993) The concept of FGM. *Ceram Trans* 34:3–10
3. Reddy JN, Chin CD (1998) Thermoelastical analysis of functionally graded cylinders and plates. *J Therm Stress* 21(6):593–626
4. Piovan MT, Sampaio R (2009) A study on the dynamics of rotating beams with functionally graded properties. *J Sound Vib* 327(1–2):134–143
5. Gayen D, Roy T, Finite element based vibration analysis of functionally graded spinning shaft system. *Proc Inst Mech Eng Part C—J Mech Eng Sci* 228(18):3306–3321
6. Boukhalfa A (2014) Dynamic analysis of a spinning functionally graded material shaft by the p-version of the finite element method. *Lat Am J Solids Struct* 11:2018–2038
7. Papadopoulos CA (2008) The strain energy release approach for modeling cracks in rotors: A state of the art review. *Mech Syst Signal Process* 22(4):763–789
8. Papadopoulos CA, Dimarogonas AD (1987) Coupled longitudinal and bending vibrations of a rotating shaft with an open crack. *J Sound Vib* 117(1):81–93
9. Jun OS, Eun HJ, Earmme YY, Lee CW (1992) Modelling and vibration analysis of a simple rotor with a breathing crack. *J Sound Vib* 155(2):273–290
10. Sinou J, Lees AW (2005) The influence of cracks in rotating shafts. *J Sound Vib* 285(4–5):1015–1037
11. Giannopoulos GI, Georgantzinou SK, Anifantis NK (2015) Coupled vibration response of a shaft with a breathing crack. *J Sound Vib* 336:191–206
12. Sekhar AS (1999) Vibration characteristics of a cracked rotor with two open cracks. *J Sound Vib* 223(4):497–512
13. Darpe AK, Gupta K, Chawla A (2003) Dynamics of a two-crack rotor. *J Sound Vib* 259(3):649–675
14. Yang J, Chen Y (2008) Free vibration and buckling analyses of functionally graded beams with edge cracks. *Compos Struct* 83(1):48–60
15. Aydin K (2013) Free vibration of functionally graded beams with arbitrary number of surface cracks. *Eur J Mech A/Solids* 42:112–124

16. Gayen D, Chakraborty D, Tiwari R (2018) Free vibration analysis of functionally graded shaft system with a surface crack. *J Vib Eng Technol* 6(6):483–494
17. Gayen D, Chakraborty D, Tiwari R (2017) Whirl frequencies and critical speeds of a rotor-bearing system with a cracked functionally graded shaft—finite element analysis. *Eur J Mech A/Solids* 61:47–58
18. Gayen D, Chakraborty D, Tiwari R (2017) Finite element analysis for a functionallygraded rotating shaft with multiple breathing cracks. *Int J Mech Sci* 134:411–423
19. Gayen D, Tiwari R, Chakraborty D (2019) Finite element based stability analysis of a rotor-bearing system having a functionally graded shaft with transverse breathing cracks. *Int J Mech Sci* 157–158:403–414
20. Touloukian YS (1967) Thermophysical properties of high temperature solid materials. Mc Millan, New York
21. Tada H, Paris PC, Irwin GR (1973) The stress analysis of cracks handbook. Del Research Corporation, Hellertown, Pennsylvania

A Coupled Field, Circuit and Rotor Model of a BCW Induction Machine



Gaurav Kumar, Karuna Kalita, Kari Tammi, and Seamus Garvey

Abstract The current trend in designing rotating machine is the integration of motor or generator into the overall machine. The use of these integrated machines is finding its applications in the development of compact drive systems in the areas, such as integrated power system for electric spacecrafts and unmanned air vehicles. These machines present great challenges and at the same time they also present great opportunities through the ability to achieve transverse actuation (in two independent directions) without any significant sacrifice. The eccentric position of the rotor with respect to the stator of electric machines makes the magnetic field distribution asymmetric and generates a force along the shortest air gap of the electrical machine. This magnetically induced force is called unbalance magnetic pull (UMP). The present work discusses the development of a coupled magnetic field, electric circuit and rotordynamic model of a 3.7 kW 4-pole induction machine with a special stator winding called bridge configured winding (BCW). This stator winding has the capability to produce torque as well as controllable transverse force. The simulation has been carried out in different eccentricity conditions. The developed model can be used for further study of vibration control or for the development of bearingless machines using BCW scheme.

Keywords Unbalance magnetic pull · Active vibration control · Bearingless machine · Rotordynamics

G. Kumar · K. Kalita (✉)

Department of Mechanical Engineering, Indian Institute of Technology, Guwahati 781039, India
e-mail: karuna.kalita@iitg.ac.in

G. Kumar

e-mail: gaurav.kr@iitg.ac.in

K. Tammi

Department of Engineering Design and Production, Aalto University, 02150 Espoo, Finland
e-mail: kari.tammi@aalto.fi

S. Garvey

Faculty of Engineering, Nottingham University, Nottingham NG7 2RD, UK
e-mail: Seamus.Garvey@nottingham.ac.uk

© Springer Nature Singapore Pte Ltd. 2021

J. S. Rao et al. (eds.), *Proceedings of the 6th National Symposium on Rotor Dynamics*, Lecture Notes in Mechanical Engineering,
https://doi.org/10.1007/978-981-15-5701-9_9

Nomenclature

D	Magnetic stiffness matrix
a	Magnetic vector potential vector
R_S	Stator coil resistance matrix
i_S	Stator circuit current vector
u_S	Stator circuit voltage vector
T_S	Transformation matrix
E	Contribution of the induced EMF
V	Transformation matrix
u_R	Rotor bar voltage vector
M	Mass matrix
G	Gyroscopic matrix
K	Stiffness matrix
f_{unb}	Unbalance force vector
f_{mag}	Magnetic force vector
d	Displacement vector
ḍ	Velocity vector
<i>x, y</i>	Displacements along <i>x</i> - and <i>y</i> -axes
<i>α, β</i>	Rotations along <i>x</i> - and <i>y</i> -axes

1 Introduction

With the advent of technology, the world is moving towards the development of integrated machines where the electric machines would be embedded on the relatively long slender shafts. The use of these integrated machines is finding its applications in the development of compact drive systems in the areas, such as integrated power system for electric spacecrafts and unmanned air vehicles [1]. These integrated machines add up challenges in terms of vibrations and reduction of critical speeds due to long slender rotors. However, this also provides an opportunity to use such machines which can be used for the vibration control without sacrificing torque production capability of the integrated electrical machine.

The eccentric position of the rotor with respect to the stator of electric machines makes the magnetic field distribution asymmetric and generates a force along the shortest air gap of the electrical machine. This magnetically induced force is called unbalance magnetic pull (UMP). The study of UMP has a long history, Fisher–Hinnen (1899) gave the first formula for the calculation of UMP for his dynamo design [2]. Many authors have studied the vibration control in electrical machines. Debortoli et al. [3] and Tenhunen [4, 5] studied the effect of rotor eccentricity, parallel paths and equalizing currents on UMP and demonstrated that the equalizing connections can change the direction of force opposite to the direction of the shortest air gap. Laiho et al. [6] utilized the dual set of winding scheme for active control of rotor

vibration in cage induction electrical machines. Oishi et al. [7] and Chiba et al. [8] developed a single set of winding scheme which can be retrofitted to (almost) any machine where all coil ends are brought out. A disadvantage of this scheme is that the “force inverter” must carry large currents. This inverter must be a “voltage source”. The machine reverts to completely conventional design if the inverter is simply short-circuited. Another single set of winding also known as bridged configured winding (BCW) which has equalizing connection in the parallel branches proposed by Khoo [9] can be used for both torque as well as radial force production. The bridge configured winding machine can accommodate two isolated power sources, (i) the main supply is used for the generation of p pole pairs of the magnetic field and (ii) the bridge supply is used for the production of $p \pm 1$ pole pairs of the magnetic field [9]. Bridged configured winding scheme has the capability to suppress the UMP passively as well as actively. In a BCW, each phase of the winding is divided into four groups, which are connected as a Wheatstone bridge in such a way that an additional power source across the bridge points of the winding would generate magnetic fields of $(p \pm 1)$ pole pairs. Several studies have been carried out on BCW scheme to investigate its behaviour in different eccentricity conditions and capability of vibration suppression [9–12]. The bridge supply has to be isolated from the main supply, i.e. the bridge supply has to have a separate ground. A three-phase bridge supply produces both $(p \pm 1)$ components of the magnetic field and this generates forces with desired frequency components. Khoo et al. [10] demonstrated the capability of force production in a 1.1 kW permanent magnet motor. Kalita et al. [11] demonstrated the capability of force production and vibration control in a 37 kW induction motor using an external supply also referred as “bridge supply” in addition to the main supply. Gaurav et al. [12] studied the generation of UMP in different eccentricity conditions in BCW induction machine using coupled magnetic field and electric circuit model. However, coupled field, circuit and rotor model are needed to study the rotor response in different eccentricity conditions.

The present work discusses the development of a coupled magnetic field, electric circuit and rotordynamic model of a 3.7 kW 4-pole induction machine with BCW. The simulation has been carried out in different eccentricity conditions. The developed model can be used for further study of vibration control or for the development of bearingless machines using BCW scheme.

2 Numerical Model

A coupled magnetic field, electric circuit and rotordynamic model have been developed in finite element environment for the study of rotor response in different eccentricity conditions. The direct coupling of the rotordynamic equation with the magnetic field and electric circuit equations provides the flexibility to simulate the rotor system accurately because the magnetic forces acting on the rotor changes with a change in the rotor position. Figure 1 represents the circuit connection of BCW machine and Fig. 2 represents the schematic representation of rotor motor system.

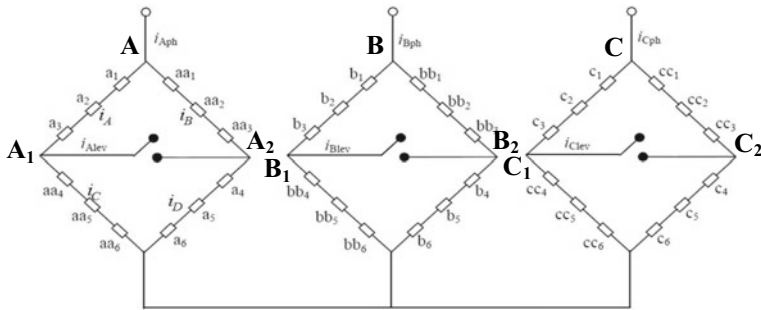
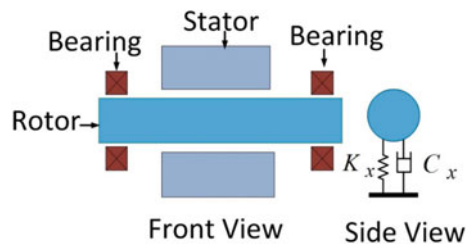


Fig. 1 Circuit diagram of a BCW in an induction machine

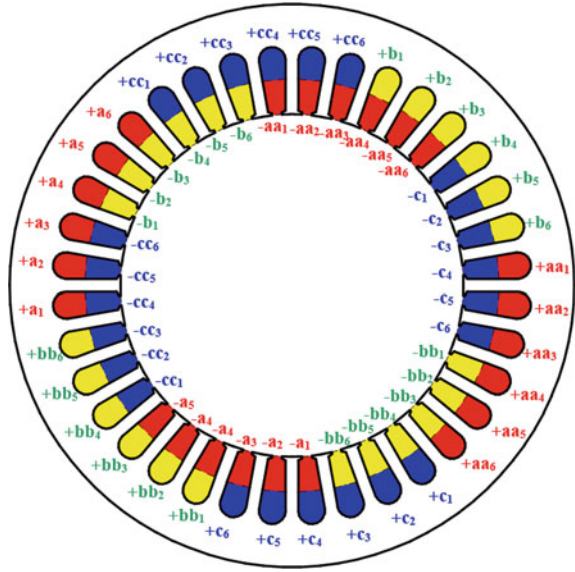
Fig. 2 Schematic representation of a motor-rotor system



The developed model is for a 3.7 kW induction motor with squirrel cage rotor which has 36 stator slots. Figure 1 shows the circuit diagram of a BCW winding scheme and Fig. 3 shows the winding connections of the BCW induction machine used for the simulation. Two power sources isolated from each other can be connected to this winding scheme. One power source is the three-phase voltage source which creates the main field and is called the main supply source, and other power source is three individual current sources and is called the bridge supply source. Points **A**, **B** and **C** represent the main supply terminals, whereas point **A₁–A₂**, **B₁–B₂** and **C₁–C₂** represent the bridge supply terminals.

A three-phase supply can be connected at the main supply terminals **A**, **B** and **C** to produces a 4-pole magnetic field, and hence interactions of this field with the rotor bar generate torque and the rotor rotates. Whereas, the bridge points of each phase **A₁–A₂**, **B₁–B₂**, and **C₁–C₂** can be excited individually using a current source, isolated from each other and also isolated from the main supply. When the bridge points are open it is referred as Bridge OFF condition, when the bridge points are short-circuited it is referred as Bridge ON condition and when a voltage source is connected across the bridge it is referred as bridge supply condition. Transverse forces in BCW electrical machines is generated when the rotor is eccentric with respect to the stator centre and forces can also be generated by connecting bridge supply through the bridge points while the rotor is concentric with the stator centre. The generation of force in an eccentric rotor condition also depends on the status of the bridge conditions, i.e. Bridge ON or Bridge OFF. If the bridge is in ON condition,

Fig. 3 Winding connections of the BCW induction machine used for numerical simulation



it passively suppresses the unbalanced magnetic pull that arises due to the eccentric position of the rotor. Figure 2 shows the schematic representation of an electrical machine consists of the bearings, rotor and stator. The rotor is modelled as a rigid rotor having four dofs (x, y, α, β). Here, x and y are the displacements along x - and y -axes, α and β are the rotations about x - and y -axes.

2.1 Coupled Magnetic Field and Electric Circuit Model

The formulation of coupled magnetic field and electric circuit equations represented in [12] has been used for the coupling of the rotor motion with the magnetic field and electric circuit equation of the machine. The magnetic field and electrical circuit equation of BCW induction motor can be represented as shown in Eqs. (1)–(4). Equation (1) is the field equation for the entire domain of the electrical machine, Eq. (2) is the stator circuit equation and Eqs. (3) and (4) are the rotor circuit equations.

$$\mathbf{D}\mathbf{a} + \mathbf{E} \frac{d\mathbf{a}}{dt} - \mathbf{P}_S \mathbf{T}\mathbf{i}_S + \mathbf{P}_R \mathbf{u}_R = \mathbf{0} \tag{1}$$

$$\mathbf{Q}_S \frac{d\mathbf{a}}{dt} + \mathbf{R}_S \mathbf{i}_S + L_{eS} \frac{d\mathbf{i}_S}{dt} = \mathbf{u}_S \tag{2}$$

$$\mathbf{Q}_R \frac{d\mathbf{a}}{dt} + \mathbf{R}_R \mathbf{i}_R - \mathbf{u}_S = \mathbf{0} \tag{3}$$

$$\mathbf{V}^T \mathbf{V} \mathbf{u}_R + 2\mathbf{R}_{eR} \mathbf{i}_R + 2\mathbf{L}_{eR} \frac{d\mathbf{i}_R}{dt} = \mathbf{0} \quad (4)$$

where \mathbf{D} is the magnetic stiffness matrix and its size is $(n \times n)$, n is number of nodes, \mathbf{a} is the magnetic vector potential vector and its size is $(n \times 1)$. \mathbf{E} represents the contribution of the induced electromotive force in the field equation due to rotor bar and its size is $(n \times n)$, \mathbf{P}_S represents the contribution of the excitation of the stator windings and its size is $(n \times q)$, q is the number of stator coil sides, \mathbf{P}_R is the contribution of the excitation at the rotor conductor, \mathbf{T}_S is the transformation matrix used for the transformation of the circuit currents to the coil side currents and its size is $(q \times m)$, m is the number of stator currents and its value is 6 in Bridge OFF condition and 9 in Bridge ON and bridge supply conditions, \mathbf{Q}_S is the contributions of induced electromotive force in the stator and its size is $(m \times n)$, \mathbf{R}_S is the stator coil resistance matrix and its size is $(m \times m)$, \mathbf{L}_{eS} is the stator end coil inductance matrix, \mathbf{i}_S is the stator circuit current vector and its size is $(m \times 1)$, \mathbf{u}_S is the stator circuit voltage vector its size is $(m \times 1)$, \mathbf{u}_R is the voltage vector where individual voltages represents the voltages across the rotor bars and its size is $(b \times 1)$, b is the number of rotor bars, \mathbf{i}_R is the rotor bar current vector and its size is $(b \times 1)$, \mathbf{R}_{eR} and \mathbf{L}_{eR} are the rotor end winding resistance matrix and inductance matrix, respectively, and their size is $(b \times b)$, and \mathbf{Q}_R is the contributions of induced electromotive force in the rotor circuit equations and its size of is $(b \times n)$ and \mathbf{V} is the transformation matrix which converts the end ring currents to the rotor bar currents and its size is $(b \times b)$.

The coupled field and circuit equation are solved for magnetic vector potential \mathbf{a} , stator circuit current vector \mathbf{i}_S , rotor bar current vector \mathbf{i}_R and rotor bar voltage vector \mathbf{u}_R using Crank–Nicolson method. The magnetic field is calculated using magnetic vector potential as,

$$\mathbf{B} = \nabla \times \mathbf{A} \quad (5)$$

where \mathbf{B} is the magnetic flux density and \mathbf{A} is the magnetic vector potential. The Maxwell stress method has been used for the calculation of forces at the air gap.

2.2 Rotordynamics Model

The magnetic forces acting on the rotor is coupled with the rigid rotor equation of motion as shown in Eq. 8. Here, m_{rot} is the mass of the rotor, I ($I_x = I_y = I$) is the mass moment of inertia of the rotor about x - and y -axes, I_z is the mass moment of inertia of the rotor about z -axis. Ω is the rotor rotational speed, l_1 and l_2 are the distance of the bearing locations from the centre of mass of the rotor, k_{x1} , k_{y1} and k_{x2} , k_{y2} are the bearing stiffness along x - and y -axes of two mechanical bearings, respectively. $f_{\text{mag}x}$, $f_{\text{mag}y}$ and $f_{\text{unb}x}$, $f_{\text{unb}y}$ are the magnetic and mass unbalanced forces acting at the centre of mass along x - and y -axes, respectively. It has been

assumed that the unbalance and magnetic forces act at the centre of mass of the rotor. Under the action of these forces, the rotor changes its position and its centre of mass moves to a new position. Also, the rotor undergoes rotations at this new position along x and y -axes by angles α and β , respectively and obtain a new orientation. x_{A1} , x_{A2} and y_{A1} , y_{A2} are the new positions of the rotor with respect to the bearing axis along x - and y -axes, respectively. Maxwell stress tensor method has been used for the calculation of transverse forces as shown in Eqs. 6 and 7 [13]. Here, σ_n and τ_t are the normal and tangential components of Maxwell stress and F_{magx} and F_{magy} are the transverse magnetic force acting along x - and y -axis, respectively. Equation 8 represents the equation of motion of the rotor with respect to the centre of mass. Here, \mathbf{M} is the mass matrix, \mathbf{G} is the gyroscopic matrix, \mathbf{K} is the stiffness matrix, \mathbf{f}_{mag} is the magnetic force vector, \mathbf{f}_{unb} is the unbalance force vector and \mathbf{d} is the vector representing the rotor displacements.

$$\sigma_n = \frac{(B_n^2 - B_t^2)}{2\mu_o} \text{ and } \tau_t = \frac{2B_n B_t}{2\mu_o} \tag{6}$$

$$F_{magx} = l \int_0^{2\pi} (\sigma_n \cos \theta - \tau_t \sin \theta) r d\theta \text{ and } F_{magy} = l \int_0^{2\pi} (\sigma_n \sin \theta + \tau_t \cos \theta) r d\theta \tag{7}$$

$$\mathbf{M}\ddot{\mathbf{d}} + \mathbf{G}\dot{\mathbf{d}} + \mathbf{K}\mathbf{d} = \mathbf{f}_{mag} + \mathbf{f}_{unb}. \tag{8}$$

$$\text{where, } \mathbf{M} = \begin{bmatrix} m_{rot} & 0 & 0 & 0 \\ 0 & m_{rot} & 0 & 0 \\ 0 & 0 & I & 0 \\ 0 & 0 & 0 & I \end{bmatrix}, \mathbf{G} = \begin{bmatrix} 0 & 0 & 0 & 0 \\ 0 & 0 & 0 & 0 \\ 0 & 0 & 0 & -I_z \Omega \\ 0 & 0 & I_z \Omega & 0 \end{bmatrix},$$

$$\mathbf{f}_{mag} = \begin{bmatrix} f_{magx} \\ f_{magy} \\ 0 \\ 0 \end{bmatrix}, \mathbf{f}_{unb} = \begin{bmatrix} f_{unbx} \\ f_{unby} \\ 0 \\ 0 \end{bmatrix}, \mathbf{d} = \begin{bmatrix} x \\ y \\ \alpha \\ \beta \end{bmatrix},$$

$$\mathbf{K} = \begin{bmatrix} k_{x1} + k_{x2} & 0 & 0 & l_1 k_{x1} - l_2 k_{x2} \\ 0 & k_{y1} + k_{y2} & l_1 k_{y1} - l_2 k_{y2} & 0 \\ 0 & l_1 k_{y1} - l_2 k_{y2} & l_1^2 k_{y1} + l_2^2 k_{y2} & 0 \\ l_1 k_{x1} - l_2 k_{x2} & 0 & 0 & l_1^2 k_{x1} + l_2^2 k_{x2} \end{bmatrix}$$

Equations 1–4 and 6–8 are solved simultaneously to calculate magnetic vector potential vector \mathbf{a} , rotor displacements vector \mathbf{d} , velocity vector $\dot{\mathbf{d}}$, stator currents vector \mathbf{i}_s , rotor bar currents vector \mathbf{i}_R and rotor bar voltages vector \mathbf{u}_R . The input of the simulation is various winding parameters, slip condition (s) and simulation time (t_f). The simulation is initialized by providing initial values of \mathbf{a} , \mathbf{d} , $\dot{\mathbf{d}}$, \mathbf{i}_s , \mathbf{i}_R and \mathbf{u}_R . Based on the requirement of force, a bridge supply along with the main supply can be given to generate transverse force on the rotor of the motor. However, if there is

no requirement of lateral force generation, only the main supply can be provided. Air gap stitching method as explained in [12] is used for the movement modelling of the rotor. After excitation conditions and rotor positions are defined, the coupled field and circuit equation are solved using Crank–Nicolson method to calculate the magnetic vector potential at each node, stator circuit current, rotor bar current and rotor bar voltage at next time step. The forces acting on the rotor is calculated by the Maxwell stress tensor method. Once the magnetic forces acting on the rotor is known, the mechanical equation of the motion has been solved by using fourth-order Runge–Kutta method to calculate the new position and velocity of the rotor.

3 Simulation Results

Simulations have been carried out using the developed coupled numerical model to study the effects of different bridge conditions on the air gap force production. The parameters of the induction machine used for simulation are considered similar to the machine used in [12]. Table 1 shows the electrical parameters of the induction machine. Table 2 shows the parameters of the rotor-bearing system.

Figures 4 and 5 represent the comparison of rotor response along the y -axis in Bridge OFF and Bridge ON conditions in static and dynamic eccentricity states, respectively. In static eccentricity condition, the rotor position has been shifted by 10^{-4} m along the x -axis and the rotor is allowed to vibrate with respect to this point subjected to eccentricity induced forces. In dynamic eccentricity condition, an unbalanced force of 0.1×10^{-4} kg m has been introduced in the rotor. This unbalance

Table 1 Electrical parameters of the induction machine

Parameters	Value
No. of poles	4
No. of stator slots	36
No. of rotor bars	26
Outer dia. of stator	160 mm
Outer dia. of rotor	103 mm
Air gap length	1 mm
Axial length of the motor	135 mm
Resistance per phase	6.8 Ω
End winding inductance	3.94×10^{-4} A/m
Resistance of each rotor bar	10^{-5} Ω
Rotor end ring resistance	2.49×10^{-6} Ω
Rotor end ring inductance	1.54×10^{-8} A/m
Main supply voltage	37 V, 50 Hz
Slip	0.02

Table 2 Parameters of the rotor-bearing system

Parameters	Value
m	0.1 kg
I	0.0433 kg m ²
I_z	0.0080 kg m ²
$l_1 = l_2$	0.1865 m
Mass unbalance	0.1 kg
Static eccentricity	1×10^{-4} m
Unbalance	0.1×10^{-4} kg m
$k_{x1} = k_{x2} = k_{y1} = k_{y2}$	1×10^8 N/m

Fig. 4 Displacement of the rotor along y-axis in static eccentricity for Bridge ON and Bridge OFF conditions

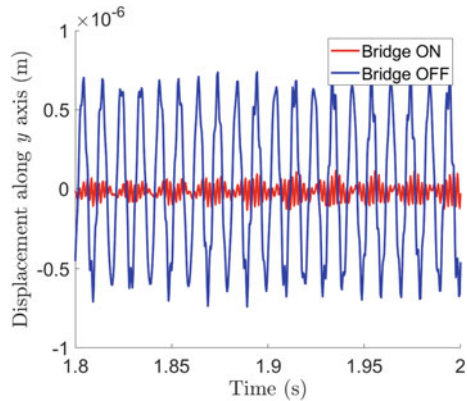
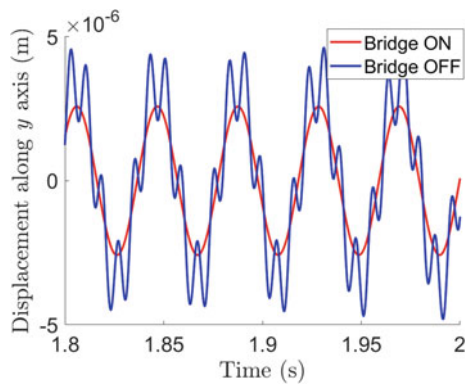


Fig. 5 Displacement of the rotor along y-axis in dynamic eccentricity for Bridge ON and Bridge OFF conditions



force-induced vibration creates dynamic eccentricity condition in the machine, and rotor is allowed to vibrate subjected to the mass unbalance force and dynamic eccentricity induced forces. It can be observed in Fig. 4 that Bridge ON condition is able to suppress the rotor vibration substantially. However, the suppression of rotor vibration

Fig. 6 Comparison of magnetic force acting on the rotor in dynamic eccentricity condition in Bridge OFF and Bridge ON condition

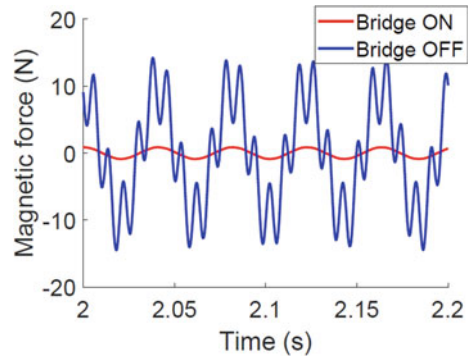
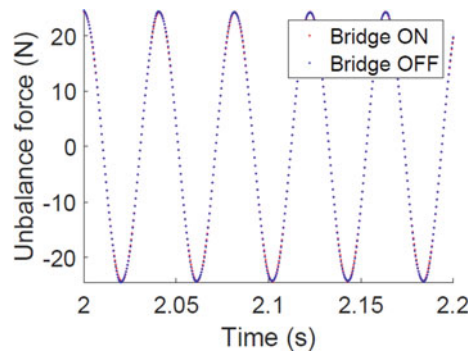


Fig. 7 Comparison of unbalanced force in acting on rotor in dynamic eccentricity condition in Bridge OFF and Bridge ON condition



is lesser in dynamic eccentricity condition as shown in Fig. 5. To investigate it further, the magnetic and unbalanced forces acting in dynamic eccentricity conditions have been compared separately in Bridge OFF and Bridge ON conditions as shown in Figs. 6 and 7, respectively. It can be observed that the reduction of magnetic forces in dynamic eccentricity condition is substantial; however, the reduction in unbalance force is quite negligible. The unbalanced force has component $Me\omega^2$, here, e is the distance between the centre of shaft and the centre of mass and M is the mass of the rotor. However, to cancel out the constant component of the unbalanced force, a bridge supply would be needed, which has not been analysed in this paper.

4 Conclusions

A coupled magnetic field, electrical circuit and rotor equation of motion model have been developed in MATLAB environment to analyse the rotor vibration in the state of static and dynamic eccentricity conditions. The developed model is generic in nature which can be used to simulate the Bridge ON, Bridge OFF and bridge supply conditions. The present work demonstrates the capability of developed code

by analysing rotor vibration in static and dynamic eccentricity conditions. The passive vibration capability of bridge configured winding has been demonstrated. Further, the developed code would be very helpful to study the transverse force generation in the bridge supply condition, which can be used for the development of bearingless electrical machines.

Acknowledgements This work was supported by the Science and Engineering Research Board, Department of Science and Technology, Government of India

References

1. Bhangu B, Rajashekara K (2014) Electric starter generators: their integration into gas turbine engines. *IEEE Ind Appl Mag* 20:14–22
2. Alexander G, Pertsch J (1918) Critical review of the bibliography on unbalanced magnetic pull in dynamoelectric machines. *Trans Am Inst Electr Eng* 37(2):1417–1424
3. Debortoli MJ, Salon SJ, Burow DW, Slavik CJ (1993) Effects of rotor eccentricity and parallel windings on induction machine behavior: a study using Finite element analysis. *IEEE Trans Magn* 29:1676–1682
4. Tenhunen A (2009) Finite element calculation of unbalanced magnetic pull and circulating current between parallel windings in induction motor with non-uniform eccentric rotor. *J Syst Des Dyn* 3:519–529
5. Tenhunen A, Holopainen TP, Arkkio A (2003) Effects of equalizing currents on electromagnetic forces of whirling cage rotor. *Proc IEMDC* 3:257–263
6. Laiho A, Sinervo A, Orivuori J, Tammi K, Arkkio A, Zenger K (2009) Attenuation of harmonic rotor vibration in a cage rotor induction machine by self-bearing force actuator. *IEEE Trans Magn* 45(12):5388–5398
7. Oishi R, Horima S, Sugimoto H, Chiba A (2013) A novel parallel motor winding structure for bearingless motors. *IEEE Trans Magn* 49:2287–2290
8. Chiba A, Horima S, Sugimoto H (2013) A principle and test results of a novel bearingless motor with motor parallel winding structure. *Energy Convers Congr Expos (ECCE)* 2013:2474–2524
9. Khoo WKS (2005) Bridge configured winding for polyphase self-bearing machines. *IEEE Trans Magn* 39:1289–1295
10. Khoo WKS, Kalita K, Garvey SD (2011) Practical implementation of the bridge configured winding for production of controllable transverse forces in electrical machines. *IEEE Trans Magn* 47(6):1712–1718
11. Kalita K, Natesan S, Kumar G, Tammi K (2015) Vibration control in electrical machines using built-in actuator. In: *Proceedings of the 9th IFToMM international conference on rotor dynamics*, vol 21, pp 1593–1603
12. Kumar G, Kalita K, Tammi K (2018) Analysis of bridge currents and UMP of an induction machine with bridge configured winding using coupled field and circuit modeling. *IEEE transactions on magnetics*, vol. 54, no. 9
13. Bastos JPA, Sadowski N (2003) *Electromagnetic modeling by finite element methods*. CRC Press, Boca Raton

Dynamic Modeling and Analysis of Propeller Shaft Supported on Rolling Element Bearings



Devendra Singh and J. Srinivas

Abstract This paper presents modeling and dynamic analysis of marine propulsion shaft supported on three radial and one thrust bearings. The motions of rotor and bearings are under the influence of each other, and therefore, such a system requires structural dynamic studies. Initially, the rotor bearing system is analyzed with finite element model to obtain the modal properties. Internal unbalance force due to mass eccentricity acts on the propeller. Unbalance response of the rotor is obtained numerically from Neumark time integration scheme. Effect of speed and bearing stiffness on the dynamic response is studied. In further case, the radial springs are replaced with three ball bearings, which are modeled by Hertz contact forces expressed in terms of the corresponding nodal displacements. The effects of disk imbalance, thrust bearing stiffness and number of propeller blades on system response are illustrated for different speeds in terms of time and frequency responses. The generalized interactive approach is useful for carrying out parametric studies.

Keywords Propulsion shaft · Hertz contact force · Dynamic response · Stability analysis

1 Introduction

Marine propulsion rotors are heavy-duty long shafts coupled to the hull and are quite difficult to analyze in practical conditions. Often, they are joined together with couplers and have uneven eccentricities. Therefore, they are mounted on several bearings in radial and axial directions. The system in its simplest form consists of the shaft, bearings and a propeller. The power from the engine is transmitted to the propeller, which generates the thrust necessary to propel. Pulsing torque of

D. Singh · J. Srinivas (✉)
Department of Mechanical Engineering, NIT Rourkela, Rourkela 769008, India
e-mail: srin07@yahoo.co.in

D. Singh
e-mail: 17.devendersingh@gmail.com

the engine, unsteady propeller thrust and imbalance of rotating parts of the system, respectively, result in torsional, longitudinal and transverse vibrations of the system. Free and forced vibration analysis of these rotors is essential to know the effects operating parameters on the vibration modes and response in order to mitigate resonance regions. The overall development and design of propeller system technology with hydrodynamic supports, strength and manufacturing aspects were given by Carlton [1]. A geometric approach of marine propeller rotor with numerical modeling of engine, propeller and control actuators was presented by Figari and Altosole [2] for nonlinear dynamic simulations of the system. Huang et al. [3] studied coupled torsional–longitudinal vibrations of ship’s propeller shaft. Sternlicht et al. [4] studied the propulsion shaft system with thrust bearing as the sole axial support. Sliding tilting pad thrust bearing was used for supporting the hull against propeller thrust. Xiao et al. [5] studied the characteristics of hybrid propulsion shaft with mathematical model and vibration equations of the shaft using lumped parameter approach. Experimental work on double diesel propulsion shafting bench was illustrated. Zou et al. [6, 7] presented coupled longitudinal and transverse vibrations of the propulsion shaft system. Chen et al. [8] analyzed vibration characteristics of propeller shaft subjected to inflow turbulence. In more recent work, Huang et al. [9] studied the coupled torsional–lateral vibrations of propeller shaft system by accounting effects of damping ratio, cross-sectional eccentricity and length to diameter ratio, etc., on the overall stability of the system. Chen et al. [10] developed a coupled longitudinal and transverse model of a submarine propeller-shaft-hull system using sub-structuring approach. In most of these works, the bearings are simply treated as linear members, and the contributory effects of supports were not studied. In practice, lateral and axial vibrations are coupled in such systems with strong nonlinearities in bearing forces. Stability studies at off-resonance states has a vital significance.

Present work focuses on the dynamic modeling of the propeller rotor shaft system. Initially, free vibration characteristics are obtained. Time and frequency domain analysis are conducted, and the effect of propeller unbalance is studied on the dynamic response. Some stability issues are discussed with respect to rotor eccentricity, number of propeller blades at different speeds of operation. The paper is organized as follows: Sect. 2 presents mathematical modeling including the energy expressions and equations of motion for finite element analysis of rotor, bearing reaction forces, etc. Section 3 describes results and discussion.

2 Mathematical Modeling

A simplified model of the rotor system is developed using Euler–Bernoulli’s beam theory. Figure 1 shows the shaft system supported on three radial bearings (back stern B1, front stern B2, middle B3) and one thruster (T1). It has propeller disk at left end and engine at the other end. Propeller is treated as rigid and shaft system is considered as flexible.

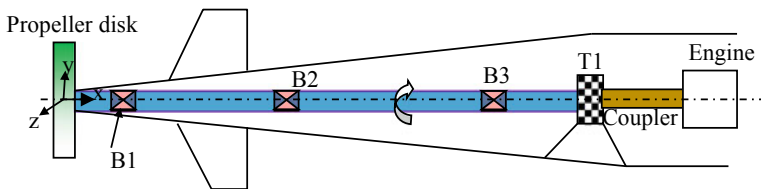


Fig. 1 Rotor dynamic system of propeller shaft

The kinetic energy and potential energy of rotor shaft element can be written in terms of material elasticity E and density ρ along with cross-sectional area A , the diameter and polar moment of inertia of the shaft are I_d and I_p , respectively. The strain energy of the shaft can be written as

$$U = U_{\text{shaft}} = \frac{1}{2} \int_0^l \left[EA \left(u'^2 + \frac{1}{4} (v'^2 + w'^2)^2 + u' (v'^2 + w'^2) \right) + EI_d (v''^2 + w''^2) \right] dx \tag{1}$$

Deflections in longitudinal, two lateral direction are u , v and w , respectively. The prime indicates derivative with respect to x . Also u , v , w are the function of x and t only. Likewise, the kinetic energy of the shaft and that of propeller disk is given by

$$T_{\text{shaft}} = \frac{\rho}{2} \int_0^l \left[A (\dot{u}^2 + \dot{v}^2 + \dot{w}^2) + I_d (\dot{v}^2 + \dot{w}^2) + I_p \Omega^2 + I_p \Omega (w' \dot{v}' - v' \dot{w}') \right] dx \tag{2}$$

$$T_{\text{disk}} = \frac{1}{2} m_d [\dot{u}^2 + \dot{v}^2 + \dot{w}^2]_{x=0} + \frac{1}{2} J_d (\dot{v}^2 + \dot{w}^2)_{z=0} + \frac{1}{2} J_p \Omega (w' \dot{v}' - \dot{v}^2 \dot{w}')_{x=0} + \frac{1}{2} J_p \Omega^2 \tag{3}$$

Here, m_d , J_d , J_p are mass, diametral and polar moment of inertia of the propeller, respectively, and Ω is the rotor speed. The external work done by unbalance forces at the propeller disk (eccentricity ‘ e ’) is given as

$$W_d = m_d e \Omega^2 (v \cos \Omega t + w \sin \Omega t)_{x=0} \tag{4}$$

As an external force, axial harmonic thrust load with the first blade passing frequency is considered. Work done by the force is

$$W_b = |F \cos(n\Omega t + \alpha) u|_{x=0} \tag{5}$$

where F is the amplitude of thrust force, α is the phase angle, n is number of blades, and $n\Omega$ is the blade passing frequency of the propeller.

The equations of motion are obtained by substituting above energy expression in the Hamilton principle

$$\delta \int_{t_1}^{t_2} (T - U + W) dt = 0 \tag{6}$$

where δ denotes the variational operator .

The resulting equations of motion of the rotor system in matrix form can be written as

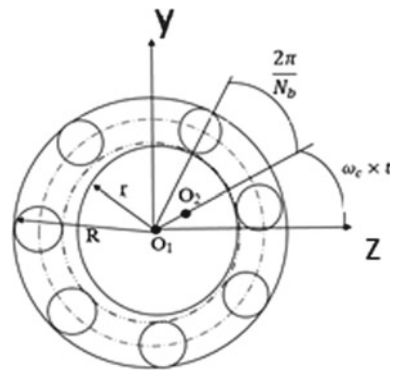
$$[M]\{\ddot{U}\} + ([C] + \Omega[G])\{\dot{U}\} + [K]\{U\} = \{f\} + \{f_b\} \tag{7}$$

Here, $[M]$, $[C]$, $[G]$ and $[K]$ are, respectively, the overall mass, damping, gyroscopic and stiffness matrices. $\{U\}$ is the displacement vector, $\{f\}$ is unbalance and blade force vector at the propeller node, while $\{f_b\}$ is components of nonlinear bearing forces.

2.1 Bearing Forces

In present context, Hertz’s contact theory is used to calculate the ball bearing forces due to the dry friction. Ball bearing consists of inner race, outer race, rolling balls and a cage as shown in Fig. 2. The outer race acts on the inner race by rolling action of the balls, and this results in interaction force which is called restoring force. Bai et al. [11] studied nonlinear dynamic response of a flexible rotor supported by ball bearings. The finite element rotor system with a shaft, one disc, two flexible bearing supports and a ball bearing element where the nonlinearities were due to both the radial clearance and the Hertzian contact between races and rolling elements. Nelson [12] used finite element model to study rotor bearing system which includes the effect of rotary

Fig. 2 Line diagram of ball bearing



inertia, gyroscopic moments and axial load using the consistent matrix approach. Liqin et al. [13] studied the nonlinear bearing forces of roller bearing and used Neumark-beta and New Raphson to solve the nonlinear equations. Tiwari [14,15] studied the nonlinear behavior of a balanced rotor by taking into the effects of internal clearances of a roller bearing and also analyzed the dynamic characteristics of an unbalance rotor. Luczko [16] developed a geometrically nonlinear model for rotating shafts, with internal resonance and self-excited vibration. Mevel and Guyader [17] studied the dynamic motion of ball bearing, which involves different mechanism in transition to chaotic behaviors, also by varying a control parameter; different routes to chaos are described.

Assume Ω as the speed of rotation of the rotor, r_i and r_o are inner and outer race radii, respectively, ω_c is the nominal cage speed, $\omega_c t$ is the cage angular position, O_1 and O_2 are the center of the two races, and then, the attitude angle for each ball is given by $\varphi_j = \frac{2\pi}{N_b}(j-1) + \Omega\left(\frac{r_i}{r_i+r_o}\right)$. In the rotor bearing system, usually, the outer race of the ball bearing is fixed to the bearing housing, and the inner race is rigidly fixed to the rotating shaft. The simplified model with two degrees of freedom has two component forces given as

$$F_{zb} = - \sum_{j=1}^{N_b} K_b \delta_j^{1.5} H(\delta_j) \cos \varphi_j \quad (8)$$

$$F_{yb} = - \sum_{j=1}^{N_b} K_b \delta_j^{1.5} H(\delta_j) \sin \varphi_j \quad (9)$$

where N_b are number of balls, K_b is load deflection factor ($N/m^{1.5}$) depends on the material properties and curvatures of the surface in contact, and also, Heaviside function (H) is defined as

$$\begin{aligned} H(\delta_j) &= 1 \text{ if } \delta_j > 0 \\ &= 0 \text{ if } \delta_j \leq 0 \end{aligned} \quad (10)$$

Here, δ_j is total elastic deformation, given as

$$\delta_j = v_b \cos \varphi_j + w_b \sin \varphi_j - r_c \quad (11)$$

with $r_c = r_{ci} + r_{co}$, is the total radial clearance between inner and outer races and ball, v_b and w_b refer to the relative displacements of the inner and outer races along y- and z-directions, respectively.

3 Results and Discussions

For dynamic analysis, the rotor is discretized into eight uniform beam elements. The propeller disk is represented as lumped mass (rigid body) located at the node 1, while the nodes 2, 6, 8 and 9 represent the bearing positions as shown Fig. 3. Each node has five degrees of freedom (DOF) including three translations (u, v, w) and two rotational degrees or slopes (v', w'). Total there are 45 degrees of freedom in the assembled system.

The assembled system of equations of motion are formulated in matrix form and solved numerically through Neumark time integration scheme with zero initial conditions via a MATLAB program. Dimension and material properties for the rotor system are shown in Table 1. The axial coordinates of each bearing support are 0.42m (node-2), 4.62m (node-6), 8.55 m (node-8) and thrust bearing at 8.8 m (node-9) from the left end.

In order to validate the finite element code, initially, the linear spring elements are used to idealize the bearings with the following stiffness coefficients from left to right: $k_{B1} = 2.5 \times 10^8$ N/m, $k_{B2} = 0.8 \times 10^8$ N/m, $k_{B3} = 3 \times 10^8$ N/m and $k_{T1} = 2.5 \times 10^8$ N/m. Table 2 shows the first few natural frequencies obtained at three different speeds of operations. The backward and forward transverse mode frequencies at 200 rpm are very close to 8.774 and 12.752 Hz at obtained by Zou et al. [7].

Further, the spring elements are replaced by ball bearings for all three radial bearings. Ball bearing parameter is shown in Table 3.

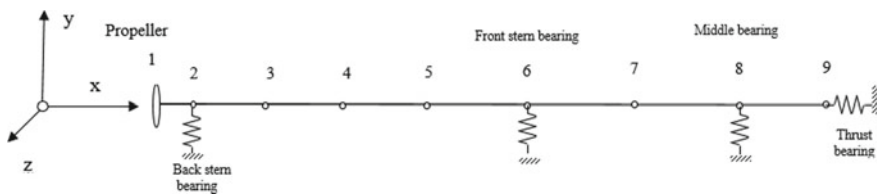


Fig. 3 Finite element model

Table 1 Geometric and material propeller shaft [7]

Property	Value	Property	Value
Density of shaft material (kg/m^3)	7800	Outer diameter of shaft (m)	0.240
Mass of propeller (kg)	6600	Inner diameter of shaft (m)	0.120
Diameter moment of inertia of propeller (kg m^2)	3000	Young's modulus of shaft (GPa)	210
Polar mass moment of inertia of propeller (kg m^2)	6000	Disk Eccentricity (m)	20×10^{-6}
Length of shaft (m)	8.8		

Table 2 First few natural frequencies (in Hz)

S. No	Rotor at rest	Speed = 200 rpm	Speed = 400 rpm
1	10.4731	8.4717	6.8886
2	10.4731	12.8400	15.3936
3	31.3386	30.8463	30.4632
4	31.3386	31.9714	32.7635
5	36.3824	36.3737	36.3767

Table 3 Ball bearing data for SKF 2500 bearing

S. No.	Properties	Value
1	Number of balls	7
2	Inner race radius (m)	2.75×10^{-3}
3	Outer race radius (m)	4.7565×10^{-3}
4	Ball radius (m)	1×10^{-3}
5	Load-deflection factor ($\text{Nm}^{-1.5}$)	1.3603×10^9

Forces considered here are unbalance due to disk eccentricity and axial blade force with amplitude $F = 1$ N, zero phase with seven blades on disk ($F = 1, \alpha = 0$ and $n = 7$). The time response in x-direction at the back stern bearing (node-2) with a rotor speed of 200 rpm is shown in Fig. 4.

It is obvious that the system is stable because the response obtained is not diverging in nature. The first dominant peak for nonlinear bearing force is obtained at 4.578 Hz. The corresponding phase plane diagram shows a limit cycle formation due to bearing nonlinearity. When speed has increased in steps of 50 starting from 250 to 400 rpm, the FFT plots at the node 2 are illustrated in Fig. 5. At 300 rpm, only single dominant peak is observed which conveys that energy is concentrated at a frequency and system is stable. As speed of the rotor is increased, the dominant peak shifts toward left, and also, multiple peaks are observed due to ball passing frequencies. The first dominant peak is found at (i) 5 Hz in 250 rpm (ii) 5.493 Hz in 300 rpm (iii) 4.833 Hz in for 350 rpm (iv) 4.578 Hz in 400 rpm.

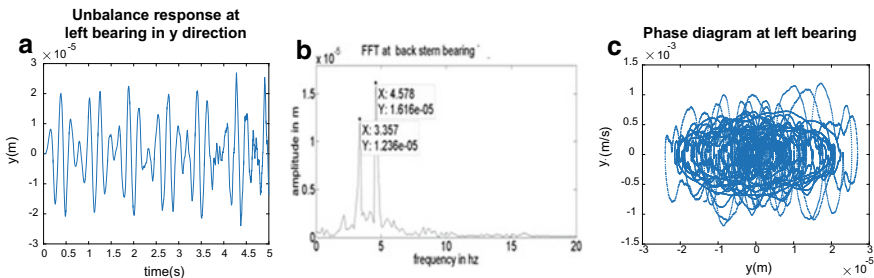


Fig. 4 Dynamic responses at node-2, **a** time response, **b** frequency spectrum, **c** phase portrait

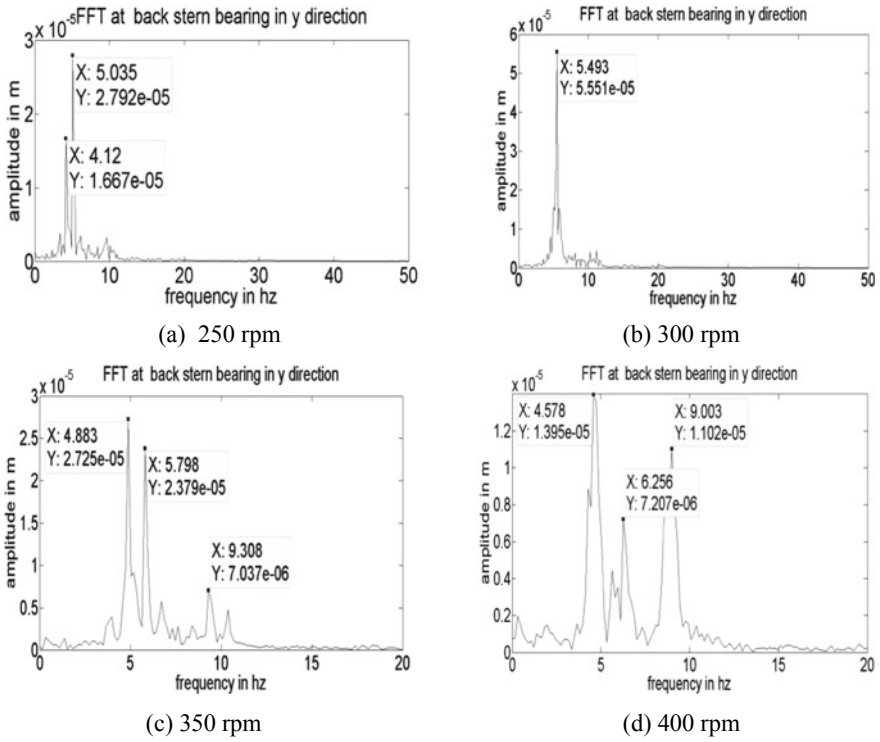


Fig. 5 Frequency spectra at different rotor speeds

As thrust bearing stiffness increases, the fundamental natural frequency increases rapidly, but afterward, it remained nearly constant. The effect of unbalance eccentricity of the rotor is studied at constant rotor speed of 300 rpm, and resultant FFT plots are shown in Fig. 6.

It is observed that as the eccentricity increases, maximum amplitudes of response increase due to increased unbalance force. Figure 7 shows the dynamic response at node 2 in axial direction at 100 rpm.

It is seen that axial response mode is having only single peak, whereas lateral responses have two distinct peaks, and small multiple peaks in y- and z-directions are due to ball passing frequencies. Figure 8 shows the effect of number of blades of propeller on the dynamic response. It is seen that the amplitude has slightly reduced as number of blades increase. Amplitude and phase have negligible effect.

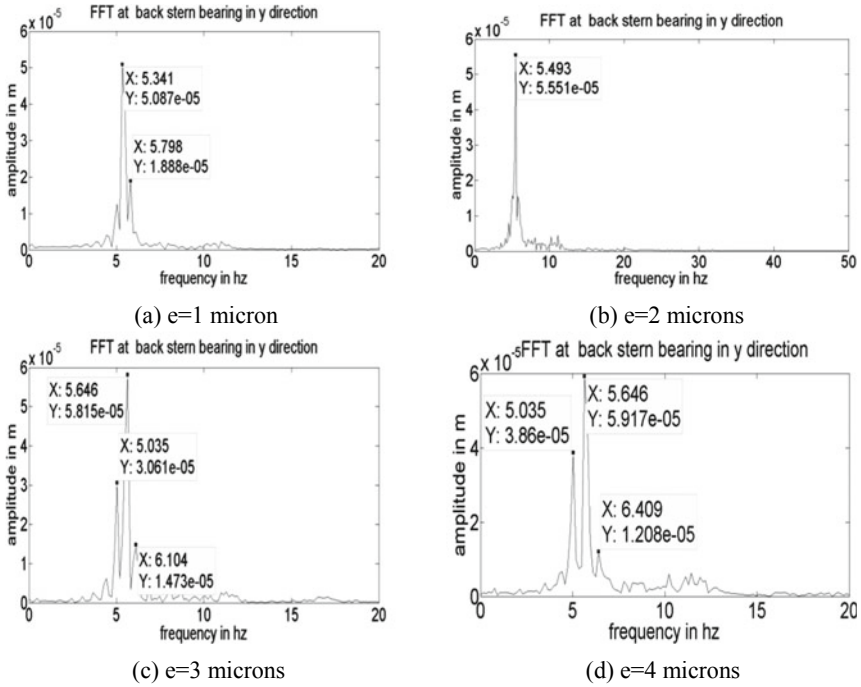


Fig. 6 Frequency spectra at different disk eccentricities

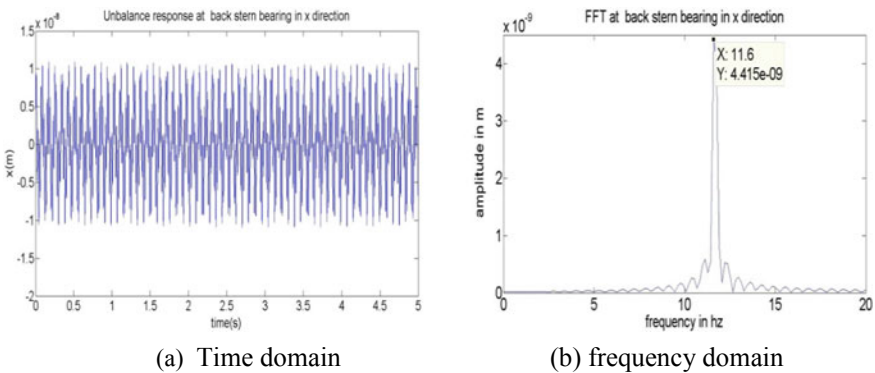


Fig. 7 Response in axial direction at 100 rpm

4 Conclusions

Present work described the coupled lateral-axial vibration analysis of propeller shaft system supported on three radial ball bearings and one thrust bearing. Dynamics and stability studies were conducted to know the effect of thrust bearing, disk unbalance

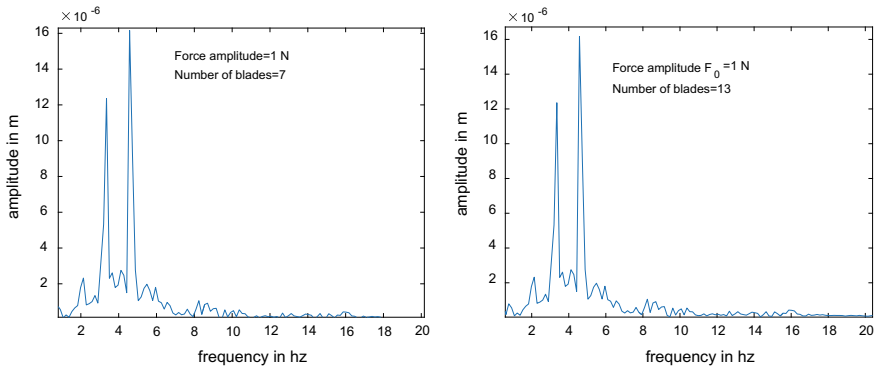


Fig. 8 Dynamic response at left bearing node at 200 rpm and $e = 20 \mu\text{m}$

eccentricity at different operating conditions. At 200 rpm, the time responses obtained for linear and nonlinear model were found to be stable in nature. By increasing the thrust bearing stiffness, fundamental natural frequency of system has also increased. Time and frequency responses obtained for axial and lateral modes at 100 rpm showed stable conditions. As a future scope of the present work, the stability of rotor may be studied with realistic thrust bearing model instead of elastic spring by including the parameters like number of pads, thickness, as well as its optimum location. An experimental work is also required with a thrust bearing to support the studies. Effect of fluid induced force transmission on the hull vibrations may also be studied in more detail.

References

1. Carlton J (2012) Marine propellers and propulsion, 2nd edn. Butterworth-Heinemann, Oxford
2. Figari M, Altosole M (2007) Dynamic behaviour and stability of marine propulsion systems, *J Eng Maritime Environ Proc IMechE, Part M* 221:187–205
3. Huang Q, Yan X, Wang Y, Zhang C, Wang Z (2017) Numerical modeling and experimental analysis on coupled torsional-longitudinal vibrations of ship's propeller shaft. *Ocean Eng* 136:272–282
4. Sternlicht B, Reid JC, Arwas EB (2009) Review of propeller shaft thrust bearings. *Naval Eng J* 71(2):277–290
5. XiaoN, Zhou R, Xu X, LinX (2016) Study on vibration of marine diesel-electric hybrid propulsion system. *Math Probl Eng*, ID 8130246, <https://doi.org/10.1155/2016/8130246>
6. Zou D, Rao Z, Ta N (2015) Coupled longitudinal-transverse dynamics of a marine propulsion shafting under superharmonic resonances. *J Sound Vibr* 346:248–264
7. Zou D, Liu L, Rao Z, Ta N (2016) Coupled longitudinal-transverse dynamics of a marine propulsion shafting under primary and internal resonances. *J Sound Vibr* 323:299–316
8. Chen Y, Wang L, Hua HX (2017) Longitudinal vibrations of marine propeller shafting system reduced by inflow turbulence. *J Fluids Struct* 68:264–278
9. Huang Q, Yan X, Zhang C, Zhu H (2019) Coupled transverse and torsional vibrations of the marine propeller shaft with multiple impact factors. *Ocean Eng* 178:48–58

10. Chen F, Chen Y, Hua H (2019) Vibration analysis of a submarine elastic propeller-shaft-hull system using FRF-based sub-structuring method. *J Sound Vibr* 443:460–482
11. Bai B, Zhang L, Guo T, Liu C (2012) Analysis of dynamic characteristics of the main shaft system in a Hydro-turbine based on ANSYS. *Procedia Engg* 31:654–658
12. Nelson HD, McVaugh JM (1975) The dynamics of rotor—bearing systems using finite elements. *J Eng Indus* 98(2):593–600
13. Liqin W, Li C, Dezhi Z, Le G (2008) Nonlinear dynamics behaviors of a rotor roller bearing system with radial clearances and waviness considered. *Chinese J Aeronaut* 21:86–96
14. Tiwari M, Gupta K, Prakash O (2000) Effect of radial internal clearance of a ball bearing on the dynamics of a balanced horizontal rotor. *J Sound Vibr* 238:723–756
15. Tiwari M, Gupta K, Prakash O (2000) Dynamic response of an unbalanced rotor supported on ball bearings. *J Sound Vibr* 238:757–779
16. Luczko J (2002) A geometrically non-linear model of rotating shafts with internal resonance and self-excited vibration. *J Sound Vibr* 255(3):433–456
17. Mevel B, Guyader JL (1993) Routes to chaos in ball bearings. *J Sound Vibr* 162(3):471–487

Rotordynamic Analysis of High-Speed Rotor Used in Cryogenic Turboexpander Using Transfer Matrix Method



Debanshu S. Khamari, Partha Sarathi Kar, Shantashree Jena, Jitesh Kumar, and Suraj K. Behera

Abstract Cryogenic turboexpander is considered as the heart of modern gas liquefier for its high thermodynamic efficiency and high reliability. The operating speed of small- and mid-sized turboexpander is usually greater than 50,000 rpm. Such high rotational speed brings constrain in the selection of the appropriate bearings. In turboexpander, gas bearings are found suitable to use, where process gas is used as a lubricant to avoid contamination. The study of rotordynamic behaviour of such high-speed turbomachinery is essential to avoid resonant conditions and predict unbalance vibrations. In the current application, transfer matrix method (TMM) is used to predict critical speed, mode shapes and unbalance response of a rotor using gas foil journal bearings. The predicted critical speeds are compared with experiments to validate the same. The rotational speed of the designed rotor is 80,000 rpm with an unbalance of 40 mg-mm at each journal bearing.

Keywords Turboexpander · Transfer matrix method · Gas foil bearings

D. S. Khamari · P. S. Kar · J. Kumar · S. K. Behera (✉)
National Institute of Technology, Rourkela, Sundergarh, Odisha 769008, India
e-mail: beherask@nitrkl.ac.in

D. S. Khamari
e-mail: debanshushekhara@gmail.com

P. S. Kar
e-mail: pskar221b@gmail.com

J. Kumar
e-mail: jiteshme23@gmail.com

S. Jena
Indira Gandhi Institute of Technology, Sarang, Dhenkanal, Odisha 759146, India
e-mail: shantashreejena@gmail.com

Nomenclature

l_n	Shaft element length
M_n	Mass of the n th element
E_n	Modulus of elasticity
K_n	Stiffness, (K_b at bearing stations and 0 at all other stations)
$M_{y,n}^L$	Bending moments on the left of the n th disc
$M_{y,n}^R$	Bending moments on the right of the n th disc
V_n^L	Shear forces at the left faces of the n th disc
V_n^R	Shear forces at the right faces of the n th disc
ω	Rotor speed
w	Deflection
θ	Slope
I_n	Area moment of inertia of the n th station
$[F]_n$	Field matrix of the n th station
$[P]_n$	Point matrix for n th station
$\{Q\}_n$	$\{w, \theta, M, V\}^T$, the state vectors at the n th node
$[T]_o$	The overall transfer matrix

1 Introduction

Transverse vibration is a significant cause of failure in high-speed turbomachinery. Therefore, a prior prediction of such failures using vibrational or rotordynamic analysis is an essential requirement for turbomachinery design. The rotordynamic analysis helps to find the possible source of failure and the solution to the same. One solution is to design rotor and bearing systems such that the operating speed of turbomachinery is far from the critical speeds of the bearing and rotor system. Apart from critical speed, the mode shapes and unbalanced response are essential for vibration analysis of the rotor. A mode shape is a definite pattern of vibration of the rotor at the critical speed which is determined by the distribution of mass and stiffness along the rotor [1, 2]. The presence of unbalanced mass causes excessive vibration in the rotating shaft. Proper rotor balancing procedure can minimize these unbalance mass. However, even small unbalance mass in the high-speed rotor can develop an unwanted vibratory response. Thus, the unbalance response analysis of the high-speed rotor is essential. There are many methods for the computation of critical speeds and unbalance response. Currently, the finite element and transfer matrix methods are two of the most prevalent methods for analysing rotor-bearing systems. Among the two, transfer matrix method is used as it is easy and requires lower computation time for the calculation.

2 Rotordynamic Analysis of Prototype Rotor

For each rotor-bearing system, there exists an infinite number of discrete natural frequencies of lateral vibration and for every natural frequency, and there is a mode shape, which can be considered as a depiction of the rotor diversion bend at the moment of most extreme strain amid the vibration. Traditional TMM has fixed matrix dimensions and is easy to solve. In this method, the rotor is modelled as discs and massless elastic elements. The first element is linked to the last element of the rotor by an overall transfer matrix. An overall transfer matrix is used to determine the critical speed and mode shapes upon applying boundary conditions. Further, this method can be easily modified to compute a response to imbalance with a known unbalance mass. In the current application, TMM [1, 2] is used for rotordynamic analysis.

2.1 Transfer Matrix Method

The prototype rotor is divided into N number of stations, where N denotes the last inertia station of the rotor. Figure 1 shows the free body diagrams of the disc (inertial element) and the elastic elements constituting the n th station.

The transfer Eq. (1) for the massless elastic shaft, element is derived using statics and beam deflection theory. The field matrix F_n relates the variable of interests (displacement, slope, bending moment and shear force) or the state vectors between right and left of the beam or between the right of the n th disc and left of the $(n + 1)$ th disc [2].

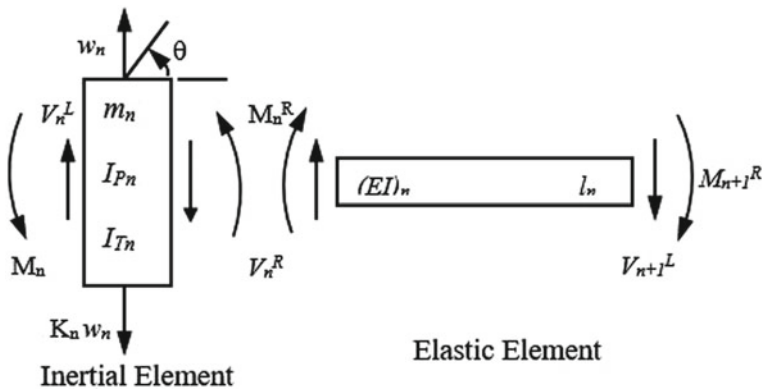


Fig. 1 Free-body diagrams of the elements in the n th rotor station [2]

$$\begin{Bmatrix} -w \\ \theta \\ M_y \\ V_z \end{Bmatrix}_{n+1}^L = \begin{bmatrix} 1 & l & l^2/(2EI) & l^3/(6EI) \\ 0 & 1 & l/(EI) & l^2/(2EI) \\ 0 & 0 & 1 & 0 \\ 0 & 0 & l & 1 \end{bmatrix}_n \begin{Bmatrix} -w \\ \theta \\ M_y \\ M_z \end{Bmatrix}_n^R \quad (1)$$

Symbolically Eq. (1) can be written as:

$$\{Q\}_{n+1}^L = [F]_n \{Q\}_n^R$$

The point matrix of Eq. (2) represents the relation between the variable of interests between right and left of the n^{th} disc [1]. The relation is derived from rigid body mechanics, and the transfer equations across the station for synchronous whirl can be expressed as:

$$\begin{Bmatrix} -w \\ \theta \\ M_y \\ V_z \end{Bmatrix}_n^R = \begin{bmatrix} 1 & 0 & 0 & 0 \\ 0 & 1 & 0 & 0 \\ 0 & (m_n \omega^2 - k_n) & 1 & 0 \\ (I_{Tn} - I_{Pn}) \omega^2 & 0 & 0 & 1 \end{bmatrix} \begin{Bmatrix} -w \\ \theta \\ M_y \\ V_z \end{Bmatrix}_n^L \quad (2)$$

Symbolically Eq. (2) can be written as:

$$\{Q\}_n^R = [P]_n \{Q\}_n^L$$

The relation between the 1st and the last element of the rotor-bearing model can be determined by multiplying all the field and point matrix. The relation can be expressed with an overall transfer matrix $[T_0]$ as:

$$\{Q\}_N^R = [T_0] \{Q\}_1^L \quad (3)$$

where

$$[T_0] = [P_N][F_{N-1}][P_{N-1}] \dots [F_1][P_1]$$

The overall transfer matrix $[T_0]$ is also 4×4 in size as the point matrix $[P]$ and field matrix $[F]$ are all 4×4 matrices. The expanded form of the Eq. (3) is written as:

$$\begin{Bmatrix} r_N \\ \theta_N \\ V_N \\ M_N \end{Bmatrix}^R = \begin{bmatrix} d_{11} & d_{12} & d_{13} & d_{14} \\ d_{21} & d_{22} & d_{23} & d_{24} \\ d_{31} & d_{32} & d_{33} & d_{34} \\ d_{41} & d_{42} & d_{43} & d_{44} \end{bmatrix} \begin{Bmatrix} r_1 \\ \theta_1 \\ V_1 \\ M_1 \end{Bmatrix}^L \quad (4)$$

In the current applications, the turbine and compressor (Fig. 2) are at the free end

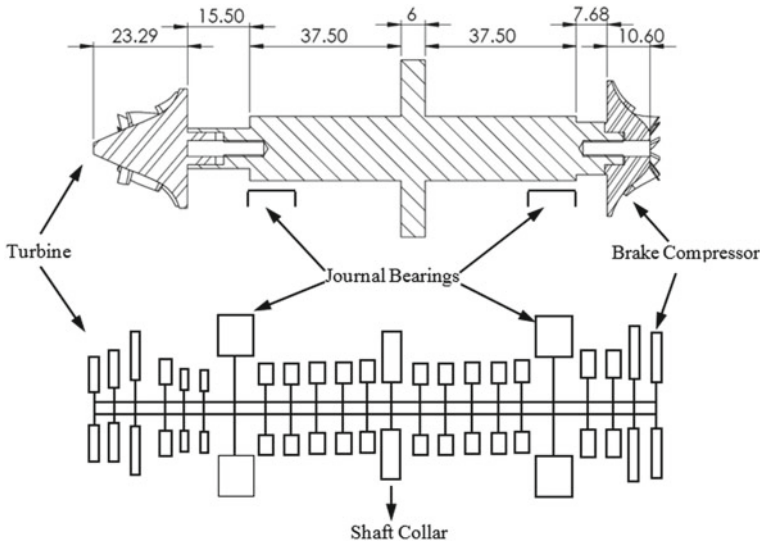


Fig. 2 Prototype rotor with stations

of the rotor, so there is no shear force and bending moment of the 1st and last element of the rotor. Hence, the boundary condition is written as:

$$\begin{Bmatrix} V_N \\ M_N \end{Bmatrix}^R = \begin{Bmatrix} V_1 \\ M_1 \end{Bmatrix}^L = \begin{bmatrix} d_{31} & d_{32} \\ d_{41} & d_{42} \end{bmatrix} \begin{Bmatrix} r_1 \\ \theta_1 \end{Bmatrix}^L = [D] \begin{Bmatrix} r_1 \\ \theta_1 \end{Bmatrix}^L = \begin{Bmatrix} 0 \\ 0 \end{Bmatrix} \quad (5)$$

For Eq. (5) to have non-zero solutions, determinant of the matrix $[D]$ should be zero, so the critical speeds are the value of ω for which the determinate of the matrix is zero. Once the critical speed is determined, the corresponding mode shapes can be evaluated by assuming unit slope at station 1 and compute the displacements at each station.

The process of computation of unbalance response using TMM is an extension of critical speed analysis. In the case of unbalance response analysis [2], the field matrix and point matrix are modified to include bending quantities of the beam and the unbalance mass m_u at an eccentricity e .

2.2 Prediction of Critical Speed, Mode Shape and Unbalance Response

For the current application, the prototype rotor is divided into 23 number of stations (Fig. 2). Each station consists of a lumped inertias (discs) and massless elastic shaft elements. The choice to divide each part into several elements is based on its shapes,

Table 1 Division of prototype rotor

No.	Rotor part description	No. of element
1	The turbine mounted on a protrusion at the cold end of the shaft	3
2	The stepped shaft region between the turbine and lower journal bearing	3
3	Lower journal bearing	1
4	Shaft region between lower journal bearing and collar	5
5	The shaft collar	1
6	Shaft region between the collar and upper journal bearing	5
7	Upper journal bearing	1
8	The stepped shaft region between journal bearing and brake compressor	2
9	The brake compressor mounted on a protrusion at the warm end of the shaft	2

dimensions and materials. The division of the rotor is as shown in Table 1. The stiffness and damping of the journal bearing are 4.02×10^5 N/m and 2.04×10^{-3} N s/m, respectively, for station no. 7 and 19. The stiffness and damping were predicted based on perturbation method and are taken as speed dependent for current analysis. The dynamic coefficients were considered at the design speed. The data for the different stations is given in Table 2. The critical speed computed using TMM are shown in Table 3.

The first two rows of the table are rigid critical speeds, and the 3rd row is the 1st bending critical speed. The mode shape of the 1st bending speed is shown in Fig. 3. The designed rotor is safe to run for the current application because the speed for the current application is 80,000 rpm, which is about 40% of 1st bending critical speed.

The analysis is further extended to predict unbalance response of the rotor with 40 mg-mm of unbalance near the bearings. The unbalance responses are predicted at various locations of the rotor such as near journal bearings of turbine and compressor sides. Figures 4 and 5 show unbalance response near journal bearing of the turbine and the compressor side. The acceptable limit of vibration amplitude is less than the radial clearance ($25 \mu\text{m}$). The maximum amplitude of vibration is nearly $5 \mu\text{m}$, and it is within the acceptable limits of the gas foil bearing design.

3 Experimental Verifications

To verify the predicted rotordynamic coefficients with experiments, a rotor along with the turbine and compressor are fabricated (Fig. 6) [3]. The assembly of turboexpander with bearing and housings is shown in Fig. 7. Pair of accelerometers and an oscilloscope is connected to the test rig. The accelerometers are mounted on the bearing housing close to the upper and lower journal bearings. The assembled turboexpander is placed at the test rig with the associated instrumentation.

Table 2 Station data of the prototype rotor

Station No.	$M \times 10^{-3}$ (Kg)	l_n (m)	I_n (mm ⁴)	I_{pn} (kgm ²)	I_m (kgm ²)	E_{jn} (N/m ²)
1	6.70E-04	7.29E-03	6.45E-11	3.04E-09	4.48E-09	6.98E+ 10
2	3.12E-03	8.00E-03	1.25E-09	6.22E-08	4.77E-08	6.98E+10
3	9.48E-03	8.00E-03	1.32E-08	6.15E-07	3.58E-07	6.98E+10
4	1.08E-02	9.00E-03	9.86E-10	3.42E-07	1.95E-07	1.79E+11
5	2.15E-03	3.25E-03	4.91E-10	2.69E-08	1.54E-08	1.79E+11
6	2.15E-03	3.25E-03	4.91E-10	2.69E-08	1.54E-08	1.79E+11
7	2.72E-02	1.60E-02	3.22E-09	8.69E-07	1.01E-06	1.79E+11
8	7.85E-03	4.63E-03	3.22E-09	2.51E-07	1.4E-07	1.79E+11
9	7.85E-03	4.63E-03	3.22E-09	2.51E-07	1.4E-07	1.79E+11
10	7.85E-03	4.63E-03	3.22E-09	2.51E-07	1.4E-07	1.79E+11
11	7.85E-03	4.63E-03	3.22E-09	2.51E-07	1.4E-07	1.79E+11
12	2.86E-03	3.00E-03	1.02E-09	5.15E-08	2.79E-08	1.79E+11
13	7.70E-02	6.00E-03	1.84E-07	1.86E-05	9.55E-06	1.79E+11
14	2.86E-03	3.00E-03	1.02E-09	5.15E-08	2.79E-08	1.79E+11
15	7.85E-03	4.63E-03	3.22E-09	2.51E-07	1.4E-07	1.79E+11
16	7.85E-03	4.63E-03	3.22E-09	2.51E-07	1.4E-07	1.79E+11
17	7.85E-03	4.63E-03	3.22E-09	2.51E-07	1.4E-07	1.79E+11
18	7.85E-03	4.63E-03	3.22E-09	2.51E-07	1.4E-07	1.79E+11
19	2.72E-02	1.60E-02	3.22E-09	8.69E-07	1.01E-06	1.79E+11
20	3.92E-03	3.84E-03	1.4E-09	8.28E-08	4.54E-08	1.79E+11
21	3.92E-03	3.84E-03	1.4E-09	8.28E-08	4.54E-08	1.79E+11
22	9.76E-03	5.28E-03	2.42E-08	8.57E-07	4.51E-07	6.98E+10
23	3.18E-03	5.28E-03	1.75E-09	7.51E-08	4.49E-08	6.98E+10

Table 3 Computed critical speed of the rotor

No.	Critical speed (Hz)	Critical speed (rpm)
1	446	26,752
2	489	29,353
3	3495	209,721

The periodic curves are plotted near the 1st and 2nd critical speed of the turboexpander which are shown in Figs. 8 and 9. The predicted 1st and 2nd critical speeds are 26,752 rpm and 29,353 rpm, respectively. The deviation of experimental 1st and 2nd critical speeds are 6% and 2%, respectively, from the predicted values. The above deviation in critical speed may be due to the deviation of predicted stiffness and damping at the bearings. The critical speeds are noted, and in the successive runs,

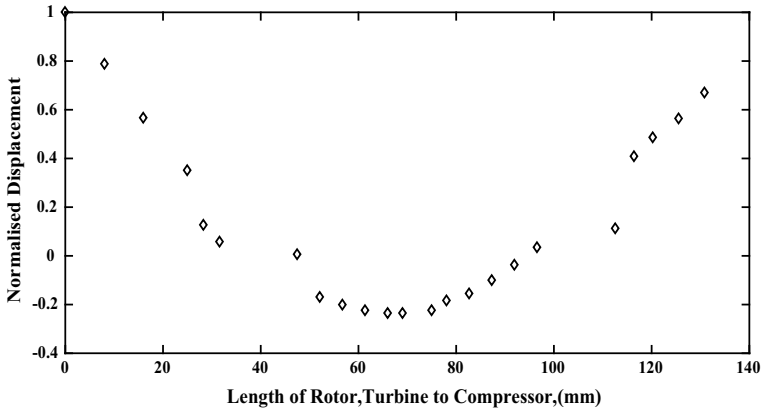


Fig. 3 Mode shape at 1st bending critical

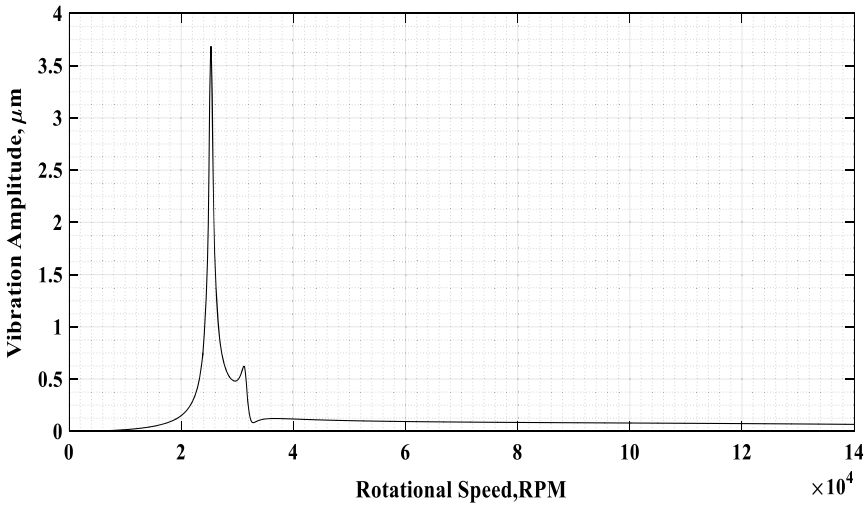


Fig. 4 Unbalance response near journal bearing on the turbine side

these speeds are quickly crossed to avoid any excessive vibration of the turboexpander. Oscilloscope is connected to the test rig to measure the amplitudes of vibration. The stable rotation is achieved at speed close to 80,000 rpm with a synchronous vibration amplitude of 85 mV near the lower journal bearing. The obtained signals are converted to acceleration, and FFT of the vibrational spectrum at 80,000 rpm is shown in Fig. 10 for response at lower journal bearing.

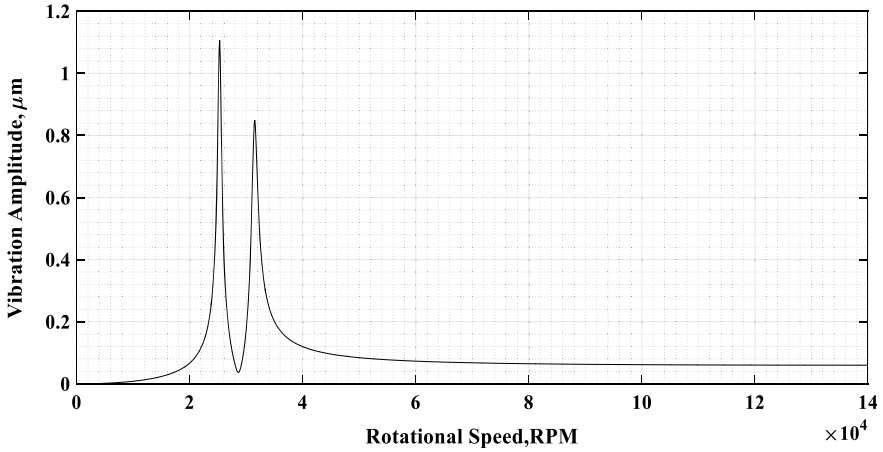


Fig. 5 Unbalance response near journal bearing on the compressor side

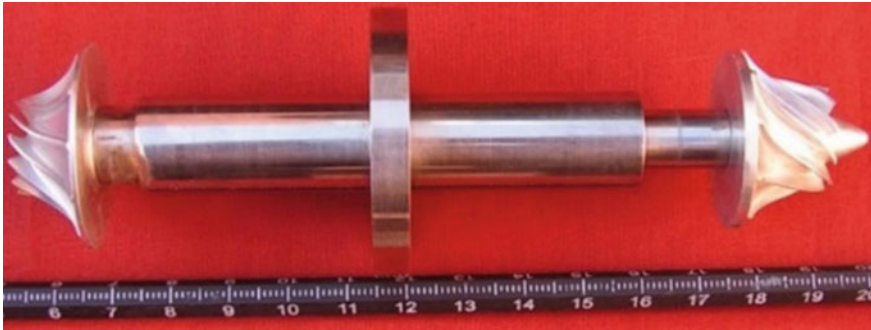


Fig. 6 Fabricated prototype rotor

4 Conclusions

The work presented in this paper is a modest attempt to validate the transfer matrix method for high-speed small-sized cryogenic turboexpander. The experimental result indicates that there are small variations in the predicted and experimented rigid critical speeds. This may be due to the variation in predicated stiffness and damping of the gas foil bearings. Therefore, the above observation proves the accuracy of the rotordynamic model as explained in this paper.

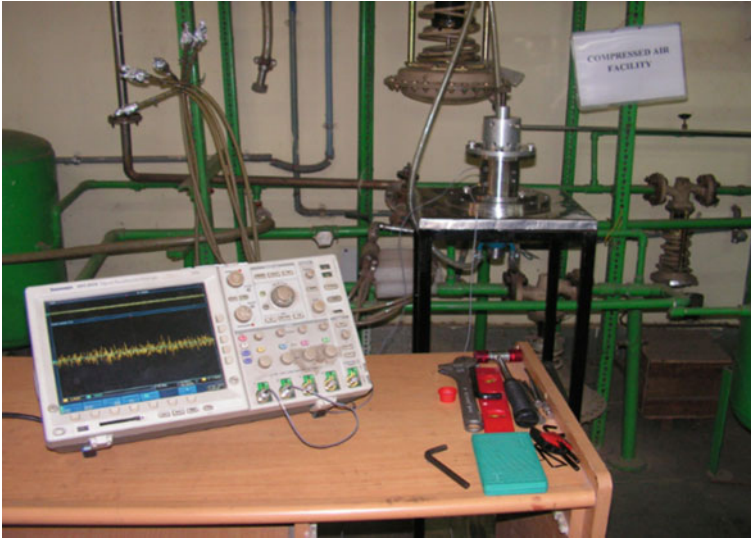


Fig. 7 Test bed with the turboexpander assembly and instrumentations

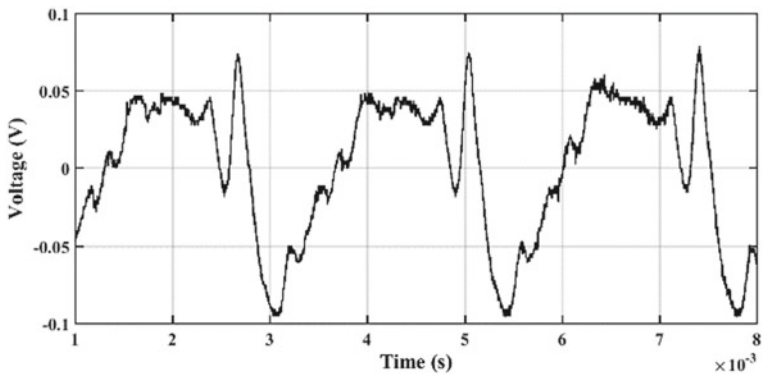


Fig. 8 Spectrum in the time domain at speed close to 1st critical speed (25,252 rpm) near lower journal bearing

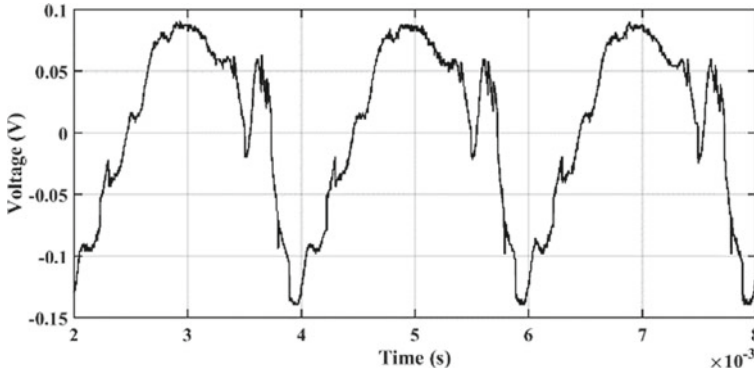


Fig. 9 Spectrum in the time domain at speed close to 2nd critical speed (29,850 rpm) near lower journal bearing

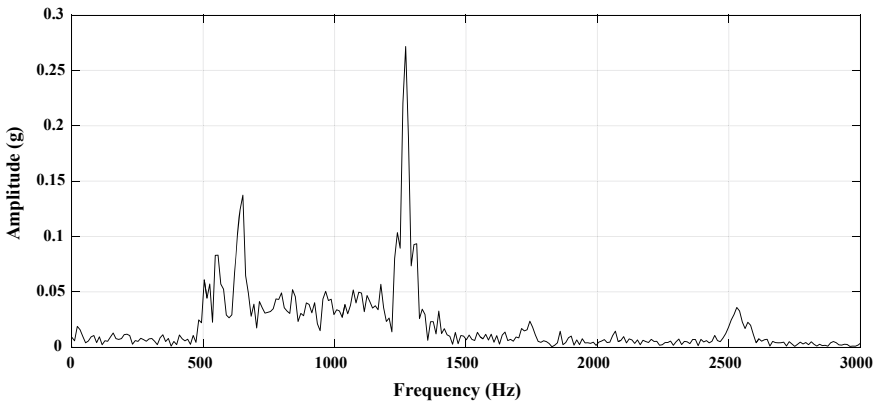


Fig. 10 FFT spectrum at a speed of 80,000 rpm speed near lower journal bearing

References

1. Vance JM (1988) Rotordynamics of turbomachinery. Wiley, Texas
2. Rao J (1983) Rotor dynamics. New Age International Publishers, New Delhi
3. Behera SK (2018) Tribology and Rotordynamics of small high-speed cryogenic turboexpander. Ph D. dissertation. NIT Rourkela
4. Bhore SP, Darpe AK (2013) Nonlinear dynamics of a flexible rotor supported on the gas foil journal bearings. *J Sound Vib* 332:5135–5150
5. Rao JS, Sharan AM (1982) Unbalance response of rotor disks supported by fluid film bearings with a negative cross coupled stiffness using influence coefficient method. *Mech Mach Theor* 17(2):143–152
6. Tiwari R, Chougale A (2014) Identification of bearing dynamic parameters and unbalance states in a flexible rotor system fully levitated on active magnetic bearings. *Mechatronics* 24(3):274–286

7. Heshmat H, Ku CP (1994) Structural damping of self-acting compliant foil journal bearings. *ASME J Tribol* 116:76–82
8. Kalita M, Kakoty SK (2004) Analysis of whirl speeds for rotor-bearing systems supported on fluid film bearings. *Mech Syst Signal Process* 18:1369–1380

Clustering in Pareto Front: Application on an Aero Engine Rotor-Bearing System for Improved Design



K. Joseph Shibu , K. Shankar, Ch. Kanna Babu, and Girish K. Degaonkar

Abstract In the aero engine rotor-bearing systems, a design modification to move the critical speed away from resonance zone and to improve the unbalance response is a practical problem for designers. The objective functions are selected as amplitude of vibration due to unbalance and second critical speed. The two selected objectives are found to be conflicting, and hence, multi-objective optimisation is used to solve this problem through numerical formulation. Diameters of the stepped shaft and stiffness of the two bearings are selected as design variables. Weight is set as a constraint, and additional constraints based on the initial design are introduced. Objectives resulting from multi-objective optimisation and corresponding design variables are clustered separately using k-means clustering algorithm. The novelty of the work is in empowering the designer to recognise the hugely diverse designs resulting in identical solutions and achieving manufacturing sovereignty in choice of design through clustering in objective and design space and their mapping.

Keywords Multi-objective optimisation · Pareto front · Clustering

K. Joseph Shibu (✉) · Ch. Kanna Babu · G. K. Degaonkar
Aero Engine Research and Design Centre, HAL, Bengaluru 560017, India
e-mail: josephshk@gmail.com

Ch. Kanna Babu
e-mail: chkannababu@gmail.com

G. K. Degaonkar
e-mail: girish.degaonkar@hal-india.com

K. Joseph Shibu · K. Shankar
Department of Mechanical Engineering, IITM, Chennai, India
e-mail: skris@iitm.ac.in

Nomenclature

NSGA	Non-dominated sorting genetic algorithm
P_{\max}	Maximum amplitude of response due to unbalance
ω_2^c	Second critical speed

1 Introduction

Aero engines are gas turbine based, and they thrive on the development of highly efficient rotor systems. Rotor systems combine shafts and discs, and the combination freely rotates about the shaft centre axis through bearings. Proper rotor dynamic analysis is performed to keep the vibration of the rotor system in control during operation. The development of scientific methods over the years replaced old trial and error methods of analysis, and the one that gained good ground is optimisation methods. Rotor system design and modification is one of the key areas of research in optimisation techniques.

An early area of research was on optimisation of shape of the rotor with constraint on critical speed [1–3]. Genetic algorithm combined with transfer matrix method was applied to shape optimisation [4]. Multi-stepped rotor was studied by the same methodology [5]. A study on weight optimisation with critical speed constraint discussed the possibility of extending single objective problem to multi-objective one [6]. These studies considered single objectives, and other parameters are either neglected or converted to constraints.

Different researchers studied the change of single parameter leading to cumulative effects on other parameters of the rotor system. The initial study on multi-objective optimisation used unbalance response and stability as two objectives and combined them using a weighted objective function [7]. Further studies on weighted objective function for multi-objective optimisation with weight and transmitted force as objectives were carried out [8]. Immune genetic algorithm was applied for the same problem by a different researcher to improve the results [9]. Weighted objective function formed for unbalance response and stability resulted in optimum solution by modifying support characteristics of rotor system [10]. These studies on weighted objective function resulted in a single optimum solution.

The quest for a set of the final solution for designer led to the generation of Pareto front with rotor system multi-objective optimisation. The multi-objective optimisation of rotor system by considering unbalance response and stability limit as two objectives improved the support characteristics and produced a Pareto front [11]. A recent study on multi-objective optimisation to diminish vibration level and transmitted force with critical speed constraint used NSGA-II optimisation algorithm and developed a Pareto front [12]. Though these studies resulted in a Pareto front, they never discussed its practical applicability from manufacturing point of view. In the real-world problems, design engineers need to understand the objective values

of the solutions and their structure, that is, how the designs appear. This leads to identification of groups called clusters that are alike both in objective values and in their structure. These clusters provide information about the relationship between the designs and regions in objective space represented by these designs.

During practical problems, the understanding of the accomplished results might be very exhausting, because the depiction of each solution is multifaceted. The rotor-bearing systems are more detailed and take more time to inspect the solutions returned by the multi-objective optimisation algorithm. Clustering is the best method to tackle this issue as it provides valuable information on the behaviour of a group of similar solutions and reduces the effort of the designer. Studies on clustering using k-means clustering algorithm discussed its suitability in design [13–16]. The grouping of the solutions is based on the centroid calculation for each cluster, and the solutions are assigned to each cluster with the closest centroid. Cluster allocation quality evaluation is performed using silhouette plot [17, 18]. Silhouette value ranges from -1 to $+1$, and a high value is preferred as it indicates good match with own cluster and poor match with other clusters.

The application of clustering in objective space and decision space and their mapping to identify the best solution from manufacturing feasibility and designer requirement considerations is an area of research which needs in-depth assessment, especially in rotor-bearing systems of aero engine application. The works in this direction are limited, and hence, the authors ventured into this pioneer work.

The novel elements of the present work are discussed here. A practical problem relevant to the aero engine application is identified and formulated for the multi-objective optimisation through in-house developed MATLAB coding. A more advanced controlled elitist genetic algorithm, a variant of NSGA-II, is used for the present work. Clustering is carried out on this practical rotor-bearing system design space as well as on objective space, and they are mapped. This mapping between design and objective space helped the designer to identify the vastly different designs producing the same solutions and entrusted him with manufacturing independence in selection of design.

2 Optimisation

A dynamic modelling procedure of rotor-bearing systems presented in reference [19], which consist of rotors modelled by circular Rayleigh beam elements, to accommodate rotary inertia effects, using finite element method with each element having four degrees of freedom and rigid discs attached to model compressor and turbine discs and discrete bearings, is followed in the present case. The presence of gyroscopic effect couples transverse motion of the beam in its two orthogonal planes, and the same is considered in the analysis.

The rotor system is of a single spool type with a distributed rotor, two bearings and three discs. The distributed rotor is modelled as a fifteen element member. The bearings at stations 6 and 9 are modelled with Rayleigh damping model and bearing

stiffness model discussed in reference [20]. Concentrated discs at stations 4, 12 and 15 have masses of 1.16, 1.13 and 1.14 kg, diametral inertias of 0.0018, 0.00158 and 0.0016 kg/m² and polar inertias of 0.00275, 0.00312 and 0.0032 kg/m³, respectively. The density of the distributed rotor made of steel alloy is 7760 kg/m³, and elastic modulus is 2.1×10^{11} N/m². A portion of the turbines is a part of the rotor and is represented by the elements 11, 12, 14 and 15 having a density of 8180 kg/m³, elastic modulus 2.05×10^{11} N/m² and is made of nickel alloy. The steel alloy part used for connecting the two turbines is represented by element 13 having a density of 7860 kg/m³ and elastic modulus 2.0875×10^{11} N/m². The stations 5 and 15 have unbalance of 1 g mm as per standard shown in reference [21].

The numerical experiment showed the importance of diameter of the shaft and bearing stiffness in the determination of critical speed and response of the system. Modal analysis identified that the second mode has large amplitude of vibration, and this mode is selected as target of the optimisation process to reduce this amplitude. Due to the complexity of design modification at bearing location and disc location, these diameters are kept constant during optimisation and other diameters of shaft are selected as design variables. Stiffness of both the bearings is selected for the initial design as 1×10^7 N/m and varied between 1×10^6 and 1×10^9 N/m independently during optimisation. The initial configuration data and bounding range for remaining design variables are showed in Table 1. The schematic of the rotor system is shown

Table 1 Initial design and bounding range for distributed rotor

Element	Initial value of inside diameter (m)	Range of inside diameter (m)	Initial value of outside diameter (m)	Range of outside diameter (m)	Axial distance (m)	Range of axial distance (m)
1	0	Kept constant	0.010	0.01–0.03	0.020	Kept constant
2	0		0.012	0.01–0.03	0.045	
3	0		0.014	Kept constant	0.073	
4	0		0.020	0.01–0.03	0.095	
5	0		0.015	Kept constant	0.1005	
6	0		0.015		0.106	
7	0		0.024	0.01–0.03	0.176	
8	0		0.015	Kept constant	0.1815	
9	0		0.015		0.187	
10	0		0.025	0.01–0.03	0.197	
11	0		0.040	Kept constant	0.212	
12	0		0.040		0.222	
13	0.020	0.01–00.03	0.050	0.04–0.06	0.242	
14	0	Kept constant	0.040	Kept constant	0.252	
15	0		0.040		0.262	

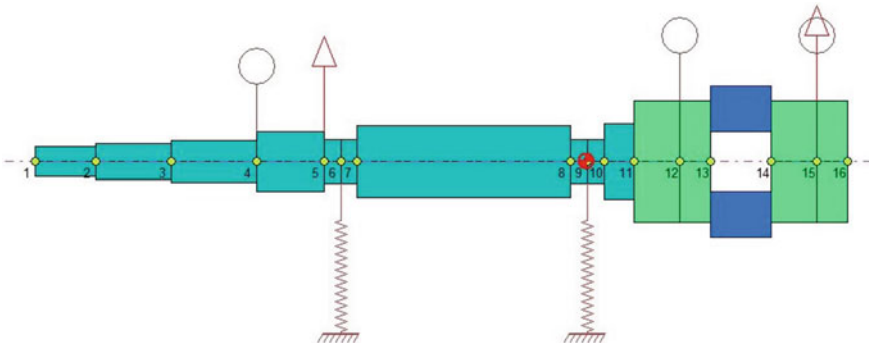


Fig. 1 Schematic of rotor-bearing system

in Fig. 1.

The objectives are maximum amplitude of response P_{\max} due to unbalance and second critical speed ω_2^c of the rotor which is selected as negative to make it a minimisation objective. The design constraints are set on weight, response and the range for second critical speed based on the initial design analysis results. Weight was limited to 1.3 kgf, response to 2.5×10^{-5} m, and the second critical is limited between 2200 and 3000 rad/s. The stress constraints may be primary for rotor system optimisation. However, in this paper, the design of an existing rotor-bearing system with satisfactory stress requirements is revised. The major changes are allowed in stiffness of the bearings, and the range of the diameters is kept close to the existing. Hence, the effect of changes of diameters of the shaft on the system stress is negligible.

Genetic algorithm-based optimisation is carried out for the present problem to generate a Pareto front. One of the most popular non-domination-based genetic algorithms for multi-objective optimisation is NSGA [22]. A modified version, NSGA-II [23] was developed with improvements over NSGA. A recent variant of NSGA-II [24] using a controlled elitist genetic algorithm is used for the present work.

3 Pareto Solutions

The result from multi-objective optimisation is a Pareto front shown in Fig. 2. Pareto front represents a set of non-dominated solutions. One objective is sacrificed for gain in another objective as we move along the Pareto front.

Pareto solutions are preferred over single solution as the designer is provided with a large number of viable solutions from which he can choose the best one. Pareto plot clearly shows the conflicting nature of the objectives.

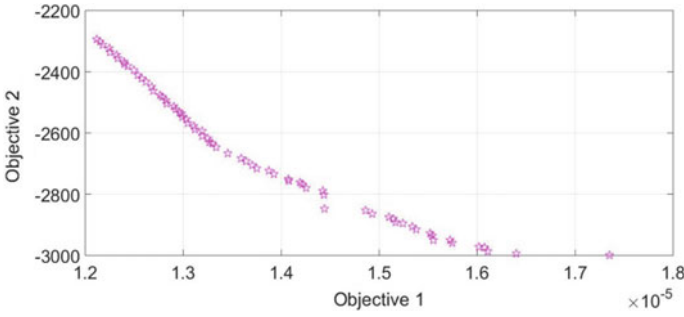


Fig. 2 Pareto front

4 Clustering

Clustering helps the designer to identify design choices leading to the strongly related solutions, the strongly different design choices achieving similar objectives, major groups, particular interested group and final solution within a group.

Cluster plot shown in Fig. 3 grouped the objectives with high response and high critical speed into cluster2 and the objectives with low response and low critical speed into cluster4. Both these clusters have high silhouette value as shown in Fig. 4. Cluster1 and cluster3 represent the trade-off solutions. Cluster1 has high silhouette value compared to cluster3. Further assessment of the objectives showed that cluster1 contains the most improved trade-off solutions compared to the initial configuration. The final solution is selected from cluster1. Thus, this methodology narrows down the Pareto front to one cluster, and the evaluation of each solution in this cluster is less time consuming and more effective.

Cluster plot of decision space shown in Fig. 5 represents the stiffness of bearing 1 plotted against the stiffness of bearing 2. The corresponding silhouette plot is shown in Fig. 6. Some of the members of cluster1 and cluster3 are found to have negative value and not belong to that group. They are grouped again and assessed separately

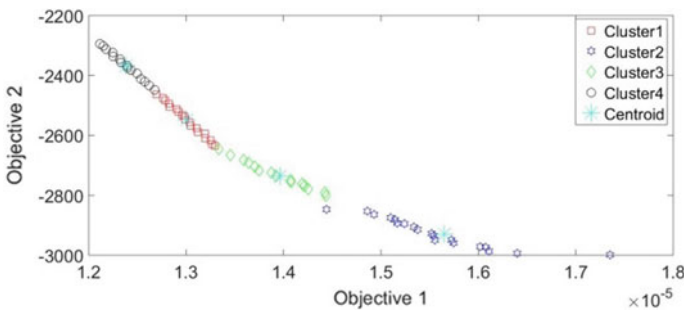


Fig. 3 Cluster in objective space

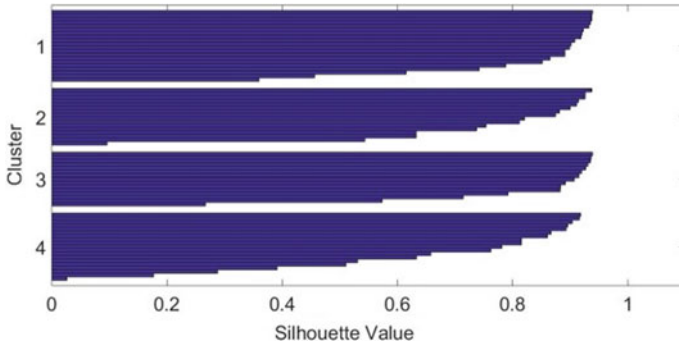


Fig. 4 Silhouette plot in objective space

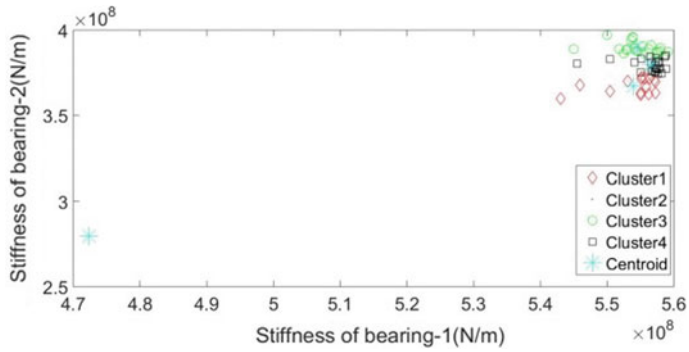


Fig. 5 Cluster in decision space for stiffness of bearings

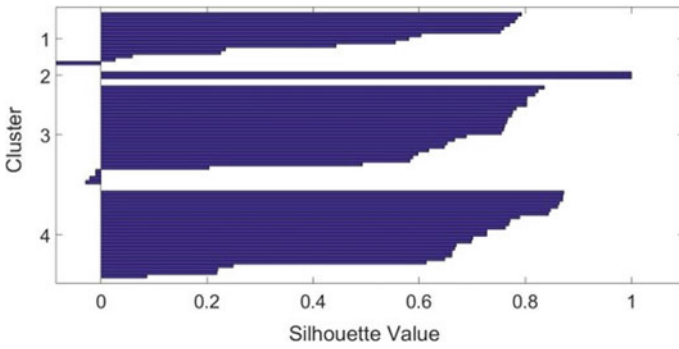


Fig. 6 Silhouette plot in decision space for Fig. 5

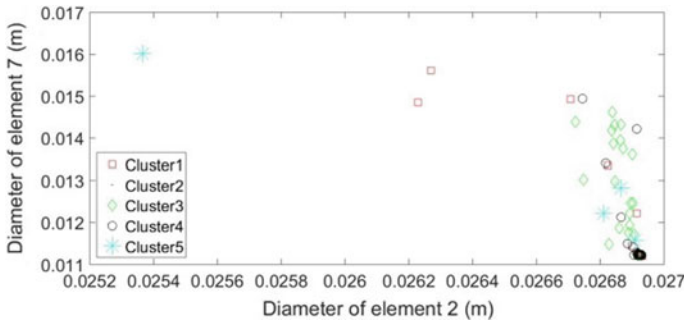
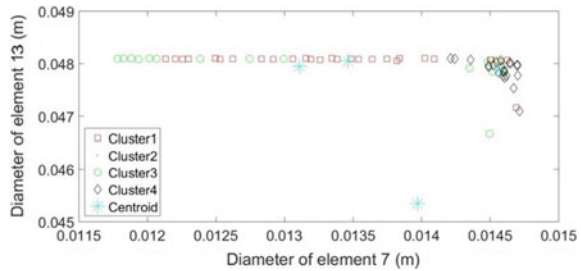


Fig. 7 Cluster in decision space for diameter of elements 2 and 7

Fig. 8 Cluster in decision space for diameter of elements 7 and 13



by mapping them in objective space. The designs are found to be similar in nature from objective space evaluation. Cluster2 of decision space corresponds to cluster2 of objective space and is found to be different from any other clusters in decision space. Other design variables are considered and plotted in clusters. Clustering plots of diameter of elements 2 and 7 and diameter of elements 7 and 13 are shown in Figs. 7 and 8. From Figs. 5, 7 and 8, it is clear that cluster1 of objective space is dominated by cluster1 in decision space.

The two designs with objective values from cluster1 corresponding to cluster1 and cluster4 in decision space are identified and selected for evaluation. Design1 and design2 were found to have similar design variables and designer left with no manufacturing liberty. Decision space clusters are closely evaluated, and it is found that the manufacturing liberty is shown by cluster2 design variables. One of the designs from cluster2 of decision space is considered for evaluation.

5 Results and Discussion

Figures 9, 10, 11 and 12 represent amplitude of vibration due to unbalance for the initial design and all the three designs selected from multi-objective optimisation Pareto front. Tables 2 and 3 represent the different designs and corresponding

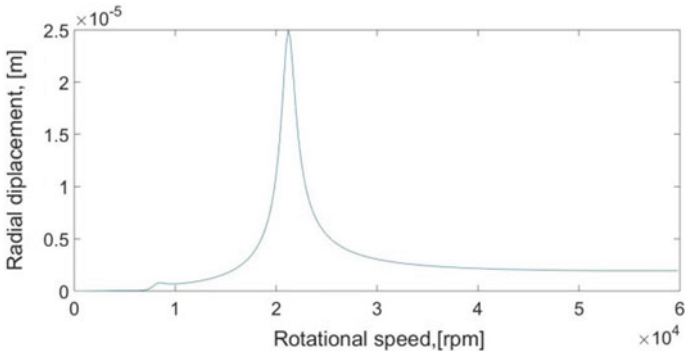


Fig. 9 Unbalance response of the initial design

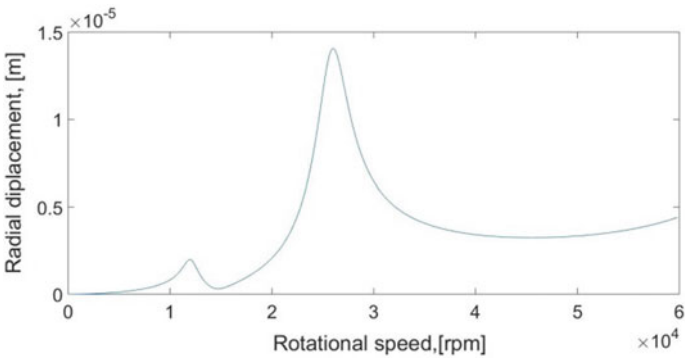


Fig. 10 Unbalance response of design1

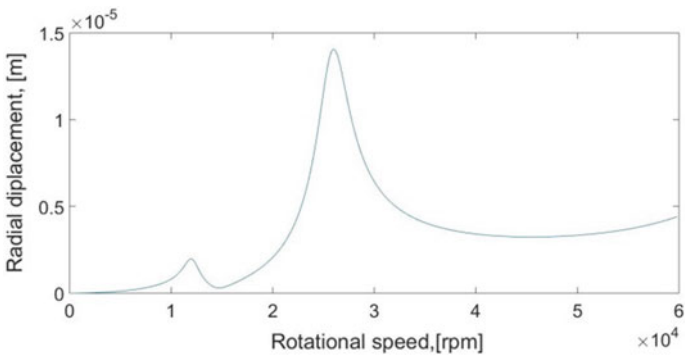


Fig. 11 Unbalance response of design2

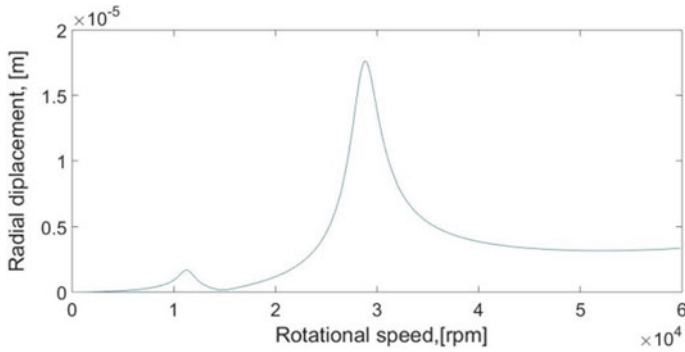


Fig. 12 Unbalance response of design3

Table 2 Different designs—critical speed, shaft weight and amplitude of vibration

Parameter	Initial design	Design1	Design2	Design3
Critical speed (rpm)	21,200	25,270	25,630	28,800
Amplitude of vibration (m)	2.5×10^{-5}	1.37×10^{-5}	1.41×10^{-5}	1.76×10^{-5}
Weight (kgf)	1.208	1.185	1.185	1.141

Table 3 Different designs—diameter of shaft element and bearing stiffness

Design variable	Element	Initial design	Design1	Design2	Design3
Outside diameter (m)	1	0.010	0.0286	0.0285	0.0277
	2	0.012	0.0269	0.0269	0.0254
	4	0.020	0.0112	0.0114	0.0160
	7	0.024	0.0144	0.0145	0.0139
	10	0.025	0.0263	0.0254	0.0233
	13	0.050	0.0480	0.0481	0.0453
Inside diameter (m)	13	0.020	0.0164	0.0164	0.0161
Stiffness (N/m)	Station 6	1×10^7	5.59×10^8	5.55×10^8	4.72×10^8
	Station 9	1×10^7	3.87×10^8	3.83×10^8	2.79×10^8

objectives and constraints. Figure 13 shows the configuration of the shaft for all the designs.

Comparing with the initial design,

- Design1: The critical speed increased by 19%, response reduced by 45% and the weight decreased by 1.9%.
- Design2: The critical speed increased by 21%, response reduced by 43.6% and the weight decreased by 1.9%.

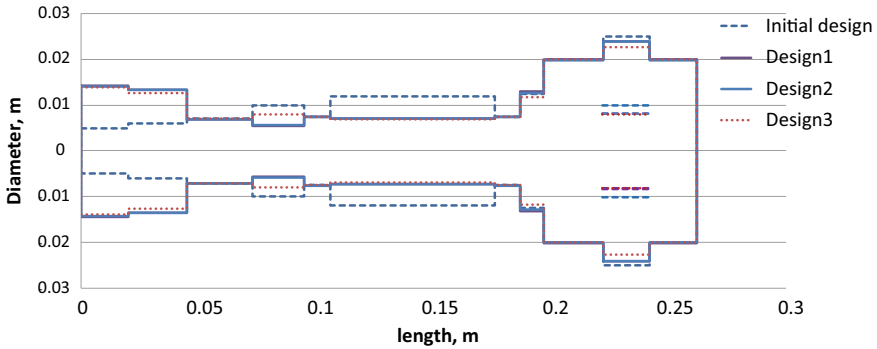


Fig. 13 Configuration of the shaft for all the designs

- Design3: The critical speed increased by 36%, response reduced by 29.6% and the weight decreased by 5.5%.

All the designs satisfied the constraints and improved the objectives. All the designs have the same mode shape for the second mode. Design1 and design2 are similar in objectives and in design variables. Design3 found to be different in terms of design variable values, especially the bearing stiffness values. Thus, the mapping of the solutions provided the designer his penchant in selecting the final design.

6 Conclusions

Multi-objective optimisation of a rotor system for aero engine application is carried out through in-house MATLAB coding using controlled elitist genetic algorithm. Three different design choices are presented to the designer for the final solution selection. Selection of first two designs is the result of mapping the objective values in decision space cluster. Design1 and design2 are from the same cluster in objective space and different clusters in decision space. They resulted in better solutions compared to the initial design with the critical speed increased by 19–21%, response reduced by 43.6–45% and the weight decreased by 1.9%. Though they belonged to different clusters in decision space, their design variable values were very close. Design3 was explored from another cluster in objective space, and the selection was based on the decision space clustering where the designs found to be different from other clusters. This design resulted in the critical speed increase of 36%, response reduction of 29.6% and the weight reduction of 5.5%. Thus, clustering of the Pareto front and the decision space resulted in strongly different design choices and liberated the designer while selecting the final solution.

Acknowledgements The authors express their gratitude to the Chief Designer AERDC, HAL, for his support and encouragement during this study and for his consent to publish this technological paper.

References

1. Shiau TN, Hwang JL (1988) Minimum weight design of a rotor bearing system with multiple frequency constraints. *Trans. ASME J Eng Gas Turb Power* 110(4):592–599
2. Shiau TN, Hwang JL (1990) Optimum weight design of a rotor bearing system with dynamic behavior constraints. *Trans. ASME J Eng Gas Turb Power* 112(4):454–462
3. Chen TY, Wang BP (1993) Optimum design of rotor-bearing system with eigenvalue constrains. *Trans ASME* 256:115
4. Choi BG, Yang BS (2000) Optimum shape design of rotor shafts using genetic algorithm. *J Vib Control* 6(2):207–222
5. Lee DS, Choi DH (2000) Reduced weight design of a flexible rotor with ball bearing stiffness characteristics varying with rotational speed and load. *J Vib Acoust* 122(3):203–208
6. Strauß Frank, Inagaki Mizuho, Starke Jens (2007) Reduction of vibration level in rotordynamics by design optimisation. *Struct Multidisc Optim* 34:139–149. <https://doi.org/10.1007/s00158-006-0065-3>
7. Shiau TN, Chang JR (1993) Multiple-objective optimization of a rotor-bearing system with critical speed constraints. *Trans ASME J Eng. Gas Turb Power* 115:246–255
8. Choi BK, Yang BS (2001) Multiobjective optimum design of rotor-bearing systems with dynamic constraints using immune-genetic algorithm. *Trans ASME* 78:123
9. Barrett LE, Gunter EJ, Allaire PE (1978) Optimum bearing and support damping for unbalance response and stability of rotating machinery. *J Eng Power* 100(1):89–94
10. Panda KC, Dutt JK (1999) Design of optimum support parameters for minimum rotor response and maximum stability limit. *J Sound Vib* 223(1):1–21
11. Babu MJ, Sekhar AS, Shankar K (2013) Multi-objective optimisation of support characteristics of rotor bearing systems. *Int J Struct Eng* 4(4):361–386
12. Zheng L, Jia S, Huang J (2017) Numerical and Experimental Study on the multiobjective optimization of a two-disk flexible rotor system. *Int J Rotating Mach* 9628181
13. Forgy EW (1965) Cluster analysis of multivariate data: efficiency vs interpretability of classifications. *Biometrics* 21(3):768–780
14. McQueen J (1967) Some methods for classification and analysis of multivariate observations. *Comput Chem* 4:257–272
15. Rahman MA, Islam MZ (2014) A hybrid clustering technique combining a novel genetic algorithm with K-Means. *Knowl-Based Syst* 71:345–365
16. Farag MA, El-Shorbagy MA, El-Desoky IM, El-Sawy AA, Mousa AA (2015) Genetic algorithm based on k-means-clustering technique for multi-objective resource allocation problems. *Br J Appl Sci Technol* 8(1):80–96
17. Milligan GW, Cooper MC (1988) A study of standardization of variables in cluster analysis. *J Classif* 5:181–204
18. Morse JN (1980) Reducing the size of the nondominated set: pruning by clustering. *Comput Oper Res* 7:55–66
19. Nelson HD, McVaugh JM (1976) The dynamics of rotor-bearing systems using finite elements. *J Eng Ind* 98:593–600
20. Shibu KJ, Shankar K, Babu CK, Degaonkar GK (2017) Multi objective optimisation of an aero engine rotor system using nondominated sorting genetic algorithm (NSGA). In: *ASME 2017 gas turbine india conference, american society of mechanical engineers*

21. ISO 1940 Mechanical vibration, Determination of permissible residual unbalances, Balance quality requirements of rigid rotors-Part 1
22. Srinivas N, Deb K (1994) Multiobjective optimization using nondominated sorting in genetic algorithms. *Evol Comput* 2(3):221–248
23. Deb K, Pratap A, Agarwal S, Meyarivan T (2002) A fast elitist multiobjective genetic algorithm: NSGA-II. *IEEE Trans Evol Comput* 6(2):182–197
24. Deb K Multi-objective optimization using evolutionary algorithms. John Wiley & Sons. ISBN 047187339

Sensitivity Analysis for Unbalance Identification of Rotor Systems



Dinesh Kumar Pasi , Manoj Chouksey, and Amit Kumar Gupta

Abstract Various types of rotor faults may appear in rotating machines over time. Unbalance is the most commonly occurring fault in rotating machines. This work proposes sensitivity analysis for unbalance identification in rotating machines using a model-based approach. The sensitivity for unbalance response has been computed as response per unit rotating unbalance force using the finite element method. The rotor system has been considered under various end supporting conditions, e.g. isotropic undamped, damped bearing and anisotropic bearing cases. Viscous form of damping has been considered to model bearing damping. The effect of gyroscopic forces has been included in the model. In the analysis, the response of the rotor system is recorded at various locations on the shaft when a unit unbalance is applied on any of the rotor disc/plane. The process has been repeated to find out the unbalance response sensitivity of the rotor system to unit rotating unbalance force at other disc/plane locations. The idea of the work involves applying the sensitivity analysis in proper selection of measurement points of unbalance responses in rotating machines in the process of unbalance identification.

Keywords Sensitivity · Sensitivity analysis · Rotor systems · Unbalance response

D. K. Pasi (✉) · M. Chouksey
Department of Mechanical Engineering, Shri G. S. Institute of Technology and Science, Indore,
India
e-mail: dkpasi25@gmail.com

M. Chouksey
e-mail: machouksey@gmail.com

A. K. Gupta
Department of Mechanical Engineering, IET-Devi Ahilya University, Indore, India
e-mail: akgupta@ietdavv.edu.in

1 Introduction

Rotors are essential components of any machine. Over time, various types of faults may develop in rotating machines, e.g. rotor crack, unbalance, rotor-bow, misalignment, etc. Unbalance is the most commonly occurring fault in rotating machines [1, 2]. If the unbalance forces are too high, the rotor and rotor–shaft experience oscillations beyond acceptable limits. Researchers have been working on identification of unbalance response in the rotor systems, and as a result of this, several techniques have been developed for the same. Identification and optimization of unbalance parameters are addressed for rotor bearing system [3]. A technique for unbalance identification is developed and experimentally verified by the author [4]. However, the unbalance response at any point depends on its location on the rotor–shaft. It implies that the unbalance sensitivity of different points on the rotor–shaft will be different. The work on sensitivity analysis for various systems can be found in the literature to predict the system’s behaviour. Sensitivity of any system may be defined as impact of any independent variable on a dependent variable under the given set of assumptions. The techniques used for the study of this impact may be called as sensitivity analysis. Data obtained from sensitivity analysis may be treated as system properties, which can further be used for the study of the system. Mottershead et al. [5] and Cheon-Hong Min [6] have used sensitivity-based approach of eigenvalues for the finite element model updating. Lu [7] presented a work on the damage identification in axially functionally graded beams using hybrid sensitivity matrix. Lü [8] describes the application of the technique for the analysis of the sensitivity of the reliability of frequencies for the prediction of failure. Various authors have been using reliability sensitivity analysis designing mechanical components, analysing vibration behaviour and predicting failures of mechanical components [8–16].

The literature survey has shown the work of sensitivity-based approach in updating finite element models and estimating reliability of the system. However, the application of sensitivity-based approach in the identification of rotor faults was not found in the literature surveyed so far. Hence, this approach extends the approach to study response sensitivity to unbalance excitations in the process of its identification.

1.1 Sensitivity Analysis

Sensitivity of any system is the effect of any independent variable on some dependent variable of interest which is needed to be studied or analysed. On the basis of recorded dependent variable, the system behaviour in any other similar conditions can be expected to be predicted.

Consider a shaft of length “*L*” supported at the ends using two bearings. Sensitivity at any point *i* is the unbalance response at the point in a particular direction, due to unit rotating unbalance at point *j*. It is denoted by *S_{ij}*. Further, in the work, *y_{ij}* denotes the sensitivity which means the unbalance response at point *i* in the *Y*-direction (vertical direction) due to rotating unbalance force at point *j*.

$$y_{ij} = \begin{bmatrix} y_{12} \\ y_{32} \\ y_{52} \end{bmatrix}; \text{ where } i = 1, 3 \text{ and } 5 \text{ for } j = 2$$

For example, if unbalance response sensitivities are computed at point (*i*) 1, 3 and 5 due to unit rotating unbalance forces at the point (*j*) 2 and 4, then the sensitivity matrix will be given by “**S**” as

$$\mathbf{S} = \begin{bmatrix} y_{12} & y_{14} \\ y_{32} & y_{34} \\ y_{52} & y_{54} \end{bmatrix}$$

The matrix *S* is termed as sensitivity matrix. Each of the elements of this matrix represents response at any location due to the force at any other location. In general terms, the response may be written as *y_{ij}*, where **i** is response location and **j** is force location.

General form of sensitivity matrix may be written as

$$S = \begin{bmatrix} y_{11} & y_{12} & y_{13} & \dots & y_{1n} \\ y_{21} & y_{22} & y_{23} & \dots & y_{2n} \\ y_{31} & y_{32} & y_{33} & \dots & y_{3n} \\ \dots & \dots & \dots & \dots & \dots \\ \dots & \dots & \dots & \dots & \dots \\ y_{m1} & y_{m2} & y_{m3} & \dots & y_{in} \end{bmatrix}$$

where *i* = 1, 2, 3, ... *m*, represents the number of points considered to find out the unbalance sensitivity.

j = 1, 2, 3, ... *n*, represents the number of points considered for the unbalance forces in the computation of sensitivities.

It may be noted that the sensitivity matrix, explained as above, is written in generalized form. In the work as explained in further sections, 12 response measurement points (corresponding to the row of the matrix) and 03 disc/unbalance locations (corresponding to the columns of the matrix) have been considered. Hence, the sensitivity matrix becomes 12 × 3 matrix.

The next section shows the concept of unbalance sensitivity analysis for the unbalance identification using an illustrative example.

1.2 Illustrative Example

The example has been considered after following the work by Lalanne [17]. The rotor system as shown in Fig. 1 comprises a shaft 1300 mm long and 50 mm diameter supported by bearings at each end. The three discs are mounted on the shaft at 200 mm, 500 mm and 1000 mm, respectively, from the left end bearing. The diameter and thickness of the discs have been shown in the Figure. The rotor and discs have material properties $E = 200$ GPa and density $= 7800$ kg/m³.

The nodal points from 2 to 13 have been considered to compute the unbalance sensitivities. The unbalance force locations have been considered on the three discs one by one, i.e. at the nodal points 3, 6 and 11.

Mass of discs at location 3, 6 and 11 (i.e. disc1, disc2 and disc3) are 14.5801 kg, 45.9457 kg and 55.1349 kg, respectively, whereas the diametral mass moment of inertia of the three discs is 0.0616 kg-m², 0.4881 kg-m² and 0.5880 kg-m², respectively. Polar moment of inertia of the disc1, disc II and disc III is 0.1232 kg m², 0.9763 kg-m² and 1.1716 kg-m², respectively.

The study has been put into two cases, namely case 1 and case 2. In case 1, the rotor system has been considered supported on undamped isotropic bearings, and it is termed as “Undamped isotropic rotor system”, whereas in case 2, the rotor is supported on damped isotropic bearings, and it is termed as “Damped isotropic rotor system”. The data for both of the cases is given below as

Case 1: Undamped isotropic rotor system The rotor–shaft system has isotropic bearing stiffness ($k_{yy} = k_{zz} = 70$ MN/m) and isotropic bearing damping ($c_{yy} = c_{zz} = 0$).

Case 2: Damped isotropic rotor system The rotor–shaft system has isotropic bearing supports with ($k_{yy} = k_{zz} = 70$ MN/m) and isotropic bearing damping ($c_{yy} = c_{zz} = 7E8$ N s/m).

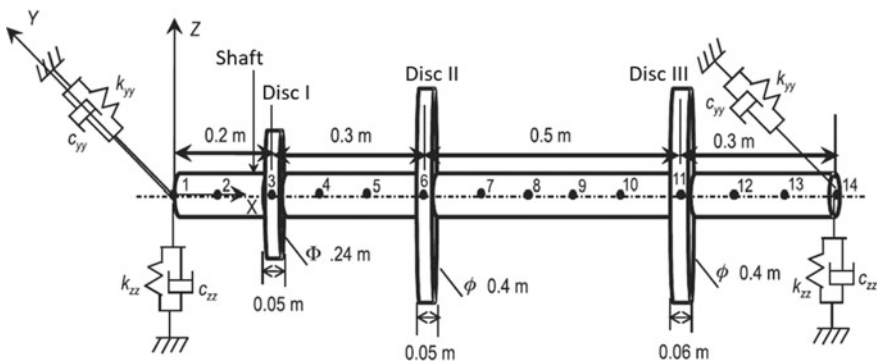


Fig. 1 The multi-disc rotor system

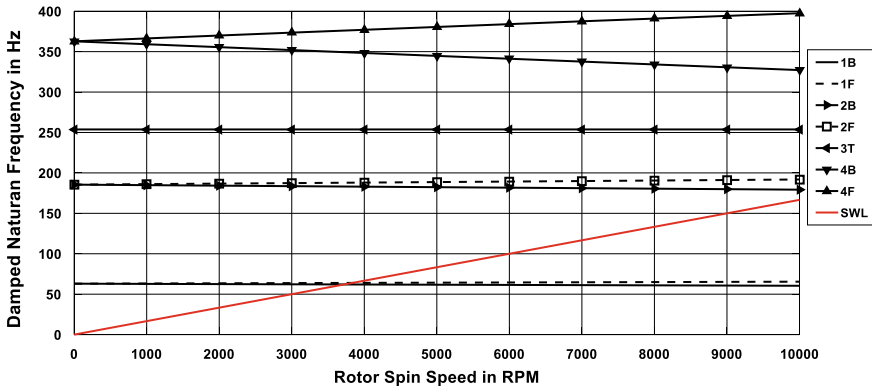


Fig. 2 Campbell diagram for isotropic undamped rotor system (case 1)

1.3 Undamped Isotropic Rotor System (Case 1)

In this section, the whirl speed map, unbalance orbit plots and the sensitivity analysis have been carried out for the undamped isotropic rotor system.

1.3.1 Whirl Speed Map

Whirl speed map, also called as Campbell diagram, is a plot between natural frequencies versus spin speed of the rotor system. Such plots are helpful in finding out the forward/backward modes and the critical speed of the system. Figure 2 shows the whirl speed map for the isotropic undamped rotor system considered. The split in the natural frequencies in various backward and forward modes is visible in the plot. It can be seen that the split is more in the higher modes, e.g. in 4F and 4B modes. This is attributed to the fact that in the higher modes, the gyroscopic couple will be of higher magnitude due to the higher angular velocity of precession which is related to the natural frequency in that mode. It may be noted that there is one torsion mode too visible in the plot. The natural frequency in this mode comes out to be uninfluenced by the spin velocity, as torsion modes remain unaffected by the gyroscopic couple. The critical speed observed from the analysis is 3722.1 rpm in first backward mode and 3837 in first forward mode.

1.3.2 Orbit Plots

Orbit plots for rotating machines provide useful information about the condition of the machine. It helps in vibration-based condition monitoring of machines. Figure 3a–c show the orbit plots of unbalance response for the case 1, i.e. for isotropic undamped rotor system when unbalance force is considered in disc I, disc II and disc III, at a

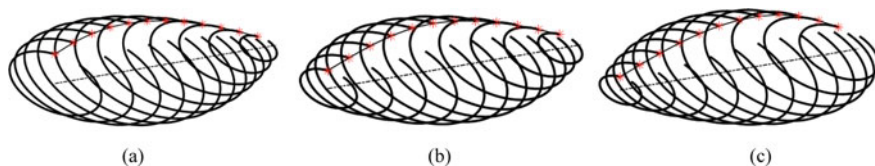


Fig. 3 Unbalance orbit plot for case 1 under unbalance in **a** disc I; **b** disc II; **c** disc III

time, respectively. It may be seen from the plots that the orbits are circular in all the three cases and unbalance response in Fig. 3b is somewhat symmetric on the rotor system, as the disc is almost on the middle of the rotor-shaft. Further in the study, unbalance sensitivity has been computed while considering unbalances in these three discs one by one.

1.3.3 Sensitivity Analysis

Figure 4 shows the unbalance response sensitivity when the unbalance is considered in disc I, disc II and disc III one by one. Unbalance response sensitivity has been computed as response at various points on the rotor system, as shown in Fig. 4, due to unit unbalance in any of the three discs at a time. It may be seen that unbalance response sensitivity is found to be the highest when the disc is considered away from the bearings. However, it depends on the location of the response point also.

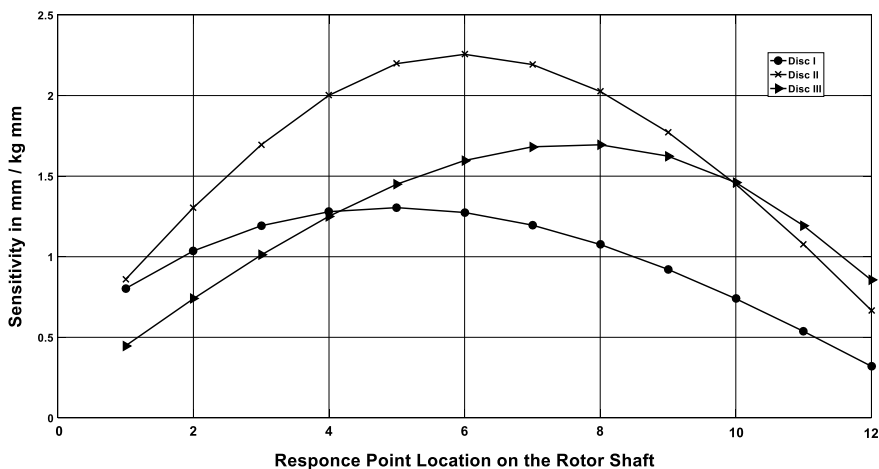


Fig. 4 Variation of unbalance sensitivity on the rotor-shaft for case 1

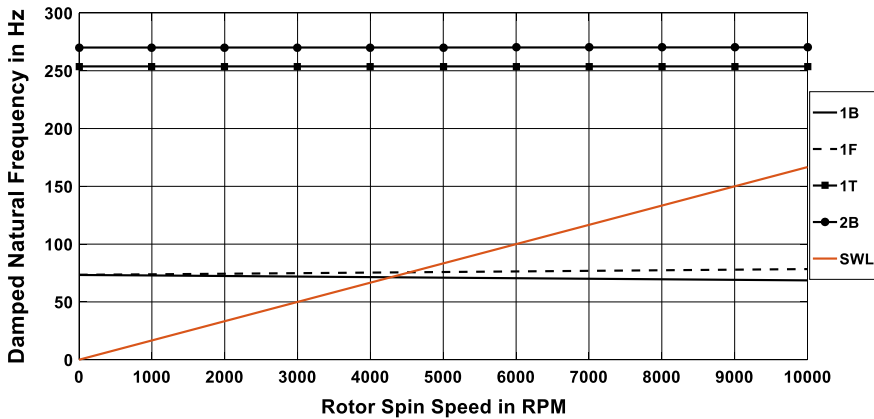


Fig. 5 Campbell diagram for isotropic undamped rotor system (case 2)

1.4 Isotropic Damped Rotor System (Case 2)

Damping is always present in practical system. Various types of damping models can be considered in modelling the system, e.g. viscous damping model, hysteretic damping model, etc. [18, 19]. In this section, viscous damping model has been incorporated to model the isotropic bearing supports. Study of sensitivity variation is conducted with higher value of damping ($7E8$ Ns/m). All other parameters are kept unchanged to see the damping effect on sensitivity due to unit unbalance at disc I, disc II and disc III applied one by one. The observations are presented below;

1.4.1 Whirl Speed Map

The whirl speed map is shown in Fig. 5, it can be observed that the critical speed in this case is shifted towards higher side. First forward mode 1F and backward mode 1B can be observed. Second backward mode and a torsional mode can also be seen in the figure. The damped natural frequencies are reducing as compared with the previous two cases due to high magnitude of damping.

1.4.2 Orbit Plot

Orbit plots for the damped isotropic rotor system are shown in Fig. 6a–c for disc I, disc II and disc III, respectively. The pattern of the orbit plot is same as observed in Fig. 3. Reduction in unbalance sensitivity can be observed from Fig. 6a–c as compared to the previous cases.

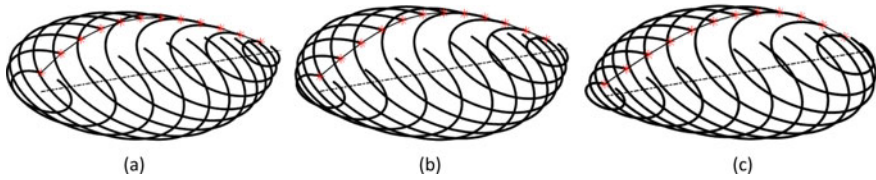


Fig. 6 Unbalance orbit plot for case 2 under unbalance in **a** disc I; **b** disc II; **c** disc III

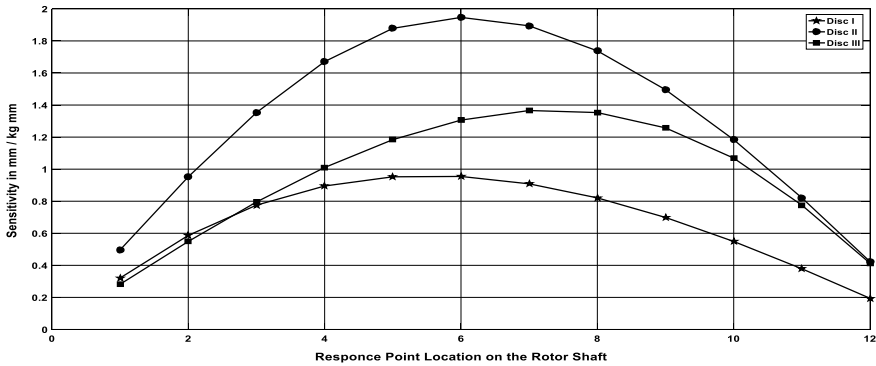


Fig. 7 Variation of unbalance sensitivity on the rotor-shaft for case 2

1.4.3 Sensitivity Analysis

The unbalance response sensitivity for the isotopic damped system with a damping coefficient 7E8 Ns/m is shown in Fig. 7. The effect of damping is observed in this Fig. 7, by comparing it with Fig. 4 in case I. In case 2, peak of the curve for disc II reaches below 2 mm, while in the case 2, it is above 2 mm. However, from the coarse observation, the sensitivity variation pattern is same as in undamped cases.

1.5 Comparison of Sensitivity with Different Damping

Comparison of the sensitivities for the damped and the undamped systems has been shown in Fig. 8a–c for the unbalance forces in disc I, disc II and disc III, respectively. It can be observed that the pattern of variation of sensitivities in the undamped and damped system is similar for unbalances on the three discs. It can be seen that the damping has significant influence on the unbalance response sensitivity in all the cases. Due to damping, the unbalance response sensitivity reduces. However, this reduction will depend on the spin speed of rotation and amount of damping present in the system. It can be observed that the unbalance response sensitivity tends to get high as the disc/unbalance location is moved towards the middle of the rotor–shaft.

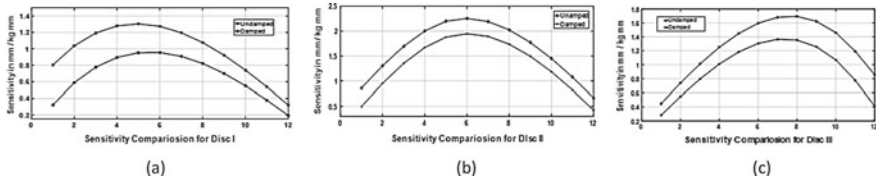


Fig. 8 Unbalance response sensitivity for undamped and damped cases with unit unbalance in **a** disc I; **b** disc II; **c** disc III

On the other hand, the more the disc/unbalance location is near to the bearing, the lower will be the unbalance response sensitivity. Such an analysis is expected to help proper selection of points for computation of unbalance response sensitivity in the process of unbalance identification.

2 Conclusion

The work included the sensitivity analysis for unbalance identification of rotor systems. A three disc rotor system has been considered in the study. Unbalance response sensitivity has been computed due to unit unbalance in various discs. The analysis has been carried out for both undamped and damped rotor system. It has been seen that the unbalance response sensitivity is high away from the bearings/support locations. The effect of damping has also been investigated to find out its influence on the unbalance response sensitivity. It has been found that due to the presence of damping, the unbalance response sensitivity reduces at any point on the rotor–shaft system. Such information expected to be helpful in proper selection of measurement points in finite element model-based unbalance identification. The approach in this work is studied using numerical simulation. However, it is the first step towards carrying out the experimental work as a future study.

Acknowledgements The research grant provided in the research promotion scheme of AICTE, New Delhi, for the work titled “A noble method for unbalance response prediction and balancing of rotor systems” is gratefully acknowledged.

References

1. Zheng GT, Wang WJ (2001) A new cepstral analysis procedure of recovering excitations for transient components of vibration signals and applications to rotating machinery condition monitoring. *J Vib Acoust* 123:222–229
2. Sinha AWLJK, Friswell MI (2004) Estimating unbalance and misalignment of a flexible rotating machine from a single run-down. *J Sound Vib* 272:967–989

3. Jianfei Yao LL, Yang F, Scarpa F, Gao J (2018) Identification and optimization of unbalance parameters in rotor-bearing systems. *J Sound Vib* 431:54–69
4. Akash Shrivastava ARM (2019) Identification of unbalance in a rotor system using a joint input-state estimation technique. *J Sound Vib* 442:414–427
5. Mottershead JE, Link M, Friswell MI (2010) The sensitivity method in finite element model updating: a tutorial. In: *Mechanical systems and signal processing*. <https://doi.org/10.1016/j.ymsp.2010.10.012> (in Press)
6. Cheon-Hong Min SH, Park S-Y, Park D-C (2014) Sensitivity based finite element model updating with natural frequencies and zero frequencies for damped beam structure. *Int J Nav Archit Ocean Eng* 6:904–921
7. Lu XXLZR, Chen YM, Huang M (2016) Hybrid sensitivity matrix for damage identification in axially functionally graded beams. *Appl Math Model* 41:604–617
8. Chunmei Lü YZ, Li H, Wang X, Liu Y (2013) Frequency reliability and sensitivity analysis on the rotor system. *Appl Mech Mater* 271–272:1296–1300
9. Changqing Su FG, Shi Q, Zhang Y (2017) Reliability sensitivity estimation of rotor system with oil whip and resonance. *Adv Mech Eng* 9(6):1–12
10. Changqing Su YZ, Zhao Q (2011) Vibration reliability sensitivity analysis of general system with correlation failure modes. *J Mech Sci Technol* 25(12):3123–3133
11. Wang ZYX, Li H, Lü C (2014) Dynamic reliability sensitivity of cemented carbide cutting tool. *Chin J Mech Eng* 27(1):79–85
12. Wang YMZXG, Yan YF, Wang BY (2008) Dynamic reliability sensitivity analysis of torsion bar. *Adv Mater Res* 44–46:275–282
13. Zhang ZYYM (2008) Reliability-based sensitivity analysis of vehicle components with non-normal distribution parameters. *Int J Autom Technol* 10(2):181–194
14. Yimin Zhang CL, Zhou N, Su C (2010) Frequency reliability sensitivity for dynamic structural systems. *Mech Based Des Struct Mach* 38:74–85
15. Zhou Yang YZ, Zhang X, Huang X (2012) Reliability-based sensitivity design of gear pairs with non-gaussian random parameters. *Appl Mech Mater* 121–126:3411–3418
16. Zhou Yang YZ, Li H, Huang J, Wang Q (2012) Reliability-based sensitivity design of coil tube-spring upon information of incomplete probability, pp 77–80
17. Lalanne GFM (1997) *Rotor dynamics prediction in engineering*. Wiley, England
18. Genta G (2004) On a persistent misunderstanding of the role of hysteretic damping in rotordynamics. *J Vib Acoust* 126(3):459–461
19. Lazan BJ (1968) *Damping of materials and members in structural mechanics*. Pergamon Press

Sommerfeld Effect Attenuation Using Switched-Stiffness Method of a Non-ideal Internally Damped Shaft–Disk System with Constant Eccentricity



Abhishek Kumar Jha and Sovan Sundar Dasgupta 

Abstract Internally, damped shaft–disk system when driven by a non-ideal power source, i.e., limited power source often exhibits complex dynamics. Upon exceeding a critical power input near resonance, the system may contribute to increasing the transverse vibration severely rather than increasing the spin speed. This phenomenon is referred to as the Sommerfeld effect. This effect can cause instability in high speed rotor system and needs to be addressed carefully for safe and smooth operations. In the present study, a semi-active control scheme based on switched-stiffness method is employed to attenuate the Sommerfeld effect of a eccentric shaft–disk system driven by a brushed DC motor. Following, the equations of motion are solved numerically to obtain time response and amplitude frequency response with a specified supply voltage. It has been shown that as the value of switched-stiffness increases, the Sommerfeld effect is found to be attenuated. However, the rotor response is corrupted with spikes as a fallout of switching stiffness technique, which may destabilize the system and becomes critical when the switching time is very fast. The attenuation of Sommerfeld effect can be further verified through the time varying potential energy plot which is seen to be diminished after crossing the critical speed owing to the dissipative characteristics of non-potential switching stiffness force.

Keywords Sommerfeld effect · Non-ideal · Internal damping · Switched stiffness · Eccentricity

Nomenclature

m Mass of the disk mounted at the mid-span
 I Mass moment of inertia of the shaft–disk system about the axis of spin

A. K. Jha · S. S. Dasgupta (✉)
School of Mechanical Engineering, VIT, Vellore, Tamilnadu, India
e-mail: sovan@vit.ac.in

A. K. Jha
e-mail: jhabhishek02@gmail.com

© Springer Nature Singapore Pte Ltd. 2021
J. S. Rao et al. (eds.), *Proceedings of the 6th National Symposium on Rotor Dynamics*, Lecture Notes in Mechanical Engineering,
https://doi.org/10.1007/978-981-15-5701-9_14

R_e	External damping
R_i	Internal or material damping
R_r	Damping offered by the bearings and medium to the system
T_m	Input torque supplied by the DC motor
T_L	Source loading torque
K	Rotor isotropic stiffness
k_1, k_2	Switched stiffness
V_s	Supply voltage
R_m	Motor armature resistance
μ_m	DC motor constant
ω_r^*	Non-dimensional rotor spin speed
β	Non-dimensional whirl amplitude
g	Acceleration due to gravity
e	Constant eccentricity
x, y	Displacement of the rotor system along the x - and y -directions, respectively

1 Introduction

The non-ideal vibrating system is characterized by its response influenced excitation in which power supply is limited. All dynamical systems are inherently non-ideal, and an additional differential equation is needed to describe the complex dynamics between drive and the system itself. The problem of passage through resonance has attracted many researchers among the mechanical engineering community for more than 150 years. But sometimes, the passage through resonance requires more input power than the driving source has available. As a result, the system cannot pass through resonance or needs a strong interaction with the non-ideal, i.e., limited source of power. In high speed rotor system, during run up/coast up operation, as the driving frequency gets closer to the critical speed, upon exceeding a critical power input, the rotor speed exhibits nonlinear jump phenomena (i.e., jumps suddenly to a much higher value, simultaneously its amplitude jumps to a much lower value) is known as Sommerfeld effect [1]. This effect may lead to catastrophic failure of the high speed rotor system.

In order to attenuate the Sommerfeld, several works have been reported based on passive, active semi-active control strategies. In 2006, a group of researchers [2] proposed tuned liquid column damper-based passive control scheme to control the structural vibration near the resonance. Afterward, Felix and Balthazar [3] employed active control technique through electromechanical vibration absorber to attenuate the non-ideal structural vibration. In 2018, Balthazar and his co-workers [4] presented an experimental method to attenuate the jump phenomena via shape memory element for a cantilever beam driven through an unbalanced DC motor. In 2019, Jha and Dasgupta [5] studied the Sommerfeld effect attenuation for an internally damped

non-ideal shaft–disk system using active PD control through a linearized model of active magnetic bearings.

Active control is considered to be one of the effective methods for suppressing the Sommerfeld effect and structural vibrations. However, their energy input is typically high and may lead to the system toward instability under certain conditions. Passive vibration control, on the other hand, though relatively simple has improved stability characteristics, but the response time is very slow. Therefore, a trade-off must be made between the active and passive control toward the development of an adaptive and semi-active alternative.

In 2000, a technique based on switched-stiffness concept [6] was proposed to attenuate the structural vibrations. This method is basically a semi-active control scheme in which the energy of the system is dissipated through changing the values of spring stiffness. The spring possesses two distinct stiffness values, low and high. The switching from low to high stiffness can be implemented through either shape memory alloys (SMA) [7] or through an electrical shunt circuit of a piezoelectric patch actuator [8] in which open circuit and short circuit states represent the high and low values of stiffness, respectively. In 1976, Wauer [9] proposed the switching stiffness method for the first time a possible attenuation of non-stationary resonance vibrations for a distributed parameter rotor model. In 1998, Wauer and Suherman [10] studied the vibration suppression of a rotating shaft driven by a non-ideal source through using switching shaft stiffness. Recently, Min et al. [11] proposed a serial stiffness switch system to reduce the structural vibration without damping. In 2019, in a different study [12], Min and his co-workers developed a semi-active shock isolation based on the serial stiffness switch system and successfully showed the efficacy of this system over a passive system.

It is evident from the earlier studies [5, 13] that internal damping of rotor–shaft in addition to non-ideal source plays a crucial role to exhibit the Sommerfeld effect. However, to the best of author’s knowledge, using switched-stiffness method, study of Sommerfeld effect attenuation for an internally damped rotor has not been reported so far. In the present study, an internally damped, eccentric shaft–disk system driven through a DC motor is presented. A pair of non-conservative springs in order to implement the switching stiffness effect is incorporated into the rotor system. The switching phenomena can be physically realized either by using SMA or piezoelectric patch into the system. The equations of motion are solved numerically along with an addition equation arising out of the complex interaction between the rotor and the non-ideal DC drive. The time response characteristics as well as amplitude with rotor speed diagrams are obtained for different values of stiffness (i.e., high as well low). As a result of increased stiffness values, the Sommerfeld effect is found to be attenuated. In addition, the potential energy (P.E.) is also found to be diminished with time after passing through the critical speed which also confirms the effectiveness of switching stiffness method in attenuation of Sommerfeld effect.

2 Mathematical Modeling of Non-ideal Shaft–Disk System with Switched-Stiffness Method

2.1 Switched-Stiffness-Based Vibration Control

The switched-stiffness method is basically a semi-active vibration control technique [14] in which the energy of the system is allowed to dissipate by incorporating a spring into it such that the stiffness of the spring switches between two distinct values, referred to as high and low stiffness thus effectively increases the energy dissipation from the system. When the system attains the maximum potential energy, the spring is switched to low stiffness state and switched to high stiffness, while the system reaches minimum potential energy. As a result, the potential energy of the system gets reduced. In turn, the reduced potential energy is then transformed into kinetic energy, which is lower than the kinetic energy of the previous cycle owing to the change of spring stiffness. This dissipation technique can be applied for the vibration attenuation of any transient system. Based on the above switching characteristics, a semi-active skyhook type control scheme can be implemented heuristically based on the position of the system with respect to its equilibrium configuration. The control law can be defined as

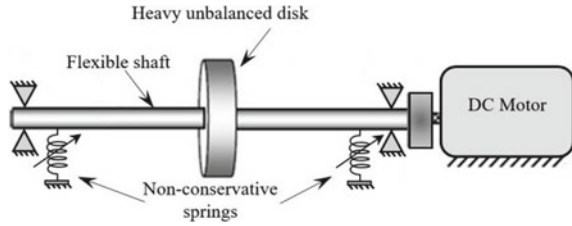
$$F(x, \dot{x}) = k(t)x = k_1x + (k_2 \text{sgn}(x\dot{x}))x, \quad \text{for } k_{\text{low}} \leq k \leq k_{\text{high}} \quad (1)$$

where $k_1 = (k_{\text{high}} + k_{\text{low}})/2$, $k_2 = (k_{\text{high}} - k_{\text{low}})/2$.

Therefore, the force due to switching stiffness is composed of two terms: a state feedback term (i.e., k_1x) and a switching term ($k_2 \text{sgn}(x\dot{x})x$) in which the product ($x\dot{x}$) represents a nonlinear sliding surface. This overall logic can be used as nonlinear switched-stiffness feedback. Using piezoelectric materials, the switching stiffness-based vibration control can also be achieved efficiently. Two piezoelectric patch actuators can be embedded into the rotor–shaft at a suitable distance from the supports. The piezoelectric patch is characterized with effective piezoelectric modulus of elasticity (\bar{Y}_p) which can be defined as $\bar{Y}_p = Y_p(1 - K^2)$ where Y_p = modulus of elasticity of the piezoelectric material and K = electromechanical coupling coefficient of the piezoelectric circuit which acts as an indicator between electrical and mechanical fields. Using an open circuit stiffness (k_{OC}) and short circuit stiffness consideration (k_{SC}), the ratio of two stiffness can be expressed as a function of coupling coefficient, i.e., $k_{\text{OC}}/k_{\text{SC}} = 1/(1 - K^2)$. Accordingly, to the control law given by Eq. (1), the effective piezoelectric Young's modulus can be switched [14] as follows:

$$\bar{Y}_p = \begin{cases} \bar{Y}_p^{\text{High}} = \bar{Y}_p/(1 - K^2) & x\dot{x} \geq 0 \\ \bar{Y}_p^{\text{Low}} = \bar{Y}_p & x\dot{x} < 0 \end{cases} \quad (2)$$

Fig. 1 Schematic of DC motor-driven shaft–rotor with non-conservative springs



The optimum value of switched-stiffness can be achieved through a suitable open circuit (high stiffness) and short circuit (low stiffness) configurations. The disadvantage of this kind of control law is it induces chatter. The faster the drive dynamics the more likely chatter to occur. To suppress the chatter, suitable anti-chatter strategies need to be adopted.

2.2 Mathematical Modeling

A non-ideal shaft–disk system (shown in Fig. 1) driven by a brushed DC motor (i.e., non-ideal energy source) is considered for the present study. A pair of non-conservative springs is also incorporated into the system to implement the proposed switched-stiffness method.

The equations of motion of the shaft–disk system [15] can be represented as follows:

$$m\ddot{x} + (R_e + R_i)\dot{x} + R_i\dot{\theta}y + (K + k_w(t))x = me(\dot{\theta}^2 \cos(\theta + \varphi) + \ddot{\theta} \sin(\theta + \varphi)) \tag{3}$$

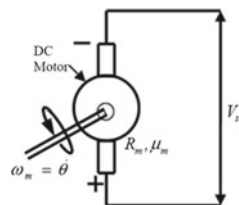
$$m\ddot{y} + (R_e + R_i)\dot{y} - R_i\dot{\theta}x + (K + k_w(t))y = me(\dot{\theta}^2 \sin(\theta + \varphi) - \ddot{\theta} \cos(\theta + \varphi)) \tag{4}$$

The complex interaction of the shaft–disk system with the non-ideal DC drive is described by the following additional equation

$$I\ddot{\theta} + R_r\dot{\theta} = T_m - T_L, \tag{5}$$

Internal damping (also known as material damping) in rotor dynamics plays a key role in determining the stability of the system. It is considered to be a function of past history of loading, strain rate and temperature of the system [15]. The notations describing the system parameters are enlisted in the nomenclature.

Fig. 2 Schematic representation of brushed DC motor



A brushed DC motor is used for the present study (shown in Fig. 2). The armature current may be expressed as [5]:

$$i_m = (V_s - \mu_m \dot{\theta}) / R_m. \quad (6)$$

The supplied torque (T_m) present in Eq. (5) provided by the DC motor becomes

$$T_m = \mu_m i_m = \mu_m (V_s - \mu_m \dot{\theta}) / R_m \quad (7)$$

The modified source loading torque (T_L) owing to the presence of switching stiffness terms may be expressed as

$$\begin{aligned} T_L = & R_i(x\dot{y} - \dot{x}y) + [(R_e + R_i)\dot{x} + (K + k_w(t))x]e \sin \theta \\ & - [(R_e + R_i)\dot{y} + (K + k_w(t))y]e \cos \theta \end{aligned} \quad (8)$$

3 Simulation Study and Results

Following representative parameters of the shaft–disk system chosen from the reference [5] are considered for numerical simulations:

$$\begin{aligned} m &= 2 \text{ kg}, K = 8 \times 10^4 \text{ N/m}, e = 0.001 \text{ m}, R_e = 50 \text{ Ns/m}, \\ R_i &= 50 \text{ Ns/m}, R_r = 2 \times 10^{-5} \text{ N m s/rad}, R_m = 40 \Omega, \\ \mu_m &= 0.1 \text{ Nm/A}, I_r = 0.004 \text{ kg m}^2 \text{ and} \\ \omega_n &= 200 \text{ rad/s}, V_s = 300 \text{ V}. \end{aligned}$$

In addition, $k_{\text{high}} = 6 \times 10^4 \text{ N/m}$ and $k_{\text{low}} = 1 \times 10^4 \text{ N/m}$. Two non-dimensional quantities are introduced here to study the Sommerfeld effect. These are the non-dimensional rotor spin speed (ω^*) = $\dot{\theta} / \omega_n$ and the non-dimensional whirl amplitude (β) = $\sqrt{x^2 + y^2} \omega_n^2 / g$, where g , the gravitational acceleration.

The Eqs. (3), (4) and (5) are solved numerically with the help of Runge-Kutta method using ode45 solver for 10 s. with time step = 0.01 s. and initial conditions ($x = y = \dot{x} = \dot{y} = \theta = \dot{\theta} = 0$).

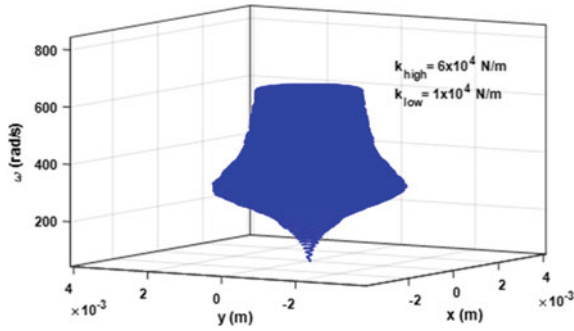


Fig. 3 Three-dimensional orbital tube representation of rotor x and y amplitudes with the rotor speed using switched-stiffness method

Figure 3 represents the three-dimensional orbital representation of an unbalanced response of the rotor system which starts at zero speed and then enlarges, taking the shape of an elliptical cross-section and tends to a circular cylindrical at high speeds. Figure 4 represents a comparison study between two time histories using with and without switching stiffness. The nature of the phase plot shown in Fig. 5 ensures the asymptotic stability of the system using switching stiffness. The variation of stiffness with time for a representative value of k_{high} and k_{low} is shown in Fig. 6. The efficacy of the switching stiffness method is confirmed through Fig. 7 in which the Sommerfeld effect is found to be attenuated gradually with relatively higher values of switched-stiffness. Additionally, it is evident from Fig. 7 that the response peak tends to shift gradually toward the right as the stiffness value increases. This result signifies that the effective critical speed tends to alter as the stiffness value changes thus helping the system to attenuate the undesirable Sommerfeld effect.

Moreover, inset of Fig. 7 shows the magnified response with spikes. These spikes in the response of the shaft–disk system ensure the presence of chatter as a consequence of the switching technique. The undesirable effect of chattering can be attenuated by using filtering, introducing a dead band around the switching points, etc. Finally, Fig. 8 illustrates how the potential energy (P.E.) is reduced due to switching stiffness however in the presence of chattering (as shown in the inset of Fig. 8) and ensures the potential energy is diminished, and in turn, the overall energy is being reduced as a result of dissipative effect of the switching stiffness.

4 Conclusions

The present study aims to attenuate the Sommerfeld effect of an internally damped unbalanced flexible shaft–disk system, driven by a DC motor using switched-stiffness method. The concept of switched-stiffness-based vibration control can be implemented using piezoelectric (i.e., PZT) material or SMA that results in significant

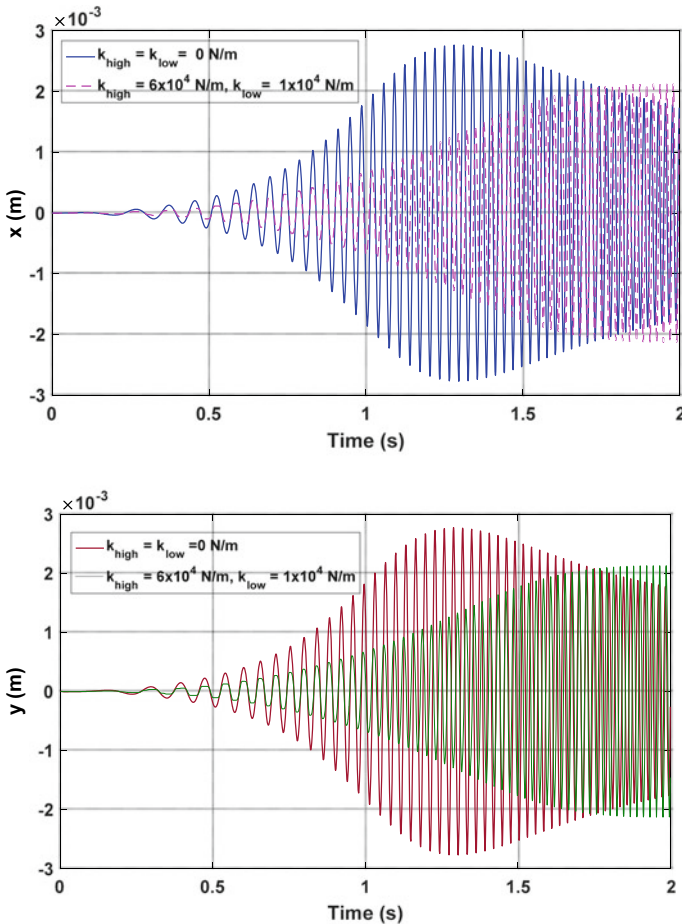


Fig. 4 **a** Time history of shaft–disk system along the x -direction. **b** Time history of shaft–disk system along the y -direction

change in effective modulus of elasticity through open circuit and short circuit configurations leading to switching of stiffness between high and low values, respectively. The equations of motion of the shaft–disk system are solved numerically along with an additional equation arising out of the complex interaction between the rotor and the non-ideal DC drive. The time response characteristics as well as amplitude with rotor speed diagrams are obtained for different values of switched-stiffness. As a result of increased stiffness values, the Sommerfeld effect is also found to be attenuated. The peak of the response is also found to be shifted toward right as the critical speeds alter gradually (i.e., increase as the stiffness increases). In addition, the potential energy (P.E.) also found to be decreased with time after passing through the critical speed which also confirms the effectiveness of switching stiffness method over the attenuation of Sommerfeld effect. However, the presence of spikes in the

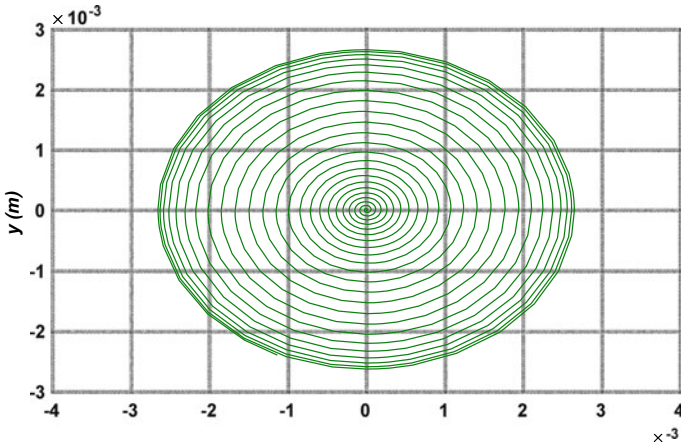


Fig. 5 Phase portrait of the shaft–disk system with switching stiffness consideration

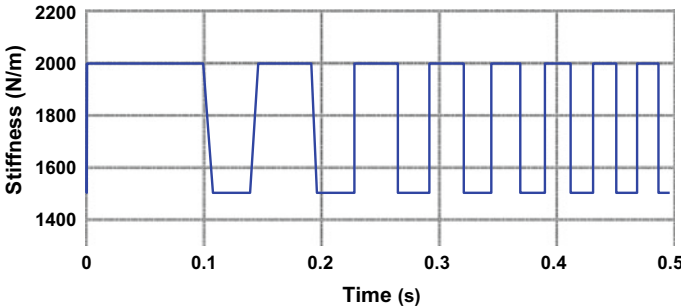


Fig. 6 Variation of switched-stiffness with time with representative values of $k_{high} = 2 \times 10^3$ N/m, $k_{low} = 1.5 \times 10^3$ N/m

frequency response and time varying potential energy clearly indicate the onset of induced chatter as a consequence of switching stiffness which in turn may destabilize the system if the switching becomes very fast. The future work can be envisioned as suppression of chatter of high speed non-ideal rotor through switching stiffness method using various anti-chattering strategies.

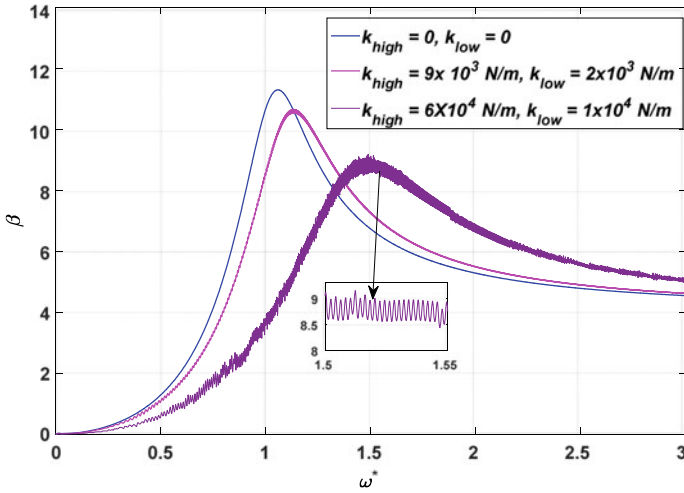


Fig. 7 Variation of amplitude of shaft–disk system for different values of switched-stiffness

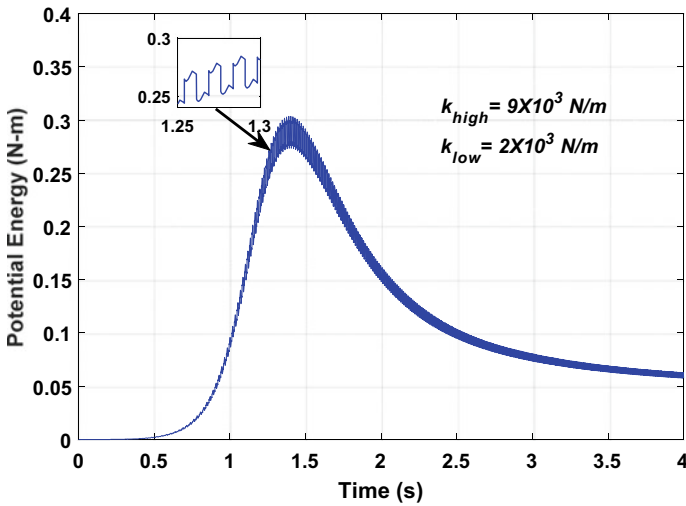


Fig. 8 Variation of potential energy with time for $k_{high} = 9 \times 10^3$ N/m, $k_{low} = 2 \times 10^3$ N/m

References

1. Sommerfeld A (1902) Beiträge zum dynamischen ausbau der festigkeitslehre. Phys Z 3:266–286
2. Felix JL, Balthazar JM, Brasil RM (2005) On tuned liquid column dampers mounted on a structural frame under a non-ideal excitation. J Sound Vibr 282:1285–1292
3. Felix JLP, Balthazar JM (2009) Comments on a nonlinear and nonideal electromechanical damping vibration absorber, Sommerfeld effect and energy transfer. Nonlinear Dyn 55(1–2):1–11

4. Kossoski A, Tusset AM, Janzen FC, Rocha RT, Balthazar JM, Brasil RM, Nabarrete A (2018) Jump attenuation in a non-ideal system using shape memory element. *MATEC Web Conf EDP Sci* 148:03003
5. Jha AK, Dasgupta SS (2019) Attenuation of Sommerfeld effect in an internally damped eccentric shaft-disk system via active magnetic bearings. *Meccanica* 54(1–2):311–320
6. Clark WW (2000) Vibration control with state-switched piezoelectric materials. *J Intell Mater Syst Struct* 11(4):263–271
7. Ramaratnam A, Jalili N, Dawson DM (2004) Semi-active vibration control using piezoelectric-based switched stiffness. *Proc Am Control Conf IEEE* 6:5461–5466
8. Caruso G (2001) A critical analysis of electric shunt circuits employed in piezoelectric passive vibration damping. *Smart Mater Struct* 10(5):1059
9. Wauer J (1976) Stationärer und instationärer Betrieb eines elastisch gelagerten Rotors. *VDI-Ber* 269:135–141
10. Wauer J, Suherman S (1998) Vibration suppression of rotating shafts passing through resonances by switching shaft stiffness. *J Vib Acoust* 120(1):170–180
11. Min C, Dahlmann M, Sattel T (2017) A concept for semi-active vibration control with a serial-stiffness-switch system. *J Sound Vibr* 405:234–250
12. Min C, Dahlmann M, Sattel T (2019) A semi-active shock isolation concept with a serial-stiffness-switch system. *J Sound Vibr* 445:117–131
13. Dasgupta SS, Samantaray AK, Bhattacharyya R (2010) Stability of an internally damped non-ideal flexible spinning shaft. *Int J Non-Linear Mech* 45(3):286–293
14. Ramaratnam A, Jalili N (2006) A switched stiffness approach for structural vibration control: theory and real-time implementation. *J Sound Vibr* 291(1–2):258–274
15. Dasgupta SS (2011) Sommerfeld effect in internally damped shaftrorotor systems. Doctoral dissertation, IIT Kharagpur

Rotor Dynamic Analysis of Rotor Assembly of a Small Liquid Metal Pump



Ashish Kumar, Y. V. Nagaraja Bhat, B. K. Sreedhar, S. I. Sundar Raj, S. Murugan, and P. Selvaraj

Abstract Fast breeder reactors (FBRs) utilize liquid metal, such as liquid sodium as the main coolant in their heat transport circuits. Choice of liquid sodium as the coolant comes due to its excellent heat transfer and neutronic properties. A 500 MWe, sodium cooled, prototype fast breeder reactor (PFBR) is being commissioned with technology inputs from Indira Gandhi Centre for Atomic Research (IGCAR). This centre has test facilities to demonstrate working and the development of components related to a fast reactor. The liquid sodium needs to be propelled in the loops of heat transport circuits of reactor and hence requires the use of pumps. Use of such pumps to propel liquid sodium has been demonstrated in one of the loops present in IGCAR. Capacity of this pump is 50 m³/h with its shaft currently being supported on top by an angular contact bearing while at bottom by hydrostatic bearing. The rated speed of operation of this pump is 2900 rpm. Use of active magnetic bearings (AMB) in place of oil lubricated bearings is being actively explored to eliminate the chances of oil leakage into the sodium. To demonstrate this concept for primary pump of PFBR, a small-scale magnetic bearing was designed and tested in the 50 m³/h pump. The shaft of this pump was modified to accommodate magnetic bearings and its associated components. Estimation of the critical speed of the shaft, both before and after modification, has been carried out using commercially available finite element analysis (FEA)-based software advanced rotating machinery dynamics (ARMD). Further, unbalance response studies have been carried out to know maximum displacement responses. The details of these analyses and results are discussed in this paper.

Keywords Rotor dynamic analysis · Active magnetic bearings

A. Kumar (✉) · Y. V. Nagaraja Bhat · B. K. Sreedhar · S. I. Sundar Raj · S. Murugan · P. Selvaraj
Fast Reactor Technology Group, Indira Gandhi Centre for Atomic Research, Kalpakkam, India
e-mail: ashishkumar@igcar.gov.in

Y. V. Nagaraja Bhat
e-mail: yvnb@igcar.gov.in

B. K. Sreedhar
e-mail: bksd@igcar.gov.in

1 Introduction

Prototype fast breeder reactor (PFBR) is a 500 MWe, sodium cooled, pool type fast reactor where liquid sodium is contained inside a main vessel and another circuit. The entire reactor core is immersed in this sodium pool. Choice of liquid sodium is derived from its excellent heat transport and neutronic properties which are prime requirements for any fast reactor. There are two main sodium circuits in PFBR, known as primary and secondary sodium circuit. Flow of liquid sodium in these circuits is achieved by the use of mechanical centrifugal pumps such as primary sodium pumps and secondary sodium Pumps. Demonstration of the use of such pumps at small scale has been carried out in the experimental facilities available at Indira Gandhi Centre for Atomic Research (IGCAR). One such pump, as shown in Fig. 1, having a capacity of 50 m³/h has been tested in sodium in one of the loops. The shaft of this pump is around 1.6 m long and is supported using typical oil lubricated angular contact bearing at the top and a hydrostatic bearing at the bottom. The hydrostatic bearing is fed by pressurized sodium of the same pump's discharge.

Use of lubricants is essential for operation of typical bearings such as angular contact bearings. With the use of such lubricants, there are chances of oil ingress in the sodium system due to various reasons such as failure of mechanical seals. This may result in a significant contamination of sodium and reactor downtime [1]. Complete elimination of the probability of such leakage can be achieved by using an alternative technique in which oil is not at all used. A combination of active magnetic bearings (AMB) and ferro fluid seal in place of oil lubricated bearings is such an option which is now being actively explored towards development of oil free pumps [2]. As a part of developmental work, AMB of small capacity was designed and tested in 50 m³/h pump. To use AMB and ferro fluid seal, angular contact bearing has to be replaced by radial and thrust magnetic bearings, and the pump shaft needs to be accordingly modified. With respect to that, magnetic bearing of small capacity was designed and assembled in 50 m³/h pump after increasing the length of the shaft.

2 Present Pump Shaft and its Modification

The 50 m³/h pump's impeller is mounted on a vertical shaft having a length of 1685 mm. The pump shaft along with various attachments is shown in Fig. 2. The attachments on this shaft are mainly impeller at bottom, mechanical sealing at top, etc. In order to replace the angular contact bearing by a radial and a thrust magnetic bearing, the shaft has to be modified. The length of modified shaft is 2100 mm, and attachment on it includes impeller, rotating parts of the radial and thrust bearing components, etc. The modified shaft along with additional bearing attachments on it is shown in Fig. 3.

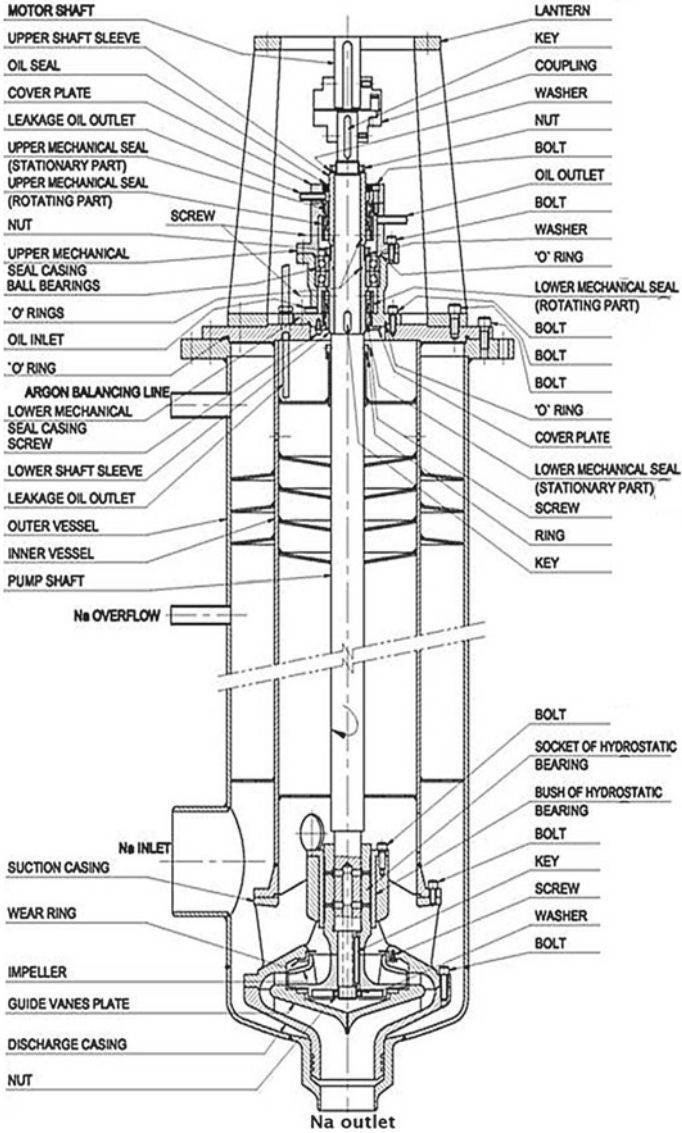


Fig. 1 50m³/h liquid metal pump assembly

3 Rotor Dynamic Analysis

Rotor dynamic analysis was carried out to obtain natural frequency before and after the modifications. Analysis was carried out in ARMD which is finite element-based software.

Fig. 2 Unmodified pump shaft

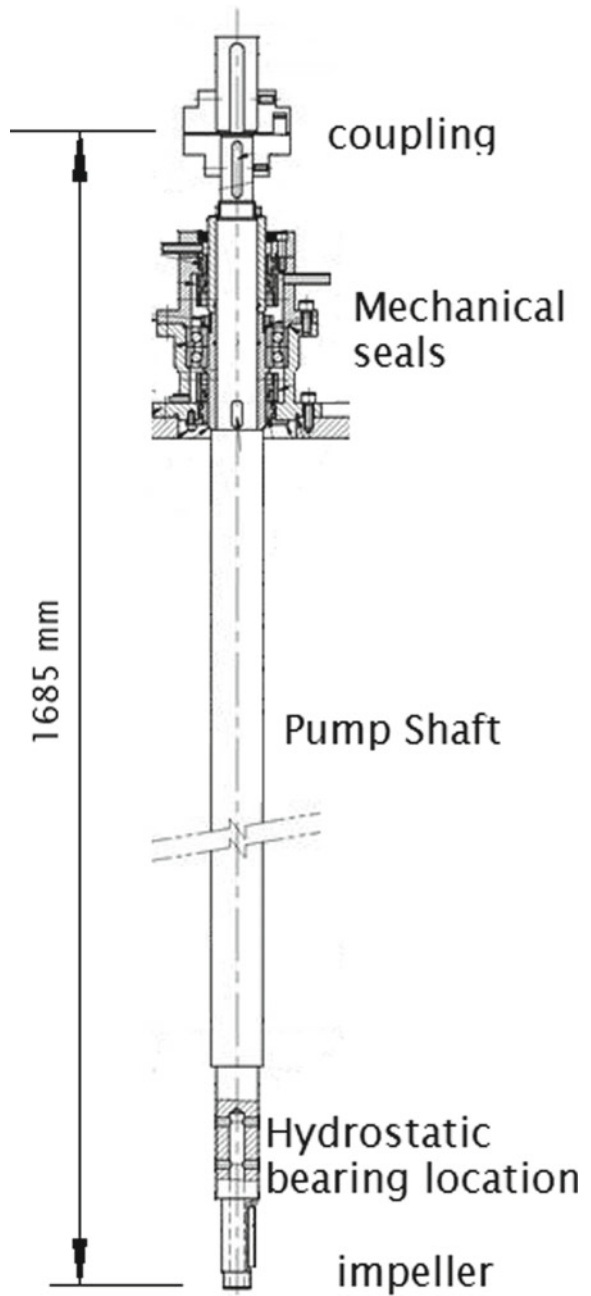


Fig. 3 Modified pump shaft

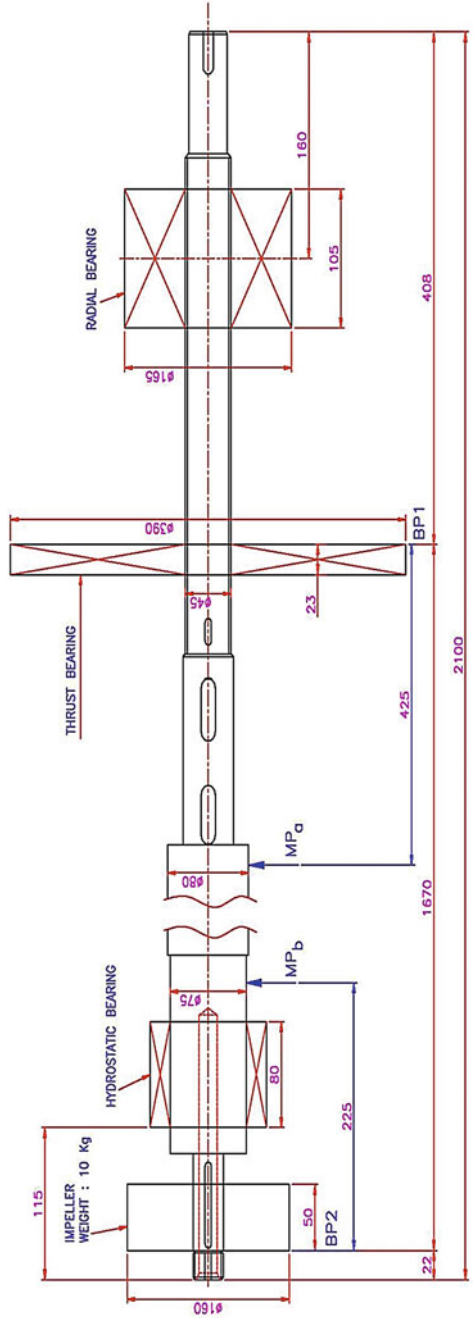


Table 1 Material property of SS 304 LN at 400 °C

S. No.	Properties	Values
1	Young's modulus	1.68×10^{11} Pa
2	Poisson's ratio	0.3
3	Density	7803 kg/m ³

3.1 Material

The material of construction of pump as well as shaft is austenitic stainless steel (SS) 304 LN. Maximum temperature pump shaft seen during reactor operation is 400 °C, hence the properties corresponding to this temperature are considered for shaft, and values are given in Table 1 [3].

3.2 Estimation of Critical Speed [4, 5]

For the estimation of critical speed, the pump shaft is modelled as a beam having different cross sections. Attachments on this shaft have been considered by attaching point masses, having same mass and moment of inertia, at their respective locations. These are given in Tables 2 and 3.

Table 2 Attachments on the unmodified pump shaft

Component	Location (node)	Disc mass (Kg)	Moment of Inertia (kg m ²)
Hydrostatic bearing	4	3.8	0.00895
Impeller	1	10	0.03313
Bottom Mech. Seal	17	1.11	0.00207
Bottom sleeve	18	2.207	0.00204
Top Mech. Seal	20	1.11	0.00207
Top sleeve	21	1.621	0.0015

Table 3 Attachments on the modified pump shaft

Component	Location (node)	Disc mass (Kg)	Moment of Inertia (kg m ²)
Impeller	1	10	0.03313
Hydrostatic bearing	4	3.8	0.00895
Thrust bearing	23	21.595	0.41604
Radial bearing	26	16.55	0.06051

3.3 Estimation of Bearing Stiffness

The unmodified shaft is supported laterally by a top radial bearing whose stiffness is 10^8 N/m, while a bottom hydrostatic bearing (HSB). The HSB gets pressurized from pump discharge of the same pump, and hence, the HSB stiffness depends on the pump speed which can be estimated using the formula given by Rowe [6] as

$$\lambda = \left(\frac{P_s L D}{h_0} \right) \left(\frac{3n^2}{2\pi} \right) \left\{ \frac{\beta \left(1 - \frac{a}{L} \right) \sin^2 \left(\frac{\pi}{n} \right)}{z + 1 + 2 \sin^2 \left(\frac{\pi}{n} \right)} \right\} \tag{1}$$

where

- D Shaft diameter
- L length of journal
- C clearance
- n number of pads
- a axial land width
- b circumferential land width

the values of z for orifice are given by

$$z = \frac{\beta}{2(1 - \beta)} \tag{2}$$

β is defined as the concentric pressure ratio $\frac{P_{r_0}}{P_s}$, where P_{r_0} is the recess pressure at a radial clearance r_0 and P_s is the supply pressure. The supply pressure is a function of pump speed which can be obtained from pump characteristics curve (discharge vs. head at various speed). The recess pressure has been taken approximately as 60% of supply pressure. By substituting various pump parameters, the following graph (Fig. 4) is obtained which shows HSB stiffness versus speed.

Direct stiffness K_{xx} and K_{yy} of radial bearing and magnetic bearing considered for the analysis are listed in Table 4. In the analysis, K_{xx} and K_{yy} are assumed as equal, and cross coupling in the stiffness is neglected. The values for hydrostatic bearing are taken from reference 7 and also estimated using theoretical formula.

Stiffness of the magnetic bearing and radial bearings will not change appreciably with increase in speed of the shaft, but hydrostatic bearing stiffness will increase, with increasing speed [7] depending on the speed of the pump shaft.

4 Results

After modelling entire shaft along with the attachments and various bearing stiffness, analysis was run in order to estimate the critical speed of rotation of both, the

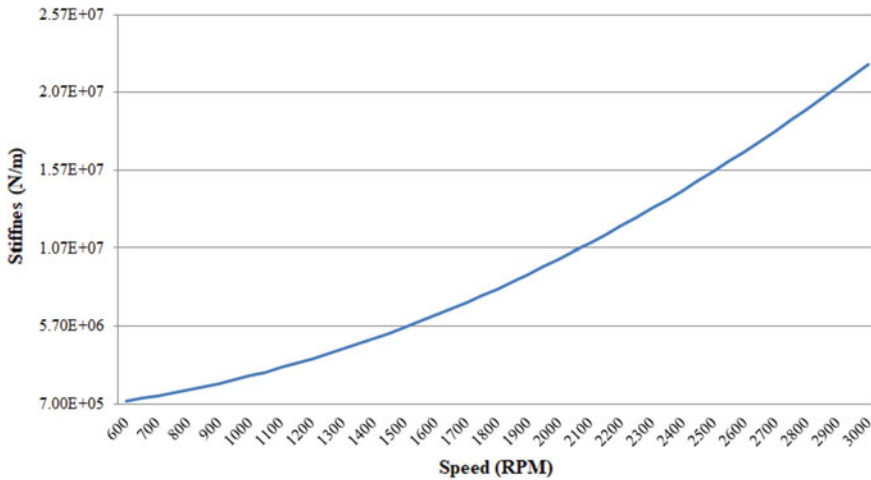


Fig. 4 Speed versus stiffness plot

Table 4 Bearing stiffness

S. No.	Type of bearing	Stiffness, K_{xx} and K_{yy} (N/m)
1	Top radial bearing	10^8
2	Bottom hydrostatic bearing	10^7
3	Magnetic radial bearing	10^6

unmodified shaft as well as modified shaft. Critical speeds were estimated with and without gyroscopic effect.

The effect of change in stiffness of HSB throughout the working range of pump which is from 580 to 2900 rpm is shown in Table 5, the stiffness of magnetic radial bearing is considered as 10^6 N/m, while stiffness of HSB varies as given in Table 6. Mode shapes for different critical speeds are given in Figs. 5, 6 and 7.

5 Unbalance Response

The critical speed of the modified shaft was analysed to be lying within the operating range of speed. Hence, to know the amplitude of maximum deflection at critical locations, unbalance response studies have been carried out. Amplitudes of maximum displacements were estimated under an unbalance of 827 g mm. This value is considered based on allowable unbalance as per 2.5 grade balanced shaft, but actual measured unbalance is much less than this value. Structural damping of 2%

Table 5 Critical speeds of the rotor assembly

Bearing Stiffness (N/m)	Mode	Whirling	With gyroscopic effect (rpm)	Without gyroscopic effect (rpm)	
<i>Unmodified shaft</i>					
Angular bearing	1×10^8	1	Backward	4459.2	4460.7
			Forward	4462.2	
Hydrostatic Bearing	1×10^7	2	Backward	5297.8	6003.2
			Forward	6078.6	
<i>Modified shaft</i>					
Magnetic bearing	1×10^6	1	Backward	1193.0	1197.7
			Forward	1202.4	
Hydrostatic bearing	1×10^7	2	Backward	2618.4	2810.6
			Forward	3002.8	

Table 6 Critical speeds of the rotor assembly of modified shaft under varying HSB stiffness

Speed (rpm)	Magnetic bearing stiffness (N/m)	HSB stiffness (N/m)	Mode 1		Mode 2	
			Backward whirl (rpm)	Forward whirl (rpm)	Backward whirl (rpm)	Forward whirl (rpm)
580	1×10^6	8.4×10^5	1170.72	1174.08	1943.58	1948.98
1160	1×10^6	3.3×10^6	1251.18	1256.46	2756.22	2833.86
1740	1×10^6	7.65×10^6	1264.8	1272.24	2976.06	3185.04
2320	1×10^6	1.35×10^7	1267.98	1277.76	2994.66	3305.22
2900	1×10^6	2.1×10^7	1268.64	1280.82	2976.84	3379.92

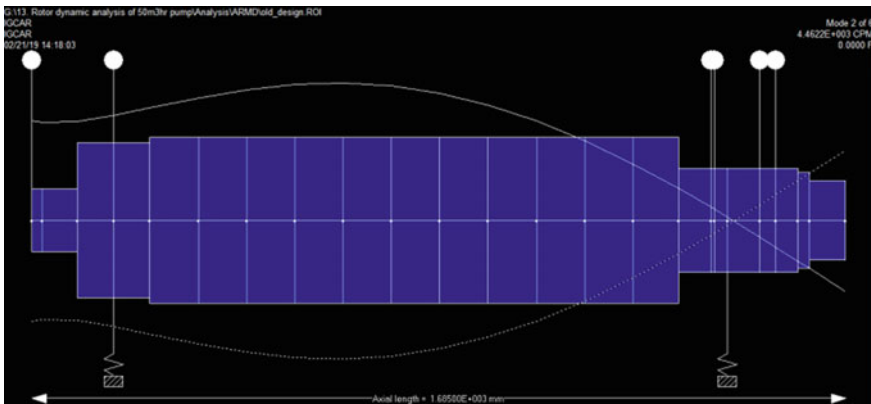


Fig. 5 Mode shape 1 of vibration of unmodified rotor assembly

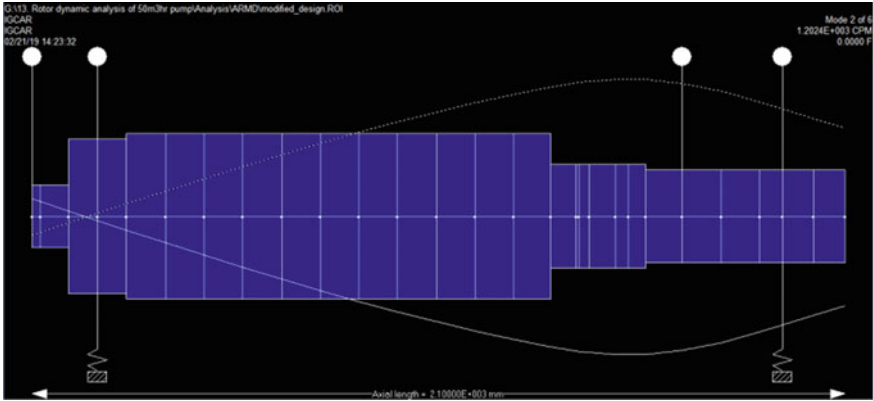


Fig. 6 Mode shape 1 of vibration of modified rotor assembly

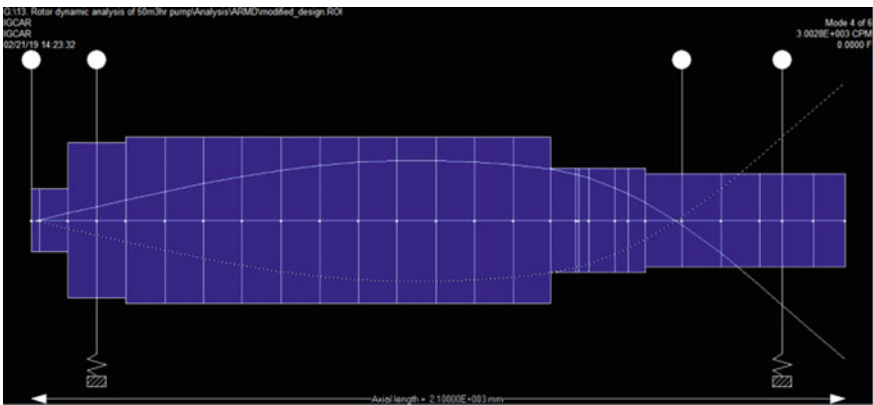


Fig. 7 Mode shape 1 of vibration of modified rotor assembly

was considered for the shaft, and viscous damping at bearing locations was neglected. Unbalance response analysis was done for two cases. In first case, the total unbalance has been concentrated at the impeller location, i.e. node 1 and in the second case, total unbalance was distributed equally at impeller location, and location of radial bearing and displacements were estimated at bearing locations. The results obtained are given in Table 7.

It can be seen from the above analysis that the maximum displacement amplitude both at the HSB location as well as active magnetic bearing are much less than the clearance provided.

Table 7 Unbalance versus deflection amplitude

Unbalance (gm mm)	Region of application	Deflection at HSB (μm) (clearance $\sim 40 \mu\text{m}$)		Deflection at magnetic radial bearing (μm) (Clearance $\sim 1 \text{ mm}$)	
		Mode 1	At maximum operating speed 2900 rpm	Mode 1	At maximum operating speed 2900 rpm
<i>At 2900 rpm (operating speed)</i>					
827	Impeller location	4.33	0.53	210	16.7
413.5	Both at impeller and radial disc location	7.81	4.92	413	85.4
<i>At 1260 rpm (1st critical speed)</i>					
827	Impeller location	0.83	–	42	–
413.5	Both at impeller and radial disc location	1.49	–	79.1	–

6 Conclusion

Use of active magnetic bearings in place of oil lubricated radial and thrust bearing is an apt option towards achieving oil free operation in critical sodium systems. To demonstrate this concept, a sodium pump having $50 \text{ m}^3/\text{h}$ capacity has been selected. The shaft of this pump has been modified to accommodate the magnetic bearings. The analysis for finding out critical speed of the pump shaft has been carried out before and after modifications. The first critical speed of the unmodified shaft is around 4460 rpm (without gyroscopic effect) which is quite away from the operating speed of the pump, i.e. 2900 rpm. With the modification of the shaft, the first critical speed has come down to 1197 rpm (without gyroscopic effect), while the second critical speed is found to be 2810 rpm (without gyroscopic effect) which has 2618 rpm backward whirl and 3002 rpm forward whirl. Since the critical speed is estimated to be very close to operating speed, an unbalance response study has been carried out. The shaft of the pump had been dynamically balanced with balance grade 2.5, maximum displacement response under an unbalance of 827 g mm was estimated, and the displacements were found to be well within the clearance provided at critical locations.

References

1. Sreedharan KV et al (2003) Conceptual design of secondary sodium pump, internal report. Indira Gandhi Centre for Atomic Research, Kalpakkam
2. Sreedhar et al BK (2013) Development of active magnetic bearing and ferrofluid seals towards oil free sodium pump. Nucl Eng Des 265
3. Kothandaraman AL et al (2000) Material properties for design, internal report. Indira Gandhi Centre for Atomic Research, Kalpakkam
4. Rao JS (1983) Rotor dynamics. Wiley Eastern Limited
5. ARMD Users Manual (Version 5.1.2600.2180), RBTS
6. Rowe WB (2012) Hydrostatic, aerostatic and hybrid bearing design. Butterworth-Heinemann
7. Chellapandi P (2004) Mechanical vibration analysis of primary sodium pump. In: Internal report. Indira Gandhi Centre for Atomic Research, Kalpakkam

Bearings, Dampers and Seals

Rotor Dynamics of Turbine–Generator Shaft with Dampers During Subsynchronous Resonance Generated by Series Capacitors



P. Manikandan  and Faheem Ahmed Khan 

Abstract Purpose In this paper, an electromechanical approach to study the turbine–generator shaft stability with and without dampers is made. The shaft is subjected to electrical disturbances created by series capacitors. The high power capacitors help the electric power system to improve the reactive power in high voltage transmission lines. **Methods** Finite element method is used to study the stability of the shaft under subsynchronous resonance when compared to the traditional methods like eigenvalue analysis, frequency scanning method and digital time simulation techniques. At the same time, it leads to subsynchronous resonance. **Results** Electromechanical stress in the rotating shaft arises when the resonance is created in the system. Maximum stress and strain of the shaft are calculated with other necessary parameters to prove the system instability. In order to maintain stability, dampers are installed at an optimum location. **Conclusion** Best location of installing damper is found using ANSYS 16.0 by modal analysis, harmonic and phase response analysis. The damper installed at the point reduces the stress caused by subsynchronous resonance and maintains the stability of the system.

Keywords Dampers · Finite element method · Generator · Shaft · Subsynchronous resonance · Turbine

1 Introduction

In dynamic systems such as the electrical power systems, the physical parameters play acute roles to study the vibration characteristics. Inspired by accurate design and aggregate demand of high proficiency in practical engineering, the vibration

P. Manikandan (✉)

Department of EEE, CHRIST (Deemed to be University), Bangalore, Karnataka, India
e-mail: manikandan.p@christuniversity.in

F. A. Khan

Department of EEE, Ghousia College of Engineering (Affiliated to Visvesvaraya Technological University, Belagavi, Karnataka), Ramanagaram, Karnataka, India
e-mail: faheemahmedkhan11@gmail.com

characteristics of rotating systems are exclusively studied both hypothetically and experimentally [1–3]. In the past years, numerous works had been carried out on various aspects of rotor systems. However, there are certain uncertainties which are unavoidable due to the practical electromechanical systems. Subsynchronous resonance occurs when series capacitors are injected to the power system and leads to a mismatch in synchronous speed of the turbo generator shaft. This causes torsional interaction between the mechanical and electrical system of a power generating unit [4]. Subsynchronous resonance was not detected till 1970s. A turbo generator shaft experienced damage in Mohave Power Station in Southern Nevada, and later, it was concluded that this damage is due to the interaction of mechanical and electrical frequencies which resulted in a resonance. The amplitude of resonance is less than the natural frequency, and hence, it is stated as subsynchronous resonance. Mechanical vibrations cause growing fatigue damage when they exceed the material exhaustion limits. This results in reduced life of shafts, blades and rotors [5–7]. In several cases, contrary interactions have led to rising oscillations and shaft damage which includes twisted couplings and broken shafts. These damages also occur in electrical lines which include HVDC converters, electric arc furnaces and cycloconverter frequency changers. Various methods like eigenvalue analysis, frequency scanning method and digital time simulation techniques have been employed to detect and damp the subsynchronous resonance [7–12].

In this study, an experimental setup of a hydro turbine–generator unit is used to study the rotor dynamics of turbine–generator shaft. 3D Model of the shaft is modelled in ANSYS 16.0. 3D model consists of shaft, springs and bearings which are subjected to vibrations [13–15]. Series capacitors are connected to the generator terminal, and resonance is induced in the circuit. The shaft model is subjected to MODAL analysis to study the mode shapes of the shaft during the resonance. Dampers are installed in the optimum point to maintain the stability of the system.

2 Physical Model

The experimental set-up consists of a complex rotor system with solid rotor and rolling bearings supported at two ends. The turbine–generator combination is fixed on the foundation by bolts. The output of the generator is loaded with both resistive and capacitive loads to ensure resonance created in the system. 3D model of the turbine and shaft is modelled by excluding the design complexities. High power turbine and generators shaft is connected with speed governors. The rotor of the generator and the turbine shaft is connected through a belt in the existing experimental set-up. To overcome the design complexity, the 3D model is designed in such a way that the turbine shaft and generator rotor are connected together, and it represents the six mass system of the turbine–generator.

3 Rotor Dynamics Under Subsynchronous Resonance

Rotor dynamics of the turbo generator shaft gives information about the adjacent and torsional vibration of rotating shafts and the modes of vibration. The study will help the operator to keep the vibration levels within acceptable limits. Certain vibrations are not easily detected until some form of damage occurs in the shaft line. Recent researchers have developed theoretical methods to study the response of torsional vibrations with low cost computing power. Precisely, torsional vibration analysis provides useful information such as eigenvalues and mode shapes. In eigenvalue analysis, both positive and negative values are derived based on the system which is under study [16–18]. Negative eigenvalue denotes the presence of subsynchronous resonance in the system. Most of the traditional methods give the information of the subsynchronous resonance with respect to its presence by considering the participation factor. In this study, point of damage on the shaft due to subsynchronous resonance is derived from the stress, strain and eigenvalues [19, 20].

4 Modal Analysis

Modal analysis gives the overview of the steady state and transient response of any static as well as dynamic system. Every rotating structure has an internal frequency or resonant frequency at which the structure starts vibrating. Modal analysis is also defined as linear dynamic response which assesses and superimposes free-vibration mode shapes to portray the displacement patterns. Mode shapes, clarifies the configurations about the construction which will naturally displace. The main purpose of a modal analysis is to find the shapes and frequencies at which the structure starts amplifying the effect of a load [21]. In general, modal analysis is useful in finding the loose components, experiencing rotational speeds which are dangerous, finding out where the maximum deformation and finding the mode. It gives an information about the frequency at which the structure will absorb the energy applied to it.

5 Experimental Setup

In the experimental set-up, Kaplan turbine is used to run the generator. The major advantage of the Kaplan turbine is the efficiency delivered during the low water speeds. The rate of rotation of the blade is high. Kaplan turbine is the modified version of Francis turbine. The technical specification of the experimental set-up is show in Table 1. The experimental set-up is self-contained in all respect except for electrical power/water supply wherever necessary to be provided during loading of the turbine (Figs. 1, 2, 3 and 4).

Table 1 Technical details of the hydro turbine-generator

Specification	Parameters
Type	Axial flow reaction turbine
Capacity	2 HP
Rated speed	2000 rpm
Discharge capacity	2000 litres per minute
Head	8 m
Loading	Electrical
Material	Cast iron
Drum size	200 mm
Generator	3 A

**Fig. 1** Experimental set-up

6 Results and Discussions

6.1 Analysis of Experimental Results

The loading pattern of hydro turbine-generator is changed to determine the resonance effect in the turbo generator shaft. Single phase capacitor banks are connected



Fig. 2 Rotor of turbo generator unit

along with the resistive load banks. Capacitors are connected to the load. The effect of capacitance increases the vibration of the shaft. The current increases when capacitance is injected into the system. Illumination of lamps also increased due to the increase in current. Since the turbine–generator rated speed is only 2000 rpm, compensation is limited to only 50%. Since the impact of resistive load is more, the rate of increase in rotational speed is not high. Considering 50% compensation case, the turbo generator runs in 1562 rpm with compensation, while the total load in the system is 1.6 kW. Without compensation, for the same load, the turbo generator runs at a speed on 1473 rpm. Current in the system increases after compensation. Head on turbine is made as constant with a pressure of 0.8 kg cm² and vacuum pressure of 10 kg/cm². Head notch is around 200 mm (Table 2).

6.2 3D Modelling of Turbine–Generator Shaft

Turbine–generator shaft is modelled with Designmodeler tool in ANSYS. Cast iron and stainless steel materials are used to determine the material properties. Stiffness coefficient is calculated based on the dimensions of the shaft. Length of the turbine



Fig. 3 Turbine—dismantled for measurements



Fig. 4 Operation of hydro turbine

Table 2 Experimental results

Head on turbine		Turbine speed rpm	Load kW	Energy metre reading		Current in amps	Head over notch 'h' in mm	Percentage of compensation (%)
Pressure 'p' kg/cm ²	Vacuum pressure P _v kg/cm ²			No. of revs	Time taken (s)			
0.8	10	1987	0.4	4	395	0.2	200	10
	10	1915	0.8	4	224	0.6	200	20
	10	1762	1.2	4	184	1.2	200	30
	10	1630	1.4	4	160	2.4	200	40
	10	1562	1.6	4	140	3.6	200	50

shaft is measured 500 mm with a diameter of 55 mm, and generator shaft is 380 mm with a diameter of 28 mm. To overcome the difficulty of design of belt-driven turbine shaft, it is assumed that both the shafts are mounted on the same without overlapping each other. Point mass is defined in the model which is of 350 kg and 0.397 kg/mm throughout the shaft line. To match with the experimental set-up, two bearings with a stiffness coefficient are attached on the both the ends of the shaft. SOLID186 model is used to mesh the shaft. Coriolis effect is enabled to ensure rotor dynamics is studied in the shaft. Modal analysis is carried out without damper as well as with damper.

6.3 Analysis of Mode Shapes

Total deformation of the shaft, stress and strain is found. Campbell diagram which shows the stability of the shaft with six modes is denoted in Fig. 5. It is noted that Mode 1 becomes unstable due to resonance created in the line. The maximum stress is distributed in the turbine shaft when compared to the generator shaft. To overcome the stress, a spring damper which is from body to ground is modelled in the shaft, and modal analysis is completed for the same speed. The Campbell diagram which is in Fig. 6 shows that all the six mode shapes are stable which is due to the damper connected to the turbine shaft. Campbell diagram numerical details are shown clearly in table. Figure 7 shows the mode shape 2, 3 and 4. It is very clear from the figure that displacement occurred at different places and the shaft is stressed more. Campbell parameters are given in Tables 3 and 4.

6.4 Analysis of Frequency Response

Frequency response analyses are used to estimate the steady-state response of a rotating structure to loads that vary sinusoidally with time, and harmonic response

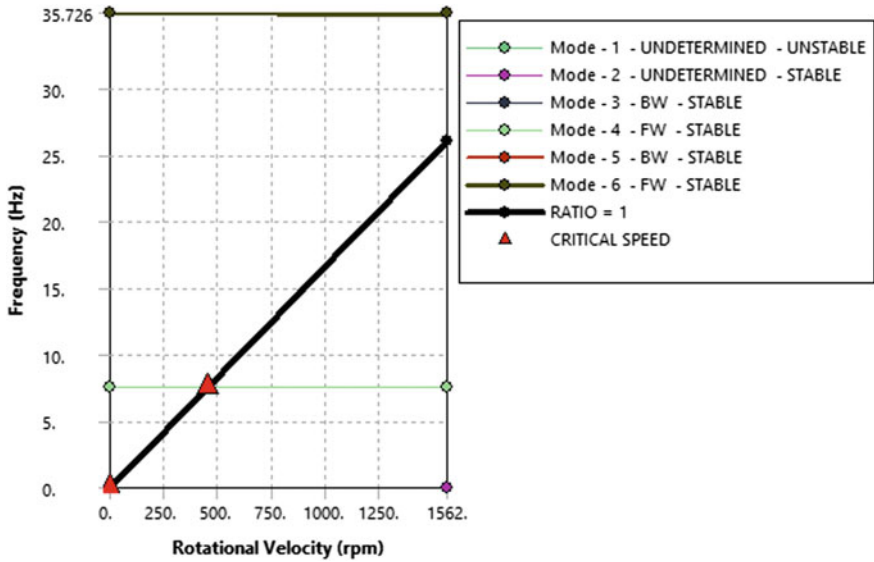


Fig. 5 Campbell diagram without damper

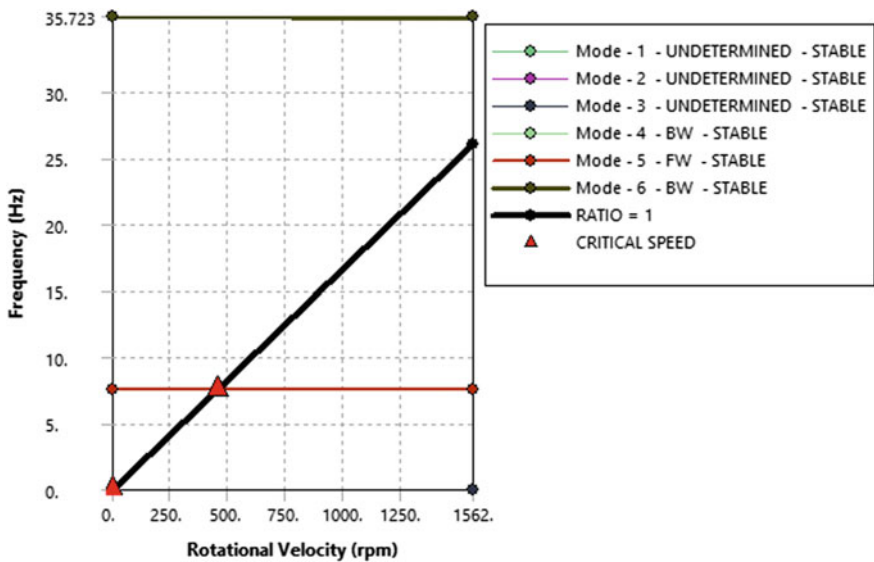


Fig. 6 Campbell diagram with damper

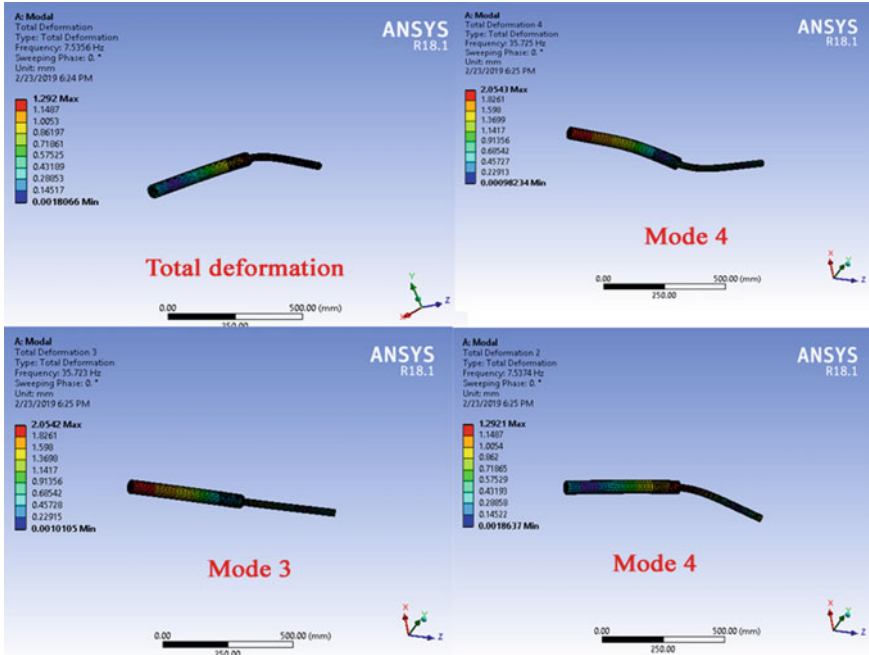


Fig. 7 Various mode shapes of the turbine–generator shaft

Table 3 Modal analysis with damper

Mode	Whirl direction	Mode stability	Critical speed	0 rpm (Hz)	1562 rpm (Hz)
1.	Undetermined	Stable	0.12349 rpm	2.0581e−003	2.0581e−003
2.	Undetermined	Stable	None	0	0
3.	Undetermined	Stable	None	0	0
4.	BW	Stable	452.13 rpm	7.5356	7.5355
5.	FW	Stable	452.25 rpm	7.5374	7.5376
6.	BW	Stable	None	35.723	35.722

Table 4 Modal analysis without damper

Mode	Whirl direction	Mode stability	Critical speed	0 rpm (Hz)	1562 rpm (Hz)
1	Undetermined	Unstable	None	0	0
2	Undetermined	Stable	0.28272 rpm	4.7119e−003	4.7119e−003
3	BW	Stable	452.13 rpm	7.5356	7.5355
4	FW	Stable	452.25 rpm	7.5374	7.5376
5	BW	Stable	None	35.723	35.722
6	FW	Stable	None	35.725	35.726

analysis during the design phase of the machine helps the user to overcome resonance, fatigue and other harmful effects of forced vibrations. The frequency response of the undamped shaft is shown in Figs. 8 and 9. Damping ratio is increased 10, 20 and 20% which is normally implemented practically by dampers and increasing lubrication. The vibration magnitude reduces when the damping ratio increases. The frequency response without dampers and with dampers is shown in the Figs. 7 and 8.

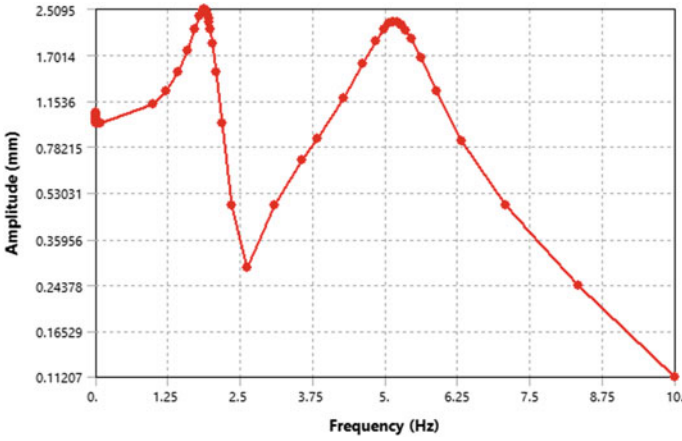


Fig. 8 Damping ratio 0.1

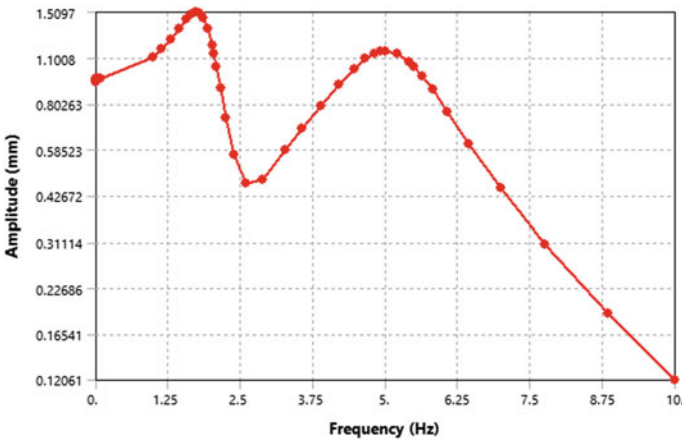


Fig. 9 Damping ratio 0.2

7 Conclusions

The dynamic characteristics of hydro turbine–generator shaft subjected to subsynchronous resonance are studied. The finite element method is utilised to solve the system differential equations. The main conclusions from this study are summarised as follows:

1. The resonance created by the series capacitors has considerable influence on the rotor system of the generator as well as the turbine, and the natural frequency interacts with the resonant frequency.
2. The excitation frequency exerts an effect on the shaft and increases the stress and strain which leads to deformation. Modal analysis results show the instability of the system during the injection of series capacitors which is meant for reactive power compensation in power systems.
3. As the compensation increases, the stress is controlled by the spring dampers installed in the shaft line. The location of installing the damper is selected from the results obtained from the stress distribution and total deformation carried during the modal analysis.
4. Frequency response analysis gives the amplitude of the vibration created in the shaft. Damping ratio must be increased by means of improving the lubrication as well as dampers. Vibration decreased when damping ratio is increased in the analysis.

Acknowledgements The authors are grateful to Department of Electrical and Electronics Engineering & Department of Mechanical engineering, School of engineering and technology, CHRIST (Deemed to be) University for providing the laboratory facilities. The authors acknowledge Department of Electrical and Electronics Engineering, Ghousia College of engineering Ramanagaram (Affiliated to Visvesvaraya Technological University), Karnataka, India.

References

1. Xie X, Zhang C, Liu H, Liu C, Jiang D, Zhou B (2016) Continuous mass model based mechanical and electrical co-simulation of SSR and its application to a practical shaft failure event. *IEEE Trans Power Syst* 31(6):5172–5180
2. Saxena Ankur, Pareya Anand, Chouksey Manoj (2016) Study of modal characteristics of a geared rotor system. *Procedia Technol* 23:225–231
3. Kirchg B (2016) Finite elements in rotor dynamics. *Procedia Eng* 144:736–750
4. Mankowski O, Wang Q (2013) Real-time monitoring of wind turbine generator shaft alignment using laser measurement. *Procedia CIRP* 11(1):291–295
5. Bai B, Zhang LX, Guo T, Liu CQ (2012) Analysis of dynamic characteristics of the main shaft system in a hydro-turbine based on ANSYS. *Int Conf Adv Comput Model Simul* 31:654–658
6. Elhefny A, Guozhu L (2012) Stress analysis of rotating disc with non-uniform thickness using finite element modeling. In: *Proceeding of the International Conference on Engineering and Technology (ICET)*, Cairo, pp 1–5

7. Karlberg (2010) Approximated stiffness coefficients in rotor systems supported by bearings with clearance. *Int J Rotating Mach*
8. Hernandez M, Guardado JL, Venegas V, Melgoza E, Rodriguez L (2008) Analysis of the torsional modes of the turbine-synchronous generator group. In: IEEE/PES transmission and distribution conference and exposition. Bogota, Latin America, pp 1–7
9. Tsai J (2007) A new damper scheme to restrict torsional torques on the turbine generator shafts and blades near a HVDC link. *Electr Eng* 89:377–387
10. Tsai JJ, Lin CH, Tsao TP (2003) Long-term fatigue life loss of turbine blades owing to non-characteristic harmonic currents in asynchronous HVDC links. *J Electr Power Syst Res* 65(2):135–147
11. Liang CC (1993) Torsional response of rotor system in steam turbine-generator. *Taipower Eng J* 538(6):35–52
12. IEEE Sub Synchronous Resonance Working Group (1992) Readers guide to sub synchronous resonance oscillations. *IEEE Trans Power Apparatus Syst* 7:150–157
13. Silva RT, Ritto TG (2018) Impact of damper seal coefficients in rotor dynamics. In: Proceedings of the joint ICVRAM ISUMA UNCERTAINTIES conference. Brazil, April 2018
14. Leader ME Evaluating and correcting subsynchronous vibration in vertical pumps. In: Dyrobes rotor dynamics software
15. Yang P, Yuan Q, Huang C (2017) Analysis of the impacts of bearing on vibration characteristics of rotor. *Shock Vibr* 22(4)
16. IEEE Sub Synchronous Resonance Working Group (1985) Second benchmark model for computer simulation of sub synchronous resonance. *IEEE Trans Power Apparatus Syst PAS* 104(5):1057–1066
17. IEEE Sub synchronous resonance working group, “Terms, definitions and symbols for sub synchronous resonance oscillations” *IEEE Transactions on Power Apparatus and Systems*, vol. PAS-104, no. 6, 1985, pp. 1326–1334
18. Lambrecht D, Kulig T (1982) Torsional performance of turbine generator shafts especially under resonant excitation. *IEEE Trans Power Apparatus Syst* 101:3689–3697
19. Glienicke J (1967) Experimental investigation of the stiffness and damping coefficients of turbine bearings and their application to instability prediction. *Proc IMechE* 181(3B):116–129
20. Assenkamp A, Hoffmann R, Kreische C, Exnowski S (2017) Simulative analyses of dynamical behavior of steam-powered turbo generators during power system incidents with a higher rate of change of frequency. In: IET international conference on resilience of transmission and distribution networks. Birmingham, pp 1–6
21. Jackson MC (1979) Turbine generator shaft torques and fatigue: part I-simulation methods and fatigue analysis. *IEEE Trans Power Apparatus Syst PAS* 98(6)

Active Control of Bridge Configured Self-bearing Motor, a Numerical Study



Gaurav Kumar, Karuna Kalita, and Kari Tammi

Abstract Vibration is a major concern of the rotating machine industry. The wear and tear of the support bearing and the eccentric motion of the rotor are among the main sources of vibration of an electrical machine. The development of a bearingless machine is a good way to address this problem. This paper mainly focuses on the development of a bearingless bridge configured winding (BBCW) induction motor. The bridge configured winding (BCW) is a specialized single set of winding scheme, which has the capability to produce the torque and the transverse force simultaneously. There are two sets of supply for this winding scheme. The three-phase main supply produces a p -pole pair of the magnetic field and is responsible for the torque-producing component. The external supply in the bridges produces a $p \pm 1$ pole pair of the magnetic field. The interaction between these two fields produces a net radial force, which is used to neutralize the various forces acting on the rotor and the weight of the rotor. The magnitude and the direction of this magnetic force can be controlled by supplying currents or voltages at different frequencies and amplitudes through the bridge points of the BCW winding. There is no study in the literature related to the development of bearingless machine using BCW scheme. In the present work, a Simulink model of a BBCW induction motor has been developed. The convergent control scheme has been used for the control of forces of various frequencies acting on the rotor. The PID controller has been used for the levitation of the rotor. The shaft of the motor has been modeled as a Euler–Bernoulli beam, and it is supported by only one isotropic bearing at the one end. The other end of the rotor has been kept unsupported to demonstrate the levitation effect.

Keywords Vibration · UMP · BCW · Electrical machine

G. Kumar · K. Kalita (✉)

Department of Mechanical Engineering, Indian Institute of Technology, Guwahati 781039, India
e-mail: karuna.kalita@iitg.ernet.in

G. Kumar

e-mail: gaurav.kr@iitg.ernet.in

K. Tammi

Department of Engineering Design and Production, Aalto University, 02150 Espoo, Finland
e-mail: kari.tammi@aalto.fi

© Springer Nature Singapore Pte Ltd. 2021

J. S. Rao et al. (eds.), *Proceedings of the 6th National Symposium on Rotor Dynamics*, Lecture Notes in Mechanical Engineering,
https://doi.org/10.1007/978-981-15-5701-9_17

203

Nomenclature

M	Mass matrix
C	Damping atrix
K	Stiffness matrix
F_{sta}	Static Force
$F_{pulsating}$	Pulsating force
$F_{bridge_x}, F_{bridge_y}$	Actuator force
K_x	Force-displacement factor
K_i	Force- current factor
T	Transformation matrix
δ_m	Mean air gap length
$\omega_1 \omega_b$	Main and bridge supply frequency
R	Outer radius of the rotor

1 Introduction

High-speed and compact drive systems are among the most emerging areas in the field of rotating machinery. Mechanical bearing inherently puts some limit on the speed of a rotating machine. The best available solution of a compact drive system is to use magnetic bearings instead of mechanical bearing with an electrical machine. However, the inclusion of magnetic bearing makes the system bulky and increases the space requirements as well. The current trend is to generate transverse force in an electrical machine itself so that the requirement of magnetic bearing or mechanical bearing can be taken care of by the electrical machine itself. Generally, the dual set of winding is used for the generation of transverse force where one set of winding is responsible for the torque generation, and another set of winding is responsible for transverse force generation [1]. Uses of the dual set of winding decrease the torque production capability of an electrical machine as the stator slot area are also shared by another set of winding which is used for transverse force generation. The bridge configured winding is a special single set of winding scheme which generates transverse force without affecting the torque production capability of the electrical machine [2]. The details of the bridge configured winding scheme has been discussed in detail in [2–4]. This winding scheme can accommodate two isolated source termed as the main supply source and bridge supply source. The main supply source is responsible for torque generation (p pole pair of the magnetic field), and the bridge supply source is responsible for transverse force generation ($p - 1$ pole pair of the magnetic field).

The present work discusses a numerical model used for levitation control and multiple harmonics vibration control in a four pole bridge configured induction machine. A MATLAB/Simulink model has been developed to study the numerical simulation. The approximation of analytical force has been used as a replica of an

electrical machine to simulate the levitation and harmonic force compensation. The magnetic field and the force have been calculated analytically, and later two control algorithms, the PID and the convergent control algorithm have been used to achieve the levitation and harmonic force compensation, respectively.

2 Force Expression

The two types of force would act on the rotor of the bearingless electrical machine, i.e., eccentricity force and actuator force. A rotor is said to be eccentric if the rotor center does not coincide with the stator center. An eccentric rotor makes the magnetic field asymmetric, and a transverse force acts in the direction of the shortest air gap. Whereas the bridge supply would generate the required controllable force is termed as actuator force.

2.1 Eccentricity Induced Force

In static eccentricity condition, the predominant component of force acts along the shortest air gap and is given by Eq. (1) [5, 6].

$$F_{\text{stat}} = \frac{\mu_0}{2\delta_m^3} \frac{A_{\text{pm}}^2 R^3 l}{p^2} \pi e \quad (1)$$

In addition to constant pull a pulsating force ($F_{\text{pulsating}}$) of double-supply frequency also acts on the rotor. By neglecting the higher order terms, it can be represented as

$$F_{\text{pulsating}} = \frac{\mu_0}{2\delta_m} \frac{\pi A_p^2 R^3 l}{p^2} \frac{\epsilon}{(1 - \epsilon^2)^{3/2}} \cos 2(\omega_1 t - \phi_p) \quad (2)$$

where δ_m is the mean air gap length, ϵ is the eccentricity ratio and A_{pm} is the amplitude of current density distribution.

$$A_p = \sqrt{2} n_0 \xi \frac{I_0 \omega_1}{\pi R} \quad (3)$$

Here, n_0 is the number of strands used in the stator winding, ξ is the winding factor, ω_1 is the angular supply frequency, R is the outer radius of the rotor, l is the length of the rotor and I_0 is the amplitude of the current. Since the constant pull is dependent on the eccentricity e , the negative magnetic stiffness coefficient K_{mag} can be obtained by differentiating the static force with respect to eccentricity, e as

$$K_{\text{mag}} = \frac{dF_{\text{stat}_x}}{de} = \frac{\mu_0}{2\delta_m^3} \frac{A_p^2 R^3 l}{p^2} \pi \quad (4)$$

2.2 Actuator Force

The actuator force can be calculated as an interaction of four pole and two pole magnetic field components. Using Maxwell's tensile stress theory, the total bridge force or actuator force over the circumference of the rotor in the x -direction can be calculated as

$$F_{\text{bridge}_x} = \int_0^{2\pi} \frac{(b_{\text{pmain}} + b_{\text{pbridge}})^2}{2\mu_0} \cos(\theta) R l d\theta \quad (5)$$

where b_{pmain} is the four pole magnetic field density due to the main supply and b_{pbridge} is the two pole magnetic field density due to the bridge supply. The four pole and two pole magnetic fields density can be approximated as sinusoidal distribution as [6]

$$b_{\text{pmain}}(\theta, t) = \beta_{\text{pm}} \cos(p\theta - \omega_1 t - \phi_p) \quad (6)$$

$$b_{\text{pbridge}}(\theta, t) = \beta_{\text{pb}} \cos(p_b \theta - \omega_b t - \phi_b) \quad (7)$$

Here, $p = 2$ is the fundamental pole pair due to the main supply, $p_b = 1$ is the fundamental pole pair due to the bridge supply, ω_1 and ω_b are the main supply and bridge supply frequency, ϕ_p and ϕ_b are the phase of main supply and bridge supply, respectively. The amplitude of main supply flux density (β_{pm}) and bridge supply flux density (β_{pb}) is given by

$$\beta_p = \frac{\mu_0 A_p R}{\delta_m p} \quad (8)$$

$$\beta_{\text{pb}} = \frac{\mu_0 A_{\text{pb}} R}{\delta_m p_b} \quad (9)$$

Here, A_{pb} is the amplitude of current density distribution due to the bridge supply,

$$A_{\text{pb}} = \sqrt{2} n_0 \xi \frac{I_b \omega_b}{\pi R} \quad (10)$$

where n_0 is the number of strands used in the stator winding, ξ is the winding factor, ω_b is the angular bridge supply frequency, R is the outer radius of the rotor, l is the length of the rotor and I_b is the amplitude of bridge supply current.

Substituting for $b_{p\text{main}}$ and $b_{p\text{bridge}}$ in Eq. (5), we get the actuator force expression along longitudinal (x -axis) direction,

$$F_{\text{bridge}_x} = \int_0^{2\pi} \frac{1}{2\mu_0} [\beta_{p\text{m}} \cos(p\theta - \omega_1 t - \phi_p) + \beta_{p\text{b}} \cos(p_b\theta - \omega_b t - \phi_b)]^2 \cos(\theta) R l d\theta \quad (11)$$

Substituting $p = 2$ for main supply and $p_b = 1$ for bridge supply, we get

$$F_{\text{bridge}_x} = \int_0^{2\pi} \frac{1}{2\mu_0} \{2\beta_{p\text{m}}\beta_{p\text{b}} R l \cos(2\theta - \omega_1 t - \phi_p) \cos(\theta - \omega_b t - \phi_b) \cos(\theta)\} d\theta \quad (12)$$

After integration of Eq. (12), we get

$$F_{\text{bridge}_x} = \frac{\beta_{p\text{m}}\beta_{p\text{b}}\pi R l}{2\mu_0} \{\cos((\omega_1 - \omega_b)t + (\phi_p - \phi_b))\} \quad (13)$$

Substituting for $\beta_{p\text{m}}$ and $\beta_{p\text{b}}$ in Eq. (13), we get the final expression of actuator force (bridge force) along the x -axis as

$$F_{\text{bridge}_x} = \left(\frac{\mu_0 A_p R}{\delta_m P}\right) \left(\frac{\mu_0 A_{p\text{b}} R}{\delta_m P_b}\right) \frac{\pi R l}{2\mu_0} \{\cos((\omega_1 - \omega_b)t + (\phi_p - \phi_b))\} \quad (14)$$

Similarly, bridge force acting in the transverse (along the y -axis) direction can be written as

$$F_{\text{bridge}_y} = \left(\frac{\mu_0 A_p R}{\delta_m P}\right) \left(\frac{\mu_0 A_{p\text{b}} R}{\delta_m P_b}\right) \frac{\pi R l}{2\mu_0} \{\sin((\omega_1 - \omega_b)t + (\phi_p - \phi_b))\} \quad (15)$$

If the bridge supply frequency is the same as that of the main supply frequency, i.e., $\omega_1 = \omega_b$, a constant force in any direction can be generated by managing the phase of the main and bridge supplies. In addition to this, the force expression, in this case, can be approximated as $K_i I_b$ where k_i can be termed as the force-current factor.

3 Rotor Model

In line with the objective of development of vibration control and bearingless simulation model, this section deals with the development of the rotor-bearing system. For the demonstration of disturbing force compensation, a meter long rotor supported by two mechanical bearings at the end has been considered. However, for the demonstration of levitation, the rotor is considered to be supported by a mechanical bearing at only one end. Figure 1 represents the rotor-bearing system considered for levitation control.

Keeping the system simple, the rotor of the motor has been modeled using the finite element method as a Euler–Bernoulli beam. The rotor has been discretized in 9 element and 10 nodes. Each node has 4 degrees of freedom, among them, first two are the transverse vibration DOF along x - and y -direction and last two are angular displacements DOF along x - and y -axes, respectively. The discretized model is represented in Fig. 2, indicating the node number of the discretization. Equation (16) represents the equation of motion of the rotor of the motor, where $[M]$ is the mass matrix, $[C]$ is the proportional damping matrix, $[K]$ is the stiffness matrix, f_{unb} is the unbalance force acting on the rotor and f_{bcw} is the sum of all the electromagnetic forces acting on the rotor.

$$[M]\{\ddot{x}\} + [C]\{\dot{x}\} + [K]\{x\} = \{f_{bcw} + f_{unb}\} \tag{16}$$

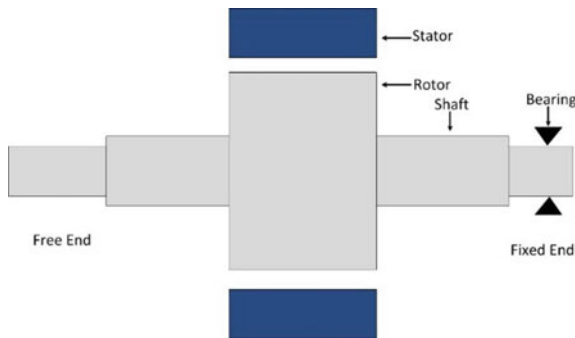


Fig. 1 Rotor model

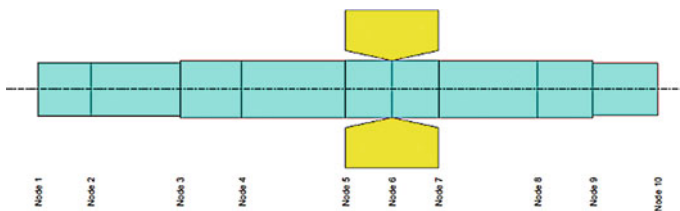


Fig. 2 Rotor discretized model

The dynamic reduction has been used to remove the unwanted degree of freedom from the rotor equation of motion. The transverse vibration degree of freedom at each node in x - and y -direction has to be retained and termed as the master degree of freedom x_m , whereas angular degree of freedom along x -axis and y -axis has to be removed and termed as slave degree of freedom x_s . To get the transformation matrix of dynamic reduction, Eq. (16) has been arranged in terms of master and slave degree of freedom as shown in Eq. (17). f_m is the combined force acting on the rotor.

$$\begin{bmatrix} M_{mm} & M_{ms} \\ M_{sm} & M_{ss} \end{bmatrix} \begin{Bmatrix} \ddot{x}_m \\ \ddot{x}_s \end{Bmatrix} + \begin{bmatrix} C_{mm} & C_{ms} \\ C_{sm} & C_{ss} \end{bmatrix} \begin{Bmatrix} \dot{x}_m \\ \dot{x}_s \end{Bmatrix} + \begin{bmatrix} K_{mm} & K_{ms} \\ K_{sm} & K_{ss} \end{bmatrix} \begin{Bmatrix} x_m \\ x_s \end{Bmatrix} = \begin{Bmatrix} f_m \\ 0 \end{Bmatrix} \quad (17)$$

Dynamic model reduction technique has been used to remove the slave degrees of freedom. Neglecting damping term in Eq. (17), we get

$$\begin{bmatrix} M_{mm} & M_{ms} \\ M_{sm} & M_{ss} \end{bmatrix} \begin{Bmatrix} \ddot{x}_m \\ \ddot{x}_s \end{Bmatrix} + \begin{bmatrix} k_{mm} & k_{ms} \\ k_{sm} & k_{ss} \end{bmatrix} \begin{Bmatrix} x_m \\ x_s \end{Bmatrix} = \begin{Bmatrix} f_m \\ 0 \end{Bmatrix} \quad (18)$$

Damping is neglected only to obtain the transformation matrix. This transformation matrix is used to reduce the degrees of freedom of the system. Writing Eq. (17) separately in master and slave degree of freedom, we get

$$\begin{aligned} M_{mm}\ddot{x}_m + M_{ms}\ddot{x}_s + K_{mm}x_m + K_{ms}x_s &= f_m \text{ and} \\ M_{sm}\ddot{x}_m + M_{ss}\ddot{x}_s + K_{sm}x_m + K_{ss}x_s &= 0 \end{aligned} \quad (19)$$

The dynamic reduction used to be carried out for a range of frequencies component or a particular frequency component. Considering the reduction for ω , Eq. (20) can be written as

$$-\omega^2 M_{sm}x_m - \omega^2 M_{ss}x_s + K_{sm}x_m + K_{ss}x_s = 0 \text{ and } x_s = A^{-1}Bx_m \quad (20)$$

where $A = (-\omega^2 M_{ss} + K_{ss})$ and $B = (-\omega^2 M_{sm} - K_{sm})$, and Eq. (22) can be used to replace slave degree of freedom by master degree of freedom. Master and slave degree of freedom can be represented with the help of master degree of freedom as

$$\begin{Bmatrix} x_m \\ x_s \end{Bmatrix} = Tx_m \quad (21)$$

where $T = \begin{Bmatrix} I \\ A^{-1}B \end{Bmatrix}$. Using Eq. (23) and pre-multiplying with T in Eq. (17), we get

$$\begin{Bmatrix} I \\ A^{-1}B \end{Bmatrix}^T \begin{bmatrix} M_{mm} & M_{ms} \\ M_{sm} & M_{ss} \end{bmatrix} \begin{Bmatrix} I \\ A^{-1}B \end{Bmatrix} \ddot{x}_m + \begin{Bmatrix} I \\ A^{-1}B \end{Bmatrix}^T \begin{bmatrix} C_{mm} & C_{ms} \\ C_{sm} & C_{ss} \end{bmatrix} \begin{Bmatrix} I \\ A^{-1}B \end{Bmatrix} \dot{x}_m$$

$$+ \begin{Bmatrix} I \\ A^{-1}B \end{Bmatrix}^T \begin{bmatrix} K_{mm} & K_{ms} \\ K_{sm} & K_{ss} \end{bmatrix} \begin{Bmatrix} I \\ A^{-1}B \end{Bmatrix} x_m = \begin{Bmatrix} I \\ A^{-1}B \end{Bmatrix}^T \begin{Bmatrix} f_m \\ 0 \end{Bmatrix} \quad (22)$$

Equation (24) can be represented in short form as

$$[M_{red}]\{\ddot{x}_m\} + [C_{red}]\{\dot{x}_m\} + [K_{red}]\{x_m\} = \{f_m\} \quad (23)$$

where

$$\begin{aligned} M_{red} &= M_{mm} + M_{ms}A^{-1}B + (A^{-1}B)^T M_{sm} + (A^{-1}B)^T M_{ss}A^{-1}B, \\ C_{red} &= C_{mm} + C_{ms}A^{-1}B + (A^{-1}B)^T C_{sm} + (A^{-1}B)^T C_{ss}A^{-1}B \\ K_{red} &= K_{mm} + K_{ms}A^{-1}B + (A^{-1}B)^T K_{sm} + (A^{-1}B)^T K_{ss}A^{-1}B \end{aligned}$$

Equation (25) can be represented in state-space form as

$$\begin{Bmatrix} \dot{x}_m \\ \ddot{x}_m \end{Bmatrix} = \begin{bmatrix} \mathbf{0} & I \\ -\frac{K_{red}}{M_{red}} & -\frac{C_{red}}{M_{red}} \end{bmatrix} \begin{Bmatrix} x_m \\ \dot{x}_m \end{Bmatrix} + \begin{Bmatrix} \mathbf{0} \\ M_{red}^{-1} \end{Bmatrix} f_m \quad (24)$$

which can be represented as

$$\dot{X} = \hat{A}X + \hat{B}u \text{ and } Y = \hat{C}X + \hat{D}u \quad (25)$$

where \hat{A} is the state matrix, \hat{B} is the input matrix, \hat{C} is the output matrix and \hat{D} is the state transition matrix. The output matrix has been chosen in such a way that vibration along x -axis and y -axis at node 4 (as shown in Fig. 4) can be separated to provide the feedback in the control loop.

4 Control Algorithm

In any bearingless machine, generally, two types of forces are required to be generated and controlled, viz. (i) a constant vertical force—for the levitation effect and (ii) revolving forces—to control revolving unbalanced and magnetic forces. In order to generate and control these two kinds of forces, two different control algorithms have been used, viz. (i) PID control—for the control of constant upward force and (ii) convergent control—for the compensation of harmonic forces.

4.1 Levitation Control—Approximation as AMB

The eccentric motion of the rotor generates two types of forces, a constant force which acts along the shortest air gap (Eq. 1) and a pulsating force (Eq. 2) which revolves at the double the supply frequency. Whereas with the help of bridge supply of the BCW induction machine, a constant as well as a revolving force can be generated, keeping the bridge supply frequency opposite or same to that of the main supply frequency, respectively.

For the development of levitation controller, the phenomena of DC component of force generation in an electrical machine is mimicked as an AMB. The force generation by an active bearing magnet (AMB) is represented as

$$f_{\text{AMB}} = -K_x X + K_i I \quad (26)$$

where K_x is the force–displacement factor, X is the displacement, K_i is the force–current factor and I is the supply current. In a similar way, the actuator force for DC component of force generation, the force-displacement factor can be represented as Eq. (4) and the force–current factor can be represented by using Eqs. 14 and 15.

4.2 Convergent Control

If the disturbance force acting on the system is of only one particular frequency, it can be controlled easily by generating the force of that particular frequency at the correct phase. However, if the phase and amplitude of the disturbance forces are not predictable, it becomes quite challenging to control it. The convergent control technique can deal with such disturbance forces which have more than one frequency components. The convergent control technique is a very effective feedforward control method to deal with such kind of problems. For multiple sinusoidal signals, the convergent control law can be written as [7]

$$U_{n+1} = \gamma U_n - \alpha g^{-1}(z_k e^{-j\omega k T}) \quad (27)$$

where T is the length of the time step, ω is the frequency of the known disturbance, γ and α are two constants and z_k is the vector of the measured signal. In case, if there is more than one frequency components of disturbance, then the control law has to be applied in parallel.

The complex multiplier g is a matrix which gives the phase and amplitude of the output as a function of the change in amplitude and phase of the control signal. For a particular frequency component ω , it can be obtained from the system's transfer function G as

$$g = G(j\omega) = C(j\omega I - A)^{-1} B \quad (28)$$

where A, B and C are the matrices of the LTI (linear time invariant) state-space model.

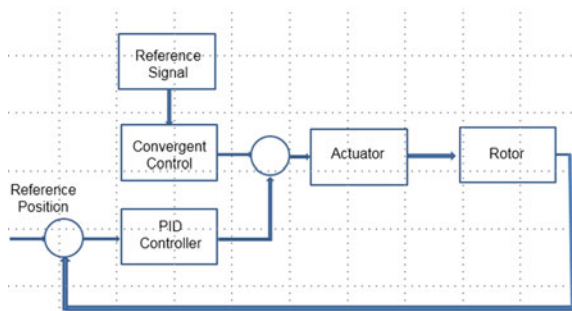
5 Simulation Results

The whole control process has been modeled using Simulink/MATLAB. The simulation parameters have been given in Table 1. Figure 3 represents the control block of the simulation model. Here, the convergent control technique is used for the compensation of discrete harmonic components of the rotor vibration. Whereas, PID controller is used as a levitation controller and works on broadband from zero up to the bandwidth of the actuator [7]. The reference signal block generates the signal of particular harmonics which is required to be compensated. Based on the reference signal harmonics, the convergent control algorithm generates a required current which is passed to the actuator. The reference position gives the command to the PID controller which in turn based on error signal passes the required current to the actuator to levitate the rotor.

Table 1 Simulation parameters

Parameters	Value	Parameters	Value
Main supply	4 Pole	Proportional gain	14.6
Bridge supply	2 Pole	Derivative gain	0.6
Rotor diameter	0.103 m	Integral gain	0
No. of slots	36	Alpha	0.01
No. of turns	50	Gamma	0.01
Air gap	1 mm	Bearing stiffness	<10 N/m
Main supply current	10 A	Main supply frequency	50 Hz
Bridge supply current	0.15 A	Bridge supply frequency	50 Hz
		Rotor weight	10 kg

Fig. 3 Control block of the simulation model



Three conditions have been simulated,

- (i) When an unbalanced force of 0.1 kg is acting on the rotor along with a double-supply frequency component of UMP. Both ends of the rotor are supported by mechanical bearings. Node 3 and node 9 are the two bearing locations as shown in Fig. 2. The unbalance has been introduced at a radius of $1e-4$ m from the rotor center along the x -axis.
- (ii) When the bearing is removed from one end of the rotor and no other disturbance forces are acting on the rotor. The mechanical bearing at node 3 is removed for the purpose of demonstration of levitation control of the rotor. The assumed air gap length of the motor is $1e-3$ m; hence, the rotor is assumed to be eccentric along the y -axis by a distance of $1e-3$ m.
- (iii) When the bearing is removed from one end of the rotor and disturbing forces (unbalanced force and double-supply frequency component UMP) are acting on the rotor. The mechanical bearing at node 3 is removed, and the simulation has been carried out considering the initial position of the rotor eccentric along the y -axis by a distance of $1e-3$ m whereas rotor is assumed to be concentric along the x -axis. The UMP control due to the eccentric rotor position for levitation and disturbance force compensation due to mass unbalance and double-supply frequency component force has been demonstrated. The mass unbalance of 0.1 kg is assumed at a radius of $1e-4$ m along the x -axis.

Figure 4a shows the rotor vibration with respect to time in x - and y -directions when only convergent control is applied. In this case, two types of forces are acting on the rotor, unbalance force which acts at the rotor spin speed, i.e., 50 Hz and unbalanced magnetic pull which acts at twice the supply frequency, i.e., 100 Hz.

Figure 4b shows the rotor vibration with respect to time when only levitation controller is applied. Considering the air gap of the machine as 0.001 m, an initial condition of 0.001 m has been applied to rotor the nodes (nodes 5, 6 and 7 as shown in Fig. 2) DOF which falls inside the motor in y -direction. It can be observed from Fig. 4b that the PID controller is able to generate the required levitation force to the rotor and rotor oscillates about the rotor center. Figure 4c shows the rotor vibration with respect to time when both levitation and convergent controllers are applied. An initial condition of 0.001 m has been given to the rotor nodes (5, 6 and 7 as shown in Fig. 2) DOF which falls inside the motor in the y -direction. Also, an unbalance force along with double-supply frequency component of UMP is acting on the rotor. It can be observed from Fig. 4c that both of the controllers combined together is able to levitate as well as able to compensate the harmonics disturbances acting on the rotor.

6 Conclusions

The present work proposes an approximate mathematical model for the analysis of bearingless bridge configured electrical machine. A simulation model has been

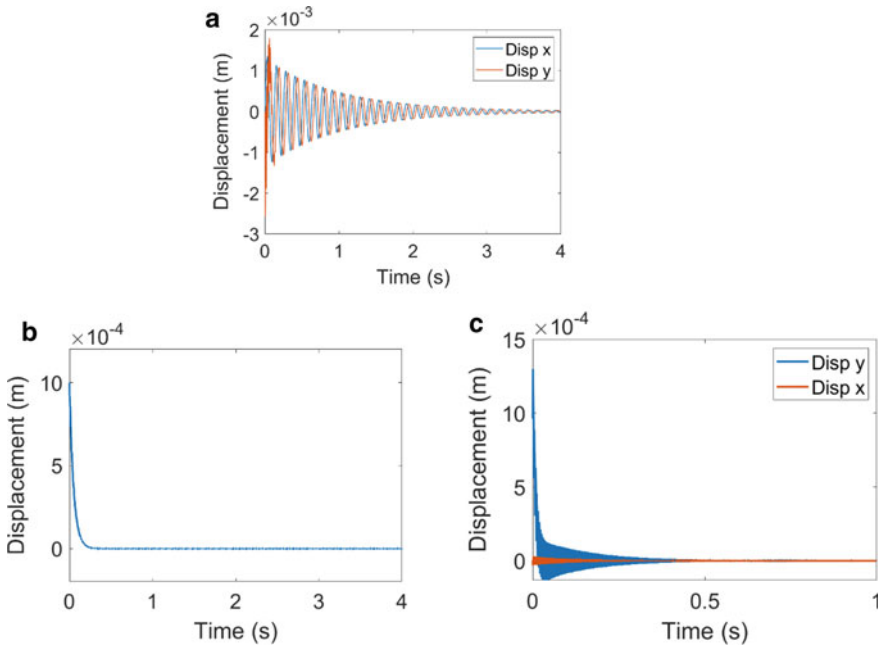


Fig. 4 **a** Rotor response with convergent control, **b** rotor response with levitation control, **c** rotor response with combined levitation and convergent control

developed in MATLAB/Simulink to demonstrate levitation and vibration control using bridge supply through the bridge terminals of the winding. The developed Simulink model can be used further for the study of the effect of rotordynamic interaction such as asymmetry in bearing stiffness in a bearingless machine or any other normal machine.


References

1. Chiba A, Rahman MA, Fukao T (1991) Radial force in a bearingless reluctance motor. *IEEE Trans Magn* 27:786790
2. Khoo W (2005) Bridge configured winding for poly-phase self-bearing machines. *IEEE Trans Magn* 41:1289–1295
3. Khoo W, Kalita K, Garvey SD (2011) Practical implementation of the bridge configured winding for production of controllable transverse forces in electrical machines. *IEEE Trans Magn* 47:1712–1718
4. Kumar G, Kalita K, Tammi K (2018) Analysis of bridge currents and UMP of an induction machine with bridge configured winding using coupled field and circuit modeling 54:1–16
5. Fruchtenicht J, Jordan H, Seinsch HO (1982) Exzentritätsfelder als Ursache Von Laufinstabilitäten bei Asynchronmaschinen. Teil 2 *Arch. Elektrotech* 65:283–292

6. Belmans R, Heylen W, Vandepuut A, Geysen W (1984) Influence of rotor-bar stiffness on the critical speed of an induction motor with an aluminium squirrel cage. *IEE Proc B Electr Power Appl* 131:203–208
7. Tammi K (2009) Active control of rotor vibrations by two feedforward control algorithms. *J Dyn Syst Measur Control* 131(5)

Stability Analysis of Partial Slip Texture Journal Bearing



T. V. V. L. N. Rao , Ahmad Majdi Abdul Rani, Norani Muti Mohamed, Hamdan Haji Ya, Mokhtar Awang, and Fakhruldin Mohd Hashim

Abstract Stability analysis of one-dimensional (long) partial slip texture journal bearing is presented. A journal bearing (one-dimensional) is analyzed considering slip on land, recess depth and extent of partial slip texture region. A modified dynamic Reynolds equation is based on theory of narrow groove approximation considering infinite cells (land with slip and recess configuration) in partial slip texture region. Pressure under static state and pressure gradients dynamic state due to journal center perturbation are derived considering Lund's method (infinitesimally small perturbation of displacements and velocities). Load capacity and linearized dynamic coefficients are derived from integration of pressure (under static state) and pressure gradients (under dynamic state), respectively. The performance characteristics (stiffness (nondimensional) and damping (nondimensional) coefficients, threshold (critical) speed and critical ratio of whirl frequency) are presented based on partial slip texture configuration parameters. Stability threshold increases for both configurations of slip and texture at higher partial slip texture extent (angular) for low-to-medium eccentricity ratio bearing operating conditions.

Keywords Partial slip texture · Coefficients under dynamic state · Threshold (critical) speed · Critical ratio of whirl frequency

T. V. V. L. N. Rao (✉)

Department of Mechanical Engineering, SRM Institute of Science and Technology,
Kattankulathur 603203, India
e-mail: tvvlnrao@gmail.com

A. M. A. Rani · H. H. Ya · M. Awang · F. M. Hashim

Department of Mechanical Engineering, Universiti Teknologi PETRONAS, 32610 Bandar Seri Iskandar, Perak Darul Ridzuan, Malaysia

N. M. Mohamed

Department of Fundamental and Applied Sciences, Universiti Teknologi PETRONAS, 32610 Bandar Seri Iskandar, Perak Darul Ridzuan, Malaysia

© Springer Nature Singapore Pte Ltd. 2021

J. S. Rao et al. (eds.), *Proceedings of the 6th National Symposium*

on *Rotor Dynamics*, Lecture Notes in Mechanical Engineering,

https://doi.org/10.1007/978-981-15-5701-9_18

Nomenclature

b	Length of slip, m
b_{ij}, \bar{B}_{ij}	Coefficients (damping) calculated under equilibrium conditions, Ns/m; $\bar{B}_{ij} = b_{ij}C^3/\mu R^3L$; $B_{ij} = \bar{B}_{ij}/W$ for $i = x, y$
C	Bearing radial clearance, m
h	Thickness of film, m; $H = h/C$
h_t	Depth of recess, m
k_{ij}, \bar{K}_{ij}	Coefficients (stiffness) calculated under equilibrium conditions, N/m; $\bar{K}_{ij} = k_{ij}C^3/\mu\omega R^3L$; $K_{ij} = \bar{K}_{ij}/W$ for $i = x, y$
M	Parameter of mass; $M = \omega_s^2 = C\omega^2/g$
p	Distribution of pressure, N/m ² ; $P = pC^2/\mu U R$
p_s, p_t	Distribution of pressure over land on bearing and recess regions, N/m ²
P_o	Distribution of pressure (nondimensional) under static state
P_j	Distribution of pressure gradients (nondimensional); $j = x, y, \dot{x}, \dot{y}$
q, Q	Flow (rate of volume per unit length) along circumferential direction, m ² /s; $Q = q/u_j C$
R	Radius of journal, m
t, T	Parameter of time, sec; $T = t\omega_p$
u_j	Velocity of journal along θ direction, m/s
w	Load (bearing) capacity, N; $W = wC^2/\mu\omega R^3L$
x, y, X, Y	Coordinates (vertical and horizontal) with reference to bearing center, m; $X = x/C, Y = y/C$
\dot{X}, \dot{Y}	Journal center nondimensional velocity direction (along x and y)
ε	Bearing eccentricity ratio
γ	Land to recess region ratio; $\gamma = \theta_s/(\theta_s + \theta_t)$
ζ	Nondimensional depth of recess; $\zeta = h_t/h$
θ	Coordinate (angular) from journal bearing maximum film thickness
θ_s, θ_t	Extents (angular) of land with slip followed by recess
θ_{st}	Extents (angular) of slip texture (partial)
θ_r	Extents (angular) of rupture film region
Θ	Coordinate (angular) considered from load line direction
ϕ	Angle of attitude
λ	Slip (nondimensional) coefficient; $\lambda = b/h$
μ	Viscosity, Ns/m ²
ω	Journal angular velocity, rad/s
ω_s	Critical (threshold) speed; $\omega_s = \sqrt{M} = \omega/\sqrt{g/C}$
ω_p	Angular velocity of whirl
Ω	Whirl ratio; $\Omega = \omega_p/\omega$

1 Introduction

Partial slip texture configuration in journal bearings is used to enhance bearing performance under lightly loaded conditions. Fortier and Salant [1] presented finite length journal bearing steady-state performance with slip/no-slip configuration considering a slip length (modified) model. Load capacity and friction are investigated with extents of slip/no-slip region on finite bearing (journal). Aurelian et al. [2] investigated the slip effects on bearings (journal) under static and dynamically loaded conditions. Lin et al. [3] investigated the effect of location of slip/texture at the region of pressure rise on improvement of journal bearing performance.

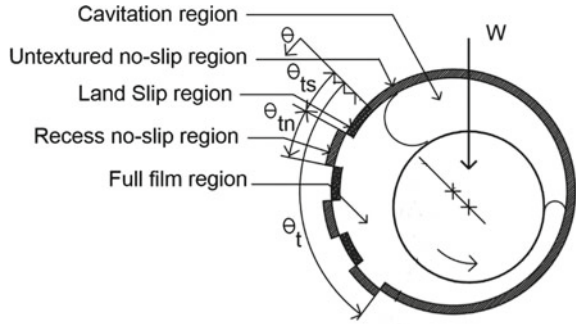
Derivation of dynamic (stiffness and damping) bearing (journal) coefficients is important to predict dynamic characteristics and stability of rotating machinery. Lund and Thomsen [4] presented dynamic coefficients data of multi-lobe journal bearing configurations based on infinitesimal perturbation of dynamic Reynolds equation. Elrod and Vijayaraghavan [5] presented stability characteristics of infinitely long journal bearing considering fluid flow in the region of cavitation. Ma et al. [6] investigated slip effects on the stability characteristics of length (finite) bearing (journal). Full slip on bearing surface reduces the load capacity as well as the rotor bearing system stability while an optimized bearing surface slip enhances load capacity and rotor bearing stability. Rao [7] derived perturbed dynamic Reynolds equation and presented stability features of bearing (journal) considering bearing surface slip extent. Bhattacharya et al. [8] investigated influence of bearing surface slip-no-slip zones on stability of short and long rotors. Matele and Pandey [9] analyzed the effect of location and geometry of the dimple on stability features of bearing (journal). Yamada et al. [10] also presented theoretical and experimental studies of texture parameters on dynamic features of bearing (journal). The impact of surface texturing on dynamic coefficients and linear stability threshold speed was investigated. Journal bearing stability improvement is investigated by varying slip extent on surface of bearing. Rao et al. [11] studied impact of slip extent on surface of bearing with three layer for stability enhancement. Rao et al. [12] investigated multi-lobe journal bearing load capacity, dynamic characteristics and stability using partial slip texture.

The dynamic Reynolds (modified) equation is derived [12] based on theory of narrow grooves [13] with large number (infinite) of slip/recess areas (regions). This paper presents stability analysis of slip texture (partial) bearing (journal) using the modified dynamic Reynolds equation [12] using narrow groove theory [13]. The coefficients under dynamic state, threshold (critical) speed and ratio of whirl frequency (critical) are presented for bearing (journal) with partial slip texture configuration.

2 Analysis

An analysis of stability of bearing (journal) under the effect of partial slip with texture configuration is presented. The diagram of a partial slip with texture bearing (journal)

Fig. 1 Schematic of partial slip texture bearing (journal)



with repeated cells of land with slip and recess with no-slip regions is depicted in Fig. 1.

The nondimensional pressure and pressure gradients of partial slip texture journal bearing are derived identical to partial slip bearing (journal) [11] and partial slip texture multi-lobe bearing (journal) [12]. The dynamic Reynolds (modified) equation (nondimensional) for partial slip texture configuration is

$$\Omega \frac{dH}{dT} + \frac{d}{d\theta} \left(\frac{\Delta_s H}{2} - \frac{\Delta_p H^3}{12} \frac{dP}{d\theta} \right) = 0 \tag{1}$$

where the coefficients are

$$\begin{aligned} \Delta_s &= \frac{(\gamma(\Delta_{1d}/\Delta_{2d}) + (1 - \gamma)(\Delta_{1t}/\Delta_{2t}))}{(\gamma(1/\Delta_{2d}) + (1 - \gamma)(1/\Delta_{2t}))}, \\ \Delta_p &= \frac{1}{(\gamma(1/\Delta_{2d}) + (1 - \gamma)(1/\Delta_{2t}))}, \Delta_{1d} = \frac{(1 + 2\lambda)}{(1 + \lambda)}, \\ \Delta_{2d} &= \frac{(1 + 4\lambda)}{(1 + \lambda)}, \Delta_{1t} = 1 + \zeta, \Delta_{2t} = (1 + \zeta)^3. \end{aligned} \tag{2}$$

The coefficients for land with slip in a cell region ($\gamma = 1$) are derived from Eq. (2) as

$$\Delta_s = \frac{(1 + 2\lambda)}{(1 + \lambda)}, \Delta_p = \frac{(1 + 4\lambda)}{(1 + \lambda)} \tag{3}$$

The coefficients for texture (recess) in a cell region ($\gamma = 0$) are derived from Eq. (2) as

$$\Delta_s = 1 + \zeta, \Delta_p = (1 + \zeta)^3 \tag{4}$$

The nondimensional pressure distribution (P_o) under steady state and the nondimensional pressure gradients (P_j for $j = x, y, \dot{x}, \dot{y}$) under dynamic conditions,

respectively, are evaluated numerically [11] using the coefficients in Eq. 2 for partial slip texture bearing (journal).

The load (nondimensional) (W) and coefficients under dynamic state for partial slip texture bearing (journal) ($\bar{K}_{xx}, \bar{K}_{yx}, \bar{K}_{xy}, \bar{K}_{yy}, \bar{B}_{xx}, \bar{B}_{yx}, \bar{B}_{xy}, \bar{B}_{yy}$) are obtained from nondimensional pressure (P_o) and nondimensional pressure gradients (P_j for $j = x, y, \dot{x}, \dot{y}$), respectively.

The ratio of whirl frequency (critical) and threshold (critical) nondimensional speed are computed [11, 12] based on Lund's methodology [14] as

$$\Omega_s = \sqrt{\frac{(K_{xx} - \kappa_o)(K_{yy} - \kappa_o) - K_{xy}K_{yx}}{B_{xx}B_{yy} - B_{xy}B_{yx}}} \quad (5)$$

$$\omega_s = \sqrt{M} = \sqrt{\frac{\kappa_o}{\Omega_s}} \quad (6)$$

where $K_{ij} = \bar{K}_{ij}/W$ and $B_{ij} = \bar{B}_{ij}/W$ for $i = x, y$, $\kappa_o = \frac{B_{xx}K_{yy} + B_{yy}K_{xx} - B_{xy}K_{yx} - B_{yx}K_{xy}}{B_{xx} + B_{yy}}$.

3 Results and Discussion

The partial slip texture configuration effect on the coefficients under dynamic state and bearing (journal) stability is studied. The significance of slip texture (partial) on the bearing (journal) stability is evaluated by considering extents (angular) of slip texture (partial) (θ_{st}) on critical (threshold) speed (ω_s) and ratio of whirl frequency (critical) (Ω_s). Results of nondimensional stiffness and damping coefficients (K_{ij} and B_{ij} for $i = x, y$), critical (threshold) speed (ω_s) and ratio of whirl frequency (critical) (Ω_s) are obtained for partial slip texture parameters: partial slip texture angular extent from line of centers at maximum film thickness ($\theta_{st} = 0^\circ - 120^\circ$); slip coefficient (nondimensional) ($\lambda = 0.1, 1$); nondimensional recess depth ($\zeta = 0, 1$); and land region with slip to cell ratio ($\gamma = 0, 1$).

Figure 2a–d illustrates K_{ij} and B_{ij} for $i = x, y$ with eccentricity ratio (ε) for slip texture (partial) geometry of a bearing (journal). The direct stiffness coefficients (K_{xx}, K_{yy}) increase with increasing eccentricity ratio. The cross-coupled stiffness coefficient (K_{yx}) is negative at low-to-medium eccentricity ratios (Fig. 2a). The nondimensional direct damping coefficient (B_{yy}), nondimensional force along the axis perpendicular to load per unit nondimensional perturbation velocity) decreases with increasing eccentricity ratios (Fig. 2b). The nondimensional damping coefficients show significant variation compared to nondimensional stiffness coefficients (Fig. 2c–d). The nondimensional damping coefficients for texture (recess) in a cell region ($\gamma = 0, \zeta = 1$) are higher than land with slip in a cell region ($\gamma = 1, \zeta = 0$).

Figure 3a–d shows the variation in threshold (critical) speed (ω_s) for extents

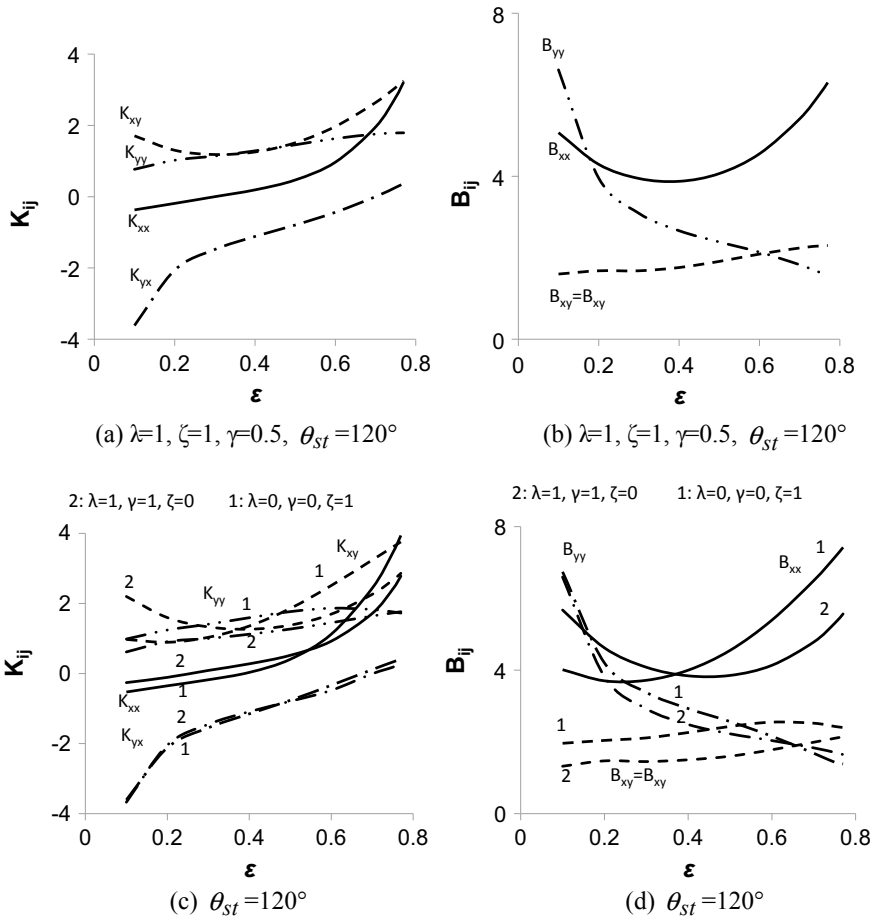


Fig. 2 Stiffness (K_{ij} for $i = x, y$) and damping (B_{ij} for $i = x, y$) coefficients of partial slip texture journal bearing

(angular) of slip texture (partial) ($\theta_{st} = 0^\circ - 120^\circ$) with nondimensional slip coefficient (λ) and nondimensional recess depth (ζ). The nondimensional threshold speed (ω_s) decreases with higher angular extent of partial slip texture ($\theta_{st} = 80^\circ - 120^\circ$) at low eccentricity ratio ($\epsilon = 0.1$) (Fig. 3a). The nondimensional threshold speed increases for both slip ($\lambda = 1$) and texture ($\zeta = 1$) configurations at $\epsilon = 0.3, 0.5$ at higher extents (angular) of slip texture (partial) ($\theta_{st} = 80^\circ - 120^\circ$) (Fig. 3b). ω_s increases with increasing θ_{st} (i) at $\epsilon = 0.1$ and $\lambda = 1, \zeta = 1, \gamma = 0.1$ (Fig. 3c) and (ii) at $\epsilon = 0.3$ and $\lambda = 1, \zeta = 1, \gamma = 0.5$ (Fig. 3d).

Figure 4a–d shows ratio of whirl frequency (critical) (Ω_s) for extents (angular) of slip texture (partial) ($\theta_{st} = 0^\circ - 120^\circ$) with nondimensional slip coefficient (λ) and nondimensional recess depth (ζ). The whirl frequency (critical) (Ω_s) decreases with increasing eccentricity ratios ($\epsilon = 0.1, 0.3, 0.5$). Lower ratio of whirl frequency

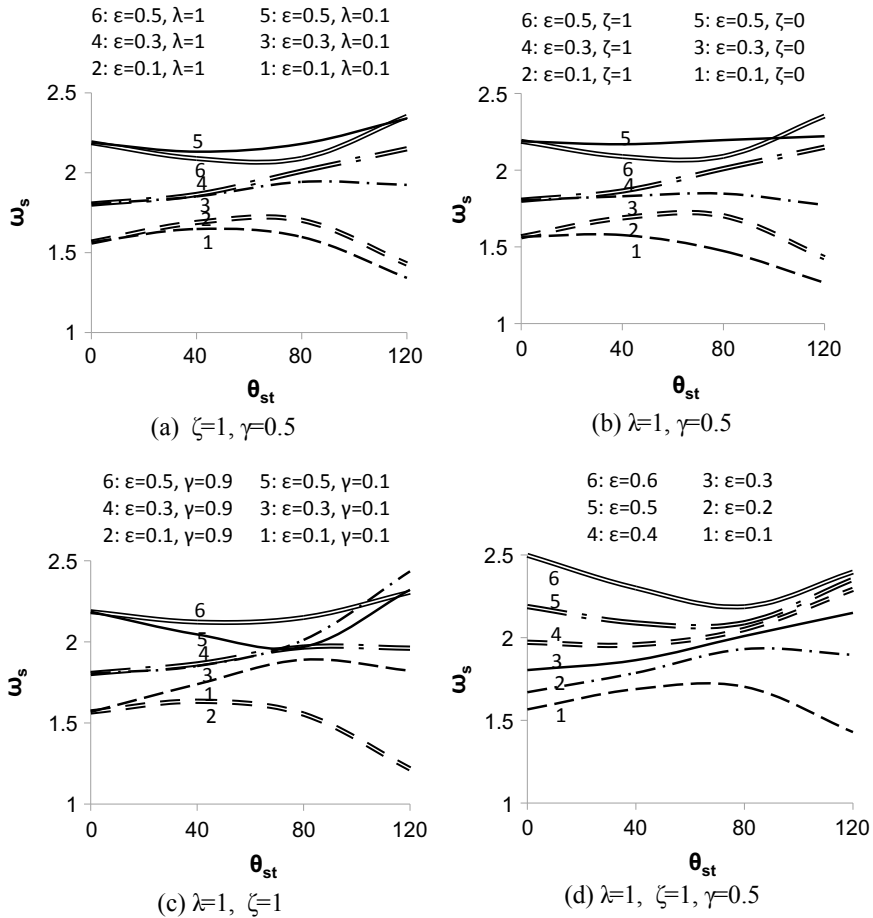


Fig. 3 Threshold speed (ω_s) of partial slip texture journal bearing

(critical) (Ω_s) is attained for both slip ($\lambda = 1$) and texture ($\zeta = 1$) configurations with higher extents (angular) of slip texture (partial) ($\theta_{st} = 80^\circ - 120^\circ$). Ω_s decreases with increasing θ_{st} (i) at $\epsilon = 0.1$ and $\lambda = 1, \zeta = 1, \gamma = 0.1$ (Fig. 4c) and (ii) at $\epsilon = 0.1 - 0.2$ and $\lambda = 1, \zeta = 1, \gamma = 0.5$ (Fig. 4d).

4 Conclusions

The influence of partial slip texture on stability characteristics of journal bearings are examined using Sommerfeld (long) bearing (one-dimensional) analysis. Both slip and texture configurations extending along the bearing surface from inlet (at

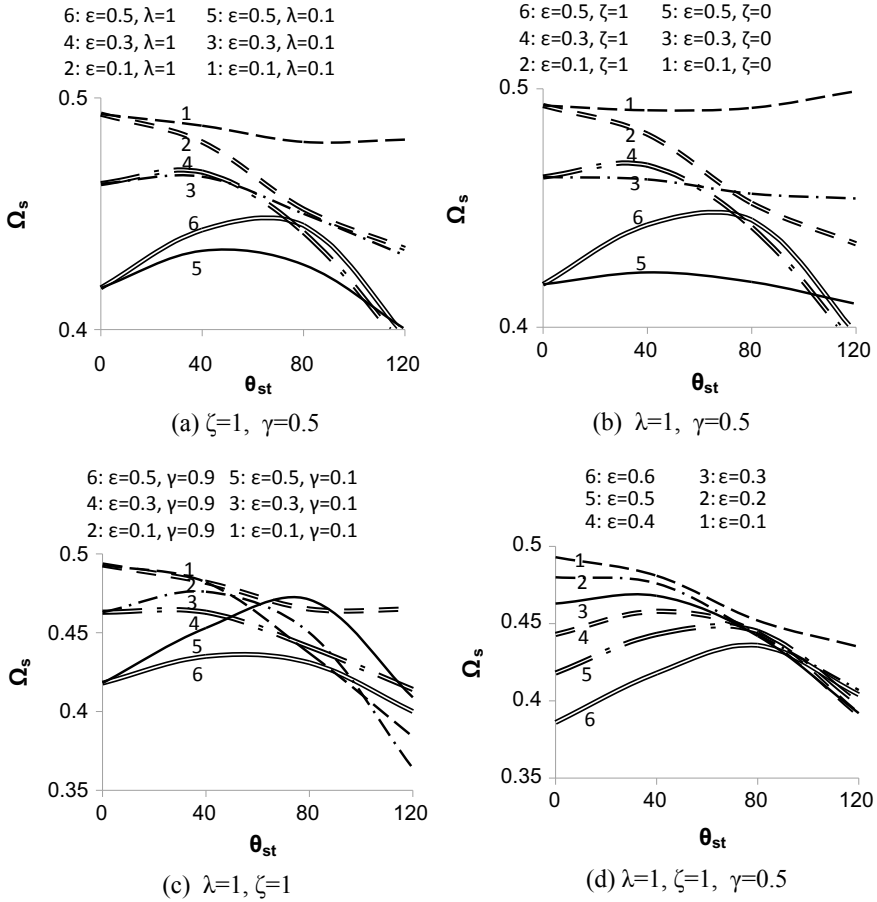


Fig. 4 Critical whirl frequency ratio (Ω_s) of partial slip texture journal bearing

maximum film thickness) has potential to increase stability threshold of bearing (journal). Slip texture (partial) on bearing surface at higher angular extents has beneficial effect for low-to-medium eccentricity ratio conditions. Maximum stability limits are obtained for an optimal extent (angular) configuration of slip texture (partial) at low eccentricity ratio.

Acknowledgements The funding for the research is obtained from Ministry of Education (MOE) Malaysia under FRGS-0153AB-K49 grant. The support of SRM Institute of Science and Technology and Universiti Teknologi PETRONAS is appreciated.

References

1. Fortier AE, Salant RF (2005) Numerical analysis of a journal bearing with a heterogeneous slip/no-slip surface. *J Tribol* 127:820–825
2. Aurelian F, Patrick M, Mohamed H (2011) Wall slip effects in (elasto) hydrodynamic journal bearing. *Tribol Int* 44:868–877
3. Lin Q, Wei Z, Wang N, Chen W (2015) Effect of large-area texture/slip surface on journal bearing considering cavitation. *Ind Lubr Tribol* 67:216–226
4. Lund JW, Thomsen KK (1978) A calculation method and data for the dynamic coefficients of oil lubricated journal bearings. In: *Topics in fluid film bearing and rotor bearing system*. ASME New York, pp 1–28
5. Elrod HG, Vijayaraghavan DJ (1994) A stability analysis for liquid-lubricated bearings incorporating the effects of cavity flow: Part I: classical one-dimensional journal bearing. *J Tribol* 116:330–335
6. Ma GJ, Wu CW, Zhou P (2008) Influence of wall slip on the dynamic properties of a rotor-bearing system. *Tribol Trans* 51:577–582
7. Rao TVVLN (2009) Theoretical prediction of journal bearing stability characteristics based on the extent of slip region on bearing surface. *Tribol Trans* 52:750–758
8. Bhattacharya A, Dutt JK, Pandey RK (2017) Influence of hydrodynamic journal bearings with multiple slip zones on rotordynamic behavior. *J Tribol* 139:061701-1-11
9. Matele S, Pandey KN (2018) Effect of surface texturing on the dynamic characteristics of hydrodynamic journal bearing comprising concepts of green tribology. *Proc iMechE Part J J Eng Tribol*. <https://doi.org/10.1177/1350650117752611>
10. Yamada H, Taura H, Kaneko S (2018) Numerical and experimental analyses of the dynamic characteristics of journal bearings with square dimples. *J Tribol* 140:011703-1-13
11. Rao TVVLN, Rani AMA, Awang M, Hashim FM (2017) Stability evaluation of three-layered journal bearing with slip/partial slip. *Ind Lubr Tribol* 69:334–341
12. Rao TVVLN, Rani AMA, Mohamed NM, Ya HH, Awang M, Hashim FM (2020) Static and stability analysis of partial slip texture multi-lobe journal bearings. *Proc Inst Mech Eng Part J: J Eng Tribol* 234:567–587
13. Vohr JH, Chow CY (1965) Characteristics of herringbone-grooved, gas-lubricated journal bearings. *J Basic Eng* 9:568–578
14. Lund JW (1987) Review of the concept of dynamic coefficients for fluid film journal bearings. *J Tribol* 109:37–41

Experimental Study of Temperature Effect on Labyrinth Seal Leakage and Vibration Characteristics of Rotor



Vivek V. Shet , A. S. Sekhar , and B. V. S. S. Prasad 

Abstract Labyrinth seals are the most widely used non-contact-type turbine seals. The main design concern is to prevent the seal rub with the stator in the range of operating conditions and to control the system rotordynamics. This work aims at experimentally evaluating the effect of thermal growth of labyrinth seal on the leakage flow rates and effect on vibration characteristics of the system. An experimental seal test rig for teeth on rotor (TOR)-type straight labyrinth seal with four flat tip teeth has been developed. Constant clearance between seal and stator is maintained and tested at different speeds and temperatures by varying the inlet air pressure. Leakage results are compared for the seal for the range of operating conditions and for a given seal radial clearance. In addition, vibration data are measured at various locations to understand the influence of seal on the vibration characteristics of the rotor system. It is seen that flow leakage rate and vibration of system are influenced by the pressure difference and the temperature.

Keywords Labyrinth seal · Leakage flow rate · Turbine seal · Turbine seal · Vibration · Thermal growth

1 Introduction

Sealing in turbomachinery is one of the most crucial design parameters. The present operating conditions of turbomachines require it to operate at high temperature of

V. V. Shet (✉) · A. S. Sekhar

Machine Design Section, Department of Mechanical Engineering, IIT-Madras, Chennai 600036, India

e-mail: vivekshet1992@gmail.com

A. S. Sekhar

e-mail: as_sekhar@iitm.ac.in

B. V. S. S. Prasad

Thermal Turbomachines Laboratory, Department of Mechanical Engineering, IIT-Madras, Chennai, India

e-mail: prasad@iitm.ac.in

© Springer Nature Singapore Pte Ltd. 2021

J. S. Rao et al. (eds.), *Proceedings of the 6th National Symposium*

on *Rotor Dynamics*, Lecture Notes in Mechanical Engineering,

https://doi.org/10.1007/978-981-15-5701-9_19

800 °C and high rotation with a shaft speed of 450 m/s [1]. So, it is very important that the sealing methods used are efficient at these conditions. There are two important reasons for turbomachinery sealing playing such an important part. First, in modern gas turbine engines, there are numerous gas-path sealing locations, so this can directly affect the efficiency of engine in terms of specific fuel consumption and engine power output. The second reason is turbomachinery seals can control the systems rotordynamics if they are designed properly [2].

Several experimental studies on labyrinth seal leakage influenced by rotation have been made. Wittig et al. [3] experimentally demonstrated the scaling effect influence on the leakage losses in labyrinth seals. High rotational speed influence on the discharge coefficients in labyrinth seals has been studied experimentally by Waschka et al. [4], and they showed that there is significant effect of rotation when the ratio of Taylor number and Reynolds number is beyond 0.2, after which it reduces the leakage rate. Zhang et al. [5] have made numerical studies on the effect of high rotation on dynamic leakage through a labyrinth seal and predicted that the leakage rate increases with increase in vibration, but the effect is more prominent at lower speed. Subramanian et al. [6] did computational studies about the influence of radial location and combined growth due to rotation and temperature on leakage characteristics of rotating labyrinth seal and showed that the radial growth and leakage rate varies significantly with increasing radius and temperature.

In the present study, effect of input pressure and temperature on labyrinth seal leakage and associated vibration characteristics have been analyzed experimentally.

2 Experimental Details

The experimental setup consists of a seal test rig as shown in Fig. 1a, with provision to run two different seal configurations in tandem. For the present study, straight labyrinth seal configuration has been used. The configuration is tooth on rotor (TOR) type. The material of construction of the seal is mild steel. The dimensional details of seal are given in Fig. 2. The initial radial clearance is 0.1 mm. The seal test rig is driven by an electric motor controlled by variable frequency drive (VFD) to vary the RPM from 0 to 3000. Compressed air from compressor is used as input flow to the seal section. The pressure can be varied from 0 to 600 kPa and temperature from 30 to 250 °C. The input airflow pressure is controlled by a pressure control gauge. Airflow at the outlet is measured using float type flow meter. Pressure transmitter is used to measure the difference in pressure across the seal for each test case.

The schematic of the rotor bearing seal system has been shown in Fig. 1b. Dimensional details are given in Table 1. Ball bearings are used at bearing location. Bearings are assumed to be rigid. First natural frequency of the system was found using impact test. The first natural frequency is around 410 Hz.

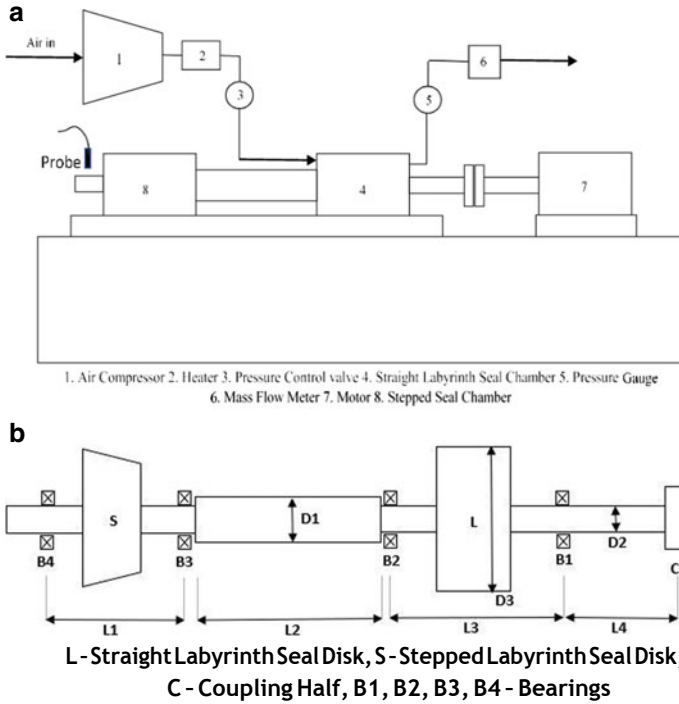


Fig. 1 a Schematic representation of test rig. b Schematic representation of test rig with dimensions

Fig. 2 Dimensional detail of labyrinth seal

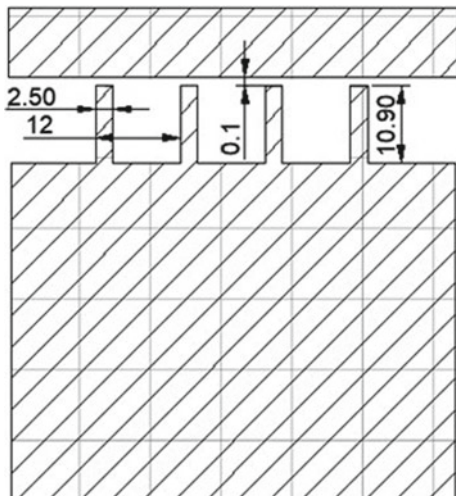


Table 1 Dimensions of the rotor

<i>L</i> 1	106 mm	D1	40 mm
<i>L</i> 2	210 mm	D2	30 mm
<i>L</i> 3	170.50 mm	D3	200 mm
<i>L</i> 4	70 mm	Shaft total length	600 mm

3 Experiments

3.1 Test at Room Temperature (30 °C)

The Initial test for seal with 0.1 mm radial clearance at room temperature of 300 K is conducted with increasing upstream pressure. Initially, test is conducted at static condition. And then, test is repeated for different rotational speed starting from 1200 to 2400 rpm in steps of 300.

In the present setup, inlet pressure is increased from 150 to 600 kPa in steps of 50 kPa. The seal rig setup is such that the upstream pressure is builtup inside the chamber. Therefore, pressure is also measured after the compressed air reaches inside the chamber, both before the seal and after the seal. Leakage flow rate is measured at each test condition. A pressure transmitter is used to measure the pressure difference across the seal. Pressure at outlet after the seal chamber is kept at atmospheric pressure.

3.2 Test at Elevated Temperature (100 °C)

Seal leakage test at elevated temperature of 100 °C (373 K) is performed. Air from the compressor is heated in an air heater before entering the labyrinth seal chamber. Like the earlier test, initially static test is performed and then repeated for different rotor speed from 1200 to 2400 RPM in steps of

300. In this experiment, sufficient time is given so that the seal is heated, and temperature reaches steady state before acquiring the data. Inlet air pressure is varied from 150 to 600 kPa in steps of 50 kPa.

3.3 Data Acquisition for Vibration Measurement

Vibration analysis is done by acquiring an accurate time-varying signal from a standard transducer or sensor on the stator. To record the response obtained from a pair of proximity probe and laser, data acquisition system (Dewe-43 V) is used. Two proximity probes are used to measure the vibration in vertical (V) and horizontal (H) direction and are positioned on the shaft at the non-drive end as shown in Fig. 3. This

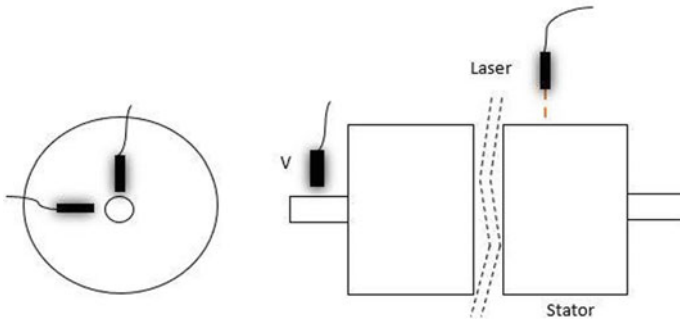


Fig. 3 Proximity probe and laser probe position on test rig (Refer Fig. 1.)

has sensitivity 7.87 V/mm. A laser signal is used to acquire stator vibration response. Acquiring response data are started once the system reached its steady-state operating condition. DEWEsoft X1 software is used to visualize, analyze and store the acquired data signals. The recorded data are then further post processed for results as presented in Sect. 4.

4 Results

4.1 Leakage Flow Results

Leakage flow rate is plotted against pressure difference across the seal at 30 °C and 100 °C for two different rotor speed, 0 and 1500 RPM, in Figs. 4 and 5, respectively. It can be observed from these figures that leakage flow rate got reduced at 100 °C for a given pressure difference across the seal compared to that at 30 °C.

The leakage flow rate reduction can be attributed to the change in the initial radial clearance between the seal and the stator due to thermal growth of the seal. Initial clearance has been kept at 0.10 mm. The seal teeth are the ones which are more subjected to hot air. The thermal growth of the teeth can be calculated using linear thermal expansion formula to calculate the reduction in clearance,

$$C_{TG} = h\alpha dT \tag{1}$$

In the above equation h = tooth height = 10.90 mm, α (mild steel) = 11.7 $\mu\text{m}/\text{m}^\circ\text{C}$ and $dT = 70^\circ\text{C}$. This gives the thermal growth value as 8.9271 μm . So the net radial clearance reduces to

$$C_{\text{net}} = C_i - C_{TG} = 0.091 \text{ mm} \tag{2}$$

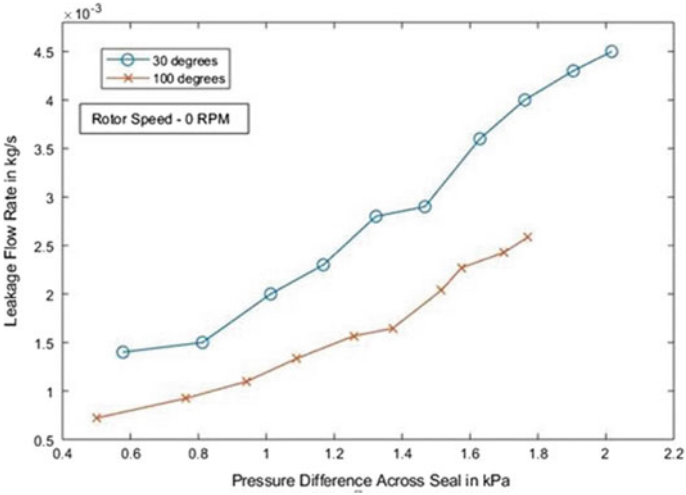


Fig. 4 Leakage flow rate versus pressure difference across seal at 0 RPM

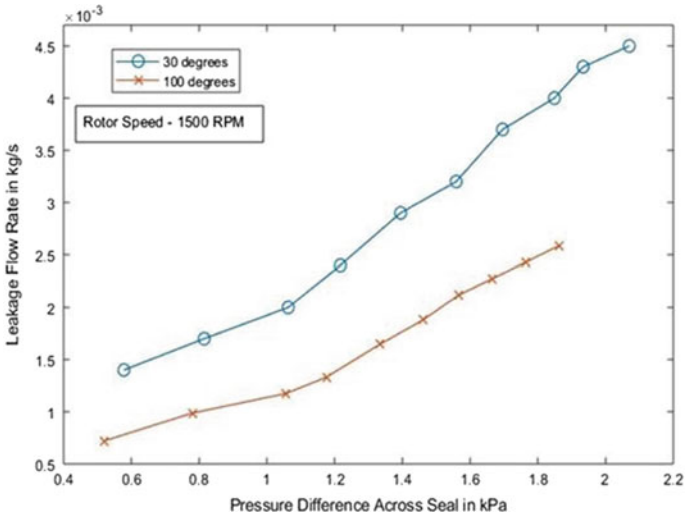


Fig. 5 Leakage flow rate versus pressure difference across seal at 1500 RPM

There is 9% reduction in radial clearance between the seal and the stator. Here, it is assumed that the stator thermal growth is negligible as the thickness of the stator is large. This leakage flow rate reduction can be attributed to this reduction in radial clearance due to growth of seal. However more studies particularly CFD analysis is needed for the estimating leakage flow and seal coefficients with thermal growth.

Figure 6 shows the variation of leakage flow rate with respect to pressure difference across the seal at 30 and 100 °C at three different rotor speed of 0, 1500 and 2400. It is

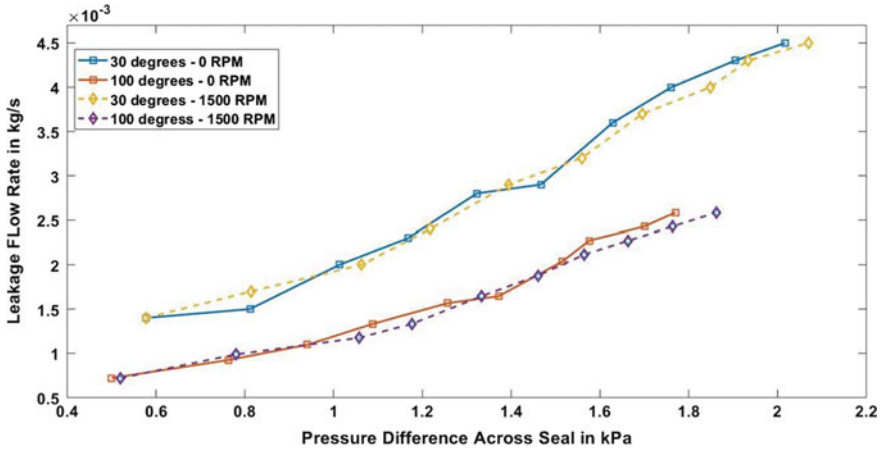


Fig. 6 Variation of leakage flow rate versus pressure difference across seal at three RPM—0 and 1500 at 30 and 100 °C

noticed that the speed variation has negligible effect on leakage flow characteristics as seen from these figures. It can be deduced that the radial growth due to centrifugal force is insignificant for the speed considered. However, there is significant influence of temperature.

4.2 Vibration Results

Vibration reading of the shaft measured by the proximity probes in vertical and horizontal direction and of the stator by the laser sensor are analyzed in MATLAB R2018a and processed to find the root mean square (RMS) value. It was seen that the stator vibration was not affected by the temperature change of the input air. RMS value of vibration for vertical is plotted for different RPM and input pressure at 30 and 100 °C as shown in Figs. 7 and 8, respectively. As seen from the plots, the vibration in vertical directions is increasing with both speed and input pressure. At static condition of rotor, the vibration is increasing with input pressure, this is due to the vibration caused by the increasing leakage flow rate through the seal. Also, as the speed of rotor is increased for a given input pressure, the vibration value has increased.

To understand the effect of temperature on the vibration, the variation of vertical vibration against increasing pressure difference across seal at 1500 RPM for 30 and 100 °C is plotted in Fig. 9. It is seen that the vertical vibration has increased with increase in temperature. As discussed in Sect. 4.1, due to the thermal growth, there is a net reduction in radial clearance. It is been proven [7] that for teeth on rotor configuration as clearances reduces the seal damping decreases. The increase in vertical vibration can be due to this decrease in seal damping. Similar trend at

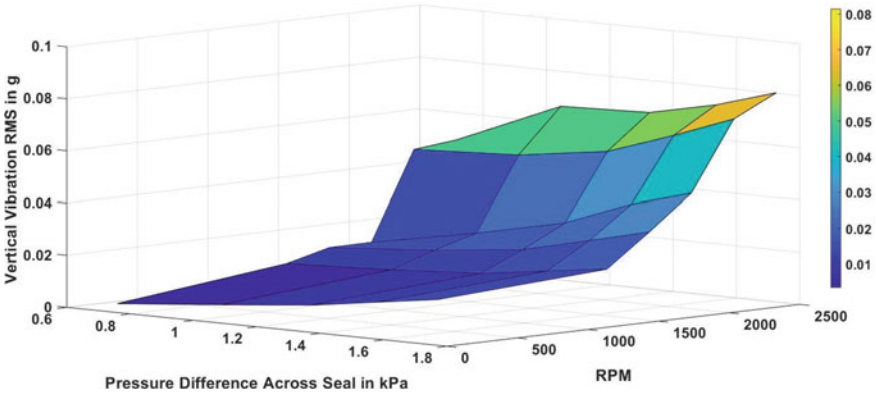


Fig. 7 Variation of vertical vibration RMS versus input pressure and RPM at 30 °C

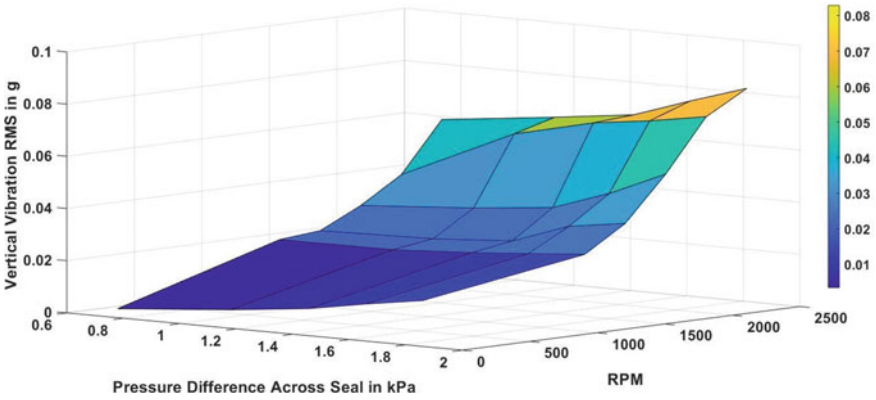


Fig. 8 Variation of vertical vibration RMS versus input pressure and RPM at 100 °C

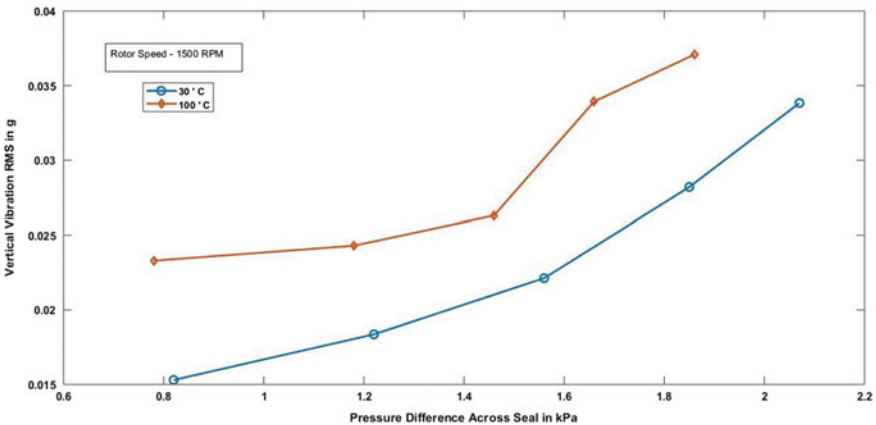


Fig. 9 Vertical vibration versus pressure difference across seal at 1500 RPM for 30 and 100 °C

these two temperatures has been observed in present experiments at different RPM of 1200, 1800, 2100 and 2400 RPM. For brevity only, a single case at 1500 RPM has been shown here.

5 Conclusion

The combined influence of input air temperature, input pressure and rotor speed on leakage rate and vibration in a straight labyrinth-rotor system have been studied experimentally. The key outcomes are:

- (1) The leakage flow rate through the labyrinth seal increases with increase in pressure difference across the seal. The same trend has been followed at elevated temperature of 100 °C.
- (2) At higher temperature, the leakage flow rate has reduced due to the thermal growth of the seal. As the temperature increases, there is net reduction in radial clearance. It is calculated that there is almost 9% reduction in radial clearance in the seal due to which the leakage rate has reduced.
- (3) As the rotor speed is increases, there is no appreciable change in the leakage flow rate. As the rotor running speeds are not high, there is very insignificant radial growth due to centrifugal forces, and hence, the radial clearance is not affected.
- (4) The vertical vibration of the rotor is increasing with rotor speed in the given speed range and pressure difference across the seal.
- (5) The vertical vibration is increasing with input air temperature at all the rotor speed. This phenomenon is due to the reduction in the seal damping which is due to the reduction in seal radial clearance.

Further, experimental studies are being carried out to understand the speed influence at higher speed values. Also, computational study on the leakage flow characteristics are being simultaneously studied to compare with experimental values.

References

1. Margaret PP (2011) Turbine seal research at NASA GRC, NASA seals and secondary flows workshop, November 2011
2. Aslan-zada FE, Mammadov VA, Dohnal F (2012) Brush seals and labyrinth seals in gas turbine applications. *J Power Eng* 227(2):216–230
3. Wittig SLK, Dorr L, Kim S (1983) Scaling effects on leakage losses in labyrinth seals. *J Eng Power* 105:305–309
4. Waschka WW, Wittig SS, Kim SS (1992) Influence of high rotational speeds on the heat transfer and discharge coefficients in labyrinth seals. *ASME, J Turbomachinery* 114(2):462–468
5. Jia X, Zhang H, Zheng Q, Fan S, Tian Z (2016) Investigation on rotor-labyrinth seal system with variable rotating speed. *Int J Turbo Jet-Eng* 36(1):19

6. Subramanian S, Sekhar AS, Prasad B (2015) Influence of combined radial location and growth on the leakage performance of a rotating labyrinth gas turbine seal. *J Mech Sci Tech* 29(6):2535–2545
7. Childs DW, Scharrer JK (1988) Theory versus experiment for the rotodynamic coefficient of labyrinth gas seals: Part II—a comparison to experiment-1. *J Vibr Acoust Stress Reliab Des* 110:281–287

Study of Static Performance Characteristics of Offset-Pressure Dam Bearing Considering Turbulent and Adiabatic Thermal Effects



Sivakumar Dakshinamurthi  and Suresh Nagesh

Abstract As there is an increasing demand for high-performance turbo-machinery, hydrodynamic bearings are expected to run at high surface speed (>100 m/s) and heavy load (>4 MPa) operating conditions. Especially, high-speed and high-power gearboxes operate at such severe operating conditions for gas or steam turbine power generation applications. Conventionally, fixed profile bearings such as pressure dam or offset bearings are used in these gearboxes. However, they have design limitation on maximum surface speed due to stability requirements at no load conditions and maximum oil film temperature at heavy load and high-speed conditions. In this paper, it is attempted to combine the offset design feature “preload” with pressure dam bearings to see that if the operational design limits could be improved. The governing mathematical model includes turbulent and adiabatic thermal effects. The static performance characteristics of combined offset pressure dam bearings are compared with individual bearings. The analytical study found that combined offset pressure dam bearing delivers better performance than the other bearings. Also, the analytical model is validated with published experimental results.

Keyword Fluid film · Hydrodynamic bearings · Stability · Turbulent effects · Thermal effects

Nomenclature

c_p	Specific heat capacity of the lubricant, kJ kg/K
T	Temperature, °C
C_R	Radial clearance at split line, mm

S. Dakshinamurthi (✉)
PES University, Bengaluru 560085, India
e-mail: dsivakumardesign@gmail.com

S. Nagesh
CORI Lab, PES University, Bengaluru 560085, India
e-mail: suresh.nagesh@pes.edu2

\bar{T}	T/T_{in} = Relative temperature
C_p	Crown clearance, mm
u, w	Velocity in circumferential and axial, m/s
D	Journal diameter, mm
\bar{u}, \bar{w}	Dimensionless velocity component in circumferential ($u/\omega R_J$) and axial ($w/\omega R_J$)
G_x, G_z	Turbulent coefficients
\bar{y}	y/h , Dimensionless coordinate across film
H	Dimensionless film thickness (h/C_R)
\bar{z}	z/R_J , Dimensionless coordinate in axial
h	Film thickness, mm
θ	x/R , Circumferential coordinate
L	Bearing length, mm
μ	Dynamic viscosity of the lubricant, Pa s
L_d	Pressure dam width, mm
μ_{in}	Dynamic viscosity of the lubricant at oil supply temperature T_{in}
m	Bearing preload, $(1 - C_R/C_p)$
$\bar{\mu}$	μ/μ_{in} = Relative dynamic viscosity
P	Dimensionless pressure ($p * C_R^2/\mu * \omega * R_J^2$)
λ	Thermal conductivity of the lubricant, W/mK
p	Oil film pressure
ψ	C_R/R_J = Relative radial clearance
R_J	Journal radius, mm
ρ	Density of the lubricant, kg/m ³
Re	Reynolds number

1 Introduction

As there is an increasing demand for high-performance turbo-machinery, hydrodynamic bearings are expected to run at high surface speed (>100 m/s) and specific load (>4 MPa) operating conditions with a lower power loss and oil flow and with excellent stability characteristics [1]. Hydrodynamic bearings that are installed in high-speed (pitch line velocity more than 125 m/s) and high-power (more than 50 MW) gear-boxes experience such operating conditions. Conventional fixed profile bore bearings such as pressure dam and offset bearings could not operate at these severe operating conditions due to operational design limits of specific bearing load, maximum oil film temperature and minimum film thickness criterion. Also, it brings the challenges on mathematical modeling to accurately predict the fluid film behavior when the bearings are operated at turbulent region with severe thermal load conditions. Currently, tilting pad journal bearings are being used for such applications which have excellent static and dynamic properties. However, these bearings are very expensive for the state-of-the-art technology and require more oil flow.

The interest in understanding turbulence and thermal effects on performance of the hydrodynamic bearings started many decades ago. One of the earliest studies was made by Elrod and Ng [2] on turbulent oil film lubrication. McCallion et al. [3] investigated the thermal effects in journal bearing by using isothermal and adiabatic thermal models. Safar and Szeri [4] made a study on thermo-hydrodynamic lubrication on laminar and turbulent regimes. Temperature and local shear-dependant viscosity is calculated through iterations of momentum and energy equations. Frene et al. [5] compared the theoretical and experimental thermo hydrodynamic performance of finite length journal bearings. They had taken into account of heat transfer between the film along with shaft and the bush, cavitation and lubricant recirculation. Mittwollen et al. [6] explained the governing equations elaborately to predict the performance of oil film journal bearings in high-speed and high-load turbomachinery. The lubricant temperature and viscosity were admitted to vary in all three dimensions, and a possible reverse flow was considered for laminar–turbulent flow transition. Khonsari [7] made a comprehensive survey on thermal effects of hydrodynamic bearings. This paper surveyed the theoretical and experimental work done on thermal effects. Zhang et al. [8] studied theoretical and experimental THD analysis of high-speed heavily loaded journal bearings. Yuan et al. [9] studied the suitability of different turbulent models for journal bearings operating at turbulent regime to calculate static and dynamic performances.

Pressure dam bearings had been investigated previously in many studies. Wilcock and Booser [10] explained theoretical background of pressure dam bearings. Allaire et al. [11] found that step inertia effect is negligible, and it becomes significant in the pressure dam pocket. Nicholas et al. [12, 13] made a study to understand the required optimum geometry parameters for stable bearings. They found that dam height ratio and the angular location of the dam play a major role for rotor-bearing stable operation. Nicholas et al. [14] studied about adiabatic thermal effects on pressure dam bearings. It is found that thermal effects have significant influence on estimating static and dynamic bearing performance characteristics. Metha et al. [15, 16] made a study on orthogonally displaced elliptical pressure dam bearings with relief track on the bottom half. The centers of upper and lower half of the bearings are displaced in both directions vertically and horizontally from the theoretical center. They found that such design improves the stability threshold speed by four times the value obtained in simple pressure dam bearings. However, this study did not consider turbulent and thermal effects. Also, the relief track on the bottom half reduces the load carrying capacity of the bearings substantially.

Though there were lots of studies made about thermal and turbulent effects on hydrodynamic bearings, only few studies are available to improve the performance of the fixed profile bearings when they operate at high rotational speed and high-load operating conditions. In this paper, it is attempted to design a fixed profile bearing having design features of both offset and pressure dam bearings. Static performance of offset, pressure dam and offset pressure dam are calculated including adiabatic thermal and turbulent effects and compared the results.

2 Theory

A schematic of offset pressure dam bearing is shown in Figs. 1 and 2. The pressure dam is located at the top half of the bearing and ends at an angle of 135° in the second quadrant as this location is found to be optimum for better stability of the bearing [12, 13]. Center of each bearing halves is offset by a distance “ d_h ” in horizontally opposite direction from the theoretical bearing center. O_L and O_U define the center of lower and upper half bearings, respectively. Two reference bearing clearances C_R at split and C_P at crown are used to define the bearing preload profile parameter “ m ”. Dam and offset features combined to improve the bearing performance characteristics at high-speed and heavy load operating conditions. If pressure dam bearing profile

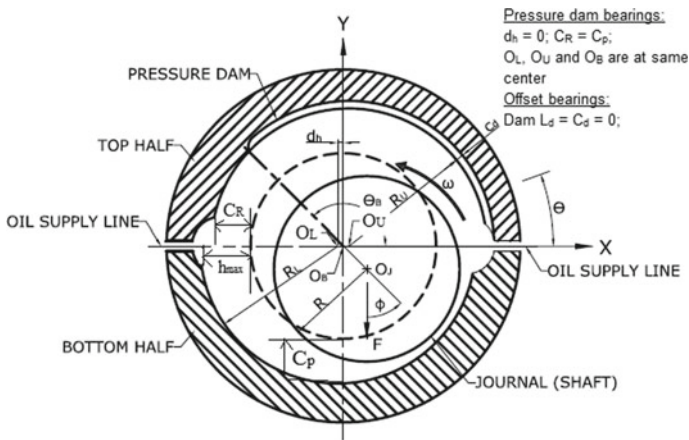
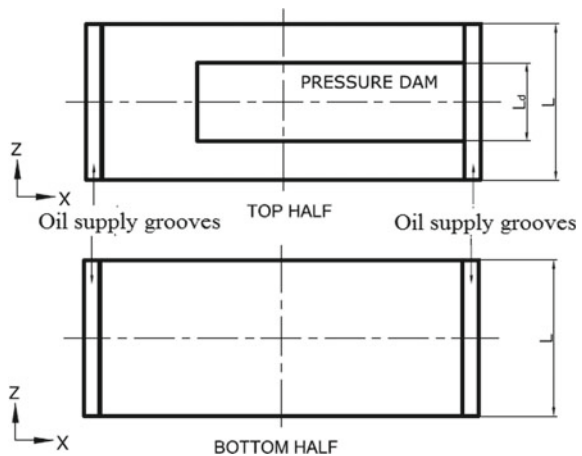


Fig. 1 Offset pressure dam bearing

Fig. 2 Offset pressure dam—mid section view



alone is considered, offset (d_h) becomes zero, and O_L , O_U and O_B are located at same geometry center. Eventually, the bearing clearances C_R and C_P become equal. In offset bearings, pressure dam parameters such dam width (L_d) and dam depth (C_d) are zero.

The eccentricity ratios and attitude angle (ϕ) are defined in Eqs. (1–3) [16].

$$\varepsilon = \frac{e}{C_R}, \quad \varepsilon_1 = \frac{e_1}{C_R}, \quad \varepsilon_2 = \frac{e_2}{C_R} \quad \text{and} \quad \delta_h = \frac{d_h}{C_R} \quad (1)$$

$$\varepsilon_1^2 = \varepsilon^2 + \delta_h^2 + 2\varepsilon\delta_h \sin \phi \quad \text{and} \quad \varepsilon_2^2 = \varepsilon^2 + \delta_h^2 - 2\varepsilon\delta_h \sin \phi \quad (2)$$

$$\phi_1 = \tan^{-1} \left[\frac{\varepsilon \sin \phi + \delta_h}{\varepsilon \cos \phi} \right] \frac{180}{\pi} \quad \text{and} \quad \phi_2 = \tan^{-1} \left[\frac{\varepsilon \sin \phi - \delta_h}{\varepsilon \cos \phi} \right] \frac{180}{\pi} \quad (3)$$

The pressure distribution of the bearing under turbulent condition is calculated with Reynolds's equation. The general non-dimensional form of the equation with turbulent effects is as follows [6]

$$\frac{\partial}{\partial \theta} \left(\frac{H^3}{12\bar{\mu}_p G_x} \frac{\partial P}{\partial \theta} \right) + \frac{\partial}{\partial z} \left(\frac{H^3}{12\bar{\mu}_p G_z} \frac{\partial P}{\partial z} \right) = \frac{1}{2} \frac{\partial}{\partial \theta} (f_c H) \quad (4)$$

$$\bar{\mu}_p = \frac{1}{12\bar{F}_2}, \quad \bar{F}_2 = \int_0^1 \frac{\bar{y}}{\bar{\mu}} \left(\bar{y} - \frac{\bar{F}_1}{\bar{F}_0} \right) d\bar{y},$$

$$f_c = 2 \left(1 - \frac{\bar{F}_1}{\bar{F}_0} \right), \quad \bar{F}_1 = \int_0^1 \frac{\bar{y} d\bar{y}}{\bar{\mu}}, \quad \bar{F}_0 = \int_0^1 \frac{d\bar{y}}{\bar{\mu}} \quad (5)$$

$$G_x = 1 + \frac{0.0136(\text{Re}_{\text{eff}})^{0.90}}{12} \quad \text{and} \quad G_z = 1 + \frac{0.0043(\text{Re}_{\text{eff}})^{0.96}}{12} \quad (6)$$

G_x and G_z are turbulent coefficients which are defined by empirical relationships in Eq. (6). Effective Reynolds number to be considered based on the flow regime defined by critical and mean Reynolds numbers as per Eqs. (1) and (2). Sneek and Vohr [17] made a good discussion on transition of laminar into turbulent region and guides to make the required modification in Reynolds equation. As per the discussion, Taylor vortex flow is developed between a rotating inner cylinder and an outer cylinder when the Taylor number exceeds 41.1. If Taylor vortices develop first, turbulence may begin at a lower value of Reynolds number. Hence, the critical Reynolds number is considered as the minimum of the two critical values calculated for Taylor onset vortices and Couette flow.

$$Re_{eff} = \begin{cases} 0 & \text{for } Re_m < Re_{cr} \\ \left(\frac{Re_m}{Re_{cr}} - 1\right) * Re_l & \text{for } Re_{cr} \leq Re_m \leq 2Re_{cr} \\ Re_l & \text{for } Re_m > 2Re_{cr} \end{cases} \quad (7)$$

Mean, global, local and critical Reynolds numbers are defined as below:

$$Re_m = \frac{2Re_o\bar{q}}{\mu_m}, \quad Re_o = \frac{\rho\omega R_J C_R}{\mu_{in}}, \quad Re_l = \frac{\rho\omega R_J h}{\mu_m}$$

and $Re_{cr} = \text{Min}\left(41.2\sqrt{(R_J/h)}, 2000\right)$ (8)

Volumetric flows in the film are defined in [6] based on the pressure gradient with turbulent coefficients in Eq. (3).

$$\bar{q} = \sqrt{\bar{q}_x^2 + \bar{q}_z^2}, \quad \bar{q}_x = -\frac{H^3}{\bar{\mu}G_x} \frac{\partial P}{\partial \theta} + \frac{f_c H}{2}$$

and $\bar{q}_z = \frac{H^3}{\bar{\mu}G_z} \frac{\partial P}{\partial \bar{z}}$ (9)

The boundary conditions that have been considered to solve the Reynolds equation are $P(\theta, \bar{z} = \pm L/D_J) = 0$ at bearing axial ends, $P = 0$ throughout cavitation region, $P = P_{in}$, oil supply pressure at grooves and $P_{rupt} = 0, \frac{\partial P}{\partial \theta}_{rupt} = \frac{\partial P}{\partial \bar{z}}_{rupt} = 0$ at film rupture. Temperature distribution is calculated by governing energy equation (4). Since the current study is mainly focused on high-speed and heavy load conditions, most of the heat generated in the oil is taken by the hot oil flows. The temperature across the film is assumed with constant temperature profile, and no heat is transferred to the adjacent solid surfaces. All the parameters in the radial direction are averaged. Neglecting conduction terms in circumferential and axial directions, the general form of the adiabatic energy equation as follows [6]:

$$\frac{\partial}{\partial \theta}(H\bar{u}\bar{T}) + \frac{\partial}{\partial \bar{z}}(H\bar{w}\bar{T}) = \frac{1}{Pr Re_o \psi} \left[\lambda \frac{\partial}{\partial \bar{y}} \left(\frac{1}{H} \frac{\partial \bar{T}}{\partial \bar{y}} \right) \right] + K_t \Phi \quad (10)$$

where

$$\text{Prandtl number} = Pr = \frac{\mu_{in} c_p}{\lambda}, \text{ heat dissipation number} = K_t = \mu_{in} \omega / \rho c_p T_{in} \psi^2 \quad (11)$$

$$\bar{u} = \frac{H^2}{G_x} \frac{\partial P}{\partial \theta} \left[\int_0^1 \frac{\bar{y} d\bar{y}}{\bar{\mu}} - \frac{\bar{F}_1}{\bar{F}_0} \int_0^1 \frac{d\bar{y}}{\bar{\mu}} \right] + \frac{1}{\bar{F}_0} \int_0^1 \frac{d\bar{y}}{\bar{\mu}} \quad (12)$$

$$\bar{w} = \frac{H^2}{G_z} \frac{\partial P}{\partial \bar{z}} \left[\int_0^1 \frac{\bar{y} d\bar{y}}{\bar{\mu}} - \frac{\bar{F}_1}{\bar{F}_0} \int_0^1 \frac{d\bar{y}}{\bar{\mu}} \right] \quad (13)$$

$$\begin{aligned} \Phi = & \left(\frac{\partial P}{\partial \theta} \right)^2 \frac{H^3}{\bar{\mu} G_x} \left(\bar{y} - \frac{\bar{F}_1}{\bar{F}_0} \right)^2 + \left(\bar{y} - \frac{\bar{F}_1}{\bar{F}_0} \right) H \left(\frac{\partial P}{\partial \theta} \right) \left(\frac{1}{\bar{\mu} \bar{F}_0} + \frac{\tau_c}{G_x \bar{\mu} \bar{F}_0} \right) \\ & + \frac{\tau_c}{\bar{\mu} H \bar{F}_0^2} + \left(\frac{\partial P}{\partial \theta} \right)^2 \frac{H^3}{\bar{\mu} G_x} \left(\bar{y} - \frac{\bar{F}_1}{\bar{F}_0} \right)^2 \end{aligned} \quad (14)$$

The velocities and dissipation function defined in Eq. (6) are calculated with a increased viscosity due to turbulence effects by using respective turbulent coefficients G_x and G_z . Couette shear stress will increase with onset of turbulent region, and it is calculated with shear stress factor τ_c as follows:

$$\tau_c = 1 + 0.0012 \text{Re}_{\text{eff}}^{0.94} \quad (15)$$

Viscosity variation with respect to the temperature is taken into account for estimating performance parameters of the bearings. It is approximated by Falz's formula [6].

$$\mu = \mu_{\text{in}} (T / T_{\text{in}})^{-1} \quad (16)$$

For the numerical solution of the Reynolds equation, it is transformed into a system of finite difference equations by means of rectangular mesh for bearing developed surface. These equations are solved by Gauss Seidel iteration procedure by over relaxation method. Turbulent coefficients are updated in the superimposed iteration loop. For numerical solutions of the temperature distributions, energy equations are discretized into finite control volumes and upwind difference scheme is employed as the convection term is predominant for taking away majority of the heat. Computer program is developed using MS Excel Visual Basic to solve these equations and calculate the bearing performance parameters.

Since the viscosity is temperature dependant, Reynolds equation and energy equations are coupled. Hence, the iterative process starts with solving the Reynolds equation first using assumed lubricant viscosity. The velocity components are calculated after the pressure distribution is obtained, and the energy equation is solved to give the temperature distribution. Then, the viscosity is recalculated and the Reynolds equation is solved again using the updated viscosity. This procedure continues till the difference between two consecutive iterations is sufficiently small. Eccentricity ratios and attitude angles are determined in such a way that sum of the oil film forces equal to the applied load in a superimposed iteration loop. The velocity components in the axial and sliding directions provide side leakage and hydrodynamic oil flow, respectively. Frictional losses are calculated by using the shear stresses at the journal surface.

3 Validation of Analytical Study with Experimental Results

The computed analytical results for pressure dam and offset bearings are validated with experimental study carried out by Ronan et al. [18]. Tested bearings were located at the middle of the shaft which is supported by other two bearings. Load was applied to the tested bearing through hydraulic cylinder and monitored by load cell. The oil supplies and drains were separate for tested and support bearings. Hence, the oil flow to each bearing and power loss can be calculated individually. The oil inlet temperature and drain temperature were monitored for each individual bearing. Oil flow and the temperature rise across the bearings are used to calculate the power loss. The tested bearings were incorporated with by passing cooling technology. Hence, the estimated power loss and maximum film temperature to be overpredicted in theory when compared to experimental results. Tested bearing geometries and experimental operating conditions are listed in Table 1.

Figures 3 and 4 compare the estimated maximum film temperatures against the experimental results. Generally, good agreement is noticed between theoretical and experimental results. The bypassing cooling technology has significant effect at higher operating speeds which results in wider gap between the results. For example, the measured maximum film temperature at 16,000 rpm in offset bearings is 15% lower than the theoretical results. Similar trend is noticed in pressure dam bearings. Figures 5 and 6 compare power loss values for the bearing specific load of 4 MPa. Here, the difference between estimated and measured power losses is observed less in offset bearings and more in pressure dam bearings. If by pass cooling technology is not available in tested bearings, good agreement is expected between theoretical and experimental results. It means that the mathematical modeling and computational methods that are considered for predicting the bearing performance under

Table 1 Tested bearing geometry and experiment details [18]

Description	Pressure dam	Offset	Description	Values
Bearing diameter, mm	152.4	152.4	Oil inlet temperature, °C	49
Bearing length, mm	152.4	152.4	Oil supply pressure, bar	1.5–2.0
Dia. clearance—split, mm	0.267	0.267	Oil viscosity @ 40 °C, Pa s	0.039
Dia. clearance—crown, mm	0.267	0.420	Specific heat capacity, kJ/kg K	2.0
Preload	–	0.35	Load range, N	8000–104,048
Pressure dam width, mm	101.6	–	Specific load range, MPa	0.35–4.48
Pressure dam depth, mm	0.305	–	Speed range, rpm	8000–16,000
Pressure dam angle, deg	135	–	Surface velocity range, m/s	65–130

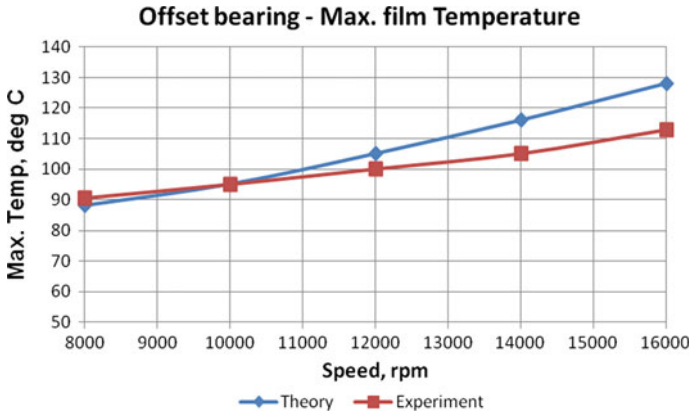


Fig. 3 Max. film temperature—offset bearing

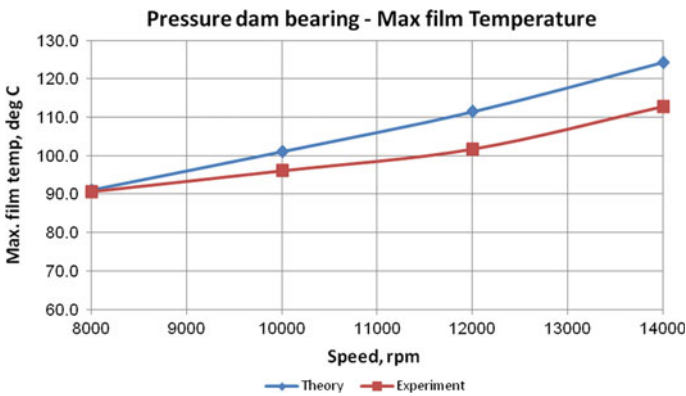


Fig. 4 Max. film temperature—PD bearing

high thermal loads are reliable for the offset pressure dam bearing’s performance calculations.

4 Results and Discussion

In this paper, it is attempted to study the performance characteristics of relatively larger size bearing with a diameter of 240 mm and length 240 mm. Usually, this bearing size is being used in high-speed and high-power gearboxes of above 40 MW turbines which run at operating speed of 7500 rpm. The bearing geometries, oil characteristics and operating conditions are listed in Table 2. Offset pressure dam

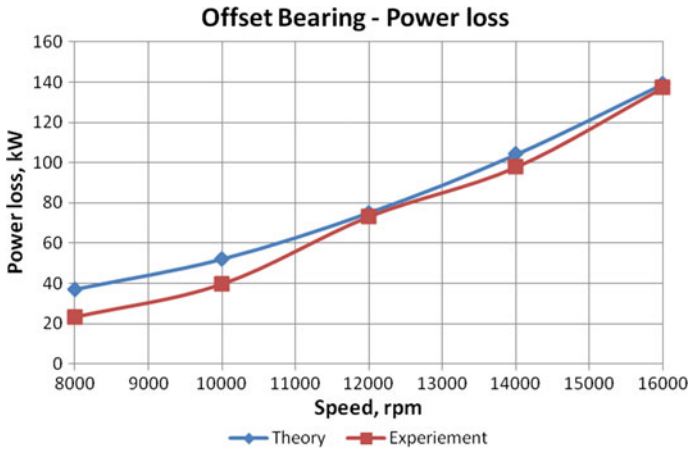


Fig. 5 Power loss—offset bearing

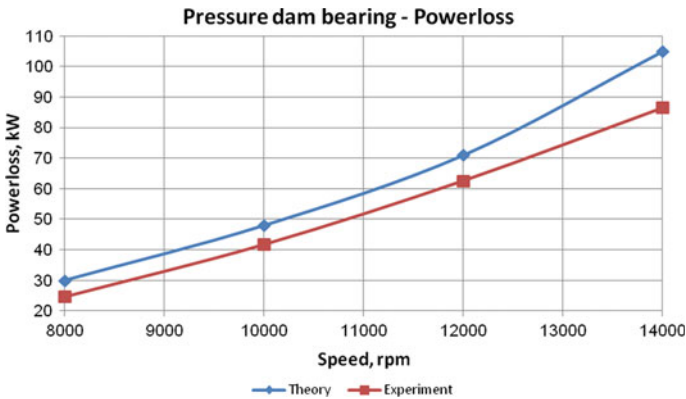


Fig. 6 Power loss—pressure dam bearing

bearing geometry parameters are selected with minimum required values of preload and pressure dam features for stable operation of the bearings.

Comparison of static performance characteristics of offset, pressure dam and offset-pressure dam bearings is presented. The performance variables such as power loss, oil flow, maximum film temperature, drain oil temperature, eccentricity ratio, attitude angle and minimum film thickness at constant specific load of 4 MPa are compared with respect to different speed conditions. The bearing eccentricity ratio and attitude angle are plotted in Fig. 7 as a function of speed for different bearings. Offset pressure dam bearing shows higher eccentricity ratio than other bearings due to high load carrying capacity which results from combined effects of preload and pressure dam. The attitude angle in offset pressure dam bearing is always lower than the other bearings. The combined performance characteristics of high eccentricity

Table 2 Bearing geometries and operating conditions

Description	Pressure dam	Offset	Offset–pressure dam	Description	Values
Bearing diameter, mm	240.00	240.00	240.00	Specific load range, MPa	0.5–4 MPa
Bearing length, mm	240.00	240.00	240.00	Operating speed range, rpm	3000–8000
Dia. clearance—split, mm	0.50	0.40	0.50	Journal velocity range, m/s	35–100
Dia. clearance—crown, mm	0.50	0.67	0.70	Oil inlet temperature, °C	49
Preload	0.00	0.40	0.29	Oil supply pressure, bar	1.5–2.0
Pressure dam width, mm	156.00	0.00	120.00	Oil viscosity @ 40 °C, Pa-s	0.039
Pressure dam depth, mm	0.50	0.00	0.40	Specific heat capacity, kJ/kg K	2.000

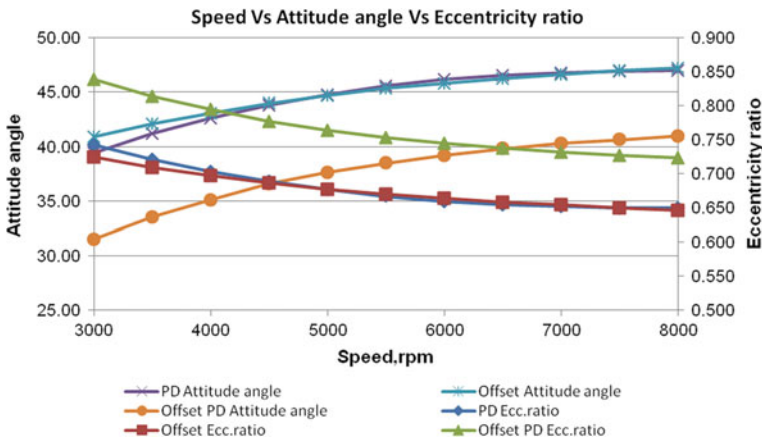


Fig. 7 Speed versus attitude angle versus eccentricity ratio

ratio and low attitude angle confirm that the offset pressure dam bearings are highly stable at all speeds.

Figure 8 compares the eccentricity ratio and attitude angle of pressure dam and offset pressure dam bearings at different loading conditions at a constant speed of 8000 rpm. It clearly indicates that offset pressure dam bearings experiences high eccentricity ratio and low attitude angle which ensures the stable operation of the

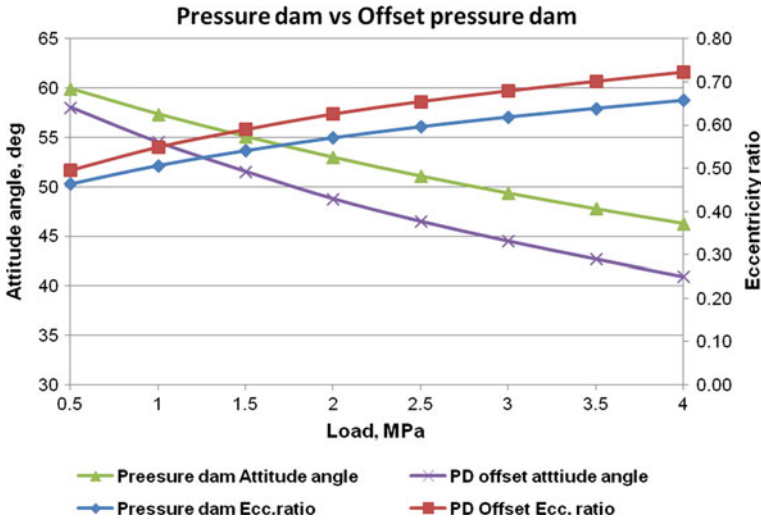


Fig. 8 Pressure dam versus offset PD at various loads

bearings. Hence, offset pressure dam bearings provide the opportunity to design engineers for wide range of severe operating conditions. Figure 10 represents the variation of power loss at different speeds. Offset pressure dam bearing shows lower power loss than offset bearing, but very close to the pressure dam bearing. It is noticed that power loss of offset pressure dam bearings is 5% lower than the pressure dam and 3% lower than the offset bearings at 8000 rpm with a surface velocity of 100 m/s. Power loss in hydrodynamic bearings is majorly dominated by the rotor speed and the shaft diameter. Here, as these two parameters are fixed in all the bearings, the low power loss in offset pressure dam bearing is influenced by operating viscosity. The preload in pressure dam reduces the turbulence effects and thus results in reduction in power loss (Fig. 9).

Figures 10 and 11 represent maximum film temperature and oil flow at various speeds for different bearings, respectively. It is noticed that offset pressure dam bearings experience low oil film temperature when compared with other two bearings. The maximum film temperature at these bearings is 88 °C at 8000 rpm against 93 °C (5% more) in pressure dam and 97 °C (8% more) in offset bearings. However, the oil flow in offset pressure dam bearings is 6% higher than the pressure dam and 15% higher than the offset bearings. This increase in oil flow is resulted from the additional preload in pressure dam bearings. If the maximum oil film temperature to be maintained less than 90 °C in pressure dam and offset bearings, the bearing clearances to be increased further. These design changes eventually result in increase in oil flow and reduce in stability of the bearings. However, offset pressure dam bearings provide better stability characteristics such as high eccentricity ratio and low attitude angle.

Figure 12 shows minimum film thickness at various operating speed conditions

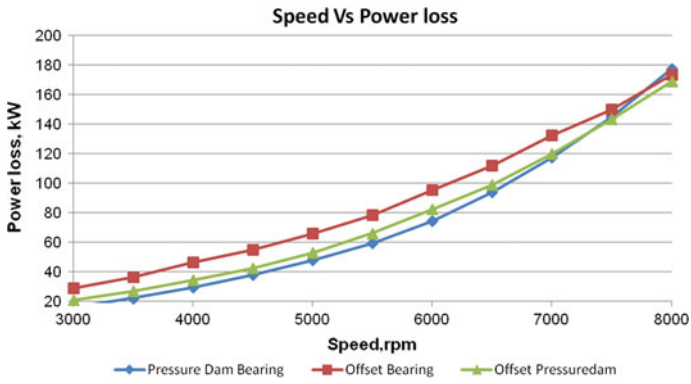


Fig. 9 Speed versus power loss

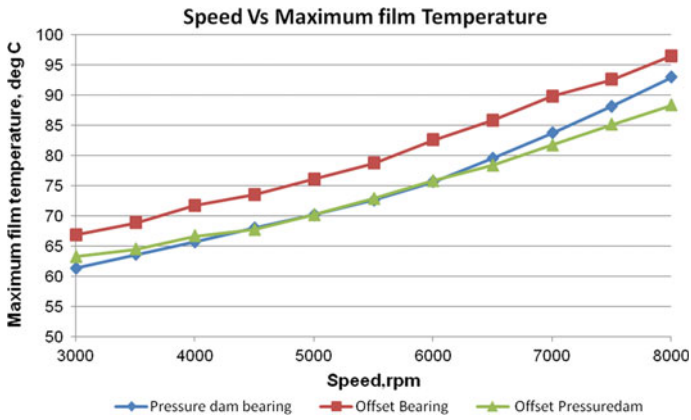


Fig. 10 Speed versus max. film temperature

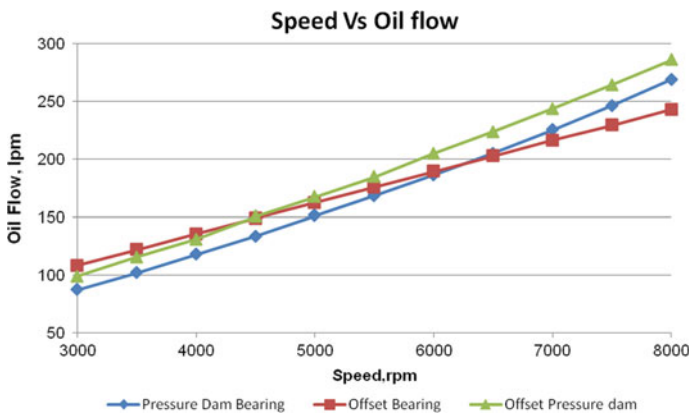


Fig. 11 Speed versus oil flow

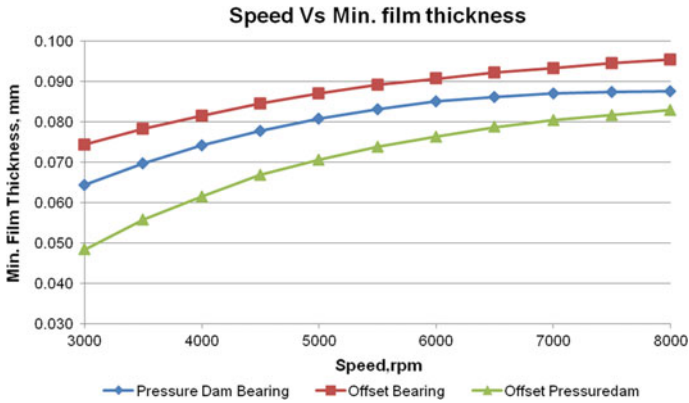


Fig. 12 Speed versus min. film thickness

for different types of bearings. Due to high eccentricity ratio, offset pressure dam bearings experience low film thickness at severe operating conditions (high load and high speed) when compared with other bearings. As the estimated minimum film thickness is greater than 0.030 mm at all operating speed conditions, the bearing are safe to operate at these operating conditions.

5 Conclusions

This study presents the benefit of preload (offset feature) in pressure dam bearing. The maximum film temperature and power loss in offset pressure dam bearing is lower than pressure dam and offset bearings. If oil film temperature is to be brought down in pressure dam and offset bearings, the clearances are to be increased further which eventually results in increase in oil flow and reduce in stability of the bearings, especially at no load high-speed conditions. However, offset pressure dam bearing provides stable operation at all operating conditions such as high journal velocity up to 100 m/s and specific load ranges from no load to maximum of 4 MPa. It could be one of the best alternatives to tilting pad bearings for high-speed applications.

References

1. He M, Cloud CH, Byrne JM. and Vázquez JA (2016) Fundamentals of fluid film journal bearing operation and modeling. In Asia turbomachinery and pump symposium 2016 proceedings, Texas A&M University
2. Elrod H, Ng C (1967) A theory for turbulent fluid films and its application to bearings. ASME J Lubric Technol 89(3):346–362

3. McCallion H, Yousif F, Lloyd T (1970) The analysis of thermal effects in a full journal bearing. *ASME J Lubric Technol* 92(4):578–587
4. Safar Z, Szeri AZ (1974) Thermo hydro-dynamic lubrication in laminar and turbulent regimes. *ASME J Lubric Tech* 96(1):48–56
5. Boncompain R, Frene J (1983) A study of the thermo hydrodynamic performance of a plain journal bearing comparison between theory and experiments. *ASME J Lubric Tech* 105(3):422–428
6. Mittwollen N, Glienicke J (1990) Operating conditions of multi-lobe journal bearings under high thermal loads. *ASME J Tribol* 112(2):330–338
7. Khonsari MM (1987) A review of thermal effects in hydrodynamic bearings, Part II. *J Bear ASLE Trans* 30(1):26–33
8. Zhang C, Yi Z, Zhang Z (2000) THD analysis of high speed heavily loaded journal bearings including thermal deformation, mass conserving cavitation, and turbulent effects. *ASME J Tribol* 122(3):597–602
9. Ji F, Guo Y, Yuan X, Yang L, Zhao W (2009) Turbulent model analysis and experimental research for lubrication performance of large power units journal bearing. In *ICIEA 2009 4th IEEE conference*, pp 206–210
10. Wilcock D, Booser E (1957) *Bearing design and application*. McGraw-Hill, New York
11. Allaire PE, Nicholas JC, Barrett LE (1979) Analysis of step journal bearings—infinite length, inertia effects. *ASLE Trans* 22(4):333–341
12. Nicholas J, Allaire P (1979) Analysis of step journal bearings—finite length stability. *ASLE Trans* 22:197–207
13. Nicholas J, Allaire P, Lewis D (1980) Stiffness and damping coefficients for finite length step journal bearings. *ASLE Trans* 23:353–362
14. Nicholas J, He M, Allaire P, Cloud CH (2004) A pressure dam bearing analysis with adiabatic thermal effects. *ASLE Trans* 47(1):70–76
15. Mehta N (1993) Static and dynamic characteristics of orthogonally displaced pressure dam bearings. *Tribol Trans* 36(2):201–206
16. Mehta NP, Singh A (1986) Stability analysis of finite offset halves pressure dam bearing. *ASME J Tribol* 108(2):270–274
17. Sneek HJ, Vohr JH (1984) *Hydrodynamic lubrication. Handbook of lubrication, vol. 2*. CRC Press
18. Ronan J, Shoup T, Perney G, Robertson C, Quoix B, Gelin A (2015) High performance bearing comparison. In *Proceedings of 44th turbomachinery symposium, Texas A&M University, Turbomachinery laboratory*

Computational Fluid Dynamics Study of Oil Lubrication in Ball and Roller Bearings



Vijay Tijare, Shanmukha Nagaraj, Mehul Pandya, and Jun Wang

Abstract Lubrication plays a significant role in performance of rolling element bearings. It is essential for proper functioning of bearings to reduce friction and to help avoid failure of bearings. Computational fluid dynamics (CFD) is one of the design and simulation tools, which is mainly used to identify proper lubrication for bearings. This work summarizes the CFD simulation results of oil transport within deep groove ball bearing and concave roller bearing. The volume fraction of oil has been predicted around the contacts at both outer and inner rings, all components and the gaps between the cage and rollers for both bearings. Drag losses (both pressure and shear drag) and film thickness have also been predicted. Cage design plays a significant role in determining the lubrication and the internal fluid drag losses in a bearing. The influence of cage design on the lubrication and the drag is evaluated by employing a metallic cage and a polymer cage. The simulation results show that oil content inside the bearing is dependent on the bearing free volume and operating speed. At lower speeds, both cage designs give similar performance; however, at the higher speed, it is different. Compared to metallic cage, polymer cage functions better in oil bath lubrication by splashing the oil on raceways at higher rotation speed. A linear decrease in oil content is observed with increased volume of polymer cage for concave roller bearing. In all case, cage and rollers experience maximum oil drag. An improved polymer cage is developed with the help of CFD to provide more oil to the cage and other bearing components.

V. Tijare (✉) · S. Nagaraj
RV College of Engineering, Bangalore, India
e-mail: vijay.tijare@skf.com

S. Nagaraj
e-mail: Shanmukhan@rvce.edu

M. Pandya
SKF Technologies, Bangalore, India
e-mail: mehul.p.pandya@skf.com

V. Tijare · J. Wang
SKF Research and Technology Development, Utrecht, The Netherlands
e-mail: jun.wang@skf.com

Keywords CFD · Volume fraction · Contact area · Contact pressure · Rolling element bearings · Finite volume method · Volume of fluid method (VOF) · Volume fraction · Drag losses · Fluid film thickness (FF)

Nomenclature

α_i	Volume fraction of phase i .
ρ_i	Density
v_i	Velocity
m_{ij}	Mass transfer rate to phase i from phase j
m_{ji}	Mass transfer rate to phase j from phase i
S_i^α	User-defined phase mass source term
p	Pressure, assumed to be equal in both phases
T_i and T_i^t	Molecular and turbulent stresses, respectively
M_i	Interface momentum transfer per unit volume
$(Fint)_i$	Internal forces
g	Gravity vector

1 Introduction

This paper elaborates a CFD approach to verify cage designs for deep groove ball bearing and concave roller bearing. The following are the objectives of work.

- Investigation of lubrication performance for concave roller bearing and deep groove ball bearing.
- Identify the cage design based on lubrication study by using CFD.

The purpose of oil using as a lubricant inside rolling bearing is to build elasto-hydrodynamic film between rolling elements and raceway and therefore minimize friction and temperature. Along with pure rolling, micro-sliding occurs in the bearing that generates heat. With insufficient lubrication, the surfaces of rolling bearing will be in intimate contact, resulting in high friction and wear at the areas where slip occurs. This produces high stresses close to the surface, leading to both reduction of fatigue life of bearing. When oil is used as lubricant in bearing, it acts as a coolant for the bearing, helping reduce temperature rise and therefore maintaining a sufficiently viscosity and film thickness. The CFD simulations of oil flow carried out in this work use the methodology developed in SKF [1].

2 Literature Survey

Wang [1] developed highly sophisticated CFD simulations to provide information of internal flow for high-speed bearings. It was observed that drag loss was mainly caused by the shearing of cage, rings and shaft. Raju et al. [2] worked on CFD simulation for needle roller bearing (NRB). Two supply holes were analyzed for lubricant supply in the bearing. The results from CFD helped in deciding right location of putting oil hole. Pang et al. [3] worked on spraying lubrication for roller bearing. As the speed increases, roller cage is shattered, which may lead to failure of bearing. This may also happen because of shortage of oil. Numerical simulation results showed that due to effect of air pressure and airflow thickness, the optimal spraying position is at region closer to inner ring of bearing. Yingyi Wen, Dr. Shinji Miyata and NSK Ltd., Japan [4] used CFD to measure torque associated with oil. CFD was used for predicting torque and tendency of lubricant flow passing through various parts of tapered roller bearing (TRB). The influence of bearing cage design on oil flow and torque was also investigated. Liebrecht et al. [5] investigated influence of oil quantity on the total friction torque on TRB by experimental results and numerical simulations. Wu et al. [6] performed CFD simulations for the oil–air flow inside multiple-point, oil-jet lubrication for ball bearing. CFD results were compared with single-point, oil-jet lubrication. The results show that distribution of oil–air for multiple-point jet was more uniform than single-point injection. Adeniyi et al. [7] carried out CFD analysis within space bounded by cage and IR for ball bearing. CFD study showed different flow behaviors where the oil inlets through a continuous slot compared to discrete entry holes. The breakup pattern of oil on cage inner surface suggested that smaller droplets should be shed at higher shaft speed. Sakai et al. [8] analyzed cavitation area in small-bore journal bearing under flood lubrication and starved lubrication using CFD. The impact of influence of setting condition of VOF, surface tension and vapor pressure was also studied and analyzed.

3 Bearings in Application and Its Kinematics

A roller bearing carries a load by placing rolling elements (such as rollers) between the inner and outer rings. The relative motion of the rings causes the rolling elements to roll with very little rolling resistance and with a little sliding resistance. Concave roller bearing consists of concave cylindrical rollers to reduce friction between two relatively rotating surfaces and is very suitable for applications with high load and a small radial clearance between two surfaces in a relative motion. It has a large surface area that is in contact with the bearing outer surfaces. The typical structure consists of a cage which orients and contains the rollers, the rollers themselves and an outer race (sometimes the housing itself). Such bearing can be used in various applications in automobile and process industry. In this bearing, surface-to-surface contact occurs; therefore, continuous lubricant supply is essential to reduce the friction and wear on

the contacts. This bearing is supposed to get higher friction than ball bearing, since it has larger elliptical contact or line contact. It is, therefore, required to lubricate its contact continuously. Lubricating oil can also dissipate the frictional heat for them. This bearing consists of a cage, concave rollers and an outer ring. The bearing can have sheet metal cage or polymer cage. The cage has pockets which hold the rollers and carry all the rollers along with the cage, while allowing the local rotation of rollers. In the present study, lubrication of this bearing is analyzed using CFD and the lubrication behavior is compared with deep groove ball bearing. Ball bearing is one of the most commonly used bearings and its lubrication behavior is known, so it was decided to compare concave roller bearing lubrication with deep groove ball bearing. Both these bearings, ball and roller bearings, are analyzed using oil bath lubrication system. Since this is a verification study, a similar oil bath level (bottom ball/roller fully submerged in both bearings) was taken for both bearings.

4 Computational Fluid Dynamics

4.1 Basic Principle

Computational fluid dynamics, usually abbreviated as CFD, is a branch of fluid mechanics that uses numerical methods and algorithms to solve and analyze problems that involve fluid flows. CFD is the term used to describe a family of numerical methods used to calculate the temperature, velocity and other fluid properties throughout a region of space, and in effect, it numerically (partly) solves the Navier–Stokes equation. Computers are used to perform the calculations required to simulate the interaction of liquids and gases with surfaces defined by boundary conditions. The present analysis was performed using STARCCM+ from Siemens. This tool performs various steps in the CFD process, e.g., fluid domain definition, meshing, running the analysis and post-processing the results. Figure 1 shows the typical steps carried out in this tool.

The Navier–Stokes equations form the basis of all CFD problems. The solution in CFD is the numerical solution to problem that is posed by mesh, boundary conditions, selection of time step and numerical scheme. The selection of the time step size for volume of fluid (VOF) method, which is used here, is one of the important steps in running CFD simulations. Accuracy of the solution is influenced by choice of the numerical scheme and time step size.

The volume of fluid (VOF) multiphase model is a simple multiphase model. It is suited to simulating flows of several immiscible fluids on numerical grids capable

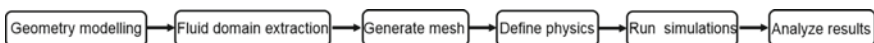


Fig. 1 Steps of CFD analysis

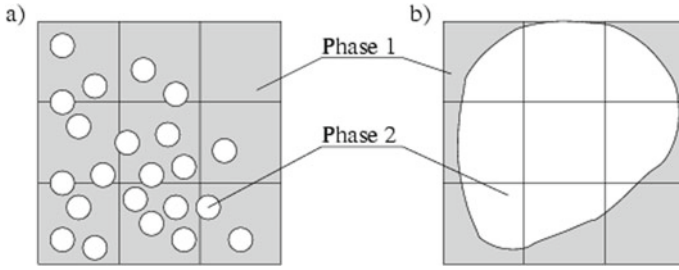


Fig. 2 Illustration for use of VOF method

of resolving the interface between the phases of the mixture. The VOF multiphase model is used to solve problems involving immiscible fluid mixtures, free surfaces and phase contact time. In such cases, there is no need for extra modeling of inter-phase interaction. Figure 2 provides an illustration of unsuitable grids (left) and suitable grid (right) for two-phase flows using the VOF model.

Volume fraction

The share of flow domain that is occupied by each phase is given by volume fraction [9].

The volume of a phase i is given by,

$$V_i = \int_V \alpha_i dV \tag{1}$$

The volume fraction of each phase must fulfill the requirement

$$\sum_{i=1}^n \alpha_i = 1 \tag{2}$$

Continuity equation

The conservation equation of mass for a generic phase i is given by,

$$\frac{\partial}{\partial t} \int_V \alpha_i \rho_i dV + \oint_A \alpha_i \rho_i v_i da = \int_V \sum_{j \neq i} (m_{ij} - m_{ji}) \cdot dV + \int_V S_i^\alpha dV \tag{3}$$

Momentum equation

The momentum balance of the generic phase i is given by,

$$\begin{aligned} \frac{\partial}{\partial t} \int_V \alpha_i \rho_i V_i dV + \oint_A \alpha_i \cdot \rho_i v_i \otimes V_i \cdot da = & - \int_V \alpha_i \nabla p dV \\ + \int_V \alpha_i \rho_i g dV + \oint [\alpha_i (T_i + T_i t)] \cdot da + \int_V M_i dV \end{aligned}$$

$$+ \int_V (F_{int})_i dV + \int_V S_i^\alpha dV + \int_V \sum_{i=1}^n (m_{ij} \cdot v_j - m_{ji} v_i) dV. \tag{4}$$

These equations are solved using STARCCM+ for the available boundary conditions on the grid using discretization techniques.

4.2 CFD Model Setup

CFD domain consists of a bearing fluid domain and an external cylindrical volume (collector/housing) around the bearing to collect the oil that leaves through the bearing outlet. The bearing volume is rotating, and the collector is stationary. A special treatment is required for the very small area where races and rollers are in contact with each other. The contact is excluded from computation domain since that would require an impractically small mesh size.

To capture the interactions between the stationary and rotating parts, two CFD regions were created. The collector and the bearing have two sets of interfaces for data exchange. It is to be noted that this analysis was carried out with metallic cage and polymer cage. Roller bearing (concave roller bearing) was analyzed with both cages, while ball bearing (deep groove ball bearing) was analyzed with metallic cage. Later, a redesigned polymer cage was also analyzed to investigate if there is any further improvement in lubrication with change in design of polymer cage. Figure 3 shows the cases studied for this analysis.

Figure 4 shows the mesh details. When creating a mesh, it is always desirable to understand the flow phenomena occurring in the fluid domain. In order to ensure a good resolution of the oil flow, it is necessary to create a fine mesh for the bearing. Particularly, fine cells are created in critical areas, such as around the contact zones, along the moving components, narrow gaps and the interfaces, and at least six layers of cells are created in the gap between rollers and races.

Figure 5 shows initial oil level for both bearings. Bottom ball/roller is submerged initially.

Table 1 shows fluid properties taken for this analysis.

In Table 2, we can see the rotational speed for which analysis was carried out. During the operation, the rollers also rotate in the opposite direction to that of the inner race along their own axis and also revolve along with the cage. CFD analyses

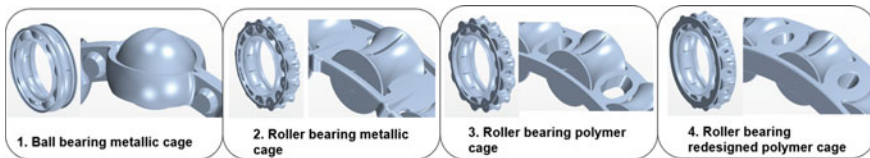


Fig. 3 Different types of cage designs investigated

Fig. 4 Computational mesh

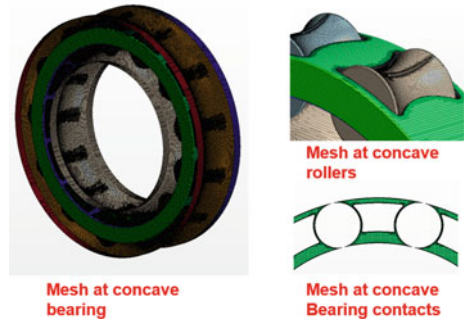


Fig. 5 Initial oil level

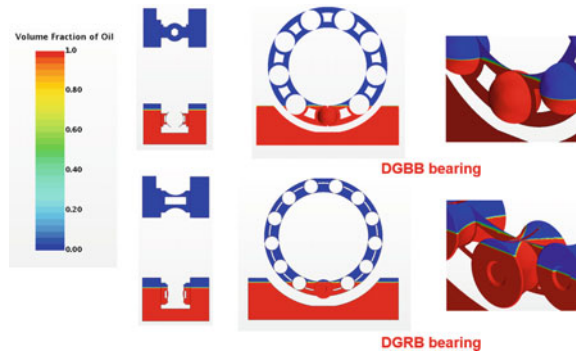


Table 1 Fluid properties

Density (kg/m ³)	872	Oil surface tension (N/m)	0.034
Dynamic viscosity (Pa-S)	0.00872	Oil–steel surface contact angle (°)	10

Table 2 Operating speed

% of operating speed	25 % speed	50 % speed	17 % speed	100 % speed
Inner ring (rpm)	3250	6500	9750	13,000

are carried out for different bearing speeds (25, 50, 75 and 100% of operating speed). Bearing operational speed is 13,000 rpm [8].

5 Results

Figure 6 shows the comparison of volume fraction plot for all cages. The red color represents the oil flow in the system, and the blue color represents the air. The following points are observed.

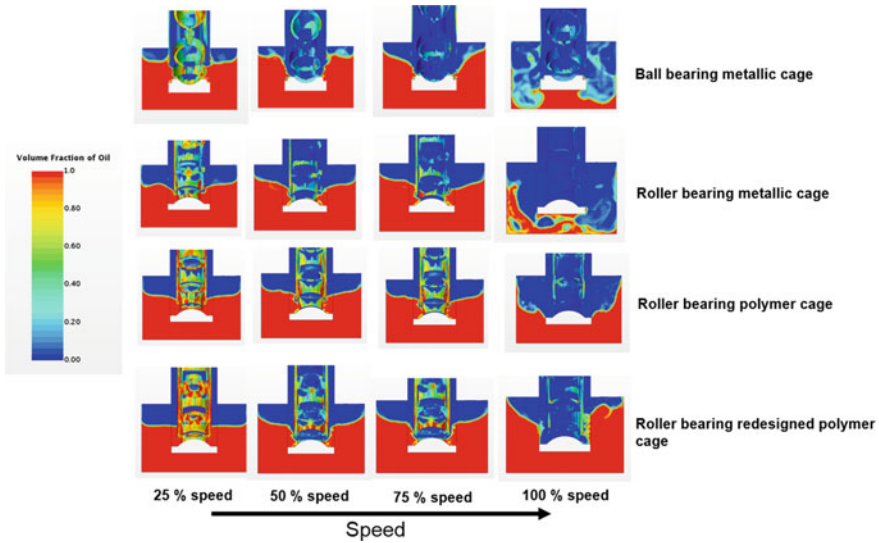


Fig. 6 Volume fraction of oil in bearing

1. When we increase speed (from 25 to 100%), the behavior becomes asymmetrical (100%) from symmetrical (25, 50 and 75%). Oil–air interface becomes unstable for 100% speed for most of cages except polymer cage and redesigned polymer cage. This is due to higher speed of bearing. Numerical diffusion is also not ruled out. This also indicates that there is a lot of splashing for ball bearing with metallic cage and roller bearing with metallic cage for higher speed.
2. As we increase speed, the volume fraction of oil decreases on bearing. That means, the oil quantity decreases in bearing.
3. The asymmetrical behavior of oil–air interface in housing for metallic cage of roller bearing is also due to higher centrifugal forces. The width of polymer cage is higher than metallic cage in radial direction, so this behavior is not happening for polymer cage cases.

Figure 7 shows the comparison of volume fraction plot for all cases. The following points are observed.

It is clearly visible that roller bearing with metallic cage has lesser amount of oil compared to ball bearing of metallic cage. This is more visible for speed of 50% and onwards. This is due to shape and geometry of cage for both bearings. For the ball bearing, the ball is better covered by metallic cage, which is not the case for metallic cage of roller bearing. The gap between cage and ball of ball bearing is responsible for holding more oil than gap between roller and cage of roller bearing. Area of balls which covered by metallic cage for ball bearing is higher than that of roller bearing, which adds more oil between balls and cage for ball bearing. Because of this, the amount of oil which should be spread on rollers and contact is less for roller bearing than ball bearing.

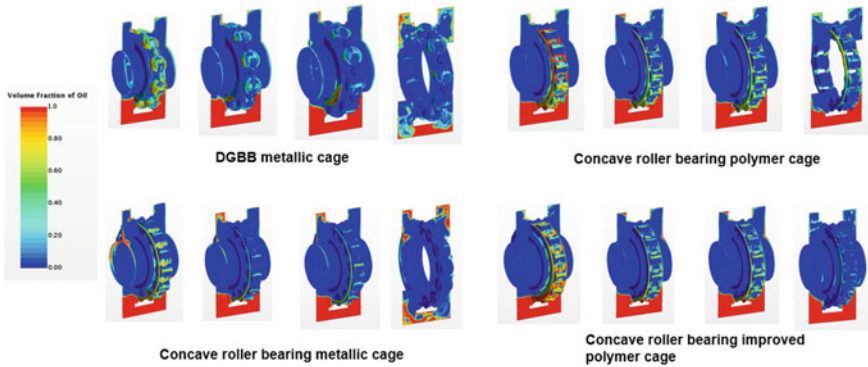


Fig. 7 Volume fraction of oil in bearing

It is observed that polymer cage gives better oil quantity than metallic cage for roller bearing. This is primarily because of higher cage width of polymer cage than metallic cage in radial direction, which is responsible to hold more oil between roller and cage. However, this is true to certain limit. Increasing width of polymer cage further, and so volume of cage, decreases amount of oil which cage can take with it initially. It also decreases oil quantity in the bearing, since cage volume has increased. So, there is a limit to increase width of cage. This is proved from redesigned polymer cage of roller bearing, where the amount of oil is reduced now, as can be seen in Fig. 7.

Figure 8 shows the average volume fraction of various components for all cases. It is observed that cage and balls have minor difference of volume fraction for ball

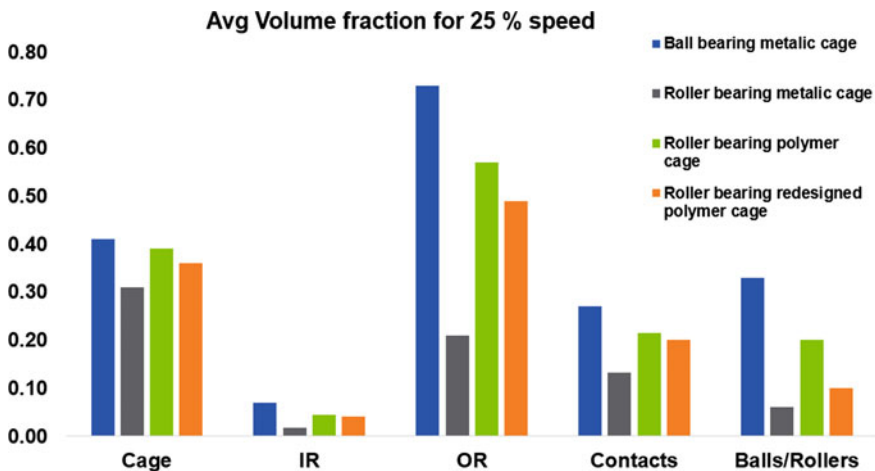


Fig. 8 Volume fraction of oil on bearing parts

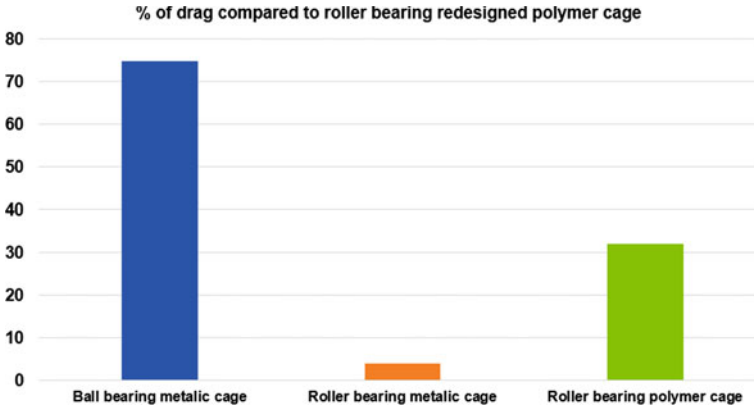


Fig. 9 % of drag comparison

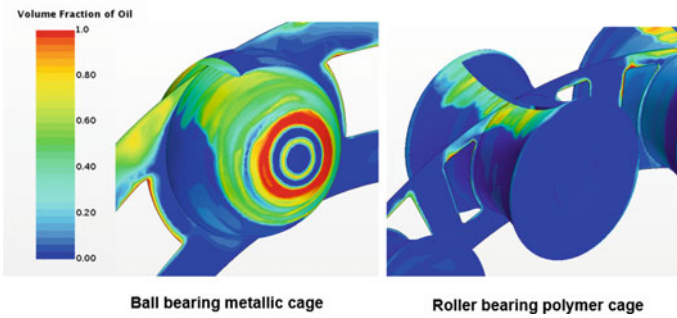


Fig. 10 % Volume fraction of oil close to contacts

bearing with metallic cage. But this is not the case with roller bearing with metallic cage. However, this is overcome when we use polymer cage for roller bearing.

Figure 9 shows the comparison of drag losses for all configurations for 100% speed. The reference bearing taken is roller bearing redesigned with polymer cage. This bearing has least drag, since it does not have much oil. So, it is taken as a reference and other bearing are compared with it. The Y-axis shows the % of drag in comparison with this bearing.

5.1 Estimation of Fluid Film Near Contacts

The approximate film thickness has been estimated at the front of the contacts of the raceways (outer race side) according to the following formula.

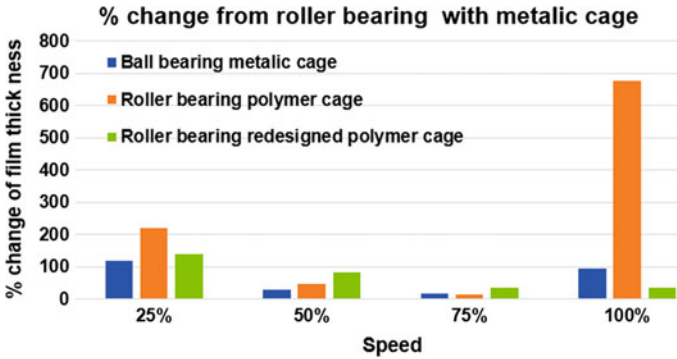


Fig. 11 % Change from roller metallic bearing

$$FF = \text{Average Volume Fraction of Oil close to contact} * \text{Height of contact.}$$

Please note that this formula gives only indication about film thickness. It does not give any actual thickness. It was observed that roller bearing with metallic cage has the lowest film thickness. Figure 11 shows % change of film thickness (Y-axis) of ball bearing with metallic cage, roller bearing with polymer cage, roller bearing redesigned with polymer cage when compared to roller bearing with metallic cage for different speeds. It shows that roller bearing with polymer cage performs better than others (Fig. 10).

5.2 Improvement in Polymer Cage

Polymer cage is further improved by extending its ends slightly upward. This was based on not to make cage so bulky and also not to occupy much oil space in bearing and allowing cage to hold more oil. This is to ensure better oil splash toward contacts and rollers. The results are shown in Fig. 12. This is even better design than concave roller bearing with polymer cage. There is higher volume fraction at contacts for this cage than the previous polymer cage.

6 Conclusion

The CFD model used here provides an opportunity to predict volume fraction of oil for different speeds of ball and roller bearings for the investigation of lubrication system.

1. As the rotational speed is increased, the volume fraction of oil is decreased.

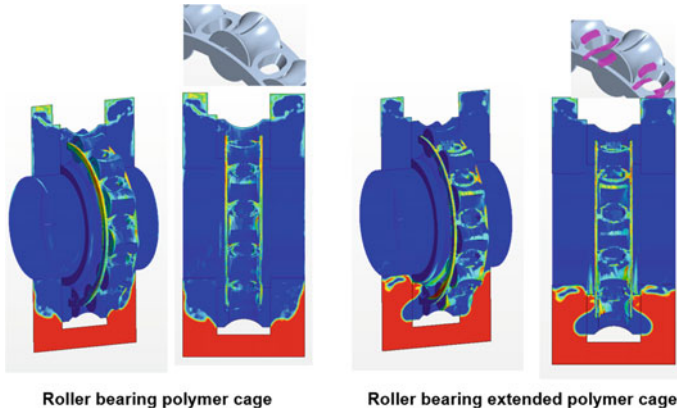


Fig. 12 Volume fraction of oil improvement in polymer cage

2. Enough oil is available for lower speed of roller bearing (metallic cage), but not with higher speed of same bearing.
3. Polymer cage of roller bearing can hold more oil than metallic cage of same bearing.
4. A new polymer cage was designed with extended width of ends in radial direction around rollers. This is useful to hold more oil, but there is a limit for this change, since more the width, less oil is available initially for the bearing.
5. Experiments on the physical prototype may be used to verify a part of the CFD observations by measuring friction torque.

Acknowledgements Authors thank SKF management to allow to work on this investigation project.


References

1. Wang J (2013) CFD analysis of Drag loss in high speed bearings. In World Tribology Congress 2013, Torino, Italy, 8–13 September 2013
2. Raju KS, Puthiya M, Ray S, Shi F (2013) Needle roller bearing lubricant flow CFD simulations. SAE Int April, 2013
3. Pang BT, Li JS, Liu HB, Ma W, Xue YJ (2008) A simulation study of an optimal oil spraying mode for high-speed rolling bearing. JAMME 31(2):553
4. Wen Y, Miyata S, NSK Ltd. (2018) Japan, CFD analysis of tapered roller bearings and ball bearings for reducing agitation torque, motion & control, No 29, June, 2018, NSK Tech J
5. Liebrecht J, Si X, Sauer B, Schwarze H (2015) Investigation of drag and churning losses on TRB. J Mech Eng 61
6. Wu M, Wu W, Yuan S, Hu J (2004) Study of multiple-point oil-jet lubrication of high-speed ball bearings. Power Trans Eng Jun 2004
7. Adeniyi AA, Morvan H, Simmons K (2016) A CFD simulation of oil-air flow between the cage and IR of aeroengine bearing. J Eng Gas Turb Power, July 2016

8. Sakai F, Ochiai M (2017) CFD analysis of Journal Bearing with oil supply groove considering 2 phase flow. In 4th International conference of design and engineering and science, ICDEs
9. Simcenter STAR-CCM+ User manual

Feasibility Studies on Newly Conceptualized Inter-shaft Squeeze Film Damper (ISSFD) Rings for Vibration Attenuation



H. M. Shivaprasad , G. Giridhara, Ajit Kumar, Praveenkumar Kamanat, and V. Arun Kumar

Abstract Squeeze film dampers (SFDs) have become very essential for high-speed turbomachinery as means of vibration energy dissipating mechanism. However, SFDs are not very common for inter-shaft bearing applications and are still in the R&D phase. It is observed that the application of SFDs for inter-shaft bearing systems is not being pursued in a real practical sense, as it becomes extremely difficult to realize a compatible component facilitating the radial squeezing mechanism—where squeeze film oil could be introduced—thus resulting in squeeze film damping. The gap that could be made available between the inner spool and inner race or the outer spool and the outer race of the inter-shaft bearing also being very little further complicates the application of a conventional squeeze film damper in the inter-shaft bearing plane. In this research work, newly conceptualized inter-shaft squeeze film damper (ISSFD) rings are fabricated and tested for evaluating their damping potential characteristics in dedicated instrumented test rig/s fabricated for the purpose. Parametric experimentations are conducted in a single-spool test rig as a proof of concept in attempting to quantitatively evaluate the damping potential of ISSFD rings and hence the suitability of their applications in inter-shaft bearing plane of two-spool system. This research study very clearly indicated the damping contribution of the ISSFD rings, and the performance of the system improved in terms of

H. M. Shivaprasad (✉) · G. Giridhara
Department of Mechanical Engineering, BMS College of Engineering, Bengaluru 560019, India
e-mail: shivaprasad.mech@bmsce.ac.in

G. Giridhara
e-mail: ggiridhar.mech@bmsce.ac.in

A. Kumar · P. Kamanat
Gas Turbine Research Establishment, Bengaluru 560019, India
e-mail: ajitkumar@gtre.drdo.in

P. Kamanat
e-mail: kamanat@gtre.drdo.in

V. Arun Kumar
Department of Mechanical Engineering, Dr. Ambedkar Institute of Technology, Bengaluru 560019, India
e-mail: arun51149@gmail.com

substantial reduction in shaft vibration amplitudes. The study also clearly indicated that the ISSFD rings contribute toward the stiffness in the bearing plane also, and as a result, the rigid body critical speed gets shifted. Parametric experimental studies brought out the effect of different geometric parameters on the stiffness and damping contribution of ISSFD rings.

Keywords Inter-shaft squeeze film damper (ISSFD) ring · Gas turbine engine · Two spools · Critical speed · Stiffness · Damping factor

1 Introduction

As SFDs have become an inevitable component in modern gas turbine engines, researchers are emphasizing on different aspects of SFDs from the point of view of improving their damping potential in the space-constrained gas turbine systems. While applications of SFD have become very common, the necessity of the same in the inter-shaft bearing plane applications, although being felt, however has still not been realized due to paucity of research from practical application point of view. Attempts however have been made by several researchers to conceptualize possible configurations of SFD suitable for inter-shaft bearing plane with practically no application potential.

Li et al. [1–3] have calculated steady-state unbalance response of the rotor system for different shaft speeds and have investigated damping effects of an inter-shaft squeeze film damper with different radial clearances under various levels of rotor unbalance. Their suggestion is that, for designing ISSFD, it should be necessary to consider the operating speed of the rotor below the threshold speed of the rotor system. Shafei et al. [4–6] have shown that the inter-shaft bearing dampers are stable supercritically only with a configuration in which the oil film does not rotate. Their ISSFD in this case is mounted in a set of double-decker rolling-element bearings with a non-rotating squeeze film. They have introduced squeeze film in between two sleeves, one on the outer race of the inner bearing and the other on the inner race of the outer bearing. These races are prevented from rotation using squirrel cages. The two sleeves are docked together to prevent their relative rotation and allow only a relative whirl between them. Defaye et al. [7] experimentally found that the efficiency of an ISSFD depends on the type of the crossing mode and on the direction of rotation of both shafts. They have suggested that an additional research effort is necessary in order to propose an optimal ISSFD technology. The influence of various parameters such as the shaft bending mode, the unbalance value and the radial clearance of the ISSFD must still be investigated. Gupta et al. [8, 9] analyzed ISSFD using Reynolds equation. They have tested an improved and inherently stable inter-shaft squeeze film damper based on El-Shafei's design in a test setup having two rolling element bearings; one each mounted on LP and HP rotor shafts. They have considered two design modifications for analysis and tested them experimentally. Jayaraman and Arunkumar [10] have discussed the concept of flexible supports/mounts which are

mounted in between the bearing and the shaft to bring down the rigid rotor critical speeds.

From the literature review, it is understood that a very few researchers have made attempts with regard to realizing SFDs for inter-shaft bearing applications. Most of these attempts do not seem to be feasible from practical application point of view, primarily because of the space constraints in the inter-shaft bearing plane and secondly because of the instability problems that exist in the existing SFD designs pertaining to oil film rotation. It is very clear from the above discussions that the efforts on developing ISSFD from practical application perspective are very scanty. As such an attempt has been made here to develop practically feasible ISSFD suitable for space-constrained gas turbines. Research effort in here basically includes conceptualization of ISSFD rings (suitable for space-constrained gas turbines), fabrication and testing for their damping potential.

2 Newly Conceptualized ISSFD Rings

Figure 1 shows schematic representation of two-spool configuration of a typical gas turbine engine in which a conventional squeeze film damper (SFD) is mounted on bearing-3. Bearing-4 represents an inter-shaft bearing, and the gap that could be made available between high-pressure (HP) spool and low-pressure (LP) spool is as low as 3–7 mm, and hence, it is a real challenge to develop a suitable squeeze film damper with a non-rotating oil film. In order to mount SFD in the inter-shaft bearing plane in such a small gap, the maximum radial space available for the damper should be well within 7 mm facilitating the squeezing action. Also, the necessity of very thin grooves for oil film needs to be created in the ring that would create squeezing action under time-dependent loading conditions. In a real practical sense, it should be a compatible component facilitating the radial squeezing mechanism, where squeeze film oil could be introduced, thus resulting in squeeze film damping.

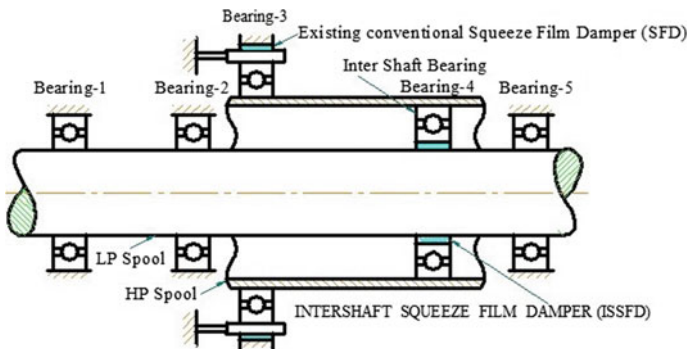


Fig. 1 Schematic of a typical two-spool gas turbine engine

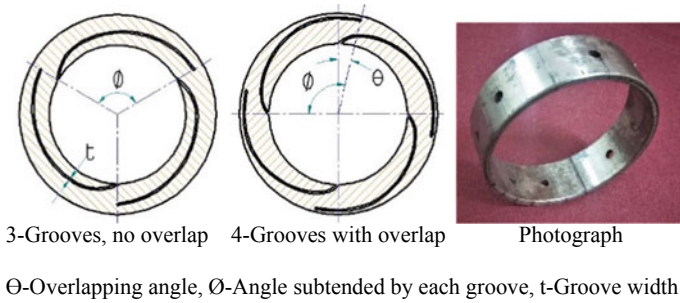


Fig. 2 Schematic/photograph of newly conceptualized ISSFD ring configurations

Figure 2 shows the schematic/photograph of the newly conceptualized ISSFD rings. The possible geometric parameters that could be varied include number of grooves, angle subtended by each of the groove/groove angle and overlapping angle of the grooves apart from groove width (nominal oil film thickness). Groove width was kept constant for the present study, while experiments have been conducted in a single-spool rig using newly conceptualized ISSFD. The assembly of ISSFD in a two-spool inter-shaft bearing (bearing-4) could be either with the LP spool or with the HP spool. It is preferable to have the ISSFD assembled with the LP spool from the point of view of assuring the presence of oil in the groove due to centrifugal action as shown in Fig. 1. The conventional squeeze film damper as well as the proposed inter-shaft squeeze film damper has rigid boundaries.

3 Test Rig and Instrumentation

To explore the suitability of ISSFD rings, two test rigs—a static test rig and a single-spool dynamic test rig—were designed and fabricated, and experiments were conducted. Basically, a static test rig is designed to evaluate the variation of static stiffness along the circumferential direction of ISSFD rings. A single-spool dynamic test rig is designed to demonstrate the damping potential of ISSFD rings defined in terms of vibration attenuation and also facilitating parametric studies.

3.1 Static Test Rig

The static test rig facilitates loading of ISSFD ring and measurement of deflection along the load line. While Fig. 3a shows the schematic of the static test rig, Fig. 3b shows the photograph of the same. The mandrel along with the ISSFD ring is supported between two V-blocks which are mounted on the base plate. The loading

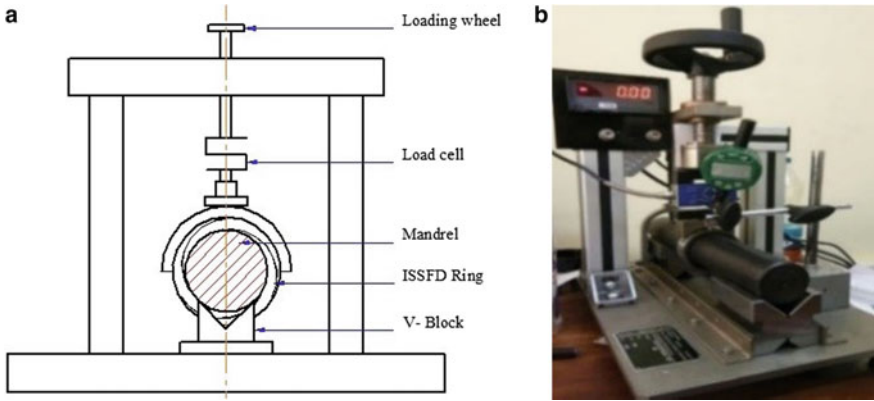


Fig. 3 a Schematic of static test rig, b photograph of static stiffness test rig

unit includes the screw rod arrangement for application of load. The instrumentation includes measurement of load and deflection along the loading direction.

3.2 Single-Spool Dynamic Test Rig

This test rig essentially consists of a horizontally configured shaft with a variable speed motor capable of running up to 16,000 rpm. The horizontally configured shaft is supported on two bearings, with one of them supporting the ISSFD ring. An oil pump provides supply of squeeze film oil, and provision of radial holes in the ring ensures continuous presence of oil in the grooves. Instrumentation basically includes measurement of speed and vibration amplitudes in two mutually perpendicular directions. Facility in the rig is provided to mount any desired amount of unbalance on either side of the bearing mounted with ISSFD ring to excite the system. While Fig. 4a shows the schematic of dynamic test rig, Fig. 4b shows the photograph of the same.

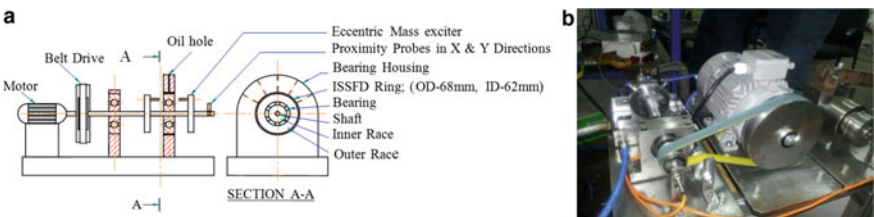


Fig. 4 a Schematic of the dynamic test rig, b photograph of the dynamic test rig

4 Results and Discussions

Experiments, parametric in nature, were conducted to evaluate the stiffness offered by the ISSFD rings (under static condition) and damping potential in terms of reduction in shaft vibration amplitudes. The system was run supercritical in order to bring out the effectiveness of the damper (as experienced by the ISSFD ring when mounted on a typical inter-shaft bearing) and hence the presence of ISSFD ring. Tests were conducted on three and four-grooved ISSFD rings, the geometric details of which are provided in Table 1.

4.1 Static Stiffness

Static stiffness details were obtained for all the four ISSFD rings with varying number of grooves, angle subtended and overlapping angles. For all the cases, the groove width was kept constant at 300 μm . Figure 5a indicates the typical load deflection pattern for a three-grooved ISSFD ring with 135° subtended angle clearly indicating relatively lower stiffness at relatively lower loads followed by a sharp increase in stiffness (very little deflection change) after certain level of loading.

This sharp change in stiffness is due to the initiation of metal to metal contact (groove closure) after a particular loading level. Figure 5b schematically shows the loading of a typical ISSFD ring. The circumferential stiffness variation is as shown in Fig. 5c. Table 2 provides the details of the stiffness values for a three-grooved ISSFD ring with 135° subtended angle.

Figure 6a, b shows the corresponding results obtained for other rings, while Table 3 shows relevant results.

Figure 7 shows the variation of average stiffness for three-grooved ISSFD rings for different values of subtended angles. By increasing the subtended angle/groove length and hence the overlap angle of grooves of ISSFD ring, the average stiffness value decreases.

Table 1 Geometric details of ISSFD rings

No. of grooves	3 grooves			4 grooves
Groove angle	135°	150°	165°	105°
Overlap angle	15°	30°	45°	15°
Outer diameter	68 mm	68 mm	68 mm	68 mm
Inner diameter	62 mm	62 mm	62 mm	62 mm
Average groove width	300 μm	300 μm	300 μm	300 μm

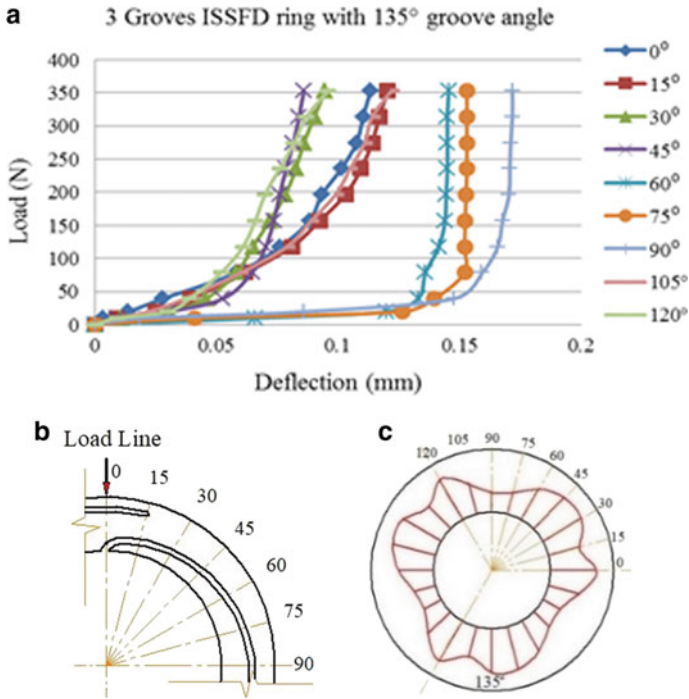


Fig. 5 a Load versus deflection pattern for three-grooved ISSFD ring with 135° subtended angle, b loading along zero degree for three-grooved 135° ring, c circumferential variation of stiffness

4.2 ISSFD Performance Evaluation

The effectiveness of the presence of newly conceptualized ISSFD rings was quantitatively estimated primarily from the point of view of vibration attenuation and shift in the rigid rotor critical speeds as a result of stiffness contribution from ISSFD squeeze film oil. Experiments were conducted on three- and four-grooved rings with different groove subtending angles (and hence overlapping angles). Figure 8 indicates the variation of shaft amplitude as a function of speed with and without the presence of oil for a three-grooved ISSFD ring with 135° subtending angle for two levels of unbalance. It is very clear that the presence of oil has attenuated the vibration levels at all speeds. It can also be observed that there is a shift in the damped critical speed (from 12,600 to 13,800 rpm) indicating the addition of stiffness in the bearing plane. Similar results were obtained when the unbalance levels were increased from 164.92 g-mm to 235.74 g-mm and that there is no change in the critical speed levels. Vibration amplitudes have attenuated by about 35% at both levels of excitation. Contribution of damping factor ‘ ξ ’ is estimated using half power method, and there is an increase in the value of ξ by 70.15% for 162.94 g-mm unbalance level and 78.43% for 235.74 g-mm unbalance level. This is due to relatively increased squeeze

Table 2 Stiffness values for three-grooved ISSFD ring with 135° groove angle

Three-grooved ISSFD ring with 135° groove angle (average $K = 3514.08$ N/mm)										
Loading line position (°)	0	15	30	45	60	75	90	105	120	
Stiffness (N/mm)	3202.08	3268.74	4618.46	4582.46	3662.82	2287.04	2063.03	3316.93	4625.75	

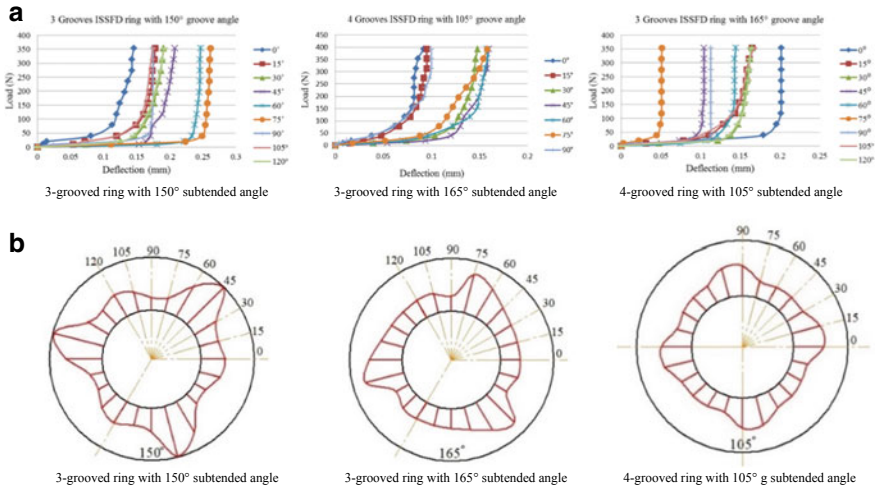


Fig. 6 a Load versus deflection curves for three-grooved and four-grooved rings, b circumferential variation of stiffness for three-grooved and four-grooved rings

velocity as a result of increased vibration levels at higher unbalance levels. Figures 9, 10 and 11 show the corresponding results obtained for other ISSFD rings.

5 Conclusion

An attempt has been made to newly conceptualize inter-shaft squeeze film damper systems in space-constrained gas turbines from practical application perspectives. The conceptualization essentially aims at realizing the presence of oil films in a suitably designed ring compatible to be accommodated in practical gas turbines. The geometrical variation considered in the newly conceptualized ISSFD ring includes number of grooves provided in the ring, angle subtended by each of the groove (and hence the overlapping angle) and groove width which actually would be the average squeeze film thickness. A dedicated instrumented test rig was designed and fabricated, wherein the speeds ranging up to 16,000 rpm could be realized. Arrangements were provided in the rig to vary unbalance levels and also the rigid rotor critical speeds. Detailed parametric experimentation was conducted to obtain the effect of different geometric parameters on the performance of the system (defined in terms of vibration attenuation) apart from estimating the stiffness of rings under static condition. The study very clearly indicated the high potential of the application of the newly conceptualized ISSFD rings for practical gas turbines in view of their suitability for space-constrained situations. The qualitative evaluation indicated substantial damping contribution (and hence the vibration reduction) and moderate stiffness contribution and hence shift in rigid body critical speeds.

Table 3 Stiffness values for three-grooved and four-grooved ISSFD rings

3 grooved ISSFD ring with 150° subtended angle (average $K = 3045.13$ N/mm)										
Loading line position (°)	0	15	30	45	60	75	90	105	120	
Stiffness (N/mm)	2201.63	2445.11	2972.11	6420.02	4405.96	1746.1	1733.87	2483.36	2980.07	
3 grooved ISSFD ring with 165° subtended angle (average $K = 2758.97$ N/mm)										
Loading line position (°)	0	15	30	45	60	75	90	105	120	
Stiffness (N/mm)	1357.32	2363.151.11	2470.18	2951.11	4096.5	4941.51	1788.45	2388.58	2473.86	
4 grooved ISSFD ring with 165° subtended angle (average $K = 2704.63$ N/mm)										
Loading line position (°)	0	15	30	45	60	75	90	105	120	
Stiffness (N/mm)	3218.69	3540.13	2300.27	2204.45	2142.09	2314.53	3212.26	-	-	

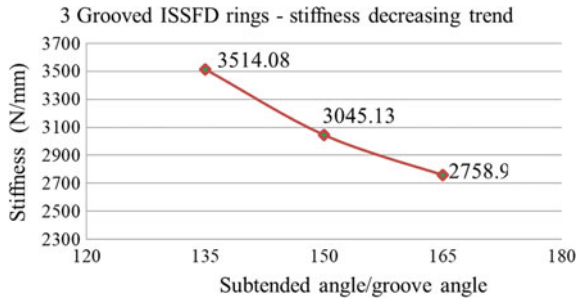


Fig. 7 Variation of average stiffness value with variation in subtended angle/groove length and overlap angle of grooves

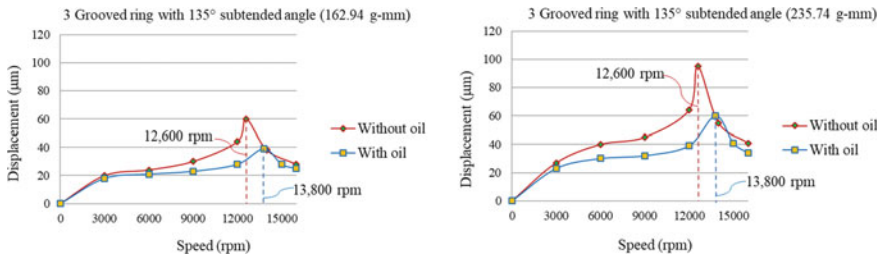


Fig. 8 Vibration amplitude for three-grooved ring with 135° subtending angle

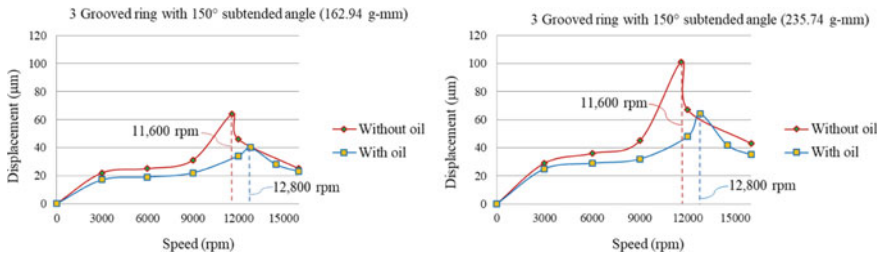


Fig. 9 Vibration amplitude for three-grooved ring with 150° subtending angle

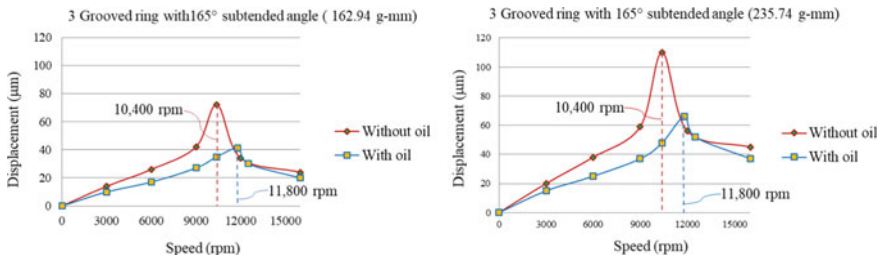


Fig. 10 Vibration amplitude for three-grooved ring with 165° subtending angle

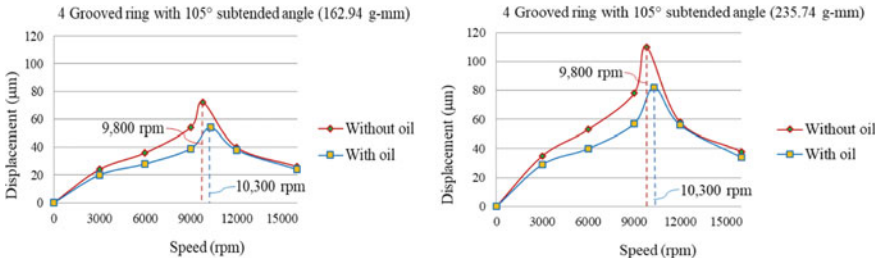


Fig. 11 Vibration amplitude for four-grooved ring with 105° subtended angle

Acknowledgements The authors immensely acknowledge the financial support received from: Gas Turbine Research Establishment (GTRE) under Gas Turbine Enabling Technology (GATET) scheme, DRDO, PO Box 9302, C. V. Raman Nagar, Bangalore-560 037 and B.M.S. College of Engineering, Bull Temple Road, Bangalore-560019.

References

1. Li Q, James YL, Hamilton F (1985) Investigation of the steady-state response of a dual-rotor system with inter-shaft squeeze film damper. In: Beijing International Gas Turbine Symposium and Exposition, Beijing, People’s Republic of China, September 1–7 1985
2. Li Q, James YL, Hamilton F (1986) Investigation of the steady-state response of a dual-rotor system with inter-shaft squeeze film damper. *J Eng Gas Turb Power* 108(4):605–612
3. Li Q, James YL, Hamilton F (1986) Investigation of the steady-state response of a dual-rotor system with inter-shaft squeeze film damper. *J Eng Gas Turb Power* 108(4):613–618
4. El-Shafei A (1991) Stability analysis of intershaft squeeze film dampers. *J Sound Vibr* 148(3):395–408
5. El-Shafei A (1988) A new design of intershaft squeeze film dampers. In: Proceedings of the Vibration Institute, pp. 15–23
6. El-Shafei A (1988) Stable intershaft squeeze film damper. United States Patent Number: 4,781,077
7. Defaye C et al (2006) Experimental study of the radial and tangential forces in a whirling squeeze film damper. *Tribol Trans* 49(2):271–278
8. Gupta K, Chatterjee S (2011) Theoretical analysis of improved designs of intershaft squeeze film damper for aero engine applications. In: Proceedings of the National Symposium on Rotor Dynamics, NSRD-2011, pp 179–190, 19–21
9. Gupta K, Chatterjee S (2006) An improved intershaft squeeze film damper device, Patent Number—199840
10. Jayaraman M, Arun Kumar V (2007) Compact flexible support for rotor bearing systems. Project Document, National Aerospace Laboratory

Characterization of a Squeeze Film Damper for Aircraft Engine Applications



Praveen Thirumalasetty, Kishore Vetcha, Mahesh Sivakumar, Tod R. Steen, and Anthony M. Metz

Abstract High-speed turbomachinery designs rely on adequate damping at the bearing supports to provide smooth operation throughout the sub-idle and normal operating speed ranges. Squeeze film damper (SFD) designs employ a thin oil film between bearing and housing that softens the bearing support and provides increase damping. During operation, the dynamic motion of the damper squeezes the thin lubricant film, thus generating hydrodynamic pressures and film forces to dissipate mechanical energy. This paper discusses test results from two different sealed SFD designs: The first design uses butt-end piston rings to seal the damper film where the oil exits the damper through a small circumferential gap in the piston rings. The second design uses an overlap piston ring design which more completely seals the oil in the damper. For this design, an alternate set of exit holes is provided to allow the oil to exit the damper. Testing was done over a range of frequencies from 20 to 300 Hz, with oil supply pressures from 14 to 140 psi, with oil temperatures from 75 to 225F and with SFD eccentricity ratios from 0.05 to 0.5, encompassing both cavitated and non-cavitated regimes of operation. The damping and added mass terms for the SFD were identified through standard data reduction algorithms. Test results indicate that for the same basic damper geometry, a significant difference in measured damping coefficient was obtained between the two different damper designs. Variation in damping using the overlap piston ring damper design was much less than

P. Thirumalasetty (✉) · K. Vetcha · M. Sivakumar
General Electric Aviation, Bangalore 560066, India
e-mail: Thirumalasetty.praveen@ge.com

K. Vetcha
e-mail: vetcha.kishore@ge.com

M. Sivakumar
e-mail: Sivakumar.mahesh@ge.com

T. R. Steen · A. M. Metz
General Electric Aviation, Cincinnati, OH 45215, USA
e-mail: tod.steen@ge.com

A. M. Metz
e-mail: Anthony.metz@ge.com

with the butt-end damper design due to the alternate set of exit holes at all operating conditions. No significant drop in damping observed at the cavitation regions for both the damper designs. Piston rings were observed to rotate. A discussion about the observed results is included.

Keywords Squeeze film damper · Damper and piston ring designs · Damping coefficient · Cavitation

Nomenclature

c	Damper clearance or damper film thickness
C	Damping coefficient
C	Damping coefficient calculated from test
C_r	Damping coefficient calculated from Reynolds solution for long bearings
F	Applied force
H	Dynamic stiffness
K	Support stiffness
M	Mass of the SFD
C_{SFD}	SFD damping coefficient
L	Damper land length
M_{SFD}	SFD added mass coefficient
R	Damper radius
x	Displacement of the damper
μ	Oil viscosity
ε/e	Eccentricity ratio
ω	Excited frequency
ω_n	Natural frequency

1 Introduction

Squeeze film dampers (SFD) are widely used in a multitude of rotating machinery, including aircraft engines and gas turbine engines used in marine and land applications and are primarily used to reduce engine/machinery vibration resulting from rotor unbalance excitations and to avoid or suppress instabilities. Squeeze film dampers are being incorporated in high-speed turbomachinery or aircraft engines as means to dissipate mechanical energy from rotor vibrations and to dampen out the structural component vibrations. Aircraft engines often have one to many squeeze film dampers with different feeding and sealing mechanisms to provide additional damping external to the bearings. The damping coefficient generated out of any SFD

should neither be low nor be high but should be optimal to be effective in isolating the vibrations.

The test objective is to measure damping coefficients of a practical squeeze film damper configuration with two different end seal concepts. The test varies operating conditions like damper oil temperature, oil pressure, damper eccentricity ratios and operating speed ranges. It is also intended to get an understanding of cavitation boundaries.

San Andrés et al. [1] summarized that the amount of damping force generated is the key criteria in designing any SFD. Damper can be characterized not only based on the input operating conditions, oil properties and damper geometry but also on the sealing arrangement, oil inlet and outlet configurations as well as cavitation. Defaye et al. [2] references that orifices and circumferential grooves are two oil feeding mechanisms into the damper cavity. Typical industrial squeeze film dampers employ several sealing configurations like piston rings, O-rings and end-plate seals to have an effective damping capacity. Jager et al. [3] attempted to explain the piston ring rotation phenomenon inside the damper grooves. Delgado et al. [4] conducted exhaustive experiments to characterize the mechanical parameters of SFD installed with an end mechanical seal and derived the damping and added mass coefficients in a frequency domain. San Andrés and Seshagiri [5] have carried out experiments to characterize the damping coefficients of a two end-sealed SFD with central groove. Two shakers in orthogonal directions are used to extract the damping parameters. Zeidan et al. [6] demonstrated the types of cavitation at different frequencies and pressure levels.

2 Test Rig

Squeeze film damper consists of an inner ring with grooves to install the butt-end piston rings which acts like a partial sealant. This inner ring is attached to the mandrel with shrink fitting assembly. A moving outer ring assembled on to the steel rods to give the system an isotropic structural static stiffness and to locate the damper. These steel rods are inserted into the mandrel that rigidly attaches to the baseplate which is grounded to the floor. The floor should have sufficient isolation capacity to isolate the vibrations from the damper to the rest of the building. A lubricant film is created by supplying oil at a specified pressure and temperature through a set of orifice feed holes from the outer ring to the clearance between the inner and outer rings. Damping is caused by the generation of dynamic tangential forces in squeezing the oil film for a given forced frequency excitation. Damper eccentricity ratio is a relative measure of the amount of squeezing inside the lubricant film (Fig. 1).

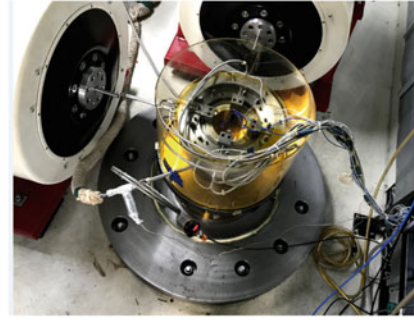
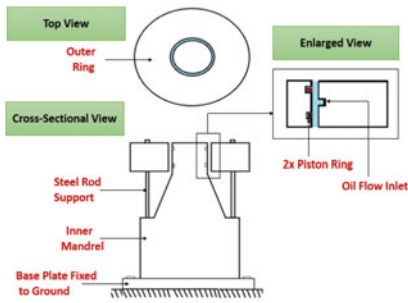


Fig. 1 SFD test rig layout

2.1 Shakers

Initially, the test rig was run with low force capability up to ~ 700 lbf which did not allow testing the damper at high eccentricity closures at high-frequency regimes above 200 Hz. Later, these are replaced with shakers with high force capability of 3000 lbf which can allow testing up to 350 Hz with a feedback-based control system that provides real-time damper displacements and orbit accuracy. These two shakers are mounted at 90° apart and impose a circular orbit to the damper outer ring with the help of long slender (stinger) rods that is mechanically coupled to the test damper. Care should be taken during stinger rods design so that it can withstand high-frequency force excitation loads in axial and lateral directions. These shakers are horizontally mounted onto the floor using isolation pads that help isolate the vibrations from the shaker. Damper can be centered using static preload from the shakers. The required shaker sizing can be evaluated based on Eq. (1) accounting for support stiffness and the weight of moving mass at various operating frequencies for a constant force. Most of the published SFD data is limited in frequency or tested with unsealed damper designs (low damping) due to limitations in available shaker force.

$$x = \frac{F}{\sqrt{(k - \omega^2 M)^2 + (\omega C)^2}} \quad (1)$$

- x Rotor orbit
- F Applied shaker force
- k Support stiffness
- M Damper assembly on centering steel rods
- C Expected damping capacity
- ω Operating frequency

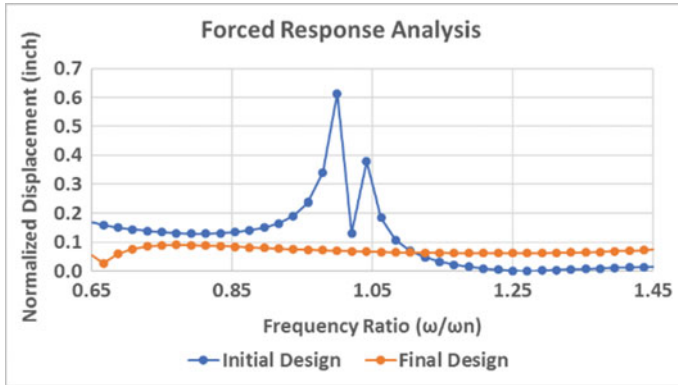


Fig. 2 Baseplate redesign analysis

2.2 Baseplate Redesign

Initially, the baseplate supporting the mandrel is a rectangular plate with gusset attachments grounded to the floor. But this fixture had a system mode within the operating regime which prevented testing above 200 Hz even to a small eccentricity levels. The baseplate was redesigned to move the system mode away from the test operating regime by simulating various design configurations using Ansys software. The final outcome of these iterations is a heavier baseplate that has overcome the design constraints. Figure 2 shows the shift in the responsive mode above 210 Hz for the final design out of the operating range. The amplitudes are range normalized.

2.3 Oil Circuit

Oil lubrication circuit mainly consists of an oil tank to store oil and has a provision to pump oil into the damper and recirculate it back to tank using variable frequency drive motors. In addition, the circuit has an inline heater for quick heating and a few filters to filter the oil going into and out of the damper. Flowmeter was installed in the oil circuit to measure the input supply flow rate for a particular operating condition. Flexible/rigid steel hose with insulation is used to supply the oil from the oil tank into the damper and recirculate it back. Thermocouple and pressure sensors were installed at the inlet to the damper supply to measure the corresponding temperatures and pressures (Fig. 3).

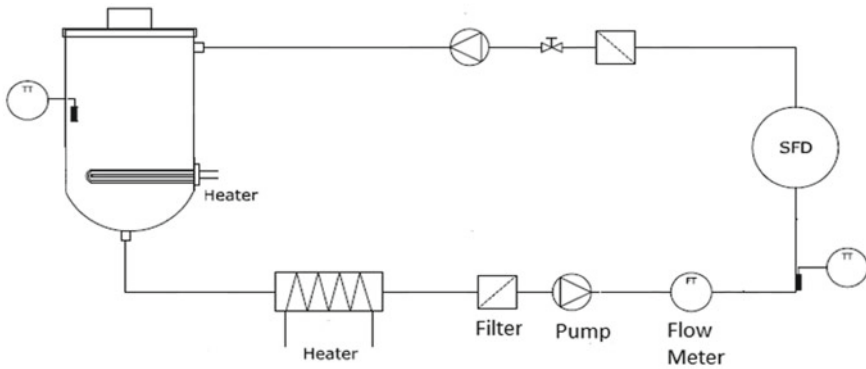


Fig. 3 Oil lubrication circuit

2.4 Sensors

Force sensors are attached to the damper outer ring to measure the applied forces from the shaker. Proximity probes are installed onto the damper test rig to measure the absolute displacements on the top and the bottom sides of the damper outer ring, accelerometers to measure the inner and the outer ring accelerations of the damper. Additional instrumentation includes thermocouples and dynamic pressure sensors installed inside the damper gap with the help of bonded adhesives to measure film temperatures and pressures.

2.5 Test Procedure

Dry tests (without oil) were conducted to estimate the stiffness and mass of the damper and were validated with hand calculations (Fig. 4).

Good correlation between model ($K-M\omega^2$) and test data is observed. Now, the oil is introduced into the damper and is force excited by the shakers in orthogonal direction to simulate the whirling motion of the damper outer ring. Shaker input force is controlled and was varied from small to very high forces resulting in low to high eccentricity ratios of the damper. This exercise will be repeated at various operating frequencies and oil supply conditions till the desired eccentricity ratio levels were reached.

The following parameters were taken during the test and were used to compute the damping through data reduction algorithms

1. Clearance closure in the damper film in orthogonal directions.
2. Applied shaker forces in two orthogonal directions
3. Acceleration of the moving inertial mass.

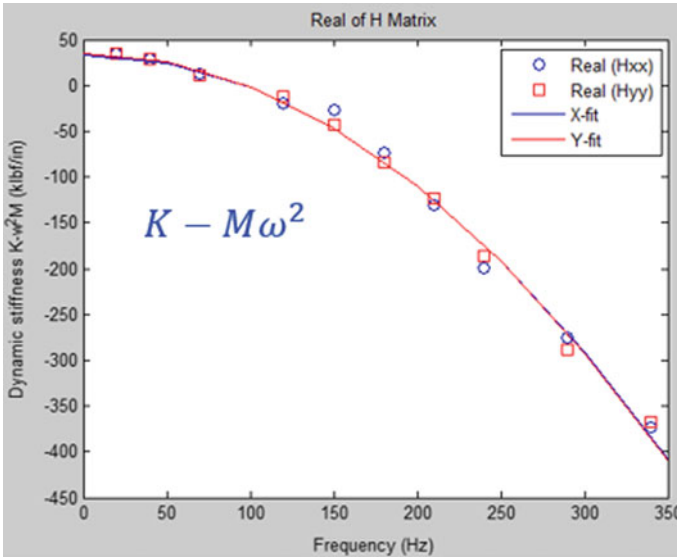


Fig. 4 Dry run test results

3 Damping Coefficient Calculation

The method to compute the damping coefficient out of the testing is as follows.

1. The inertial contribution of the moving outer ring can be subtracted out from the applied direct forces, resulting in a direct measurement of the damper forces

The dynamic coefficients are identified from Eq. (2) as in Ref. [7].

$$\begin{bmatrix} H_{xx} & H_{xy} \\ H_{yx} & H_{yy} \end{bmatrix} = \begin{bmatrix} \bar{F}_{x_1}^\circ & \bar{F}_{x_2}^\circ \\ \bar{F}_{y_1} & \bar{F}_{y_2} \end{bmatrix} \begin{bmatrix} \bar{x}_1^\circ & \bar{x}_2^\circ \\ \bar{y}_1 & \bar{y}_2 \end{bmatrix}^{-1}$$

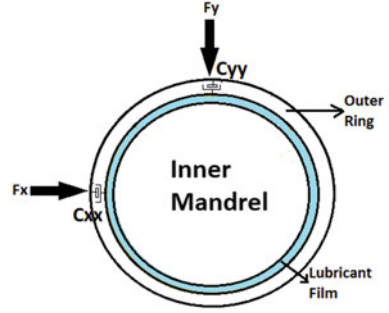
$$H_{ij}(\omega) = k_{ij} - \omega^2 M_{ij} + i\omega C_{ij}$$

Complex Dynamic Stiffness Matrix (2)

However, the total SFD forces acting in the system are combination of damping and inertia forces (Fig. 5)

$$\begin{Bmatrix} F_x \\ F_y \end{Bmatrix} = \begin{bmatrix} C_{SFD_{xx}}(e) & C_{SFD_{yx}}(e) \\ C_{SFD_{xy}}(e) & C_{SFD_{yy}}(e) \end{bmatrix} \begin{Bmatrix} \dot{x} \\ \dot{y} \end{Bmatrix} + \begin{bmatrix} M_{SFD_{xx}} & M_{SFD_{yx}} \\ M_{SFD_{xy}} & M_{SFD_{yy}} \end{bmatrix} \begin{Bmatrix} \ddot{x} \\ \ddot{y} \end{Bmatrix} \quad (3)$$

Fig. 5 Damper sketch



4 Test Results

In general,

1. Increased temperature reduced the damping till 0.1 eccentricity ratios as expected from a low viscous oil. But test results indicate that as the eccentricity ratio increases beyond 0.1, cold oil damping coefficient tends to be closer to hot oil damping (Fig. 6).
2. As eccentricity increases, damping stabilizes till the damper cavitates. Post-cavitation, we observed slight drop in damping.
3. Increase in supply pressure increases the amount of damping force till 80 psi, and beyond 80 psi, higher supply pressure has limited impact on the damping force (Fig. 7).
4. Higher the input excitation frequency, higher the damping force and viscous damping coefficient for a given supply oil condition.
5. Damping coefficient does not scale linearly with oil viscosity.

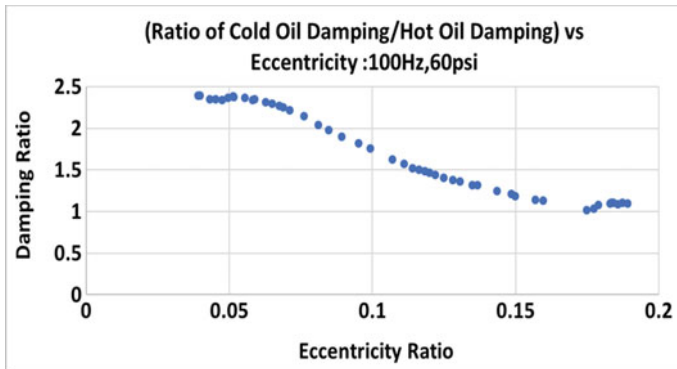


Fig. 6 Damping ratio versus eccentricity ratio at two different supply oil temperatures

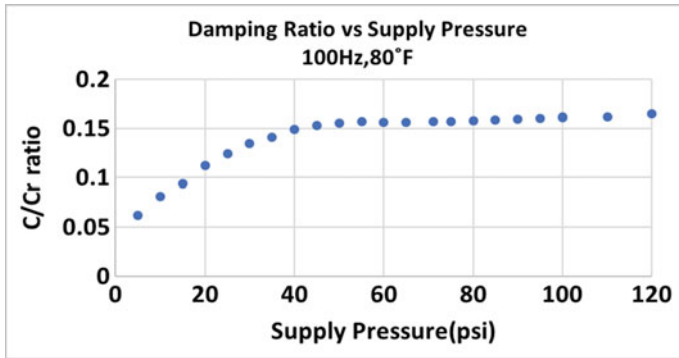


Fig. 7 Normalized damping (measured/theoretical) versus supply pressure

4.1 Damper Design's Comparison

The first damper design has a piston ring with a circumferential gap to allow oil exit, whereas the second damper design has an overlap piston ring that completely seals the oil flow with an alternate set of exit holes through them. Both the designs have the same radius, land length and film thickness (Figs. 8 and 9).

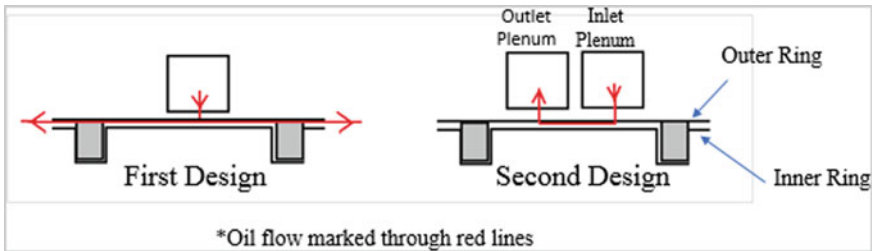


Fig. 8 Two damper designs with oil flow

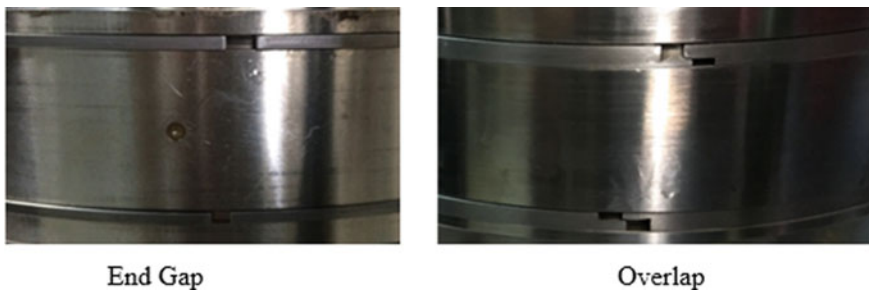


Fig. 9 Piston ring configurations

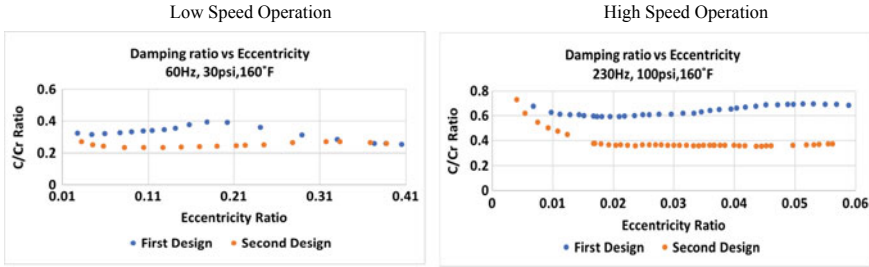


Fig. 10 Damping versus eccentricity ratio for low-speed and high-speed operating conditions: test results

In the first damper design, the relative position of the piston ring gap and the supply feed holes was observed to influence the effective damping, whereas, in the second damper design, as the piston rings do not have oil bleed gaps, damping was observed to be independent of the piston ring clock position.

Damping is ~45% lower in the second design compared to the first damper design as in Fig. 10 due to differences in additional oil exit holes and additional volume under the piston rings, and this effect is consistent with the CFD studies carried in reference [8]. Damping variation is less in the second design due to an alternate set of exit plenum under similar operating conditions. This overlap piston ring damper was observed to be less sensitive to the supply pressure variations and eccentricity variations compared to the butt-end seal damper.

Damping coefficient ratio is damping obtained from rig test data (C) to the damping obtained from Reynold’s long bearing solution (Cr) based on Eq. (2) for both the damper designs at various eccentricity ratio’s which is compared as below.

$$Cr = \frac{12\pi \mu R^3 L}{c^3(2 + \varepsilon^2)\sqrt{1 - \varepsilon^2}} \tag{4}$$

4.2 Cavitation Phenomena

The pressure profile in the squeeze film dampers has increasing pressures downstream of the minimum film gap up to a peak value and then reduces back up to the minimum film thickness. The low-pressure regions may contain low-pressure zones that are lower than vapor pressure of the oil. These lower than vapor pressure zones are prone to vapor cavitation. The cavitation zones thus formed keep rotating in the circumferential direction along with the damper shaft motion. The other form of cavitation that is observed is gaseous cavitation due to the presence of air as an impurity in the incoming oil. The cavitated zones would have lower viscosity and hence affect the damping characteristics. The onset and extent of cavitation depend on

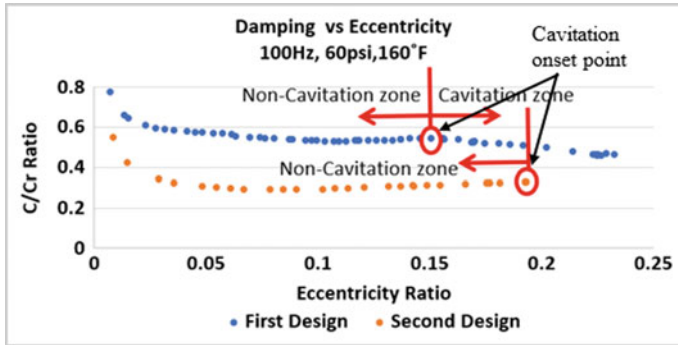


Fig. 11 Damping variation with cavitation

the inlet supply pressure and damper sealing mechanism. The operating eccentricity ratio and frequency are also important factors to understand cavitation.

Cavitation starts at lower eccentricity with low supply pressure and lower temperatures as well as with higher frequency excitation. Cavitation pressure distribution was captured with the installed dynamic pressure sensor instrumentation inside the film thickness.

Piston ring starts rotating as soon as the damper cavitates. Piston ring rotation was observed through the oil jet leak out of the piston ring. Piston ring rotational speed increases with increase in excitation frequency, and the max rotational speed went till ~10 Rev/h. Both the butt-end and the overlap piston ring rotate during cavitation, but the rotational speed of the overlap piston ring is lower compared to the butt-end design. Cavitation starts at a higher eccentricity in the second design than the first for the same operating condition as in Fig. 11.

One important observation is that damping did not decrease significantly with the damper going into cavitation zone, and transition from non-cavitation zone to a cavitation zone is gentle as shown in the below plot.

The damper film pressures were extracted from the dynamic pressure sensor instrumentation inside the damper film and Fig. 12 shows the change in film pressure over time domain (pseudo-time) transitioning smoothly from non-cavitated to cavitated zone with increase in eccentricity ratios for the first design. Damper film pressures saw some fluctuations on the maximum/minimum pressure side as soon as the damper cavitates, and the max pressure increases with increase in eccentricity ratios. The following plot is normalized to maximum pressure observed for the entire testing.

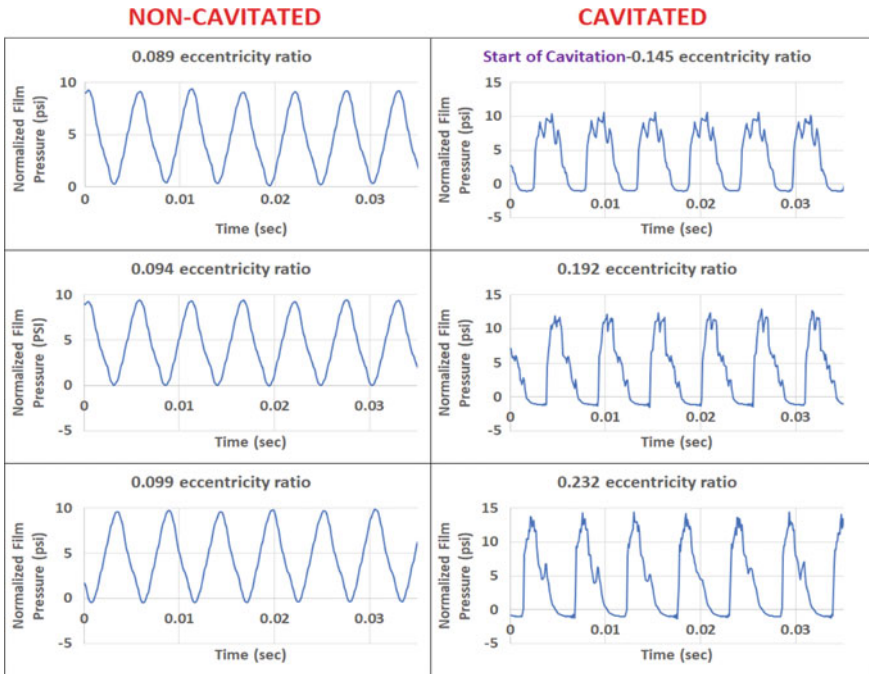


Fig. 12 Damper film pressure variation with cavitation

5 Conclusions

Transition from non-cavitation to cavitation takes place over a range of eccentricities with a smooth transition, and damping coefficient does not drop during cavitation unlike the theoretical predictions (Fig. 11).

Subtle changes in damper design lead to $2\times$ change in measured damping coefficient (Fig. 10), and this change in damping value is consistent with the parametric studies conducted based on the piston ring/groove dimensions and supply design. Test results point to the need for more sophisticated damping models able to capture the effects observed in these tests.

By completely understanding various damper piston sealing effects, one can improve the damper design to regenerate the damping force that will meet the requirements at all possible operating conditions within the design space. Extensive research is being conducted with various dampers of different hole sizes and different hole positions to validate the feasibility of the design.

References

1. San Andrés L, Den S, Jeung S-H, Savela G (2016) Squeeze film dampers: an experimental appraisal of their dynamic performance. *Asia Turbomachinery & Pump Symposium*, pp 22–25. <https://doi.org/10.21423/r12q4n>
2. Defaye C, Laurant F, Carpentier P, Arghir M, Bonneau O, Colboc S (2004) Squeeze-film damper predictions for simulation of aircraft engine rotor dynamics. *Proc Asme Turbo Expo Vienna Austria*. <https://doi.org/10.1115/GT2004-53447>
3. Jäger S, Bruchmüller T, Albers A (2012) Dynamic behavior and sealing performance of piston rings used in squeeze-film-dampers. *Sealing Technol* 9–13. [https://doi.org/10.1016/s1350-4789\(12\)70485-3](https://doi.org/10.1016/s1350-4789(12)70485-3)
4. Delgado A, San Andrés L (2010) Identification of force coefficients in a squeeze film damper with a mechanical seal: large contact force. *Asme J Tribol* <https://doi.org/10.1115/1.4001458>
5. San Andrés L and Sanjeev Seshagiri (2013). Damping and inertia coefficients for two end sealed squeeze film dampers with a central groove: measurements and predictions. *J Eng. Gas Turbines Power* 135(11), Paper No: GTP-13-1173; <https://doi.org/10.1115/1.4025033>
6. Zeidan FY, Vance JM (1989) Cavitation leading to a two-phase fluid in a squeeze film damper. *Tribol Trans* pp 100–104. <https://doi.org/10.1080/10402008908981868>
7. Delgado A, San Andrés L (2010) Identification of squeeze film damper force coefficients from multiple-frequency noncircular journal motions. *ASME J Eng Gas Turbines Power*. <https://doi.org/10.1115/1.3159374>
8. Lee GJ, Kim J, Steen T (2017) Application of computational fluid dynamics simulation to squeeze film damper analysis. *J Eng Gas Turbines Power* 139(10):102501-11. <https://doi.org/10.1115/1.4036511>

Stability of Parametrically Excited Active Magnetic Bearing Rotor System Due to Moving Base



Tukesh Soni, J. K. Dutt, and A. S. Das

Abstract Active magnetic bearings (AMBs) offer contact-less functioning and active vibration control capability while supporting and levitating a rotor. This is the reason that the AMBs are being progressively researched for novel and challenging applications in the industry. In application areas, such as ships, airplanes and space crafts, the rotor is mounted on a moving base, which causes parametric excitation to the system. This, in turn, is generally known to cause stability issues in a rotor shaft system. The present work thus attempts to conduct stability analysis of a rotor shaft system supported by an AMB and is parametrically excited due to the presence of periodically varying base motion. The finite element model for a generic rotor shaft system mounted on a moving base is first presented, and the time-periodic state matrix for the system is found. The Floquet–Liapunov method of analyzing stability of a periodically varying system is used to find the stability boundaries for the system with two widely used control laws for the AMB. The analysis reveals that it is important to consider the parametric excitation caused to the system when the AMBs are being designed for applications involving large base motions.

Keywords Active magnetic bearing · Parametric stability · Rotor dynamics

T. Soni (✉)
UIET, Panjab University, Chandigarh 160014, India
e-mail: tukeshsoni@gmail.com

J. K. Dutt
Department of Mechanical Engineering, Indian Institute of Technology Delhi, New Delhi 110016, India
e-mail: jkdutt@gmail.com

A. S. Das
Department of Mechanical Engineering, Jadavpur University, Kolkata 700032, India
e-mail: anindya990052003@yahoo.com

1 Introduction

Active magnetic bearings (AMBs) offer some major advantages over conventional bearings, namely contact-less support and an opportunity to actively control vibrations in the system. This results in lesser vibration and noise levels in the rotor system. This is also the reason that the AMBs are researched for novel and challenging applications in the industry. Reference [1] provides an excellent introduction to the AMBs. A detailed review on recent research advancements in the application areas of the AMB can be found in [2]. Rotor shaft systems subject to large base motion have been shown to be parametrically excited [3]. It is also well known that parametric excitation to rotor shaft systems may also lead the system to instability [4]. It is therefore necessary to conduct a thorough stability analysis of an AMB levitated rotor system, which is mounted on a moving base.

The issue of stability has been a concern for the researchers in the field of rotor dynamics for many decades [5–8]. Two major sources of instabilities have been clearly identified and extensively studied in the literature on rotor dynamics, namely the instability due to internal material damping and the instability due to rotor–fluid interaction in the fluid film type-bearings. The varying parameters of a system for example varying stiffness lead to another type of instability in rotors called the parametric instability. When the cross section of the rotor shaft is not axisymmetric, then the bending stiffness of the rotor shaft varies with the rotation of the rotor shaft and thus leads to parametric instability in such systems [9, 10].

Kamel and Bauomy [11] analyzed the stability of a nonlinear AMB-supported rigid rotor system with varying stiffness. Investigations into the steady-state stability with varying parameters were carried out. Bauomi [12] considered a similar system and studied the effect of cubic and quadratic nonlinearity of the stiffness on the dynamics of a rigid rotor-AMB system. Duchemin et al. [3] and later Driot et al. [13] analyzed the dynamics and stability of a rotor shaft system subject to periodic base motion. The rotor was considered to be simply supported. The equations of motion for a generic rotor shaft system with base motion were derived. However, Rayleigh–Ritz method was used to simplify the equations of motion to conduct the stability analysis. Han and Chu [14] conducted the stability analysis of parametrically excited flexible rotor shaft system with conventional bearings mounted on a base with periodic angular motion. Stability boundaries were drawn for various cases of periodic base motion frequency and amplitude. The authors used dynamic state transition matrix (DSTM) method to find the instability regions of the rotor shaft system. An interesting problem of stability of an aircraft rotor during the maneuvering of the aircraft is analyzed by Hou et al. [15]. In the work, the bearings were modeled as a Duffing-type nonlinear spring and dampers and the aircraft maneuver was modeled as a sine wave. The variation in bifurcation diagram for the system with respect to the aircraft maneuver was reported.

To the best of authors knowledge, the existing literature has a shortcoming that these research activities do not consider the stability analysis of a rotor shaft system levitated on an AMB and subject to parametric excitation due to large generic base

motion. Recently, Soni et al. [16] conducted parametric stability analysis of a rotor-AMB system subject to periodic base motion. However, the stability boundaries of the system with respect to base motion parameters were not reported. This research gap has inspired the authors to report the present work. This paper, therefore, conducts a stability analysis of a flexible rotor system which is levitated by an AMB and is aboard a moving base. Finite element model governing the motion of a generic rotor mounted on a moving base is first presented. Mathematical model of the force–current relationship of an AMB is then discussed. An efficient numerical algorithm based on the Floquet–Liapunov method of analyzing stability of a periodic system is introduced [17]. Results pertaining to the stability boundaries of the system are then presented.

2 Finite Element Model of a Rotor with Moving Base

The equation of motion of a rotor with large generic base motion has been derived in [18]. The resulting finite element model for such a system is reproduced in this section. A schematic of a rotor shaft system levitated and supported by an AMB with moving base is shown in Fig. 1. Three coordinate frames are defined and are also shown in Fig. 1. Frame, F_i , is the inertial reference frame, and F_{AMB} (with unit vectors $i_A - j_A - k_A$) is the coordinate frame attached to the rotor base at the left AMB, coordinate frame F attached to the rotor shaft. The global finite element matrices are given as:

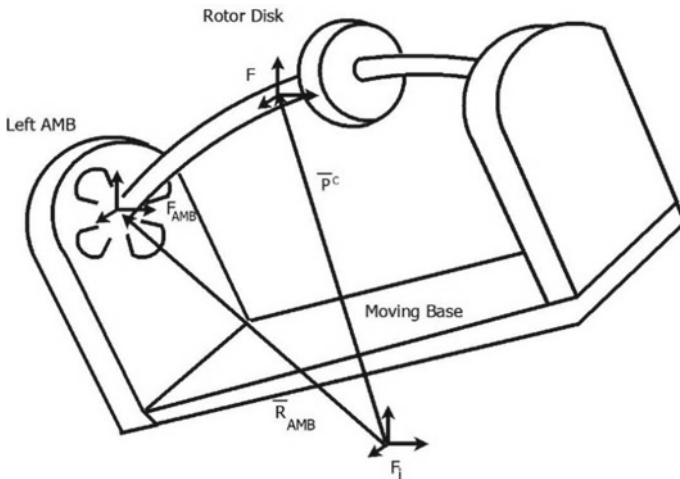


Fig. 1 Rotor disk system supported on AMB with base motion

$$[M] = \sum_D [M]_D + \sum_e [M]_S^e \quad (1)$$

$$[D] = (\Omega_{X_b}^b + \dot{\phi}) \left(\sum_D [G]_D + \sum_e [G]_S^e \right) + 2\Omega_{X_b}^b \left(\sum_D [C]_D + \sum_e [C]_S^e \right) + [D]_{\text{brg}} \quad (2)$$

$$[K] = - \left\{ (\ddot{\phi} + \dot{\Omega}_{X_b}^b) \left\{ \sum_D [H]_D + \sum_e [H]_S^e \right\} - \dot{\Omega}_{X_b}^b \left\{ \sum_D [C]_D + \sum_e [C]_S^e \right\} \right\} \\ \left\{ \Omega_{X_b}^{b^2} \left\{ \sum_D [M]_D + \sum_e [M]_S^e \right\} + \Omega_{Z_b}^{b^2} \left\{ \sum_D [K_{p11}]_D + \sum_e [K_{p11}]_S^e \right\} \right\} \\ \left\{ \Omega_{Y_b}^{b^2} \left\{ \sum_D [K_{p22}]_D + \sum_e [K_{p22}]_S^e \right\} - \Omega_{Y_b}^b \Omega_{Z_b}^b \left\{ \sum_D [K_{p12}]_D + \sum_e [K_{p12}]_S^e \right\} \right\} \\ + \{ [K_B]_S^e + [K]_{\text{brg}} \} \quad (3)$$

where $\dot{\phi}$ is the rotor spin speed and $\Omega^b = \Omega_{X_b}^b i_A + \Omega_{Y_b}^b j_A + \Omega_{Z_b}^b k_A$ is the angular velocity of the frame F_{AMB} with respect to inertial frame F_i .

Equation (1) gives the global mass matrix for the system $[M]$, $[D]$ is the global damping matrix and $[K]$ is the global stiffness matrix. From Eqs. (2) and (3), it can be seen that global stiffness and damping matrix contain the time-varying base motion parameters, and this leads to parametric excitation to the system. The objective of the present work is to study the stability of the system; therefore, the global force vector acting on the system by the virtue of base motion is not given here. Details regarding the other matrices are given in the Appendix.

3 Active Magnetic Bearing (AMB)

Active magnetic bearing is a mechatronic device which provides contact-less levitation of a rotor shaft system and has the active vibration control capability. The basic components of an AMB are the electromagnet pole pairs (radially arranged around the rotor shaft), proximity displacement sensors, power amplifiers, data acquisition system and the controller. A schematic of an AMB is shown in Fig. 2.

Linearized expressions for the force exerted by the AMB electromagnet can be written as [1],

$$F_Y = k_i i_{cY} - k_Y y_{\text{AMB}}; F_Z = k_i i_{cZ} - k_Z z_{\text{AMB}} \quad (1)$$

where k_i , k_Y and k_Z are constants for an electromagnet and depend upon the bias current (i_0) and the nominal air gap (g_0). Expressions for k_i , k_Y and k_Z are given

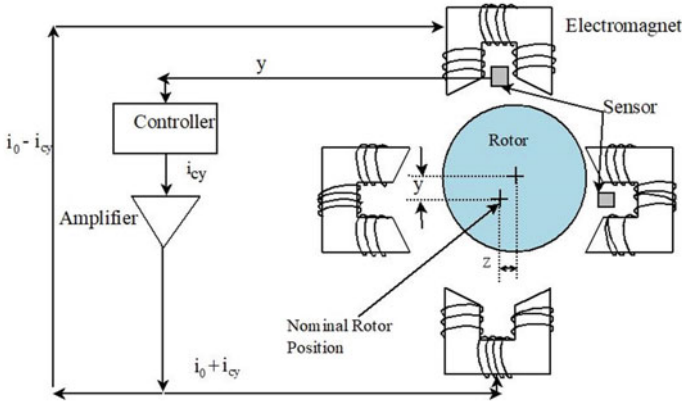


Fig. 2 Schematic representation of an AMB

in Eq. (5). i_{cY} and i_{cZ} are the control current provided to the vertical and horizontal electromagnet pairs. y_{AMB} and z_{AMB} are the corresponding excursions of the rotor at the location of the AMB proximity sensor (assumed to be collocated with the AMB, in the present study).

$$k_i = 4k_{mag} \frac{i_0}{g_0^2}; k_Y = k_Z = k_s = -4k_{mag} \frac{i_0^2}{g_0^3} \tag{2}$$

where $k_{mag} = \frac{\mu_0 A_p N^2}{4}$ is a constant for an electromagnetic actuator. A_p is the face area of the electromagnetic pole (m^2), N is number of coil turns and μ_0 is magnetic permeability of air. The control law decides the relationship between the control current i_{cY} and the displacement at the AMB location. For the case of a simple PID control law,

$$i_{cY} = -(k_p y_{AMB} + k_I \int y_{AMB} dt + k_d \dot{y}_{AMB}); i_{cZ} = -(k_p z_{AMB} + k_I \int z_{AMB} dt + k_d \dot{z}_{AMB}) \tag{3}$$

where k_p , k_I and k_d are the proportional, integral and derivative gains of the PID control law. Then, the assembled equations of motion for the rotor shaft system levitated by an AMB and mounted on a moving base can written as,

$$[M]\{\ddot{\Gamma}\} + [D]\{\dot{\Gamma}\} + [K]\{\Gamma\} + [C]\{\Gamma\} = \{0\} \tag{4}$$

where $\{\Gamma\}$ is the global displacement vector and the $[C]$ matrix represents the contribution of force on the rotor shaft due to the AMB. At the AMB node, the elemental $[C]$ matrix is given as,

$$[C]_{\text{AMB}}^e = \begin{bmatrix} k_i(k_p + k_1 \frac{1}{\mathcal{D}} + k_d \mathcal{D}) - k_Y & 0 & 0 & 0 \\ 0 & k_i(k_p + k_1 \frac{1}{\mathcal{D}} + k_d \mathcal{D}) - k_Z & 0 & 0 \\ 0 & 0 & 0 & 0 \\ 0 & 0 & 0 & 0 \end{bmatrix} \quad (5)$$

where \mathcal{D} is the differentiation operator, equal to $\frac{d}{dt}$.

4 Parametric Stability Analysis of Periodic Systems

The assembled equations of motion of the rotor-AMB system in Eq. (4) can be transformed into the state space form as follows,

$$\dot{x}(t) = A(t)x(t) \quad (6)$$

which represents a time-varying linear system. For the case of periodic base motion, the state matrix $A(t)$ is also periodic with $A(t + \mathcal{T}) = A(t)$ and \mathcal{T} is the fundamental time period of the state matrix. Efficient numerical method for ascertaining the stability of periodic system has been described by Friedmann et al. [17]. The method can be considered as a numerical counterpart to the Floquet–Liapunov’s theory of stability of linear periodic systems. The method is based on the eigenvalues of the state-transition matrix of the system. However, for a complex system, it may not be always possible to find the state-transition matrix; therefore, in this numerical method an estimated state-transition matrix is found. The method to find the estimated state-transition matrix is outlined in Fig. 3.

After the estimated state-transition matrix has been deduced, the stability regions can be found using the eigenvalues of the estimated state-transition matrix. The system is considered to be in a stable state if the following condition is satisfied,

$$\max(|\sigma + j\omega|) < 1 \quad (7)$$

where $\sigma + j\omega$ is the eigenvalue of the estimated state-transition matrix of the system.

5 Results and Discussion

5.1 System Details

An overhung rotor shaft system is considered for the stability analysis in this work [19]. The details of the rotor shaft system and the AMB used for simulation in this work are given in Table 1. Finite element discretization of the rotor shaft system is depicted in Fig. 4. The periodic base motion analyzed in this work is (a) periodic

Fig. 3 Steps to find the estimated state-transition matrix

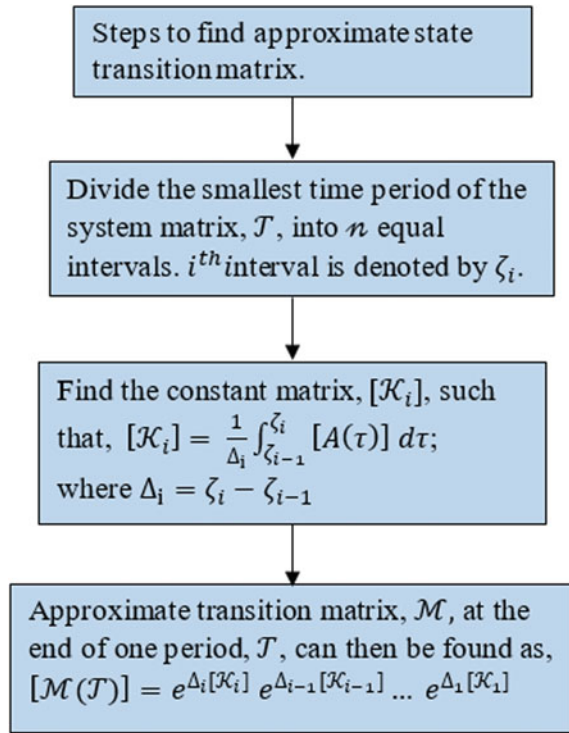


Table 1 Rotor shaft disk and AMB details

Rotor shaft disk details		AMB details	
Shaft length	1.5 m	Pole face area, A_p	500 mm ²
Shaft diameter	0.03 m	Current stiffness, k_i	177.4 N/A
Disk diameter	0.5 m	Displacement stiffness, k_s	-1.388 kN/mm
Disk thickness	0.07 m	Bias current, i_0	5 A
Young's modulus of elasticity	211 GPa	Radial air gap, g_0	2.5 mm
Density	7810 kg/m ³	AMB node location	1.5
Rotor spin speed	1000 rev/min		

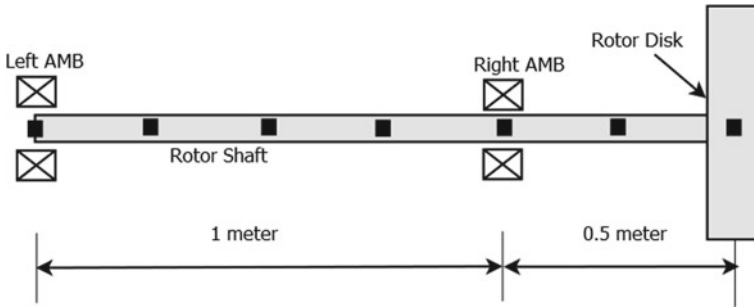


Fig. 4 Overhung rotor shaft AMB system with finite element discretization

pitch motion of the base (A_P —amplitude, ω_P —frequency), (b) periodic roll motion of the base (A_R —amplitude, ω_R —frequency) and (c) periodic yaw motion of the base (A_Y —amplitude, ω_Y —frequency).

5.2 Parametric Stability Boundaries

Figure 5 shows the stability boundaries for the overhung rotor system levitated by an AMB and subject to periodic base pitching. The condition of stability as per the Floquet–Liapunov method detailed in the previous section is that the maximum of absolute eigenvalue of the estimated state-transition matrix must be less than one (see Eq. 7). Therefore, it can be seen from Fig. 5, that for the case of periodic base pitching, the rotor shaft becomes unstable at the lowest frequency of around 15 rad/s for 0.4 rad base amplitude. Similar plots for the case of periodic base roll and yaw motion are shown in Figs. 6 and 7, respectively. For the case of base roll motion, the rotor-AMB system becomes unstable for a base roll frequency value as low as 3 rad/s for a 0.25 rad amplitude.

5.3 Free Vibration Response

To validate that estimated eigenvalue correctly predicts the stability of the rotor-AMB system, response due to initial conditions (free vibration) is simulated. To this end, an initial displacement of 1 mm in both horizontal and vertical directions is imposed at the rotor disk, and consequent response of the rotor disk is numerically simulated using the Newmark-beta method. The free vibration plot for the case of periodic base pitching with a frequency of 24.5 rad/s and an amplitude of 0.3 rad is shown in Fig. 8. As predicted by the value of the approximate eigenvalue (refer Fig. 5), unstable response at the rotor disk is observed. It must be noted the rotor-AMB system has

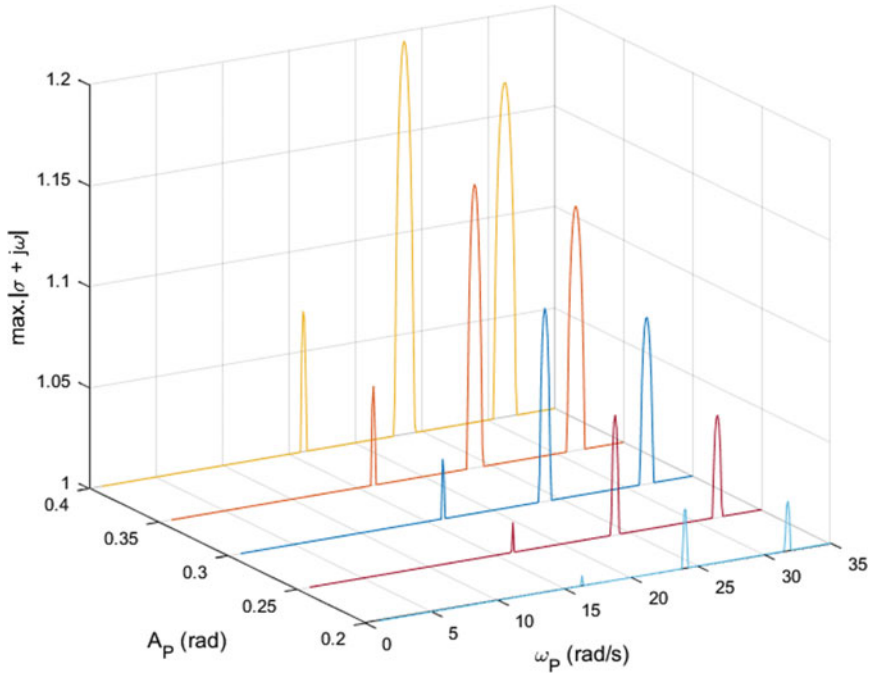


Fig. 5 Stability regions for case of base pitching

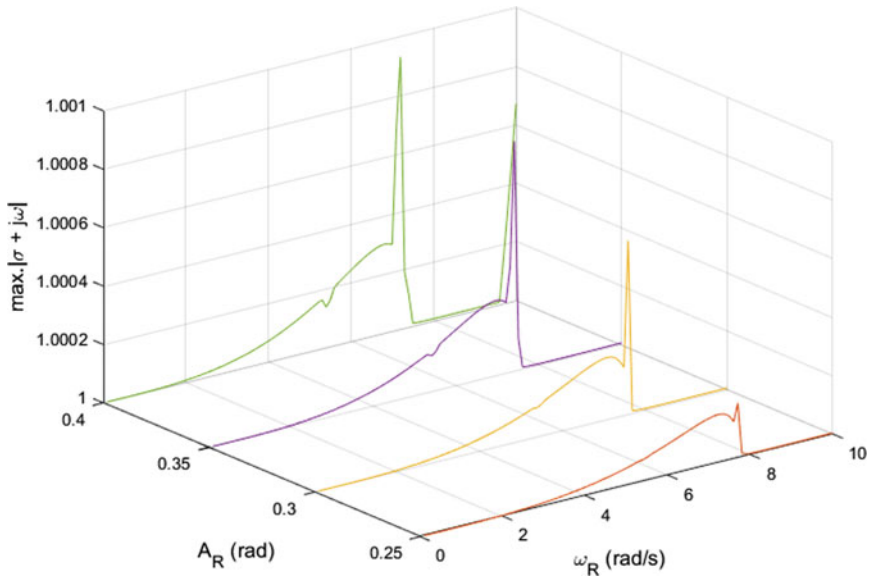


Fig. 6 Maximum absolute eigenvalue for periodic roll base motion

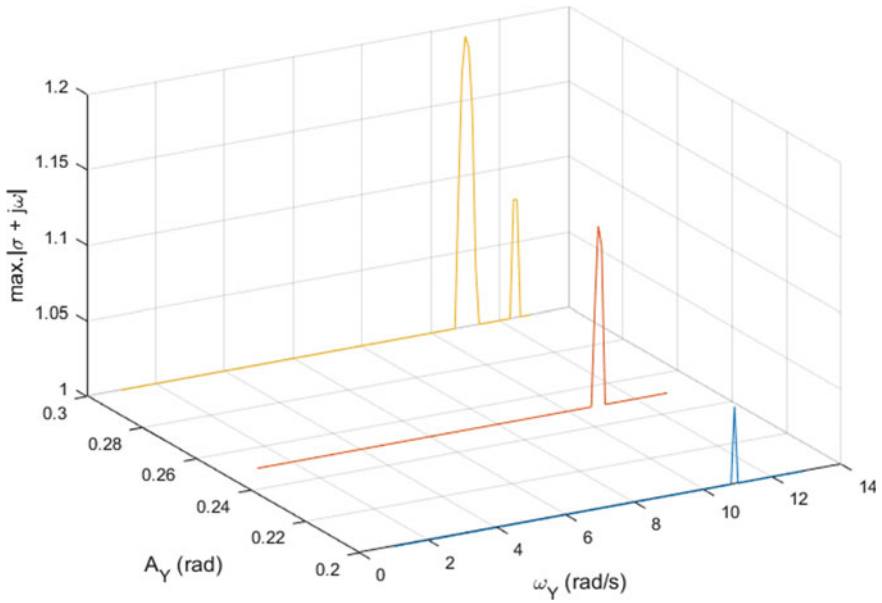


Fig. 7 Maximum absolute eigenvalue for periodic yaw base motion

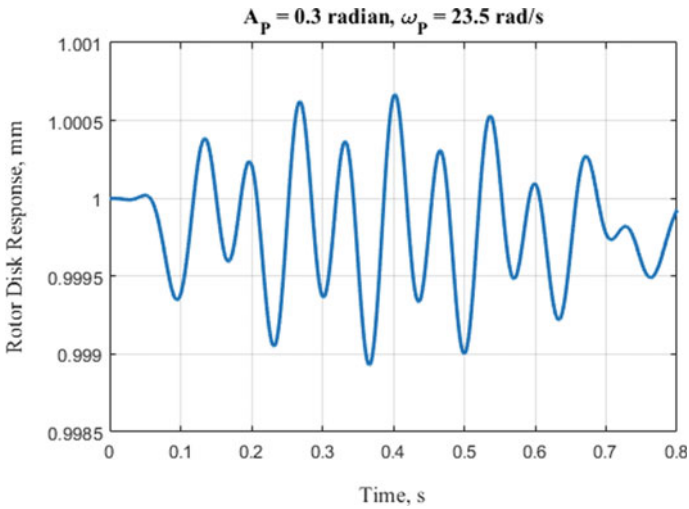


Fig. 8 Free vibration unstable response at the rotor disk due an initial displacement

been considered to be reasonably balanced, and only, the parametric excitation to the system is considered.

6 Conclusion

The following conclusions are drawn from this work:

1. Base motion in a rotor shaft bearing system causes parametric excitation to the system, which may result in excessive vibrations even in a reasonably balanced rotor.
2. While designing AMBs for the applications involving base motion, an exhaustive parametric stability analysis of the system must be conducted.
3. Depending upon the type of base motion, the rotor shaft system levitated on an AMB may become unstable at lower combinations of amplitude and frequency of the base motion. For example, for the case of periodic base rolling motion, the rotor-AMB system becomes unstable for frequency values as low as 3 rad/s and amplitude 0.25 radians.

Appendix

Details of the matrices used for finding the global matrices given in Eqs. (1)–(3).

Shaft Inertia matrix: $[M]_S^e = \int_0^l m[\psi(x)]^T[\psi(x)]dx + \int_0^l i_d[\psi'(x)]^T[\psi'(x)]dx$ where $[\psi]$ is the shape function matrix, gyroscopic matrix: $[G]_S^e = \int_0^l i_p[\psi']^T \begin{bmatrix} 0 & -1 \\ 1 & 0 \end{bmatrix} [\psi']dx$; $[H]_S^e = \int_0^l i_p[\psi']^T \begin{bmatrix} 0 & 0 \\ 1 & 0 \end{bmatrix} [\psi']dx$ bending stiffness matrix: $[K_B]_S^e = \int_0^l EI[\psi'']^T[\psi'']dx$; $[\psi''] = \frac{d^2[\psi(x)]}{dx^2}$.

Circulatory matrix: $[K_C]_S^e = \int_0^l EI[\psi'']^T \begin{bmatrix} 0 & -1 \\ 1 & 0 \end{bmatrix} [\psi'']dx$

Coriolis matrix: $[C]_S^e = \int_0^l m[\psi(x)]^T \begin{bmatrix} 0 & -1 \\ 1 & 0 \end{bmatrix} [\psi(x)]dx + \int_0^l i_d[\psi'(x)]^T \begin{bmatrix} 0 & -1 \\ 1 & 0 \end{bmatrix} [\psi'(x)]dx$

Parametric stiffness matrix due to base motion:

$$[K_{p11}]_S^e = \int_0^l m[\psi(x)]^T \begin{bmatrix} 1 & 0 \\ 0 & 0 \end{bmatrix} [\psi(x)]dx + \int_0^l i_p[\psi'(x)]^T \begin{bmatrix} 0 & 0 \\ 0 & 1 \end{bmatrix} [\psi'(x)]dx$$

$$[K_{p22}]_S^e = \int_0^l m[\psi(x)]^T \begin{bmatrix} 0 & 0 \\ 0 & 1 \end{bmatrix} [\psi(x)] dx + \int_0^l i_p [\psi'(x)]^T \begin{bmatrix} 1 & 0 \\ 0 & 0 \end{bmatrix} [\psi'(x)] dx$$

$$[K_{p12}]_S^e = \int_0^l m[\psi(x)]^T \begin{bmatrix} 0 & 1 \\ 1 & 0 \end{bmatrix} [\psi(x)] dx + \int_0^l (i_p - i_d) [\psi'(x)]^T \begin{bmatrix} 0 & 1 \\ 1 & 0 \end{bmatrix} [\psi'(x)] dx$$

Rotor disk finite element matrices

Inertia matrix: $[M]_D = \begin{bmatrix} m_D & 0 & 0 & 0 \\ 0 & m_D & 0 & 0 \\ 0 & 0 & I_d & 0 \\ 0 & 0 & 0 & I_d \end{bmatrix};$

Gyroscopic matrix: $[G]_D = \begin{bmatrix} 0 & 0 & 0 & 0 \\ 0 & 0 & 0 & 0 \\ 0 & 0 & 0 & -I_p \\ 0 & 0 & I_p & 0 \end{bmatrix};$

Coriolis effect matrix: $[C]_D = \begin{bmatrix} 0 & -m_D & 0 & 0 \\ m_D & 0 & 0 & 0 \\ 0 & 0 & 0 & -I_d \\ 0 & 0 & I_d & 0 \end{bmatrix};$ Parametric stiffness

matrix: $[K_{p11}]_D = \begin{bmatrix} m_D & 0 & 0 & 0 \\ 0 & 0 & 0 & 0 \\ 0 & 0 & I_p & 0 \\ 0 & 0 & 0 & 0 \end{bmatrix}; [K_{p22}]_D = \begin{bmatrix} 0 & 0 & 0 & 0 \\ 0 & m_D & 0 & 0 \\ 0 & 0 & 0 & 0 \\ 0 & 0 & 0 & I_p \end{bmatrix}; [K_{p12}]_D =$

$$\begin{bmatrix} 0 & m_D & 0 & 0 \\ m_D & 0 & 0 & 0 \\ 0 & 0 & 0 & I_p - I_d \\ 0 & 0 & I_p - I_d & 0 \end{bmatrix}$$



References

1. Schweitzer G et al (2009) Magnetic bearings: theory, design and application to rotating machinery. Springer, Berlin
2. Siva Srinivas R, Tiwari R, Kannababu C (2018) Application of active magnetic bearings in flexible rotordynamic systems—a state-of-the-art review. *Mechan Syst Signal Process* 106:537–572
3. Duchemin M, Berlioz A, Ferraris G (2006) Dynamic behaviour and stability of a rotor under base excitation. *ASME J Vibr Acoust* 128(5):576–585
4. Sinha SC, Marghitu DB, Boghiu D (1998) Stability and control of a parametrically excited rotating beam. *J Dyn Sys Meas Control* 120(4):462–470
5. Kirk RG, Gunter EJ (1974) Transient response of rotor-bearing systems. *J Eng Ind* 96(2):682–690

6. Vance JM, Zeidan FY, Murphy B (2010) Machinery vibration and rotordynamics. Wiley, Hoboken
7. Genta G (2007) Dynamics of rotating systems. Springer Science and Business Media, Berlin
8. Lalanne M, Ferraris G (1998) Rotordynamics prediction in engineering. Wiley, Hoboken
9. Muszynska A (2005) Rotordynamics. CRC Press, Boca Raton
10. Rao JS (1996) Rotor dynamics. New Age International
11. Kamel M, Bauomy HS (2009) Nonlinear oscillation of a rotor-AMB system with time varying stiffness and multi-external excitations. *J Vib Acoust* 131(3):031009
12. Bauomy HS (2012) Stability analysis of a rotor-AMB system with time varying stiffness. *J Franklin Inst* 349(5):1871–1890
13. Driot N, Lamarque CH, Berlioz A (2006) Theoretical and experimental analysis of a base excited rotor. *ASME J Comput Nonlinear Dyn* 1(3):257–263
14. Han Q, Chu F (2015) Parametric instability of flexible rotor-bearing system under time-periodic base angular motions. *Appl Math Model* 39(15):4511–4522
15. Hou L, Chen Y, Fu Y, Li Z (2016) Nonlinear response and bifurcation analysis of a Duffing type rotor model under sine maneuver load. *Int J Non-Linear Mech* 78:133–141
16. Soni T, Dutt JK, Das AS (2019) Parametric stability analysis of active magnetic bearing-supported rotor system with a novel control law subject to periodic base motion. *IEEE Transactions on Industrial Electronics*, p 1
17. Friedmann P, Hammond CE, Woo T-H, Efficient numerical treatment of periodic systems with application to stability problems. *Int J Numer Method Eng* 11:1117–1136
18. Das AS, Dutt JK, Ray K (2010) Active vibration control of flexible rotors on maneuvering vehicles. *Am Insti Aeronaut Astronaut (AIAA)* 48(2):340–353
19. Friswell MI, Penny JET, Garvey SD, Lees AW (2010) Dynamics of rotating machines. Cambridge University Press, Cambridge

Experimental Investigation on the Effect of Housing Profile and Its Relative Position on the Performance of Semi-Active Journal Bearing



Raghu Yogaraju , L. Ravikumar , G. Saravanakumar, and V. Arun Kumar

Abstract Demand for higher speeds, reduced noise and improved reliability along with other safety requirements necessitates an effectively controlled rotor dynamics system. The desired requirements are often not met by using conventional bearings which are passive in nature. Additional improvements can be achieved only with the aid of active or semi-active controls. A new concept adopted here is to conceptualize a semi-active journal bearing to simulate a multi-lobed journal bearing. This research work attempts to develop a semi-active journal bearing by modifying the profile of the bearing and position of the bearing with respect to the shaft. The performance is here defined in terms of attenuation of the vibration amplitude in the bearing plane. For different bearing profiles and various bearing positions, rotor responses are acquired experimentally and FE method is used to obtain extent of simulation with the experimental results. The study is predominantly experimental in nature, and a simple versatile instrumented test rig is designed and fabricated for the purpose. The results indicate a high potential toward practically realizing a semi-active control on journal bearing profile, resulting in quantitative reduction of vibration amplitudes and also benefits derived from optimally positioning the bearing.

Keywords Semi-active · Multi-lobed · Journal bearing · Initial eccentricity · Two-lobe bearing · Preload

R. Yogaraju (✉) · L. Ravikumar · G. Saravanakumar
Department of Mechanical Engineering, BMS College of Engineering, Bengaluru 560019, India
e-mail: raghuyogaraj.mech@bmsce.ac.in

L. Ravikumar
e-mail: lrkmech@gmail.com

G. Saravanakumar
e-mail: gurusaravana@yahoo.co.in

V. Arun Kumar
Department of Mechanical Engineering, Dr. Ambedkar Institute of Technology, Bengaluru 560056, India
e-mail: arun51149@gmail.com

1 Introduction

Most of the medium- to large-sized rotating machinery is supported on conventional journal bearings (basically passive in nature) in view of their simplicity in terms of geometry, design, load carrying capabilities and inherent presence of damping. In view of obtaining better control on vibrations arising out of varieties of reason, there exists a need to alter the bearing dynamics in terms of stiffness and damping leading to a requirement of active bearing systems. The active control aims at varying quantitative values of stiffness and damping by varieties of mechanisms.

The effective way to achieve active control on synchronous vibration depends mainly on variation of geometry of the bearing, controlling the position of the journal with respect to bearing or vice versa and control on the effective shaft length. The vibration due to self-excitation in rotor-bearing system can be reduced during operation by appropriate control on the flexible sleeve and choice of optimal hydraulic damper parameters [1]. The controlled position of bearing with respect to rotor will culminate in vibration reduction. The control over the bearing position can be achieved by using actuators like piezoelectric material and giant magnetostrictive materials (GMM)-based actuators [2–4]. The rotor-bearing system with certain mechanism developed to position a sliding bearing support such that the rotor lateral dynamics can be modified by controlling the effective rotor length. The natural frequencies can be arbitrarily shifted, where the resonance can be passed and vibration attenuation during operations can be achieved [5]. The isotropic, orthotropic and fluid film bearings positioned at different locations are modeled, analyzed (harmonic analysis) and compared using FE method [6]. Smaller clearance simply means higher Babbitt temperature, whereas inducing non-circularity by increase in lobe preload affects both static and dynamic characteristics [7]. The elliptical journal bearing is analyzed using the FEM by the application of linearized perturbation method on the classical Reynolds equation. Steady-state and dynamic performance characteristics give insight into the behavior of elliptical journal bearing with different preloads [8].

In the present work, an attempt is made toward conceptualizing a semi-active control journal bearing with a provision to realize varying housing profiles and also obtain varying relative shaft-bearing positions. A dedicated test rig designed facilitating the above requirement is fabricated for the purpose.

2 Test Rig Details

The test setup consists of a horizontally configured shaft supported on the test bearing as shown in Fig. 1a and driven by suitable motor as shown in 1b. The test bearing, which is of semi-active type consists of a thin cylinder (sleeve, part 1) surrounding the shaft, in between which a thin oil film (the journal is fed with oil through grooves on the sleeve and oil supply to grooves are provided using oil supply port, part 5) exists. The circular sleeve is connected to the housing (part 2) through one rigid support,

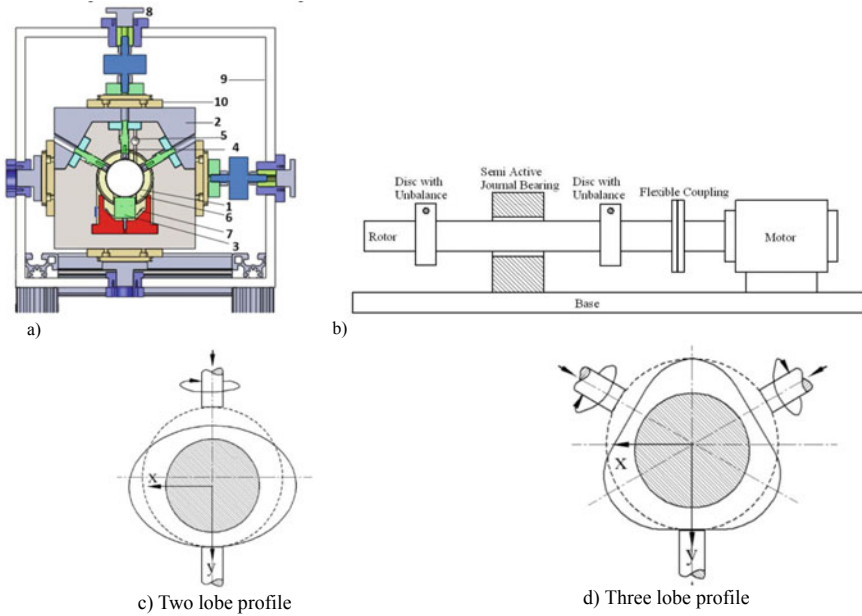


Fig. 1 Schematic and profiles of test rig

(part 3) and three non-rigid (part 4) supports and surrounded by elastomer, (part 6), to damp out chattering if any that may be induced during journal rotation. The non-rigid supports are provided with the knobs and shoes, and the shoes are designed such that it has an area contact with the cylindrical sleeve to attain non-circular profile modifications. The knobs have graduation to obtain different preloads, and these knobs are provided at 120° (10 ‘o’ clock position), 180° (12 ‘o’ clock position), 240° (2 ‘o’ clock position) from rigid support in anti-clockwise direction, to create two-lobe and three-lobe journal bearing profiles as shown in Figs. 1c, d. For example, to obtain a two-lobe bearing profile, the support at 180° (from the rigid support) has to be brought in contact with sleeve, by keeping the rigid support unaltered and the three-lobe bearing profile can be obtained by using non-rigid supports at 120° and 240°. The rotation of calibrated graduation knob on non-rigid support preloads the sleeve.

The shaft is provided with disk to mount desired unbalance mass for the purpose of excitation. The rig is also having facility to alter the position of the bearing housing with respect to shaft. In view of the equivalent stiffness being very low (cantilever type), the shaft would be sitting on the bearing under zero speed condition. The flexibility in realizing different eccentric positions is obtained using bearing displacement knobs (part 8) mounted on the rigid frame (part 9). The alteration in relative position of the shaft with respect to bearing center can be provided by change in the eccentricity in both x- and y-directions using four bearing displacement knobs (provided at top, bottom, left and right of rigid frame). For frictionless movement of bearing housing,



Fig. 2 Semi-active journal bearing test rig

Table 1 Details of test journal bearing system

Shaft material	Mild steel
Young's modulus	200 GPa
Shaft length	0.316 m
Shaft radius	0.0396 m
Disk mass	0.3 kg

the rig is provided with linear movement guides (part 10) in all four directions of test bearing, (part 2).

The instrumentation includes measurement of operating (speed, preload and shaft-bearing position) and response (amplitude of vibrations) parameters. The response parameters obtained would be utilized in evaluating test bearing performance quantitatively. As said earlier, the performance here is quantified in terms of vibration attenuation levels for different combinations of the operating parameters. The experimental study is parametric in nature, covering a wide range of operating parameters suitable for a typical steam turbine journal bearing. The instrumented test rig photograph is shown in the Fig. 2, and the details of rotor-bearing system are shown in Table 1. The journal displacement with respect to shaft in x and y are presented in Table 2 in terms of eccentricity (e) and attitude angle (ϕ).

3 Performance Studies

The methodology to estimate semi-active journal bearing performance in terms of reduction in vibration amplitudes is presented in this section.

Table 2 Journal displacement terminology

x, y	e, ϕ
0,0	0, 0°
0,100	0.5, 0°
25,100	0.52, 14°
50, 100	0.56, 26°
75, 100	0.625, 37°
100, 100	0.707, 45°

3.1 Experimentation

Experiments, parametric in nature, were conducted to obtain the effect of the ovality ratio, speed and relative initial position of shaft-bearing centers (different combinations of eccentricity and attitude angle). While the speed was varied up to 6000 rpm, the value of ovality ratio was kept in range 1.5–2 with the eccentricity and attitude angle varying from 0 to 0.9 and 0 to 90°, respectively. The unbalance mass was kept constant all through the experimentation at 55 g-mm (2 g mass located at radial distance of 27.5 mm). The relative position of shaft and bearing centers is designated as 2-x-y (x and y indicating horizontal and vertical distance of shaft and bearing centers from which eccentricity and attitude angles could be obtained, 2 indicating added unbalance is 2 g). The amplitude time history and phase information are acquired in x and y -directions. The leading edge of the reflecting tape produces the reference pulse. 1X amplitude and phase as a result of swept sine excitation are provided directly from the synchronous order analysis. The measured data was used to quantitatively evaluate stiffness and damping.

3.2 Harmonic Analysis Using Finite Element Method

The rotor-bearing system is modeled using FE method as shown in Fig. 3 for harmonic analysis. The rotor shaft is modeled using beam element; the rotor is supported on the bearing element at node 3, which supports both direct and cross-coupling coefficients. The evaluated stiffness and damping coefficients using experimental data are the inputs for bearing elements [9]. The disk is modeled using an element called mass element at node 2 and 4, and unbalance force is also applied at the same nodes. The harmonic analysis was performed for rotor spin speeds ranging from 0 to 6000 rpm with subset of 500 rpm. The critical speed analysis was carried out for different combinations of stiffness and damping and compared with the experimental critical speeds.

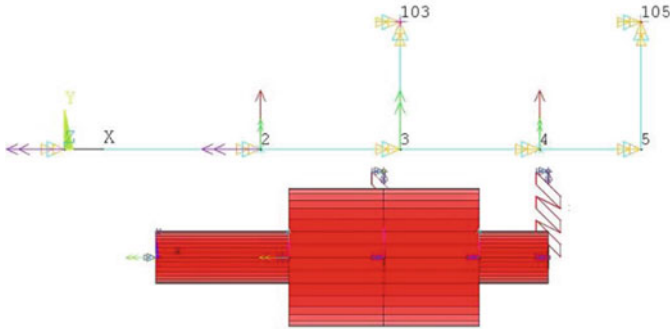


Fig. 3 FE model of test rig

4 Results and Discussions

The performance of the test journal bearing defined in terms of shaft vibration attenuation in the bearing plane (or the increase in load levels to realize similar vibration levels) obtained as a function of different influencing parameters like shaft speed, ovality ratio and relative position is presented here

4.1 Experimentation

Figures 4a–e shows variation of amplitude of vibration as a function of speed for circular (ovality ratio, $R = 1$) and two-lobe bearing with ovality ratio 1.25, 1.5, 1.75 and 2 and for different relative shaft-bearing positions (0–100 μm with intervals of 25 μm in both x and y -directions).

Figure 4a gives the complete details of the variation of vibration amplitudes as a function of speed for a circular bearing ($R = 1$) for different relative positions of shaft-bearing centers. It is very clearly observed that the maximum amplitude of vibration occurs when shaft center is very close to bearing center (x and y approaching zero) and vibration attenuation taking place for other combinations of x and y . Relatively, the highest level performance of the bearing (maximum attenuation in vibration amplitude) is observed with both x and y approaching 100 μm (i.e., at eccentricity = 0.707 and attitude angle = 45°). Further increase in x and y would probably yield better performance, but the same was restricted to 100 μm in order to compare with performance obtained with bearing with other ovality ratio. Figures 4b–e shows similar results obtained for bearings with different ovality ratios. The increased ovality ratio has dominant effect on vibration attenuation levels as the critical speed has shifted beyond the operating speed range. While the combination of circular bearing and x and y displacements of bearing with respect to shaft (eccentricity) being zero results

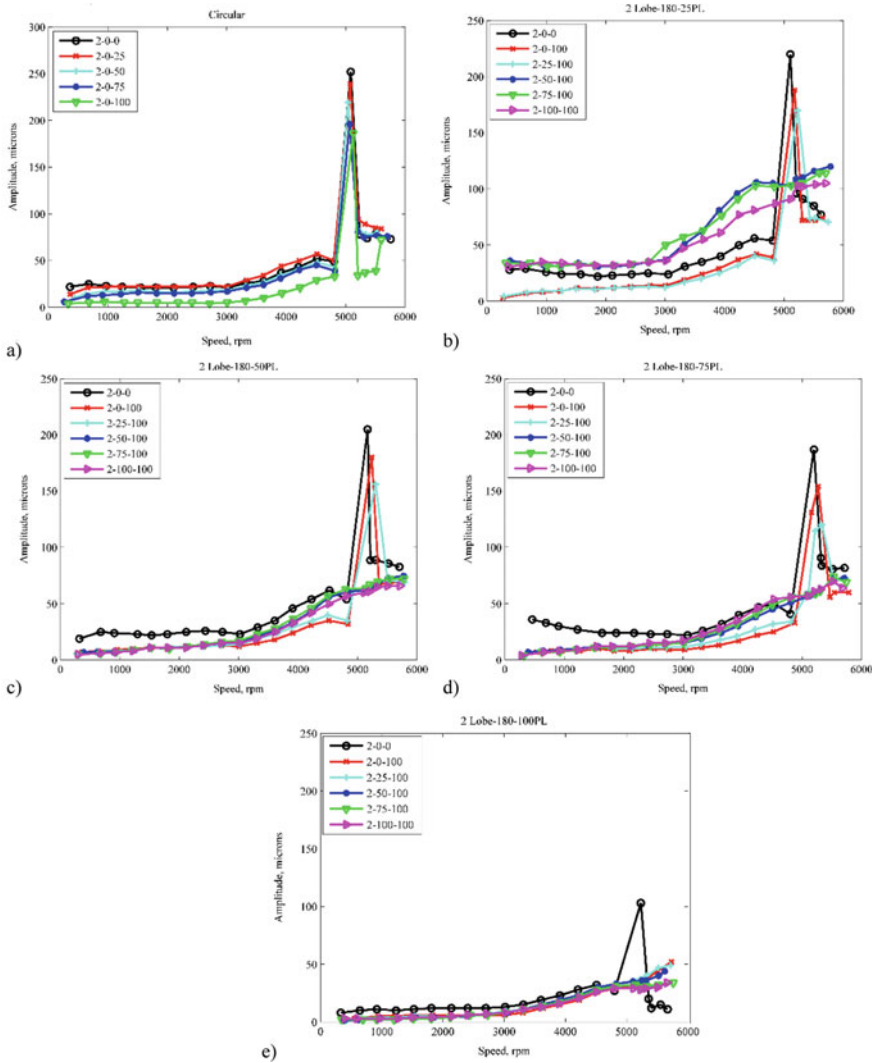


Fig. 4 Amplitude response as a function of speed for different preloads and relative positions of the shaft with respect to housing **a)** circular, $R = 1$, **b)** elliptical, $R = 1.25$, **c)** elliptical, $R = 1.5$, **d)** elliptical, $R = 1.75$, **e)** elliptical, $R = 2$

in the lowest performance level, the bearing with the ovality ratio ‘2’ and x and y positions approaching 100 μm provides higher performance level.

4.2 FEM Approach

Figure 5a shows response amplitude for circular profile indicating the maximum amplitude of vibration at 4920 rpm (as against experimentally observed speed of 5060 rpm-refer Fig. 4a). Similarly, Figs. 5b–e shows the amplitude response for ovality ratios 1.25, 1.5, 1.75 and 2, respectively. It is clearly observed that increased ovality ratio increases the critical speed as well as decreases amplitude of vibration. The FEM results are well validated with that of experimental.

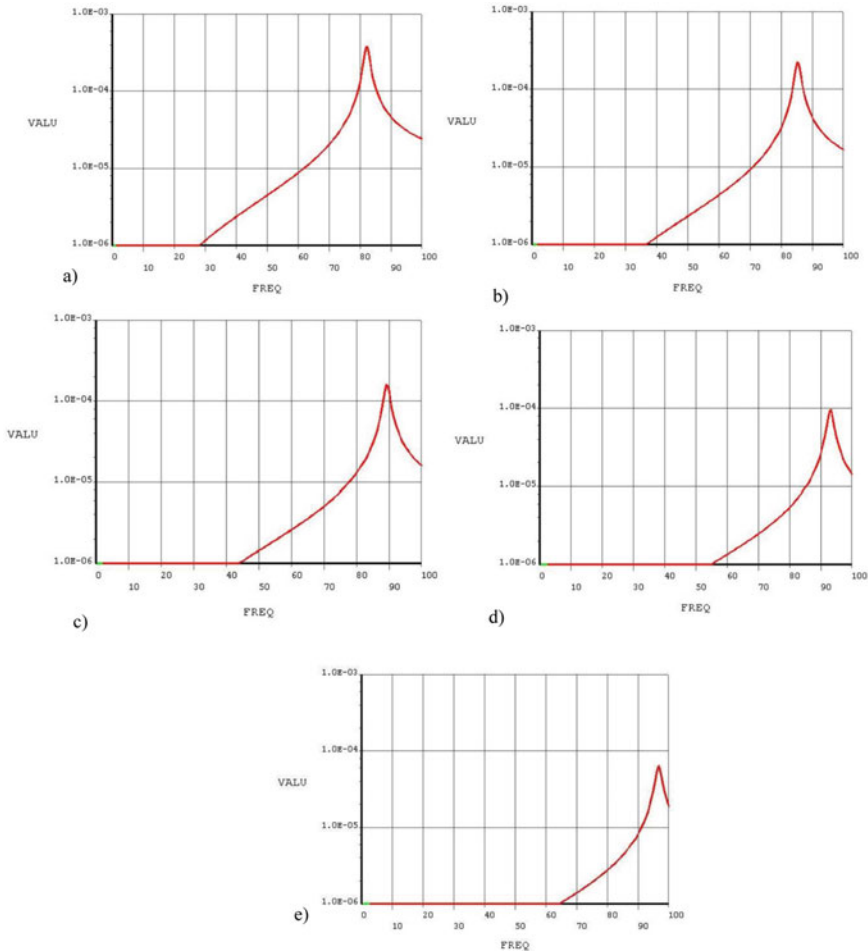


Fig. 5 Amplitude response as a function of speed of the system for different ovality ratios using FEM, a) circular, $R = 1$, b) elliptical, $R = 1.25$, c) elliptical, $R = 1.5$, d) elliptical, $R = 1.75$, e) elliptical, $R = 2$

The results revealed that the increase in ovality ratio increases the dynamic stiffness (reason for increase in critical speed) and damping (known by reduced amplitude) parameters compared to the case of circular profile. The results proved that the dynamic stiffness and damping parameters can be semi-actively controlled in a journal bearing by varying the ovality ratio and shaft-bearing relative position.

5 Conclusions

A dedicated instrumented test rig was designed and fabricated for the purpose of conducting experiments, and to obtain the effect of the variation in different parameters on the performance levels of semi-active journal bearings. Different parameters considered were speed (varied up to 6000 rpm), ovality ratios (1–2) and relative shaft-bearing positions (0–100 μm in x - and y -direction, varies eccentricity and attitude angle). The increase in ovality ratio results in improved performance levels in addition to the benefits realized from increase in eccentricity ratio. The effort has indicated very high potential toward practical applications.

Acknowledgements The authors acknowledge the financial support received from TEQIP-III, BMS College of Engineering and all the authorities who have helped to file a patent on this work.

References

1. Krodkiewski JM, Cen Y, Sun L (1997) Improvement of stability of rotor system by introducing a hydraulic damper into an active journal bearing. *Int J Rotating Mach* 3:45–52. <https://doi.org/10.1155/S1023621X97000055>
2. Lau HY, Liu KP, Wang W, Wong PL (2009) Feasibility of using GMM based actuators in active control of journal bearing system. In: *Proceedings of the World Congress on Engineering*. <https://pdfs.semanticscholar.org/3c0d/cec45325ba081e2bb90bb7e138900da6493c>
3. Alkhfaji SS, Garvey SD (2011) Vibration control of rotating machines using actuated bearing seating's. *The International conference surveillance*, 25–26 October 2011. https://www.researchgate.net/publication/269986689_Vibration_Control_of_Rotating_Machines_Using_Actuated_Bearing_Seatings
4. Zhou Hua, Zhao Sanxing, Hua Xu, Zhu Jun (2004) An experimental study on oil-film dynamic coefficients. *Tribol Int* 37:245–253. <https://doi.org/10.1016/j.triboint.2003.08.002>
5. Silva-Navarro G, Lopez-Medina F, Cabrera-Amado A (2010) Unbalance compensation in a rotor-bearing system by dynamic stiffness control and acceleration scheduling. *Dynamics of Rotating Machinery. Proceedings of ISMA*. http://past.isma-isaac.be/downloads/isma2010/papers/isma2010_0625
6. Ghade U, Gangrade AK (2016) Performance analysis of non-circular hydrodynamic journal bearing using CFD. *Int J Adv Technol Eng Sci* 4:502–508. 1459266587_410N
7. He M, Cloud CH, Byrne JM (2015) Fundamentals of fluid film journal bearing operation and modeling. In: *Proceedings of thirty-fourth Turbomach symposium*, 155–175. https://www.researchgate.net/publication/294890540_Finite_Element_Analysis_of_Oil-Lubricated_Elliptical_Journal_Bearings

8. Faria MTC (2015) Finite element analysis of oil-lubricated elliptical journal bearings. *Int J Mech Mechatron Eng* 9(5):716–721. https://www.researchgate.net/publication/294890540_Finite_Element_Analysis_of_Oil-Lubricated_Elliptical_Journal_Bearings
9. Yogaraju R, Ravikumar L, Saravanakumar G, Shravana Kumar C, Arun Kumar V (2016) Feasibility and performance studies of a semi-active journal bearing. *Proc Technol* 25:1154–1161. <https://doi.org/10.1016/j.protcy.2016.08.233>

Some Fundamental Issues in Foil Bearings



P. Samanta, N. C. Murmu, and M. M. Khonsari

Abstract While the foil bearing technology is well established, some inherent issues must be addressed at the design stage to vastly expand its utilization. This paper highlights the need for one of the critical problems dealing with the need for accurate prediction of maximum temperature of the shaft and bearing to avoid failure due to thermoelastic instability (TEI). A brief description of the cause and consequence of TEI along with a simple prediction methodology is presented.

Keywords Foil bearing · Thermoelastic instability · Transient analysis

Nomenclature

W	Heat flux, W/m^2
μ	Viscosity of air, $N\cdot s/m^2$
h	Film thickness, m
ε	Coefficient of thermal expansion, $1/^\circ C$
k	Thermal diffusivity, m^2/s
K	Thermal conductivity, $W/m\cdot K$
R_o	Outer radius of bearing, m
R_s	Inner radius of bearing, m
T	Temperature, $^\circ C$
t	Thickness of foil, m

P. Samanta (✉) · N. C. Murmu
Surface Engineering and Tribology, CSIR-Central Mechanical Engineering Research Institute,
MG Avenue, Durgapur 713209, WB, India
e-mail: p_samanta@cmeri.res.in

N. C. Murmu
e-mail: murmu@cmeri.res.in

M. M. Khonsari
Department of Mechanical and Industrial Engineering, LSU, Baton Rouge, USA
e-mail: khonsari@lsu.edu

- (_b) Subscript b stands for bearing
- (_j) Subscript j stands for journal
- ' Term with prime indicates due to perturbation

1 Introduction

The history of foil bearing (FB) development goes back to more than sixty years ago when Block and Von Rossum investigated the effect of flexibility on the hydrodynamic film in the 1950s [1]. The concept of introducing flexibility on hydrodynamic film was, next, taken a newer height by Gross [2]. After twenty years, the FB was put to use in the air handling system of aircrafts for the first time [3]. The initial designs of FB were primarily tension dominated. Today's most of FBs are of bending-dominated where the rigid surface is replaced by this metal foil supported by a corrugated foil as shown in Fig. 1 [4, 5]. The interested reader is referred to a recent article on the evaluation of foil bearing [6].

Although the geometric configuration of an FB is quite simple, the intricate coupling of the foil structures with compressible hydrodynamic film renders the analysis and performance prediction very difficult. Hence, the technology remains to be highly specialized, and unlike the conventional rolling element and oil-lubricated hydrodynamic bearings, one cannot easily select and order an FB from a catalog [7]. Each FB must be designed explicitly for a distinct application. Indeed, the design and development of an FB require thorough analysis and testing, making the development costly. The interested reader can refer to the work of Radil and DellaCorte who recommended a four-step process for development a new FB to mitigate the failure risk of the bearing [8]. Those four steps include (1) rotor dynamic feasibility and layout trade study, (2) bearing sizing and testing, (3) experimental rotor dynamic simulator validation tests, and (4) system-level demonstration. In addition, this article points to the need for evaluating the thermoelastic instability (TEI) potential at the stage. A simple strategy for preliminary evaluation of TEI is outlined.

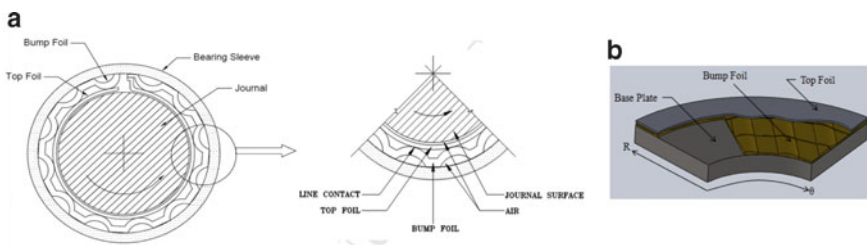


Fig. 1 Configuration of foil journal and thrust bearings. **a** Foil journal bearing [4]. **b** Foil thrust bearing [5]

2 Thermoelastic Instability

Thermoelasticity deals with the response of the elastic body in a non-uniform temperature field. In case of an FB, this non-uniform temperature field is created due to viscous shearing in a non-uniform pressure or stress field. The non-uniform pressure or stress field is created due to the non-uniform film thickness. The physical sources of this non-uniformity are described in details in the next sub-section. When the heat generated due to viscous shearing in the clearance propagate in the non-uniform stress field, heat will accumulate in the high-stress zone and create a thermal gradient. This excessive thermal gradient can diminish the air film and lead to high-speed rubbing and ultimately cause failure often with catastrophic consequences. This phenomenon is called thermoelastic instability (TEI). While fairly rich volumes of published theoretical works dealing with TEI for dry contact in seal-like structures [9–11], lubricated sliding contact [12] with provision for surface roughness in this sliding contact [13] exist, available work on the nature of TEI dealing with compressible fluid is far less. Surprisingly, however, there is ample experimental evidence of occurrences of TEI in FBs. Dykas and Howard observed the repeated failure of bearing during testing of bearing at high temperature (538 °C) at high speeds (60,000 rpm) and moderate loads (222 N) [14]. In one application, although the operating temperature was 538 °C, the temperature at the mid-section of the journal, due to TEI, reached its melting point (~1400 °C) and a dime-sized hole was created. This cause of failure of the journal is described in the following sub-section. Lee et al. also experienced TEI phenomenon during experiments with foil journal bearing at speed of 35,000 rpm and load of 97.7 N [15]. Their theoretical model on TEI predicts the air film breakdown at a load of 106.6 N. Similar TEI in foil thrust bearing is also observed by other researchers [16, 17]. Clearly, a methodology for predicting TEI in foil bearings that can be used at the design is crucially needed to provide insight into the experimental observations and guard against such failures.

2.1 *Relative Expansion of Journal Surface*

Physically, in FBs the transient clearance loss due to the expansion of bearing surface lags relative to journal surface during start-up or growth of surface wave. This is due to the non-uniform temperature field in high sliding speeds. In this section, we will scrutinize the details of this phenomenon. An FB is essentially a high-speed air bearing. The internal temperatures of the bearing are mainly dependent upon the surrounding environment temperature and the heat generated due to viscous shearing. Although the viscosity of air is low, a significant amount of heat is generated due to high surface speed. Since thermal capacity of air is also low, it has limited capability to carry the heat out of the bearing. Thus, the generated heat must necessarily be absorbed by the bounding metal surfaces of journal and bearing. A simplified formula

for the heat flux generated due to viscous shear loss is given by the following equation [18]:

$$W = \frac{\mu U^2}{h} \tag{1}$$

The rate of expansion of journal and bearing surface due to this heat input is given by the following expressions. The reader may refer to Ref. [18] for its detailed derivation.

$$\left(\frac{dr}{dt}\right)_j = \frac{2\varepsilon_j W_j k_j}{K_j} \tag{2}$$

$$\left(\frac{dr}{dt}\right)_b = \frac{2\varepsilon_b W_b k_b}{K_b \left[\left(\frac{R_o}{R_s}\right)^2 - 1 \right]} \tag{3}$$

where W is distributed between the journal and bearing surface, hence $W = W_j + W_b$.

Substituting the expression for heat flux from Eq. 1 and using the material properties of Inconel into Eq. 2, one can obtain the expansion rate of the journal. The expressions for k and K are obtained from Ref. [19].

$$\mu = \frac{1.462 \times 10^{-6} (T + 273.15)^{1.5}}{T + 273.15 + 112} \tag{4}$$

$$k = -10^{-14} T^3 + 10^{-11} T^2 + 5 \times 10^{-10} T + 2.96 \times 10^{-6} \tag{5}$$

$$\varepsilon = -10^{-15} T^3 + 10^{-12} T^2 - 7 \times 10^{-9} T + 1.1226 \times 10^{-5} \tag{6}$$

$$K = 11.45 + 1.156 \times 10^{-2} T + 10^{-6} T^2 \tag{7}$$

The expression for ε is obtained from Ref. [20].

Figures 2 and 3 show the rate of expansion of the journal with a surface speed of the journal and temperature, respectively. From these plots, it is observed that the effect of speed variation on the journal expansion is higher than the temperature. Thus, when the bearing speed is above a threshold speed, the bearing will become susceptible to TEI. A closed-form expression for predicting the critical speed at which TEI occurs is given by the following expression [4]:

$$U_{cr} = h\Omega \sqrt{\frac{K}{\alpha\mu R} \left(\frac{1 - \sqrt{1 - 8F}}{4F} \right)} \tag{8}$$

For detail of the above expression, the reader may refer Ref. [4].

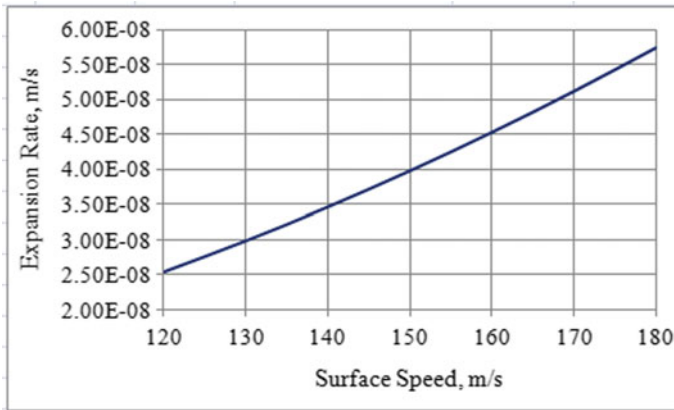


Fig. 2 Journal expansion rate with speed

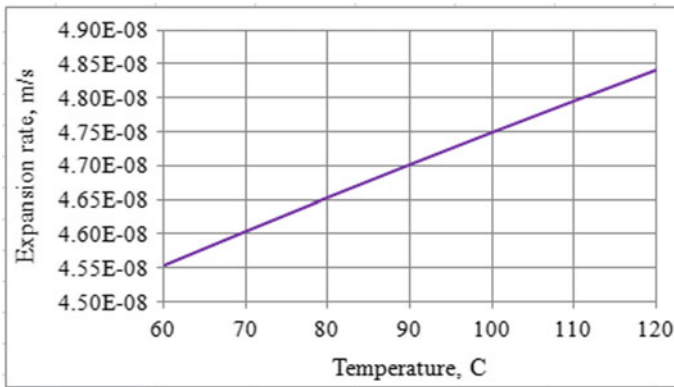


Fig. 3 Journal expansion rate with temperature

2.2 Transient Expansion of the Journal and Bearing

When the bearing and journal are made of the same material and the perturbed heat is equally distributed among bearing and journal, the expressions for transient expansion of journal and bearing will be obtained from Eqs. 2 and 3 as follows:

$$\left(\frac{dr'}{dt}\right)_j = \frac{\varepsilon W'k}{K} \tag{9}$$

$$\left(\frac{dr'}{dt}\right)_b = \frac{\varepsilon W'k}{K \left[\left(\frac{R_o}{R_s}\right)^2 - 1 \right]} \tag{10}$$

By subtracting the expansion rate of journal given in Eq. 9 from bearing in Eq. 10, one can have the rate of change of film thickness as follows [18]:

$$\frac{dh'}{dt} = -\frac{\varepsilon W'k}{K} \left[\frac{(R_o/R_s)^2 - 2}{(R_o/R_s)^2 - 1} \right] \tag{11}$$

The thermal resistance of heat transfer through the air is high compared to that of a solid. From Fig. 1a, it is observed that the top foil is supported by a very narrow area of the crest of the bump foil. The maximum space between the top and the bump foil is filled by air. Since air is a poor conductor of heat, the conduction path from film to the sleeve surface is significantly restricted. The outside surface of the top foil is exposed to an open atmospheric condition and acts as an outside surface of a sleeve like the conventional bearing from heat transfer point of view. Therefore, R_o in Eq. 11 can be considered as $R_o = R_s + t$, where t is the foil thickness. Substituting this value in Eq. 11 and rearranging the Eq. 11, one arrives at the following equation:

$$\frac{dh'}{dt} = -\frac{\varepsilon W'k}{K} \left[1 - \frac{R_s}{2t} \right] \tag{12}$$

where the term $\left(\frac{t}{R_s}\right)^2$ is neglected since $\frac{t}{R_s} \ll 1$.

When the perturbation is superimposed in clearance, the increased heat dissipation is obtained from Eq. 1 as follows [17]:

$$W + W' = \frac{\mu U^2}{h + h'} \tag{13}$$

For small perturbation condition, $h' \ll h$ and $W' \ll W$;

$$W' = -\frac{Wh'}{h} \tag{14}$$

Substituting Eqs. 14 and 1 into Eq. 12, one will obtain the following expression for perturbed film thickness variation as follows:

$$\frac{dh'}{dt} = \frac{\varepsilon \mu U h' k}{K h^2} \left[1 - \frac{R_s}{2t} \right] \tag{15}$$

Since non-prime terms are from steady-state condition, the above equation will be satisfied by:

$$h' = h'_0 e^{\alpha t} \tag{16}$$

Taking the derivative of Eq. 16 with respect to time, one can have

$$\frac{dh'}{dt} = \alpha h' \quad (17)$$

Comparing Eqs. 17 and 15, one will have

$$\alpha = \left(\frac{U}{h}\right)^2 \left(\frac{\mu \varepsilon k}{K}\right) \left(1 - \frac{R_s}{2t}\right) \quad (18)$$

In practice, the value of the ratio $\frac{R_s}{t}$ is typically of the order of 10^3 . The last terms contained in the parenthesis in Eq. 18 will be negative, i.e., α will become negative. From Eq. 16, it is observed that for the negative value of α , the perturbation will decay. Therefore, in practice, the maximum damage due to TEI in foil bearing resulting from the growth of surface wave happen in the journal, not in the foil. Radil et al. observed the effects of different journal cooling methods on the foil bearing experimentally by impinging air directly to the journal as well as through support structure [21]. They reported that the direct cooling of the journal reduced both bearing temperature and thermal gradient, whereas the encroaching the cooling air through support structure has limited ability to reduce the thermal gradient. The authors also concluded that full understanding of both the static and transient thermal operational environment is needed to implement the appropriate cooling methodology in the bearing system. These experimental findings attest the validity of the proposed model. The developed theoretical model provides a simplified theoretical model for initial selection of the proper thermal management technique.

2.3 Causes of Non-uniform Film Thickness and Heat

The causes of the generation of non-uniform film thickness are manifold. The primary cause is due to the unavoidable surface roughness produced based on the manufacturing accuracy. The statistical average of surface roughness may be represented as a sine wave. The longer wavelength is likely to contribute in the generation of non-uniform pressure or stress field. Secondary waves are caused by: (i) nonlinear heating when the journal, even if a perfect cylinder is pushed through one side of the film and create a wave peaks whereas the thick film ditch is situated diagonally opposite to it as shown in Fig. 4 [4]; (ii) nonlinear heating also may be caused due to elliptical journal with two peaks and two troughs as shown in Fig. 5. When this elliptical configuration grows due to thermal expansion, the bearing may lose its clearance near these two peaks [18]; (iii) non-cylindrical shape of bearing sleeve may cause waviness even when heat flux is uniform in the bearing clearance; (iv) mechanical constraints against the expansion of bearing sleeve; and (v) centrifugal growth of journal [18]. Although these issues may not appear to be severe during the start-up, when the system tries to equilibrate against the strong thermal gradient in the bearing, those waves will grow and activate a long-delayed TEI. This TEI can be avoided using detailed nonlinear thermo-elastic hydrodynamic analysis which will

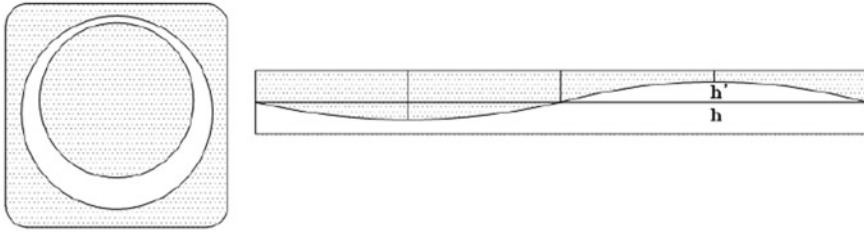


Fig. 4 Eccentric position of shaft and corresponding wave profile [18]

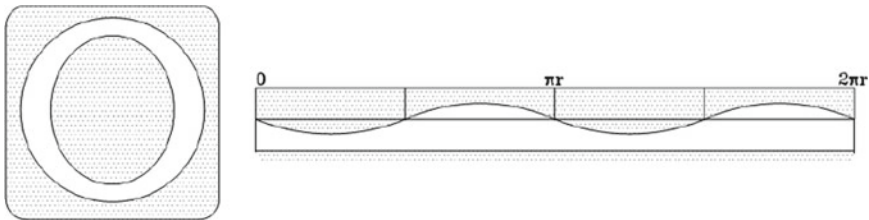


Fig. 5 Elliptical journal of shaft and corresponding wave profile [18]

include hydrodynamic, thermal, and structural deformation features of the bearing [6].

3 Conclusions

This paper highlights the possible causes of thermoelastic instability in foil bearing. A foil bearing is prone to TEI if precautionary measures are not taken into account at the design stage. Due to its typical structure, it is shown that the journal is more prone to damage due to TEI rather than foil. Therefore, to avoid TEI, cooling the journal by passing forced air through inside the hollow shaft or other means rather than through bottom of the top foil may be needed.

Acknowledgements The authors would like to thank CSIR, New Delhi, India, for sponsoring the fund of the Raman Research Fellowship under which the proposed works were carried out.

References

1. Blok H, Van Rossum JJ (1953) The foil bearing—a new departure in hydrodynamic lubrication. *Lubr Eng* 9:316–320
2. Gross WA (1962) *Gas film lubrication*. Wiley, New York, pp 114–138

3. Barnett MA, Silver A (1970) Application of air bearings to high speed turbomachinery. SAE Paper 700720
4. Samanta P, Khonsari MM (2018) On the thermoelastic instability of foil bearings. *Tribol Int* 121:10–20
5. Samanta P, Khonsari MM (2017) The limiting load carrying capacity of foil thrust bearings. *Proc IMechE Part J* 1–7
6. Samanta P, Murmu NC, Khonsari MM (2019) The evaluation of foil bearing technology. *Tribol Int* 135:305–323
7. Barber-Nichols Inc (2013) Guidelines for determining foil bearing applicability
8. Radil KC, Dellacorte C (2010) A Three-dimensional foil bearing performance map applied to oil-free turbomachinery. *Tribol Trans* 53(5):771–778
9. Davis CL, Krousgrill CM, Sadeghi F (2002) Effect of temperature on thermoelastic instability in thin disks. *ASME J Tribol* 124:429–437
10. Jang JY, Khonsari MMA (2003) Generalized thermoelastic instability analysis. *Proceeding Royal Society, London, Vol A459*, pp 309–329
11. Kao TK, Richmond JW, Douarre A (2000) Brake disc hot spotting and thermal judder: an experimental and finite element study. *Int J Veh Des* 23:276–296
12. Banerjee BN, Burton RA (1976) An instability for parallel sliding of solid surfaces separated by a viscous liquid film. *J Lubr Technol* 98:157–166
13. Jang JY, Khonsari MM (2004) Thermoelastic instability of two-conductors friction system including surface roughness. *ASME J Appl Mech* 71(1):57–68
14. Dykas B, Howard S (2004) A journal design considerations for turbomachine shafts supported on foil air bearings. *STLE Tribol Trans* 47(4):508–516
15. Lee D, Kim D, Sadashiva RP (2011) Transient thermal behavior of preloaded three-pad foil bearings: modeling and experiments. *J Tribol* 133:021703
16. Dykas BD (2006) Factors influencing the performance of foil gas thrust bearings for oil free turbomachinery applications. Ph.D. Thesis, Case Western Reserve University
17. Cable TA, San Andrés L (2018) On the design, manufacture, and premature failure of a metal mesh foil thrust bearing—how concepts that work on paper, actually do not. *J Eng Gas Turbines Power* 140(12):121007–121007-13
18. Burton RA (2000) Heat, bearings, and lubrication, engineering analysis of thermally coupled shear flows and elastic solid boundaries. Springer, New York
19. Sweet JN, Roth EP, Moss M (1987) Thermal conductivity of Inconel 718 and 304 stainless steel. *Int J Thermophys* 8(5):593–606
20. Raju S, Sivasubramanian K, Divakar R, Panneerselvam G, Banerjee A, Mohandas E, Antony MP (2004) Thermal expansion studies on Inconel-600 by high temperature X-ray diffraction. *J Nucl Mater* 325:18–25
21. Radil K, Dellacorte C, Zeszotek M (2007) Thermal management techniques for oil-free turbomachinery system. *Tribol Trans* 50:319–327

Condition Monitoring, Diagnostics and Prognostics of Rotors

Study of Turbocharger Fully Floating Hydrodynamic Bearing Oil Whirl Behavior—Test and Prediction



Lokesh Chandrasekaran, Praveen Kumar Selvaraj, Prasanth R. Vengala,
and Subramani D. Arthanarisamy

Abstract Automotive engines are facing increased design focus toward downsizing, higher performance and lower emissions, in the process challenging turbocharger technology to their limits. The exhaust-driven turbine energy must transmit to the compressor stage with minimal losses through the bearing system. In general, two types of bearings are used in turbocharger applications, namely semi-floating rotary bearings (SFRB) and fully floating rotary bearing (RFRB) system. In the latter, bearing is suspended in the lubricant, and by virtue of its rotational speed, brings down the angular speed of the fluid in the clearances between the shaft and the bearings. The ring rotates in the range from 0.25 to 0.4 times the shaft speed, and as a result has a positive effect on lubricant drag. On the other hand, this bearing system now has two spinning oil films and has to sustain the dual self-excited oil whirl vibrations in the inner and outer clearances that have a reciprocal influence on each other. The final evaluation calls for application specific validation either on the respective engine or vehicle system, as the system peripherals could resonate at the same frequencies and amplify these waves. This work describes the oil whirl-related sub-synchronous investigations of the RFRB on turbochargers. A brief theoretical

L. Chandrasekaran

Senior Simulation Engineer, ER&D, Turbo Energy Private Limited, Old Mahabalipuram Road, Paiyanur, Chennai 603104, India

e-mail: lokesh.c@turboenergy.co.in

P. K. Selvaraj

Test Engineer, ER&D, Turbo Energy Private Limited, Old Mahabalipuram Road, Paiyanur, Chennai 603104, India

e-mail: Praveenkumar.S@turboenergy.co.in

P. R. Vengala

Head of NVH & Simulation, ER&D, Turbo Energy Private Limited, Old Mahabalipuram Road, Paiyanur, Chennai 603104, India

e-mail: Prasanth.VR@turboenergy.co.in

S. D. Arthanarisamy (✉)

Director, Head of R&D, Turbo Energy Private Limited, Old Mahabalipuram Road, Paiyanur, Chennai 603104, India

e-mail: Subramani.Dr@turboenergy.co.in

© Springer Nature Singapore Pte Ltd. 2021

J. S. Rao et al. (eds.), *Proceedings of the 6th National Symposium*

on *Rotor Dynamics*, Lecture Notes in Mechanical Engineering,

https://doi.org/10.1007/978-981-15-5701-9_27

explanation followed by numerical rotor dynamic simulations on two bearing designs using AVL Excite simulation tool is discussed, and thus, obtained results are later validated through tests at the turbocharger sub-system-level evaluations on gas stand.

Keywords Turbocharger · Rotor dynamics · Hydrodynamics bearings · Numerical calculation · Sub-synchronous · Noise

Nomenclature

x, y and z	Directions in circumferential, radial and axial
i and o	Inner and outer joints
p	Oil pressure
ϵ	Oil fill ratio
η	Dynamic viscosity
h	Nominal clearance gap height between the two sliding surfaces
u	Surface velocity
φ	Flow factor
h_T	Local oil film thickness
σ	Composite roughness value

1 Introduction

In recent years, the number of turbocharged combustion engines has dramatically increased in the passenger car segment. To achieve better emission norms, high-power output with engine downsizing is main reason for the implementation. Such an engine critical flow requirement is satisfied with the help of smaller compressor and turbine wheels by operating at higher rotational speed. For such high-speed applications, hydrodynamic bearings offer better trade-off in terms of manufacturing cost and performance. Furthermore, rotating floating ring bearings (RFRB) offer better damping and lower friction power loss and are studied in this paper.

Hydrodynamics bearings in general are subject to various nonlinear effects such as self-excitation vibration, oil whirl/whip, sub- and super-harmonics, and jump phenomena as explained in [1, 2]. Several bifurcations with the occurrence of different types of oscillations which are caused by instability due to inner and outer oil films of the fully floating bearing system are detailed in [3–5]. In turbocharger system, sub-synchronous oscillations from inner oil whirl are the main reason for the acoustic problem detailed in [6, 7].

Rajasekhara and Srinivas [8] computed the nonlinear hydrodynamic journal bearing forces using discretized equations of motion using finite element method

solved in time integration approach. Lubos et al. [9] solved the Reynolds equation to predict the effect of outer bearing clearance and bearing clearance ratio on sub-synchronous components in rotor's response. Constant amplitude of sub-synchronous vibration induced by nonlinear hydrodynamics support on forced response of extend flexible rotor model is explained by Agnieszka et al. [10].

Due to high nonlinearity of the hydrodynamics bearings, mathematical models were validated with the experiments to arrive at calibrated simulations in [5, 9, 11]. Accurate prediction of shaft deflection and oil film temperatures of each joint by solving the differential algebraic equations (DAE) for flexible rotor and average Reynolds equation for non-linear hydrodynamic contacts (EHD) was presented by Bukovnik [12]. Influence of circumferential groove on the outer bearing width was studied, and the results [13] are compared with the plain journal bearing where effective outer bearing width in the both the designs is equal ($X = 2Y$) as shown in Fig. 1.

In this paper, numerical simulation was conducted using the same tool as in [12] for two RFRB designs—plain (Design A) and circumferential groove (Design B). It is worth noting that Design B bearing here has lesser effective outer bearing width ($2Y < X$) as shown in Fig. 5. Deeper insights of the EHD joints are presented through simulations in terms of RSR, MOFT, eccentricity ratio, asperity contact pressure in the bearings, and overall oil flow rate. Also, experimental results from hot gas stand test bench run-up were compared with simulation results.

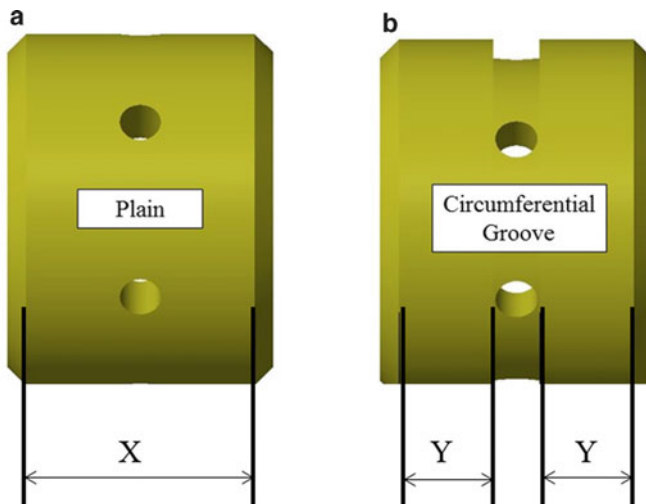


Fig. 1 Effective outer bearing width [13]. **a** plain journal bearing and **b** circumferential groove bearing

2 Sub-synchronous Phenomena

In fully floating bearing turbocharger, shaft assembly is supported by means of sleeve or bush on both compressor and turbine side which are suspended in a lubricant. The bush rotates in the range from 0.25 to 0.4 times the shaft speed, and as a result has a positive effect on lubricant drag. On the other hand, this bearing system now has two spinning oil films and have to sustain the dual self-excited oil whirl vibrations in the inner and outer clearances.

Figure 2 shows two-dimensional waterfall spectrum shows the turbocharger modes shapes and its corresponding frequency. When the turbocharger speed is gradually increased, the unbalance force excites the rotor with a harmonic vibration that is synchronous with the rotor speed at the frequency order of 1X. Oil whirl is the kind of self-excited vibration with the frequency order less than 1X. The rotational kinetic energy of the oil whirling excites the rotor and induces the sub-synchronous oscillation or vibration. When the whirling frequency equals the first critical bending frequency of the rotor, oil whip takes place in which rotor amplitude continuously increases with time as shown in Fig. 2. Initially, during the ramp up, inner oil film temperature is higher than the outer oil film temperature due to the larger bearing friction in the inner oil film. So, the damping coefficient of the inner oil film decreases. As soon as the destabilizing force induced by the cross-couple stiffness coefficient exceeds the damping force, the inner oil whirl occurs in the frequency range between 200 and 500 Hz at inner clearance, which is Sub 1 as shown in Fig. 2.

Further, increasing the rotor speed, the rotor unbalance becomes larger and the vibration mode of the inner oil whirl changes from the conical to the cylindrical mode. It leads to the jump of the inner oil whirl frequency which occurs between 600 and 1100 Hz regions, which is Sub 2 as shown in Fig. 2. Similarly, oil whirling in the outer clearance has the conical mode shape and occurs in the frequency range

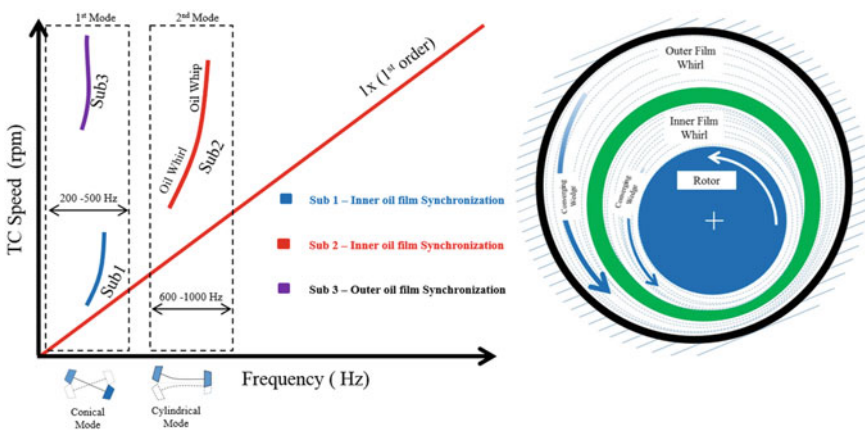


Fig. 2 Typical waterfall spectrum—shaft deflection

between 200 and 500 Hz in the higher turbocharger speeds known as Sub 3. The outer clearance plays the important role in the rotor deflection amplitudes, and also the outer oil whirl is less noisy than the inner oil whirl because it occurs at very low frequency.

3 Numerical Simulation Setup and Results

3.1 Simulation Methodology

Below differential (DAE) algebraic Eq. (1) [12] allows us to solve both global motion and local elastic deformation of the rotor system. M_R , D_R , and K_R are the time-invariant mass, damping, and stiffness matrices that are calculated for the rotor with the help of in-built FEM software at the pre-processing step in the commercially available AVL Excite tool used in this study.

$$M_R \ddot{q} + D_R \dot{q} + K_R q = f^* + f^a + f^{\text{gyro}} - f^{\text{rbAcc}} \quad (1)$$

On the other side of the equation, f^{gyro} is gyroscopic force of the rotor assembly, f^{rbAcc} denotes the global motion and rigid body acceleration of the rotor, f^a is the force induced in the radial and axial directions from the compressor and turbine wheels, and f^* denotes force occurring due to contact with other component surfaces. Hydrodynamic bearing are formulated using average Reynolds equation [12] with respect to outer sliding body coordinate system,

$$\begin{aligned} & -\frac{\partial}{\partial x} \left(\frac{\theta \cdot \varphi_x \cdot h^3}{12\eta} \frac{\partial p}{\partial x} \right) - \frac{\partial}{\partial z} \left(\frac{\theta \cdot \varphi_z \cdot h^3}{12\eta} \frac{\partial p}{\partial x} \right) + \frac{u_i - u_o}{2} \frac{\partial((h_T + \sigma \cdot \varphi_s) \cdot \theta)}{\partial \bar{x}} \\ & + \frac{\partial(h_T \cdot \theta)}{\partial t} = 0 \end{aligned} \quad (2)$$

From the above Eq. (2), first and second terms of the above equation represent sliding in x-direction, and cross-direction along z-axis which are commonly denoted by Poiseuille term. Third and fourth terms denote the wedge (clearance change) and squeeze of the joint, respectively.

3.2 Simulation

Figure 3 shows AVL Excite simulation tool, schematic model for turbocharger rotor, and bearing system. Housings and rotor are modeled as flexible element, which itself is supported by two bearings. Each bearing consists of two joints which are inner and outer oil films and a floating bushing that is also a flexible body. Inner and outer

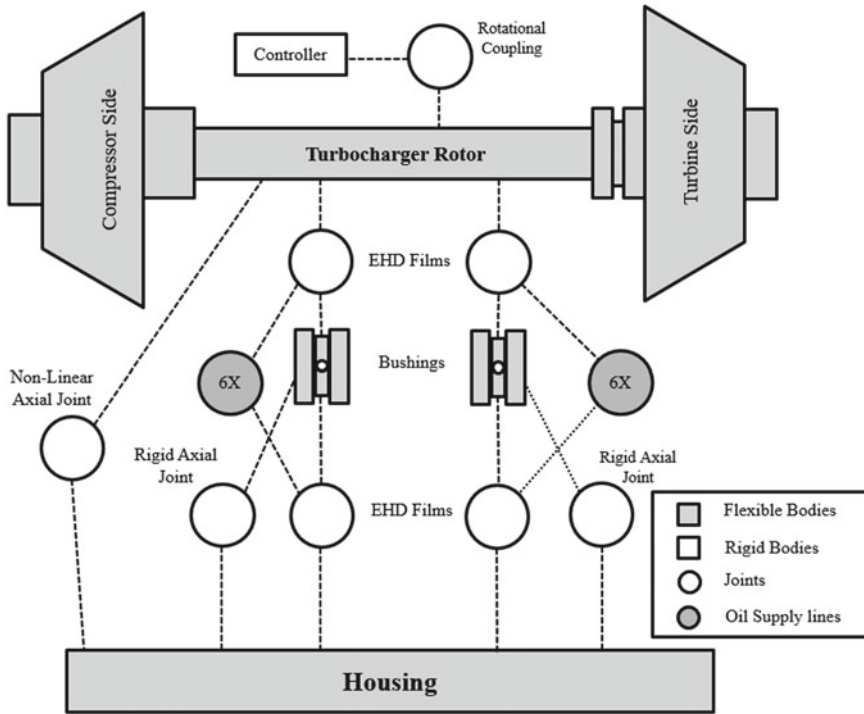


Fig. 3 Schematic model for fully floating bearing

oil films are connected via six oil holes in the bushing, respectively. Rotating parts of rotor components are discretized into FE model with multiple journal components in shaft modeler section in modeling turbocharger rotor. In discretized model, wheel contour captured to match the eigenmodels of the rotor with massless element. Mass of the compressor and turbine wheel is assigned at center of gravity location of the wheels, respectively. Unbalance for the rotor system is defined in shaft modeler. Flexible model for housing and bushing is imported from FE tool by condensation process together with the thermal and structural boundary condition for surface of the housing. Rigid axial joint is used to position the bushes, and nonlinear axial bearing is used between the housing and rotor when assumed zero thrust load condition.

Figure 4 shows Design A and Design B ($2Y \neq X$) that are investigated in this study. Outer bearing joint modeling for the both designs is shown in Fig. 5. Constant speed simulation is conducted from 40 to 260 krpm with the increment of 20 krpm. Initial speed of rotor and floating bushings needs to be defined. Calculations are performed for few revolutions till stable ring speed ratio is arrived at each speed.

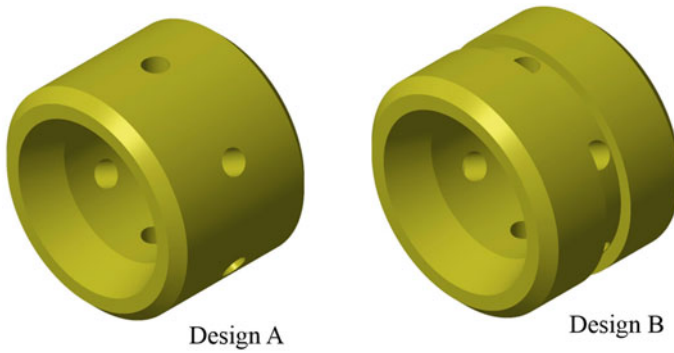


Fig. 4 RFRB TC. a Design A and b Design B

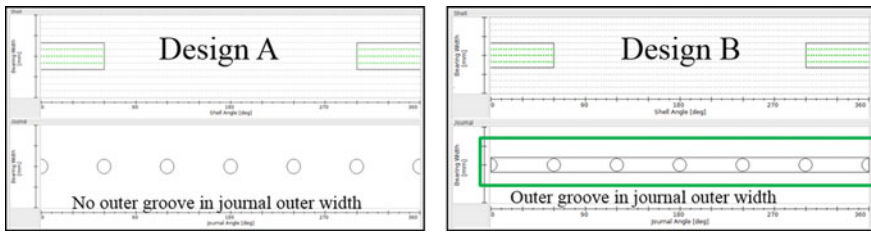


Fig. 5 Outer joint modeling for Design A and Design B

3.3 Waterfall Spectrum

From simulation, both shaft deflection spectrum maps and orbit plot overlaid for designs A and B in Fig. 6. In this spectral map, X, Y, Z denote frequency in Hz, speed in rpm, and color intensity which show displacement amplitude where blue to red denotes the raise in displacement amplitude from low to high. For both designs,

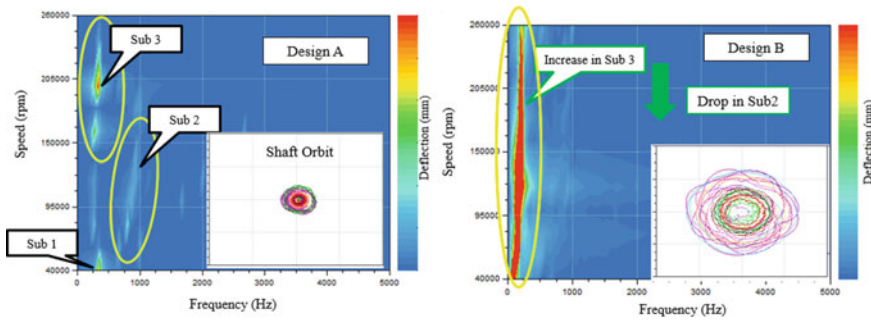


Fig. 6 Shaft deflection on compressor side color map (Design A and Design B)

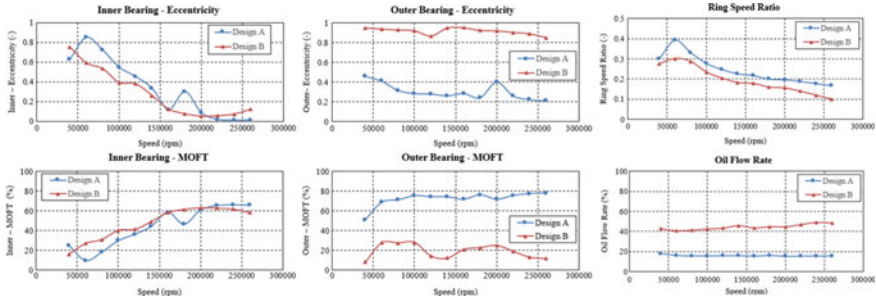


Fig. 7 Simulation—EHD joint results comparison

same amount of unbalance considered from the balancing results. For results, Design A has slightly higher unbalance deflection, while compared with Design B at low speed. Unbalance deflection are negligible while compared with the sub-synchronous deflection. Design A shows that Sub 2 inner bearing deflection appears from 60 to 180 krpm at around 0.3X and Sub 3 appears from 60 krpm till the max speed of 260 krpm around at 0.1 X. Providing circumferential groove in Design B reduces Sub 2, i.e., inner oil whirl deflection and on the other hand, a stronger Sub 3 outer bearing deflection was observed from the lower speed. Design B has drop the load bearing capacity as a result of reduced effective outer bearing width, as shown in Fig. 5. As a result, Design B system has a larger shaft orbit when compared with Design A due to higher Sub 3.

3.4 EHD Joint Results

As shown in Fig. 7, introducing circumferential groove in the outer bearing of Design B reduces the load bearing capacity of the outer bearing. That has resulted in higher eccentricity ratio in the outer bearing and lower MOFT. Ratio between the angular velocity of bush and angular velocity of shaft (RSR) also drops, reducing the circumferential velocity of the inner oil whirl. In addition, introducing groove in outer bearing increases the axial flow rate. Both the drop in RSR and increased oil flow rate have positive effect on Sub 2.



Fig. 8 Hardware and sensor instrumentation

4 Experimental Setup and Results

4.1 Data Acquisition and Instrumentation

Figure 8 shows the LMS SCADAS XS hardware, eddy current displacement sensors, and accelerometer on the compressor side of the TC. Turbocharger speed is measured as well.

4.2 Test Results Comparison on Hot Gas Stand

Both designs A and B are assembled with nominal inner and outer bearing clearances, and run-up test was conducted for operating points of the compressor characteristic map on the basis of full-load line of the scheduled engine for the oil inlet temperature and pressure of 120 °C and 2 bar. For simulating the vehicle condition, run-up was conducted from 60 to 260 krpm with fired/hot test condition. Both systems are balanced for nearly equal unbalance condition. For results, Design A has slightly higher unbalance deflection while compared with Design B. Unbalance deflection is negligible while compared with the sub-synchronous deflection. With Design A, higher Sub 2, inner oil whirl appears below 1000 Hz and Sub 3 occurs from 75 to 260 krpm. In Design B, Sub 2, inner oil whirl appears below 1000 Hz with lower amplitudes and Sub 3 begins from lower speed with higher amplitude similar to the test results. Similarly, orbit plot shows that Design B larger orbit compared to Design A which is mainly comes from the outer bearing due of drop in load carrying capacity of the outer bearing.

5 Test Versus Prediction—Correlation Discussion

Figures 6, 7 and 9 show good qualitative agreement between simulation and test results. Similar to test results, simulation predicted the higher Sub 2, inner oil whirl

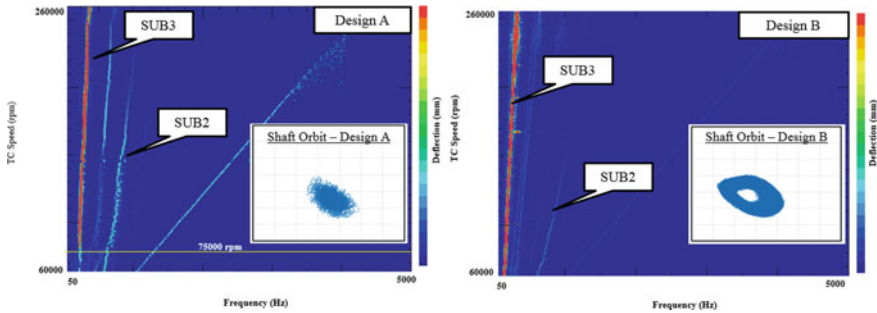


Fig. 9 Test results—spectral map and orbit comparison (Design A versus Design B)

deflection with Design A. Good correlation is observed in terms of Sub 2 improvement with the Design B. Simulation provides better insights for the oil film joints results.

6 Conclusion

For fully floating bearing turbocharger, oil whirl-related instabilities were discussed in detailed manner. Rotor dynamics simulation methodology was developed successfully for the turbocharger fully floating bearing system with the help of commercially available software. Simulation results validated well against the hot gas stand test results. From both simulation and testing, Design A has higher Sub 2 inner oil whirl deflection which will cause sub-synchronous vibration and could result in noise with overall lower shaft deflection. But Design B has much lower Sub 2 inner oil whirl deflection and higher Sub 3 outer oil whirl deflection which will result in larger shaft orbit and poor load bearing capacity. While comparing both designs, Design B is a better option in terms of sub-synchronous noise behavior.

References

1. Khonsari MM, Booser ER (2001) Applied tribology: bearing design and lubrication. Tribology in Practice Series 2001
2. Szeri AZ (2013) Fluid film lubrication. Cambridge University Press, Cambridge
3. Boyaci A, Seemann W, Proppe C (2010) Stability analysis of rotors supported by floating ring bearings. In: Proceedings of the 8th IFToMM Inter Conference on Rotordynamics, Seoul
4. Schweizer B (2010) Dynamics and stability of automotive turbochargers. Arch Appl Mech 80(9):1017–1043
5. Schweizer B, Sievert M (2009) Nonlinear oscillations of automotive turbocharger turbines. J Sound Vib 321:955–975
6. Nguyen-Schäfer Hung (2012) Rotordynamics of automotive turbochargers. Springer, Heidelberg

7. Schweizer B (2009) Dynamics and stability of turbocharger rotors - Published online: 28 August 2009. Springer, Berlin
8. Rajasekhara, Srinivas (2015) Vibration analysis of a support excited rotor system with hydrodynamic journal bearing. In: 12th International Conference on vibration problems ICOVP
9. Kirk RG (2013) Experimental evaluation of hydrodynamic bearings for a high speed turbocharger. In: Proceedings of ASME Turbo Expo 2013. San Antonio, Texas, USA, June 3–7, pp. 1–9
10. Agnieszka (Agnes) (2005) Muszynska – Rotordynamics. Taylor & Francis Group, LLC
11. Köhl K (2014) Experimental and numerical investigations on an automotive turbocharger with a transparent bearing section. In: IMechE, 11th international conference on turbochargers and turbocharging. London, UK, May 13–14, pp 349–359
12. Bukovnik S, Offner G, Turbocharger dynamic analysis: advanced design simulation in time domain using CFD predicted thermal boundary conditions
13. Nowald B, Schmoll K, Schweizer (2015) Influence of circumferential grooves on the non-linear oscillation of turbocharger rotor in fully floating bearings. 14th IFToMM Oct 2015

Rolling Element Bearing Fault Diagnosis by Different Data Fusion Techniques



Sandaram Buchaiah  and Piyush Shakya 

Abstract Rolling element bearing is a crucial element of rotating machinery. A sudden failure of the bearing may result in a catastrophic failure. Therefore, the identification of bearing failure in the incipient stage is essential. The vibration signal generated by bearing fault is used for condition monitoring and fault diagnosis. The parameters extracted from vibration data provide the fault indication. However, a single parameter may miss useful information, resulting in less accurate fault diagnosis. The fused parameters after data fusion of individual parameters are more informative and efficient than a single parameter. Mahalanobis–Taguchi–Gram–Schmidt method, principal component analysis, and independent component analysis are the most popular data fusion techniques, and these techniques are applied to three most occurring fault data such as the outer race, the inner race, and rolling elements. The bearing vibration data, available on the NASA Web site, are used for the data analysis and extracting parameters. A comparison is made on the effectiveness of various data fused parameters obtained from different data fusion techniques. The best data fusion technique with respect to each type of defect (inner race, outer race, and ball) is identified.

Keywords Rolling element bearing · Fault diagnosis · Mahalanobis-Taguchi-Gram-Schmidt method · Principal component analysis · Independent component analysis

1 Introduction

The rolling element bearing is ubiquitous in rotating machinery. The function of a bearing is to support the machines and to constrain the relative motion to only a

S. Buchaiah (✉) · P. Shakya
Department of Mechanical Engineering, Indian Institute of Technology Madras, Chennai 600036, India
e-mail: me16d021@smail.iitm.ac.in

P. Shakya
e-mail: pshakya@iitm.ac.in

© Springer Nature Singapore Pte Ltd. 2021
J. S. Rao et al. (eds.), *Proceedings of the 6th National Symposium on Rotor Dynamics*, Lecture Notes in Mechanical Engineering,
https://doi.org/10.1007/978-981-15-5701-9_28

341

desired direction (rotational motion). More than 90% of bearings used in machines are rolling element bearings [1]. The sudden failure of a rolling element bearing may result in catastrophic failure of the rotating machinery. In rolling element bearings, defects may occur on the outer race, inner race, rolling elements, and cage. When rolling elements periodically passes over the defects that create impact vibrations [2, 3]. Fault indication parameters extracted from vibration signal in time domain, frequency domain, and time–frequency domain are used for fault diagnosis. However, a single fault indication parameter directly extracted from vibration signal processing techniques may miss some information, which results in less accurate fault diagnosis. A fault identification based on the fusion of multiple parameters is better on the count of accuracy. Data fusion is intermixing of multivariate data into a more informative single dataset. Several data fusion techniques are available for fusing multiple parameters into a single parameter. Mahalanobis–Taguchi–Gram–Schmidt method, principal component analysis, and independent component analysis techniques are the most popular techniques. Mahalanobis distance (MD) indicates the similarity between two datasets, and it measures the distance between a point and a dataset. The MD is used for the fusion of multiple parameters, and it is calculated by using Mahalanobis–Taguchi–Gram–Schmidt method. The principal component analysis is a variable dimension reduction procedure, which converts multidimensional observations into set of uncorrelated variables. The independent component analysis divides the multivariate data into different subcomponents called independent components. These three techniques are applied to outer race, inner race, and rolling elements fault data; and the best data fusion technique with respect to each type of defect (inner race, outer race, and ball) is identified.

2 Mahalanobis–Taguchi–Gram–Schmidt Method

In this method, the MD is calculated by Gram–Schmidt orthogonal process (GSO). The GSO is an orthogonalization process which transforms the linearly independent vectors into orthogonal vectors [4].

Data normalization: The healthy dataset X_{ij} for reference is selected. In this study, the data collected at an initial stage of new bearing with proper lubrication is selected as healthy dataset. The data is normalized by subtracting the mean of the health data and dividing with the standard deviation of healthy data from each characteristic of full data to make data as zero mean and unit standard deviation and construct normalized matrix Z_{ij} .

Orthogonal vectors: The vectors of normalized matrix Z_{ij} are treated as independent vectors, and orthogonal vectors are calculated by the following equations.

$$U_1 = Z_1 \tag{1}$$

$$U_2 = Z_2 - \frac{Z_2^T U_1}{U_1^T U_1} U_1 \tag{2}$$

$$U_k = Z_k - \frac{Z_k^T U_1}{U_1^T U_1} U_1 - \dots - \frac{Z_k^T U_{k-1}}{U_{k-1}^T U_{k-1}} U_{k-1} \tag{3}$$

where

$Z_k = (Z_{k1}, Z_{k2}, Z_{k3}, \dots, Z_{kn})$ is the k th set of normalized vector,

$U_k = (U_{k1}, U_{k2}, U_{k3}, \dots, U_{kn})$ is the k th set of orthogonalized vector.

Mahalanobis distance: The MD of j th observation is given by the following equation,

$$MD_j = \frac{1}{k} \left(\frac{U_{1j}^2}{S_1^2} + \frac{U_{2j}^2}{S_2^2} + \dots + \frac{U_{kj}^2}{S_k^2} \right) \tag{4}$$

where U_{kj} is an element of orthogonalized vector U_k , S_k is a standard deviation of U_k , and k the is number of variables [5, 6].

3 Principal Component Analysis

Principal component analysis is used to reduce the dimension of a multivariate dataset and to identify a pattern in the random data. The PCA converts dimension of a multivariable dataset (X_{ij}) to a lower dimension dataset (P_{ik}) without loss of useful information [3, 7].

Principal component analysis procedure:

- Initially, the original dataset as a matrix (X_{ij}) is taken, where i is the number of observations and j is the number of characteristics.
- A normalized matrix (Z_{ij}) is found by subtracting mean from each characteristic.
- The covariance matrix (C) of the normalized matrix is found. The eigenvalues of the covariance matrix are computed and arranged in order from higher to lower. The eigenvectors for each eigenvalue and form an eigenvector matrix (W_{jj}) is calculated.
- The principal components (P) by multiplying each vector of the eigenvector matrix with normalized matrix are computed.

$$P_{ji} = W Z_{ij}^T \tag{5}$$

- The dimension (k number of reduced characteristics) of dataset (P_{ik}) is chosen from obtained principal component set (P_{ij} is transpose of P_{ji})($k < j$) by calculating proportion of variation explained by each eigenvalue such that the number

of eigenvalues giving max proportion value indicates the number of principal components to choose.

- In this case, the first principal component (PCA1) is used for fault diagnosis, which justifies the maximum variance.

4 Independent Component Analysis

Independent component analysis (ICA) is a statistical method which is used to dissociate the multivariate signal into individual non-Gaussian subcomponents called independent components. The ICA initially developed for blind source separation [8]. For measuring mutual information, the ICA algorithm uses maximum entropy and Kullback–Leibler divergence; and kurtosis and negentropy are used for measuring non-Gaussianity. In this case, fast ICA algorithm is used for calculating independent component analysis.

The mathematical model simple noiseless ICA is given by the equation,

$$X = AS \quad (6)$$

where $X = [x_1, x_2, \dots, x_n] \in R^{m \times n}$ is data matrix, $S = [s_1, s_2, \dots, s_n] \in R^{m \times n}$ is independent components matrix, and $A = [a_1, a_2, \dots, a_l] \in R^{m \times n}$ is mixing matrix [10].

Both independent matrix (S) and mixing matrix (A) are unknown; these are estimated by using data matrix (X), these are possible by finding the de-mixing matrix (W) which is the inverse matrix of mixing matrix [9].

$$S = WX \quad (7)$$

5 Results and Discussion

The intelligent maintenance systems (IMS) bearing data are taken from the NASA Web site [10]. In this case, for analysis October dataset of the third bearing x -axis, fourth bearing x -axis, and February dataset of the first bearing x -axis (these datasets are inner race defect, ball defect, and outer race defect, respectively) are taken. Eleven parameters are extracted; seven parameters in time domain (standard deviation, RMS, kurtosis, skewness, peak factor, shape factor, and RMS * kurtosis), two parameters in frequency domain (amplitude of defect frequency (outer race or inner race or ball, whichever is the case) of FFT and HFRT spectrum corresponding to the dataset) and two parameters in time–frequency domain (amplitude of defect frequency (outer race or inner race or ball, whichever is the case) of HFRT spectrum of CWT and DWT corresponding to the dataset).

The February dataset (from NASA Web site) contains 984 files, for every 10 min, dataset of 1-s is extracted with a sampling frequency of 20 kHz. The October dataset contains 2156 data files, for every 10 min' dataset of 1-s is extracted (except the first 43 files were extracted every 5 min).

The percentage of variation (Δ) calculated by taking percentage variation in means (μ) of the respective stages of fused parameters.

$$\Delta_i = \left(\frac{\mu_{i+1} - \mu_i}{\mu_i} * 100 \right) \tag{8}$$

Here Δ_1 is the percentage of variation in means of the healthy stage and stage 1, and Δ_2 is the percentage of variation in means of stage 1 and stage 2. Stages are divided based on visual identification of patterns.

5.1 Outer Race Defect

The data fusion techniques are applied on IMS bearing fault data of the February dataset (first bearing). Single parameter patterns are shown in Fig. 1. Three parameters MD, PCA1, and ICA1 are calculated; and respective patterns are given in Fig. 2.

The trends of fused parameters healthy stage and defective stage for outer race defect are shown in Fig. 2. The early fault detection point (initiation of defect progression), the percentage of variation in trend, and bearing failure points are shown in Table 1. Out of these three parameters, MD is the better early fault detection. The percentage of variation in each stage is more in MD in comparison with other methods.

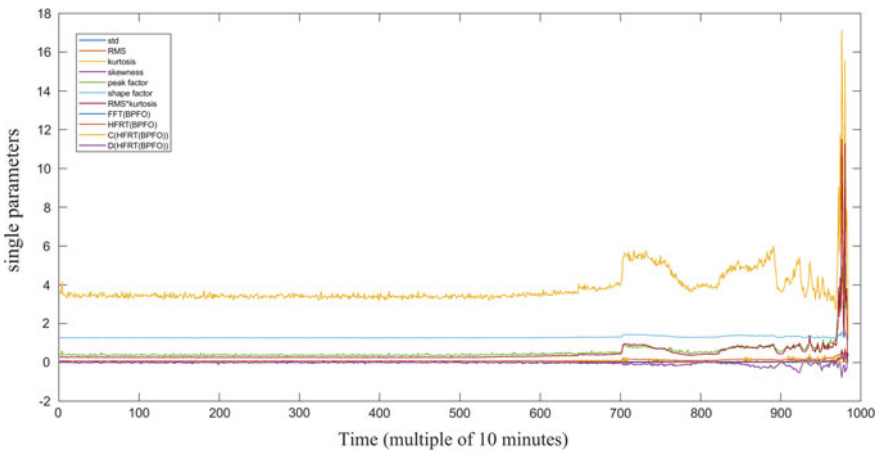


Fig. 1 Patterns of single parameters for outer race defect

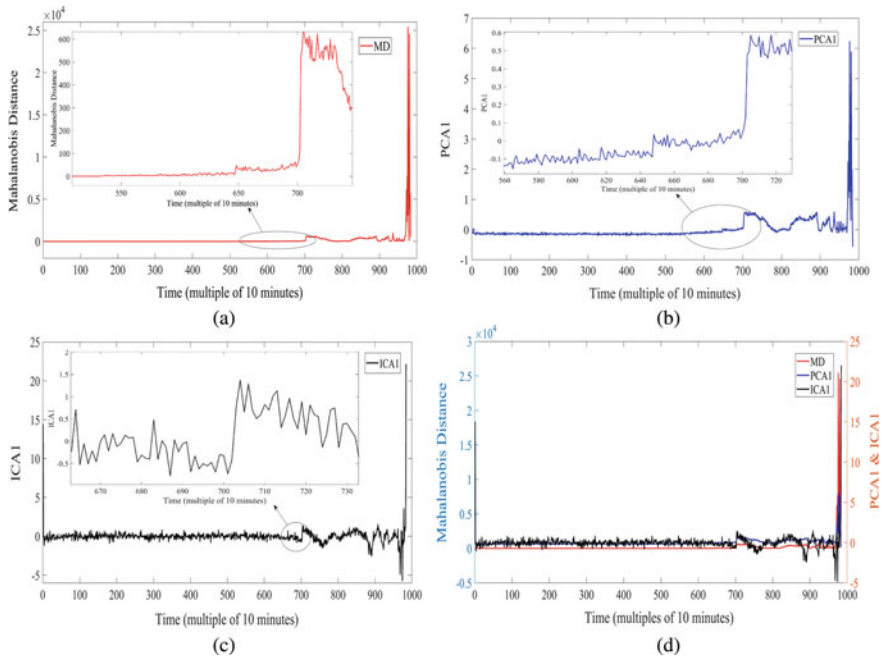


Fig. 2 Trends of fused parameters for outer race defect. **a** Trend of Mahalanobis distance, **b** trend of first principal component, **c** trend of the first independent component, **d** trends all three parameter

Table 1 Comparison of fused parameters for outer race defect

Observation	MD	PCA1	ICA1	
Early (initial) defect detected at	5310 min	5420 min	6990 min	
Percentage of variation (Δ)	Stage 1	5310–6450 min	5420–6440 min	5420–6440 min
	Δ_1	470%	27.41%	0%
	Stage 2	6450–6980 min	6440–6980 min	6440–6990 min
	Δ_2	406%	92%	0%
	Stage 3	6980–9650 min	6980–9660 min	6990–9800 min
	Δ_3	559%	452%	558%
	Stage 4	9650–9760 min	9660–9760 min	9800–9840 min
	Δ_4	9658%	2688%	1806%
Bearing failure point detected at	9760 min	9760 min	9840 min	

5.2 Inner Race Defect

The data fusion techniques are applied on IMS bearing fault data of the October dataset (third bearing x-axis). Eleven single parameter patterns are shown in Fig. 3.

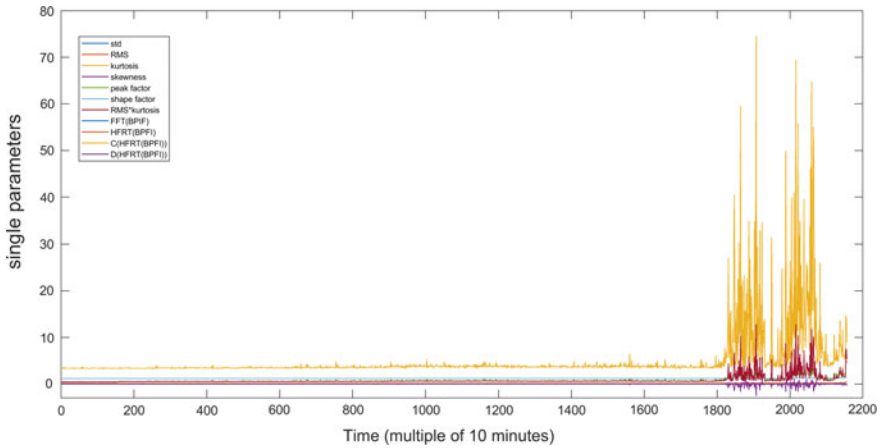


Fig. 3 Patterns of single parameters for inner race defect

Three fused parameters MD, PCA1, and ICA1 are calculated, and respective patterns are given in Fig. 4.

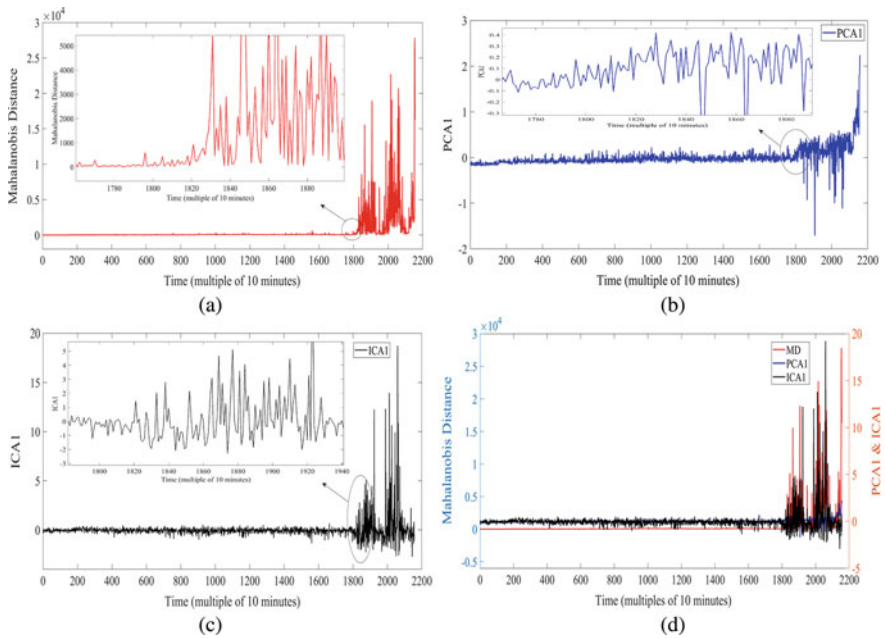


Fig. 4 Trends of fused parameters for inner race defect. **a** Trend of Mahalanobis distance, **b** trend of first principal component, **c** trend of the first independent component, and **d** trends all three parameters

Table 2 Comparison of fused parameters for inner race defect

Observation		MD	PCA1	ICA1
Early (initial) defect detected at		17,715 min	17,835 min	17,975 min
Percentage of variation (Δ)	Stage 1	17,930–19,300 min	18,050–19,320 min	18,190–19,330 min
	Δ_1	3974.5%	406%	466%
	Stage 2	19,300–21,030 min	19,320–21,060 min	19,330–20,490 min
	Δ_2	91.2%	24%	78%
	Stage 3	21,030–21,540 min	21,060–21,560 min	20,490–20,590 min
Δ_3	1222.3%	933.6%	1070%	
Bearing failure point detected at		21,325 min	21,345 min	20,375 min

The trends of fused parameters for healthy stage and defective stage for inner race defect are shown in Fig. 4. The early detection point (initiation of defect progression), percentage of variation in trend, and bearing failure points are shown in Table 2. Out of the three parameters, MD gives the early fault detection. The percentage of variation in each stage is more in MD comparative to other methods.

5.3 Ball Defect

The data fusion techniques are applied on IMS bearing fault data of the October dataset (fourth bearing *x*-axis). Patterns of single parameters are shown in Fig. 5. Three parameters MD, PCA1, and ICA1 are computed, and the corresponding patterns are given in Fig. 6.

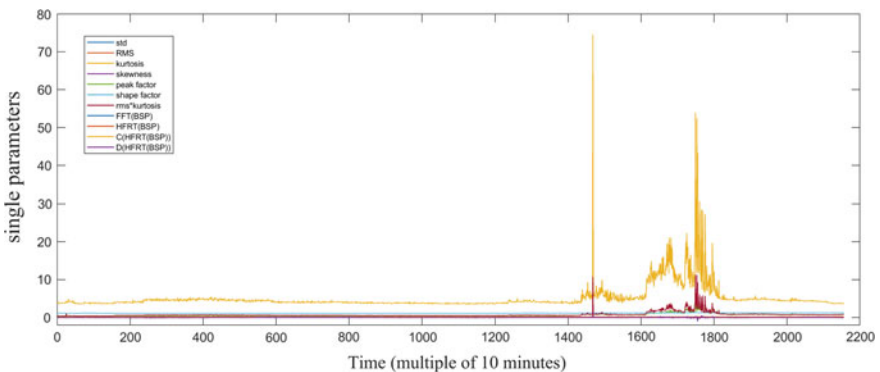


Fig. 5 Patterns of single parameters for ball defect

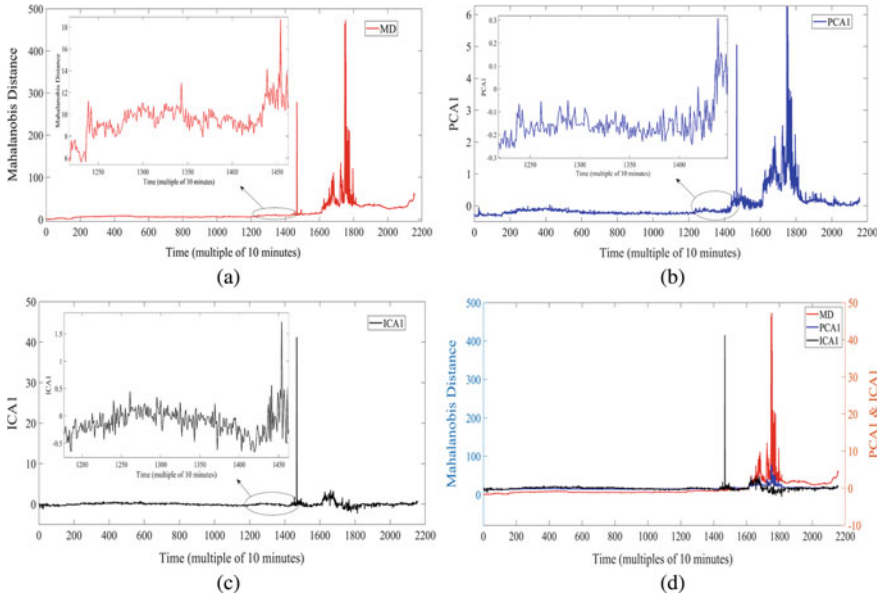


Fig. 6 Trends of fused parameters of ball defect. **a** Trend of Mahalanobis distance, **b** trend of first principal component, **c** trend of the first independent component, and **d** trends of all three parameters

The trends of fused parameters healthy stage and defective stage for ball defect are shown in Fig. 6. The early fault detection point (initiation of defect progression), percentage of variation in trend, and bearing failure points are shown in Table 3. All three parameters are showing same the early fault detection, but the percentage of variation in PCA is more. MD and PCA are showing the same bearing failure points,

Table 3 Comparison of fused parameters for ball defect

Observation	MD	PCA1	ICA1	
Early (initial) defect detected at	12,135 min	12,135 min	12,135 min	
Percentage of variation (Δ)	Stage 1	12,350–14,340 min	12,350–14,340 min	12,350–14,170 min
	Δ_1	61%	63%	15%
	Stage 2	14,340–16,100 min	14,340–16,100 min	14,170–16,100 min
	Δ_2	53.53%	174.5%	123%
	Stage 3	16,100–17,440	16,100–17,440 min	16,100–16,770 min
	Δ_3	228%	715.58%	233%
	Stage 4	17,440–17,490 min	17,440–17,490 min	16,770–17,770 min
	Δ_4	741%	550%	0%
Bearing failure point detected at	17,275 min	17,275 min	17,555 min	

and the percentage of variation at failure is more in MD. An outlier is identified in all parameters at 14680 min.

6 Conclusion

In this study, three data fusion techniques are applied to three types of bearing fault data. Data fusion techniques are applied to eleven parameters to fuse these into a single parameter; these fused parameters provide a better pattern in comparison with single parameters. The percentage of variation in means (μ) of stages divided based on visual identification is taken for analyzing the results. MD performs better for the outer race and inner race defect (early fault detection and percentage of variation in trend). PCA performs better for ball defect. The effectiveness of ICA in comparison with other techniques is low.

References

1. Gupta P, Pradhan MK (2017) Fault detection analysis in rolling element bearing: a review. *Mater Today: Proc* 4:20852094
2. Howard I (1994) A Review of rolling element bearing vibration detection, diagnosis and prognosis. DSTO Aeronautical and Maritime Research Laboratory, GPO Box 4331, October 1994
3. Jiang L, Xinxin F, Jianguo C, Zhonghai F (2012) Fault detection of rolling element bearing based on principal component analysis. In: 24th Chinese control and decision conference (CCDC)
4. Shakya P, Kulkarni MS, Darpe AK (2015) Bearing diagnosis based on Mahalanobis–Taguchi–Gram–Schmidt method. *J Sound Vib* 337:342–362
5. Soylemezoglu A, Jagannathan S, Saygin C (2010) Mahalanobis Taguchi System (MTS) as Prognostics tool for rolling element bearing failure. *J Manuf Sci Eng* 132:051014-1
6. Taguchi G, Rajesh J (2002) *The Mahalanobis-Taguchi strategy a pattern technology system*. Wiley, Hoboken
7. Zvokelj M, Zupan S, Prebil I (2010) Multivariate and multiscale monitoring of large-size low-speed bearings using ensemble empirical mode decomposition method combined with principal component analysis. *Mech Syst Signal Process* 24:1049–1067
8. Wangn Z, Chen J, Dong G, Zhou Y (2011) Constrained independent component analysis and its application to machine fault diagnosis. *Mech Syst Signal Process* 25:2501–2512
9. Guo Y, Jing N, Bin L, Fung RF (2014) Envelope extraction based dimension reduction for independent component analysis in fault diagnosis of rolling element bearing. *J Sound Vib* 333:2983–2994
10. IMS (Intelligent Maintenance Systems), Bearing Data Set, NASA Ames Prognostics Data Repository. Available online: <https://ti.arc.nasa.gov/tech/dash/groups/pcoe/prognostic-data-repository/>

Diagnosability Index and Its Application to Bearing Fault Diagnosis



Ankush C. Jahagirdar  and K. K. Gupta 

Abstract Bearings are essential component of rotating machines and are often prone to failure. Early detection of bearing faults thus becomes important for predictive maintenance strategies. Conventionally, vibration measurement is considered to be the most reliable and widely used indicator of fault signatures, which are to be extracted from the raw signal. Traditional signal processing techniques, like envelope spectrum, are employed for extraction of such features. However, selection of optimal band and center frequency remains the main objective of research in the field. Use of spectral kurtosis (kurtogram) is now a standard method for this selection. However, a benchmark study on Case Western Reserve University dataset shows several non-diagnosable cases using kurtogram method. The purpose of this study is to quantify diagnosability in the form of an index and use it as a selection criterion for getting optimal band and center frequency. The proposed method is validated using non-diagnosable cases of the benchmark study, and the results are compared with that of conventional Hilbert transform method and autogram method.

Keywords Fault diagnosis · Diagnosability index · Vibration monitoring

Nomenclature

BPFI	Ball pass frequency inner race
BPFO	Ball pass frequency outer race
BSF	Ball spin frequency
HT	Hilbert transform
SES	Squared envelope spectrum
DI	Diagnosability index

A. C. Jahagirdar (✉) · K. K. Gupta
Birla Institute of Technology & Science, Pilani, Rajasthan 333031, India
e-mail: ankush.chandrakant@pilani.bits-pilani.ac.in

K. K. Gupta
e-mail: kgupta@pilani.bits-pilani.ac.in

© Springer Nature Singapore Pte Ltd. 2021
J. S. Rao et al. (eds.), *Proceedings of the 6th National Symposium on Rotor Dynamics*, Lecture Notes in Mechanical Engineering,
https://doi.org/10.1007/978-981-15-5701-9_29

1 Introduction

Vibration signals are most reliable way of monitoring faults in rotating machinery. When a fault occurs on either the inner raceway, outer raceway, or on the rolling element of a bearing, it can be captured using accelerometer sensor located in contact with the machine. The high-frequency shock signal generated due to impact of fault is very peculiar and often shows amplitude modulation. The cyclostationary nature of such signals is well known and of specific interest from signal processing point of view. Complex nature of these signals and random interfering noise makes it difficult to model such signals. It is often very difficult to find the optimum resonance band for filtering out undesired components from the signal. State-of-the-art research focuses mainly on this aspect of finding the optimum center frequency and bandwidth, and the various statistical features are used to guide this optimization process. Kurtosis is one such feature which is very widely used. A study on Case Western Reserve University dataset uses spectral kurtosis as a benchmark and classifies the cases into easily diagnosable, partially diagnosable and non-diagnosable [1, 2]. This benchmark method mainly relies on kurtosis as an indicator of fault in time domain signal and thus finds optimal band and center frequency by finding the maximum value of kurtosis. However, there are several cases in which this method fails, and thus, this method of kurtogram was further modified into infogram [3], sparsogram [4, 5], and autogram [6].

Different signal processing methods are proposed to extract bearing fault features such that the size and type of fault is faithfully represented. A detailed analysis of different cepstral editing methods is discussed in [7]. On the other hand, signal processing methods based on probability distribution function of the fault signal are also being explored [8]. Cepstral analysis is used a way of filtering different than traditional Fourier spectrum based methods [9–13]. A brief history of few such methods is discussed by Randall in [14]. Out of these, automated cepstral editing procedure [15] and cepstral prewhitening [11] are important signal preprocessing methods which try to improve the diagnosability by removing stationary harmonic component from the signal.

Unlike these methods, the proposed method focuses on features local to each potential fault frequency. Though, in the benchmark study, the classification of cases is based on classical fault signatures like fault frequency and harmonics, sidebands, etc., it is not possible to quantify all of these. Thus, we define diagnosability in terms of simple quantifiable parameters like amplitude at fault frequency, deviation of fault frequency from the theoretical value, and number of significant peaks in the spectrum. The diagnosability index, thus designed, is used as a feature to select optimum band and center frequency. Cases in which the proposed method performs better than the benchmark method are discussed.

2 Diagnosability

A close observation of the CWRU dataset reveals that the fault diagnosis largely depends on following factors:

1. Amplitude at fault frequency and its harmonics,
2. Deviation of peak frequency from theoretical fault frequency,
3. Number of other significant peaks in the spectrum,
4. Sidebands in case of inner race and ball fault signals.

Based on this observation, the diagnosability index is proposed as:

$$DI = A.D.P \tag{1}$$

where, A is the amplitude at the fault frequency, D is derived from the deviation of fault frequency from its theoretical value, and P is derived from the number of other significant peaks in the spectrum.

The block diagram of the proposed method is shown in Fig. 1. As the fault signal is modulated, the conventional method of band-pass filtering and demodulating is used to find the squared envelope spectrum (SES) of the vibration signal. Full-tree wavelet packet transform (WPT), with db1 as mother wavelet, is applied to decompose the signal without reducing the length of the signal. The decomposed signal is then Hilbert transformed to find its envelope. To find out this values of A , D and P , the value of fault frequency has to be known. As the fault frequencies of inner race fault, outer race fault and rolling element fault are different, three different values of diagnosability index DI_I , DI_O and DI_R are calculated respectively.

The values of fault frequencies are theoretically calculated based on the geometry of the bearing using following formulae [16].

$$f_{or} = f_s \frac{N_b}{2} \left(1 - \frac{B_d}{P_d} \cos \emptyset \right) \tag{2}$$

$$f_{ir} = f_s \frac{N_b}{2} \left(1 + \frac{B_d}{P_d} \cos \emptyset \right) \tag{3}$$

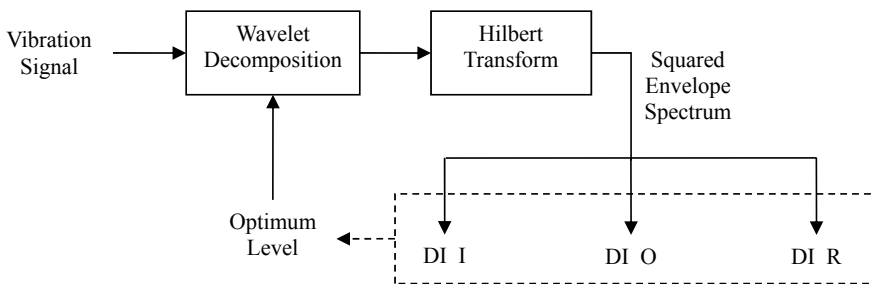


Fig. 1 Block diagram of the proposed method

$$f_{re} = f_s \frac{P_d}{2B_d} \left(1 - \frac{B_d^2}{P_d^2} (\cos \emptyset)^2 \right) \quad (4)$$

where f_s is the rotational speed in Hz, N_b is the number of rolling elements, B_d is the diameter of rolling elements, P_d is the pitch diameter, \emptyset is the contact angle, and f_{or} , f_{ir} , f_{re} are the fault frequencies of outer race fault, inner race fault, and rolling element fault (BPFI, BPFO, and BSF), respectively.

2.1 Amplitude (A)

To ensure that the diagnosability index (DI) has a value in the interval [0,1], each feature is scaled in this interval by simple linear transformation. The amplitudes of spectral peaks are scaled by dividing each value by the maximum value. This feature tells how significant the peak at the fault frequency is and it directly affects diagnosis, in a sense, that if there is a large peak at the fault frequency, then it signifies presence of fault.

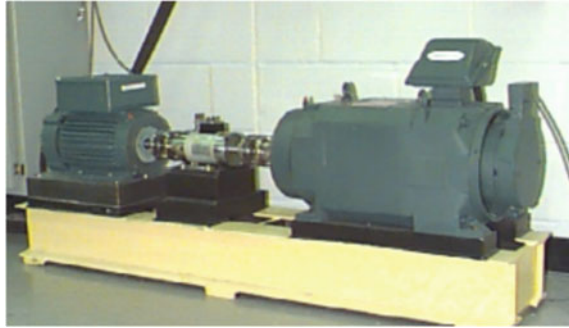
Though the theoretical value of the fault frequency is known, it is often observed that the actual value of fault frequency is slightly different. This is because of two main reasons—first, the uncertainty and error associated with the speed sensor and second, the cyclostationary nature of the signal. As mentioned by Randall et al. [16], this deviation is generally 1–2%. Considering this, we have introduced a tolerance of ± 2 Hz, and taken the maximum peak in the frequency interval of $[f - 2, f + 2]$.

2.2 Deviation (D)

As the fault frequency is bound to have some uncertainty in its value, it is very difficult, especially cases where the fault signal is submerged in noise, to pinpoint this frequency in the spectrum. With the introduction of tolerance band, there is a possibility of choosing a wrong value of frequency. To avoid this, the proposed index linearly penalizes the deviation of frequency from its theoretical value assuming that large deviation from the theoretical value means that it is unlikely to be the fault frequency. This difference in theoretical and actual frequencies is also scaled to [0,1] interval.

$$D = \frac{2 - |(\text{Actual} - \text{Theoretical})|}{2} \quad (5)$$

Fig. 2 Case Western Reserve University experimental set-up



2.3 Peaks (P)

It is quite clear that the amplitude of fault peak alone is not sufficient to quantify diagnosability. It has to be observed in relation to other significant peaks in the spectrum. If the number of significant peaks other than the fault harmonics is more, then that case is either partially or not diagnosable. Thus, the third feature to calculate DI is selected to be number of other significant peaks in the spectrum. This feature has inverse relation with diagnosability and is thus calculated similar to Eq. (2), that is, number of significant peaks is subtracted from a tolerance value and then divided by the same value to scale it down to [0,1].

It should be noted that, significance is a relative term and for the purposes of this study, it is assumed to be 20% of the maximum spectral amplitude.

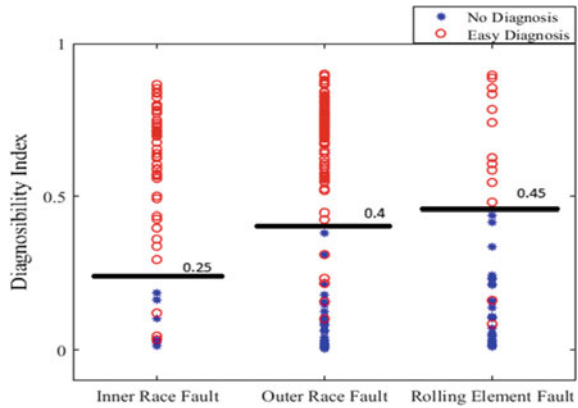
3 Bearing Fault Data

To substantiate the importance of the proposed method, we have used a standard dataset on bearing faults provided online by Case Western Reserve University [17]. The dataset contains vibration signals from a 2 hp electric motor setup as shown in Fig. 2 with 6205-2RS JEM SKF deep groove ball bearing at the drive end and 6203-2RS JEM SKF deep groove ball bearing at the fan end.

4 Results

The diagnosability index (DI) is first verified using a benchmark study on CWRU dataset [1]. In this study, each signal is classified into easily diagnosable, partially diagnosable, and non-diagnosable case. Figure 3 shows DI values for easily diagnosable and non-diagnosable cases of inner race, outer race, and rolling element faults. It can be observed from the figure that, barring few cases, the diagnosable

Fig. 3 Diagnosis based on diagnosability index



and non-diagnosable cases are fairly separable from each other based on the diagnosability index. Also, the value of proposed diagnosability index (DI) is larger for easy diagnosis as compared to non-diagnosable cases.

Figure 4 shows the performance of conventional Hilbert transform, the proposed method and the autogram method for three non-diagnosable cases of the benchmark study.

Case 1 is a case of drive end bearing with an outer race fault located opposite to the load zone with fault size of 7 mil, under 1 hp load. The accelerometer is located at the baseline of the setup, and it captures the raw vibration of the setup sampled at 12,000 Hz. This case is classified as a non-diagnosable case by the benchmark study because even after the decomposition, the envelope spectrum shows no classical spectrum features, like the peaks at the fault frequency and its harmonics. The location of the fault frequency and its harmonics are shown by arrows in Fig. 4. The autogram method also fails, as seen in Fig. 4c. This means that the optimum level (7) and corresponding optimum node (111) selected by the autogram method fails to enhance the fault features. The proposed method, however, chooses level 3 and node 4 of wavelet decomposition, and significant fault peaks can be observed in the envelope spectrum of the decomposed signal in Fig. 4b.

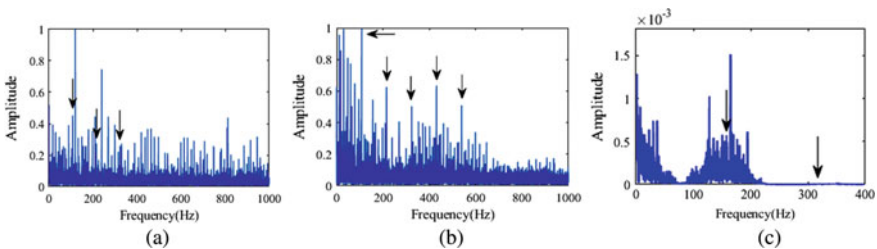


Fig. 4 Envelope spectra for Case 1 using **a** conventional Hilbert transform, **b** proposed method, **c** autogram method

Case 2 is a case of drive end bearing with a rolling element fault of 7 mil, under 2 hp load. The accelerometer is located at the baseline of the setup, and it captures the raw vibration of the setup sampled at 12,000 Hz. The cases of rolling element faults are difficult to diagnose, because the rolling element fault behaves very similar to Gaussian noise in terms of its distribution. The distribution in such cases does not show peakedness and thus kurtosis-based methods, like kurtogram and autogram, seem to fail. From Fig. 5b, it can be observed that the proposed method identifies the optimal band as (7, 44), and the envelope spectrum of the decomposed signal shows significant fault features compared to the Hilbert transform and the autogram methods.

Case 3 is a 14 mil outer raceway fault at drive end bearing, in the load zone, and the data is collected at the baseline accelerometer. The autogram method chooses the optimum level-node pair as (7, 126) which clearly removes the fault harmonics from the spectrum as shown in Fig. 6c. The optimum node chosen by the proposed method is (7, 54). At this node, we can observe maximum peak at 1X fault frequency and small peaks at second and third harmonics as shown in Fig. 6b. This result is evidently better compared to the conventional Hilbert transform, as the fault peaks are not submerged in other peaks as shown in Fig. 6a.

As the selection of optimum node depends on maximum value of the diagnosability index, the resultant spectrum should have more peak amplitude and less number of other peaks. This can be observed in all the three representative cases.

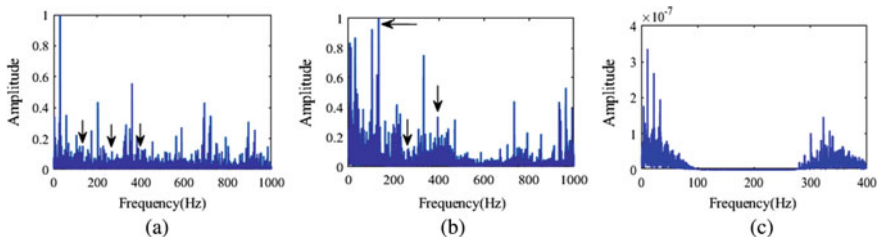


Fig. 5 Envelope spectra for Case 2 using a conventional Hilbert transform, b proposed method, c autogram method

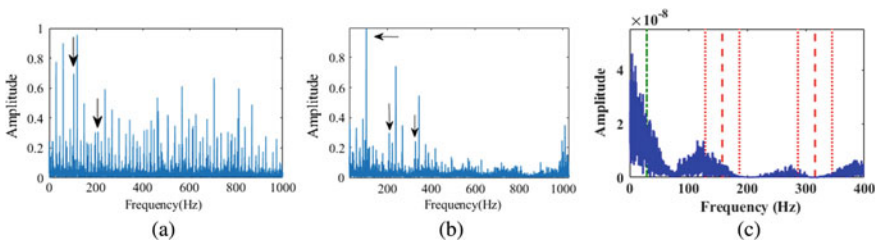


Fig. 6 Envelope spectra for Case 3 using a conventional Hilbert transform, b proposed method, c autogram method

Comparison of conventional Hilbert transform spectrum and proposed method spectrum reveals that the fault peaks become more prominent compared to other peaks in the spectrum.

5 Conclusions

Current research in bearing fault diagnosis focuses mainly on the objective of finding optimum band and center frequency so that the raw vibration signal can be decomposed to show prominent fault features in the envelope spectrum. The benchmark, kurtogram method, and its modification, the autogram method, use kurtosis to guide the selection of this optimum band. However, in various non-diagnosable cases, these methods fail. To overcome this problem, the proposed method looks at local spectrum features like the fault peak amplitude, its deviation from the theoretically calculated fault frequency, and number of other significant peaks in the spectrum. A diagnosability index is designed using these parameters such that its value is larger for easily diagnosable cases than for the non-diagnosable cases. This index is used to guide the selection of optimum band. With the help of three non-diagnosable cases, the improvement in fault features is demonstrated using the proposed method over the autogram method. The diagnosability index can be improved, in future, to provide improved classification between the easily diagnosable and non-diagnosable cases and also to incorporate the partially diagnosable cases.

References

1. Smith WA, Randall RB (2015) Rolling element bearing diagnostics using the Case Western Reserve University data: a benchmark study. *Mech Syst Signal Process* 64–65:100–131
2. Antoni J, Randall RB (2006) The spectral kurtosis: application to the vibratory surveillance and diagnostics of rotating machines. *Mech Syst Signal Process* 20(2):308–331
3. Antoni J (2016) The infogram: entropic evidence of the signature of repetitive transients. *Mech Syst Signal Process* 74:73–94
4. Tse PW, Wang D (2013) The design of a new sparsogram for fast bearing fault diagnosis: Part 1 of the two related manuscripts that have a joint title as “Two automatic vibration-based fault diagnostic methods using the novel sparsity measurement—Parts 1 and 2”. *Mech Syst Signal Process* 40(2):499–519
5. Tse PW, Wang D (2013) The automatic selection of an optimal wavelet filter and its enhancement by the new sparsogram for bearing fault detection: Part 2 of the two related manuscripts that have a joint title as “Two automatic vibration-based fault diagnostic methods using the novel sparsity measurement—Parts 1 and 2”. *Mech Syst Signal Process* 40(2):520–544
6. Moshrefzadeh A, Fasana A (2018) The autogram: an effective approach for selecting the optimal demodulation band in rolling element bearings diagnosis. *Mech Syst Signal Process* 105:294–318
7. Peeters C, Guillaume P, Helsen J (2017) A comparison of cepstral editing methods as signal pre-processing techniques for vibration-based bearing fault detection. *Mech Syst Signal Process* 91:354–381

8. Mohanty S, Gupta KK, Raju KS (2017) Effect of unitary sample shifted Laplacian and rectangular distributions in bearing fault identifications of induction motor. *IET Sci Meas Technol* 11(4):516–524
9. Morsy ME, Achtenova G (2015) Rolling bearing fault diagnosis techniques—autocorrelation and cepstrum analyses. In: 23rd Mediterranean conference on control and automation, MED, pp 328–334
10. Salah M, Bacha K, Chaari A (2014) Cepstral analysis of the stator current for monitoring mechanical unbalance in squirrel cage motors. In: 1st International Conference on Green Energy, ICGE, pp 290–295
11. Borghesani P, Pennacchi P, Randall RB, Sawalhi N, Ricci R (2013) Application of cepstrum pre-whitening for the diagnosis of bearing faults under variable speed conditions. *Mech Syst Signal Process* 36(2):370–384
12. Hwang YR, Jen KK, Shen YT (2009) Application of cepstrum and neural network to bearing fault detection. *J Mech Sci Technol* 23(10):2730–2737
13. Li H, Ai S (2008) Application of order bi-cepstrum to gearbox fault detection. In: Proceedings of World Congress on intelligent control and automation, vol 2, No. 1, pp 1781–1785
14. Randall RB (2017) A history of cepstrum analysis and its application to mechanical problems. *Mech Syst Signal Process* 97:3–19
15. Ompusunggu AP (2015) Automated cepstral editing procedure (ACEP) as a signal pre-processing in vibration-based bearing fault diagnostics. In: International conference of surveillance, pp 1–11
16. Randall RB, Antony J (2011) Rolling element bearing diagnostics—a tutorial. *Mech Syst Signal Process* 25(2):485–520
17. Loparo KA. Bearings vibration data set. Case Western Reserve University. Available: <http://csegroups.case.edu/bearingdatacenter/pages/12k-drive-end-bearing-fault-data>

Gearbox Health Condition Monitoring Using DWT Features



Setti Suresh  and V. P. S. Naidu 

Abstract The gearbox is an accessory drive, used widely for power transmission in industries and vehicles. Since its invention in the twentieth century, it brought major changes in the field of mechanical engineering. At the same time as the gearbox evolution continues, people are focusing on customized operation with less maintenance cost. Instead of the traditional approach (scheduled and unscheduled maintenance), the industry is looking for condition-based preventive maintenance. Therefore, it is important to monitor the health condition of the gearbox. This paper presents three different architectures to diagnose the gearbox vibration signal between healthy and damaged condition. Fifteen wavelet features are extracted from the segmented signal and tested with infinite latent feature selection (ILFS) algorithm to find useful features based on ranking. Feature classification was done using a support vector machine (SVM) algorithm. The ideology of the round-robin technique was implemented in architecture-2. The result shows that, among the three developed architectures, the first architecture with discrete wavelet transform (DWT—1D) followed by the SVM model is providing better classification accuracy than the other two architectures. The results were presented with 100 Monte Carlo runs.

Keywords Condition monitoring · Gearbox fault diagnosis · SVM classifier

Nomenclature

DWT Discrete wavelet transform
ILFS Infinite latent feature selection
NREL National Renewable Energy Laboratory

S. Suresh (✉)

School of Avionics, Institute of Science and Technology, JNTUK, Kakinada, India
e-mail: settisuresh1@gmail.com

V. P. S. Naidu

Multi Sensor Data Fusion Lab, FMCD, CSIR-National Aerospace Laboratories, Bangalore, India
e-mail: vpsnaidu@gmail.com

PCA	Principal component analysis
SVM	Support vector machine
UCI	University of California Irvine
W_{SHE}	Shannon entropy
W_{LEE}	Log energy entropy
W_{TE}	Threshold entropy
W_{SE}	Sure entropy
W_{NE}	Norm entropy
W_E	Wavelet energy
W_P	Wavelet power
W_V	Wavelet variance
W_{STD}	Standard deviation
W_{IQR}	Interquartile range
W_M	Wavelet mean
W_{HM}	Harmonic mean
W_{SK}	Skewness
W_{KUR}	Kurtosis
W_{CV}	Coefficient of variation

1 Introduction

The gearbox is one of the important parts of the rotating machinery, which plays a major role in the transportation and processing industries. As the gearbox is an active component in the automatic transmission, its failure could cause the entire machinery to shut down. Partial failure of the gearbox may lead to inefficient operation of the machinery associated with it and deteriorates the performance of the system, which is not cost effective. In any mechanical system, the fault cannot happen suddenly. When the system is prone to minor impact and if early detection of the fault does not happen, it may lead to failure of the whole system. Even though the gearbox (as a subsystem) is designed for a particular span of time to work effectively but it may lead to failure in working conditions due to several external factors. The failure of the gearbox can affect the overall efficiency of the industry in terms of maintenance delay, cost and loss of equipment. Therefore, it is crucial to monitor the gearbox health and detect the faults in the early stage. Some of the applications with gearbox include aircraft (engine accessory drives), automobile gear system, wind turbine, etc.

There are different conditions monitoring techniques used in the industry to monitor the health of the rotating machinery. The sensor mechanisms used for monitoring the rotating machinery consist of thermal, acoustic and vibration analyses. Among the three, vibration analysis is the most widely used condition monitoring technique as it contains information regarding the characteristic vibrations of each component. The accelerometers mounted on the gearbox in different direction acquire

the composite vibration signal, which is a combination of gear, bearing and shaft characteristic frequencies. Each component has its own characteristic vibration, and it is very difficult to find out where the fault has occurred really from the composite signal. In addition, the varying load on the gearbox has an effect on the measured vibration signal. As the load on the gearbox increases, the induced vibrations in each component change, and they are reflected in the acquired vibration signal. All these scenarios have to be considered while analyzing the vibration signal. The application of wavelet transform to the residual signal and fault diagnosis using fault growth parameter, statistical and kurtosis features for varying load of gearbox dataset has been presented in [1]. The bearing fault diagnosis using wavelet decomposition, discrimination of signal using basic mean and standard deviation features computed for the wavelet coefficients were asserted in [2]. The fault classification in gears using SVM with feature vector containing seven statistical features in the time domain, ten-frequency domain features and standard deviation of wavelet coefficients in time–frequency domain with a feature selection technique based on Euclidean distance has been proposed in [3]. The researchers [1–3] proposed different approaches to find their own way in the fault diagnosis of the vibration signal.

In this paper, the effect of overlapping epochs and wavelet decomposition applied to each epoch is discussed. Fifteen information theoretic features are computed from detailed and approximation wavelet coefficients for all levels and concatenated to form a feature vector. To remove the unwanted features from the vector, a feature selection algorithm is used. Three different fault classification algorithms (architectures) are developed and evaluated for gearbox health condition monitoring. The consistency in the fault detection accuracy of the developed algorithm is illustrated using 100 Monte Carlo runs [4]. The datasets used in this paper are vibration signals collected from UCI machine learning repository [5] (dataset-1) and NREL—wind turbine benchmarking gearbox datasets [6] (dataset-2).

2 Methodology

In general, the sequence of steps involved in gearbox health condition monitoring is acquiring sensor data, preprocessing the data, feature extraction and selection, followed by feature classification to detect the fault.

2.1 Data Acquisition

Vibration data was collected using the accelerometer sensor and a high-speed data acquisition system. In this paper, two different datasets are used for gearbox health condition monitoring from two sources.

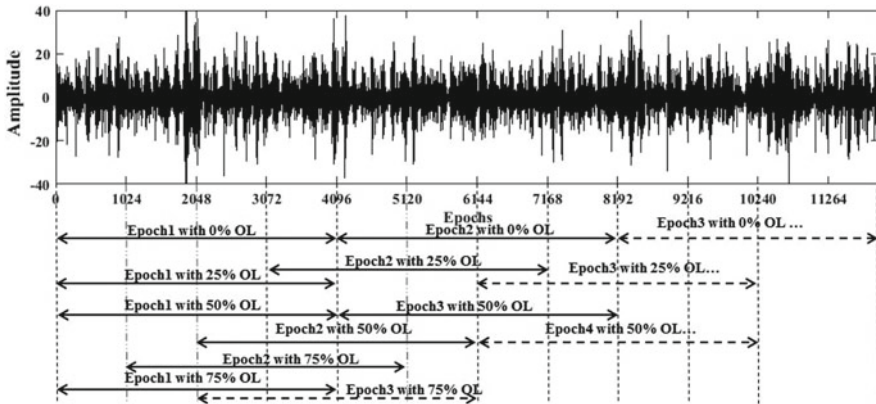


Fig. 1 Data preprocessing

Dataset-1: This gearbox dataset is collected from the UCI machine learning repository archives [5]. The dataset consists of healthy and broken tooth cases of a gearbox. The vibration data has been recorded using four different sensors placed in four different directions, by varying the load from ‘0’ to ‘90’ percent. ‘0’ stands for free rotation of the gearbox. There are ten healthy and broken teeth data files, and each file has four sensors data.

Dataset-2: Wind turbine gearbox dataset is obtained from NREL [6]. The vibration data was collected from healthy and damaged wind turbine gearbox by using accelerometer sensors with a dynamometer test facility. Eight accelerometer sensors were mounted on the surface of the gearbox in different directions covering low-speed shaft, intermediate shaft and high-speed shaft gear assemblies. The data was recorded at a sampling frequency of 40 kHz per channel. Ten 1-min datasets are available for both healthy and damaged gearbox.

2.2 Preprocessing

Data preprocessing is an important step in the data mining process. The raw vibration signal is divided into overlapping (OL) epochs/segments with 0, 25, 50 and 75% overlap. Figure 1 shows the overlapping epochs of the gearbox vibration signal.

2.3 Feature Extraction

Feature extraction is one of the important issues in machine health condition monitoring. The main purpose of extracting features from a signal is that they will provide

necessary discriminative information for classifying the fault to have better classification accuracy [7]. The segmented vibration data is decomposed into approximation and detailed coefficients using DWT. The features, described in Table 1, are computed

Table 1 Wavelet domain features

S. No.	Features	Formula	Ref.
1	Shannon entropy	$W_{SHE}(s) = - \sum_{i=1}^n s_i^2 \log(s_i^2)$	[8–10]
2	Log energy entropy	$W_{LEE}(s) = \sum_{i=1}^n \log(s_i^2) \dots$ with the convention $\log(0) = 0$	[8]
3	Threshold entropy	$W_{TH}(s_i) = 1 \text{ } s_i > p$ and 0 otherwise $W_{TH}(s) = \sum_{i=1}^n W_{TH}(s_i)$ Or $W_{TH}(s) = \#(i \text{ such that } s_i > p)$	[8]
4	Sure entropy	$W_{SU} = n - \#(i \text{ such that } s_i \leq p) + \sum_{i=1}^n \min(s_i^2, p^2)$	[8]
5	Norm entropy	The concentration in l^p norm entropy with $1 \leq p$ equivalent to $(l, p)^p$ $W_{NE} = \sum_{i=1}^n s_i ^p$	[8]
6	Wavelet energy	$W_E(s_k) = \sum_{i=1}^n a_k(i)c_k(i)^2$	[10]
7	Wavelet power	$W_P(s_k) = \frac{1}{n} \sum_{i=1}^n a_k(i)c_k(i)^2$	–
8	Wavelet variance	$W_V(s_k) = \frac{1}{n} \sum_{i=1}^n (c_k(i) - \overline{c_k(i)})^2$	[9, 11]
9	Interquartile range	$W_{IQR}(s_k) = Q_U - Q_L$ $Q_U = \frac{n_U+1}{2}, Q_L = \frac{n_L+1}{2}$	–
10	Mean	$W_M(s_k) = \frac{1}{n} \sum_{i=1}^n c_k(i)$	[2, 3, 9, 12]
11	Harmonic mean	$W_{HM}(s_k) = \frac{n}{\sum_{i=1}^n \frac{1}{c_k(i)}}$	[9]
12	Standard deviation	$W_{STD}(s_k) = \sqrt{\frac{\sum_{i=1}^n (c_k(i) - \overline{c_k(i)})^2}{n-1}}$	[2, 3, 9, 12]
13	Skewness	$W_{SK}(s_k) = \frac{\frac{1}{n} \sum_{i=1}^n (c_k(i) - \overline{c_k(i)})^3}{\left[\frac{1}{n} \sum_{i=1}^n (c_k(i) - \overline{c_k(i)})^2 \right]^{\frac{3}{2}}}$	[3, 9, 12]
14	Kurtosis	$W_{KUR}(s_k) = \frac{\frac{1}{n} \sum_{i=1}^n (c_k(i) - \overline{c_k(i)})^4}{\left[\frac{1}{n} \sum_{i=1}^n (c_k(i) - \overline{c_k(i)})^2 \right]^2}$	[3, 9, 12]
15	Coefficient of variation	$W_{CV} = \frac{W_{STD}}{W_M}$	[9]

Note: s_i = i th coefficient associated with each signal; n = number of observations in each wavelet coefficient; n_U and n_L = upper and lower half observations in each wavelet coefficient; a_k = approximation scaling coefficient of level k ; Q_U and Q_L = median of upper half and lower half observations of the wavelet coefficient; k = decomposition levels; c_k = coefficients at level k

for the wavelet coefficients at different levels of decomposition. The first five features are based on entropy criteria, and the remaining ten are statistical features.

The decomposition levels are decided based on the numerical values of gear mesh frequencies, their harmonics and sidebands of the gearbox. For dataset-2, the sampling frequency is 40 kHz and lowest gear mesh frequency is 2.103 Hz (computed from the specifications of the gearbox in dataset-2) lead to choosing 12 decomposition levels. For dataset-1, there are 61 features in a feature vector that contains [4 (approximation + 3 detailed) \times 15 (features) + 1 (load)]. Similarly, for dataset-2, there are 195 features in a feature vector that contains [13 (approximation + 12 detailed) \times 15 (features)].

2.4 Feature Selection

The feature selection is used to reduce the dimension of the feature vector using the feature selection algorithm. Instead of using all the features that might result in overfitting, the useful features from the estimated feature vector are sorted based on ranking. An infinite latent feature selection (ILFS) algorithm [13] is used to reduce the size of the feature vector and to arrange the features based on ranking.

2.5 Feature Classification

Support vector machine (SVM) [12], most commonly used supervised machine learning algorithm, is used for feature classification. The extracted wavelet features are divided into training and testing set. From the total available observations for each sensor, the SVM model is trained with 70% of random permutation observations along with labels. The remaining 30% of observations are used to test the SVM classifier. The SVM model accuracy is verified with 100 Monte Carlo runs.

3 GHCM Architectures

In this paper, three different gearbox health condition monitoring (GHCM) architectures are presented and evaluated. Figure 2 shows the information flow diagram of architecture-1, where the raw sensor vibration data is preprocessed into overlapping epochs. Features (discussed in Sect. 2.3) are computed using DWT with different decomposition levels for every epoch. These features are computed for different gearbox conditions (healthy and damage) and form the feature set. This feature set is divided into training and testing sets. The training set is used to train the SVM model along with labels of gearbox faults, and the trained SVM model is tested with a testing set.

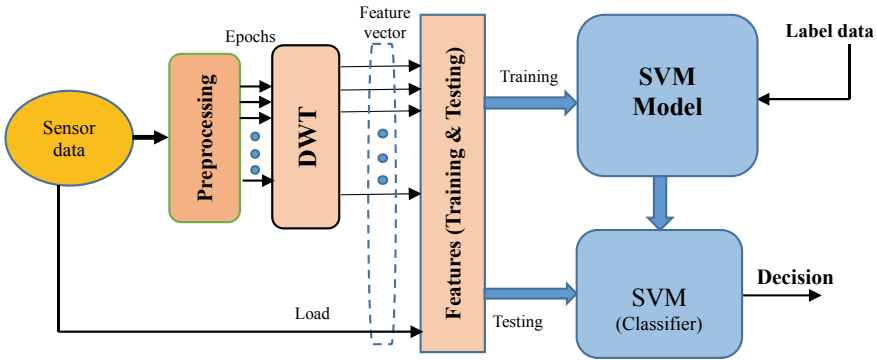


Fig. 2 Architecture-1 (A₁)

The second architecture (A₂) as shown in Fig. 3 depicts the analogy of feature combination with round-robin [14] technique. The ideology behind this is to give priority to all the features in stating the condition of the gearbox. The sequence of operations up to feature vector formation and generating training and testing data is the same as that of architecture-1. In round-robin technique block if there are n features, ' N ' ($N = {}^n C_2$) feature combinations are formed to generate ' N ' SVM models. For 195 features (all features of dataset-2), we will have a combination of ${}^{195}C_2 = 18915$ SVM models. Therefore, for each observation (row) we will get 18,915 decisions. All the decisions are fused to have a combined decision by keeping a threshold of more than 50% (voting methodology), and the resulting accuracy is granted as a final decision (healthy or damaged). Therefore, developing a combinational feature model to classify the data between healthy and broken tooth case of the gearbox.

The third architecture (A₃) as shown in Fig. 4 is developed using principal compo-

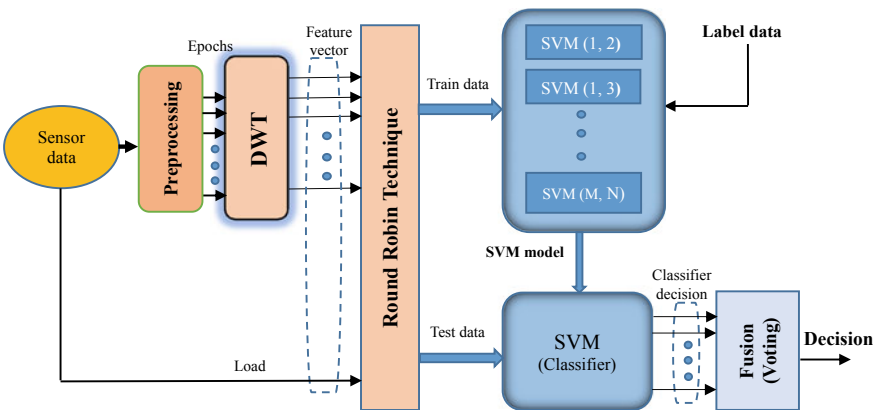


Fig. 3 Architecture-2 (A₂)

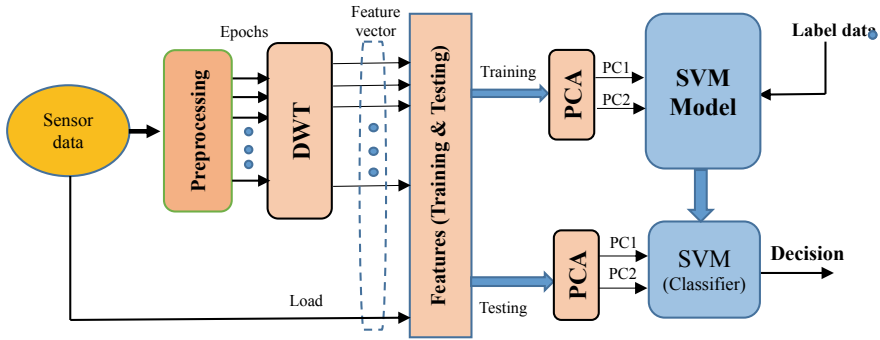


Fig. 4 Architecture-3 (A₃)

nent analysis (PCA) which is a data reduction technique [15], implemented to convert the set of observations of correlated variables (features) into linearly uncorrelated variables called principal components. The first two principal components, which contain 80 percent of the total feature vector information, are used to train the SVM model. The rest of the process is similar to A₁.

4 Results and Discussion

The proposed three GHCM architectures (A₁, A₂ and A₃) are tested using dataset-1 and dataset-2, and the results are presented in this section. Table 2 shows the classi-

Table 2 Classification accuracy of overlapping epochs with A₁ and A₃ using 100 Monte Carlo runs

	S ₁ (%)	S ₂ (%)	S ₃ (%)	S ₄ (%)	All sensors
Overlapping of epochs in percentage = 0%					
A ₁	100 ± 0.00	99.96 ± 0.17	99.92 ± 0.25	NC	99.85 ± 0.31
A ₃	100 ± 0.00	100 ± 0.00	100 ± 0.00	65.04 ± 3.23	100 ± 0.00
Overlapping of epochs in percentage = 25%					
A ₁	99.99 ± 0.07	99.99 ± 0.07	99.89 ± 0.24	NC	99.97 ± 0.12
A ₃	100 ± 0.00	99.97 ± 0.12	76.51 ± 19.42	64.43 ± 2.53	100 ± 0.03
Overlapping of epochs in percentage = 50%					
A ₁	99.99 ± 0.06	99.87 ± 0.21	99.93 ± 0.14	NC	99.90 ± 0.17
A ₃	100 ± 0.00	100 ± 0.00	100 ± 0.00	64.40 ± 2.21	100 ± 0.00
Overlapping of epochs in percentage = 75%					
A ₁	99.92 ± 0.12	99.96 ± 0.09	99.91 ± 0.14	NC	99.92 ± 0.10
A ₃	100 ± 0.00	99.96 ± 0.08	70.51 ± 18.77	65.34 ± 1.80	100 ± 0.00

A₁ = Architecture-1; A₃ = Architecture-3; S₁, S₂, S₃, S₄ = Sensors; NC no convergence

Table 3 Feature selection using ILFS algorithm (for dataset-2)

FP	F	Wavelet Coefficients (level-12)												
		D ₁	D ₂	D ₃	D ₄	D ₅	D ₆	D ₇	D ₈	D ₉	D ₁₀	D ₁₁	D ₁₂	A ₁₂
1-13	W _{SHE}	★	★	★	★	★	★	★ ₇	★	X	X	X	X	X
14-26	W _{LEE}	★	★	★	★ ₂	★	★	★	★	X	X	X	X	★
27-39	W _{TE}	★	★	★	★	★ ₆	★ ₃	★ ₈	X	X	X	X	X	★
40-52	W _{SE}	X	★	★	★ ₄	★	★	★	★	X	X	X	X	★
53-65	W _{NE}	★	★	★	★	★	★	★	★	X	X	X	X	X
66-78	W _E	★	X	X	X	X	X	X	★	★	★ ₅	X	X	X
79-91	W _P	X	★	★	★	★	★	★ ₉	★	X	X	X	X	X
92-104	W _V	★	★	★	★	★	★	★ ₁₀	★	X	X	X	X	X
105-117	W _{CV}	X	X	X	X	X	X	X	X	X	X	X	X	X
118-130	W _{SK}	X	X	X	X	X	X	X	X	X	X	★	X	X
131-143	W _{KUR}	X	★	★	X	X	X	★	X	X	X	X	X	X
144-156	W _{IqR}	★	★	★ ₁	★	★	★	★	★	X	X	X	X	X
157-169	W _{HM}	X	X	X	X	X	X	X	X	X	X	X	X	X
170-182	W _M	X	X	X	X	X	X	X	X	X	X	X	X	X
183-195	W _{STD}	★	★	★	★	★	★	★	★	X	X	X	X	X

★: selected features, X: omitted features, FP: feature position in the feature vector, F: feature

fication accuracy of overlapping epochs for individual sensors and all sensors data using A₁ and A₃ with 100 Monte Carlo runs for dataset-1 with consideration of all features. A₂ is omitted from 100 Monte Carlo loops due to its time constraint of generating feature combination SVM models. It is observed that 0% of overlapping provides better classification accuracy. Similarly, for dataset-2, 25% of overlapping epochs provides better classification accuracy. Therefore, the overlapping effect is a data-driven phenomenon. Table 3 shows the feature selection using the ILFS algorithm for dataset-2. The first two columns in the table show the feature and its position in the feature vector. From 195 features, the features indicated with a star are selected as useful features with a classification accuracy of 99%. All the remaining features are omitted (indicated with a cross) for classification. The top ten features (star with suffix) are also shown in the table. It is observed from the results that the wavelet features such as skewness, coefficient of variation, kurtosis, harmonic mean and mean will not provide good classification, and similar observation is made from dataset-1.

The features in feature vector are rearranged based on feature ranking provided by ILFS algorithm. Figure 5 shows the SVM classification for A₁. From the figure, it can be inferred that superior ranking features provide perfect classification and satisfactory ranked features showing moderate classification followed by inferior ranking features showing poor classification. Table 4 shows the classification accuracy by considering all features and by considering useful features using ILFS algorithm for dataset-1. It is observed that by considering useful features, the proposed GHCM architectures provide better classification accuracy than considering all the features. GHCM architecture A₁ for sensor 4 is unable to converge while considering all

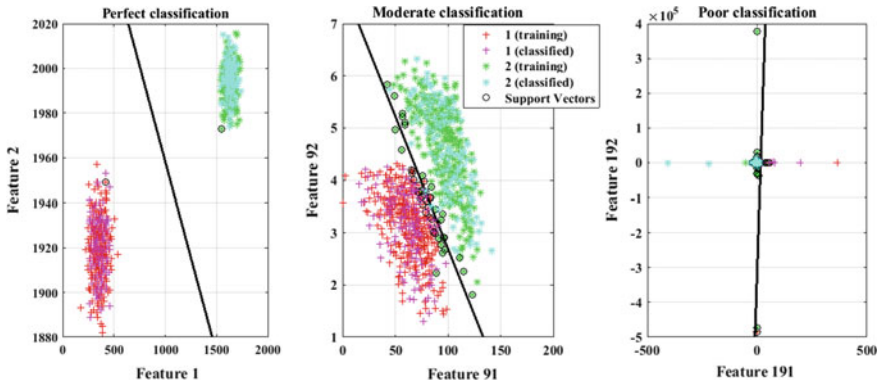


Fig. 5 SVM classification for dataset-2 (sensor 1)

features as shown in Table 4. The fault classification accuracy using all and useful features for dataset-2 is shown in Table 5. It is observed that by considering useful features, the classification accuracy is 100% than considering all features. It is also observed that A_2 is unable to converge the solution when considering all features.

Figure 6 shows the SVM classification for all sensors in case of dataset-1 with the first two superior features. It is observed that sensor 1, 2 and 3 are able to classify the signal (healthy and damaged) and sensor 4 is unable to classify the signal. It is understood that sensor 4 is far away from the fault location and not able to capture the faulty vibration signal. A similar classification is made for dataset-2, and all sensors are successful in classifying the gearbox condition between healthy and damaged signal. From the results, it can be inferred that, among the three architectures, the A_1 is giving better fault classification accuracy followed by A_3 . Architecture-2 (A_2) may not be useful for real-time gearbox fault diagnosis due to its time constraint limitation to generate multiple SVM models and poor classification (considering all features).

5 Conclusion

Three gearbox health condition monitoring architectures had been developed and tested using two different datasets, and the results were presented with 100 Monte Carlo runs. The phenomenon of overlapping segments has been exercised for the vibration signal of the gearbox and realized that the overlapping effect is a data-dependent preprocessing. The segmented signal over a fixed length has converted into information theoretic wavelet features at different levels of decomposition. The notion of feature selection algorithm (ILFS) has applied to the computed features to get useful features, which resulted in the improved SVM fault classification accuracy. The ideology of the round-robin technique has been used with architecture-2 for gearbox health condition monitoring. It is concluded that Architecture A_1 provides

Table 4 Classification accuracy with all and useful features (dataset-1)

	With all features (61)				With useful features (41)			
	$S_1(\%)$	$S_2(\%)$	$S_3(\%)$	$S_4(\%)$	$S_1(\%)$	$S_2(\%)$	$S_3(\%)$	$S_4(\%)$
A_1	100 ± 0.00	99.96 ± 0.17	99.92 ± 0.25	NC	100 ± 0.00	100 ± 0.00	100 ± 0.00	81.85 ± 2.71
A_2	100	100	97.92	52.78	100	100	100	55.56
A_3	100 ± 0.00	100 ± 0.00	100 ± 0.00	64.78 ± 3.05	100 ± 0.00	100 ± 0.00	100 ± 0.00	64.85 ± 3.06

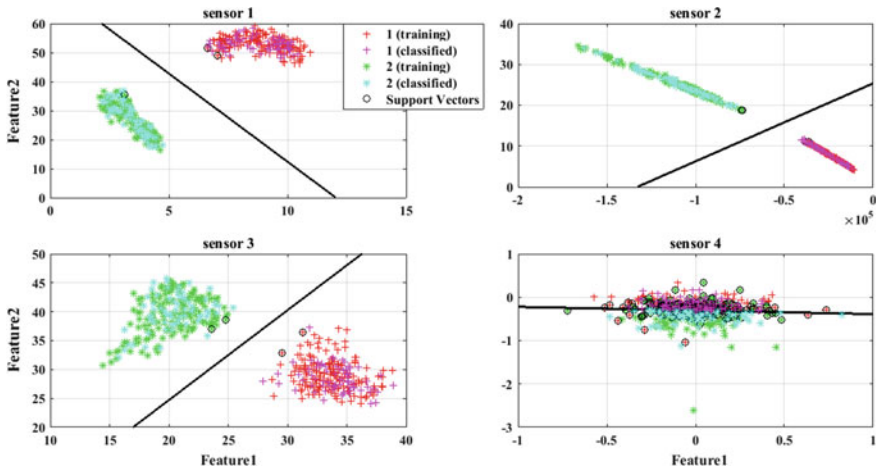


Fig. 6 SVM classification for all sensors (dataset-1)

better fault classification accuracy followed by A_3 and Architecture A_2 may not be feasible for real-time application because of its time complexity.

Acknowledgements The authors would like to acknowledge the U.S. Department of Energy’s National Renewable Energy Laboratory (NREL) for providing the Wind Turbine Gearbox Vibration Condition Monitoring Benchmarking Datasets in this research.

References

1. Wang X, Makis V, Yang M (2010) A wavelet approach to fault diagnosis of a gearbox under varying load conditions. *J Sound Vib* 329(9):1570–1585
2. Shanmukha Priya V, Mahalakshmi P, Naidu VPS (2015) Bearing health condition monitoring: wavelet decomposition. *Indian J Sci Technol* 8. <https://doi.org/10.17485/ijst/2015/v8i26/81712>
3. Soleimani A, Mahjoob MJ, Shariatpanahi M (2009) Fault classification in gears using support vector machines (SVMs) and signal processing. In: 2009 Fifth International Conference on Soft Computing, Computing with Words and Perceptions in System Analysis, Decision and Control, Famagusta, pp 1–4 (2009)
4. Anderson HL (1986) Metropolis, Monte Carlo and the MANIAC. *Los Alamos Sci* 14:96–108
5. <https://data.world/gearbox/gear-box-fault-diagnosis-data-set>. Accessed 06 Mar 2019
6. Sheng S (2012) Wind turbine gearbox vibration condition monitoring benchmarking datasets. National Renewable Energy Laboratory, USA. <https://openei.org/datasets/dataset/wind-turbine-gearbox-condition-monitoring-vibration-analysis-benchmarking-datasets>
7. Li W, Shi T, Liao G, Yang S (2003) Feature extraction and classification of gear faults using principal component analysis. *J Qual Maint Eng* 9:132–143. <https://doi.org/10.1108/13552510310482389>
8. Mathworks (2019) “Wentropy”, Mathworks. Available: <https://in.mathworks.com/help/wavlet/ref/wentropy.html>. Accessed 06 Mar 2019

9. Afghah F, Razi A, Soroushmehr R, Ghanbari H, Najarian K (2018) Game theoretic approach for systematic feature selection; application in false alarm detection in intensive care units. *Entropy* 20(3):190
10. Ekici S, Yildirim S, Poyraz M (2008) Energy and entropy-based feature extraction for locating fault on transmission lines by using neural network and wavelet packet decomposition. *Expert Syst Appl* 34(4):2937–2944
11. Rajani J, Srinivas M, Naidu VPS (2018) Gearbox health condition monitoring: vibration analysis. In: National conference on VLSI design, signal processing, image processing, communication & embedded systems (NCVSPICE-2018). ISBN: 978-93-85100-99-4, JNTUK, Kakinada, 19–20 July 2018, pp 68–71
12. Rajani J, Naidu VPS (2017) Bearing health condition monitoring using time domain analysis & SVM. *Control Data Fusion (e-Journal)* 1(5):02–11. ISSN: 2581-5490, Sept–Oct 2017
13. Roffo G, Melzi S, Castellani U, Vinciarelli A (2017) Infinite latent feature selection: a probabilistic latent graph-based ranking approach. In: 2017 IEEE international conference on computer vision (ICCV), Venice, pp 1407–1415 (2017)
14. Oyague F, Butterfield CP, Sheng S (2018) gearbox reliability collaborative analysis Round Robin. National Renewable Energy Laboratory, Golden, CO, Report No. NREL/CP-500-45325
15. Qian H, Liu Y, Lv P (2006) Kernel principal components analysis for early identification of gear tooth crack. In: 2006 6th World Congress on Intelligent Control and Automation, Dalian, pp 5748–5751 (2006)

Gas Turbine Engine Fan Blade Flutter Detection Using Casing Vibration Signals by Application of Recurrence Plots and Recurrence Quantification Analysis



A. N. Viswanatha Rao, V. P. S. Naidu, and Soumendu Jana

Abstract Gas turbine aero engines are a specific class of turbomachinery wherein compression system and turbine are realized as spinning discs on an interconnecting shaft. Fan-bladed disc undergoes an unsteady aeroelastic phenomenon known as flutter during various operational regimes, which might lead to structural failure of blades. Study of this mode of flutter induced structural response by measuring casing vibration is of interest in health monitoring of aero engines. In this paper, authors present a novel application of detecting the rotating blade flutter based on the feature space constructed using statistical parameters, recurrence plots (RP) and recurrence quantification analysis (RQA) of engine casing vibration data. Feature vectors thus obtained are visualised in several 3D vector space plots to cluster the data points which separate flutter mode from the normal mode of operation. Results obtained through the proposed method have been compared with engine flutter test results obtained through dedicated rotating blade strain gauge instrumentation.

Keywords Flutter · Recurrence plots · Bladed disc · Casing vibration · Low-pressure compressor (LPC) · High-pressure compressor (HPC)

A. N. Viswanatha Rao (✉) · V. P. S. Naidu · S. Jana
Academy of Scientific and Innovative Research (AcSIR), Ghaziabad 201002, India
e-mail: vishwanatha@gtre.drdo.in

V. P. S. Naidu
e-mail: vpsnaidu@nal.res.in

S. Jana
e-mail: sjana@nal.res.in

A. N. Viswanatha Rao
DRDO—Gas Turbine Research Establishment, Bengaluru 560093, India

V. P. S. Naidu · S. Jana
CSIR—National Aerospace Laboratories (NAL), Bengaluru 560017, India

Nomenclature

<i>1F</i>	First flexural mode
<i>2F</i>	Second flexural mode
<i>1T</i>	First torsional mode
N_L	LPC spool speed
N_H	HPC spool speed
<i>RPS</i>	Revolutions per second
<i>EO</i>	Engine orders
ksp/s	Killo samples per second

1 Introduction

Gas turbine engine-based propulsion system of an aircraft is one of the flight safety critical systems, which encompass various disciplines of science and technology. A developmental aero engine under consideration is an augmented low bypass ratio twin spool turbofan with a dry thrust rating of 51 kN and maximum after burner thrust of 81 kN. The engine has been configured with an axial flow fan of three stages and six stages of core compressor. It has an annular combustor, single-stage cooled high-pressure turbine operating at maximum temperature of 1700 K and a single-stage unshrouded low-pressure turbine [1].

In order to meet the requirements of high thrust to weight ratio (>7), aero engine structures are designed to operate with lower factor of safety margins. Cyclic load experienced during vibration of engine components leads to fatigue failure. Engine rotating blades get excited by aerodynamic instabilities like rotating stall, surge and by aeroelastic instability termed as flutter [2].

Bladed disc assemblies experience system level vibratory modes referred to as nodal diameters. Generally, at any particular rotational speed of engine, if a resonant condition of blades exists, then such a crossover may lead to high cycle fatigue failure. The Campbell diagram graphically represents such resonance crossover condition of blades. It is a 2D plot, where in measured or predicted natural frequencies of blades and corresponding excitation by engine rotational speed are presented. Blades can vibrate in flexural modes 1F and 2F and torsional modes 1T. While in operation, excitation by rotor at harmonics of the rotational speed can also excite the vibration, and these excitation lines are termed 2EO, 3EO, 4EO and so on [2]. There are several sources of excitation during engine operation, which can lead to vibration of blades. A case study of aeroelastic flutter in a transonic axial compressor rotor based on analytical methods has been discussed in. The unsteady airflow that leads to aerodynamic force fluctuation close to fan blade natural frequency, resulting in excitation of the blades, has been discussed at length. A study of the structural and dynamic behaviour of bladed disc assembly is crucial to decide whether the response is due to flutter or not [3].

Structural health monitoring of the engine is of paramount importance during developmental tests. Hence, in order to monitor the blade vibration and flutter phenomenon, extensive instrumentations are carried out during developmental tests. Engine test data obtained during development phase forms the basis for life and usage monitoring algorithms, which would be used during subsequent operational phase. One of the critical health monitoring instrumentations that would be employed during operational phase of the engine is the casing vibration [4]. In this paper, data analysis algorithm of detecting flutter signatures from the casing mounted vibration sensor has been developed and validated with known cases of flutter. Gas turbine engines used for aircraft propulsion application must meet safety and reliability requirements. High degree of reliability is achieved by suitable design and proper maintenance schedules. When any fault is reported by the monitoring instrumentation, detailed fault diagnosis is undertaken which is complex and time-consuming. In order to aid the fault diagnosis, statistical methods that rely on feature extraction technique have evolved over the past two decades [5].

2 Flutter in Fan of a Gas Turbine Engine

The fan of a gas turbine engine under consideration is shown in Fig. 1a. In this configuration, fan blades are assembled on to the disc through a dovetail interface to form a bladed disc assembly as shown in Fig. 1b. Due to the complex geometry and twist of fan blades, the aerodynamic load, centrifugal forces acting during rotation result in blades experiencing both bending and torsion motions. First stage of the fan-bladed disc assembly is of particular interest since this is the highly loaded stage, which handles the entire mass flow into the engine, and is having the longest blades, which vibrate with high amplitude and at relatively low frequency.

Flutter is a self-induced vibration due to instability in the bladed disc system in any turbomachinery and is usually associated with one of the blade's fundamental

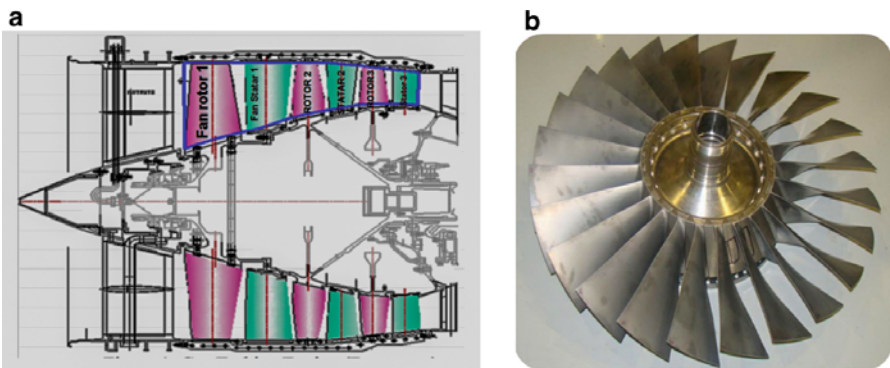


Fig. 1 a Third-stage axial fan of a gas turbine engine. b First-stage fan rotor blade disc

modes (bending or torsion) with a frequency close to the natural frequency. During flutter, condition aerodynamic forces induced due to blade vibration feed energy back into the bladed disc structure itself. This leads to stress pile-up in each cycle of vibration and can result in structural damage. One noticeable feature of flutter induced vibration is that it is non-integral to the engine rotational speed [6, 7].

3 Instrumentation to Acquire Flutter Signals

Engine is instrumented extensively during developmental tests with a suitable data acquisition system to obtain high-quality aerodynamic performance data for the fan module under tests. Transient dynamic data from strain gauges, casing flush-mounted high-frequency response pressure transducers and casing vibration are acquired with wide bandwidth data acquisition systems. Rotational speed of the engine is a fundamental parameter for blade health monitoring. Blade vibration measurement requires a reference signal, which is essentially a once-per-revolution (1/rev) signal from fan-bladed disc. It is an eddy current sensor, which senses the passing of a reference feature on the low-pressure compressor shaft. This signal gives an angular reference point on the spool, which would be useful for identifying the exact blade in the rotating disc [8].

Engine casing structural vibration level on the fan casing is measured by a piezo-electric accelerometer (CA 134/5 of Vibrometer©, USA make). The sensor has a wide dynamic range of measurement up to 500 g and sensitivity of 10pc/g and a bandwidth of 6 kHz. The bandwidth requirements for casing vibration are ~2 kHz which can sense tenth harmonic of LPC spool speed and eighth harmonic of the HPC spool speed when engine is tested 10–100% speed. In addition to the vibration, casing flush-mounted miniature piezo-resistive pressure sensors (XT-190-25G) are used for detecting unsteady aerodynamic phenomena like rotating stall, surge and flutter [8].

3.1 Rotor Blade Vibration

Traditionally, blade vibration is measured using strain gauges during initial phases of engine development. Strain gauge measures strains experienced by rotor blades. During the experimental evaluation of the fan, foil-type strain gauges of karma© (74 Ni, 20 Cr, 3 Al, 3 Fe) with a gauge factor of 2 were used. These are small in size, low in mass, easy to attach to fan blade through an adhesive [9]. Gauges are placed on specific locations based on finite element studies to capture various modes of blade vibration [10]. Lead wires from the strain gauges are routed through the blade root dovetail to the rotating slip ring/telemetry system to transfer the data from rotating system to the static frame as shown in Fig. 2.

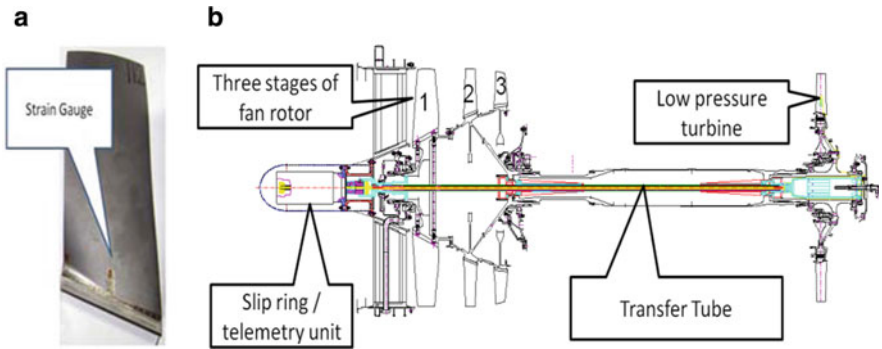


Fig. 2 a Fan rotor blade strain gauge. b Fan rotor blade strain gauge and rotating instrumentation arrangement. *Courtesy* GTRE

In order to evaluate the presence of flutter in the fan, elaborate testing procedure is required. It is established both analytically and experimentally that fan blade flutter occurs at a defined corrected rotational speed [2]. During engine test at the normally aspirated test cell, speed is gradually increased, while carefully watching the build-up of flutter signals simultaneously through strain signals from blades and casing mounted vibration sensors. Upon appearance of flutter signals, engine is accelerated away from the flutter speed band. Since strain gauge measurement is in rotating frame of reference, the sensors would pick up the strain response of the blades as single tone signature when blades vibrate. The Campbell diagrams shown in Fig. 3a, b indicates marginal strain build-up at 2EO crossover and flutter occurring at 1.8EO asynchronously.

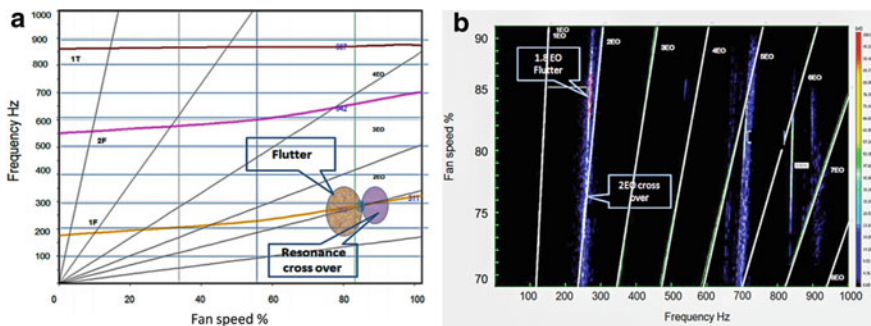


Fig. 3 a Campbell diagram of the fan blades (theoretical estimates). b Non-synchronous (1.8 EO) blade response shown flutter in fan blades (Experimental results)

4 Casing Vibration Signals

Rotation of the engine is the excitation for any vibratory response of engine subsystems. Hence, it is an industry practice to analyse the vibratory response by using the concept of engine order tracked RMS levels. It can be seen from Fig. 4a that when the engine fan speed crosses the flutter speed band, RMS level of the casing

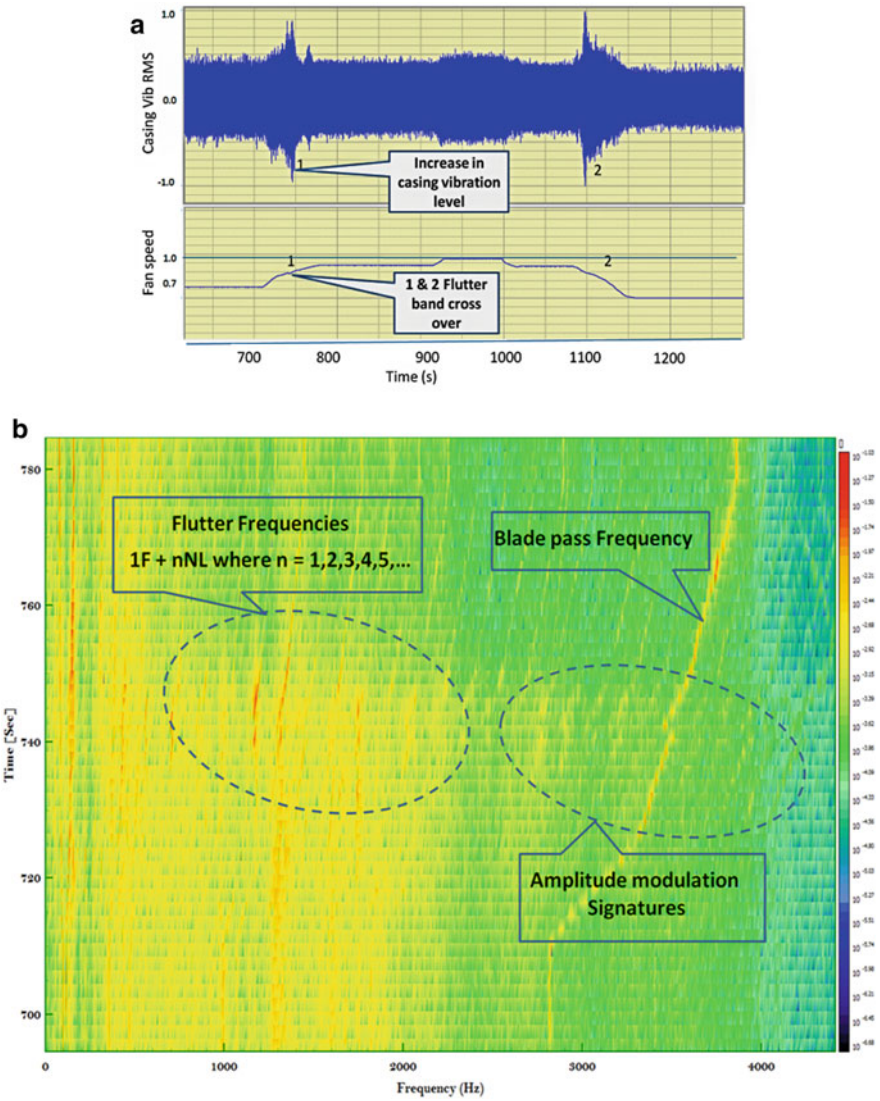


Fig. 4 a Engine casing vibration RMS value trend analysis and b spectrogram of the casing vibration on fan

vibration increases. Such a response is due to pressure wave prevailing inside the engine during flutter which acts on the inner surface of the engine casing forcing it to respond by casing vibration. During this state of the engine, the spectrogram of the casing vibration shown in Fig. 4b has several frequency components as defined in Ref. [6]. During flutter, one or more circumferential travelling pressure waves set in, each with a specific nodal diameter as described in Ref. [7]. It has been shown by analysis in ref [7] that the frequency of the signals sensed by the casing mounted sensors is given by Eq. 1, in a stationery frame of reference can be computed as follows:

$$f_s = f_b + nN_L \tag{1}$$

where

- f_s frequency sensed by a casing mounted sensor in Hz
- f_b frequency of vibrating blade in Hz
- n 1, 2, 3, 4...
- f frequency in Hz and
- N_L Rotational speed in RPS.

5 Flutter Analysis Frame Work

Initially, data analysis was carried out on four engine tests by conventional time–frequency methods using well-established analysis algorithms provided DATS framework by PROSIG© [11] which conclusively identified the existence of flutter of the fan blades based on the theoretical Campbell diagram 3(a) and experimental results shown in Fig. 3b. Further an exploratory analysis was taken up on casing vibration data patches extracted at instances 1 and 2 as shown in Fig. 4a. Test cases of flutter-free operation of fan as well as flutter condition were analysed as per the analysis framework shown in Fig. 5.

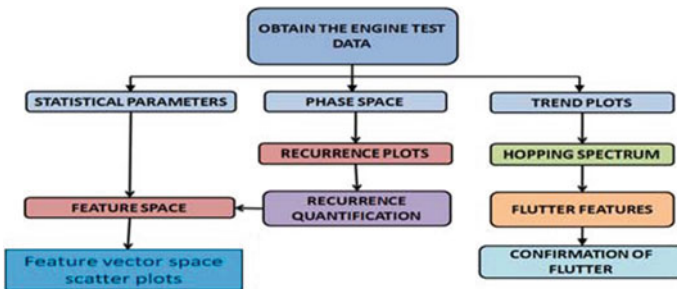


Fig. 5 Flow chart of the fan flutter signal analysis framework

6 Recurrence

Recurrence is an inherent property of any dynamical processes in nature. Many dynamic phenomena in complex systems, natural or engineered, have these two patterns, i.e. (1) recurrence wherein a set of states occur and repeat often and (2) the trajectory of states, which evolve, follows a specific pattern. In a dynamical system, there are a set of states between which it dwells often. By observing a few significantly contributing patterns in a time domain signal, it is possible to determine the tendency of a system towards a particular state [12]. Recurrence-based analysis method has emerged as powerful tool for visualization as recurrence plots (RP) and analysis of complex dynamical systems. Further, the quantification of recurrence that has led to a new analysis tool called recurrence quantification analysis (RQA), which is effective to detect transitions in the dynamics of systems from a time series data. This method has been demonstrated to work effectively even with one-dimensional (1D) time series data [13]. However, there are not much research publications on usage of RP for diagnosis of gas turbine engine faults. In this research work, recurrence plots and associated analysis have been carried out on vibration data from casing mounted sensors during flutter as described in Fig. 5.

6.1 Phase Space

Sampled data obtained by a sensing system is a time series, which describes the changes of the systems over a period. This data is transformed to the phase space by use of time delay approach based on the Takens' embedding theorem [14] in given by Eq. 2:

$$\begin{aligned}
 X(1) &= \{x(1), x(1 + \tau), x(1 + 2\tau), x(1 + 3\tau), \dots, x(1 + (m - 1)\tau), x(1 + m\tau)\} \\
 X(2) &= \{x(2), x(2 + \tau), x(2 + 2\tau), x(2 + 3\tau), \dots, x(2 + (m - 1)\tau), x(2 + m\tau)\} \\
 X(3) &= \{x(3), x(3 + \tau), x(3 + 2\tau), x(3 + 3\tau), \dots, x(3 + (m - 1)\tau), x(3 + m\tau)\} \\
 &\vdots \\
 X(i) &= \{x(i), x(i + \tau), x(i + 2\tau), x(i + 3\tau), \dots, x(i + (m - 1)\tau), x(i + m\tau)\} \quad (2)
 \end{aligned}$$

where X is a state vector of dimension m ; x is the instantaneous data; $i = 1, 2, 3, \dots, N$; m is the dimension parameter; τ is the delay parameter.

For the analysis of time series, the parameters, i.e. embedding dimension m and the delay time τ have to be chosen appropriately.

6.2 Recurrence Plot (RP)

In the study of recurrences in dynamical systems, recurrence plot was constructed based on phase space. It is a technique to visualize the behaviour of m -dimensional phase space trajectories. It is a graphical representation of such points in time, when the trajectory recurs in a ε -neighbourhood to a former state. The state of a system at i th instance of time, and at another instance of time j is depicted in a two-dimensional plot of black and white spots, where black spot marks repeated occurrence. Here both X - and Y -axes are the time as shown in Fig. 7.

A recurrence instance can be mathematically given in Eq. 3:

$$R_{i,j}(\varepsilon) = \Theta(\varepsilon \|x_i - x_j\|), i, j = 1, Z, \quad (3)$$

where Z is the number of considered states x_i , ε is a threshold distance, $\|\cdot\|$ is a norm and $\Theta(\cdot)$ the Heaviside function. A comprehensive discussion on the recurrence plots and their interpretation is described in Ref. [14].

6.3 Recurrence Quantification Analysis (RQA)

The recurrence quantification analysis (RQA) is a process of data analysis where quantification of the number and duration of recurrences of a dynamical system are presented by its state space trajectory. Small cluster of points, such as diagonal lines, horizontal and vertical lines, random points in the recurrence plots are used to quantitatively describe recurrence plots and arrived at the framework of quantification. The RQA method has been enhanced since inception by introduction of several quantification measures such as determinism (DET), recurrence rate (RR), laminarity (LAM), RP entropy (RP-ENT), length of diagonal lines (RP- L_{\max}), trapping time (TT). Details on the RQA are available in Ref. [14].

6.4 Recurrence Analysis of Casing Vibration Data

As the name suggests, the recurrence plot is a pictorial representation of repeated occurrence of a state in a system. When engine is operating normally, as the fan blades rotate at a constant angular velocity, each blade passes over a reference point as a repeating phenomenon. A cyclic phenomenon of bladed disc rotation coupled with vibrating blades, i.e. repetition of few cycles of blade vibration while completing one rotation of the disc, needs to be captured by the RP. It may be recalled that blades vibrate due to resonance when engine speed and natural frequency of blades cross over. Design guidelines itself ensure that selection and placement of any two adjacent blades on the fan disc to be slightly apart in order not to have all blades

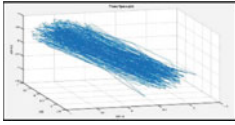
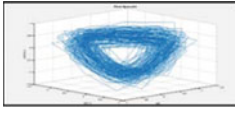
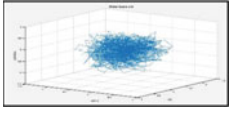
getting excited together. However, during flutter mode of excitation, all blades of the fan disc go into a single frequency of vibration close to its natural frequency. By exploiting this unique feature of blade vibration during flutter, recurrence plots can be constructed effectively.

In order to identify the possible flutter crossover band, RMS value of the casing vibration was considered to identify the speed band (82–89% of N_L) where sudden increase in casing vibration RMS level is shown in Fig. 4a. During most of the tests, engine speed was scheduled for crossover at a ramp rate of 20 rpm/s which lasted for a duration of ~ 40 s from 70 to 90% of power setting. This mode of operation was essential to avoid pile-up of blade strain levels which could lead to failure of the blades and also to get confirmed flutter data. During most of the engine tests, flutter band crossover occurs four times, i.e. two acceleration and two decelerations. Data was sampled at 8.823 ksp/s. Since engine speed is continuously accelerating or decelerating throughout the flutter data capture duration, it is essential to have a quasi-steady condition for the RP to be effectively obtained. Each revolution during flutter crossover is about 7 ms (time for one rotation around flutter speed $\sim 145 \pm 3$ Hz), and each blade would be passing across the vibration sensor at time interval of 0.291 ms (7/24). By the prior knowledge, the flutter frequency at $1F$ mode is $\sim 290 \pm 5$ Hz, and the frequency of the signal felt by the stationary frame of reference would be 570–590 Hz ($1F + 2N_L$). When engine casing vibrates during flutter, accelerometer mounted on the casing would sense the harmonics of flutter signal. Since the vibration signal has several other frequency components, it is essential to capture the frequency of interest.

In order to effectively capture recurrence feature in a signal, embedding dimension m and delay parameter τ need to be iteratively and intuitively varied to arrive at an optimum combination. A parametric study was carried out by constructing recurrence plots with delay parameter τ varied from 1 to 100 and embedding parameter fixed at 3. Observations made on the phase space trajectories during this study are shown in Table 1.

Autocorrelation of the signal was carried out in order to get an explanation for observations made in Table 1. When engine is operating in flutter-free speed band (N_L speed in the range 149–151 RPS), the correlation peaks in a repetitive manner once in 58 samples are shown in Fig. 6a. Inter-sample gap of 58 gives a time period of ~ 6.6 ms ($1/8823 * 58$) which is the time taken for one rotation of LPC spool ($N_L = 149$ RPS). Further, autocorrelation study of signals during flutter speed band ($N_L \sim 142$ – 148 RPS) shows a cyclic peaking pattern every 7.5 samples as shown in Fig. 6b. It can be inferred from the autocorrelation results that when the embedding parameter $\tau = 15$ (which is 2 times 7.5) gives a time period of ~ 1.7 ms ($15 * 1/8823$) which corresponds to the flutter frequency band 588 ± 1 Hz (which is 292 Hz + $2X$ 148 Hz, i.e. $1F + 2N_L$) observed in a stationary frame of reference. Methodology of constructing recurrence plots requires to set the delay parameter τ which is the index of the data array to an integer number only. Since the embedding dimension m is 3, it is essential to have three data samples which are separated by the delay parameter τ within contiguous 15 samples. Based on the constraints as discussed, τ

Table 1 Parametric study to arrive at optimal value of τ

Dimension parameter m	Delay parameter τ	Phase space image	Observations	Remarks
3	15, 30, 45, 60, 75, 90		Cylindrical image	τ set at exactly at the flutter signature frequency based on autocorrelation
3	1 to 100 excluding 15, 30, 45, 60, 75, 90		Toroid image	τ not set away from the flutter signature frequency based on autocorrelation
3	1–100		Spherical Image	No flutter. When τ is in the range 52–53, the image takes the shape of a toroid

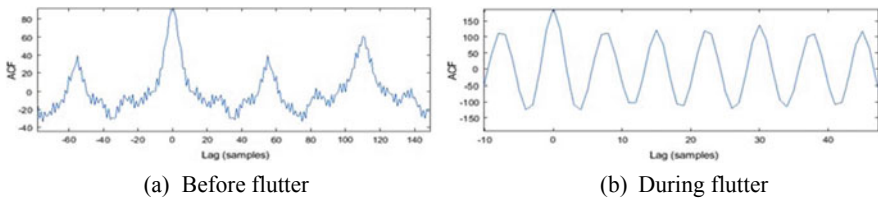


Fig. 6 Autocorrelation of the casing vibration

is optimally arrived at 5 which gives the phase space vector the data with indices as $n + 1, n + 6$ and $n + 11$ where $n = 1, 2, 3, 4$, till end of data array.

Two windows of data just before occurrence of flutter and during flutter are taken for analysis. The window size is optimally fixed at 13,000 samples, which amounts to about 200 revolutions of engine test where the assumption of quasi-steady state of the engine can be made with fair degree of certainty. During each window of data, 13 contiguous sets of 1000 samples are extracted as pages for the RPs. During RP construction with casing vibration data, embedding dimension of 3 and delay parameter of 5 were decided based on the parametric study carried out as described earlier. The delay parameter of 5 gives a clear evolution of the phase space into an ellipsoid-shaped image as can be seen in Fig. 7a–f.

It can be seen from the phase space, colour RP and binary RP that there are significant features in the images which differentiate the flutter condition from the normal operation. Such 52 plots were constructed for each engine test which has two crossovers. After a careful visualization study, in order to aid an automated

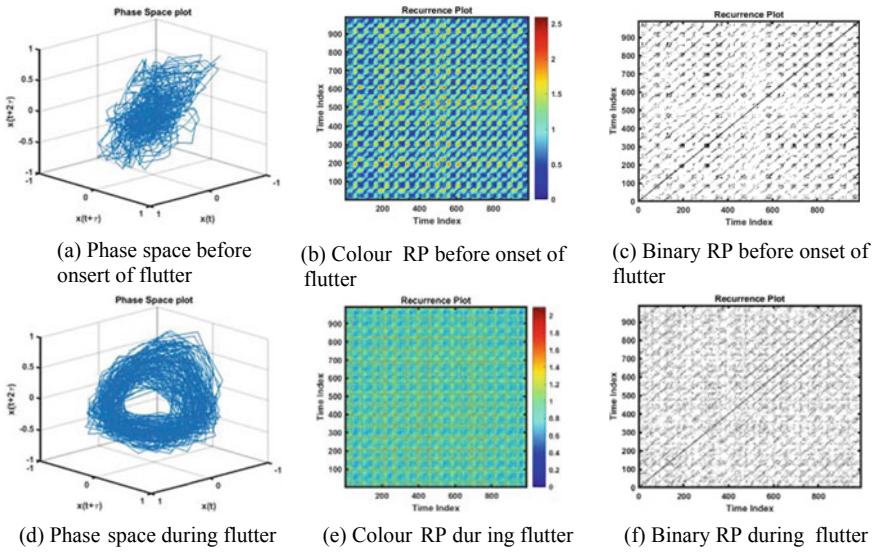


Fig. 7 Phase space, colour RP and binary RP for flutter crossover

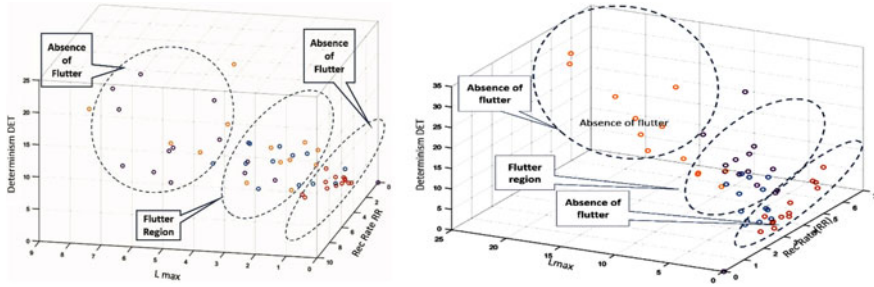
decision-making process, RP images were processed by the RQA which extract several features as described. These features vectors are extracted from each RP. Totally, 104 engine test data points were processed to demonstrate the efficacy of the RP-based flutter analysis. Among the 104 data sets, 52 data sets are taken just prior to flutter excitation and 52 data sets are during flutter mode of blade vibration.

6.5 Results of Recurrence Quantification Analysis

Among all the RQA parameters, three parameters RR, DET and L_{max} were found to have noticeable variations between the presence and absence of flutter. In order to visualize the RQA features, a 3D feature space was constructed as shown in Fig. 8. Even though there is a clear clustering of data points separating flutter region from normal region, a distinct clustering of RQA features was not being emerged, and there were few outliers.

6.6 Statistical Analysis of Vibration Signal During Flutter

In addition to the RQA features, general statistical features such as mean, variance, RMS, skewness, kurtosis and entropy for the data were also analysed for the casing vibration signals during flutter test of fan. These statistical features are analysed



(a) Engine test #1 for Flutter Evaluation

(b) Engine test #2 for Flutter Evaluation

Fig. 8 Clustering of RQA features

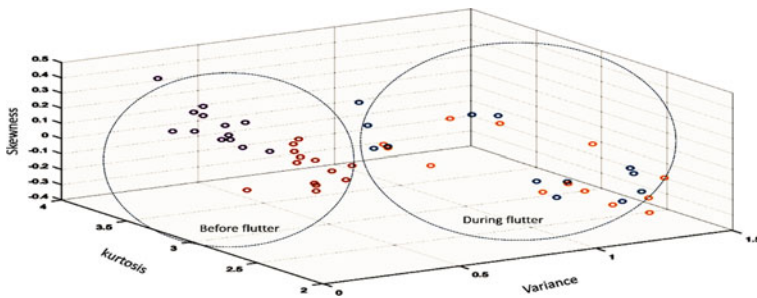


Fig. 9 Statistical features to distinguish between presence and absence of flutter

for their sensitivity and clustering, i.e. their ability to classify the flutter state of the engine from normal state. A 3D feature space of statistical features was created using selected feature vectors, which exhibited noticeable variations. It is clear from Fig. 9 that the feature vectors of selected statistical features in the 3D scatter plot show a good separation between flutter condition and otherwise with few outliers.

6.7 Feature Vector Fusion

In order to improve the clustering of flutter condition data points, a fusion of RQA features and statistical features was taken up for a study. Two 3D scatter plots were constructed with kurtosis, variance and RQA- L_{max} as a one feature vector as shown in Fig. 10a and RQA- L_{max} , variance and kurtosis as the other feature vector as shown in Fig. 10b. It can be seen that there is a clear demarcation of data points, which separate presence and absence of flutter condition.

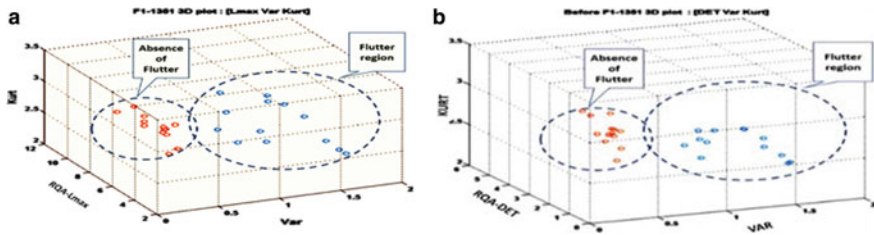


Fig. 10 **a** Fusion of variance, kurtosis and RQA- L_{\max} . **b** Fusion of RQA-DET, variance and kurtosis

7 Conclusions and Future Work

In order to avoid premature failure of rotor blades due to fatigue caused by flutter induced vibration, a framework of online monitoring and offline analysis is essential. Such a framework essentially would be an interdisciplinary analysis methodology of structural and aerodynamic phenomenon. Engine test engineers are generally constrained by limited instrumentation, lack of validated monitoring methodologies during initial developmental engine tests. Under such circumstances, analysis based on statistical methods, feature recognition and multi-sensor data fusion enhance the decision-making process of the test engineers. An engine-monitoring framework, which has been discussed in this paper, helps in decision making whether flutter exists or not with fair degree of certainty based on casing vibration data alone. The analysis needs a small data slice acquired during test and a general analysis algorithm, which can be implemented easily for online monitoring. Upon detection of flutter signatures online, detailed investigation can be taken up with a comprehensive rotating instrumentation to sense and quantify resulting blade deformation and prevailing aerodynamic conditions dedicated instrumentation. The parametric study conducted on selecting delay parameter τ has revealed unique phase space images. There is a need to explore this further and extract features on these geometric images as a measure of flutter magnitude. Usage of RP can be extended to cross RP wherein the phase space can be constructed from two or three identical sensors located circumferentially around the engine casing to fuse multi-sensor data towards enhancing the confidence level.

Acknowledgements The authors are thankful to the director, Gas Turbine Research Establishment (GTRE), Bangalore, and National Aerospace Laboratories (NAL), Bangalore, who has given an opportunity to take up this research work. They also thank Mr. Vikas, scientist, working in the instrumentation and control engineering group of GTRE for helping in various data analysis work.

References

1. Technology Focus Gas Turbine Research Bulletin of Defence Research and Development Organisation DRDO, Ministry of Defence, India, vol 17, no 5 October 2009. ISSN 0971-4413
2. Srinivasan AV (1997) Flutter and resonant vibration characteristics of engine blades. In: AnIGTI scholar paper, 97-GT-533, Presented at the international gas turbine & aero engine congress & exhibition, Orlando, FL 2–5 June 1997
3. Purushotaman K, Jeyaraman SK, Pratap A, Deshkulakarni KP (2017) Aeroelastic flutter investigation and stability enhancement of a transonic axial compressor rotor using casing treatment. In: Paper No. GTINDIA 2017–4767, pp V001 T0 1A015, <https://doi.org/10.1115/gtindia2017-4767> presented during ASME 2017 gas turbine india conference, Bangalore, India, 7–8 Dec 2017. ISBN 978-0-7918-5850-9
4. Viswanatha Rao AN et al. Challenges in engine health monitoring instrumentation during developmental testing of gas turbine engines. In: Paper no 153, proceedings of the 2nd national aero propulsion conference, NAPC-2018 7–19 Dec 2018, IIT Kharagpur, West Bengal (proceedings yet to be released)
5. Riazet S et al (2017) Vibration feature extraction and analysis for fault diagnosis of rotating machinery—A literature survey. *Asia Pac J Multi Research* 5(1):103–110
6. Jha BK, Rao ANV, Mohana TR, Singh AK, Khorikov AA. Development of instrumentation to capture unsteady & flutter phenomena in the fan rotors of Gas Turbine Engines Book ISSN 1091-5281. ISBN 978-1-4244-7933-7 <https://doi.org/10.1109/imtc.2011.5944006>
7. Gill JD, Capece VR, Fost RB (2004) Experimental methods applied in a study of stall flutter in an axial flow fan. *Shock Vib* 11(2004):597–613. ISSN 1070-9622/04/2004 (IOS Press)
8. recommended practices for measurement of gas path pressures and temperatures for performance assessment of aircraft turbine engines and components, AGARD AR-245, 1990
9. Holanda R. Analysis of strain gage reliability in F-100Jet engine testing at NASA Lewis Research Centre, 1983 NASA Technical Memorandum 83325
10. Kumar D, Barad S, Suresh TN (2013) Gas turbine blade damper: a design optimization study to mitigate high resonance blade vibration. In: Proceedings of ASME. 35161; ASME 2013 gas turbine India conference, V001T05A018, 05 Dec 2013, GTINDIA2013-3748. <https://doi.org/10.1115/gtindia2013-3748>,
11. <http://prosig.com/wp-content/uploads/pdf/datasheets/prosigDatsTimeFreq.pdf>. Accessed on 22 Feb 2019
12. Marwan N, Carmen Romano M, Thiel M, Kurths J (2007) Recurrence plots for the analysis of complex systems. *Elsevier Phys Rep* 438(2007):237–329. Nonlinear Dynamics Group, Institute of Physics, University of Potsdam, Potsdam 14415, Germany
13. Marwan N, Saperin P, Kurths J (2005) Generalisation of recurrence plot analysis for spatial data international symposium on nonlinear theory and its applications (NOLTA2005) Bruges, Belgium, 18–21 Oct 2005
14. www.recurrence-plot.tk

Condition Monitoring of Rolling Contact Bearing by Vibration Signature Analysis



Kashinath Munde and Ganesh Kondhalkar

Abstract Bearing condition monitoring is the useful technique for maintaining the health of the machines. A machine is similar to a human body as far as condition monitoring is concerned. The sensors act as stethoscope for machines, which provides the machine health-related information. The vibration information helps the analyst to predict the exact condition of machine. Condition monitoring plays a vital role in automation of medium to large-scale industries. Vibration signature is commonly used parameter for identification of fault in rotating machines. Hertzian contact deformation theory is used to calculate contact force. The mathematical model considers frequency as well as acceleration magnitude of bearing vibration. The model developed shows the nature of vibration for both defective and defect-free bearing. The results are presented in frequency domain for simulated defect on the raceways. The effects of defect location and rotating speed are investigated by using theoretical model. The actual rotor with defective bearing is tested at constant speed under known load. The wire cut EDM process is used for creation defects in the bearing. The results obtained in theoretical are validated through the experimentation. The model developed can be used for the signature pattern database development which will act as knowledge base for the future studies in the field.

Keywords Condition monitoring · Fault detection · Bearing vibration · Rotor dynamic model · Dynamic load analysis · Defect analysis

K. Munde (✉)
Savitribai Phule Pune University, Pune 411007, India
e-mail: kashinathmunde@gmail.com

G. Kondhalkar
Koneru Lakshmaiah Education Foundation (Deemed to be University), Vaddeswaram, Guntur Dt.,
A.P, India
e-mail: ganeshkondhalkar@gmail.com

Nomenclature

K	Load-deflection factor or constant for Hertzian contact elastic deformation
δ_r	Radial deflection or contact deformation
D_S	Defect size
RW_R	Raceway radius
Q	Contact force
F_m	Inertia force
K	Load-deflection ‘factor’ or load-deflection ‘constant’ for Hertzian contact elastic deformation
δ_r	Radial deflection or contact deformation
n	Load-deflection exponent = 3/2 for all bearings and 10/9 for roller bearings
c	Damping coefficient
k	Stiffness coefficient

1 Introduction

Condition monitoring is the process of monitoring one or more parameters that define condition of the machinery, such that a significant change is indicative of an existing or developing failure. Condition monitoring is one of the major components of predictive maintenance. Overall vibration measurements were first recognized and used in 1950s using simple vibration meters. The unit of measurement was either in thousands of an inch when measuring displacement or sometimes in inches per second also called IPS while measuring vibration velocity. Personal computing became prevalent in 1970s leading to faster and accurate digital signal processing that led to the development of FFT analyzer. The analyzers calculated frequency spectrums from any recorded and saved vibration signal very quickly. Being primitive and at the very beginning stages, those analyzers were weighing as high as 40 kilograms, making them suited only for laboratory instruments, and difficult to be used as portable units for in situ field use. As the microprocessor generation came to picture in 1980s, it exploited development on a single silicon chip and powered by battery, making it truly portable digital signal analyzer. This device can now be coupled with a data storage mechanism along with computer program which simplified the logistics of vibration data collection and monitoring. This development brought in a revolutionary change in machinery diagnosis through application of vibration analysis.

Gao and Holm-Hansen [1] used structurally integrated force sensor to analyze the vibrational behavior of deep groove ball bearing. The findings were used to validate the approach of online bearing condition monitoring by integrated sensing. The combined work theoretically and experimentally established a strong basis for the development and practical application of an integrated online bearing condition monitoring system. Prabhakar et al. [2] presented the detection of race faults in ball bearing by the application of discrete wavelet transform. Ball bearings with

single point and multiple defects on different locations like inner race, outer race, balls and combination of faults were considered for this analysis using vibrations. McInerny and Dai [3] presented a laboratory module for detection of rolling element bearings faults. The study highlighted shortcomings of conventional spectral analysis by generating synthetic signals using MATLAB. Shrinidhi et al. [4] discovered how progressing malfunctions can be used to acquire information early in the stage. The results were used to demonstrate detection of problems in antifriction bearings using each of these techniques.

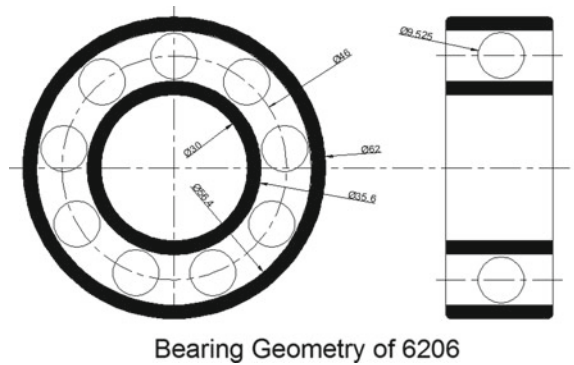
Kenneth et al. [5] used fuzzy inference and wavelet transformation to present a technique for diagnosing bearing faults. The diagnostic method was developed to separate reliably various fault conditions and under presence of load variations. Narayanana et al. [6] established procedures that could prevent malfunction and catastrophic failures during operation of machines by using condition monitoring techniques. The results established from experimentation and spectrum analysis were then compared with feature extraction data. Markov models were used to present bearing fault monitoring using an alternate method of pattern recognition. Purohit and Purohit [7] analyzed the vibration in radial and axial direction of rigid shaft simply supported on ball bearings. The effect on vibrations due to preload variations and effects due to change in number of balls in the ball bearings was investigated [8]. The vibration amplitudes, during the experimentation, are presented as reduced considerably upon correct selection of preload and number of balls in the bearings [9, 10]. Wang et al. [11] developed and presented a method that was focused on compressed vibration signals for detecting faults in rolling element bearings. Fault characteristic frequencies within vibration signals are often represented by harmonics. Firstly, a compressed vibration signal is acquired from sensing matrix and then a sensing frame of characteristic harmonics is proposed to detect bearing faults.

2 Mathematical Model for Rotor Bearing System

The objective of work is to build theoretical model for the bearing fault vibration signature to identify localized defects on the bearing and validate with experimental results. For developing mathematical model, the contacts of rollers and races are assumed to be nonlinear springs. Hertzian contact deformation theory is used for calculating the contact forces. The work is focused toward developing a theoretical model in order to analyze the different effects on vibration due to defect size in the bearing.

The model can be used for acceleration magnitudes and frequency of vibration components of bearing. Defect itself is modeled as part of sinusoidal wave, instead of using periodically repeated impulse function for the impulses generated due to defect. The present model is relatively limited in treating the ball skidding effect. The model is aimed to achieve a theoretical model that enables study of effects due to varying load, different defect sizes and rotating speed variation. This study is limited to the bearing vibration and prediction of its spectral components. The model is

Fig. 1 Bearing SKF 6206 geometry



done carefully with a lot of attention to include the ball raceway interaction and ball skidding phenomenon. However, at any future time, this model can be upgraded to incorporate the effects of ball skidding for predicting the spectral components of defective bearing.

Figure 1 shows bearing SKF 6206 geometry.

- Z 9 mm
- d 9.525 mm
- D 46 mm
- d_i 30 mm
- d_o 62 mm

2.1 Frequency Model

Researchers pointed out that in most of the cases, the practical values of the characteristic frequencies are either more or less than the theoretical values. As the bearing is fitted on the shaft with a certain fit [mostly interference fit], this fit will vary when the bearing is in working condition, affecting the bearing characteristic frequency. The slip between rolling element and bearing races affects the bearing frequency. So it is important to take into account these changes in the characteristic frequency. As a result, following factors also play important role in BCF equation for changes in fits of mounting and bearing elements during working condition.

Speed Factor (SF) This factor considers the variation in the RPM of the elements of the bearing [10].

$$SF = 3.218 \left(\frac{1}{N} \right)^{1/3} \quad (1)$$

$$SF = 1 + \left(\frac{SF}{3} \right) \quad (2)$$

Fit Factor (FF) Fit factor takes care of bearing geometry other than standard equation. The fit is selected on following factors:

- Rotation—outer/inner
- Bearing internal clearance
- Rotating load
- Stationary load
- Temperature
- Material shaft and housing
- Running accuracy.

The interference is related to the magnitude of the load, i.e., for heavier load [mainly shock type load], the greater interference will be required.

$$KM = \frac{d_i}{k(d_o - d_i) + d_i} \quad (3)$$

$$FF = 1 + \left(\frac{KM}{6} \right) \quad (4)$$

$k = 0.3$ (ball bearing).

The modified equation by considering speed factor and fit factor, which gives higher limit (HL) and lower limit (LL), is as follows:

$$BCF - HL = BCF \times SF \quad (5)$$

$$BCF - LL = BCF/SF \quad (6)$$

$$BCF - HL = BCF \times FF \quad (7)$$

$$BCF - LL = BCF/FF \quad (8)$$

These equations can be used as basic equations for finding characteristic frequency.

2.2 Amplitude Model

As per Hertzian contact deformation theory, the nonlinear load-deformation relation is given by,

$$F = K \delta_i^n$$

where the load-deflection factor, K , depends on the contact geometry.

The effective elastic modulus K for the bearing system is written as

$$K = \frac{1}{\left[\frac{1}{K_i^{1/n}} + \frac{1}{K_o^{1/n}} \right]^n}$$

The elastic modulus for the contact of inner race and a ball is

$$K_i = 3.587 \times 10^7 (\Sigma\rho)^{-1/2} (\delta_i^*)^{-3/2}$$

for the contact of a outer race and ball is

$$K_o = 3.587 \times 10^7 (\Sigma\rho)^{-1/2} (\delta_o^*)^{-3/2}$$

δ^* is a function of curvature difference $F(\rho)$ is given as

$$F(\rho) = \frac{(\rho_{I1} - \rho_{I2}) + (\rho_{II1} - \rho_{II2})}{\Sigma\rho}$$

Hertz assumed the deformation and stress in the perfectly contacting surfaces are elastic solids, smooth and ellipsoidal. The stress calculation for of the bearings and its components is based on classical theory of elasticity. So, the point of contact of the ball and races makes a contact area of elliptical shape with a as semi-major axis and b as semi-minor axis. The curvature difference and sum are necessary to have the contact force of the elements. The curvature sum is given by

$$\Sigma\rho = \rho_{I1} + \rho_{I2} + \rho_{II1} + \rho_{II2} = \frac{1}{r_{I1}} + \frac{1}{r_{I2}} + \frac{1}{r_{II1}} + \frac{1}{r_{II2}}$$

The parameters of r and ρ are dependent upon the type of race in consideration (inner or outer).

The contact deformation between steel bodies and the approach between two deforming and contacting surfaces are given by

$$\delta = 2.787 \times 10^{-8} Q^{2/3} (\Sigma\rho)^{1/3} \delta^*$$

The contact force Q is given by

$$Q = \{3.587 \times 10^7 (\delta^*)^{-3/2} (\Sigma\rho)^{1/2}\} \delta^{3/2}$$

The effective elastic modulus (K) for a bearing SKF 6206 system using physical and geometrical parameters is given by

$$K = 7.41 \times 10^{10} \text{ N/m}^{3/2}$$

As the inner race is fixed on shaft, it rotates with shaft. The balls are rolling on the inner race and transmitting the force to outer race by point contact. As the balls are moving in restricted area of the cage, they are revolving along their own axis and hitting with inner and outer race. The radial deflection at any angle θ_i for the ball is given by

$$\delta_r = [(x \cos \theta_i + y \sin \theta_i) - R_c]$$

The deflection along X and Y -axis are x and y and internal radial clearance is R_c . According to the Hertz contact theory,

$$F = K[(x \cos \theta_i + y \sin \theta_i) - R_c]^{3/2}$$

The total restoring force equals the sum of restoring forces from each of rolling elements. The components of restoring force along X and Y -axis are given by

$$F_X = \sum_{i=1}^Z K[(x \cos \theta_i + y \sin \theta_i) - R_c]^{3/2} \cos \theta_i$$

$$F_Y = \sum_{i=1}^Z K[(x \cos \theta_i + y \sin \theta_i) - R_c]^{3/2} \sin \theta_i$$

The above equations give a circumferential half sinusoidal wave without defect. To consider the effect due to defect on races, the above equation should be modified by considering total deflection considered. The resulting distortion is obtained by considering radial displacement. For the bearing race with defect, the restoring force is given as

$$F_{XD} = \sum_{i=1}^Z K[(x \cos \theta_i + y \sin \theta_i) - (R_c + H_D \sin(\pi/\gamma(\theta_t - \theta_i)))]^{3/2} \cos \theta_i$$

$$F_{YD} = \sum_{i=1}^Z K[(x \cos \theta_i + y \sin \theta_i) - (R_c + H_D \sin(\pi/\gamma(\theta_t - \theta_i)))]^{3/2} \sin \theta_i$$

$$\gamma = D_S/RW_R$$

$$\theta_t = \omega_c t + 2\pi/Z(Z - i)$$

where $i = Z$ to 1.

By using the above value of θ_t , the restoring force at outer race will be calculated.

It is clear that the inner race rotation speed is equal to the shaft speed. Also, the speed of ball center should be equal to the speed of the rotation of cage. Consider a point on the inner race and simultaneously consider a point at the ball center such that they are at the same distance from the X -axis at time $T = 0$, it can be easily noticed

that after a certain time t , the point located on ball center will lag the point marked on the inner race by an angle of $-(\omega - \omega_c)$. This can now be used for calculating the restoring forces generated due to defects on inner race by substituting

$$\theta_t = (\omega_c - \omega)t + 2\pi/Z(Z - i)$$

By considering above equations, the variation in frequency can be found as 6%, due to existence of slip between the bearing inner race and the rolling element. There is also a large difference in amplitude of vibration as predicted by the model and by the experimentation because it is difficult to consolidate the different effects of the entire rotor bearing system into the theoretical model.

Figure 2 presents the basic modeling process. The signal modeling process combines the rotor dynamic forces and the impulse response. Firstly, rotor dynamic forces were analyzed as main influence of bearing load. Then, as the bearing load conditions are obtained, it is combined with the impulse signal model. Fault signals are modeled based on the above attainments. The resulting fault signal model can then be used for predicting fault signals and also to simulate fault signals in rolling bearings.

According to the Newton's theorem, the term mew^2 in the equation can be considered rotating inertia force. Then, this inertia force F_m can be represented as

$$F_m = mew^2$$

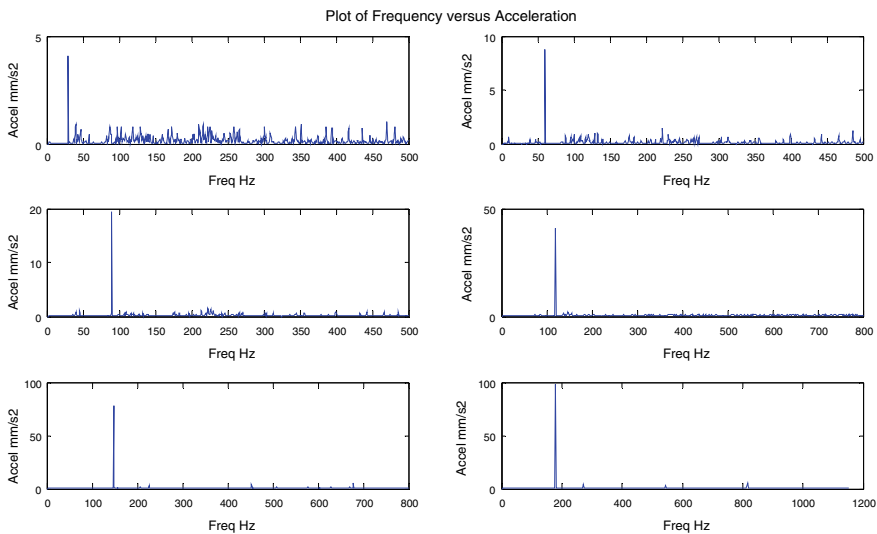


Fig. 2 Outer race MATLAB graphs for 0.5 mm load 2 kg speed 500–3000 RPM (Sequence of Figs from left top to right bottom with increment of 500 RPM)

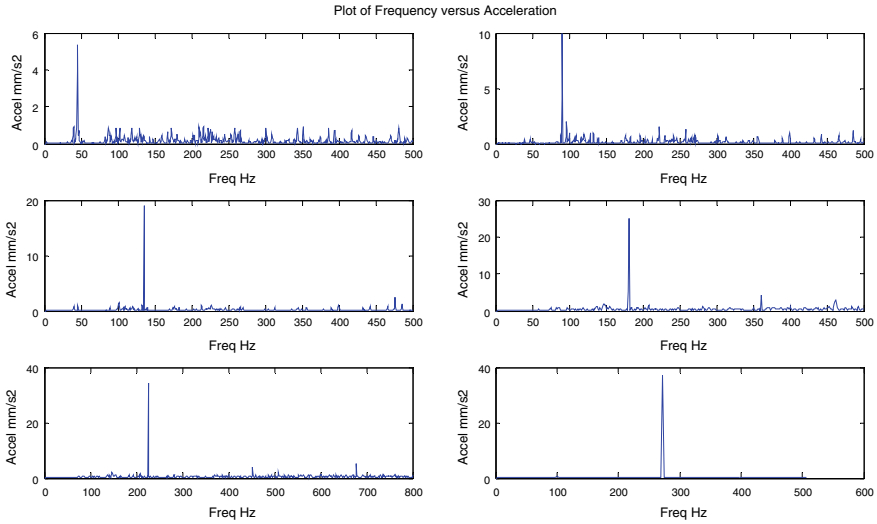


Fig. 3 Inner race MATLAB graphs for 0.5 mm load 2 kg speed 500–3000 RPM (Sequence of Figs from left top to right bottom with increment of 500 RPM)

The direction of the rotating inertia force changes when the mass center rotates with the geometrical center. The inertia force will also have a periodic characteristic when the rotor bearing system runs at a constant speed. Figure 3 shows a schematic diagram of the force analysis on rolling element bearing. As described, the bearing load consists of two parts:

- a. the constant (system gravity) and
- b. the alternate load (inertia force).

The detailed calculation equation can be concluded as follows:

$$F_y = W + F_m \cos\theta$$

$$F_x = F_m \sin\theta$$

Some of the parameters can be obtained by considering the basic theorem of gravity and the rotation features

$$W = mg$$

$$\theta = 2\pi f_s t$$

2.3 Equations of Motion

The prediction of the actual amplitudes of vibration is not possible by the models reported in the literature so far because it is difficult to incorporate the effect of rotor bearing system. It would include components like motor, shaft, bearing, supporting frame, etc.

However, model presented helps to predict the effect of defect position and size and the generated spectral components due to defect.

2.4 Proposed Model

The equation of motion for a two DOF, degree of freedom, system can be written as, for the bearing race without defect,

$$\begin{aligned}
 m\ddot{x} + c\dot{x} + F_X &= F_m \sin\theta_i \\
 m\ddot{x} + c\dot{x} + \sum_{i=1}^Z K[(x \cos \theta_i + y \sin \theta_i) - R_c]^{3/2} \cos\theta_i &= F_m \sin\theta_i \\
 m\ddot{y} + c\dot{y} + F_Y &= W + F_m \cos\theta_i \\
 m\ddot{y} + c\dot{y} + \sum_{i=1}^Z K[(x \cos \theta_i + y \sin \theta_i) - R_c]^{3/2} \sin\theta_i &= W + F_m \cos\theta_i
 \end{aligned}$$

For the bearing race with defect,

$$\begin{aligned}
 m\ddot{x} + c\dot{x} + F_{XD} &= F_m \sin\theta_i \\
 m\ddot{x} + c\dot{x} + \sum_{i=1}^Z K[(x \cos \theta_i + y \sin \theta_i) - (R_c + H_D \sin(\pi/\gamma(\theta_i - \theta_i)))]^{3/2} \cos\theta_i &= F_m \sin\theta_i \\
 m\ddot{y} + c\dot{y} + F_{YD} &= w + F_m \cos\theta_i \\
 m\ddot{y} + c\dot{y} + \sum_{i=1}^Z K[(x \cos \theta_i + y \sin \theta_i) - (R_c + H_D \sin(\pi/\gamma(\theta_i - \theta_i)))]^{3/2} \sin\theta_i &= w + F_m \cos\theta_i
 \end{aligned}$$

The initial displacement conditions are as follows.

Displacement $X_0 = Y_0 = 10^{-6}$ Velocity $\dot{X}_0 = \dot{Y}_0 = 0$.

2.5 Theoretical Results

The defect size considered is 0.5–2 mm with incremental 0.5 mm and width = 1 mm and depth = 1 mm. After solving above equations in MATLAB the following results are obtained for Bearing SKF 6206.

2.5.1 Outer Race Graphs of Defect Size 0.5 mm Load 2 kg Speed 500–3000 RPM

Figure 2 shows the nature for amplitude for bearing defects of 0.5 mm and 2 kg load. The frequency for outer race 29.76, 59.51, 89.27, 119.02, 148.78 and 178.53 and corresponding amplitude accelerations are 4.08, 8.76, 19.42, 41.05, 78.34 and 98.46, respectively. It is observed that the defect frequency as well as amplitude of vibration increases with speed.

2.5.2 Inner Race Graphs of Defect Size 0.5 mm Load 2 kg Speed 500–3000 RPM

Figure 3 shows the nature for amplitude for bearing defects of 0.5 mm and 2 kg load. The frequency for inner race 45.24, 90.49, 135.73, 180.98, 226.22 and 271.47 and corresponding amplitude accelerations are 5.33, 9.97, 18.89, 25.11, 34.21 and 37.21, respectively. The trend displays stepping up frequency with respect to speed and the amplitude of vibration arguments in relation to speed.

3 Experimental Setup

The experimental setup consists of three-phase induction motor with armament for applying loading as shown in Fig. 4. The SKF Microlog AdvisorPro is used for data acquisition. The amplitudes of vibration measured indicate the severity of the machine defect. Smooth operation confirms the defects-free operation of machine. Machinery vibration can be considered as the ‘heartbeat’ of a machine. The vibration pattern depends on its health, and the monitoring of machinery vibration gives a clear indication of the defects in the machine. The experimental parameters used in this vibration analysis are speed, load and defect size.



Fig. 4 Experimental setup

3.1 Results of Inner Race (IR) and Outer Race (OR)

Figure 5 shows the vibration amplitude and frequency for bearing with defects of 0.5 mm size under 2 kg load at 1500 RPM. Frequencies observed with inner race defect are 135.73, 271.74 and 407.21 Hz. The corresponding acceleration amplitudes are 34.54 mm/s², 37.91 mm/s² and 36.85 mm/s², respectively. Similarly, Fig. 6 shows the nature of vibration with outer race bearing defect of 0.5 mm and 2 kg load at 1500 RPM. The frequencies present in outer race signature are 89.27 Hz, 178.53 Hz and 267.80 Hz and their corresponding amplitudes are 31.23 mm/s², 32.26 mm/s² and 34.55 mm/s², respectively. The peak at particular race frequency is an indication of the presence of defect. The defect frequency is independent of defect size and applied load but the amplitude is directly proportional to the defect size and applied load.

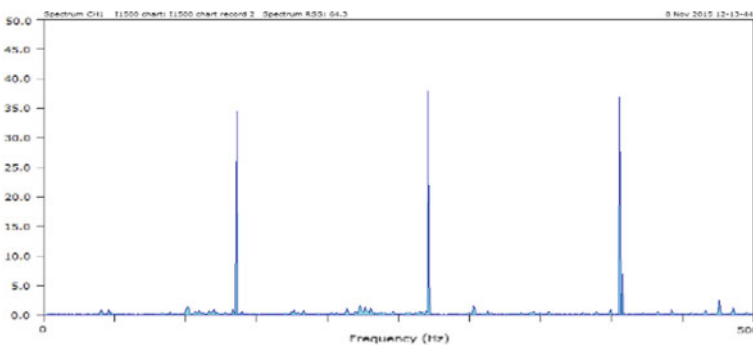


Fig. 5 Inner race

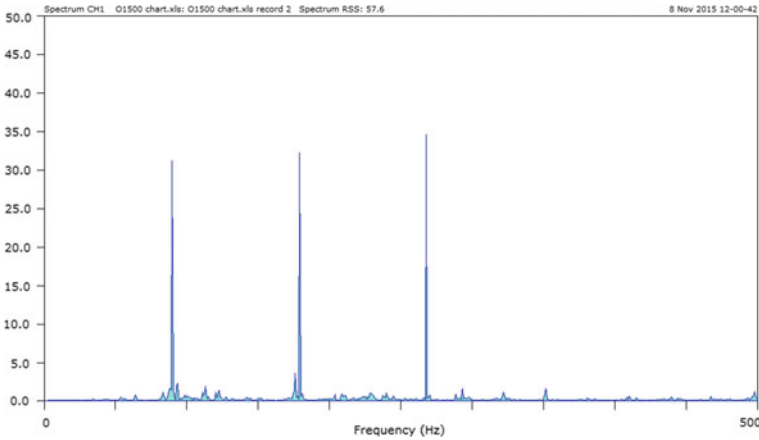


Fig. 6 Outer race

4 Conclusion

The results show that as the speed increases, the amplitude of vibration increases. The peak at particular race frequency is an indication of the presence of defect. The amplitude at defect frequency increases with shaft speed. The effort is made to build the defective bearing model to develop database for localized defects occurring in bearing, which will be useful in real-time analysis of bearing faults.

In theoretical analysis, bearing characteristic frequencies are modified to consider the bearing fits and speed variation. The speed factor (SF) takes care of change in speed of bearing components, and the fit factor (FF) considers the change in bearing mounting fit and bearing component fits. These modified equations are useful in investigating the cause of frequency variation and predict their results precisely by stating the exact cause of frequency variation during experimentation. The outer race defective bearings have higher amplitudes of vibration in comparison with inner race defective bearings for the same speed and size of defect. It can be attributed to the longer travel path of the vibration signal. It is also noticed that at constant defect size and speed, radial load has negligible influence on bearing vibration amplitude. Hence, it can be concluded that the defect on outer race is easier to identify compared to inner race.

References

1. Holm-Hansen BT, Gao RX (2000) Vibration analysis of a sensor-integrated ball bearing. *Trans ASME* 122:384–392
2. Prabhakar S, Mohanty AR, Sekhar AS (2002) Application of discrete wavelet transform for detection of ball bearing race faults. *Tribol Int* 35:793–800

3. McInerny SA, Dai Y (2003) Basic vibration signal processing for bearing fault detection. *IEEE Trans Educ* 46(1):149–156
4. Amamath M, Shrinidhi R, Ramachandra A, Kandagal SB (2004) Prediction of defects in antifriction bearings using vibration signal analysis. *IE(I) J MC* 85:88–92
5. Lou X, Loparo KA (2004) Bearing fault diagnosis based on wavelet transform and fuzzy inference. *Mech Sys Signal Process* 18–5:1077–1095
6. Purushothama V, Narayana S, Prasad SAN (2005) Multi-fault diagnosis of rolling bearing elements using wavelet analysis and hidden Markov model based fault recognition. *NDT&E Int* 38:654–664
7. Purohit RK, Purohit K (2006) Dynamic analysis of ball bearings with effect of preload and number of balls. *Int J Appl Mech Eng* 11(1):77–91
8. Vibrations of gears and bearings, diagnostic maintenance and monitoring of machines, Chap. 3. IIT Roorke. <http://www.iitr.ac.in/outreach/web/CIRCIS/UG/DMM/Diagnostic%20Maintenance%20and%20Monitoring%20of%20Machines-3.pdf>
9. Tiwari R (2008) Vibration measurement equipment and signal processing. In: Theory & practice of rotor dynamics. IIT Guwahati. <http://www.iitg.ernet.in/engfac/rtiwari/resume/rtiwari03.pdf>
10. Shaft and housing fits. MRC Bearing Services. <http://www.skf.com/binary/tcm:12-97852/520033/index.html>
11. Tang G, Hou W, Wang H, Luo G, Ma J (2015) Compressive sensing of roller bearing faults via harmonic detection from under-sampled vibration signals. *Sensor* 15:25648–25662

Misalignment, Rotor-Bow, Crack, Rub-Imapct

Dynamic Response Analysis of an Unbalanced and Misaligned Rotor Supported on Active Magnetic Bearings and Touchdown Bearings



Prabhat Kumar and Rajiv Tiwari

Abstract This paper investigates a study of the simultaneous interaction between active magnetic bearing (AMB) and touchdown bearing (TDB) in an unbalanced and misaligned rotor system. Numerous practical importance of the working together of both bearings in high-speed rotating machinery, such as the turbines and pumps, can be explained by examining two cases depending upon the types of touchdown bearings. The first case is to consider a faulty rotor supported by active magnetic bearings and conventional touchdown bearings (rolling element bearings) as backup support, in which AMB is active but conventional touchdown bearing is inactive during operation. The second case is considering foil bearings as touchdown bearings, in which AMB and foil bearing both are in action during operation. The hydrodynamic principle of air in foil bearing while rotation of the rotor causes to make it in working condition. Mathematical modelling of the unbalanced and misaligned rigid rotor with a disc at middle supported on both bearings has been done for this investigation purpose. Misalignment has been considered between the rigid rotor and active magnetic bearings. The dynamic equations of motion are developed to numerically generate rotor displacement and current responses of the system. It has been found that simultaneous working of AMB and foil touchdown bearings helps in suppressing the vibration response of the rotor system, increasing the reliability of the machine and making more energy efficiently. It is also observed that current consumption is less in the second case than the first.

Keywords Active magnetic bearing · Foil bearing · Misalignment · Touchdown bearing · Unbalance

P. Kumar · R. Tiwari (✉)
Department of Mechanical Engineering, Indian Institute of Technology Guwahati, Guwahati,
Assam 781039, India
e-mail: rtiwari@iitg.ac.in

© Springer Nature Singapore Pte Ltd. 2021
J. S. Rao et al. (eds.), *Proceedings of the 6th National Symposium on Rotor Dynamics*, Lecture Notes in Mechanical Engineering,
https://doi.org/10.1007/978-981-15-5701-9_33

1 Introduction

High-speed rotating system is quite common in use in various applications based on mechanical system, which includes industrial turbomachinery, i.e. turbines, compressors as well as aircraft gas turbine engines and pumps. Usually, these rotating machines have conventional bearings for providing a firm support to the rotor through physical contact, but the recent research trend is towards using active magnetic bearings (AMBs), which levitates the rotor in air due to electromagnetic forces [1]. Thus, the rotor does not feel any frictional resistance, while in rotation and can be operated at very high speeds. AMBs supported system offers several advantages over conventional bearings, such as it helps in reducing vibration and making system more stable at high speeds through active and adjustable stiffness and damping coefficients employing a controller.

Rotor system may experience several faults while in operation that includes unbalance, misalignment, crack, bow in rotors, etc. A rotor system with any of these faults or together is often noisy, unsafe and short-lasting and requires more maintenance. The unbalance leads to drastic vibration at high rotational speed of rotor as it is directly proportional to the square of rotor spin speed. An experimental investigation based on an adaptive open-loop control method was performed by Knospe et al. [2] to minimize the high amplitude vibration due to unbalances in rotor supported by two radial magnetic bearings. De Queiroz [3] explained the effect of unbalance fault on rotor and developed a method for identification of the unknown values of unbalance parameters in a simple Jeffcott rotor by exploiting a dynamic robust control mechanism.

Misalignment fault in rotor system may also affect the efficiency of the system and can cause hazardous health effect to operators. It may occur when axes of two coupled rotors are not aligned with each other or the rotor axis and supported bearings axis are not in alignment. A finite element model with incorporation of reaction forces and moments arising due to the coupling misalignment in a rotor system was developed by Sekhar and Prabhu [4]. They observed that $2\times$ vibration response indicates the presence of misalignment between two shafts. Patel and Darpe [5] executed an experimental investigation on a misaligned coupled rotor-bearing system and obtained several orbit plots for diagnosing the misalignment fault. They observed that the frequency spectrum of response for the misaligned rotor contains several harmonics. Recently, Tuckmantel and Cavalca [6] presented dynamics of rotor-coupling-bearing system integrated with an electromagnetic actuator under the combined effect of unbalance and angular misalignment. They also validated the finite element simulated various vibrational patterns with developed experimental test rig measurements.

It is mandatory to use touchdown bearings (TDBs) in AMBs supported rotor system, so that it would protect the AMB stator and rotor laminations in failure condition of AMBs due to power cut or overload condition cases. For fulfilling this motive, it is certainly needed to keep the air gap between rotor and touchdown bearings lesser than AMBs air gap [7]. Several kinds of research have been found in

the field of utilizing rolling element bearings as backup bearings, where AMBs was inactive during rotor operation [8, 9]. There are multiple disadvantages of rolling element bearings such as ball skidding, destructive wear of rotor and bearing surface and useful for low-speed applications, etc., and to overcome these limitations, nowadays new research is being conducted to use foil bearings as touchdown bearing [10, 11]. However, AMBs were not working during investigation of dynamic analysis of rotor-AMB system. Keeping in mind this lack of research in the field of working together of backup bearings and active magnetic bearings, the present paper immensely focusses on simultaneous interaction of foil bearings and active magnetic bearings during operation of rotor since it has practical importance.

To elaborate the significance of simultaneous working of backup bearings and active magnetic bearings in a rotor-AMB-TDB system, two cases have been considered depending upon the types of touchdown bearings. The first case is to use conventional touchdown bearings (rolling element bearings) as backup support during operation and utilizing foil touchdown bearings as backup support in the second case. The hydrodynamic principle of air in foil bearings while rotation of the rotor causes to make it in working condition along with the operation of active magnetic bearings. For this investigation purpose, mathematical modelling of an unbalanced and misaligned rigid rotor with a rigid disc at middle supported on touchdown bearings and active magnetic bearings has been done. Rigid rotor is misaligned with active magnetic bearings. Equations of motion of the rotor system are derived and numerically simulated by building SIMULINKTM model to generate the time domain displacement and current responses of the system for both cases. The main objective of the proposed work is to explore the practical importance of the working together of touchdown bearings and AMBs. The second case helps in suppressing the vibration response of the rotor system more than the first case. The current consumption is also less in the second case than the first.

2 System Configuration and Mathematical Modelling of the Rotor System

To investigate and explore the dynamic analysis for both cases, a rigid rotor with a rigid disc at middle position supported on two misaligned active magnetic bearings (AMBs) and two touchdown bearings (TDBs) is considered as shown in Fig. 1. The motion of rigid rotor is taken in two transverse directions, i.e. vertical (x) and horizontal (y) directions for the analysis purpose. Here, B_1B_2 is the central axis of both AMBs, and OZ is the operating axis of rotor and central axis of touchdown bearings. Active magnetic bearing axis is misaligned by an amount of radial distance ' a ' from operating axis. Both TDBs are assumed to be identical in its stiffness and damping coefficients. It is to be noted that the rotor is perfectly aligned with TDBs but only misaligned with AMBs, so there is no effect of this misalignment on TDBs. Further, the dynamic characteristics of both AMBs are assumed to be same, and it is

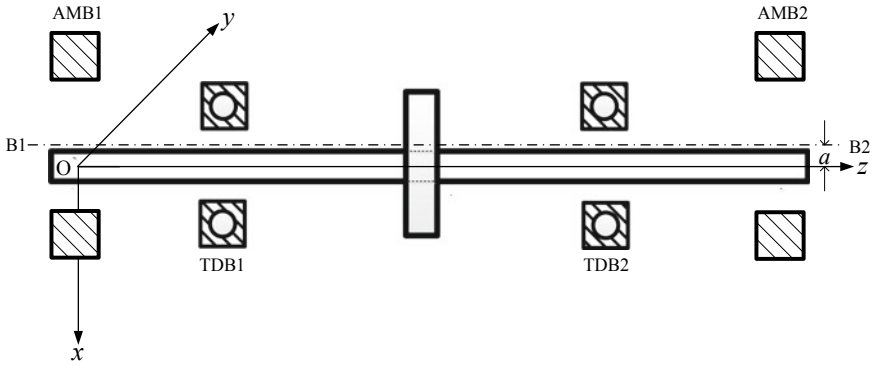


Fig. 1 Schematic diagram of a misaligned rotor-AMB-TDB system

also assumed that the displacements in the x - and y -directions are not coupled with each other.

2.1 Unbalance Force

The force exciting on rotor due to unbalance in the x - and y -directions can be written as

$$f_{unbx} = m_d e \omega^2 \cos(\omega t + \beta); \quad f_{unby} = m_d e \omega^2 \sin(\omega t + \beta) \quad (1)$$

where the disc mass and the eccentricity are represented by m_d and e , respectively. The phase of unbalance and the spin speed of rotor are represented by β and ω , respectively.

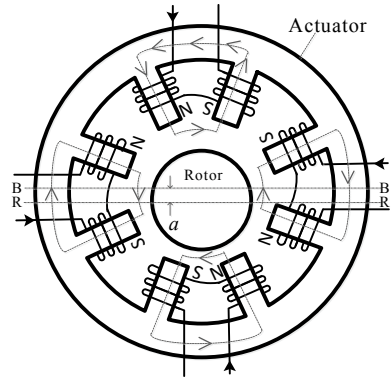
2.2 Force on Rotor Due to Misaligned AMB

The force due to AMB on the rotor in x -direction, when rotor axis is perfectly aligned with AMBs [1], can be expressed as

$$f_x = k \left\{ \frac{(i_0 + i_x)^2}{(s_0 - u_x)^2} - \frac{(i_0 - i_x)^2}{(s_0 + u_x)^2} \right\}; \quad k = \frac{1}{4} \mu_0 N^2 A_a \cos \frac{\alpha}{2} \quad (2)$$

where μ_0 is the vacuum permeability and equal to $4\pi \times 10^{-7}$ H/m, N is the number of turning coils, A_a is the cross-sectional area of magnetic pole, α is the angle between two adjacent magnetic poles, and i_0 and i_x are the bias and controlling currents, respectively. AMB air gap is denoted by s_0 and u_x is the displacement in x -direction.

Fig. 2 Misaligned rotor actuator model



Now simplifying and linearizing Eq. (2) with assumption that $u_x \ll s_0$, it gives

$$f_x = k_a u_x + k_i i_x \tag{3}$$

where the force–displacement constant k_a and force–current constant k_i are

$$k_a = \frac{4ki_0^2}{s_0^3}; \quad k_i = \frac{4ki_0}{s_0^2} \tag{4}$$

Similarly, the force due to AMB on rotor in y -direction in perfectly aligned case can be written as

$$f_y = k_a u_y + k_i i_y \tag{5}$$

where u_y and i_y are the displacement of rotor and controlling current in y -direction, respectively.

The side view of actuator misaligned with rotor is shown in Fig. 2. Here, the rotor is misaligned radially with AMBs axis by an amount of distance ‘ a ’. Thus, there is a change in air gap of AMB. The lower air gap of AMB is $(s_0 - a)$, and the upper air gap is $(s_0 + a)$. Based on this consideration, the force on rotor due to misaligned AMB in the x -direction can be written as

$$f_{mx} = k \left\{ \frac{(i_0 + i_x)^2}{(s_0 - a - u_x)^2} - \frac{(i_0 - i_x)^2}{(s_0 + a + u_x)^2} \right\} \tag{6}$$

On simplifying Eq. (6) and neglecting the higher-order terms of u_x^2 with assumption that $u_x \ll (s_0 - a)$ and $u_x \ll (s_0 + a)$, we get

$$f_{mx} = k \left\{ \frac{4s_0 i_0^2 u_x}{(s_0 - a)^2 (s_0 + a)^2} + \frac{4i_0 (s_0^2 + a^2) i_x}{(s_0 - a)^2 (s_0 + a)^2} + \frac{4s_0 a i_x^2 + 4s_0 u_x i_x^2 + 4i_0 a i_x u_x + 4s_0 a i_0^2}{(s_0 - a)^2 (s_0 + a)^2} \right\} \quad (7)$$

On neglecting the higher-order terms, i.e. i_x^2 , $u_x i_x^2$ and $i_x u_x$, Eq. (7) can be written in a linear form as

$$f_{mx} = k \left\{ \frac{4s_0 i_0^2 u_x}{(s_0 - a)^2 (s_0 + a)^2} + \frac{4i_0 (s_0^2 + a^2) i_x}{(s_0 - a)^2 (s_0 + a)^2} + \frac{4s_0 a i_0^2}{(s_0 - a)^2 (s_0 + a)^2} \right\} \quad (8)$$

On substituting Eq. (4) into Eq. (8), the force on rotor due to misaligned AMB in the x -direction can be given as

$$f_{mx} = k_{ma} u_x + k_{mi} i_x + F_m; \\ \text{with } k_{ma} = \frac{k_a}{(1 - a_1^2)^2}; \quad k_{mi} = \frac{k_i (1 + a_1^2)}{(1 - a_1^2)^2}; \quad F_m = \frac{F_a a_1}{(1 - a_1^2)^2}; \\ F_a = \frac{4k i_0^2}{s_0^2}; \quad a_1 = \frac{a}{s_0} \quad (9)$$

Similarly, the force on rotor due to misaligned AMB in y -direction can be given as

$$f_{my} = k_{ma} u_y + k_{mi} i_y + F_m \quad (10)$$

So, it can be observed from Eqs. (9) and (10) that the force due to misaligned AMB in x - and y -direction contains a modified force–displacement stiffness constant k_{ma} and force–current stiffness constant k_{mi} together with a constant force term F_m . Controlling current outputs [1] from PID controller in the x - and y -directions are expressed as

$$i_x = - \left(k_P u_x + k_I \int u_x dt + k_D \dot{u}_x \right); \quad i_y = - \left(k_P u_y + k_I \int u_y dt + k_D \dot{u}_y \right) \quad (11)$$

where k_P , k_I and k_D are the proportional, integral and derivative factors of PID controller.

2.3 Equations of Motion of the Rotor-AMB-TDB System

With inclusion of the inertia force, unbalance force, forces due to AMBs [1] and TDBs exciting on rotor, the equations of motion of the rotor-AMB-TDB system are described in the following section.

2.3.1 Case I: Considering Conventional Touchdown Bearings (Rolling Element Bearings)

In this case, conventional touchdown bearings (rolling element bearings) are considered as backup support in the rotor-AMB system as shown in Fig. 1. While the rotor is in operation being levitated by AMBs, there is negligible effect of conventional TDBs in comparison with AMBs on the rotor system, due to the presence of air gap between the rotor and conventional TDBs. So, the equations of motion the rotor-AMB-TDB system in the x - and y - directions can be written as

$$m\ddot{u}_x = f_{\text{unbx}} + 2f_{mx}; \quad m\ddot{u}_y = f_{\text{unby}} + 2f_{my} \quad (12)$$

where m is the mass of rotor.

2.3.2 Case II: Considering Foil Bearings as Touchdown Bearings

Foil bearings have been considered as touchdown bearings in this case. While the rotor is in operation, both foil bearings along with active magnetic bearings exert forces on the rotor. The stiffness coefficient k_f and damping coefficient c_f of foil bearings are present throughout the rotor motion. With this approach, the equations of motion of the rotor-AMB-TDB system in the x - and y - directions can be written as

$$m\ddot{u}_x + 2c_f\dot{u}_x + 2k_f u_x = f_{\text{unbx}} + 2f_{mx}; \quad m\ddot{u}_y + 2c_f\dot{u}_y + 2k_f u_y = f_{\text{unby}} + 2f_{my} \quad (13)$$

3 Analysis of Numerically Generated Responses

Equations (12) and (13) have been solved to generate rotor displacements and currents in the x - and y -directions for both cases using a SIMULINK™ model as shown in Fig. 3. The purpose of this simulation is to show how case II is more effective and energy efficient than the case I through comparison in responses. Table 1 summarizes

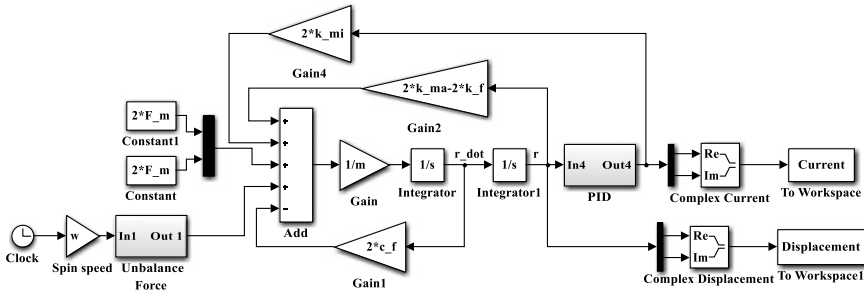


Fig. 3 SIMULINK model of the considered rotor-AMB-TDB system

Table 1 Rotor-AMB-TDB system parameters for the simulation purpose

Rotor-TDB parameters	Assumed values	AMB parameters	Assumed values
Rotor mass (m)	2.845 kg	AMB force displacement constant (k_s)	175,440 N/m
Disc mass (m_d)	2.1 kg	AMB force displacement constant (k_i)	35.09 N/A
Disc eccentricity (e)	100 μ m	Proportional gain of PID controller (k_p)	10,000 A/m
Unbalance phase (β)	30°	Derivative gain of PID controller (k_D)	3 A-s/m
Stiffness coefficient of foil bearing (k_f)	1×10^5 N/m	Integral gain of PID controller (k_I)	25,000 A/m-s
Damping coefficient of foil bearing (c_f)	50 Ns/m	Amount of radial offset of AMBs (a)	1.5×10^{-4} m

the assumed values of rotor-AMB-TDB system parameters utilized for the simulation purpose to generate system responses in the time domain. It can be observed that Table 1 does not include the data for conventional TDBs (e.g. rolling element bearings), as they are inactive while the rotor is in operation due to the presence of relatively smaller air gap. A fourth-order Runge–Kutta ordinary differential equation solver with a fixed step size of 0.0001 s is used for obtaining displacement and current responses of the system. The simulation was run for 5 s for the analysis purpose using data given in Table 1.

The displacements and the controlling currents in the x - and y -directions for case I (conventional touchdown bearings) and case II (foil bearings as TDBs) at a spin speed of 350 rad/s are shown in Fig. 4. It is noticeable from Fig. 4a, b that the maximum absolute value of displacement in the x - and y -directions caused due to simultaneous presence of unbalance and misalignment faults for case I is 9.03×10^{-5} m, but it is only 5.28×10^{-5} m for case II. Thus, the displacement has been suppressed almost half using the second case.

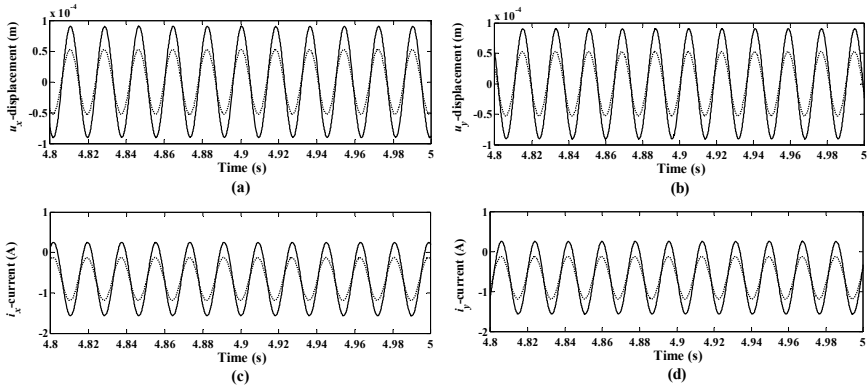


Fig. 4 Rotor system response with conventional TDBs (solid line) and foil bearings as TDBs (dotted line). **a** x-direction displacement, **b** y-direction displacement, **c** x-direction current, **d** y-direction current

It is noticeable from Fig. 4c, d that the maximum absolute values of current response in both directions for case I and case II are 1.57 A and 1.19 A, respectively. Thus, the current consumption for operating the rotor system in the second case is found to be less than the first case. Rotor displacement orbit and AMB current orbit for both cases are represented in Fig. 5. It can be followed from these attenuated responses that the simultaneous working of foil bearings and active magnetic bearings for rotor supporting purpose is more effective and energy efficient.

Further, the present analysis was explored for the lower and higher values of the stiffness and damping coefficients of foil bearings, i.e. 5×10^4 N/m and 40 Ns/m as well as 3×10^5 N/m and 60 Ns/m, respectively, which is reported in Fig. 6. The maximum absolute value of the rotor displacement and current responses in

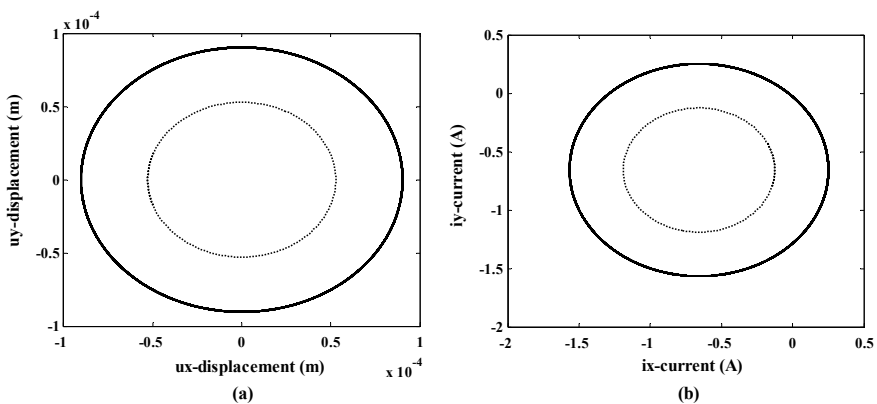


Fig. 5 System orbital response with conventional TDBs (solid line) and foil bearings as TDBs (dotted line). **a** Rotor displacement orbit, **b** AMB current orbit

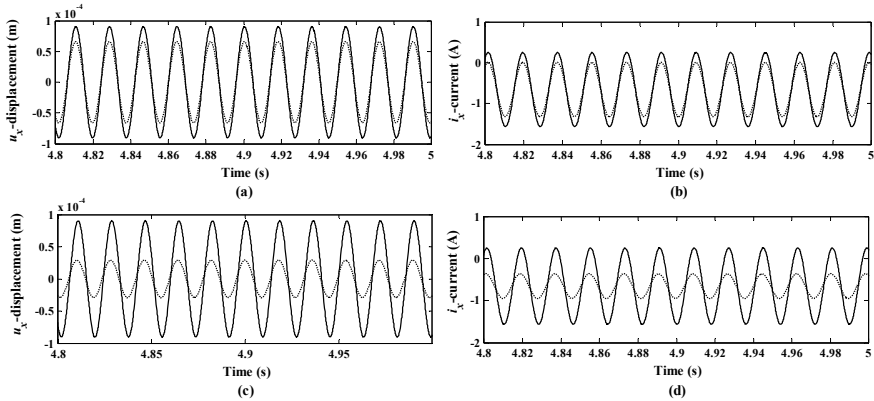


Fig. 6 Response of the system with conventional TDBs (solid line) and foil bearing as TDBs (dotted line) for lower stiffness and damping values. **a** x -direction displacement, **b** x -direction current, and for higher dynamic values of foil bearings, **c** x -direction displacement, **d** x -direction current

x -direction, for the lower stiffness and damping values for the case II are 6.61×10^{-5} m and 1.32 A, which are more than the obtained values from Fig. 4. Thus, it is observed that at low dynamic values of foil bearings, the suppression in the rotor displacement and the current consumption will be less. For higher values of the dynamic coefficients, the maximum absolute value of displacement and current responses in x -direction for the second case are 2.92×10^{-5} m and 0.95 A, which is lesser than the obtained values from Fig. 4.

Therefore, the salient remark can be adopted from this investigation that the suppression in rotor displacement response increases and the current consumption decreases as the value of dynamic coefficients of foil bearings increased. Noting that the present study concludes by examining the importance of working together of AMBs and foil touchdown bearings, which helps in the suppression of the displacement response as well as the current consumption of AMBs. The main cause of this benefit is that the loads on rotor are shared with both the foil bearings and AMBs while rotor is in operation. In the analysis, the values of stiffness and damping parameters of foil bearings are chosen only to show the comparison of responses for conventional TDBs and foil bearings as TDBs. It is interesting to mention that the stiffness and damping coefficients of foil bearings may decrease simultaneously in the light load condition and at low speeds [12]. The factors that determine the stiffness of foil bearings are the film thickness, pressure in the film, projected surface area of the bearings and deformation of the top and bump foils during operation [13]. At low speeds and in the light load condition, the deformation of foils will be less, which lowers the film thickness and consequently the stiffness value. Similarly, the relative motion between the top foil and bump foil or between the bump foil and the bearing inner wall surface arises the damping in the foil bearing [14]. This relative motion will be little at low speeds and light load conditions and thus lowers the damping value of foil bearings. One of the most advantages of the simultaneous working of foil

bearings and AMBs is that this novel idea can eliminate the coating wear problem of foil bearings because the active magnetic bearing supports the rotor loads at start-up and during low speeds. Thus, the life of foil bearings may also improve due to the minimization of initial rubbing between the foil bearing and shaft. One more point can be emphasized from the present work that the study is truly based on the rotor with AMB and conventional TDBs (e.g. rolling element bearings) as well as the rotor with AMB and foil bearings as TDBs. But, the conventional touchdown bearings for case I are inactive and foil bearings are active for case II while the rotor operation, in the considered rotor-AMB-TDB system. Therefore, it is safe to say that the study boils down to rotor with AMB versus rotor with AMB and foil bearings support.

4 Conclusions

The present paper is concluded with the modelling and dynamic analysis of an unbalanced and misaligned rotor supported on two active magnetic bearings and two touchdown bearings. Dynamic analysis of the rotor system is performed based on two cases in which the first case is to use conventional touchdown bearings (rolling element bearings) and foil bearings are to be utilized as touchdown bearings for the second case. Misalignment is considered between the rotor and active magnetic bearings. Mathematical modelling for the rotor system is done, and equations of motion are derived to numerically generate the displacement response and current response of the system. It is found that the suppression in the rotor displacement response is more and current consumption is less when both the foil touchdown bearings and active magnetic bearings are working together while rotor is in operation. Thus, the second case is more effective and energy efficient than the first case. The novel idea of the simultaneous working of foil bearings and AMBs may eliminate the wear problem of foil bearings and improve their life aspect. In the future research, a flexible rotor-AMB-TDB system with an offset disc can be considered using the finite element modelling to study the dynamic response analysis, for the cases when the rotor is supported by AMBs and conventional TDBs as well as the rotor with AMBs and foil bearings as TDBs.

Acknowledgements The first author acknowledges the members of Vibration Laboratory of IIT Guwahati, for their sublime support and help.

References

1. Tiwari R (2017) Rotor systems: analysis and identification. CRC Press, Boca Raton
2. Knospe CR, Hope RW, Fedigan SJ, Williams RD (1995) Experiments in the control of unbalance response using magnetic bearings. *Mechatronics* 5:385–400

3. De Queiroz M (2009) An active identification method of rotor unbalance parameters. *J Vib Control* 15:1365–1374
4. Sekhar AS, Prabhu B (1995) Effects of coupling misalignment on vibrations of rotating machinery. *J Sound Vib* 185:655–671
5. Patel TH, Darpe AK (2009) Experimental investigations on vibration response of misaligned rotors. *Mech Syst Signal Process* 23:2236–2252
6. Da Silva Tuckmantel FW, Cavalca KL (2019) Vibration signatures of a rotor-coupling-bearing system under angular misalignment. *Mech Mach Theory* 133:559–583
7. Bleuler H, Cole M, Keogh P, Larsonneur R, Maslen E, Okada Y et al (2009) *Magnetic bearings: theory, design, and application to rotating machinery*. Springer, Berlin, Heidelberg
8. Kärkkäinen A (2007) Dynamic simulations of rotors during drop on retainer bearings. In: *Acta Universitatis Lappeenrantaensis*
9. Kärkkäinen A, Helfert M, Aeschlimann B, Mikkola A (2008) Dynamic analysis of rotor system with misaligned retainer bearings. *J Tribol* 130:021102
10. San Andrés L, Kim TH (2005) Gas foil bearings: limits for high-speed operation. In: *World tribology congress III*, pp 71–72
11. Swanson E, Heshmat H (2002) Oil-free foil bearings as a reliable, high performance backup bearing for active magnetic bearings. In: *ASME turbo expo 2002: power for land, sea, and air*, pp 589–598
12. Peng JP, Carpino M (1993) Calculation of stiffness and damping coefficients for elastically supported gas foil bearings. *J Tribol* 115:20–27
13. Peng ZC, Khonsari MM (2004) Hydrodynamic analysis of compliant foil bearings with compressible air flow. *J Tribol* 126:542–546
14. Rubio D, San Andrés L (2006) Bump-type foil bearing structural stiffness: experiments and predictions. *J Eng Gas Turbines Power* 128:653–660

Finite Element Modeling and Analysis of Coupled Rotor System Integrated with AMB in the Presence of Parallel and Angular Misalignments



R. Siva Srinivas, Rajiv Tiwari, and Ch. Kanna Babu

Abstract Misalignment is one of the commonly encountered faults in rotor systems. The standard techniques that are used to detect misalignment are loopy orbits, multiple harmonics with predominant 2X and high axial vibration. In real rotor systems, it is caused due to improper seating of bearing housing on foundation or lack of concentricity between bearing and its housing. This chapter presents a numerical model of the coupling, which mimics the forces/moments produced due to parallel and angular misalignment. The coupling connects two rotor systems each with a centrally mounted disk and simply supported on two flexible bearings. The rotor train is modeled with two-node Timoshenko beam finite elements. An AMB is used as an auxiliary support on rotor-2. The coupling connecting the two rotor systems is modeled by a stiffness matrix, which has both static and additive components. While the static component is unchanging during operation, the additive component displays multi-harmonic behavior and exists only in the presence of misalignment. The multi-harmonic nature of coupling's misalignment force/moment is mathematically modeled by an appropriate steering function. The development of mathematical model is followed by some response analysis, which shows lateral vibration of rotor, current signal of AMB and the orbit plots of rotor in the presence of misalignment and unbalance.

Keywords Misalignment · Active magnetic bearing · Full spectrum

R. Siva Srinivas · R. Tiwari (✉)

Department of Mechanical Engineering, Indian Institute of Technology Guwahati, Guwahati 781039, India

e-mail: rtiwari@iitg.ac.in

R. Siva Srinivas

e-mail: wydeek@gmail.com

Ch. Kanna Babu

Aero Engine Research and Design Centre, Hindustan Aeronautics Limited, Bangalore 560093, India

e-mail: chkannababu@gmail.com

© Springer Nature Singapore Pte Ltd. 2021

J. S. Rao et al. (eds.), *Proceedings of the 6th National Symposium*

on Rotor Dynamics, Lecture Notes in Mechanical Engineering,

https://doi.org/10.1007/978-981-15-5701-9_34

Nomenclature

η_0^c	Static deflection vector at coupling
$\eta(t)$	Vibratory deflection vector in real coordinates
\mathbf{u}	Vibratory deflection vector in complex coordinates
k_s	AMB displacement stiffness
k_i	AMB current stiffness
i_c	AMB current in complex form
\mathbf{K}_c	Coupling static stiffness matrix
\mathbf{C}	Damping matrix
\mathbf{G}	Gyroscopic matrix
\mathbf{T}	Transformation matrix
$\Delta\mathbf{k}_c(t)$	Coupling additive stiffness matrix
\mathbf{M}	Mass matrix
\mathbf{K}	Stiffness matrix

Subscripts

<i>ACS</i>	Additive coupling stiffness
<i>SCS</i>	Stiffness matrix
<i>rad</i>	Radial
<i>ang</i>	Angular

1 Introduction

Condition monitoring (CM) essentially involves identification of various faults in rotating machinery, which is followed by corrective measures toward the rectification of the faults. Reference [1] is one of the few textbooks that serve to instruct the reader on various aspects of CM. References [2, 3] are fully devoted to the subject of misalignment. The literature available on the research work conducted on misalignment is extensive. A brief review of a few among the many important papers is given here.

Reference [4] has performed the identification of coupling parameters in a turbo generator (TG) from the forced response due to the disk unbalance using frequency domain least-squares regression. The forces and moments in the coupling produced due to the misalignment have been derived from these identified coupling parameters. Reference [5] measured the forces and moments under the bearing pedestal using a six-axis load cell. The forced response due to offset and angular misalignment was shown on full spectrum plots. In Ref. [6] the stiffness of rigid coupling in the presence of misalignment is modeled as having two components: static and

additive. Reference [7] has performed experiments on the misalignment response in Jeffcott rotors. Reference [8] used higher-order elements with 8-dof per node to model rotor system. The forces and moments are derived and introduced in the finite element model. In Refs. [9, 10] three-dimensional orbits and full spectra are used to study parallel and angular misalignment in a machinery fault simulator. In Ref. [11] different time-frequency techniques were used to monitor misalignment from the run-up data of the rotor. In Ref. [12] orbits and full spectra are used to study the behavior of coupled Jeffcott rotors supported on hydrodynamic bearings. The effect of various coupling geometries on the response due to parallel and angular misalignment is studied theoretically. Reference [13] uses bi-spectrum and tri-spectrum to identify crack and misalignment in an experimental rotor setup. Reference [14] provides a comprehensive review of the applications of active magnetic bearings (AMB) in the field of CM of flexible rotors.

The objective of this work is to model the behavior of a coupled rotor system integrated with an AMB. The development of mathematical model of coupling in the presence of parallel and/or angular misalignment between bearing centers is an important portion in this paper. An appropriate steering function is used to model the multi-harmonic nature of misalignment force as reported in various experimental studies Refs. [5, 9, 12]. Under weight dominance assumption, the additive forces and moments are written as the product of additive stiffness coefficients, an appropriate steering function and the static deflections at the coupling nodes. Assigning values to additive stiffness coefficients in a particular direction would physically represent the existence of fluctuating forces/moments in that direction.

This coupling model is then integrated into the finite element model of coupled rotor. An AMB used as an auxiliary support on rotor-2 serves to attenuate the rotor vibration as well as for the condition monitoring. A Simulink model has been built from the global EOM to generate rotor vibration at nodal locations and AMB current responses in time domain. Orbits and full spectrum plots of vibration and current are analyzed.

2 System Configuration and Mathematical Modeling

An industrial turbine generator (TG) has a train of multiple rotors seated on bearings and connected by intermediate couplings. In the present work, a simplified model of TG integrated with an AMB on rotor-2 is chosen (Fig. 1). The coordinate system followed in this work is shown in Fig. 2. A coupling connects two rotor systems that are simply supported on two bearings, each with a centrally mounted disk. The rotor system is discretized into finite elements using Timoshenko beam elements. The real elemental matrices are of the size 8×8 and are given in Refs. [15, 16]. Alternatively, matrices of size 4×4 , corresponding to complex nodal displacement vector, as given in Refs. [17, 18] can be used for modeling each finite element. Besides reducing the computational effort, complex notation helps in identifying the coefficients of positive and negative harmonics of full spectrum arising due to

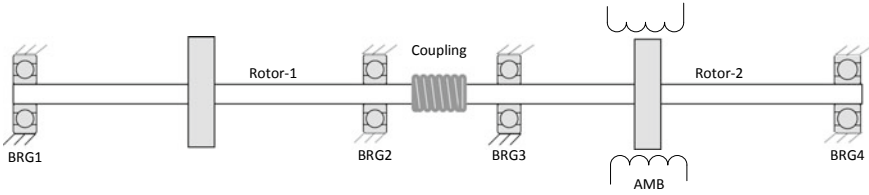
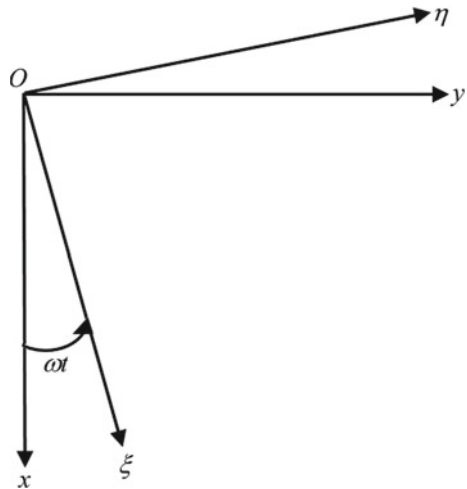


Fig. 1 Coupled rotor system integrated with AMB

Fig. 2 Inertial and rotating frames of reference



multi-harmonic forcing due to misalignment. In Ref. [17], nodal displacements of the left node are arranged in real domain and those of the right node are arranged in imaginary domain as shown in Eq. (1).

$$\mathbf{u}^e = \mathbf{u}_{left} + j\mathbf{u}_{right} = \{x_1 \varphi_{x1} \ x_2 \ \varphi_{x2}\}^T + j\{y_1 \ \varphi_{y1} \ y_2 \ \varphi_{y2}\}^T \tag{1}$$

In Ref. [18], nodal displacements of x - z plane are arranged in real domain and those of y - z plane in imaginary domain as shown in Eq. (2). While the matrices in Ref. [17] have imaginary terms, the elemental matrices in Ref. [18] have real terms, and these are used in the present work.

$$\mathbf{u}^e = \mathbf{u}_{xz} + j\mathbf{u}_{yz} = \{x_1 \ \varphi_{y1} \ x_2 \ \varphi_{y2}\}^T + j\{y_1 \ \varphi_{x1} \ y_2 \ \varphi_{x2}\}^T \tag{2}$$

Likewise, the mass and gyroscopic matrices of disks, as given in Ref. [19], are used. In the presence of misalignment, the coupling has static coupling stiffness (SCS) and time-dependent additive coupling stiffness (ACS) components Ref. [6]. This assumption that when misalignment exists between bearing centers there is an additive stiffness component in a coupling besides its static stiffness is the basis of

the present formulation. When the bearing centers are perfectly aligned, there is only the static stiffness component as shown in Eq. (3).

$$\mathbf{f}_{\text{coupling}} = \mathbf{K}_c \{ \boldsymbol{\eta}_0 + \boldsymbol{\eta}(t) \} \quad (3)$$

When there is misalignment between bearing centers, then the additive component comes into play. In such case, we have

$$\begin{aligned} \mathbf{f}_{\text{coupling}} &= [\mathbf{K}_c + \Delta \mathbf{k}_c(t)] \{ \boldsymbol{\eta}_0 + \boldsymbol{\eta}(t) \} \\ &= \underbrace{\mathbf{K}_c \boldsymbol{\eta}(t)}_{\mathbf{f}_{SCS}} + \underbrace{\Delta \mathbf{k}_c(t) \boldsymbol{\eta}_0 + \Delta \mathbf{k}_c(t) \boldsymbol{\eta}(t)}_{\mathbf{f}_{ACS}} \end{aligned} \quad (4)$$

2.1 Static Stiffness Force of Coupling

Static stiffness force of coupling in Eq. (4), \mathbf{f}_{SCS} takes the following *real* form as shown below.

$$\mathbf{f}_{SCS}^r = \mathbf{K}_c \boldsymbol{\eta} = \begin{bmatrix} k_{xx} & k_{xy} & 0 & 0 & -k_{xx} & -k_{xy} & 0 & 0 \\ k_{yx} & k_{yy} & 0 & 0 & -k_{yx} & -k_{yy} & 0 & 0 \\ 0 & 0 & k_{\varphi_y \varphi_y} & 0 & 0 & 0 & -k_{\varphi_y \varphi_y} & 0 \\ 0 & 0 & 0 & k_{\varphi_x \varphi_x} & 0 & 0 & 0 & -k_{\varphi_x \varphi_x} \\ -k_{xx} & -k_{xy} & 0 & 0 & k_{xx} & k_{xy} & 0 & 0 \\ -k_{yx} & -k_{yy} & 0 & 0 & k_{yx} & k_{yy} & 0 & 0 \\ 0 & 0 & -k_{\varphi_y \varphi_y} & 0 & 0 & 0 & k_{\varphi_y \varphi_y} & 0 \\ 0 & 0 & 0 & -k_{\varphi_x \varphi_x} & 0 & 0 & 0 & k_{\varphi_x \varphi_x} \end{bmatrix} \begin{Bmatrix} x_1 \\ y_1 \\ \varphi_{y1} \\ \varphi_{x1} \\ x_2 \\ y_2 \\ \varphi_{y2} \\ \varphi_{x2} \end{Bmatrix} \quad (5)$$

The size of the above matrix reduces by half when converted to *complex* form. In complex notation, the above matrix takes the following form, where $u_{c_i} = x_{c_i} + j y_{c_i}$, $\varphi_{c_i} = \varphi_{y_i} + j \varphi_{x_i}$. If cross-coupled coupling coefficients are not considered, then $k_{xy} = k_{yx} = 0$. For a symmetric coupling, $k_{xx} = k_{yy} = k_{rad}$ and $k_{\varphi_{yy}} = k_{\varphi_{xx}} = k_{\varphi_{ang}}$.

$$\mathbf{f}_{SCS}^c = \begin{bmatrix} k_{rad} & 0 & -k_{rad} & 0 \\ 0 & k_{ang} & 0 & -k_{ang} \\ -k_{rad} & 0 & k_{rad} & 0 \\ 0 & -k_{ang} & 0 & k_{ang} \end{bmatrix} \begin{Bmatrix} u_{c_1} \\ \varphi_{c_1} \\ u_{c_2} \\ \varphi_{c_2} \end{Bmatrix} \quad (6)$$

2.2 Additive Stiffness Force of Coupling

Additive stiffness force of coupling in Eq. (4) can be expanded as

$$\mathbf{f}_{ACS} = \Delta \mathbf{K}^c(t) (\boldsymbol{\eta}_0^c + \bar{\eta}^c e^{ij\omega t}) \quad (7)$$

If the weight dominance criterion is assumed, then we have

$$\bar{\eta}^c \ll \boldsymbol{\eta}_0^c \quad (8)$$

and

$$\mathbf{f}_{ACS} = \Delta \mathbf{K}^c(t) \boldsymbol{\eta}_0^c \quad (9)$$

where $\Delta \mathbf{K}^c(t)$ in Eq. (9) can be written as the product of a steering function $s(t)$ and a matrix of constant coefficients as shown in Eq. (10).

Parallel misalignment generates additive coupling stiffness coefficients $\Delta k_{T\xi}$ and $\Delta k_{T\eta}$ in the rotating frame of reference. Likewise, $\Delta k_{R\eta}$ and $\Delta k_{R\xi}$ are additive coupling stiffness coefficients and are generated due to the angular misalignment. In the most general case, unequal amounts of misalignment exist in X-Y and X-Z planes, and therefore, the coefficients are assumed to be unequal, $\Delta k_{T\xi} \neq \Delta k_{T\eta}$, $\Delta k_{R\xi} \neq \Delta k_{R\eta}$ which makes the total number of direct ACS coefficients to four. All cross-coupling coefficients are ignored in this work.

$$\Delta \mathbf{K}_{Rot}^c(t) = s(t) \begin{bmatrix} \Delta k_{\xi\xi} & 0 & 0 & 0 & -\Delta k_{\xi\xi} & 0 & 0 & 0 \\ 0 & \Delta k_{\eta\eta} & 0 & 0 & 0 & -\Delta k_{\eta\eta} & 0 & 0 \\ 0 & 0 & \Delta k_{\varphi\eta\varphi\eta} & 0 & 0 & 0 & -\Delta k_{\varphi\eta\varphi\eta} & 0 \\ 0 & 0 & 0 & \Delta k_{\varphi\xi\varphi\xi} & 0 & 0 & 0 & -\Delta k_{\varphi\xi\varphi\xi} \\ -\Delta k_{\xi\xi} & 0 & 0 & 0 & \Delta k_{\xi\xi} & 0 & 0 & 0 \\ 0 & -\Delta k_{\eta\eta} & 0 & 0 & 0 & \Delta k_{\eta\eta} & 0 & 0 \\ 0 & 0 & -\Delta k_{\varphi\eta\varphi\eta} & 0 & 0 & 0 & \Delta k_{\varphi\eta\varphi\eta} & 0 \\ 0 & 0 & 0 & -\Delta k_{\varphi\xi\varphi\xi} & 0 & 0 & 0 & \Delta k_{\varphi\xi\varphi\xi} \end{bmatrix} \quad (10)$$

The above matrix is in rotating frame of reference. We convert Eq. (10) from the rotating to stationary frame of reference using the transformation matrix given in Ref. [20].

$$\Delta \mathbf{K}_{Stat}^c = \mathbf{T}^T \Delta \mathbf{K}_{Rot}^c(t) \mathbf{T} = s(t) (\mathbf{T}^T \Delta \mathbf{K}_{Rot}^c \mathbf{T}) \quad (11)$$

The additive coupling force in the real form is given by

$$\mathbf{f}_{ACS}^r = s(t) \Delta \mathbf{K}_{Stat}^c \boldsymbol{\eta}_0^c \quad (12)$$

where

$$\mathbf{\eta}_0^c = \{ \delta x_1 \ \delta y_1 \ \delta \varphi_{y_1} \ \delta \varphi_{x_1} \ \delta x_2 \ \delta y_2 \ \delta \varphi_{y_2} \ \delta \varphi_{x_2} \}^T \quad (13)$$

For horizontal rotor, self-weight acts in the vertically downward direction, the static deflections and slopes in the horizontal direction are zero. As per the convention followed in this work (Fig. 2)

$$\delta y_1 = \delta y_2 = \delta \varphi_{x_1} = \delta \varphi_{x_2} = 0 \quad (14)$$

The remaining coefficients of the vector given by Eq. (13) are the static deflections and slopes at the coupling nodes (indicated by super script c) due to the self-weight of the coupled rotor system. These are obtained from catenary curve, which is the graphical representation of the static deflections and slopes due to self-weight at each node along the length of the rotor modeled by finite elements. This is obtained by solving the equation

$$\mathbf{\eta}_{8 \times 1}^{ne} = -(\mathbf{K}_{8 \times 8}^{ne})^{-1} (\mathbf{M}_{8 \times 8}^{ne}) \{ \mathbf{g}_{8 \times 8}^{ne} \} \quad (15)$$

where

$$\mathbf{g}^{ne} = \{ 0 \ 9.81 \ 0 \ 9.81 \ 0 \ 9.81 \ 0 \ 9.81 \}^T \quad (16)$$

In Eq. (15), elemental matrices of Ref. [16] are used. The superscript ne is used to avoid confusion. Upon solving Eq. (15), we obtain the static deflections at coupling nodes. The static deflections in X-Y plane are zero, and those in X-Z plane are substituted in Eq. 12 to obtain additive coupling stiffness force vector of size 8×1 . Finally, the force vector due to additive coupling stiffness in the complex form is given by

$$\mathbf{f}_{ACS}^c = 0.5s(t) \left\{ \begin{array}{l} (\delta x_1 - \delta x_2) \{ \Delta k_{T\xi}(1 + e^{j2\omega t}) + \Delta k_{T\eta}(1 - e^{j2\omega t}) \} \\ (\delta \varphi_{y_1} - \delta \varphi_{y_2}) \{ \Delta k_{R\xi}(1 + e^{j2\omega t}) + \Delta k_{R\eta}(1 - e^{j2\omega t}) \} \\ (\delta x_2 - \delta x_1) \{ \Delta k_{T\xi}(1 + e^{j2\omega t}) + \Delta k_{T\eta}(1 - e^{j2\omega t}) \} \\ (\delta \varphi_{y_2} - \delta \varphi_{y_1}) \{ \Delta k_{R\xi}(1 + e^{j2\omega t}) + \Delta k_{R\eta}(1 - e^{j2\omega t}) \} \end{array} \right\} \quad (17)$$

where the steering function is assumed to be square wave with 40% duty cycle as shown in Fig. 3. The Fourier expansion of the wave is as follows

$$\begin{aligned} s(t) = & 0.5 + 0.6055 \cos(\omega t) + 0.1871 \cos(2\omega t) - 0.1247 \cos(3\omega t) \\ & - 0.1514 \cos(4\omega t) + 0.1009 \cos(6\omega t) + 0.0535 \cos(7\omega t) - 0.0468 \cos(8\omega t) \\ & - 0.0673 \cos(9\omega t) + 0.055 \cos(11\omega t) + 0.0312 \cos(12\omega t) \\ & - 0.0288 \cos(13\omega t) - 0.0432 \cos(14\omega t) + 0.0378 \cos(16\omega t) + 0.022 \cos(17\omega t) \end{aligned} \quad (18)$$

Upon rewriting Eq. (17) in terms of exponential series, we have

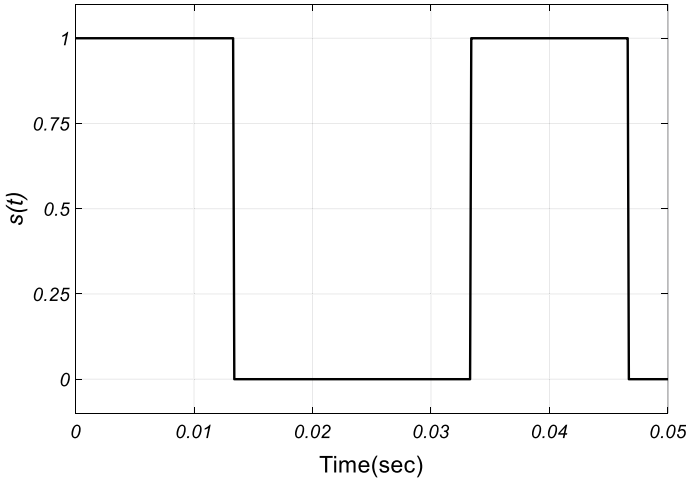


Fig. 3 Square wave with 40% duty cycle

$$\mathbf{f}_{ACS}^c(t) = 0.5 \left\{ \begin{array}{l} (\delta x_1 - \delta x_2) \left(\Delta k_{T\xi} \sum_{i=-n}^{i+n} p_i e^{ij\omega t} + \Delta k_{T\eta} \sum_{i=-n}^{i+n} q_i e^{ij\omega t} \right) \\ (\delta \varphi_{y_1} - \delta \varphi_{y_2}) \left(\Delta k_{R\xi} \sum_{i=-n}^{i+n} p_i e^{ij\omega t} + \Delta k_{R\eta} \sum_{i=-n}^{i+n} q_i e^{ij\omega t} \right) \\ (\delta x_2 - \delta x_1) \left(\Delta k_{T\xi} \sum_{i=-n}^{i+n} p_i e^{ij\omega t} + \Delta k_{T\eta} \sum_{i=-n}^{i+n} q_i e^{ij\omega t} \right) \\ (\delta \varphi_{y_2} - \delta \varphi_{y_1}) \left(\Delta k_{R\xi} \sum_{i=-n}^{i+n} p_i e^{ij\omega t} + \Delta k_{R\eta} \sum_{i=-n}^{i+n} q_i e^{ij\omega t} \right) \end{array} \right\} \quad (19)$$

In Eq. (19), in the above equation, p_i and q_i denote the participation factors of the steering function. The physical interpretation of Eq. (19) is as follows: In the presence of parallel and/or angular misalignment, a time varying additive stiffness component arises in the coupling. It follows that the parallel misalignment produces translational *additive* stiffness in x and y directions. Likewise, rotational *additive* stiffness about x and y directions arises from the angular misalignment. Under the weight dominance assumption, the additive forces and moments are written as product of additive stiffness coefficients, an appropriate steering function and the static deflection at the coupling nodes. Assigning values to the additive stiffness coefficients in a particular direction would physically represent the existence of fluctuating forces/moments in that direction.

2.3 *AMB Force*

The lateral force exerted by the AMB on the rotor has two components: the one which depends on the rotor vibration at the AMB location and the other due to current in the actuator, which depends on the control law implemented.

$$\mathbf{f}_{AMB} = k_s u_{AMB} - k_i i_c \quad (20)$$

where u_{AMB} is the complex displacement at the nodal location of AMB. The complex current i_c is obtained as per the PID control law. The AMB constants used in this work are taken from Ref. [21].

2.4 *Unbalance Force*

The unbalance force vector due to the disk eccentricity at the nodal location of i^{th} disk is

$$\mathbf{f}_{umb_i} = m_{d_i} e_{d_i} \omega^2 e^{j\omega t} e^{j\beta} \quad (21)$$

2.5 *Bearing Force*

The force acting at the bearing nodal location due to the stiffness of i^{th} bearing is

$$\mathbf{f}_{b_i} = 0.5 \{ k_{1xx}(u_{b_i} + \bar{u}_{b_i}) - jk_{1xy}(u_{b_i} - \bar{u}_{b_i}) + jk_{1yx}(u_{b_i} + \bar{u}_{b_i}) + k_{1yy}(u_{b_i} - \bar{u}_{b_i}) \} \quad (22)$$

where u_{b_i} is the complex translational displacement at the nodal location of the i^{th} bearing. $k_{i_{xx}}, k_{i_{xy}}, k_{i_{yx}}, k_{i_{yy}}$ represent the direct and cross-coupled stiffness coefficients of bearing. We assume that rolling element bearings have no cross-coupled coefficients. In such case

$$\mathbf{f}_{b_i} = 0.5 \{ k_{i_{xx}}(u_{b_i} + \bar{u}_{b_i}) + k_{i_{yy}}(u_{b_i} - \bar{u}_{b_i}) \} \quad (23)$$

2.6 Global EOM and Simulink Model

The global EOM in complex form is mounted by assembling the sub-system matrices as described in Ref. [20].

$$\begin{aligned}
 &(\mathbf{M}_{shaft} + \mathbf{M}_{disc})\mathbf{R} + [\mathbf{C}_{brg} + \mathbf{C}_{cpg} + \mathbf{C}_{shaft} - j\omega(\mathbf{G}_{shaft} + \mathbf{G}_{disc})]\dot{\mathbf{u}} \\
 &+ (\mathbf{K}_{brg} + \mathbf{K}_{SCS} + \mathbf{K}_{shaft})\mathbf{u} + s(t)\Delta\mathbf{K}_{Stat}^c\boldsymbol{\eta}_0^c = \mathbf{f}_{unb} + \mathbf{f}_{AMB} \tag{24}
 \end{aligned}$$

Damping coefficient in anti-friction bearings is $(0.25-2.5)\times 10^{-5}sec \times k$ [10], where k is the linear bearing stiffness. This bearing damping \mathbf{C}_{brg} is lower than is found in journal bearings and so is ignored in the present work. Likewise, the equivalent viscous damping of coupling \mathbf{C}_{cpg} is ignored. Equation (24) then becomes

$$\begin{aligned}
 &(\mathbf{M}_{shaft} + \mathbf{M}_{disc})\mathbf{R} + [\mathbf{C}_{shaft} - j\omega(\mathbf{G}_{shaft} + \mathbf{G}_{disc})]\dot{\mathbf{u}} \\
 &+ (\mathbf{K}_{brg} + \mathbf{K}_{SCS} + \mathbf{K}_{shaft})\mathbf{u} = \mathbf{f}_{unb} + \mathbf{f}_{AMB} - \mathbf{f}_{ACS} \tag{25}
 \end{aligned}$$

Equation (25) can be rewritten as

$$\begin{aligned}
 &(\mathbf{M}_{shaft} + \mathbf{M}_{disc})\mathbf{R} + [\mathbf{C}_{shaft} - j\omega(\mathbf{G}_{shaft} + \mathbf{G}_{disc})]\dot{\mathbf{u}} + \mathbf{K}_{shaft}\mathbf{u} \\
 &= \mathbf{f}_{unb} + \mathbf{f}_{AMB} - \mathbf{f}_{BRG} - \mathbf{f}_{SCS} - \mathbf{f}_{ACS} \tag{26}
 \end{aligned}$$

From Eq. (25), it can be seen that the external forces acting on the system are (i) unbalance force (ii) force due to static coupling stiffness (iii) the force due to additive coupling stiffness (iv) force due to AMB and (v) force due to bearings. The global EOM is obtained by assembling the sub-system matrices as described in Ref. [20].

A Simulink model as shown in Fig. 4 is built using the above equations to generate time domain responses of vibration at each node along the length of rotor-bearing-coupling-AMB system. Additionally, the current at AMB location can be obtained.

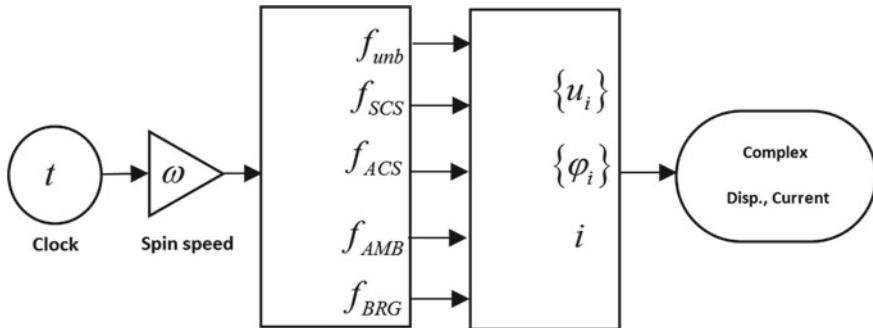


Fig. 4 Simulink model of rotor-bearing-coupling-AMB system

3 Results and Discussion

The geometric properties of rotors are given in Table 1. Figures 5 and 6 show the stiffness values of bearings and coupling. Figure 7 shows the orbits at disk locations at 3000 rpm. The orbits are close to circular in shape since the synchronous unbalance response dominates the multi-harmonic misalignment response. The orbit at the nodal location of disk-2 is smaller than that of disk-1 which demonstrates the effect of AMB. Figure 8 shows the full spectrum plot of disk-1 vibration and AMB current. The amplitude and phase of forward and backward whirl frequencies can be seen. The full spectrum plots obtained from simulation look similar to the plots in Refs. [5, 9, 12], which are obtained by performing FFT on experimental data.

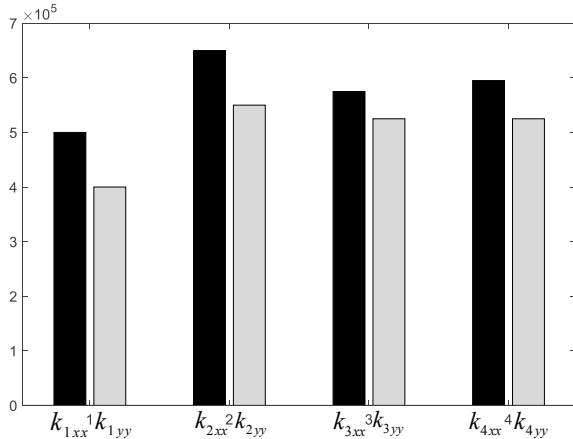
4 Conclusions

A coupled rotor system representative of a TG is modeled with finite elements. The mathematical model of coupling in the presence of angular and parallel misalignments is developed. The multi-harmonic component of coupling forces/moments

Table 1 Rotor geometric properties

Parameters	Values	Parameters	Values	Parameters	Values
m_{d1} (kg)	2.25	I_{p2} (kg m ²)	0.006	d (m)	0.016
I_{d1} (kg-m ²)	0.0024	e_1 (kg-m)	0.00008	l_e (m)	0.1
I_{p1} (kg-m ²)	0.0045	e_2 (kg-m)	0.00006	k_p (A/m)	12,200
m_{d2} (kg)	1.25	β_1 (rad)	$\pi/6$	k_i (A/m-s)	2000
I_{d2} (kg-m ²)	0.003	β_2 (rad)	$\pi/4$	k_d (A-s)/m	2

Fig. 5 Stiffness of bearings in N/m



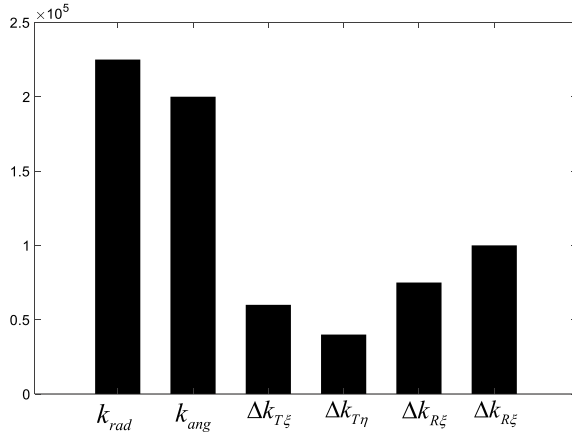


Fig. 6 Static and additive stiffness coefficients of coupling

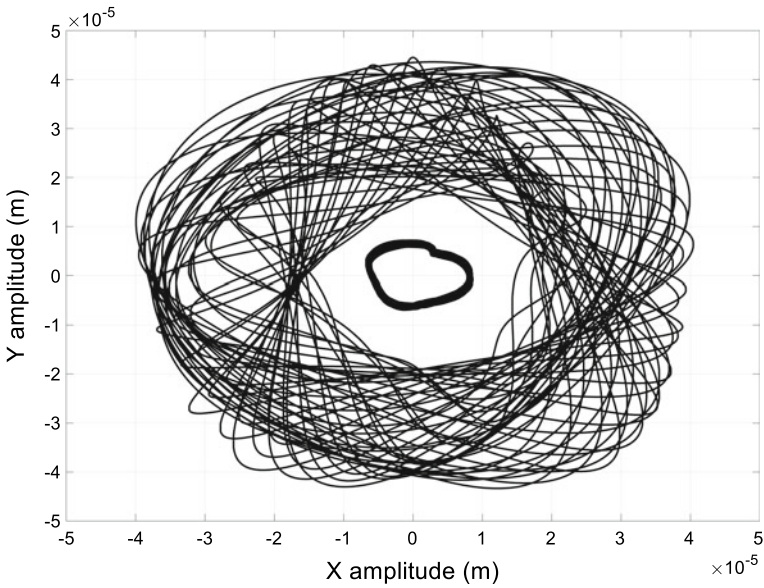


Fig. 7 Orbits at disk-1 and disk-2 locations

depends on the static deflections at the coupling locations and the additive stiffness coefficients. A Simulink model is built from the EOM. From the time domain data, orbits and full spectrum plots at various nodal locations are plotted. AMB is shown to be effective at reducing the amplitude of the orbit at its nodal location.

The modeling of coupling to account for its dynamic behavior in the presence of parallel and angular misalignments is the novelty of the present work. The magnitude

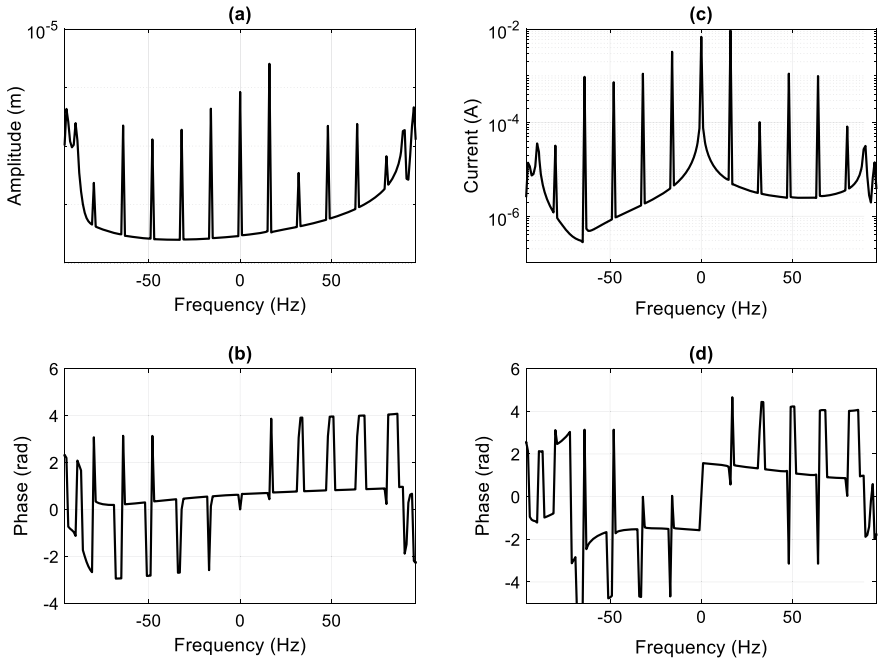


Fig. 8 Full spectrum plot at 16 Hz **a** amplitude at disk-1 location, **b** phase at disk-1 location, **c** amplitude of AMB current, **d** phase of AMB current

of additive stiffness of coupling is proportional to the amount of misalignment in a specific direction. In other words, its magnitude in a given direction indicates the severity of misalignment in that direction. This assumption is central in the development of the present mathematical formulation. The steering function is chosen in such a way that full spectra obtained from simulation shall look akin to the experimental spectra.

This mathematical model can be rearranged in the form $\mathbf{Ax} = \mathbf{b}$ where \mathbf{A} and \mathbf{b} are matrix/vector of known quantities and \mathbf{x} is the vector of physical parameters of rotor, bearing, AMB and coupling, which are the unknown quantities. The vibration and current data obtained from experiments at various speeds are the inputs to the matrices. By solving the above mentioned equation, the magnitude of the ACS coefficients that depend on the amount of misalignment present between bearing centers can be estimated experimentally.

Acknowledgements The authors thank the reviewers for their valuable comments.

References

1. Tiwari R (2017) Rotor systems: analysis and identification, 1st edn, Taylor & Francis Group, CRC Press, Boca Raton
2. Macmillan RB (2003) Rotating machinery: practical solutions to unbalance and misalignment, 1st edn, Fairmont Press, Georgia
3. Piotrowski S (2006) Shaft alignment handbook, 3rd edn, CRC Press, Boca Raton
4. Lal M, Tiwari R (2012) Multiple fault identification in simple rotor-bearing-coupling systems based on forced response measurements. *Mech Mach Theory* 51:87–109
5. Patel T, Darpe AK (2009) Experimental investigations on vibration response of misaligned rotors. *Mech Syst Signal Process* 23:2236–2252
6. Lees AW (2007) Misalignment in rigidly coupled rotors. *J Sound Vib* 305:261–271
7. Rao JS, Sreenivas R, Chawla A Proceedings of ASME Turbo Expo, June 4–7, 2001, Louisiana
8. Sekhar AS, Prabhu BS (1995) Effects of coupling misalignment on vibrations of rotating machinery. *J Sound Vib* 185(4):655–671
9. Monte M, Verbelen F, Vervisch B (2015) Detection of coupling misalignment by extended orbits, experimental techniques, rotating machinery, and acoustics. In: Proceedings of the society for experimental mechanics series, vol 8, pp 243–250
10. Monte M, Verbelen F, Vervisch B (2014) The use of orbitals and full spectra to identify misalignment. *Struct Health Monitor* 5:215–222
11. Chandra NH, Sekhar AS (2016) Fault detection in rotor bearing systems using time frequency techniques. *Mech Syst Signal Process* 72-73:105–133
12. Tuckmantel FWS, Schoola CG, Cavalca KL (2019) Flexible disc coupling model in rotating shafts. In: Proceedings of the 10th international conference on rotor dynamics, mechanisms and machine science, IFToMM 2018, vol 61, pp 502–517
13. Sinha JK (2007) Higher order spectra for crack and misalignment identification in the shaft of a rotating machine. *Struct Health Monitor* 6:325–334
14. Siva Srinivas R, Tiwari R, Kannababu Ch (2018) Application of active magnetic bearings in flexible rotordynamic systems—a state-of-the-art review. *Mech Syst Signal Process* 106:537–572
15. Chen WJ, Gunter EJ (2007) Introduction to dynamics of rotor bearing systems, Trafford Publications
16. Nelson HD, McVaugh JM (1976) The dynamics of rotor bearing systems using finite elements. *J Eng Industr* 593–600
17. Nelson HD (1985) Rotor dynamics equations in complex form. *J Vib Acoust Stress Reliab Design Tech Brief* 107:460–461
18. Chen WJ (1998) A note on computational rotor dynamics. *J Vib Acoust* 120:228–233
19. Singh S, Tiwari R (2016) Model based switching crack identification in a Jeffcott rotor with an offset disc integrated with an active magnetic bearing. *J Dyn Syst Measure Control* 138:031006-1–031006-11
20. Friswell MI, Penny JET, Garvey SD, Lees AW (2010) Dynamics of rotating machines, 1st edn, Cambridge University Press, New York
21. Bordoloi DJ, Tiwari R (2013) Optimization of controller parameters of active magnetic bearings in rotor bearing systems. *Adv Vib Eng* 12:319–327

Detection of Fatigue Crack in the Shaft Using Time-Frequency Analysis



Sagi Rathna Prasad  and A. S. Sekhar 

Abstract Rotating shafts operating under complex loading conditions are susceptible to develop fatigue cracks at the localized stress concentration points. Fatigue cracks are the prime sources for catastrophic failures. Therefore, it is vital and challenging for the early fatigue crack detection to prevent costly machinery breakdowns. A rotor test rig with a facility of introducing stochastic loads on to the rotating shaft is designed and developed to induce fatigue crack on the shaft is utilized for this study. Accelerated fatigue tests are performed, along by introducing stochastic loads, on a shaft specimen seeded with circumferential V-notch configuration. The methodology for early crack detection is based on analyzing the steady-state vibration data acquired, till the shaft specimen develops fatigue crack, from various locations of the test rig using different sensors like miniature accelerometers, wireless telemetry strain gauge, and laser vibrometer. In the present study, signal processing tools like continuous wavelet transforms (CWT), Hilbert–Huang transform (HHT), and short-time Fourier transform (STFT) are employed for the early fatigue crack detection. Wavelet packet (WP) analysis is used to decompose the experimental vibration response data into narrow frequency band signals before the processing of CWT, HHT, and STFT analyses. In addition, these techniques are compared to evaluate their detection performance when employed directly on raw data and preprocessed data using WP analysis. Finally, this paper provides a detailed description and comprehensive selection of time-frequency techniques for the early fatigue crack detection.

Keywords Fatigue crack · Stochastic loads · V-notch · Wavelet packet · Condition monitoring

S. R. Prasad (✉) · A. S. Sekhar

Department of Mechanical Engineering, Indian Institute of Technology, Madras, Chennai 600036, India

e-mail: aerorathan.sagi@gmail.com

A. S. Sekhar

e-mail: as_sekhar@iitm.ac.in

© Springer Nature Singapore Pte Ltd. 2021

J. S. Rao et al. (eds.), *Proceedings of the 6th National Symposium*

on Rotor Dynamics, Lecture Notes in Mechanical Engineering,

https://doi.org/10.1007/978-981-15-5701-9_35

1 Introduction

From the literature, it is evident that the many recommendations and rules have been proposed for the early crack detection. However, industrial rotors fail without exhibiting detectable changes in some of the key vibration parameters. Therefore, this indicates the problem of early fatigue crack detection is not fully addressed, and no general detection technique is found in the literature. Hence, it is vital and challenging to discover a signal processing technique, for fault detection, suitable for the dynamic response of the rotating shaft subjected to the elevated stress conditions. Many researchers modeled and studied the dynamic responses of the cracked rotors using different approaches [1, 2]. From the literature, it is suggested to track the operating frequency harmonic components such as $1\times$, $2\times$, and $3\times$ for primary indicators of shaft cracks in the isotropic rotors [3–5]. As time information is lost while performing fast Fourier transform (FFT), it cannot represent the variation of these components ($1\times$, $2\times$, and $3\times$) with time. Also, it is unable to effectively characterize non-stationary vibration signals and temporal transients using FFT analysis. Therefore, for the time as well as frequency-dependent nature of rotor faults time-frequency techniques with high resolution in both time and frequency are ideal for their detection. An extensive review on crack detection in shafts using time-frequency techniques, such as CWT, HHT, and STFT, is presented by Sabnavis et al. [6]. In rotors, each fault has a certain frequency band. Hence, it is essential to extract fault features from these bands for effective fault diagnosis. In recent years, the wavelet packet (WP) analysis has attracted much attention and has been used for feature extraction. Gao et al. [7] performed a comparative study between WP analysis and other time-frequency techniques like HHT, STFT for bearing health monitoring and their results showed that WP analysis could identify fault induced transient components buried within the signal. WP analysis can also be used as a preprocessor tool to decompose the vibration into narrow frequency band signals to improve the performance of CWT, STFT, and HHT [8]. The performance of wavelet transforms in detecting rotor cracks using transient response is well documented by Prabhakar et al. [9]. Liu et al. [10] adopted combined HHT, and WP analysis for the structural crack detection and their findings proved that the amplitude of intrinsic mode functions (IMF) are much sensitive to the presence of a crack. From earlier publications, it is evident that the time-frequency analysis techniques such as STFT, HHT, CWT, and WP analysis have been investigated for the condition monitoring of rolling bearings, gear boxes, and power transformers [11–13]. In addition, authors in their earlier work [14] applied enhanced spectral kurtosis (SK) (a frequency domain statistical parameter sensitive for transients in the signal) for fatigue crack detection in the shaft for the same experimental data used in this study. In all the above-mentioned literature, each of these techniques, employed either collectively or individually, displayed certain effectiveness in extracting fault features hidden within the transients or non-stationary signals. However, no detailed studies have been conducted to detect fatigue cracks, that develop in the shafts subjected to external random excitation while operating at a constant rotating speed, by applying time-frequency techniques such as CWT, HHT

and STFT. In this paper, analysis of early detection of shaft crack developed during an accelerated fatigue test is performed by investigating three time-frequency techniques such as short-time Fourier transform (STFT), continuous wavelet transform (CWT), and Hilbert–Huang transform (HHT). Wavelet packet analysis is used as a preprocessing tool to decompose the raw vibration signal into finer frequency bands, which consist of incipient crack features. A comparative study on the effectiveness of the selected time-frequency techniques in detecting the shaft fatigue crack, when employed directly on raw vibration signals and on decomposed signals using wavelet packet analysis, is presented

2 Description of Time-Frequency Techniques

The procedure for the decomposition of signals using wavelet packet analysis is presented in Sect. 2.1. Description of three selected time-frequency techniques followed by a comparative study on their performance of early crack detection using raw and reconstructed signals from WP analysis is presented in the subsequent sections.

2.1 Wavelet Packet Analysis

Wavelet packet analysis is a classical two-band method used for the multistage filtering process employed for obtaining hidden fault features in noisy signals. The detailed description of wavelet packet decomposition can found in [15, 16]. Wavelet packet analysis presents a finer frequency band partitioning over the entire frequency band of the signal by splitting into both low (approximation) frequency and high (detail) frequency bands, hence, enhancing the frequency resolution. The wavelet packet function expressed mathematically is shown in Eq. (1):

$$W_{j,k}^n(t) = 2^{\frac{j}{2}} W^n(2^j t - k) \quad (1)$$

where W is the wavelet packet function, j and k are the scale and translation parameters, respectively; $n = 0, 1$, is the oscillation parameter. Two prime parameters, such as the selection of mother wavelet and the level of decomposition, can significantly influence the wavelet packet analysis. Therefore, in this study, the optimal mother wavelet is chosen based on its signal-to-noise ratio (SNR) characteristic. For a chosen mother wavelet, SNR is calculated for a reconstructed signal from a terminal node of the wavelet packet tree containing the highest percentage of energy. And the number of levels of decomposition is selected based on the Shannon entropy criteria [17]. In the present study, after careful investigation, discrete Meyer wavelet showed the highest SNR for an optimal decomposition level of nine. Using discrete Meyer

wavelet, the vibration signal is decomposed into nine wavelet levels giving a total of 512 wavelet sub-bands at the terminal node (9th level). The range of frequency band for each terminal node is given by $0.5 * F_s/2^L$, where F_s is the sampling frequency and L is the optimal decomposition level. Signals are reconstructed from the frequency bands of interest at the terminal node containing fault information. This reconstructed signal is further used in other time-frequency techniques, selected in this study, for crack detection.

2.2 Short-Time Fourier Transform

STFT employs a sliding window function $g(T - t)$ centered at a time 't' to perform time localized Fourier transform of the signal $x(t)$ consecutively, and the result reveals the variation of the signal's frequency content with time. The mathematical equation for STFT is given in Eq. (2).

$$\text{STFT}_x(t, f) = \int_{-\infty}^{\infty} x(\tau)g(\tau - t) \exp^{-2\pi\tau t} d\tau \quad (2)$$

Time and frequency resolutions of the decomposed signals are directly affected by the choice of window size [18]. Smallest window size provides good time resolution, whereas the largest window size provides good frequency resolution. Thus, the choice of the window is a vital parameter for an effective STFT analysis.

2.3 Continuous Wavelet Transform

Unlike STFT, where the window size is fixed, the wavelet transform enables variable window sizes in analyzing different frequency components within the signal. The CWT employs wavelets as a basis instead of complex exponential functions [19]. It adds a scale parameter along with a time translation parameter to the analysis. Hence, it is best suited for time-frequency analysis and is effective in analyzing non-stationary signals like run-up response of the rotor. Continuous wavelet transform of a signal $x(t)$ is given in Eq. (3).

$$\text{WT}(s, \tau) = \frac{1}{\sqrt{s}} \int x(t)\psi^*\left(\frac{t - \tau}{s}\right) dt \quad (3)$$

where $\psi^*(\cdot)$ denotes the complex conjugation of the mother wavelet $\psi(t)$, τ is the shifting parameter, and $s > 0$ represents the scaling parameter. The parameter 's' determines the time-frequency resolutions of the scaled mother wavelet $\psi^*(t - \tau)/s$. In the present study, Morlet mother wavelet is chosen as the base wavelet.

2.4 Hilbert–Huang Transform

Hilbert–Huang transform is an adaptive nonparametric time-frequency technique that combines the empirical mode decomposition (EMD) with the Hilbert transform [20]. To perform this transformed signal, it should have at least two extrema, that is, one is maximum and one minimum. HHT empirically decomposes a signal into several intrinsic mode functions (IMFs), with each IMF being a mono-component function, calculated as the difference between the signal and mean envelope values. EMD is designed to decompose a signal $x(t)$ into a collection of IMF components and a final residue R_L , which is the mean trend of the original signal. The IMFs $C_1, C_2, C_3 \dots C_L$ have different frequency bands ranging from high to low. The sum of all IMFs and the final residue can be represented, as shown in Eq. (4). The Hilbert transform of the intrinsic mode function $C_1(t)$ is also shown in Eq. (4).

$$x(t) = \sum_{l=1}^L C_l(t) + R_L(t) \quad H[C_l(t)] = \frac{1}{\pi} \int \frac{C_l(\tau)}{t - \tau} d\tau \quad (4)$$

Hilbert–Huang transform of reconstructed signal from an IMF can be expressed, as shown in Eq. (5).

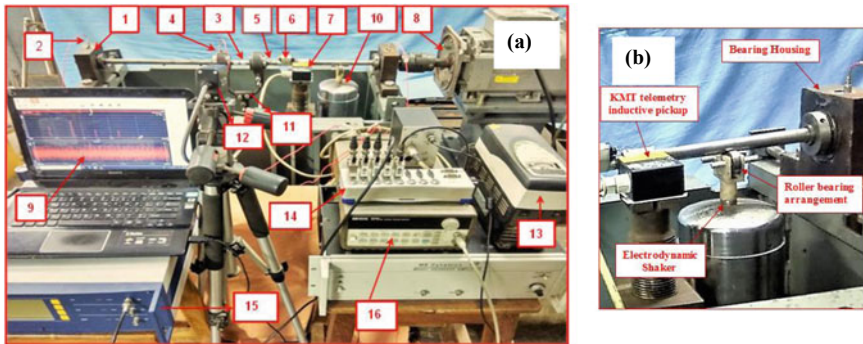
$$\text{HHT}(t, \omega) = \sum_{l=1}^n a_l(t, \omega_l) \quad (5)$$

where $a_l(t, \omega_l)$ is the amplitude of l th IMF at the time t with frequency ω_l .

3 Experimental Details

A rotor test rig, as shown in Fig. 1a, is designed and developed according to the function specification proposed by ASTM E468-11. A shaft (AISI 1020 Bright Steel) of diameter 0.016 m and length 1 m is mounted on two main bearings as shown in Fig. 1. All the bearings used are self-sealed spherical roller types which have a high load carrying capacity. A combination of weight hanger and slotted dead weights is used to apply the static load on the shaft through two auxiliary load carrying bearings (see Fig. 1a). In addition to this, contact type electrodynamic exciter, as shown in Fig. 1, is employed to excite the shaft randomly during the operation. Circumferential V-notch with notch root radius (0.02 mm) and with an open angle (60°) is seeded at the designated location on the three shaft specimens.

Data acquisition system (DAQ) Dewe-43 V is used to record the vibration response measured using the accelerometer (DYTRAN 3145AG), rotational laser vibrometer (RLV-5500), and KMT telemetry strain gauge (T1-PCM-IND). These sensors are mounted at different locations of the test rig, as shown in Fig. 1. Laser vibrometer



1. Bearing housing 2. Accelerometer 3. Notch Location 4. Auxiliary bearing 5. Strain Gauge 6. KMT telemetry 7. Inductive pickup 8. Motor 9. Computer 10. Electrodynamic shaker 11. Weight hanger 12. Laser sensor 13. RPM controller 14. DAQ 15. Sensor head (RLV-500) 16. Waveform generator 17. Power Amplifier

Fig. 1 **a** Experimental rotor test rig and **b** shaker arrangement for transmitting random excitation to the shaft

is used to measure vibration velocity, and KMT telemetry unit is used to measure the strain caused due to lateral vibrations of the shaft. HP 33120A function/arbitrary waveform generator is used to excite the shaker. A sampling frequency of 5 kHz is chosen for all the analog channels.

4 Results and Discussion

Fatigue test is conducted on a shaft specimen fabricated with circumferential V-notch depth of 1.5 mm. Shaft carrying a dead weight of 120 N is subjected to random excitation from electrodynamic shaker along with the predominant unbalance forces that arise in accelerated fatigue test conditions. The random excitation is transmitted to the shaft through a two roller bearing arrangements, as shown in Fig. 1b. Shaped burst random profile is chosen from waveform generator, to excite the shaft, in a frequency band of 10–500 Hz. The power amplifier is used to enhance the excitation level. Excitation unit is operated under its optimal power rating conditions. An excitation level of 1.5 g is noticed at the notch location when the shaft is subjected only to the shaker excitation (i.e., under zero operating speed). This level of excitation is maintained throughout the fatigue test. Before the fatigue test, the vibration response induced only due to random excitation is acquired using accelerometer mounted at the auxiliary bearing and is shown in Fig. 2a. The power spectrum of this vibration response, as shown in Fig. 2b, reveals the natural frequencies of the rotor. From Fig. 2b, it is observed that the first two natural frequencies of the rotor are 18.75 and 174.5 Hz. To perform an accelerated fatigue test, all the three experiments are conducted at an operating speed (16.5 Hz), which is close to the first natural frequency. To maintain the stability of the test rig, an operating speed of 990 rpm (16.5 Hz) is selected by performing a series of run-up tests covering the first critical speed. Due to safety

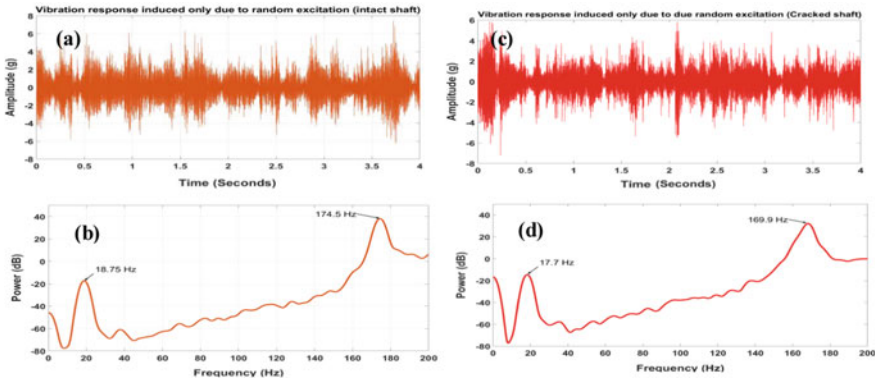


Fig. 2 a Vibration response of intact shaft, b power spectrum of the intact shaft, c vibration response of cracked shaft, and d power spectrum of cracked shaft

reasons, experiments are conducted only till shaft develops transverse fatigue crack at the V-notch location. Fatigue test is ceased after cautious observation of abrupt changes in time-domain statistical parameters like root-mean-square value, and crest factor is observed. To ascertain the development of fatigue crack, power spectrum of vibration response (see Fig. 2c) induced only due to random excitation on the shaft after the experiment without any rotation is plotted in Fig. 2d. It can be observed clearly from Fig. 2b, d, the occurrence of a shift in the natural frequencies from 18.5 and 174.5 Hz of the intact shaft to 17.7 and 167.9 Hz due to the crack that developed during a fatigue test.

The entire acceleration time history (raw data) of the fatigue test acquired at the auxiliary bearing location is shown in Fig. 3a. From the total vibration data length of 6393 s, two data sets of length 20 s (as shown in Fig. 3b, c) are taken at initial zone (Data#1 represents healthy condition of shaft) and end zone (Data#2 with shaft crack information) are considered for investigating the development of fatigue crack using time-frequency analysis. The fast Fourier transform (FFT) evaluated for Data#1 and

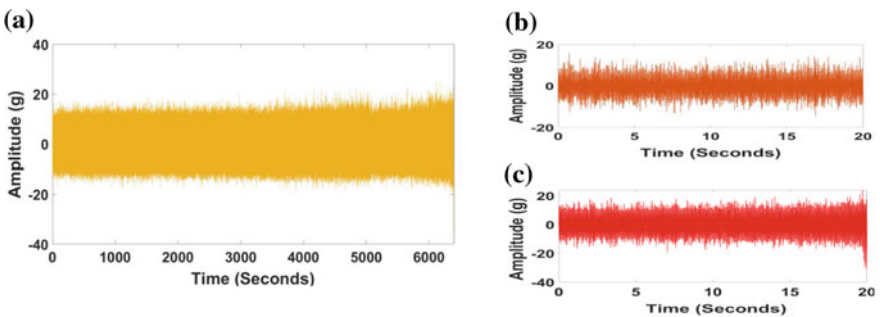


Fig. 3 a Acceleration time history, b initial 20 s data (Data#1), and c final 20 s data (Data#2)

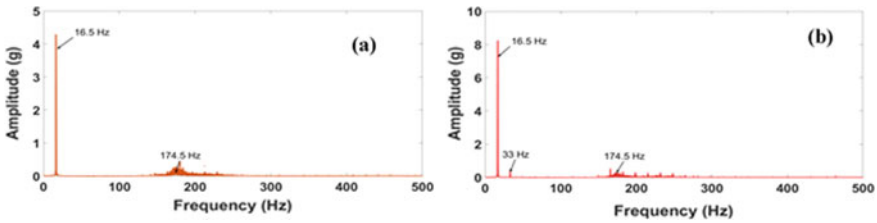


Fig. 4 a FFT of Data#1 and b FFT of Data#2

Data#2, plotted for a frequency scale of 0–500 Hz, are shown in Fig. 4a, b. From Fig. 4a, only $1\times$ multiple of operating speed is seen in a frequency span of 0–500 Hz. Although the stochastic loads applied in the 0–500 Hz frequency band, its influence on the shaft is not visible in 0–100 Hz frequency span of the amplitude spectrum. This is due to the predominant unbalance force that has developed under the operating conditions surpasses the level of random excitation. However, due to random excitation, the second natural frequency (174.5 Hz) component is observed in the frequency spectrum. As Fig. 2d, affirms the development of fatigue crack during the test; therefore, Data#2 is expected to have the details of the fatigue crack. From the FFT of Data#2, as shown in Fig. 4b, a very small value of the $2\times$ component is also noticed; however, the magnitude of $2\times$ is not that significant to attribute the presence of a crack. As small misalignment/looseness caused during operation can also result in the rise of $2\times$ harmonic component. Also, temporal variations of the magnitudes of these harmonics are not known using FFT analysis. Therefore, to ascertain the development of fatigue crack, high-resolution time–frequency techniques are employed on Data#2. Time–frequency techniques such as CWT, HHT, and STFT are performed on the Data#2, and the obtained results plotted for the frequency range of (0–100 Hz) are shown in Fig. (5a–c). From Fig. (5a–c), crack indicators like $2\times$ and $3\times$ are not found, thus, indicating the poor performance of these time–frequency techniques in detecting fatigue crack when employed on the raw data (Data#2). Therefore, as discussed in Sect. 2, wavelet packet analysis is performed on Data#2 to decompose the signal into high-resolution frequency bands. For 5 kHz sampling rate, the frequency band for each terminal node (9th level) of the wavelet packet tree is (0–5 Hz). Signals are reconstructed from the three terminal nodes whose indices in wavelet packet tree

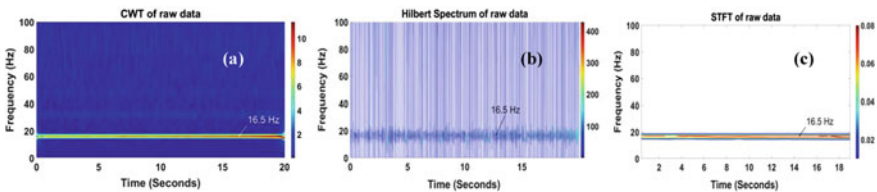


Fig. 5 a CWT of Data#2, b HHT of Data#2, and c STFT of Data#2

are (9, 3), (9, 6), and (9, 9), and their corresponding frequency bands are (15–20 Hz), (30–35 Hz), and (45–50 Hz), respectively.

These frequency bands contain the details of shaft crack indicators such as $1\times$, $2\times$, and $3\times$ components. The CWT, HHT, and STFT are performed on these reconstructed signals, and the obtained results are shown in Figs. 6a–c, 7a–c, and 8a–c, respectively. In HHT analysis, the Hilbert spectrum is evaluated for the IMF possessing the largest percentage of signal energy. A window size of 2048 is chosen for STFT analysis for better frequency resolution. From Figs. 6, 7 and 8, crack indicators ($1\times$, $2\times$, and $3\times$) are observed from all the time-frequency techniques. Hence, the WP analysis enhances the performance of all the three techniques in identifying the crack features. However, temporal variations in the magnitude of the first three operating speed harmonics are clearly observed only in CWT analysis. These temporal variations in magnitudes of $1\times$ and $2\times$ components CWT coefficients are plotted in Fig. 9. From Fig. 9, it can be noticed that a significant rise of the $1\times$ component after 11th second onwards.

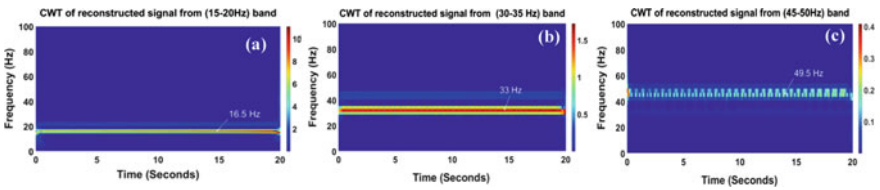


Fig. 6 CWT of reconstructed signal from frequency band of **a** (15–20 Hz), **b** (30–35 Hz), and **c** (45–50 Hz)

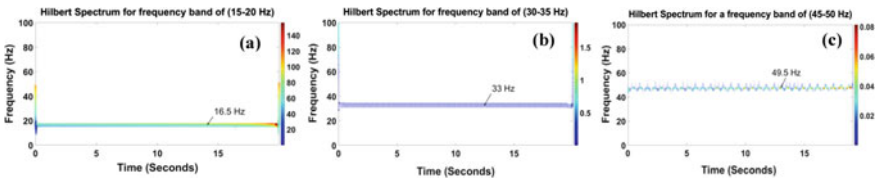


Fig. 7 HHT of reconstructed signal from frequency band of **a** (15–20 Hz), **b** (30–35 Hz), and **c** (45–50 Hz)

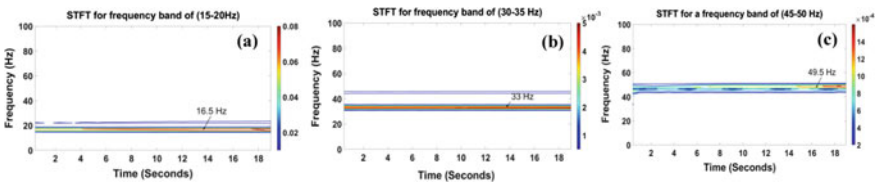


Fig. 8 STFT of reconstructed signal from frequency band of **a** (15–20 Hz), **b** (30–35 Hz), and **c** (45–50 Hz)

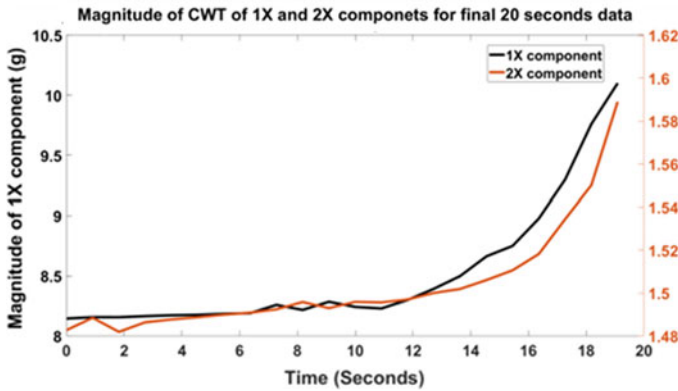


Fig. 9 Variation in magnitude of $1\times$ and $2\times$ CWT coefficients

Further, a steep rise in $2\times$ component is noticed from the 16th second, because of shaft asymmetry developed due to crack. Thus, the combination of WP and CWT analysis is most effective in the early fatigue shaft crack detection compared to the rest of all the techniques investigated. Similar analyses are performed for the vibration data acquired using other sensors like laser vibrometer and KMT telemetry strain gauge. Results of these analyses are found to be alike with that of Figs. 6, 7 and 8.

5 Conclusions

A rotor test rig, with stochastic loading facility, is designed and developed to instigate shaft fatigue crack is reported in this paper. Accelerated fatigue test is conducted on a shaft specimen seeded with circumferential V-notch configuration. Raw vibration data acquired from various locations of the test rig, using different sensors, like miniature accelerometers, laser vibrometer, and wireless telemetry strain gauge, are used for crack detection analysis. Signal processing tools like continuous wavelet transforms (CWT), Hilbert–Huang transform (HHT), and short-time Fourier transform (STFT) are investigated for the early fatigue crack detection. Wavelet packet (WP) analysis is used to decompose the original vibration response data into narrow frequency band signals containing fault information before the processing of CWT, HHT, and STFT analyses. It is found that the direct application of CWT, HHT, and STFT on raw data cannot identify the crack features. However, all three techniques could extract fault features when employed on the reconstructed signals from WP analysis. WP analysis, when used as a signal preprocessing tool, enhances the performance of time-frequency techniques for the shaft crack detection in an accelerated fatigue test. CWT employed on reconstructed signals from WP analysis shows better resolution for temporal changes in the magnitudes of $1\times$, $2\times$, and $3\times$ running speed

components. Finally, the combination of WP and CWT analysis is best suited for early shaft fatigue crack detection.

References

1. Wauer J (1990) On the dynamics of cracked rotors: a literature survey. *Appl Mech Rev* 43(1):13–17
2. Gasch R (1993) A survey of the dynamic behaviour of a simple rotating shaft with a transverse crack. *J Sound Vib* 160(2):313–32
3. Dimarogonas AD (1996) Vibration of cracked structures: a state of the art review. *Eng Fract Mech* 55(5):831–857
4. Lazzeri L, Cecconi S, Faravelli M, Scala M (1992) Second harmonic vibration monitoring of a cracked shaft in a turbogenerator. *Proc Am Power Conf* 54:1337
5. Saavedra PN, Cuitiño LA (2002) Vibration analysis of rotor for crack identification. *J Vib Control* 8(1):51–67
6. Varney P, Green I (2012) Crack detection in a rotor dynamic system by vibration monitoring—part II: extended analysis and experimental results. *J Eng Gas Turbines Power* 134(11):112501
7. Sabnavis G, Gordon Kirk R, Kasarda M, Quinn D (2004) Cracked shaft detection and diagnostics: a literature review. *Shock Vib Dig* 36(4):287–296
8. Gao RX, Yan R (2006) Non-stationary signal processing for bearing health monitoring. *Int J Manufact Res* 1(1):18–40
9. Peng ZK, Peter WT, Chu FL (2005) A comparison study of improved Hilbert-Huang transform and wavelet transform: application to fault diagnosis for rolling bearing. *Mech Syst Sig Process* 19(5):974–988
10. Prabhakar S, Sekhar AS, Mohanty AR (2001) Detection and monitoring of cracks in a rotor-bearing system using wavelet transforms. *Mech Syst Sig Process* 15:447–450
11. Liu L, Dong DS (2012) Structural crack detection using Hilbert-Huang transform method and wavelet analysis. *Appl Mech Mater* 105:710–713 (Trans Tech Publications)
12. Lou X, Loparo KA (2004) Bearing fault diagnosis based on wavelet transform and fuzzy inference. *Mech Syst Sig Process* 18(5):1077–1095
13. Chen D, Wang WJ (2002) Classification of wavelet map patterns using multi-layer neural networks for gear fault detection. *Mech Syst Signal Process* 16(4):695–704
14. Satish L (1998) Short-time Fourier and wavelet transforms for fault detection in power transformers during impulse tests. *IEEE Proc Sci Measur Technol* 145(2):77–84
15. Rathna Prasad S, Sekhar AS, Diagnostics of fatigue crack in the shaft using spectral kurtosis. In *ASME Turbo Expo 2019: Turbomachinery Technical Conference and Exposition*. American Society of Mechanical Engineers Digital Collection
16. Misiti M, Misiti Y, Oppenheim G, Poggi JM, Wavelet toolbox for use with MATLAB. The Mathworks Inc., USA
17. Leamed RE (1992) Wavelet packet based transient signal classification. Master's thesis. Massachusetts Institute of Technology
18. Coifman RR, Victor Wickerhauser M (1992) Entropy-based algorithms for best basis selection. *IEEE Trans Inf Theory* 38(2):713–718
19. Cohen L (1989) Time-frequency distributions—a review. *Proc IEEE* 77(7):941–981
20. Feng Z, Liang M, Chu F (2013) Recent advances in time-frequency analysis methods for machinery fault diagnosis: a review with application examples. *Mech Syst Signal Process* 38(1):165–205

Coupling Misalignment Detection and Condition Monitoring of a Rotor Assembly Using FEA-Based Reduced-Order Modeling Methods



Anil Kumar, Dinesh Kumar, and Ravindra Masal

Abstract Coupling misalignment is a common issue in rotating assemblies connected to driving shafts via coupling systems. Keeping the level of misalignment within safe thresholds is a major requirement for the reliable functioning of rotating systems. Coupling misalignments can result in sub- and super-synchronous excitations (displacements, velocity and acceleration, reaction forces at critical locations) that can be used to ascertain the level of misalignment for a given coupling type. Coupling misalignment happens due to frictional interaction of the coupling spider from driving and driven side. To model it in full generality, it will require nonlinear transient analysis of actual 3D CADs of the couplings with frictional contacts. Challenge to model such systems using FEA is that it requires full nonlinear FEA analysis and is very time-consuming. In the present study, a full 3D nonlinear transient analysis is first done to capture the effect of misaligned coupling and proposes various methodologies that can be employed to reduce the solution times. Component mode synthesis (CMS) is employed to model the stationary part to reduce the solve times considerably. Further effect of varying levels of misalignment on the results is studied. Result trends are studied to explore the possibility of creating reduced-order models (ROMs) from such design of experiments (DoE) study for real-time physics-based condition monitoring of rotating machinery.

Keywords Coupling misalignment · Reduced-order model (ROM) · Design of experiments (DoE) · Nonlinear FEA · Rotordynamics · Digital twin (DT) · Component mode synthesis (CMS)

A. Kumar (✉) · D. Kumar · R. Masal
ANSYS Inc., Pune, India
e-mail: anil.kumar@ansys.com

D. Kumar
e-mail: dinesh.kumar@ansys.com

R. Masal
e-mail: ravindra.masal@ansys.com

Nomenclature

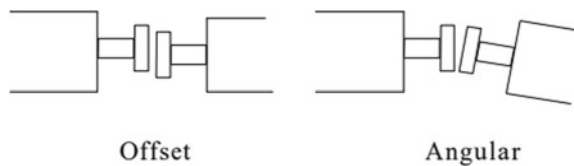
$[M]$	Mass matrix
$[C]$	Damping matrix
$[K]$	Stiffness matrix
$[m]$	Mass matrix of sub-system
$[c]$	Damping matrix of sub-system
$[k]$	Stiffness matrix of sub-system
m	Master DOFs defined only on interface nodes
s	All DOFs that are not master DOFs
c	Damping parameter
$\{y_\delta\}$	Truncated set of generalized modal coordinates
$\{\phi_s\}$	Fixed-interface normal modes (eigenvectors obtained with interface nodes fixed)

1 Introduction

Misalignment of the components like shafts, bearings, etc., in the rotary machinery, is the most common cause of machine vibration. Researches have shown that 30–50% of the machine downtime and breakdown is subjected to the misalignment problems [1, 2]. The two most common types of the shaft/ bearing misalignments are parallel and angular. Figure 1 shows parallel offset misalignment, in which the shafts of the two machines are on two separate but parallel centerlines; and angular misalignment, in which the centerlines of the two shafts intersect at their coupling point and are at an angle to each other. In real assemblies, combined misalignment is present.

Some of the typical reasons for the alignment issues could be thermal distortions, movement during operation, manufacturing tolerances, and improper machine assembly. The vibration caused by the misalignment can severely affect the long-term reliability, production output and increase maintenance costs. It can result in many failures like leakages, bearing failures, energy loss, structural induced noise, and excessive heating. Therefore, it becomes necessary for the engineers to have in-depth understanding of the root causes of the misalignments and their effects, timely prediction, and fixing the problem. There has been a series of the studies to understand the effect of misaligned shafts and bearings on the overall vibration

Fig. 1 Types of shaft misalignment



characteristics of the machine, its prediction via theory and finite element analysis and fixing the problems.

Hariharan and Srinivasan [2] verified and investigated rotordynamic characteristics related to misalignment throughout the experimental and simulation works. Experimental predictions are good agreement with the numerical results. In their study, a newly self-designed pin type of flexible coupling is used for simulation using ANSYS by introducing the bearing and coupling elements into the model as the misalignment effects. Both the measured and ANSYS results spectra show that misalignment can be characterized primarily by $2 \times$ shaft running speed. Vaziri and Patil [3] did the experimental process to obtain the RMS acceleration values of vibration of cracked shaft. This study showed that the position and the depth of the crack affects the stiffness of the shaft and that would result in the different vibration signatures. Dere and Dhamande [4] considered both parallel and angular misalignment of the rotating bearings. The study proposes a methodology to predict the faults in machinery. Irvin Redmond in [5] presented the results of a theoretical study on a simple linear rotordynamic model, capable of simulating the effects of parallel and angular misalignment across a flexible-element coupling connecting drive and driven rotors. The study is targeted to reduce the turnaround time of the numerical simulations of the complex systems specially during the present of variability in system. However, the model is mostly limited to the linear systems. Other studies [6, 7] have also carried out the effort on the misalignment but are mostly limited to the component level analyses and it does not include the complex parts of the full machinery.

The scope of the current work is to extend misalignment study onto fully complex pump assembly. Challenge to model such complex systems using FEA is that it requires full nonlinear FEA analysis and is very time-consuming. On other hand, modeling variabilities become almost computationally impossible. These challenges are addressed to some extent in current study using component mode synthesis (CMS) to make it computationally manageable.

It is always desired to predict the cause of certain vibration problems by examining the signature of the vibrations, so that a proactive action can be taken before the downtime of the critical components. This demands significant amount of experiments or time-consuming FE simulations to prepare look up IoT tables, ROMs, or training set for machine learning. The current work also proposes a methodology to address these challenges, by using simulations to prepare physics-based ROMs of complex rotating machines to create accurate digital twins.

2 Modeling Approach

3DCAD model of a centrifugal pump assembly (Fig. 2) is considered for FE modeling in current study. Assembly consists of both stationary and rotary parts (Fig. 3).

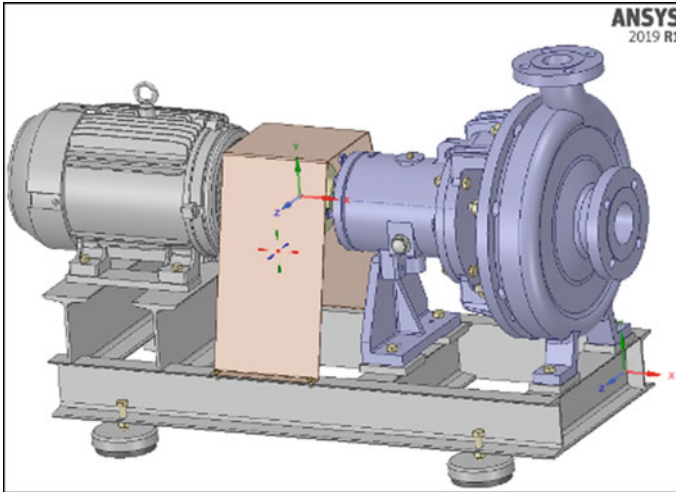


Fig. 2 Full 3D CAD model of pump-stator assembly

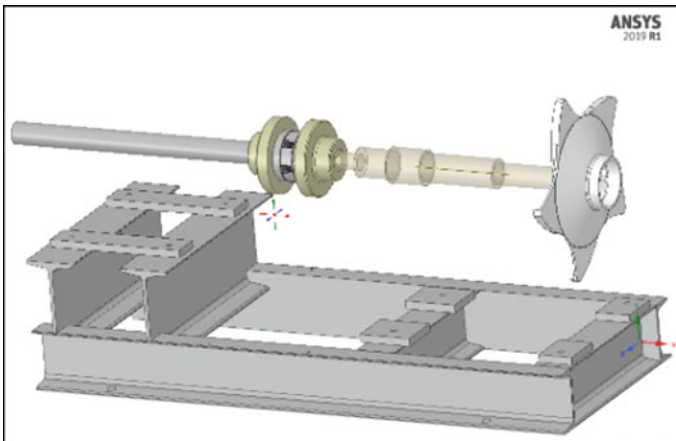
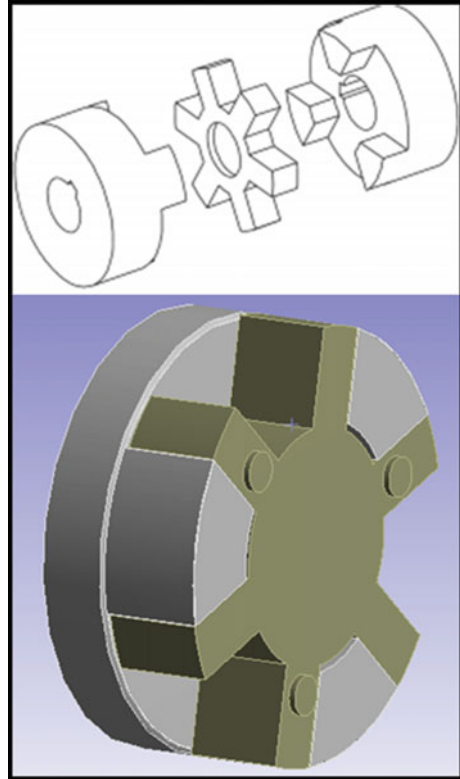


Fig. 3 Rotating portion and base

Coupling between motor shaft and pump shaft is modeled using ideal jaw flexible coupling composed of two three-jaw hubs and one six-legged intermediate elastomeric spider (Fig. 4).

CAD is imported into ANSYS Spaceclaim[®] and some cleanup like removing small insignificant parts like bolts, nuts, etc., is carried out. Solid rotating shafts are converted into equivalent line bodies for saving time in subsequent FE analysis. Spider and coupling jaw interact by a frictional contact (Fig. 5).

Cleaned up CAD is then imported into ANSYS Mechanical[®] for finite element modeling. Solid parts in CAD are modeled using SOLID186 and SOLID187

Fig. 4 Coupling connection

elements. Line bodies are modeled using BEAM188 and ball bearings are modeled assumed symmetric in bearing planes and modeled using two COMBIN14 elements for each ball bearing [8, 9]. There are 2 bearings on motor and 3 on the pump side that connect the rotating shafts with the stator assembly (Fig. 6). Spider and coupling jaws are modeled using SOLID 186/187 elements and frictional contact is used for their interaction. Impeller is modeled using equivalent point mass. FE mesh is shown in Fig. 7. All parts are assigned standard steel material properties. Spider is modeled using linear BUNA material. Only source of physical damping in system is frictional contacts between the coupling and the spiders. No other physical damping mechanisms were used in current study (Table 1).

Disconnected FE mesh domains in the assembly are connected using appropriate contact elements TARGE170, CONTA174, and joints using MPC184 elements. Frictional coefficient of 0.15 is used and contact stiffness updated at each iteration [10]. Coupling connection is shown in Fig. 5. Resultant FE model has about 15 K nodes and 11 K elements. As dynamic response typically involves solving of thousands of time points, analysis can be very time-consuming as the FE model size increases. Solution times can be considerably minimized using CMS which helps to replace thousands of DOFs of flexible stator body with just tens of DOFs still representing

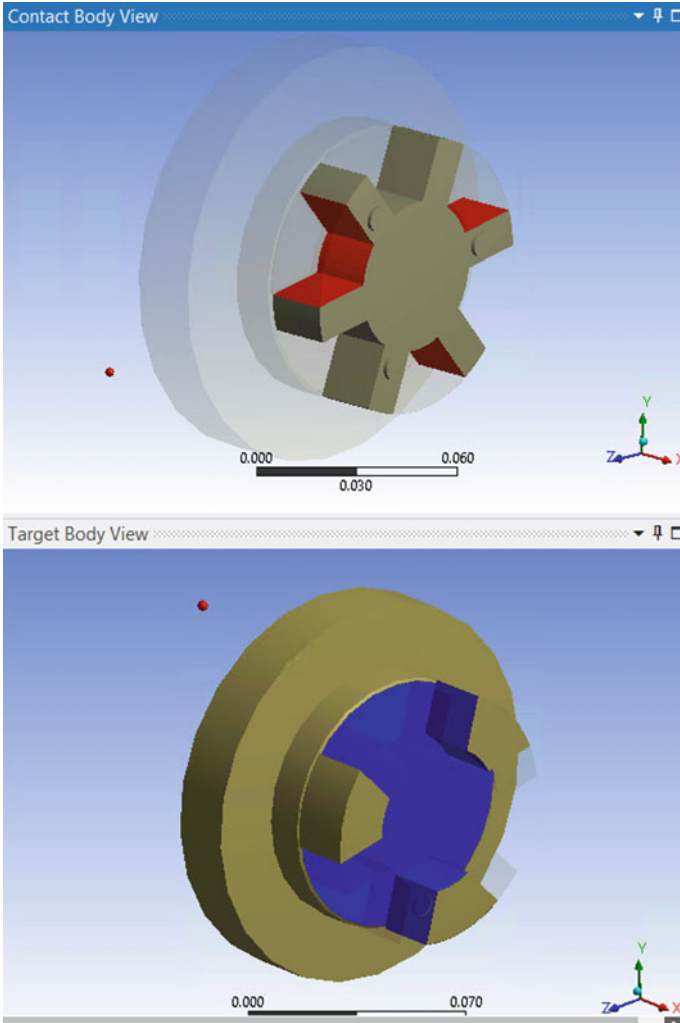


Fig. 5 Red are contact faces and blue are target faces

its dynamic response accurately. A superelement simply represents a collection of elements that are reduced to act as one element [11].

Full nonlinear transient analysis [9] is carried out to analyze the effect of misalignment on the pump assembly. Full transient analysis solves below general second-order equation.

$$[M]\{\ddot{U}(t)\} + [C]\{\dot{U}(t)\} + \{F^i(t)\} = \{F^a(t)\} \tag{1}$$

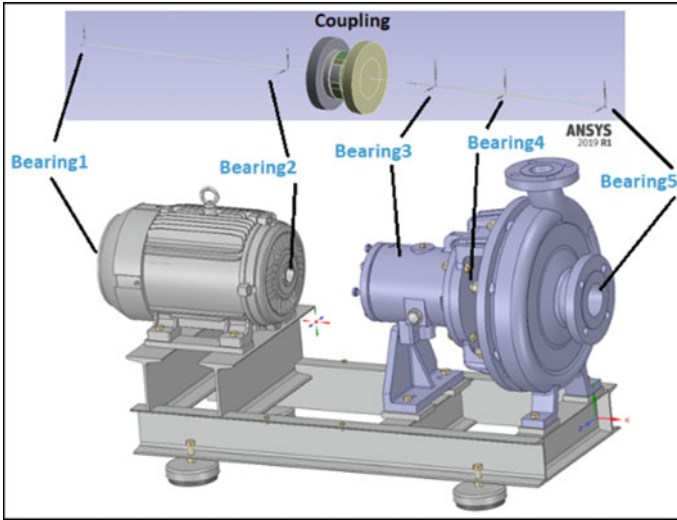


Fig. 6 3D CAD of stator and rotor with bearing locations

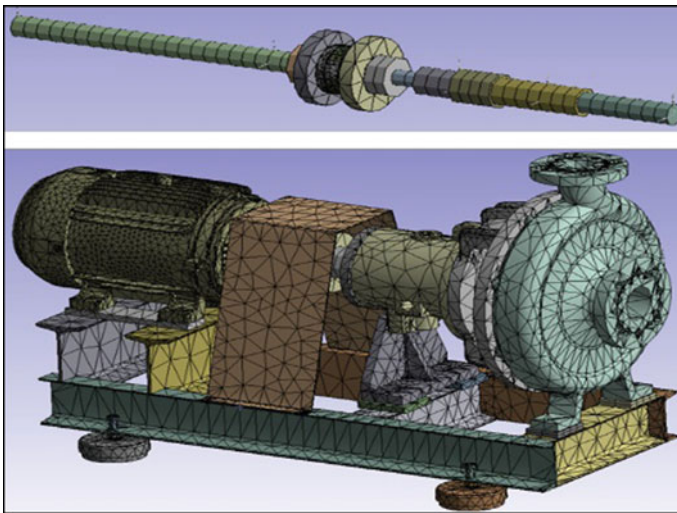


Fig. 7 Finite element model of assembly with rotating subassembly shown separately

Table 1 Material properties

Material	Young's modulus (MPa)	Poisson's ratio	Density (Kg/m ³)
Structural steel	2e5	0.3	7850
BUNA	1.1e9	0.42	950

For a sub-system defined as superelement, its FE matrices can be represented as [11]:

$$[m]\{\ddot{u}\} + [c]\{\dot{u}\} + [k]\{u\} = \{f\} \tag{2}$$

These are partitioned into interface and slave DOFs, written as

$$\{u\} = \begin{Bmatrix} \{u_m\} \\ \{u_s\} \end{Bmatrix} = [T] \begin{Bmatrix} \{u_m\} \\ \{y_\delta\} \end{Bmatrix}; \quad [T] = \begin{bmatrix} [I] & [0] \\ [G_{sm}] & [\phi_s] \end{bmatrix} \tag{3}$$

The nodal displacement vector, $\{u\}$, may be represented in terms of master DOFs completed by component generalized coordinates (3). Finally, the reduced matrices for sub-system for a Craig and Bampton method [11–13] can be as:

$$[\hat{k}] = [T]^T [k] [T]; \quad [\hat{m}] = [T]^T [m] [T]; \quad [\hat{c}] = [T]^T [c] [T]; \quad \{\hat{f}\} = [T]^T \{f\} \tag{4}$$

These new reduced matrices replace the non-reduced sub-assembly matrices (as shown in Eq. 2) in the full system matrices of Eq. (1), resulting in reduced number of DOFs in Eq. (1).

In present study, all stationary parts are converted to a single superelement (Fig. 8). The boundary condition and bearing connection locations on stator are defined as its interface nodes or master nodes.

Shafts are perfectly alignment at the CAD level. So, misalignment is introduced by applying a displacement condition to one end of the pump side gearbox part. This represents the common practice in testing apparatus to introduce misalignment by introducing machined shims of given thickness [14]. Misalignment level is varied from 0.01 to 3 mm. Assembly is applied fixity at the four legs at base. Constant RPM

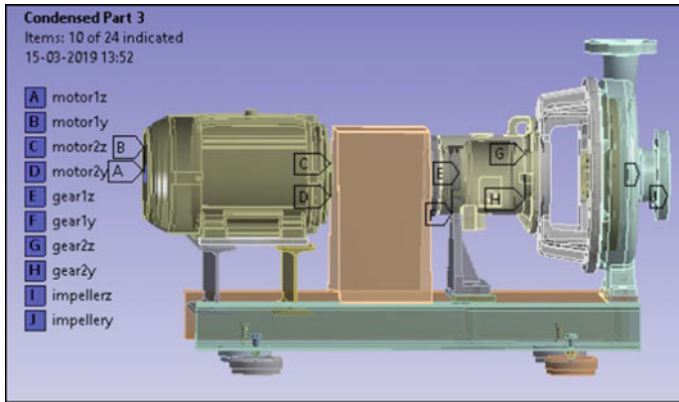


Fig. 8 Stator (motor; base; gearbox; impeller housing)

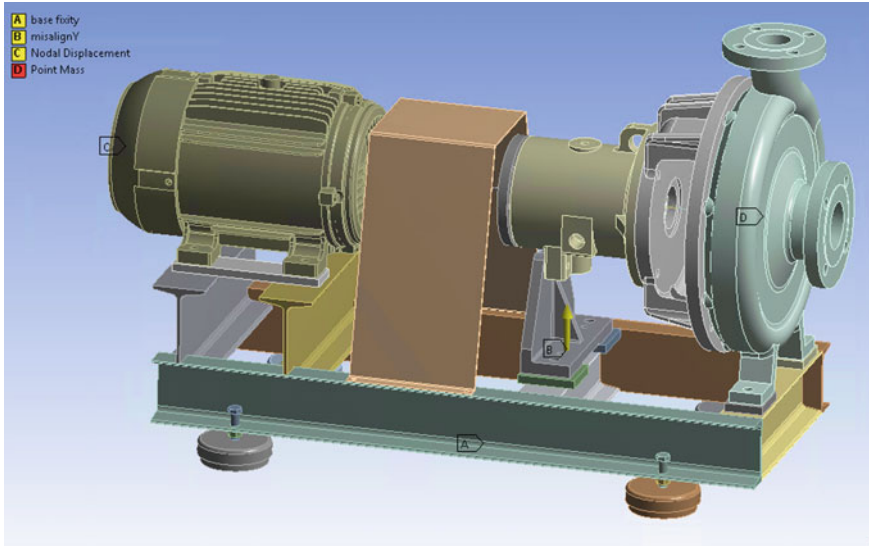


Fig. 9 BCs (fixity at legs; misalignment; rotation)

of 30 Hz is introduced by applying rotation to one end of the shaft at the motor side. All the boundary conditions are shown in Fig. 9. Misalignment is known to cause periodic variations due to the coupling spider-jaw frictional interaction while rotating. This excites harmonics of rotating speed in the acceleration, bearing reaction, etc., responses of the assembly.

3 Results and Discussion

The overall deformation plot at one of the time points is shown in Fig. 10. It shows rotating 3D coupling and shafts. Results on stator are not shown as it is a superelement. One may need to expand the solution to get results on slave nodes of superelement. If there are any points of interest on stator (e.g., sensor points), it is suggested to define master node/interface on stator. One misalignment transient analysis for 0.5 s end time took about 8 h on a 4-core workstation. CMS stator mode was found to be 11 times faster per iteration with respect to a non-CMS stator model under same compute settings. For FFT constant timestep of $1e-4$ s was used and 4096 result points used for carrying out FFT with resolution of about 2.441 Hz.

Generally, condition monitoring sensors like accelerometers are put near the bearing locations to capture any anomaly like imbalance, misalignment, and bearing failures in rotating machinery like pumps. Thus, the transient results of bearing reactions forces and accelerations are shown in Figs. 12, 13 and 14 are obtained at one of the bearing locations as shown in Fig. 11. Misalignment results in excitation of

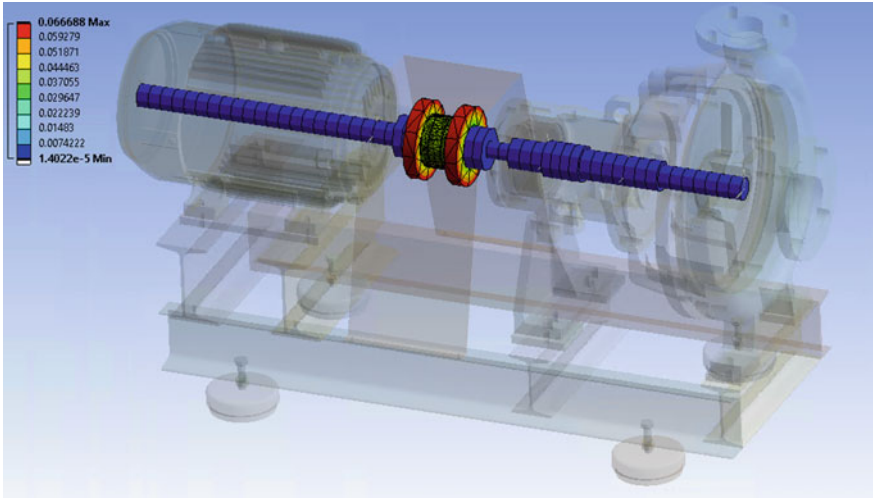


Fig. 10 Deformation plot at $T = 0.5$ s

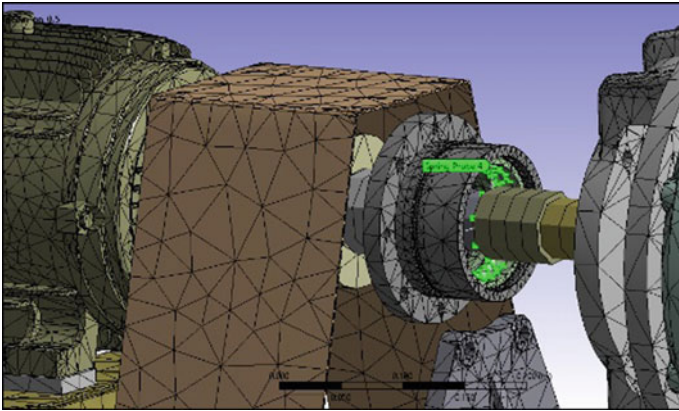


Fig. 11 Bearing-3 location at gearbox

Fig. 12 X-direction acceleration results at bearing-3

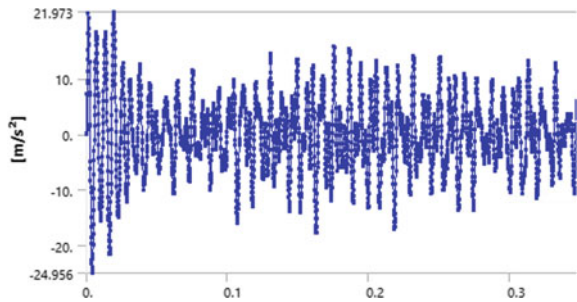


Fig. 13 Z-direction acceleration at bearing-3

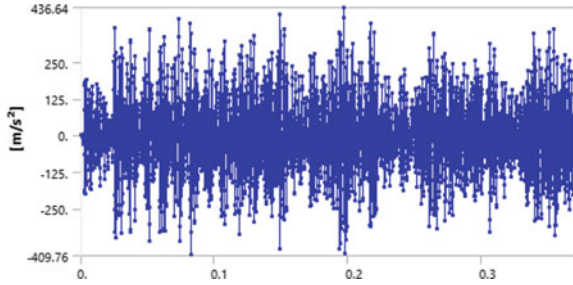
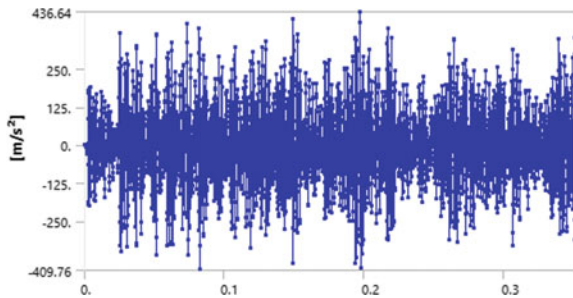


Fig. 14 Ball-bearing reaction force (FY) at bearing-3



multiple harmonics of the RPM like $1\times$, $2\times$, $3\times$, and so on [1–4, 6, 14–16]. These harmonics depend on the type of the coupling and its interaction with connecting jaws, misalignment type, bearings, assembly, etc. To understand the behavior in frequency domain, fast Fourier transform (FFT) of time transient results was carried out.

Figures 15, 16 and 17 show the FFT of the results at bearing-3 in the gearbox housing. $1\times$ is absent, as misalignment is not considered in beam element rotors. But results clearly show that $3\times$, $6\times$, $9\times$, and so on, harmonics are excited. This partially agrees with findings in literature on misalignment which reported higher harmonics with misalignment [2, 6, 14, 17]. But, it does not show any $2\times$ vibrations as also reported in some literature [15, 16]. This can be attributed to fact that these harmonics strongly depend on (a) coupling kinetics and (b) the way misalign excitation is

Fig. 15 FFT of bearing forces (RY)

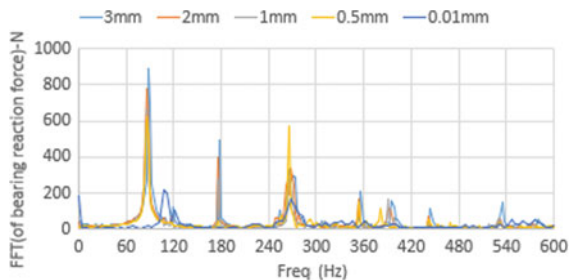


Fig. 16 FFT of bearing forces (RZ)

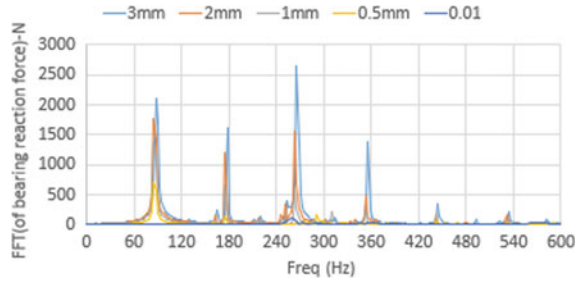
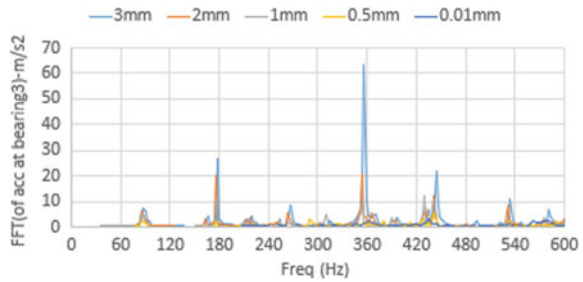


Fig. 17 FFT Z-direction acceleration

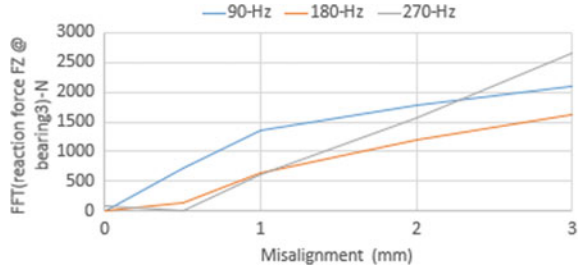


modeled, and (c) model itself. Probably in the model under study, misalignment is more of an angular misalignment and thus do not show the $2\times$ response like in Ref. [16]. For example, a direct $2\times$ term introduced in the force terms in Ref. [17] excites a $2\times$ response. In current study, as no such assumptions was made on nature of coupling nonlinearity, the result represents true assembly behavior, for given spider and assembly. Additionally, different levels of misalignment lead to near same FFT excitations. From this, one can conclude that a kind of misalignment can be clearly identified with their FFTs or vibration signature, and only the level of FFTs will change.

However, FFT in misalign direction can be slightly different than on the transverse direction as indicated by the FFT of bearing reaction forces in F and Z -direction, respectively. Z -direction is consistently having higher value for higher misalignment level, but Y -direction suddenly shows relatively bigger peak at 270 Hz. This, however, can be attributed to highly nonlinear behavior of the frictional contact.

FFT values at different harmonics of 90, 180, and 270 Hz are plotted against the misalignment level and shows monotonic increase in the values with misalignment. The slopes, however, vary, so the behavior cannot be said to be linear dependent on misalignment. Once enough, such data is generated, it can be used to create a reverse reduced-order model (ROM) for evaluating the misalignment levels by feeding in a sensor FFT output that can be coming from actual sensor on real asset (Fig. 18).

Fig. 18 Bearing force RZ at $3\times$, $6\times$, $9\times$ -RPM versus misalignment



4 Conclusions

Misalignment behavior of a rotating shaft with spider coupling in a pump assembly was effectively modeled using nonlinear transient FE analysis. CMS reduction of the stator proved very effective in reducing and solving the time by 11 times as compared to that of a full FE stator model. It is imperative to use it to solve dynamic analysis involving complex assembly like the one considered in this study.

FFT of the results like acceleration and reaction forces showed harmonics excitations in form of $3\times$, $6\times$, $9\times$, etc., of RPM. Vibration signature seems to be highly coupling and assembly dependent as no $2\times$ excitations are seen, as reported in literature. FFT signature at different misalignment levels was found to be qualitatively similar. This observation could be explored further to create accurate physics-based ROMs that can evaluate misalignment levels based on the FFT data. And the data can come either from real-time field mounted sensors on assemblies or from FE simulations.

In current study, coupling is modeled with solid FE elements with frictional contact. This causes considerable increase in solve times both due to number of DOFs and frictional contact. Though current study is done using accurate 3D coupling model, further reduction in solution times can be achieved by creating equivalent nonlinear 1D coupling. An equivalent 1D model was created to explore this. Modal analysis results proved equivalence as seen in Table 2. However, 1D equivalent coupling for misalignment analysis would require a nonlinear stiffness that replicates the 3D actual coupling. Such a study in the future can be useful to explore further time reduction of misalignment analysis so that more scenarios can be analyzed in a shorter time. These models can then be used to create accurate digital twins in

Table 2 Modal analysis results comparison of a full 3D coupler and equivalent 1D coupler

Solid coupler Freq (Hz)	1D equivalent coupler Freq (Hz)
27.228	27.228
74.009	74.009
96.23	96.986
101.74	104.55
115.16	116.63

such highly coupling and assembly dependent systems that account for large range of faults like misalignment, unbalance, crack, bearing faults, etc., and prove helpful for predictive maintenance of critical rotating equipment.

Acknowledgements The authors are grateful to Grab CAD user Royston Scudder for permitting use of the CAD geometry for this study.

References

1. Pruftechnik LTD (2002) A practical guide to shaft alignment
2. Hariharan V, Srinivasan PSS (2009) Vibration analysis of misaligned shaft–ball bearing system. *Indian J Sci Technol* 2(9):45–50
3. Vaziri A, Patil MJ (2013) Vibration analysis of a cracked shaft. *Int J Adv Eng Technol* IV(II):103–104
4. Dere SD, Dhamande L (2017) Rotor bearing system FEA analysis for misalignment. *IJARIIIE* 3(4). ISSN (O)-2395-4396
5. Redmond I (2007) Shaft misalignment and vibration—a model. Dynamic Analysis Unit, Consulting Services Department, Saudi Arabian Oil Company
6. Hariharan V, Srinivasan PSS (2011) Vibration analysis of parallel misaligned shaft with ball bearing system. *Songklanakarin J Sci Technol* 33(1):61–68
7. (Indian Academy of Sciences)
8. ANSYS rotordynamics analysis guide. R2019
9. ANSYS structural analysis guide. R2019
10. ANSYS contact technology guide. R2019
11. ANSYS substructuring analysis guide. R2019
12. Craig RR, Bampton MDD (1968) Coupling of substructures for dynamic analysis. *AIAA J* 12:1313–1319
13. Craig RR (1987) A review of time domain and frequency domain component mode synthesis methods. *Int J Anal Exp Modal Anal* 2(2):59–72
14. Patel TH, Darpe AK (2009) Experimental investigations on vibration response of misaligned rotors. *Mech Syst Signal Process* 23:2236–2252
15. Al-Hussain KM, Redmond I (2002) Dynamic response of two rotors connected by rigid mechanical coupling with parallel misalignment. *J Sound Vib* 249(3):483–498
16. Khot SM, Khaire P (2015) Simulation and experimental study for diagnosis of misalignment effect in rotating system. *J Vib Anal Measur Control* 3(2):165–173
17. Sekahar AS, Prabhu BS (1995) Effects of coupling misalignment on vibrations of rotating machinery. *J Sound Vib* 185(4):655–667

Vibration Control Using Active and Semi Active Methods

Vibration Reduction in Indigenous Wankel Rotary Combustion Engine with Structured Layer Damping



Sadanand Kulkarni, S. Satish Kumar, S. Santhosh Kumar, Umesh Kumar Sinha, Brijeshkumar Shah , K. Satish Kumar, A. J. Steve Mithran, and K. Monickavasagom Pillai

Abstract Rotary engines are simpler in design and operation compared to the gas turbines. Rotary engines propel many monoplanes, power hang gliders, and unmanned aerial vehicles (UAV). In an indigenization effort, a 65 hp Wankel rotary combustion engine (WRCE) was successfully developed in the country for a wheeled version of Nishant UAV. As a part of the testing and certification process, three engines were required to be tested in the test bed for a stipulated number of hours. The engine was mounted in the test bed on two cantilever bolts in horizontal and two in the vertical direction with equi-frequency anti-shock mounts. During testing without the alternator, it was observed that the vibrations are higher with 1X amplitude of 24 g. To identify the source of vibration, a detailed modal analysis was carried out. Impact test data showed the existence of dominating frequency around 138 Hz. To reduce the vibrations, the engine mount is modified suitably, and structured layer damping is introduced between the engine mount and support structure.

S. Kulkarni (✉) · S. Satish Kumar · S. Santhosh Kumar · U. K. Sinha · B. Shah · K. Satish Kumar · A. J. Steve Mithran · K. Monickavasagom Pillai
Propulsion Division, CSIR-National Aerospace Laboratories, Bangalore 560017, India
e-mail: sadanandsk@nal.res.in

S. Satish Kumar
e-mail: satishkumar@nal.res.in

S. Santhosh Kumar
e-mail: santyssk@nal.res.in

U. K. Sinha
e-mail: umeshsinha@nal.res.in

B. Shah
e-mail: shahbrij@nal.res.in

K. Satish Kumar
e-mail: ksatishk@nal.res.in

A. J. Steve Mithran
e-mail: stevemithran@nal.res.in

K. Monickavasagom Pillai
e-mail: kmpillai@nal.res.in

This modification resulted in increased damping leading to vibration reduction to the acceptable level. Testing of Wankel engine with alternator up to the required speed was completed successfully using the structured layer damping method.

Keywords Rotary engine · Unmanned aerial vehicle (UAV) · Modal analysis · Critical speed

1 Introduction

The lightweight aerial vehicles, mainly UAVs, have seen phenomenal growth and improvements in their performance in the past couple of decades. The UAV's find the utility in defense and civil sector, especially for surveillance and carrying the payloads [1]. High demand for UVA's is a driving force for the continuous efforts toward their performance improvement. One of the rationales behind the performance enhancement is the vehicle's propulsion system. The power plant requirements for the UAVs are very demanding. Some of the major considerations in the power plant design are high specific power, low specific fuel consumption (SFC), lower frontal area, minimum noise and vibration, high reliability, low maintenance, and ease of serviceability. Wankel rotary combustion engine (WRCE) is one of the promising contenders that satisfy a large number of requirements of a small aircraft power plant. Hence, WRCE is being considered for powering many aircraft such as UAVs, microlights, and hang gliders all over the world. It is also used as APU for the aircraft.

Activities toward the development of WRCE have begun in CSIR-NAL couple of decades ago. As on today, CSIR-NAL has developed 55 and 65 hp water-cooled rotary combustion engines for UAV applications successfully. Currently, 30 hp air-cooled engine is under development. This paper deals with the case study on the vibration issues developed during the trials on the 65 hp WRCE in the testbed and methodology implemented for rectifying the high vibration problem.

2 Details of 65 hp WRCE

The 65 hp WRCE consists of the core engine, reduction drive, water pump, and fan [2]. The in-built reduction drive system has a speed reduction of 1:2 to keep the propeller speed lower. Water cooling system is used to maintain the housings operating temperature under safe limits. The air cooling system cools the rotor and also aids in the flow of lubricant to various bearings of the engine. The complete engine model indicating the critical parts is shown in Fig. 1. Detailed specifications for this engine are given in Table 1.

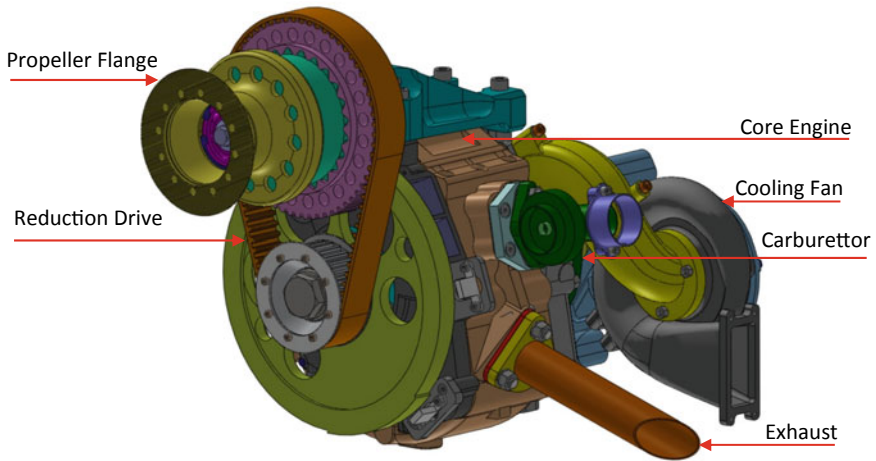


Fig. 1 Engine assembly indicating major parts

Table 1 Engine specifications

Parameter	Details
Engine type	Wankel rotary combustion engine
Thermodynamic cycle	Otto cycle
Max power (hp/kW)	65/48.5 @ 8000 rpm at sea level (without exhaust muffler)
Cylinder capacity (cc)	397
No. of rotors	1
Operating temperature	-40 to +55 °C
Fuel supply system	Diaphragm type carburetor
Fuel	100 LL gasoline
Specific fuel consumption (g/kWh) (lb/hp h)	335-365 g/kWh (0.55-0.60)
Engine lubrication system	Total loss lubrication
Engine aspiration	Naturally aspirated
Engine cooling	Liquid cooled
Ignition system	Capacitive discharge ignition (CDI)
Propeller speed (rpm)	4000 @ max. engine speed
Engine dry weight (kg)	29-30
Engine installed weight (kg)	39-40

3 Experimentation with WRCE

The designed WRCE engine is modeled and analyzed for the thermal and structural aspects to ensure its safe working until the maximum operating speed of 8000 rpm. After the analysis, the various engine components are fabricated and assembled into a WRCE. The performance of the designed WRCE is evaluated by mounting the engine on the thrust cradle simulating the actual engine configuration as shown in Fig. 2.

The mounting arrangement of the engine on the vehicle is shown in Fig. 3. It consists of two horizontal and two vertical bolts projecting from the DS frame which is a part of the UAV structure. To reduce the transmission of the engine vibration to the vehicle, an equi-frequency mount is provided at the engine mounting locations. These equi-frequency mounts have same stiffness in both the radial and axial directions for the specified load range. The mounting selected in this case has a stiffness of 14 N/mm and natural frequency of 15 Hz, which provides 50% isolation [3]. Details of the equi-frequency mounting arrangement are shown in Fig. 3.

In WRCE performance evaluation phase, the bare engine was run up to the full speed. Vibrations of WRCE without alternator were observed to be higher at full speed. The spectrum plot of engine vibration acquired at 8000 rpm is shown in Fig. 4. Spectrum plot shows that 1X is the dominant frequency with 24 g as the amplitude of vibration. The amplitude of vibration observed is higher compared to the sponsor recommended values of 10 g.

In order to find the critical structural frequencies getting excited during running, an impact hammer study was carried out using OROS vibration analyzer [4]. Figure 5

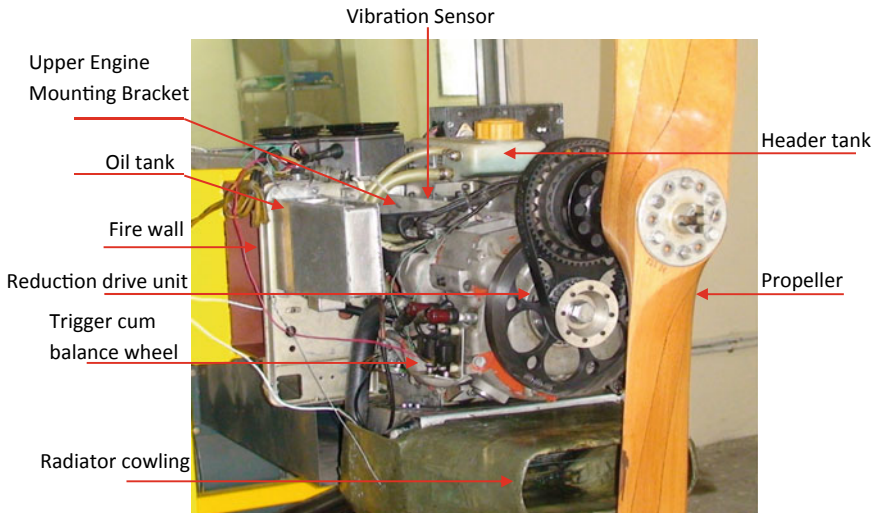


Fig. 2 Engine mounted on the thrust cradle

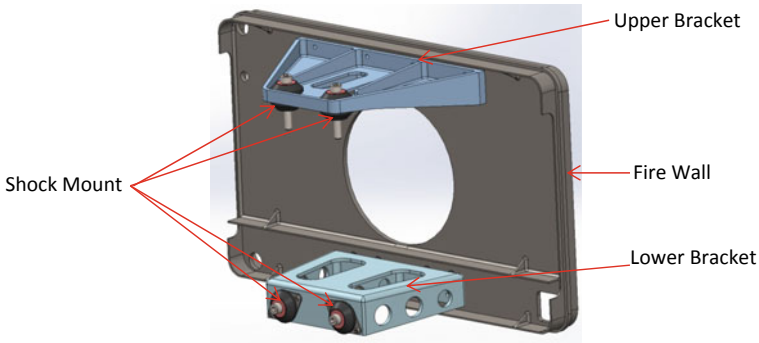


Fig. 3 Mounting of engine with frame

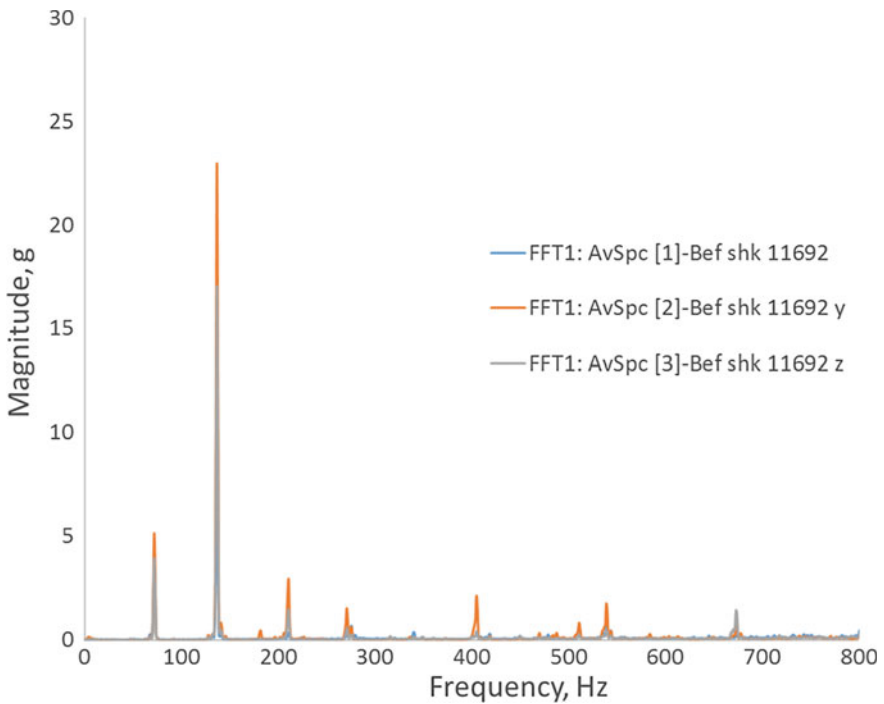


Fig. 4 Frequency plot of the WRCE (without alternator) running at speed of 8000 rpm

shows the results from the impact hammer experiments performed at stationary conditions with the sensor mounted on the firewall and also hit on the firewall to determine the point FRF. It can be seen that a frequency of about 138.75 Hz is evident in the impact experiments. This frequency is likely to get excited when the engine operates at full speed of 8000 rpm. Hence, it was decided to alleviate this frequency by introducing structured layer damper between the engine mount and the lower bracket in

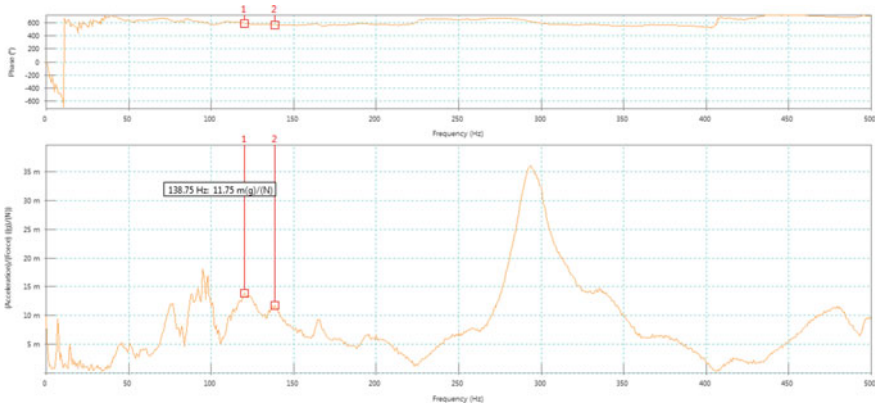


Fig. 5 Frequency response plot of the engine without alternator

the horizontal plane by replacing the shock mounts. A Turcite sheet of 150 mm × 50 mm × 4 mm is sandwiched between the engine mount and lower bracket as shown in Fig. 6. The experiments are repeated without the alternator. Figure 7 shows the results of experiments performed at full speed with structured layer damping in place. It can be seen that the magnitude of vibration has decreased from 24 g to about 14 g.

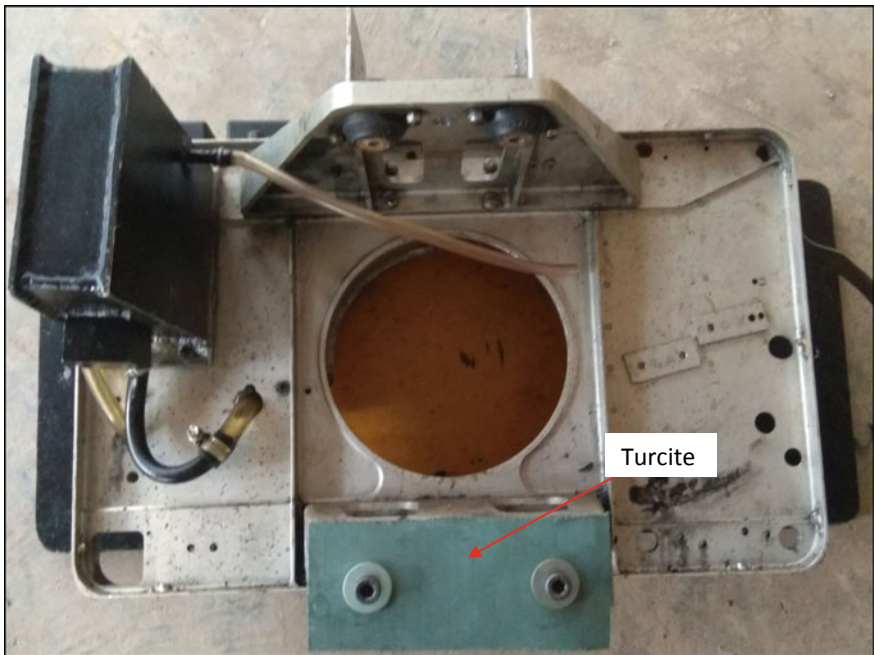


Fig. 6 Engine firewall fitted with structured layer damper (Turcite)

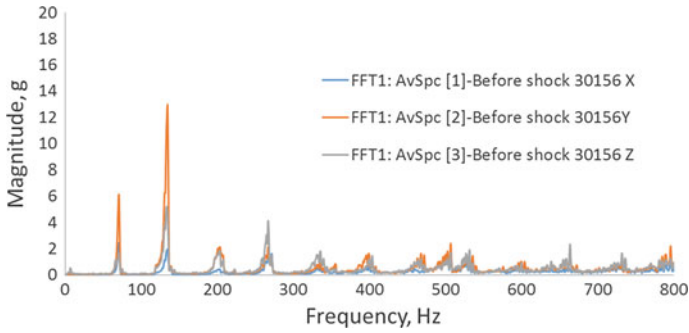


Fig. 7 Frequency plot of the WRCE at running speed of 8000 rpm with structured layer damping without alternator

This confirms that the structured layer damping is effective in reducing the vibration levels in the engine.

As per the mission requirements, the testing has to be carried out with the alternator. In the next phase of testing, the engine is fitted with an alternator and experiments are performed with structured layer damping in place. Figure 8 shows the vibration levels encountered when the engine is running at full speed. From frequency plot, it can be seen that the overall vibration levels have been reduced further with a maximum 1X amplitude of around 6 g, which is well within the prescribed limits of 10 g.

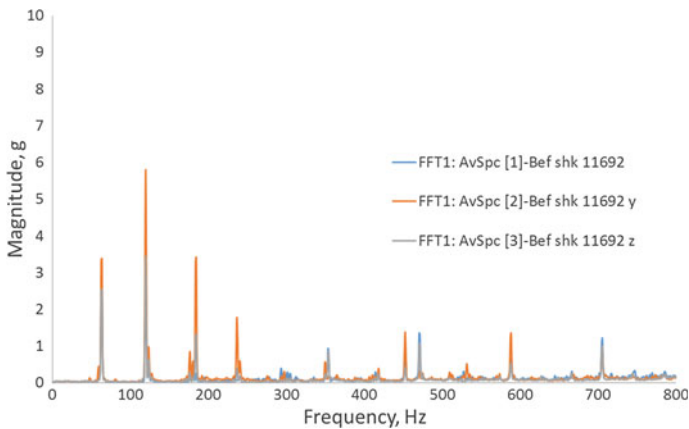


Fig. 8 Frequency plot of the WRCE at running speed of 8000 rpm with structured layer damping with alternator

4 Conclusions

The systematic approach of modal frequency identification with fundamentals of vibration analysis was followed to identify the source of vibration during the testing of indigenously developed Wankel engine. The mounting stiffness in the horizontal direction was identified as a controlling stiffness. The mounting stiffness and damping are improved by adopting the structured later damping. Demonstration of Wankel engine with the alternator is completed successfully up to full speed by adopting the structured layer damping.

Acknowledgements The authors acknowledge the support and encouragement of The Director, CSIR-NAL, and Head, Propulsion Division throughout this activity. Authors also acknowledge the active participation of Propulsion Workshop during the fabrication and inspection of the various engine components. Special thanks to ADE, Bangalore for sponsoring the 65 hp Wankel engine development program.

References

1. Bright sparks: revolutionary rotary engines for UAVs, DEVELOP3D (February 2015)
2. Detailed design report on 65 hp wankel rotary combustion engine. Propulsion Division, CSIR-NAL, Bangalore
3. Datasheet-“equi-frequency™ Mountings”. Trelloborg Inc
4. User Manual “OROS-35-portable noise and vibration analyser”. Grenoble, France

Characteristic Parameters Estimation of Active Magnetic Bearings for Varying Controlling Parameters



Sampath Kumar Kuppa and Mohit Lal

Abstract Online condition monitoring of rotor systems with the help of active magnetic bearings (AMBs) has been achieved more importance for the last few decades due to its ability to work in a feedback loop. Proportional-integral-derivative (PID) has three characteristic gain parameters, namely proportional (K_P), integral (K_I) and derivative (K_D). The main purpose of the controller is to provide current for the steady operation of the system. The stability condition of the system is achieved by applying Routh–Hurwitz stability criteria. The stable responses of the system are obtained by tuning the PID controller. Ziegler–Nichols tuning method is used to acquire the least settling time for different controlling parameters. Two different sets of PID controlling parameters are considered for tuning the system against different sets of frequency range. For identifying the characteristic parameters, two different sets of PIDs are selected for the frequency range of 35–51 Hz. A total of 10 operating speeds are selected randomly between the frequency ranges to generate the independent responses that are used in identification algorithm. In this article, a numerical experiment has been performed to identify characteristic parameters of the active magnetic bearing (AMB) along with dynamic parameters of coupling misalignment. An approach is proposed to evaluate the unknown parameters for two different sets of PIDs.

Keywords Flexible rotor-bearing-coupling · AMB · PID controller · Inherent unbalances · Settling time

S. K. Kuppa · M. Lal (✉)

Industrial Design Department, National Institute of Technology Rourkela, Odisha 769008, India
e-mail: lalm@nitrkl.ac.in; dr.mohitlal@gmail.com

S. K. Kuppa

e-mail: 515ID1003@nitrkl.ac.in

1 Introduction

In recent trends, the online conditioning is foremost in the high speed rotating machinery such as cryogenic engines, power generation units, space equipment and underwater vehicle. In online conditioning, the balancing of the rotor system for a wide range of frequency and consequently the selection of proportional-integral-derivative (PID) parameters is the real challenge otherwise it will lead to the increased settling time. The settling time is directly related to the exposure time to exaggerated vibration. In high speed rotating machineries, the major faults in the system are inherent unbalance, fatigue crack propagation, misalignment at the bearing and coupling location, rubbing of the components, etc. AMBs are utilized to provide contactless motion in high speed machineries to avoid/reduce wear and tear of components [1–3].

The authors of article [4, 5] developed a misaligned rotor system integrated with a different radial AMB for its performance and robustness. The EOMs are derived to determine the misalignment in terms of frequency responses utilizing Newmark method. Authors of [6] proposed a methodology to evaluate speed-dependent parameters of rotor-AMB system. Here, the proposed algorithm is tested against a different measurement noise for its robustness. Article [7] proposed an algorithm based on force response to estimate the AMB dynamic parameters, theoretically and experimentally. Based on experimental results concluded, AMB can be used as an exciter and also used a controller for stabilization of the rotor system at high speed operating conditions. Reference [8] proposed a methodology to evaluate the AMB characteristics using rotor unbalance response. Here, finite element rotor model was adopted to develop methodology and compared experimentally the identified parameters based on unbalance response.

In present study, the flexible rotors are modelled according to Euler Bernoulli beam theory with gyroscopic effect (due to the rigid discs). The finite element method (FEM) is used to derive the equations of motion (EOMs). SIMULINK model is developed for the system EOM and solved by Runge–Kutta method of fourth order to obtain time-series displacement and current response. Fast Fourier transformation (FFT) is used to convert the time-series signal into frequency-series. The online conditioning technique is proposed based on frequency responses to identify the characteristic fault parameters (unbalance, AMB (displacement and current stiffness) and coupling (stiffness and damping)) of an AMB-rotor-bearing-coupling system. The numerical simulations have been performed to illustrate the effectiveness of the methodology by varying the PID controlling parameters.

2 Modelling of the AMB-Rotor-Bearing-Coupling System

In this section, the assumptions involved in modelling of the AMB-rotor-bearing-coupling system and its considerations have been stated.

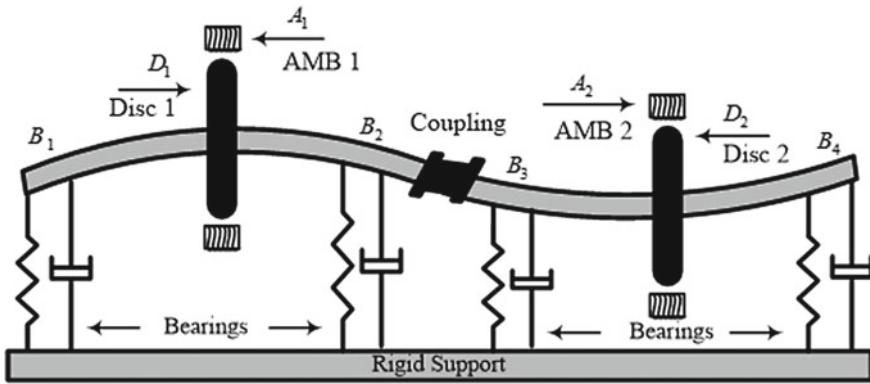


Fig. 1 Flexible rotor-bearing-coupling system with AMB

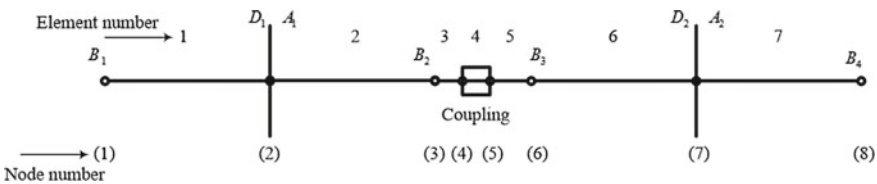


Fig. 2 FE model of the AMB-rotor-bearing-coupling system

2.1 Assumptions and Description of the Model

A flexible rotor-coupling system along with AMB considered for numerical simulation is shown in Fig. 1. The finite element (FE) model with the elemental and nodal description is shown in Fig. 2. Euler Bernoulli beam theory is applied in the modelling of the shaft. The torsional and longitudinal vibration effect and its effect on transverse direction have not been incorporated in this study. Cross-coupled parameters of bearing and coupling are not considered in the present study.

2.2 System EOM

The EOMs for the individual substructures, viz. the shaft, disc, bearing, coupling, AMB and inherent unbalance are derived in [1, 9–12]. The assembled EOMs with boundary conditions may be given as

$$M^G \ddot{\eta} + (C^G - j\omega G^G) \dot{\eta} + K^G \eta = f_{unb} + f_{AMB} \tag{1}$$

Here, M^G , C^G , G^G and K^G are the overall mass, damping, gyroscopic and stiffness matrices, and f_{unb} , f_{AMB} and η are the inherent unbalance force, AMB controlling force and global displacement vector.

The radial eight-pole electromagnets are considered to define the characteristic parameters of AMB [11, 12]. The AMB force could be given as,

$$f_{\text{AMB}} = -k_s \eta + k_i i_c \quad (2)$$

with

$$i_c = k_P \eta + k_D \dot{\eta} + k_I \int \eta$$

where k_P , k_D , k_I and i_c are gain parameters of controller, namely proportional gain, derivative gain, integral gain and controlling current, respectively. k_s and k_i are displacement and current stiffness of AMB, respectively. Here, η is the time-series displacement vector at AMB location.

In Eq. (1), substituting the unbalance force, displacement and current response as, $\{f_{\text{unb}}(t)\} = \{F_{\text{unb}}(t)\}e^{j\omega t}$, $\{\eta^c(t)\} = \{N^c(t)\}e^{j\omega t}$ and $\{i_c(t)\} = \{I_c(t)\}e^{j\omega t}$, respectively. The EOMs in frequency-series may be obtained as

$$[(-\omega^2 M^G) + j\omega(C^G - j\omega G^G) + K^G]N^c = F_{\text{unb}} + F_{\text{AMB}} \quad (3)$$

3 Simulated System Responses Based on Settling Time

Mathematical rearrangement may modify Eq. (1) as expressed below,

$$\ddot{\eta}^c(t) = \frac{1}{M^G} \{f_{\text{unb}}(t)\} + \{f_{\text{AMB}}(t)\} - (C^G - j\omega G^G)\dot{\eta}(t) - K^G \eta(t) \quad (4)$$

Conferring Eq. (4), to attain responses time-series, a SIMULINKTM model is designed as presented in Fig. 3. The PID controller is in parallel mode because in this condition the output of one controller does not affect the output of the other (Fig. 4). This allows the controller to control the parameters independently. The responses obtained in time-series are transformed into frequency-series by using the fast Fourier transformation (FFT) technique. The system specifications are presented in Table 1. Reference value presented for different parameters in Table 1 is taken from article [9, 13].

A characteristic linear displacement and phase response against the spin speed at bearing location 1 is shown in Fig. 5. The natural frequencies observed from Fig. 5 are $\omega_{nf1} = 66.08$ rad/s, $\omega_{nf2} = 200.00$ rad/s, $\omega_{nf3} = 347.48$ rad/s, $\omega_{nf4} = 517.37$ rad/s, $\omega_{nf5} = 795.16$ rad/s and so on. To have the effect of forward and backward whirl in

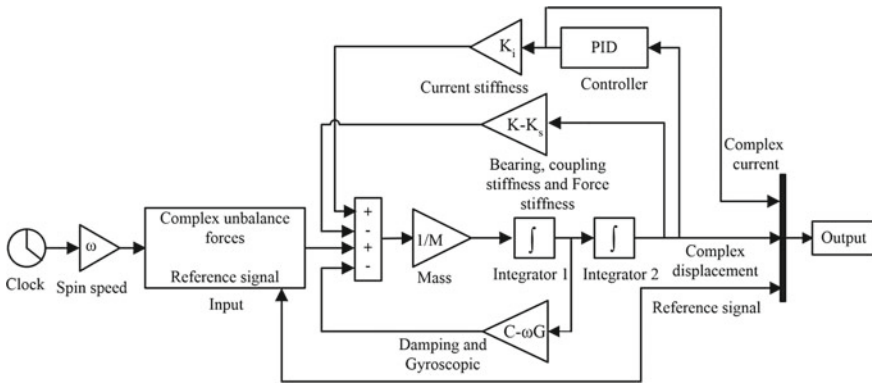


Fig. 3 SIMULINK diagram for AMB-flexible rotor system

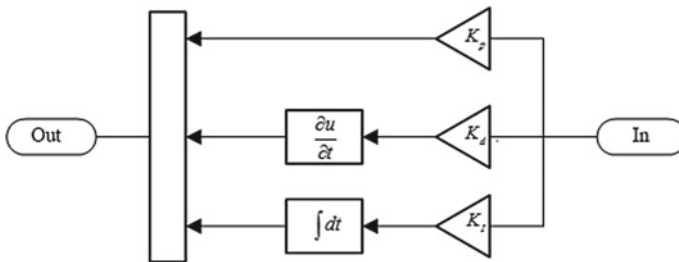


Fig. 4 PID controller for AMB

the estimated parameters, responses are generated at selected operating speeds (in between second and third natural frequency).

The responses in time-series are obtained with the help of SIMULINK model. The stability of the system is analysed based on the Routh–Hurwitz stability criteria [14] as

$$M > 0, k_D > 0, k_I > 0 \text{ and } k_P > \frac{1}{k_i k_s k_{sn}} \left(\frac{M k_I}{k_D} + K \right) \quad (5)$$

Here, M , k_P , k_D and k_I are mass of the rotor, proportional, derivative and integral gain of PID, respectively. For estimating the optimal characteristic parameters of the system, the parameters are tuned with different PID controller parameters (Table 2) for stabilization and lesser steady-state error. The Ziegler–Nichols (Z–N) tuning method [15, 16] is used to tune the PID controller for a stable performance of the system at different running conditions. In Ziegler–Nicholas criterion, the PID parameters are tuned by keeping the value k_P value as constant and varying the k_I and k_D values alternatively until the system response becomes steady. The stable characteristic response of the system with lesser steady-state error can be obtained

Table 1 Specifications of the numerical model considered

Parameters	Values (units)	Parameters	Values (units)
<i>Rotor</i>			
Disc mass m_1 and m_2	2 kg	Shaft length l	2.5 m
Polar moment of inertia I_p	45×10^{-4} kg-m ²	Disc eccentricity e_1 and e_2	24 μ m
Diametrical moment of inertia I_d	0.0024 kg-m ²	Shaft diameter d	0.016 m
Shaft density ρ	7850 kg-m ³	Phase change β_1 and β_2	30° and 36°
Rayleigh's coefficients for the damping proportional:		$a_0 = 0.154,$	$a_1 = 0.00001$
<i>AMB</i>			
PID-I (controller gains)		PID-II (controller gains)	
Proportional, K_p	4200 A/m	Proportional, K_p	10,200 A/m
Derivative, K_D	1 A-s-m ⁻¹	Derivative, K_D	8 A-s-m ⁻¹
Integral, K_I	1200 A/(m-s)	Integral, K_I	7400 A/(m-s)
Actuator forces			
Current factor, k_i	48 N/A	Displacement factor, k_s	105,210 N/m
<i>Bearing</i>			
Stiffness parameters (N/m)			
K_x^{b1}	2.21×10^5	K_y^{b1}	2.35×10^5
K_x^{b2}	2.35×10^5	K_y^{b2}	2.42×10^5
K_x^{b3}	2.13×10^5	K_y^{b3}	2.24×10^5
K_x^{b4}	2.01×10^5	K_y^{b4}	2.20×10^5
Damping parameters (Ns/m)			
C_x^{b1}	280	C_y^{b1}	350
C_x^{b2}	287	C_y^{b2}	350
C_x^{b3}	225	C_y^{b3}	275
C_x^{b4}	315	C_y^{b4}	290
<i>Coupling</i>			
Stiffness parameters			Damping parameters
K_{lx}^{co}	2.12×10^5 N/m	K_{ly}^{co}	1.99×10^5 N/m
$K_{\phi y}^{co}$	2.2×10^5 Nm/rad	$K_{\phi x}^{co}$	2.50×10^5 Nm/rad
		C_{lx}^{co}	150 Ns/m
		$C_{\phi y}^{co}$	150 Ns/m

with the help of rise time (T_r) and settling time (T_s). The T_r and T_s should be as less as possible for faster stabilization of the system. The steady-state error, settling time and rise time are calculated for different sets of PID for range of operating speed. For brevity and completeness, the worst and best cases are presented in Figs. 6 and 7, respectively. From Fig. 6, it may conclude that the settling time varies with operating condition. As settling time plays a major role in stabilization and identification of the system parameters, the PID control parameters are tuned to obtain the longer steady-state response at lesser settling time.

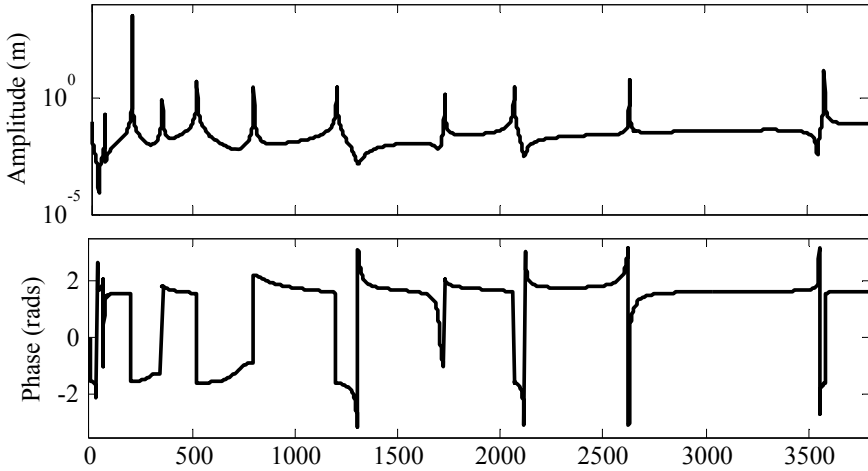


Fig. 5 Amplitude and phase plot with spin speeds

Table 2 Reference PID values

Set	1	2	3	4	5	6	7	8
K_p	4200							
K_i	1200	2100	2900	3800	4700	5600	6500	7400
K_d	1	2	3	4	5	6	7	8

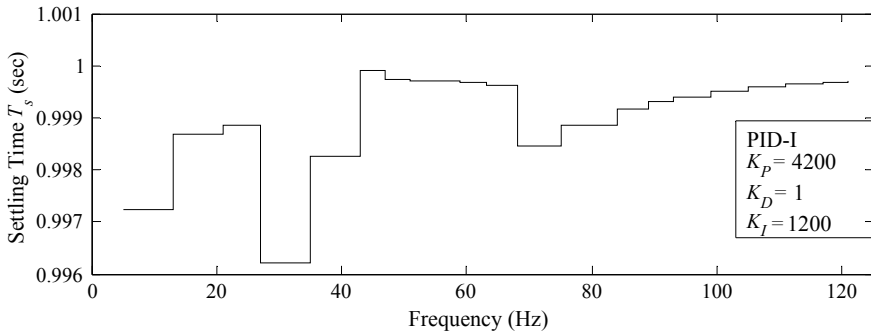


Fig. 6 Variation of settling time with the spin speed for PID-I

These two sets of PID control parameters are considered to estimate the characteristic parameters. By comparing Figs. 6 and 7, it can be observed that PID-II is better set of control parameters because the settling time is constant for longer speed range.

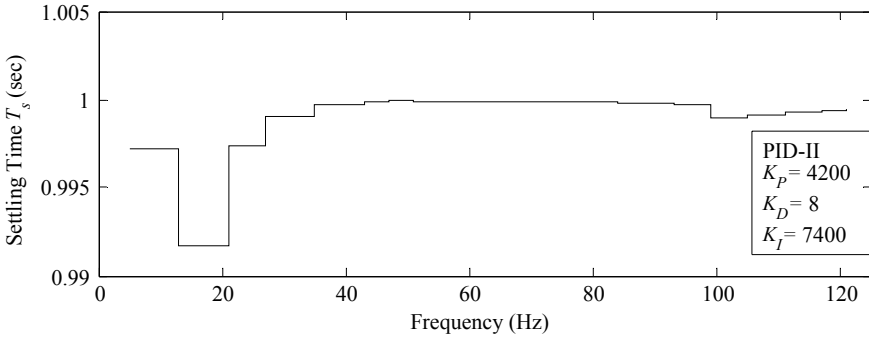


Fig. 7 Variation of settling time with the spin speed for PID-II

4 Formulation of Identification Algorithm

For developing identification algorithm, the governing Eq. (3) can be rearranged to retain the unknown system parameters, namely coupling (stiffness and damping), AMB and unbalance force to left side, and known parameters, namely the global mass, rotor (stiffness and damping) and bearing (stiffness and damping) to the right side. These rearrangements in the above equation are to generate the regression equation. The regression equation may be presented as

$$-\{F_{unb}\} - \{F_{AMB}\} + ([K^c] + j\omega[C^c])\{N\} = (\omega^2[M^G] - [K^B] - j\omega[C^B] - \omega^2[G^G])\{N\} \quad (6)$$

Equation (6) may be expressed in regression form as

$$[A(\omega_i)]\{X\} = [B(\omega_i)] \quad (7)$$

with

$$\{X\} = \{e_{1r} \ e_{1i} \ e_{2r} \ e_{2i} \ K_{s1} \ K_{i1} \ K_{s2} \ K_{i2} \ K_{Lx} \ K_{Ly} \ K_{\phi x} \ K_{\phi y} \ C_{Lx} \ C_{Ly}\}$$

In Eq. (7), regression matrix $[A]$ and vector $\{B\}$ are in complex form and represented in [11, 13]. The characteristic parameter vector $\{X\}$ requires set of independent response data for estimation. To generate the required responses for developed algorithm, a suitable simulation procedure needs to be designed. The following section deals with the suitable model development to fulfil above purpose.

5 Characteristic Fault Parameter Identification

A methodology is developed to identify the characteristic fault parameters (i.e., dynamic coupling, AMB and inherent unbalance) of the system, using least squares method. The efficiency of the algorithm is analysed against different PID controllers (PID-I and PID-II) for a range of operating speeds. The estimated parameters are presented in Figs. 8 and 9 for PID-I and PID-II, respectively. From Figs. 8 to 9, it may be observed that the AMB parameters exhibit good agreement with the addition of measurement noise as well as by varying the PID tuning parameters. The inherent unbalance parameters and coupling angular stiffness parameters are varying with the addition of measurement noise for both the PID-I and PID-II. The maximum error obtained in the estimated parameters is around 5% for coupling angular parameter with the addition of measurement noise. The identification algorithm is verified against faulty signal and found to be robust for varying PID tuning parameters.

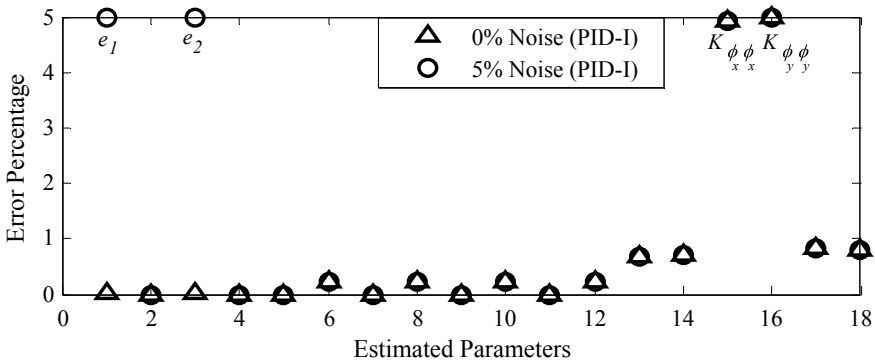


Fig. 8 Estimated parameters for different levels of measurement noise for PID-I

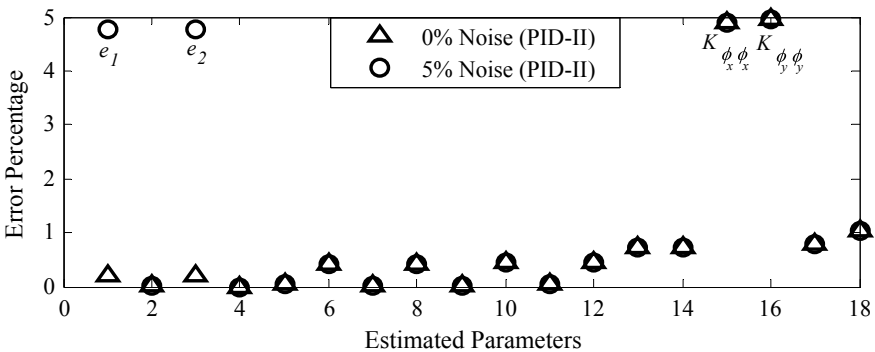


Fig. 9 Estimated parameters for different levels of measurement noise for PID-II

6 Conclusions

An online conditioning technique is proposed for simultaneous estimation of unbalance, dynamic AMB and coupling parameters in an AMB-rotor system for varying PID control parameters. The current and frequency responses along with rotor model information are utilized for developing the identification technique. A finite element model is developed with the Euler Bernoulli beam theory for proposed AMB-rotor system. An identification technique is proposed to identify the various faults parameters of the AMB-rotor system using least squares method. The effective changes in the settling time against different PID control parameters for range of operating speeds are calculated. The fault parameters such as dynamic coupling, AMB and inherent unbalance parameters are estimated. The proposed technique is tested against different levels of noise percentage and the measurement errors obtained from the estimated parameters are found to be robust.

References

1. Rao JS (1996) Rotor dynamics. New Age International
2. Bleuler H, Cole M, Keogh P, Larsonneur R, Maslen E, Okada Y, Schweitzer G, Traxler A (2009) Magnetic bearings: theory, design, and application to rotating machinery. Springer Science and Business Media
3. Polajžer B (2010) Magnetic bearings, theory and applications. IntechOpen
4. Bouaziz S, Messaoud NB, Mataar M, Fakhfakh T, Haddar M (2011) A theoretical model for analyzing the dynamic behavior of misaligned rotor with active magnetic bearing. *Mechatronics* 21:899–907
5. Bouaziz S, Messaoud NB, Choley JY, Mataar M, Haddar M (2013) Transient response of a rotor-AMBs system connected by a flexible mechanical coupling. *Mechatronics* 23:573–580
6. Tiwari R, Talatam V (2015) Estimation of speed-dependent bearing dynamic parameters in rigid rotor systems levitated by electromagnetic bearings. *Mech Mach Theory* 92:100–112
7. Jin C, Xu Y, Zhou J, Cheng C (2016) Active magnetic bearing stiffness and damping identification from frequency characteristics of control system. *Shock Vibr* 2016
8. Xu Y, Zhou J, Di L, Zhao C (2017) Active magnetic bearings dynamic parameters identification from experimental rotor unbalance response. *Mech Syst Signal Process* 83:228–240
9. Lal M, Tiwari R (2012) Multi-fault identification in simple rotor-bearing-coupling systems based on forced response measurements. *Mech Mach Theory* 51:87–109
10. Lal M, Tiwari R (2013) Quantification of multiple fault parameters in flexible turbo-generator systems with incomplete rundown data. *Mech Syst Signal Proc* 41:546–563
11. Kuppa SK, Lal M (2017) Characteristic parameter estimation of AMB supported coupled rotor system. In: ASME 2017 gas turbine India conference, American society of mechanical engineers, pp V002T05A010-V002T05A010
12. Kuppa SK, Lal M (2018) Characteristic parameters estimation of uncertainties present in an active magnetic bearing integrated flexible rotor system using dynamic reduction technique. In: international conference on rotor dynamics. Springer Cham, pp 234–248
13. Tiwari R, Chougale A (2014) Identification of bearing dynamic parameters and unbalance states in a flexible rotor system fully levitated on active magnetic bearings. *Mechatronics* 24:274–286

14. Tiwari R (2017) Rotor systems: analysis and identification. CRC Press
15. Ziegler JG, Nichols NB (1942) Optimum settings for automatic controllers. Trans ASME 64(11)
16. Levine WS (2010) The control systems handbook: control system advanced methods. CRC Press

Characterization of Digital Power Amplifier-Based Active Magnetic Bearings



Pravina R. Mali , Balaji Sankar , Gurunayk Nayak, Soumendu Jana, and A. S. Sekhar 

Abstract Active magnetic bearings (AMB's) are used to support rotors using magnetic forces, without any solid to solid contact. The AMB system has four main components: power amplifier, electromagnetic actuator, sensor and controller. In this work, the characterization of power amplifier for the AMB system is undertaken. The gain and phase lag of the power amplifiers over the operating frequency is obtained experimentally. Equivalent circuit models are made for the power amplifier. These characteristics of the amplifiers are used in developing the control algorithm for the AMB. The experimental results of these characterizations will help in understanding the gain of the power amplifier and also the lag between the signal input and the output signal over the desired frequency range.

Keywords Magnetic bearing · MATLAB/simulink model · Power amplifier · Step response

1 Introduction

The AMB system consists of electromagnetic actuator, sensor, AMB controller device and power amplifier. The power amplifier plays a significant role in the active magnetic bearing system. It receives control signals of low strength from the controller and drives the desired current in the electromagnetic actuator in order to maintain the shaft at levitated condition. The study of the response characteristics

P. R. Mali (✉) · G. Nayak
M. S. Ramaiah Institute of Technology, Bengaluru, India
e-mail: star.pravina@gmail.com

B. Sankar · S. Jana
Propulsion Division, CSIR—National Aerospace Laboratories (NAL), Bengaluru 560017, India

A. S. Sekhar
Department of Mechanical Engineering, Indian Institute of Technology Madras, Chennai, Tamil Nadu, India

of power amplifier is necessary for selection of suitable power amplifier for a specific AMB application.

Changsheng and Zhiwei [1] proposed a two-level PWM switching power amplifier with an inner feedback loop composed of inner controller, drive circuit, power main circuit and feedback circuit to improve the characteristics of the power amplifier. The current loop can be used in voltage-controlled mode or current controlled mode, with characteristics satisfying the requirements of industrial AMB switching power amplifiers for the rotational speed of up to 60,000 RPM. In “study on three-level power amplifier of magnetic bearings for high speed machine” [2], the three-level switching power amplifier is designed by using carrier triangular wave phase shift method to meet the requirement of the magnetic bearings which are used in high speed machines. The comparative study of the two-level and three-level switching power amplifier was carried out that shows two-level has large current ripple which causes the fluctuation of the rotor position and three-level has reduced current ripple because of the increased zero level switching. The three-level switching power amplifier can satisfy the requirements of the magnetic bearing system.

Ren et al. [3] analyzed the principle of three-level power amplifier and designed a circuit based on the three-level PWM modulation technique. The designed circuit uses two triangular carriers that are formed by the triangular wave superimposing the positive and negative voltage bias and the two drives are formed by comparing the current error signal and the two triangular carriers based on the voltage comparator. It reduces the output current ripple and has good dynamic characteristics, tracking characteristics and steady-state characteristics. Wentao et al. [4] proposed a similar three-level PWM signal generation algorithm, designed the gate-driven circuits with negative bias and built a three-level magnetic bearing power amplifier. The full-bridge circuit model and current sampling circuit model were created by using power system block set library in the MATLAB/Simulink. Also, it used M-file function of MATLAB to simulate the data flow of the FPGA chip digital control in the power amplifier. The use of FPGA chips to design power amplifier has easy programming and flexibility of generating PWM signal.

In “the design and research of switching power amplifier used on magnetic suspension support” [5], the switching power amplifier was used for the magnetic suspension support to improve the frequency response bandwidth. The circuit simulation was done in MULTISM software. Since most of the energy in the magnetic suspension support would be utilized by the power amplifier the efficiency of the power amplifier should be good with fast output current response speed. The switching power amplifier is more advantageous as compared to the analog power amplifier since the power consumption is low with high efficiency and small volume. But the disadvantage of the switching power amplifier is switches are subjected to significant interference. In the simulation, they have used the sine input and also step response. From the experiment results, the waveforms of input and output show that the output can follow input with less distortion. The control performance can be assessed by the step response. The time required for the systems to be in the stable states can be done by testing step response. The shorter the rise time is, the higher the cut off frequency is, i.e., the frequency band is wider.

Cao and Lee [6] developed a power amplifier based on IGBT power modules and applied in an actual AMB system which has characteristics such as high-power capacity with current greater than 10 A and power supply voltage greater than 48 V with wide variable carrier frequency up to 200 kHz. The design has taken considerations of the effect of the ripple current, electrical stresses on power semiconductor devices and power loss of the amplifier. Zhang and Jiang [7] discussed a similar two-level power amplifier for a magnetic bearing and its working. He applied the control method for the power amplifier which used DSP controller for the control action. The design scheme used switching frequency of 50 kHz, high speed optocoupler isolation device HCPL4504 and bipolar *H*-type structure for the power amplifier. The current rate of the change of the coil current was analyzed which shows that in order to improve the response speed of the current, the inductance value of the electromagnetic coils should be minimized. Zhao et al. [8] analyzed the working principle of the switching power amplifier that was based on the power system simulation method. It was achieved in MATLAB/Simulink software. The dynamic performance of the power amplifier was simulated and experimented, with overshoot, rise time and bandwidth analyzed and compared separately which showed small error between simulation and experiments and resulted in more accuracy.

In “research on MATLAB simulation of three-level power amplifier for magnetic bearing” [9], the simulation for the data flow of the FPGA chip digital control in the power amplifier for magnetic bearing was carried out by using MATLAB function file. The design of the three-level PWM power amplifier included AD sampling circuit for the conversion of coil current signals into digital signals and then transfer to FPGA chip, FPGA control circuit for processing/generating the PWM output signals and full-bridge circuit. The simulated and experimented waveforms coincided and show the accurate results for the simulation and experiment.

Wang and Xu [10] proposed an accurate system model of three-level switching power amplifier for active magnetic bearing. The operating principle was analyzed using equivalent switching model and math models of half-bridge circuits are obtained. The PI controller was designed in order to increase the stability domains of the system and to improve the system response time. The simulation results matched with the experiment and the model helps to design the required stability and dynamic property of the system for magnetic bearing.

2 Equivalent Circuit for the Load on a Power Amplifier

The equivalent circuit for the load on an analog power amplifier consists of the inductor coil in series with its internal resistance and additional external resistance. The transfer function of the system is

$$T(s) = \frac{I(s)}{V(s)} = \frac{1}{(R_{in} + R_{ex}) + sL} \quad (1)$$

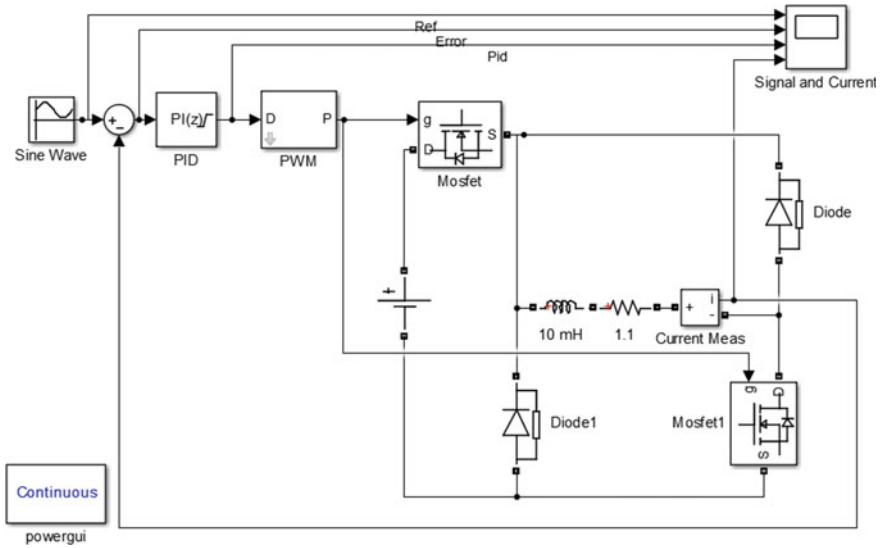


Fig. 1 Simulink model for the digital power amplifier

Equation (1) shows the transfer function of the load on power amplifier where $I(s)$ is the output current and the $V(s)$ is the input voltage to the power amplifier. R_{in} is the internal resistance of the actuator coil and L is the inductance of the actuator coil. R_{ex} represents the external resistance which also acts as a load. From the equivalent circuit of the power amplifier, a Simulink model was built in MATLAB software. The parameters of the designed circuit are: input voltage (V_{in}) = 1 V (peak-peak), offset voltage (V_{off}) = 0.5 V, inductance (L) = 571 μ H, internal resistance (R_{in}) = 0.1 Ω and external resistance (R_{ex}) = 1 Ω . The Simulink model for digital power amplifier was built and simulated as shown in Fig. 1 and the simulation results for it is shown in Fig. 2. The waveforms shown in Fig. 2 are (i) input signal given to the amplifier with the help of NI-cDAQ, (ii) error signal, (iii) PI signal given to the PWM generator and (iv) current signal taken from load output.

3 Experimental Verification

The experimental setup for the characterization of power amplifier is as shown in Fig. 3. The analog power amplifier used for this experiment requires ± 12 V. The signal excitation for power amplifier is given with the help of analog output card through NI-cDAQ. The power supply to the power amplifier was supplied by two batteries connected in series for +12 and -12 V to get a common point. The load connected to the power amplifier was electromagnetic actuator in series with the rheostat and an ammeter. The output signals for the measurements were taken across

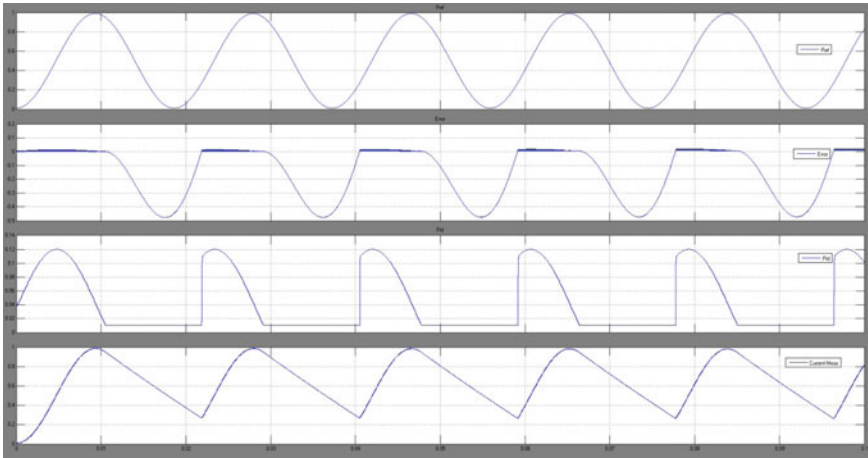


Fig. 2 Simulation results for digital power amplifier

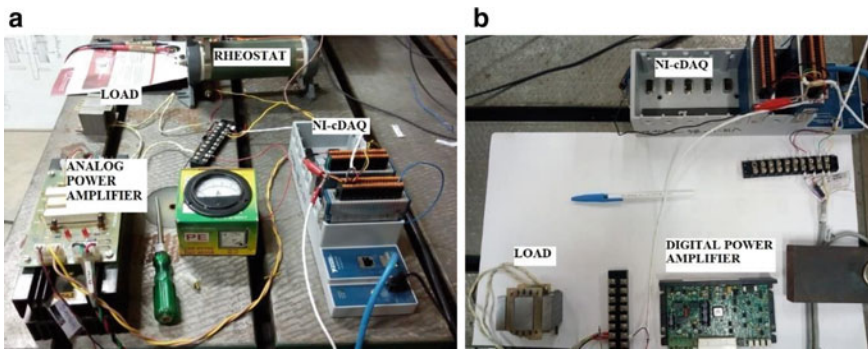


Fig. 3 a Experimental setup for analog power amplifier, b experimental setup for digital power amplifier

the rheostat through NI-cDAQ analog input card and the input signals were given from the analog output card through NI-cDAQ. The NI-cDAQ was connected to the PC with the help of Ethernet. In the same way for the digital power amplifier, the circuit connections are similar.

The experiment is carried out at multiple frequencies in the desired range. For comparison purpose, the results for only few of the frequencies are shown. The experiment result for analog power amplifier has two set of values, one without thrust plate and with thrust plate. The thrust plate represents the magnetic shaft of an AMB system. Figure 4 shows the experiment results without thrust plate for analog power amplifier. The waveforms in Fig. 4 are (i) input signal given to the power amplifier and its fast Fourier transform (FFT) signal, (ii) load signal across the electromagnetic actuator and its FFT signal, (iii) drop across the resistor and its

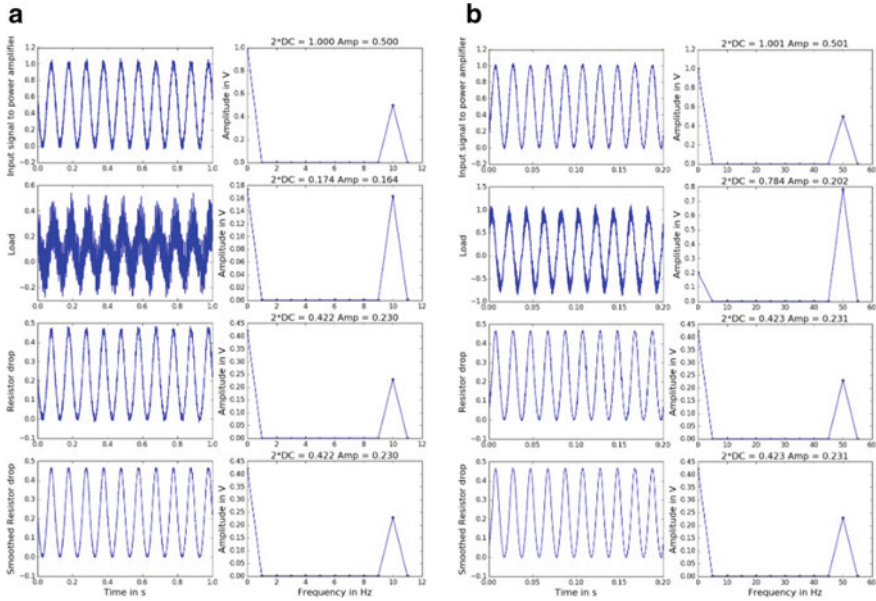


Fig. 4 **a** Experiment results for analog power amplifier without thrust plate for 10 Hz (y-axis is in volts), **b** experiment results for analog power amplifier without thrust plate for 50 Hz (y-axis is in volts)

FFT signal and (iv) smoothed resistor drop and its FFT signal. Similarly, for Fig. 5, experiment results with thrust plate for analog power amplifier are shown. The FFT signals helped in analyzing the input and output frequency. From Fig. 4a, it can be seen clearly that the frequency of the output signal was same as the input signal (peak at 10 Hz). Also, for the output signals across the resistor, the FFT signals clearly say that amplitude at low and high frequencies without thrust plate on actuator does not show a significant dip in output voltage amplitude. But from Fig. 5, it is clear that there is a significant dip across the output voltage amplitude for high frequencies with thrust plate on the actuator. Also, the time plot of load versus time in Fig. 4a looks noisy so there are possibilities of multiple frequencies in FFT plot at higher frequencies but the plot is limited to 12 Hz and hence is not visible.

Based on the data collected for the analog power amplifier, the input and output voltage amplitude with and without thrust plate are tabulated for all of the desired frequencies as shown in Table 1. From the following table, it is clear that for over a desired frequency range the gain of the analog power amplifier is constant with nearly zero phase lag between its input and output signals. The same experiment is carried out for digital power amplifier for the set of desired frequency range as shown in Fig. 6a, b. The waveforms in Fig. 6 are (i) voltage drop, i.e., output signal taken across the load consisting of electromagnetic actuator without thrust plate on top, (ii) input signal given from the analog output card through NI-cDAQ and (iii) the load signal after the removal of outlier. Figure 7 (a) and (b) shows the waveforms of (i)

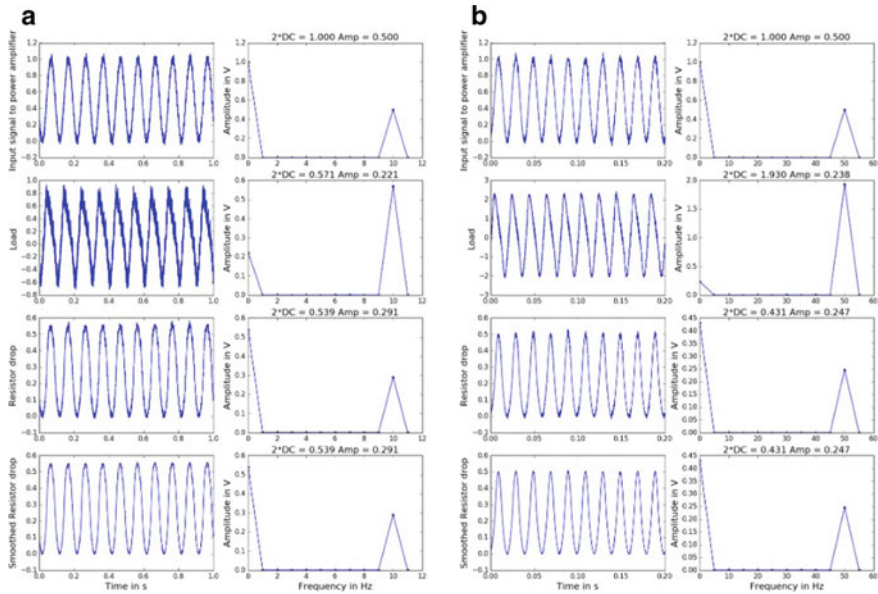


Fig. 5 **a** Experiment results for analog power amplifier with thrust plate for 10 Hz (y-axis is in volts), **b** experiment results for analog power amplifier with thrust plate for 50 Hz (y-axis is in volts)

Table 1 Output voltage amplitude for analog power amplifier for desired frequency range

Frequency (Hz)	Input voltage amplitude (V)	With thrust plate	Without thrust plate
		Output voltage amplitude (V)	Output voltage amplitude (V)
0.1	0.5	0.229	0.24
0.2	0.5	0.228	0.203
0.5	0.5	0.217	0.252
0.7	0.5	0.229	0.26
1	0.5	0.229	0.276
2	0.5	0.229	0.292
5	0.5	0.249	0.303
7	0.5	0.259	0.298
10	0.5	0.249	0.302
20	0.5	0.247	0.312
30	0.5	0.246	0.318
40	0.5	0.245	0.296
50	0.5	0.245	0.291

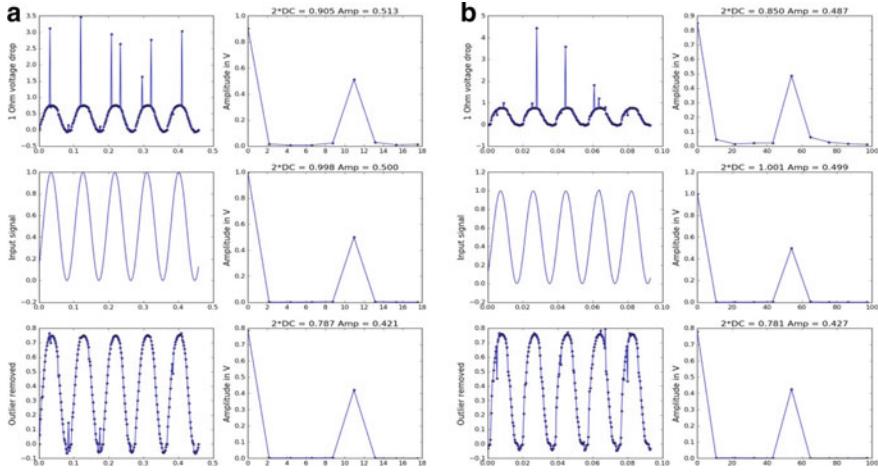


Fig. 6 **a** Experiment results for digital power amplifier without thrust plate for 10.9 Hz (y-axis in volts), **b** experiment results for digital power amplifier without thrust plate for 53.7 Hz (y-axis in volts)

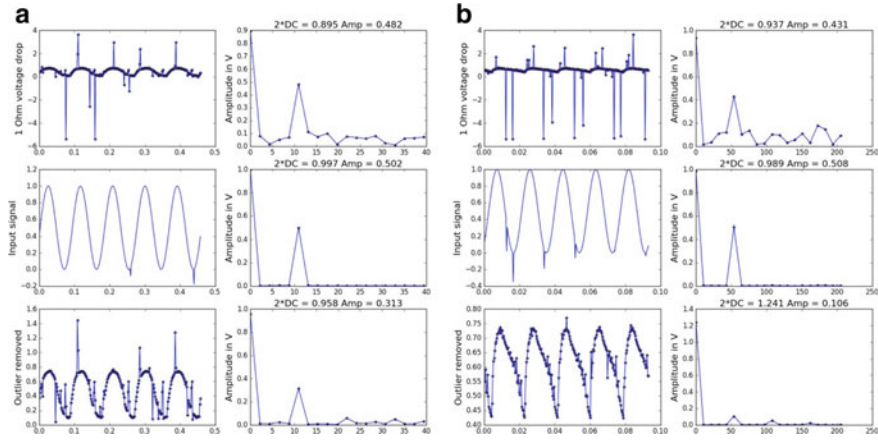


Fig. 7 **a** Experiment results for digital power amplifier with thrust plate for 10.9 Hz (y-axis in volts), **b** experiment results for digital power amplifier with thrust plate for 53.7 Hz (y-axis in volts)

voltage drop, i.e., output signal taken across the load when thrust plate is kept on the top of it, (ii) input signal given from the analog output card through NI-cDAQ and (iii) the load signal after the removal of outlier. The MOSFET-based digital power amplifier is used here with a high PWM switching frequency and 24 V power supply. It is clear from Fig. 6 that for low and high frequencies without thrust plate on the actuator the inductance is less and the output signal is following the input signal. And from Fig. 7, it is clear that for low frequencies with thrust plate on the actuator

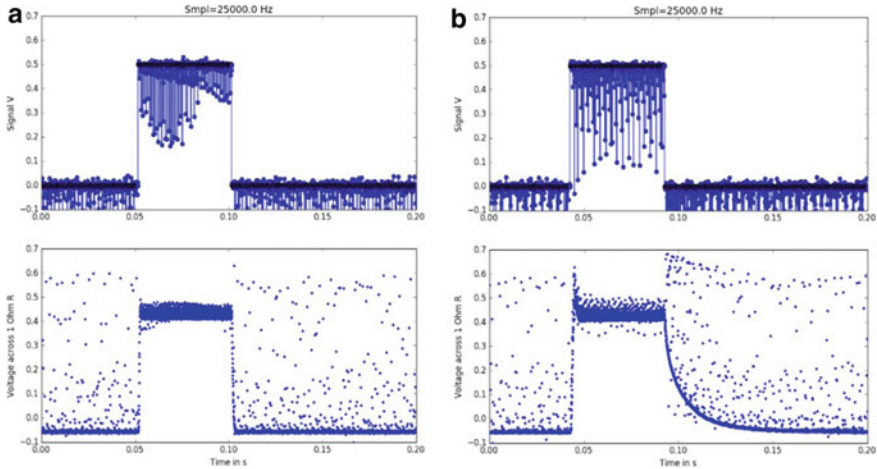


Fig. 8 **a** Step response for digital power amplifier without thrust plate (y-axis in volts), **b** step response for digital power amplifier with thrust plate (y-axis in volts)

the output signal is following the input signal but for the high frequencies the output signal is not able to follow the input signal cleanly because of the effect of high inductance. The peaks that are seen for 1 Ω voltage drop signal in Figs. 6 and 7 is the noise due to high switching frequency of the digital power amplifier. Also, the noise content has increased significantly when the actuator has thrust plate on top of it.

The step response analysis is common tool to characterize the dynamic behavior of the power amplifier. The step responses have been plotted for the digital power amplifier in Fig. 8. The step responses are shown for (a) actuator without thrust plate and (b) with thrust plate on top of it. The waveforms in Fig. 8 are (i) signal voltage and (ii) voltage across the resistor.

To estimate the inductance values with thrust plate and without thrust plate, a MATLAB code was written. This program simulated the decay of current from the initial constant current case for different values of inductances. By comparing the current decay trend with experimentally obtained curves, the equivalent inductance of the coil was estimated. Figure 9 shows the comparison of the decay of current trends from simulation and experiment for the estimated inductances values. From this study, it was estimated that the inductance of the actuator with thrust plate on top of actuator was 10 mH and without thrust plate it was 0.8 mH.

4 Conclusion

The frequency response of the analog and digital power amplifiers was studied experimentally. The analog power amplifier was given constant amplitude input signals of various frequencies, and the experimental results show nearly constant gain and

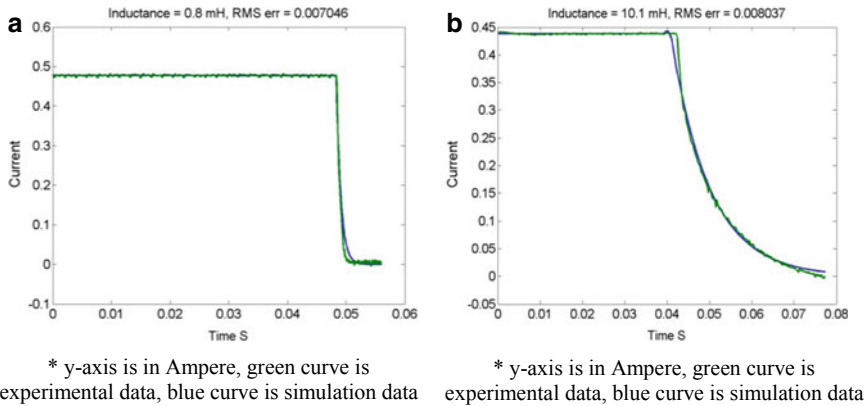


Fig. 9 **a** Comparison of inductances for the simulated and the experimented without thrust plate, **b** comparison of inductances for the simulated and the experimented with thrust plate

zero phase lag over the desired range of frequencies. The FFT of input and output signal shows no change in frequencies or any addition of undesired frequencies in the response. Similar study was conducted for digital power amplifier and the current response showed significant distortion compared to the input signal at high inductance levels. Similar behavior was seen in the simulation model developed for the digital power amplifier. This study helps us in choosing the power amplifier based on our power requirement and coil inductance.

References

1. Changsheng Z, Zhiwei M (2005) A PWM based switching power amplifier for active magnetic bearings. In: 2005 international conference on electrical machines and systems, vol 2. IEEE
2. Wang D, Wang F, Zhao Y (2010) Study on three-level power amplifier of magnetic bearings for high speed machine, In: 2010 3rd international conference on computer science and information technology, vol 1. IEEE
3. Ren X, et al (2015) Design of the power amplifier for magnetic bearings based on the three-level PWM modulation. In: 3rd international conference on mechatronics, robotics and automation. Atlantis Press
4. Wentao, Y, Hongwei L, Shuqin L (2016) The development of power amplifier for the high-power magnetic suspension bearing blower. DEStech transactions on engineering and technology research (mccemic)
5. Wang ZY, Wu GQ (2012) The design and research of switching power amplifier used on magnetic suspension support. Appl Mech Mater 150. Trans Tech Publications
6. Cao G, Lee CW (2004) Development of PWM power amplifier for active magnetic bearings. In: Fifth world congress on intelligent control and automation (IEEE Cat. No. 04EX788), vol 4. IEEE
7. Zhang JS, Jiang DJ (2012) Research on power amplifier for AMB based on DSP. Appl Mech Mater 150. Trans Tech Publications
8. Zhao Z, et al (2014) Simulation and experiment of power amplifier for magnetic bearings. Adv Mater Res

9. Yu W, et al (2010) Research on matlab simulation of three level power amplifier for magnetic bearing. In: 2010 Asia-pacific power and energy engineering conference, IEEE
10. Wang J, Xu L (2009) Analysis and modeling of a switching power amplifier for magnetic bearing. In: 2009 4th IEEE conference on industrial electronics and applications, IEEE

Nonlinear, Parametric Effects on Rotor

Effect of Sinusoidal and Non-sinusoidal Periodic Forces on the Stability of Gas Foil Bearing



Kamal Kumar Basumatary, Sashindra K. Kakoty,
and Manash Pratim Ghosh

Abstract The effect of unidirectional sinusoidal and non-sinusoidal external periodic forces on the stability of gas foil bearing has been investigated using the nonlinear transient analysis. In the case of sinusoidal forces, the loading is considered to follow a sine wave. In the case of non-sinusoidal forces, the periodic forces are assumed to follow square and triangular wave. The spatial domain and time domain terms of the governing Reynolds equation have been discretized using the finite difference method and the Crank–Nicholson method, respectively. The Reynolds equation and the equation of film thickness have been coupled with the elastic deformation of the bump foil structure as the deformation of the bump foil structure is a function of hydrodynamic pressure. The stability of the bearing has been investigated for different loading frequency ratio and loading amplitude. Trajectories are obtained for different values of journal speed to ascertain if the rotor-bearing system is in the stable, unstable, or in critically stable condition. The effect of loading frequency ratio and loading amplitude on the minimum film thickness is also presented.

Keywords Gas foil bearing · Periodic loading · Sinusoidal forces · Non-sinusoidal forces

Nomenclature

C Bearing radial clearance (m)
 e, ε Bearing eccentricity (m), e/C

K. K. Basumatary (✉) · S. K. Kakoty · M. P. Ghosh
Department of Mechanical Engineering, Indian Institute of Technology, Guwahati, India
e-mail: k.basumatary@iitg.ac.in

S. K. Kakoty
e-mail: sashin@iitg.ac.in

M. P. Ghosh
e-mail: manasp@iitg.ac.in

$F_\varepsilon, F_\phi, \tilde{F}_\varepsilon, \tilde{F}_\phi$	Hydrodynamic forces in ε, ϕ coordinate system (N), $\tilde{F}_\varepsilon = \frac{F_\varepsilon}{P_a R^2}, \tilde{F}_\phi = \frac{F_\phi}{P_a R^2}$
H, \tilde{H}	Film thickness (m), $\tilde{H} = H/C$
L_a	Amplitude of periodic loading
M	Mass of rotor per bearing (kg), $\tilde{M} = MC\omega^2/W$
O	Center of bearing
O'	Center of journal
P	Hydrodynamic pressure of the gas film (N/m^2), $\tilde{P} = P/P_a$
P_a	Atmospheric pressure in gas film (N/m^2)
R	Radius of journal (m)
S	Compliance coefficient Number, $\alpha P_a/C$
t	Time (s), $\tau = \omega t$
w_t	Transverse deflection of foil (m), $\tilde{w}_t = S(\tilde{P} - 1)$
W_0	Steady-state load carrying capacity (N), $\tilde{W}_0 = W/P_a R^2$
Z, \tilde{Z}	Axial coordinate of bearing, $\tilde{Z} = Z/R$
α	Compliance of the bump foil (m^3/N)
Λ	Bearing number, $\frac{6\mu\omega}{P_a} \left(\frac{R}{C}\right)^2$
μ	Gas viscosity, (N s/m^2)
ϕ	Attitude angle (rad)
θ	Angular coordinate of bearing (rad), x/R
ω	Rotor angular velocity, (rad/s)
ω_p	Frequency of periodic loading
Ω	Frequency ratio, ω_p/ω

1 Introduction

The recent need for high-speed oil-free technology has endorsed the application of gas foil bearings (GFBs) in air cycle units and auxiliary power units, turbo-expanders and turbochargers [1]. In general, it consists of three parts, viz. top foil, bump foil, and bearing housing. The bump foil provides the compliance to the top foil, which increases the load-carrying capacity of GFBs compared to the conventional rigid gas bearing, thus providing maintenance-free and low power loss operation. Although the applications of GFBs are numerous, the design of GFBs is mainly empirical due to mechanical complications. Moreover, due to its low damping capabilities, rotors supported on GFBs have low stability, which concerns the researchers and engineers.

The linearized method and nonlinear transient method are the two methods that are generally used to investigate the stability of the rotor. The linearized method specifies the dynamic coefficients that are used to predict the rotor-bearing stability. The nonlinearized approach provides information and details about the whirl orbit of the rotor. The nonlinear transient analysis is, however, time-consuming but predicts the stability of the rotor better than the linearized method [2, 3]. In many applications,

the rotor-bearing system has to undergo various loading conditions. As a result, the stability of the rotor gets altered. In this regard, the stability of the rotors supported on the oil film bearings under different loading conditions has been investigated [4–6]. The investigation showed that the loading conditions greatly influenced the stability of the rotor-bearing system. In another investigation, Vijayaraghavan and Brewe [6] established that the loading patterns greatly affect the film thickness. Zarbane et al. [7] found that the load capacity of the bearing is directly proportional to the oscillating frequency of the periodic squeezing of the fluid film, whereas inversely proportional to the mean film thickness. Further, Bhole and Darpe [8] compared the linear and nonlinear frequency response of different frequency and amplitude of sinusoidal excitation. The analysis showed a strong dependence of nonlinear frequency function on the rotor supported on GFBs. Most recently, Basumatary et al. [9] compared the stability of GFB under unidirectional sinusoidal load and constant load. It was found that under high periodic load, the stability of rotor decreases. Moreover, higher compliance coefficient of the bump foil also decreases the stability.

In the present investigation, the stability of the rotor supported on GFB under sinusoidal and non-sinusoidal periodic forces has been investigated. In the case of sinusoidal forces, the loading is considered to follow a sine wave. In case of non-sinusoidal forces, another two kinds of periodic forces vis-a-vis square and triangular wave are analyzed. The stability analysis has been investigated for different frequency and amplitude of sinusoidal and non-sinusoidal periodic loading. The time domain and spatial domain of the governing Reynolds equation have been discretized using the Crank–Nicholson method, respectively. The deformation of the bump foil structure has been coupled with the film thickness equation to evaluate the hydrodynamic pressure. In this regard, the effect of sinusoidal and non-sinusoidal forces on minimum film thickness has also been investigated.

2 Mathematical Model

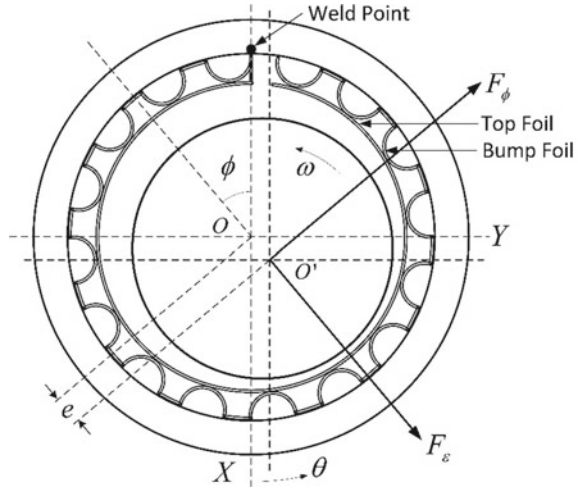
The schematics of the bump type gas foil bearing has been shown in Fig. 1. The Reynolds equation for isothermal perfect gas is the governing equation that describes the generation of the gas pressure in GFBs. The Reynolds equation can be written in non-dimensional form as,

$$\frac{\partial}{\partial \theta} \left(\tilde{P} \tilde{H}^3 \frac{\partial \tilde{P}}{\partial \theta} \right) + \frac{\partial}{\partial \tilde{Z}} \left(\tilde{P} \tilde{H}^3 \frac{\partial \tilde{P}}{\partial \tilde{Z}} \right) = \Lambda \frac{\partial \tilde{P} \tilde{H}}{\partial \theta} + 2\Lambda \frac{\partial (\tilde{P} \tilde{H})}{\partial \tau} \quad (1)$$

Equation (1) has been discretized and rearranged for (m, n) th node or k th node to obtain a quadratic form as,

$$(\tilde{P}_k^e)^T A_k^e \tilde{P}_k^e + b_k^e \tilde{P}_k^e = \frac{\partial \tilde{P} \tilde{H}}{\partial \tau} \quad (2)$$

Fig. 1 Schematic of the bump type GFB



where $P_k^e = \{ P_{(m,n-1)} P_{(m-1,n)} P_{(m,n)} P_{(m+1,n)} P_{(m,n+1)} \}^T$

$$A_k^e = \begin{bmatrix} \frac{\tilde{H}_{(m,n-1)}^3}{4(\Delta Z)^2} & 0 & 0 & 0 & -\frac{\tilde{H}_{(m,n-1)}^3}{4(\Delta Z)^2} \\ 0 & \frac{\tilde{H}_{(m-1,n)}^3}{4(\Delta\theta)^2} & 0 & -\frac{\tilde{H}_{(m-1,n)}^3}{4(\Delta\theta)^2} & 0 \\ \frac{\tilde{H}_{(m,n)}^3}{(\Delta Z)^2} & \frac{\tilde{H}_{(m,n)}^3}{(\Delta\theta)^2} & -\frac{2\tilde{H}_{(m,n)}^3}{(\Delta\theta)^2} - \frac{2\tilde{H}_{(m,n)}^3}{(\Delta Z)^2} & \frac{\tilde{H}_{(m,n)}^3}{(\Delta\theta)^2} & \frac{\tilde{H}_{(m,n)}^3}{(\Delta Z)^2} \\ 0 & -\frac{\tilde{H}_{(m+1,n)}^3}{4(\Delta\theta)^2} & 0 & \frac{\tilde{H}_{(m+1,n)}^3}{4(\Delta\theta)^2} & 0 \\ -\frac{\tilde{H}_{(m,n+1)}^3}{4(\Delta Z)^2} & 0 & 0 & 0 & \frac{\tilde{H}_{(m,n+1)}^3}{4(\Delta Z)^2} \end{bmatrix}$$

$$b_k^e = \begin{bmatrix} 0 & \frac{\Lambda\tilde{H}_{(i-1,j)}}{2(\Delta\theta)} & 0 & -\frac{\Lambda\tilde{H}_{(i+1,j)}}{2(\Delta\theta)} & 0 \end{bmatrix}$$

The right-hand side of Eq. (2) has been discretized using Crank–Nicholson method. Applying the boundary conditions given in Eqs. (3), (2) has been solved using Newton–Raphson method [9],

$$\begin{aligned} \tilde{P} &= 1 \text{ at } (\tilde{Z} = \pm L/2, \theta) \\ \tilde{P} &= 1 \text{ at } (\tilde{Z}, \theta = \pi) \\ \tilde{P} &= \bar{P} \text{ at } (\tilde{Z}, \theta = 0) \text{ and } (\tilde{Z}, \theta = 2\pi) \end{aligned} \tag{3}$$

The film thickness equation in non-dimensional form is expressed as,

$$\tilde{H} = 1 + \varepsilon \cos(\theta - \phi) + \tilde{w}_t \tag{4}$$

In the current analysis, the bump foil structure has been considered as the simple foundation model [10]. The deformation of the foil structure is mainly dependent

on the compliance of the bump structure and the average fluid film pressure along the width of the bearing. Therefore, the deflection of the bump structure in the non-dimensional can be written as,

$$\tilde{w}_t = S(\tilde{P} - 1) \tag{5}$$

Therefore, the deflection of the bump structure is coupled to the Reynolds equation through the film thickness Eq. (4). The pressure field thus obtained from solving the Reynolds equation is integrated using Simpson’s 1/3rd rule to calculate the fluid film forces of the bearing, $\tilde{F}_\varepsilon, \tilde{F}_\phi$ in the ε and ϕ direction, respectively, using Eqs. (6) and (7).

$$\tilde{F}_\varepsilon = - \int_0^{2\pi} \int_0^{L/R} \tilde{P}(\theta, \tilde{Z}) \cos(\theta - \phi) d\theta d\tilde{Z} \tag{6}$$

$$\tilde{F}_\phi = - \int_0^{2\pi} \int_0^{L/R} \tilde{P}(\theta, \tilde{Z}) \sin(\theta - \phi) d\theta d\tilde{Z} \tag{7}$$

Assuming, the rotor to be rigid while mass of M kg acting on each bearing, the journal trajectory has been calculated using the following non-dimensional form of equations of motion [3].

$$\tilde{M} \tilde{W}_0 [\ddot{\varepsilon} - \varepsilon (\dot{\phi})^2] = \tilde{F}_\varepsilon + \tilde{W}_c \cos \phi \tag{8}$$

$$\tilde{M} \tilde{W}_0 [\varepsilon \ddot{\phi} + 2\dot{\varepsilon} \dot{\phi}] = \tilde{F}_\phi - \tilde{W}_c \sin \phi \tag{9}$$

where \tilde{W}_0 is the non-dimensional load and $\tilde{W}_c = \tilde{W}_0(1 + L_a F(t))$, in which the $F(t)$ is the function of periodic load and L_a is the loading amplitude.

The equations of motion are solved under sinusoidal load and non-sinusoidal periodic load to obtain the attitude angle, ϕ and the eccentricity ratio, ε for each time step for the various values of mass parameter, \tilde{M} , which is a function of speed. Thus plotting ϕ and ε for every time step, the journal trajectories are obtained for every \tilde{M} . It has been observed that for a certain value of \tilde{M} , the journal orbit ends in a limit cycle and above which the transition of the rotor motion from stable to unstable state occurs [9]. The corresponding value of \tilde{M} at the transition is known as the critical mass parameter. Hence, the critical mass parameter has been found for different frequency ratio and amplitude of loading.

The three loading conditions that have been investigated in this work are described as follows:

Case 1: Sinusoidal Periodic Load [6]:

$$F_{st}(t) = \sin \Omega \omega t \quad (10)$$

Case 2: Triangular Periodic Load [11]:

$$F_{sst}(t) = \begin{cases} \frac{2t}{T_0} & 0 < t < \pi/\omega, \\ \frac{2t}{T_0} - 2 & \pi/\omega < t < 2\pi/\omega, \end{cases} \quad (11)$$

where t is taken as mod $(2\pi/\omega)$ and T_0 is the time period of the periodic force.

Case 3: Square Periodic Load [11]:

$$F_{sq}(t) = \begin{cases} 1, & 0 < t < \pi/\omega, \\ -1, & \pi/\omega < t < 2\pi/\omega, \end{cases} \quad (12)$$

where t is taken as mod $(2\pi/\omega)$.

3 Results and Discussion

The simulation for the rotors supported on GFB under unidirectional constant load has been validated by the authors in earlier publications [9, 12]. In the present analysis, the length to diameter ratio and compliance coefficient has been considered as 1. The eccentricity ratio has been considered as 0.3 for all the cases. In Fig. 2, the load cycle for the three loading conditions with the loading frequency ratio and loading amplitude of 1 has been shown. The loading frequency ratio indicates the load cycle per revolution of the journal. As for example, the loading frequency ratio of 0.25 means four-load cycle occurs in one journal revolution. The loading amplitude indicates the amplitude of loading compared to the mass of the rotor. Therefore, the loading amplitude 0.25 means the periodic load is one-fourth of the rotor mass.

In Fig. 3, the rotor trajectories for different loading conditions with the loading frequency ratio and loading amplitude, 1 for the mass parameter 2.1, have been shown. It has been observed that the rotor traverses a different trajectory for different loading conditions, although the mass parameter is the same. The trajectory of the rotor under square loading shows higher orbit radius than the other two loading cases (Fig. 3c). Similarly, in case of loading frequency ratio 0.5 and loading amplitude 1, the rotor trajectory under sinusoidal loading just touches the clearance circle

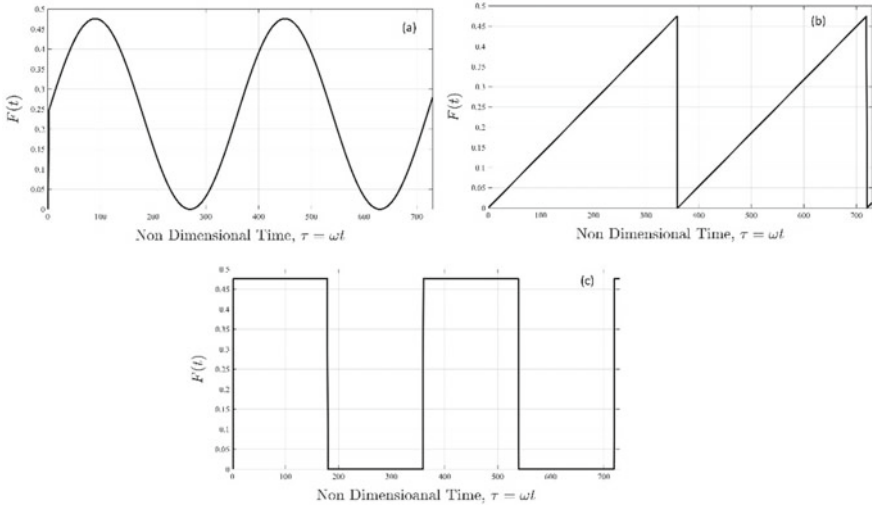


Fig. 2 Load cycle **a** sinusoidal load, **b** triangular load, **c** square load

(Fig. 4a). Under the same loading condition, the trajectory for triangular loading is well below the clearance circle while in case of square loading, the trajectory crosses the clearance, suggesting the instability. Figure 5 shows the rotor trajectories for loading frequency ratio 1, and loading amplitude of 0.5 has been shown. The radius of the orbit of the rotor under triangular loading is less compared to other orbits (Fig. 5b).

3.1 Effect of Loading Frequency Ratio

The loading frequency ratio is the ratio of the frequency of the journal and the loading frequency. In order to investigate the effect of loading frequency ratio, the loading amplitude is assumed to be 1. The effect of the loading frequency ratio on the mass parameter for different loading conditions has been shown in Fig. 6. It has been observed that at low-frequency ratio the critical mass parameter is low. However, as the loading frequency is increased the critical mass parameter increases. In case of square loading, the mass parameter is always lower than the other two cases for all the loading cases. In case of the triangular loading, the mass parameter is higher than the other two cases for all loading frequency ratios. Therefore, it can be concluded that the rotors supported on GFB have low stability when the loading frequency ratio is low.

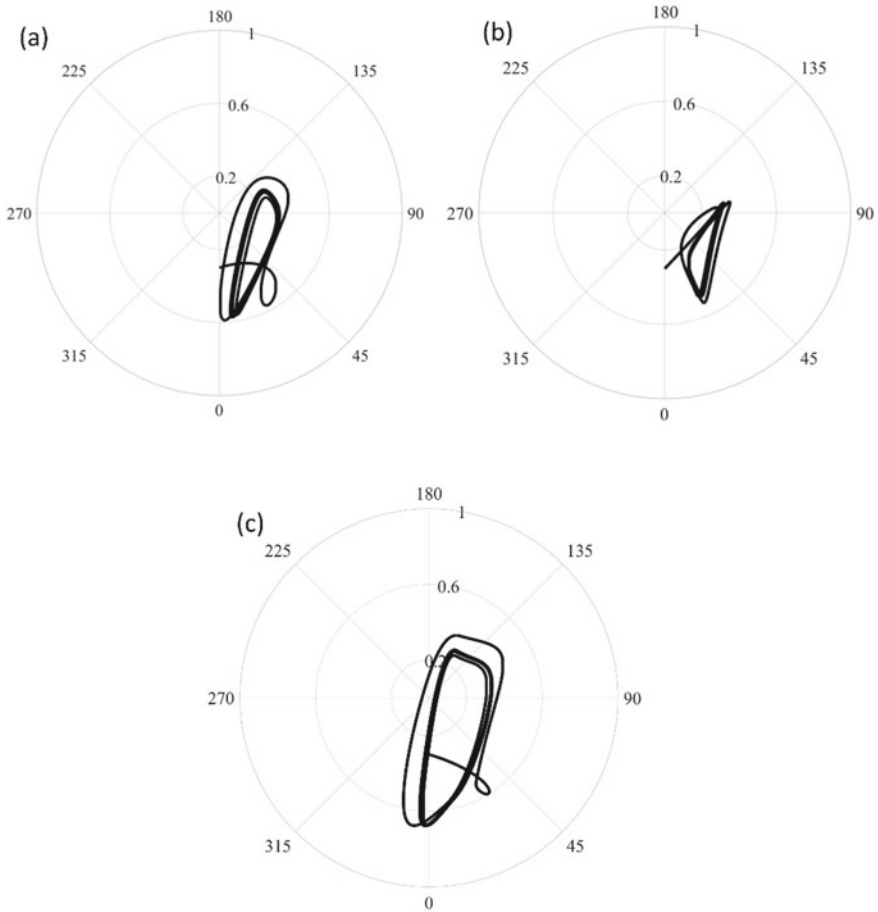


Fig. 3 Rotor trajectories for loading frequency ratio of 1 and loading amplitude 1 **a** sinusoidal, **b** triangular, **c** square

3.2 Effect of Loading Amplitude

The loading amplitude ratio is the ratio of loading and mass of the rotor. In order to investigate the effect of loading amplitude ratio, the loading frequency ratio is kept constant at 1. Figure 7 shows the effect of loading amplitude ratio on the mass parameter for different loading conditions. The mass parameter decreases as the loading amplitude increases for all the loading cases. In case of square loading, as the loading amplitude is increased beyond 1, the critical mass parameter decreases drastically. Nonetheless, the critical mass parameter of square loading is lower than the other two cases for all the loading amplitude. The critical mass parameter of triangular loading has been found to be higher than the other two cases. Therefore,

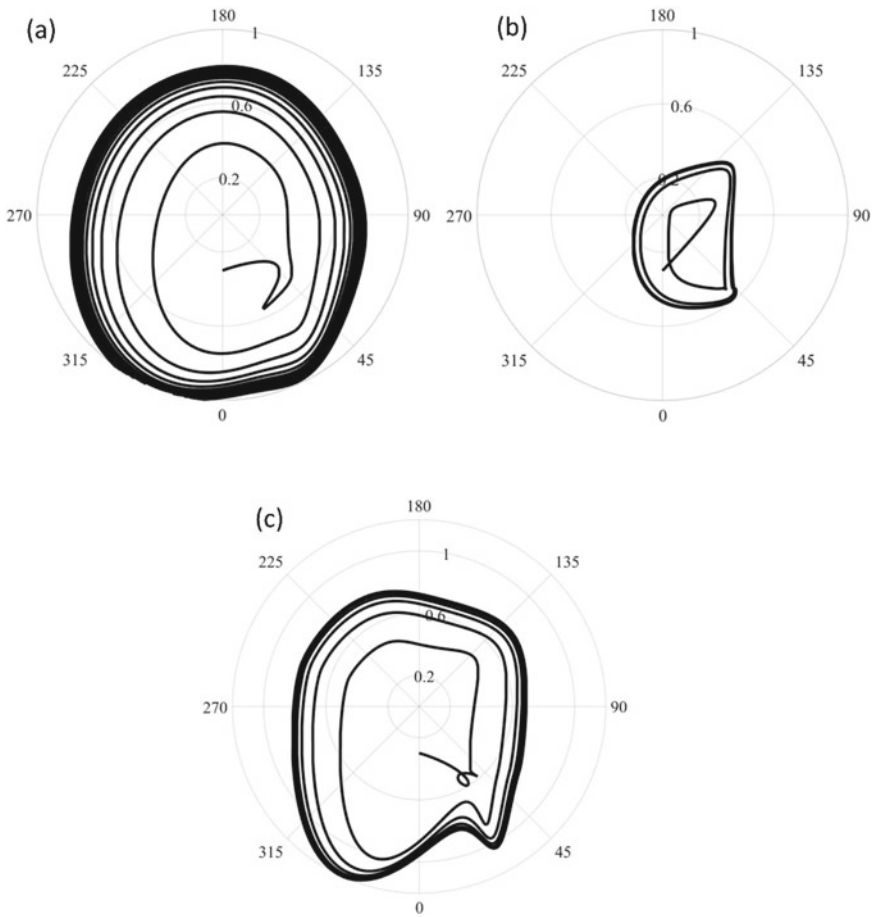


Fig. 4 Rotor trajectories for loading frequency ratio of 0.5 and loading amplitude 1 **a** sinusoidal, **b** triangular, **c** square

the rotor supported on GFB is better in sustaining triangular loading rather than square or sinusoidal loading.

3.3 *Effect on Minimum Film Thickness*

In case of hydrodynamic bearings, the fluid film prevents the journal surface from getting in contact with the bearing inner surfaces and also helps in the generation of the fluid film forces. Therefore, the loading patterns also influence the fluid film thickness. Hence, an investigation of the minimum film thickness under different loading conditions has been carried out. Figure 8 shows the minimum film thickness

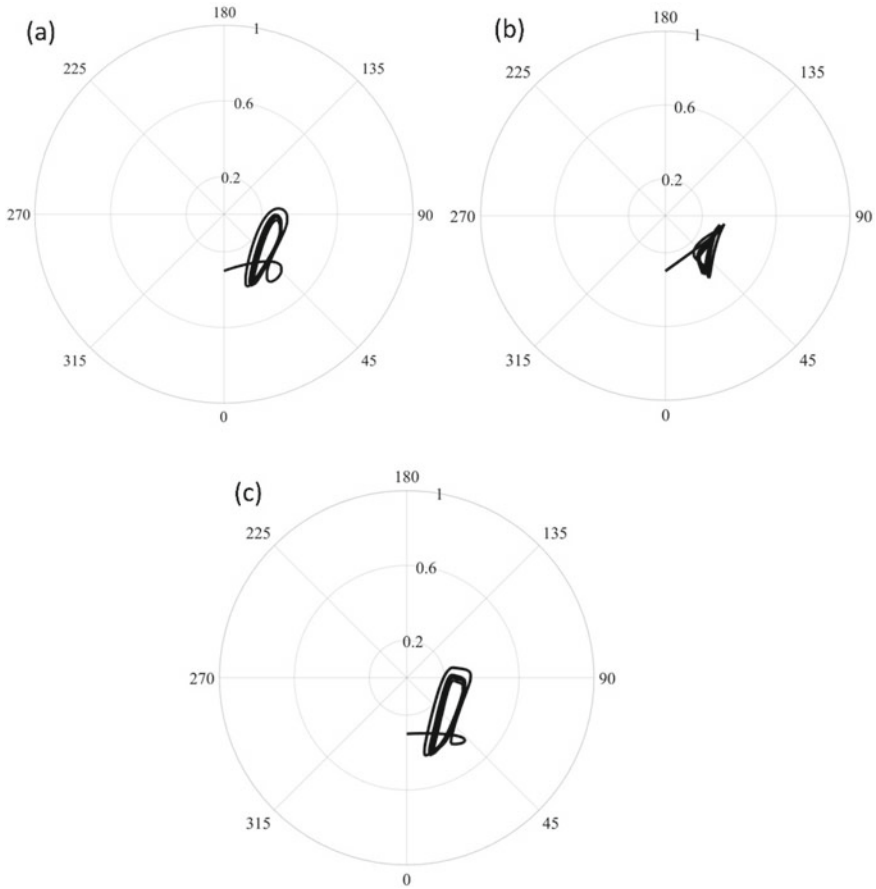


Fig. 5 Rotor trajectories for loading frequency ratio 1 and loading amplitude 0.5 **a** sinusoidal, **b** triangular, **c** square

under different loading conditions for the same mass parameter. In Fig. 8a, the effect of loading frequency ratio of 0.5 and loading amplitude of 1, on the minimum film thickness has been shown. The variation of film thickness is different for the different loading conditions. It has been observed that the minimum film thickness in case of square loading reduces beyond zero indicating the journal surface rubbing the top foil surface of the GFB which leads to the failure of the bearing. In Fig. 8b, the effect of loading frequency ratio 1 and loading amplitude of 1.5 on the minimum film thickness have been shown. The film thickness in case of square loading shows the lowest value of the minimum film thickness for the same amplitude of loading. It has also been observed that, although the mean value of the film thickness is the same for the same amplitude of loading, the fluctuations of the minimum fluid film thickness are different. Therefore, while considering the dynamic loading patterns

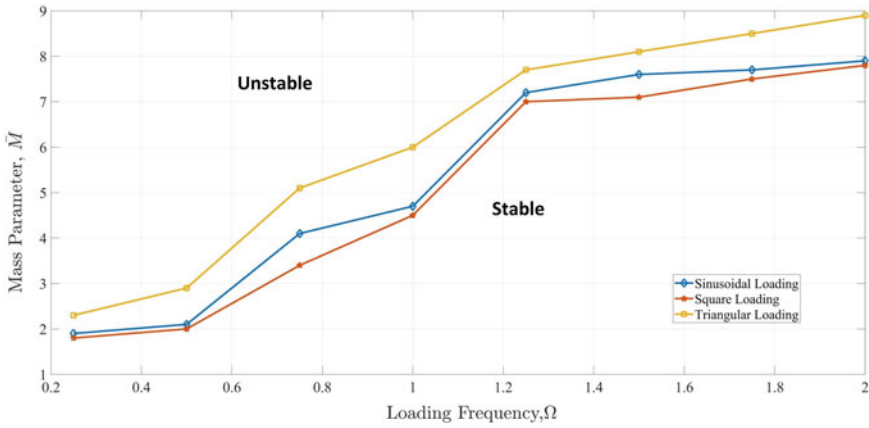


Fig. 6 Effect of loading frequency ratio due to different loading conditions

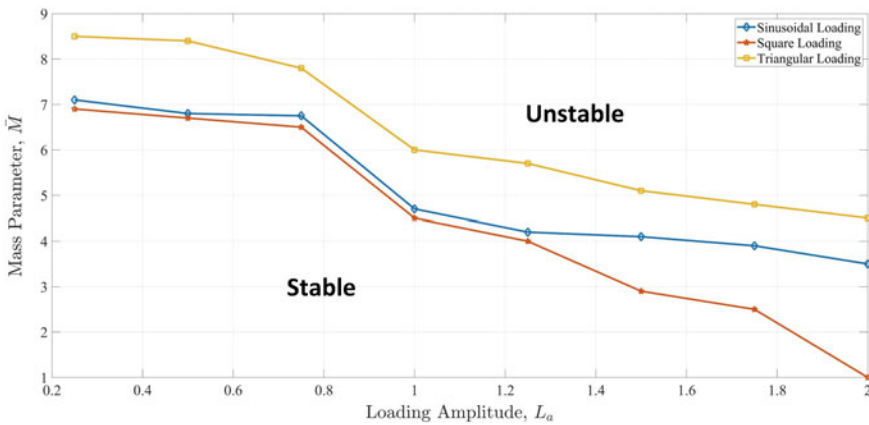


Fig. 7 Effect of loading amplitude due to different loading conditions

the fluid film thickness is greatly affected. Decrement in fluid film thickness leads to the rubbing of top foil with the journal which in turn leads to instability.

4 Conclusion

The stability analysis of rotor undergoing dynamic loading is essential for engineers to understand the system response and predict the instabilities. In this paper, the effect of sinusoidal, triangular, and square loading conditions on the stability of rotor supported on GFB has been studied. It has been observed that as the loading frequency ratio is increased the stability of the rotor also increases. Moreover, the

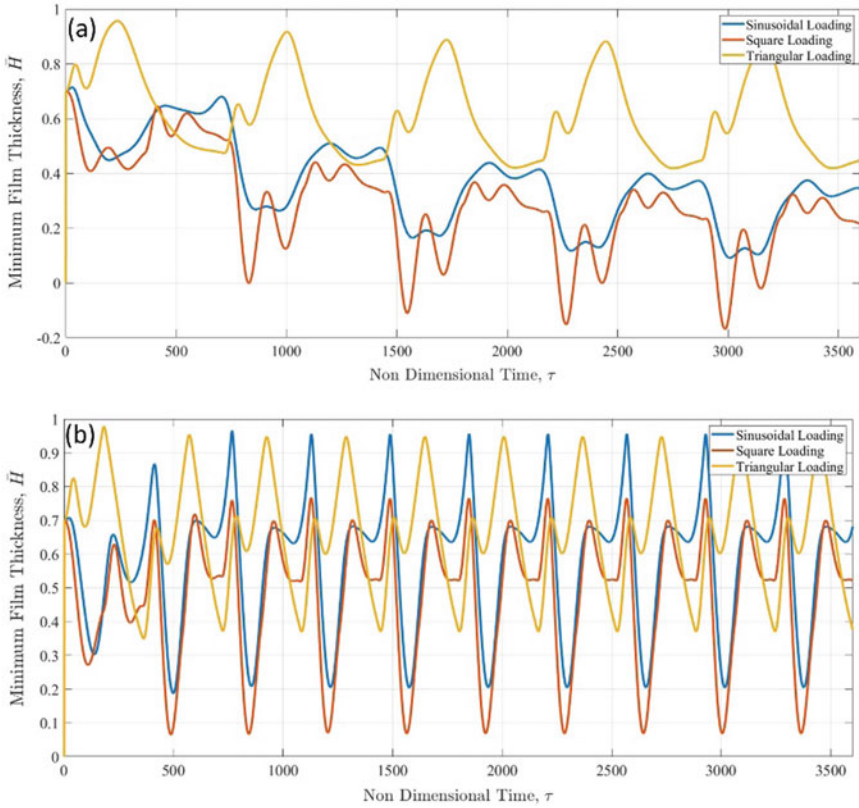


Fig. 8 Minimum film thickness under different loading conditions

high amplitude of loading decreases the stability. The rotor supported on GFB shows better performance under triangular loading rather than sinusoidal or square loading. On the other hand, the GFB supported rotor is susceptible to instabilities due to square loading. Therefore, square loading has to be avoided in rotor supported on GFB. The loading frequency ratio and amplitude greatly affect the film thickness. For the same frequency ratio of loading, the mean film thickness is different for different loading patterns. Although the mean film thickness is the same for the same amplitude of loading, the variations in film thickness are, however, different. The effect of compliance of the bump foil and bearing number on the stability under different loading conditions can be investigated.

References

1. Agrawal GL (1997) Foil air/gas bearing technology—an overview. In: Proceedings of the ASME Turbo Expo, Orlando, Florida, USA, Paper no. 97-GT-347
2. Larsen JS, Santos IF, Osmanski SV (2016) Stability of rigid rotors supported by air foil bearings: comparison of two fundamental approaches. *J Sound Vib* 381:179–191
3. Majumder BC, Brew DE (1987) Stability of a rigid rotor supported on oil-film journal bearings under dynamic load. NASA Technical Memorandum 102309
4. Pai R, Majumdar BC (1992) Stability of submerged four-lobe oil journal bearings under dynamic load. *Wear* 154:95–108
5. Ramesh J, Majumder BC, Rao NS (1995) Non-linear transient analysis of submerged oil journal bearings considering surface roughness and thermal effects. *Proc Inst Mech Eng Part J J Eng Tribol* 201(1):53–61
6. Vijayaraghavan D, Brew DE (1992) Frequency effects on the stability of a journal bearing for periodic loading. *J Tribol* 114:107–115
7. Zarbane K, Zeghloul T, Hajjam M (2011) A numerical study of lubricant film behaviour subject to periodic loading. *Tribol Int* 44:1659–1667
8. Bhore SP, Darpe AK (2012) Nonlinear frequency response analysis of rotor supported on air foil journal bearing under amplitude and frequency dependent external disturbances, (ISMA2012), 17–19 Sept 2012, Leuven, Belgium, pp 1323–1336
9. Basumatary KK, Kakoty SK, Kalita K (2017) Stability analysis of a rigid rotor supported on gas foil bearings under different loading conditions. In: Proceedings of iNaCoMM, 3rd international and 18th national conference on machines and mechanisms, BARC, Mumbai, 13th to 15th Dec, 2017, Paper ID-23. (ISBN No. 978-981-10-8597-0, ISSN-2195-4356. <https://doi:10.1007/978-981-10-8597-0>)
10. Heshmat H, Walowit JA, Pinkus O (1983) Analysis of gas lubricated foil journal bearings. *ASME J Lubricant Technol* 105:647–655
11. Srinivasan K, Thamilmaran K, Venkatesan A (2009) Effect of nonsinusoidal periodic forces in Duffing oscillator: numerical and analog simulation studies. *Chaos Solitons Fractals* 40:319–330
12. Basumatary KK, Kumar G, Kalita K, Kakoty SK (2017) A numerical study on effect of electromagnetic actuator on rigid rotor supported on gas foil bearing. In: ASME gas turbine India conference 2017, Bangalore, India, 7th to 8th Dec, 2017, Paper No. GTINDIA2017-4607, pp V002T05A006. <https://doi:10.1115/GTINDIA2017-4607>

Modal Response of a 4-DOF Cantilever Rotor System with 2 Bearing Support Under Rotor Rub Impact with Unbalance



Aman K Srivastava, Mayank Tiwari, and Akhilendra Singh

Abstract This paper studies the modal response of rotor systems such as turbine engines during rubbing due to unbalance. Rubbing in rotor introduces nonlinearity in the system which leads to phenomena such as rotor stiffening. Experimentation for such cases bears huge cost; hence, nowadays simulation results are widely acceptable. In this paper, a cantilever rotor with 2 bearing support model has been studied for unbalance due to rub in the rotor. Response of such system has been studied on MATLAB. The results reveal the dependence of natural frequency on additional parameter, modal amplitude, which usually is dependent on rotor spin speed in case of linear systems. Effect of parameters such as external damping, stiffness, friction coefficient between the rotor and stator on the modal response of such system has also been presented. The modal response clearly brings out the nonlinear behavior of the rotor system.

Keywords Fan blade off · Cantilever rotor · Rotor dynamics · Stability

1 Introduction

The clearance between rotor and stator is a very critical parameter. Modern-day aero-engine needs to deliver high performance which results in very small clearance. This increases the chances of impact rub between rotor and stator, which introduces unpredictability in the rotor system and can often lead to catastrophic failure. The response in such cases is nonlinear, and system shows many dynamic behaviors such as rotor stiffening, partial rub, annular rub, dry whip, backward whirl, quasi-periodic

A. K. Srivastava (✉) · M. Tiwari · A. Singh
Department of Mechanical Engineering, Indian Institute of Technology, Patna, India
e-mail: 1821me20@iitp.ac.in

M. Tiwari
e-mail: mayankt@iitp.ac.in

A. Singh
e-mail: akhil@iitp.ac.in

and chaotic motion. For many decades now, researchers have been studying the nonlinear behavior of rotors in case of rub impact. Muszynska [1] studied the rotor-stator rub and deduced the stiffening of rotor with increasing speed which introduces nonlinearity in the system. Grazing bifurcation, chaotic and quasi-periodic response of nonlinear rotor with impact rub was studied by Chu and Zhang [2]. Jiang [3] studied the different types of rub in nonlinear rotors such as partial rub, full annular rub, dry whip analytically. Black [4] studied the dry whip of rotors and concluded that it occurs in a particular frequency band between individual natural frequency of rotor/stator to next combined rotor/stator system natural frequency. Using Black's model, Zhang [5] identified multiple modes in dry whip and labeled the whirl region as black. Physical reason for the existence of dry whip in rotor with impact rub was identified to be backward whirl with negative natural frequency of rotor by Jiang [6]. Periodic variation of rotor's stiffness in partial rotor rub which introduces instability was studied by Bently [7].

During impact rub, the modes are not the typical normal linear modes. Instead, nonlinear normal modes (NNM) are found due to additional constraint in the system introduced by impact-rubbing. First mathematical framework to obtain NNM was formulated by Rosenberg [8] and further developed by Shaw and Pierre [9]. Many approximate methods have been developed to formulate NNM [10–12], such as method of multiple scales, numerical methods, and harmonic balance method. Tiwari [13] applied the harmonic balance method along with alternating frequency time domain method (HB-AFT) to solve the nonlinearity introduced due to IRC of ball bearing. Similar nonlinearity can be observed between rotor/stator clearance systems. Hou [14] applied HB-AFT method to study the resonance of dual-rotor system. Cameron [15] applied HB-AFT method to study the steady-state response of nonlinear dynamic systems. Hong [16] studied the complex nonlinear modes of a simply supported rotor with impact rub. He observed the onset of dry whip in case of negative backward whirl.

Harmonic balance method is one of the most tried and tested methods to solve nonlinear dynamic systems. Only prerequisite is the solution should be harmonic. But often the additional constraint such as rub between the rotor/stator leads to nonlinear rub forces. Solving it simultaneously requires the implementation of AFT along with harmonic balance. Nayfeh and Mook [17] have given the harmonic balance method for solving such systems.

Very few literature is available which studies the impact of rotor rub on modal characteristics of rotor with additional constraint. Hong [16] studied such system but with a simply supported rotor with 2-DOF. Hence, the understanding of complex modes in cantilever rotors with nonlinearity due to additional constraint is still limited. This paper aims to study the modal characteristics of such complex nonlinear modes, excited by unbalance leading to impact rub and introduction of additional constraint in cantilever lever rotor with -4 DOF. This type of study holds importance as during events such as FBO, the unbalance leads to rubbing between the stator and rotor, and hence, the nonlinearity in system is introduced.

2 Rotor Model with Additional Constraint

The rotor system here is modeled as a cantilever rotor with circular stator, and the stiffness for rotor/stator interaction is K_c as shown in Fig. 1. The rotor is supported with two ball bearings, and K, C are the stiffness and damping of rotor system. Clearance between the rotor and stator is r_o . The shaft is massless, and disk has a mass m . The stator is a rigid ring and has no mass. Degrees of freedom of rotor are $[x, y, \theta, \Psi]$.

During impact rub, relative motion is observed between the stator and rotor, the relative velocity is given by v_{rel} . This motion causes friction between stator and rotor. And the impact induces normal and tangential additional forces into the system. So, the forces in y also affect the forces in x by μF_y . The other two degrees of freedom become less significant as the forced excitation is applied only in X and Y .

The equation of motion for such impact rub system is given as [16]:

$$m\ddot{x} + c\dot{x} + kx + H(r - r_o)k_c\left(1 - \frac{r_o}{r}\right)(x - \text{sign}(v_{rel})\mu y) = me\omega^2 \cos\omega t$$

$$m\ddot{y} + c\dot{y} + ky + H(r - r_o)k_c\left(1 - \frac{r_o}{r}\right)(y + \text{sign}(v_{rel})\mu x) = me\omega^2 \sin\omega t$$

$$v_{rel} = \omega_w r + \omega r_d$$

where x and y are transverse displacements, r is radial displacement given by $\sqrt{x^2 + y^2}$, v_{rel} is the relative speed at contact point between rotor and stator. μ is friction coefficient. Radius of disk is r_d , ω_w is the whirl angular speed. $H()$ is Heaviside function, and $\text{sign}()$ is symbolic function given by:

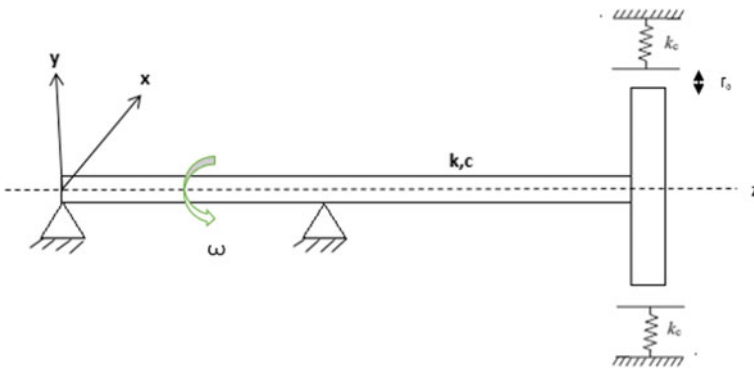


Fig. 1 Schematic representation of cantilever rotor with rotor stator clearance and additional constraint

$$H(x) = \begin{cases} 0 & x \leq 0 \\ 1 & x > 0 \end{cases}$$

$$\text{Sign}(x) = \begin{cases} -1 & x < 0 \\ 0 & x = 0 \\ 1 & x > 0 \end{cases}$$

From the governing equations, it can be seen that additional constraint comes into play only when radial displacement is more than radial clearance. For parametric study, we will convert equation into non-dimensional form [16]:

$$\ddot{X} + 2\zeta \dot{X} + \gamma X + H(R - R_o) \left(1 - \frac{R_o}{R}\right) (X - \text{sign}(V_{\text{rel}})\mu Y) = \Omega^2 \cos \Omega T$$

$$\ddot{Y} + 2\zeta \dot{Y} + \gamma Y + H(R - R_o) \left(1 - \frac{R_o}{R}\right) (Y + \text{sign}(V_{\text{rel}})\mu X) = \Omega^2 \sin \Omega T$$

Non-dimensional variables are given as:

$$X = \frac{x}{e}, Y = \frac{y}{e}, R = \frac{r}{e}, R_o = \frac{r_o}{e}, \omega_1 = \sqrt{\frac{k_c}{m}}, 2\zeta = \frac{c}{\sqrt{k_c m}}$$

$$\Omega = \frac{\omega}{\omega_1}, Y = \frac{k}{k_c}, R = \sqrt{X^2 + Y^2}, T = \omega_1 t$$

$$V_{\text{rel}} = \Omega R_d + \omega R, R_d = \frac{r_d}{e}, \omega = \frac{\omega_w}{\omega_1}$$

2.1 Harmonic Balance Method

In order to study the modal characteristic of a rotor in impact rub, we use the knowledge of complex nonlinear modes proposed by Laxalde [18]. Here the eigenvalue and the characteristic equation are defined in the following form:

$$\lambda = -\beta + i\varpi$$

$$\ddot{X} + 2\zeta \dot{X} + \gamma X + H(R - R_o) \left(1 - \frac{R_o}{R}\right) (X - \text{sign}(V_{\text{rel}})\mu Y) = 0 \quad (1)$$

$$\ddot{Y} + 2\zeta \dot{Y} + \gamma Y + H(R - R_o) \left(1 - \frac{R_o}{R}\right) (Y + \text{sign}(V_{\text{rel}})\mu X) = 0 \quad (2)$$

Here, $\beta = \zeta \omega_o$ is modal damping ratio and $\varpi = \omega_o \sqrt{1 - \zeta^2}$, ω_o is the natural frequency of the rotor without impact rub. Now as per the understanding of complex nonlinear modes, the solution of the above problem can be expressed in the form of a Fourier series:

$$X = a_x^o + \sum_{k=1}^l e^{-k\beta T} (b_x^k \cos k\omega T) \tag{3}$$

$$Y = a_y^o + \sum_{k=1}^l e^{-k\beta T} (b_y^k \cos k\omega T) \tag{4}$$

Similarly, since the rub forces are dependent on x and y only, they can also be expressed in the form of Fourier series:

$$F_x = p_x^o + \sum_{k=1}^l e^{-k\beta T} (q_x^k \cos k\omega T) \tag{5}$$

$$F_y = p_y^o + \sum_{k=1}^l e^{-k\beta T} (q_y^k \cos k\omega T) \tag{6}$$

Putting Eqs. (3) and (4) back into Eqs. (1) and (2), applying harmonic balance on the left- and right-hand side (putting coefficients of sine, cos, and constant term to zero), we get nonlinear algebraic equations of the form:

$$K A_o + P_o = 0 \tag{7}$$

$$\begin{bmatrix} k^2(\beta^2 - \omega^2)\mathbf{M} - k\beta\mathbf{D} + \mathbf{C} & 2k^2\beta\omega\mathbf{M} - k\omega\mathbf{C} \\ k\omega\mathbf{C} - 2k^2\beta\omega\mathbf{M} & k^2(\beta^2 - \omega^2)\mathbf{M} - k\beta\mathbf{C} + \mathbf{K} \end{bmatrix} \begin{bmatrix} b_x^k \\ b_y^k \end{bmatrix} + \begin{bmatrix} q_x^k \\ q_y^k \end{bmatrix} = 0, k = 1, \dots, l$$

where M, K, C are the mass, stiffness, and damping matrices. A_o and P_o denote constants of displacement and rub forces.

The rub forces are dependent on displacement in time domain only. In order to find its value in frequency domain, alternating frequency time (AFT) domain method is used. Firstly, we find out values of x in frequency domain, then we go back to time domain using inverse Fourier transform (IFT) and calculate rub forces and again using Fourier transform, we put the values of rub forces in frequency domain. These steps are done simultaneously. Further, Newton–Rhapson method is used to solve these algebraic equations. For our current study, we have used harmonic balance method to obtain the algebraic equation and get the characteristic equation after solving the coupled equations. That gives us the modal response of the system.

3 Results

The values of the parameters used for HBM method has been listed in Table 1. It can be observed that in case of a nonlinear rotor, the modal frequency of the system varies with the modal amplitude R . While in linear rotor, the modal frequency only varies with the spin speed of the rotor. The modal frequency, before the rubbing starts, remains constant as expected from a linear system. After the modal amplitude crosses the clearance R_o , the response becomes nonlinear and the modal frequency increases and attains a maximum value in case of forward whirl as observed in Fig. 2. The possible explanation for this effect is stiffening of rotor as the rubbing starts.

The modal frequency in this case varies with parameters such as stiffness ' γ ' (Fig. 3), friction coefficient between the rotor and the stator ' μ ' (Fig. 4) and modal damping ' β ' (Fig. 5). As we can clearly observe that the increase in stiffness causes the maximum value of modal frequency to increase.

The modal frequency of the rotor starts decreasing as we start increasing the damping ratio, which is not the case with other two parameters, friction coefficient and stiffness.

Table 1 Values of non-dimensional parameters for modal response

S. No	Parameter	Value
1	R_o	1
2	β	0.1
3	μ	0.15
4	γ	0.1

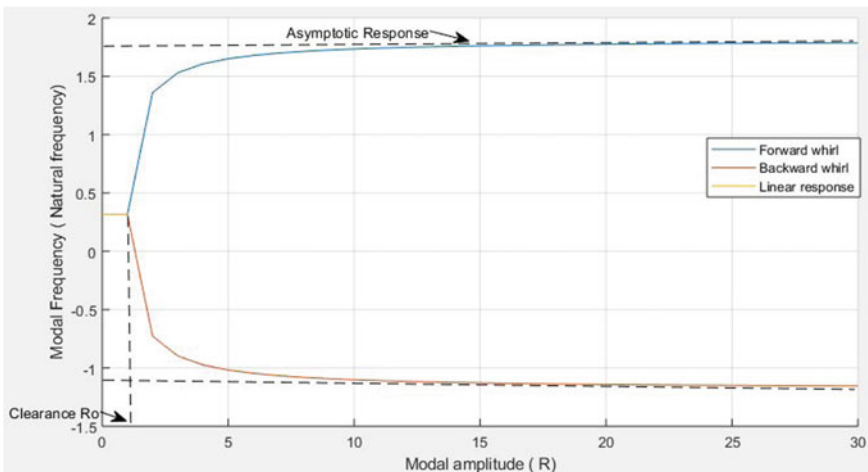


Fig. 2 Modal frequency versus modal amplitude

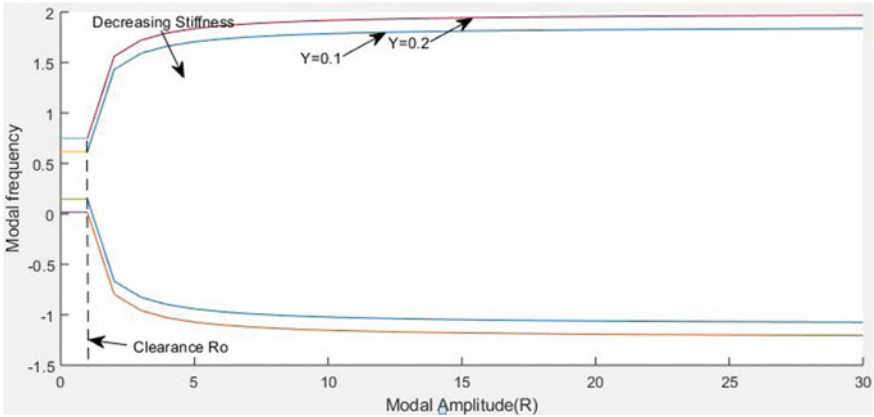


Fig. 3 Effect of variation of stiffness of rotor on modal frequency

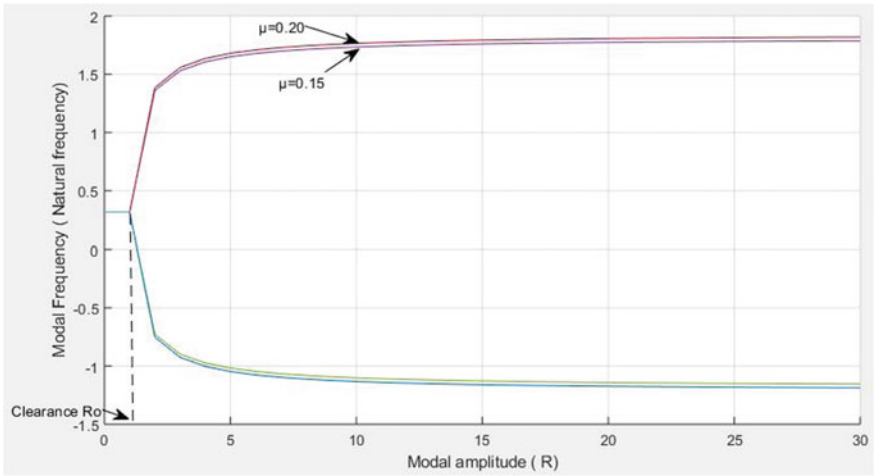


Fig. 4 Effect of variation of friction coefficient between rotor/stator on modal frequency

4 Conclusion

1. The modal response of rotor shows that the modal frequency increases nonlinearly with modal amplitude instead of spin speed of rotor. The physical reason behind such variation is stiffening of the rotor with increase in modal amplitude. The modal frequency reaches a maximum value which is dependent on the parameters such as damping and stiffness.
2. Modal damping causes reduction in the modal frequency. Slight change in the maximum value of modal frequency can also be observed. While in linear rotor case, damping barely affects the natural frequency of the rotor.

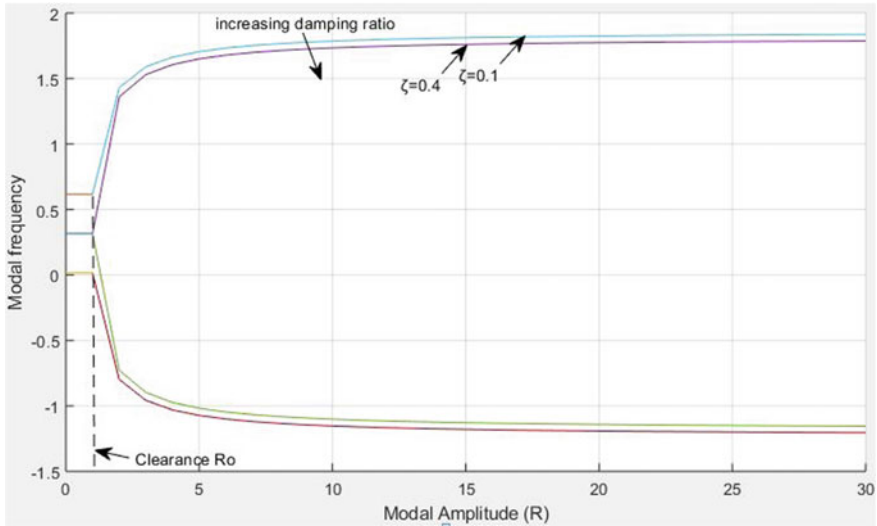


Fig. 5 Effect of variation of damping of rotor on modal frequency

- Friction coefficient between the rotor and the stator also affects the modal frequency. An increase in friction coefficient causes an increase in modal frequency. Hence, the material for the rotor and the stator should be chosen with utmost carefulness as it might lead to instability of the rotor.

The amplitude of the vibration, X and Y , has been assumed in such a way to simplify the model. However, in further study, the solution should be assumed of the form which should comprise of both sine and cosine terms along with decay in order to study the phase response of the rotor.

The current study only determines the modal response of the system, and the forced response or unbalance response will be studied in future work.

References

- Muszynska A (2005) Rotordynamics. Taylor and Francis, New York
- Chu F, Zhang Z (1997) Periodic, quasi-periodic and chaotic vibrations of a rub impact rotor system supported on oil-film bearings. *Int J Eng Sci* 35(10):963–973
- Jun Jiang, Yanhua Chen (2013) Advances in research on nonlinear phenomena in rotor/stator rubbing systems. *Adv Mech* 1:132–148
- Black HF (1968) Interaction of a whirling rotor with a vibrating stator across a clearance annulus. *J Mech Eng Sci* 10(1):1–12
- Zhang W (1988) Dynamics instability of multi-degree-of-freedom flexible rotor systems due to full annular rub. *IMechE C252(88)*:305–308
- Jiang J, Ulbrich H (2005) The physical reason and the analytical condition for the onset of dry whip in a rotor-to-stator contact system. *J Vibr Acoust* 127(6):594–603

7. Bently D (1974) Forced subrotative speed dynamic action on rotating machines. ASME paper 74-PET-16; Petroleum mechanical engineering conference, Dallas, TX, 15–18 Sept 1974
8. Rosenberg RM (1959) Normal modes of nonlinear dual-modes systems. Institute of Engineering Research, University of California
9. Shaw SW, Pierre C (1991) Non-linear normal modes and invariant manifolds. *J Sound Vibr* 150(1):170–173
10. Greenberg HJ, Yang TL (1971) Modal subspaces and normal mode vibrations. *Int J Non Linear Mech* 6(3):311–326
11. Nayfeh AH (1995) On direct methods for constructing nonlinear normal modes of continuous systems. *Modal Anal* 1(4):389–430
12. Slater JC (1996) A numerical method for determining nonlinear normal modes. *Nonlinear Dyn* 10(1):19–30
13. Tiwari et al (2000) Effect of radial internal clearance of a ball bearing on the dynamics of a balanced horizontal rotor. *J Sound Vibr* 238(5):723–756
14. Hou L et al (2017) Application of the HB-AFT method to the primary resonance analysis of a dual rotor system. *Nonlinear Dyn* 88(4):2531–2551
15. Cameron TM, Griffin JH (1989) An alternating frequency/time domain method for calculating the steady-state response of nonlinear dynamic systems. *J Appl Mech Am Soc Mech Eng* <https://doi.org/10.1115/1.3176036>. hal-01333697
16. Hong J et al (2019) Nonlinear Dynamic analysis using the complex nonlinear modes for a rotor system with an additional constraint due to rub-impact. *Mech Syst Signal Process* 116:443–461
17. Nayfeh AH, Mook DT (1995) *Nonlinear oscillations*. Wiley Classic Library
18. Laxalde D, Thouverez F (2009) Complex non-linear modal analysis for mechanical systems: application to turbomachinery bladings with friction interfaces. *J Sound Vibr* 322(4):1009–1025

Dynamic Response Analysis of Rotating Shaft-Bearing System with an Open Crack



S. Bala Murugan , R. K. Behera , and P. K. Parida

Abstract The best of effective design and practices of constructive methods in the analysis of rotor excessive vibration will yield the solutions for the dynamic problems. The extensive effusion of the finite element method (FEM) strongly induced in the area of rotordynamic studies and can give accurate results. Diagnosis of a rotor shaft with crack for its operating conditions is essential to the dynamic systems design. This paper carries the analysis of a finite element model of a flexible rotor-bearing system with a transverse open crack by accounting the various crack depths and internal damping of the shaft. The effect of transverse crack on the system instability regions was found out. It is noted that the natural whirl speeds reduce with increase in crack depths. The system unbalance response and damped natural whirl speeds are presented with undamped orthotropic bearings. The stability of the rotating shaft-bearing system with transverse open crack has also been studied for the various spin speeds and disk eccentricity with the time integration procedure. The phase-plane portraits and frequency-domain diagrams are drawn to study the dynamic behavior. Further, the study is yet to be extended to a fully levitated rotor model supported in active magnetic bearings (AMBs).

Keywords Rotor-bearing system · Transverse crack · Internal damping · Whirl speeds · Stability

1 Introduction

The growing direction of rotating dynamic systems, steer into a complicated analysis of design for the smooth operation. Dynamic analysis of rotating systems has had an extensive investigation over the last few decades. Several methods were developed

S. Bala Murugan (✉) · R. K. Behera
National Institute of Technology, Rourkela, Odisha 769008, India
e-mail: balamurugan8202@gmail.com

P. K. Parida
College of Engineering and Technology, Bhubaneswar, Odisha 751003, India

for the study of shaft-disk-bearing systems over the past few decades. Effective modeling procedures can be split into two significant classes. Finite element method (FEM) is one among them, in which the rotor elements are subdivided into finite number of degrees of freedom and the system motions are represented by ordinary differential equations. Rotating structures are employed broadly through industries from all around the world for energy generation and power transmission. The large vibration amplitudes in rotating systems will lead the shaft/rotor to the propagation of cracks. Followed by these great amplitudes due to cracks allow to unpredicted shutdown and feasible damage of machine elements. The shaft with an open crack is one of the vicious havoc situations in rotordynamic systems analysis particularly in transverse direction.

An important study of the modeling and investigation to get the perfect results for multi-stepped rotor systems was carried for distributed parameters. In his three instances, first, the system is validated with FEM analysis. Second a parametric study in variation of shaft length consists of two different shafts with different diameters. And finally, an unbalance response analysis was carried out by Hong and Park [1]. A new approach for extracting the critical speeds of flexible rotor-bearing system with the transverse shear effect and distributed mass and inertia of the shaft were presented. The external loads are considered with bearing mass, damping, and coupling flexibilities. The critical speeds with the effect of coupling flexibilities were investigated by Joshi and Dang [2]. Modal analysis for continuous rotor-bearing systems for isotropic and anisotropic natural boundary conditions was analyzed. The backward and forward whirl speeds, and mode shapes are calculated for varying rotational speed and boundary conditions by Lee and Jei [3]. The finite element method is used as a key to extract the eigenvalue and stability investigation of rotors by accounting distributed stiffness of bearing and damping. For the two models of rotor on cylindrical journal bearings, tilting pad journal bearings, offset and three-lobe journal bearings were analyzed with (i) uniform and (ii) parabolic distributions, followed by the stability limits were studied by Rao et al. [4]. Sekhar and Dey [5] investigated the rotor-bearing system with transverse crack for the stability threshold by FEM analysis by accounting the different crack parameters, internal dampings and geometric parameters. They found that, the instability is reduced reasonably with an increase of crack depth.

Analysis of flexible rotor-bearing system with symmetrical single-disk derived by lump mass method including shaft stiffness and damping, bearing linear oil-film forces was used to find out the unbalance responses and the feasibilities are discussed by Sanxing et al. [6]. Nelson and McVaugh [7] presented the dynamic modeling of the shaft-disk system supported on bearings which gave the basic idea in this field of rotor dynamics. They suggested a Rayleigh shaft element for modeling a rotating shaft-disk system. The study of rotor model with finite elements incorporates the effects of rotatory inertia, axial load, and gyroscopic moments by applying the consistent matrix method. Natural whirl speeds and unbalance response were presented for two sets of undamped bearing stiffness. However, it excludes the axial torque or shear deformation effect. By employing Timoshenko beam theory, the above approach hypothesizes his previous study to obtain the shape functions by

Nelson [8]. Dimarogonas [9] has presented a review article for crack in a structural member as vibration of cracked structures. He had mentioned about the two families of subharmonic critical speed. A transient vibration analysis of rotor with crack which is passing over critical speeds was studied by Sekhar and Prabhu [10]. The work from the authors shows that the time histories with harmonics and frequency spectrum of model can be obtained with further analysis. The analysis of asymmetric cracked rotor shaft systems for stability concern is much interested topic to study by the rotordynamicists: Some basic cases have been discussed in [11, 12] which generally gives the parametric instability.

2 Finite Element (FE) Model of the Shaft-Bearing System

Finite element method (FEM) is predominantly influenced in rotordynamic analysis. The spinning structures are composed of numerous particles. The equation of motion of the total particles allows the conclusion in the equilibrium of the system. Structures with 'n' numbers of particles will have the generalized coordinates q_i which consists of nodal translational and nodal rotational displacement variables. Displacement components of the nodal commonly chosen by order to be translations and followed by rotations.

2.1 Energy Equations

All rotating particles are part of the structural system, and that it undergoes for elastic deformations. By implementing the linear stress-strain relationship to the system, the elastic potential energy of the structure can be derived. The derivative of this elastic potential energy gives the finite element stiffness matrix of the structure. The dissipative force which acts on the structure indicates the energy lost in it. The kinetic energy of these particles is damped by the above-mentioned forces.

2.2 System Configuration and Coordinates

In present work, a typical flexible overhanging rotor-bearing model is analyzed to understand the system dynamic stability situation. The segment incorporates the discrete bearing, discrete disks with mass unbalances and incorporates a transverse open crack in one of the element. The dynamic equations are solved using the implied time integration procedure, and the stability at different speeds of operation is studied using phase-plane portraits and frequency response. A simplified rotor system by finite element can be standardized using Timoshenko beam theory. Figure 1 shows the typical rotor element model.

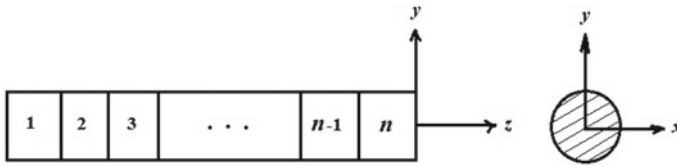


Fig. 1 Turbocharger schematic diagram

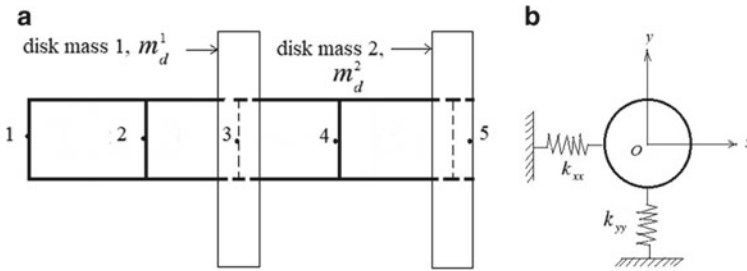


Fig. 2 a Rotor-disk finite element system. b Bearing model of the system

The finite element method is used to model the rotor-disk-bearing system. Here, rotor mass is M and entire length L is divided into n -number of elements along $n + 1$ total node for the rotor z -axis which shown in Fig. 2a. By considering the bending and shearing effects, the kinetic energy (T_s) and potential energy (U_s) of the elements (shaft) in rotation are given as:

$$T_s = \frac{1}{2} \int_0^\ell \rho \{ A(\dot{v}^2 + \dot{w}^2) + I_D(\dot{\theta}_y^2 + \dot{\theta}_z^2) + I_P[\Omega^2 + \Omega(\dot{\theta}_z\theta_y - \dot{\theta}_y\theta_z)] \} ds \quad (1)$$

$$U_s = \frac{1}{2} \int_0^\ell \{ EI(\theta_y'^2 + \theta_z'^2) + kGA[(\theta_y - w')^2 + (\theta_z + v')^2] \} ds \quad (2)$$

2.3 Disk Model

The rigid disk with four degrees of freedom is kept in the respective elemental nodes. Since the disk is rigid, the mass/inertia center of the disks is placed on the particular node which is connecting two elements as shown in Fig. 2a. The disk kinetic energy is given as:

$$T_d = \frac{1}{2}m_d(\dot{v}^2 + \dot{w}^2) + \frac{1}{2}J_d(\dot{\theta}_y^2 + \dot{\theta}_z^2) + \frac{1}{2}J_p[\Omega^2 + \Omega(\dot{\theta}_z\theta_y - \dot{\theta}_y\theta_z)] \tag{3}$$

The work generated by the disk with eccentricity of mass is:

$$W_d = m_d r_d \Omega^2 (w \cos \Omega t + v \sin \Omega t) \tag{4}$$

$$[M_d] = \begin{bmatrix} m_d & & & \\ & m_d & & \\ & & J_d & \\ & & & J_d \end{bmatrix}; [G_d] = \begin{bmatrix} 0 & & & \\ & 0 & & \\ & & 0 & J_p \\ & & -J_p & 0 \end{bmatrix} \tag{5}$$

2.4 Bearing Model

The bearings considered in this analysis which is in Fig. 2b are restricted to follow the governing equations. The bearings were linearized and the stiffness alone is taken into account for the analysis. The stiffness matrix of the bearing elements as follows,

$$[K^b] = \begin{bmatrix} k_{VV}^b & k_{VW}^b \\ k_{WV}^b & k_{WW}^b \end{bmatrix} \tag{6}$$

2.5 System Modeling

The shaft model is expressed with beam elements of circular in cross section. The strain energy and kinetic energies are needed to take into account when modeling a shaft element. The distinctive shaft elemental cross section is estimated with the following equation(s):

$$\begin{Bmatrix} v \\ w \end{Bmatrix} = [N_t(s)]\{q\}; \begin{Bmatrix} \theta_y \\ \theta_z \end{Bmatrix} = [N_r(s)]\{q\} \tag{7, 8}$$

where $[N_t(s)]$ and $[N_r(s)]$ are the shape functional matrices of translation and rotation. These shape functions are well-established by Nelson [8]. By using the above set of equations and by doing the integration along the total length by implementing Hamilton’s principle, the below equations for the finite system, disk, and bearings are obtained:

$$[M_s]\{\ddot{q}_s\} + \Omega[G_s]\{\dot{q}_s\} + [K_s]\{q_s\} = \{F_s\} \quad (9)$$

$$[M_d]\{\ddot{q}_d\} + \Omega[G_d]\{\dot{q}_d\} = \{F_d\} \quad (10)$$

where

$$[M_s] = \int_0^\ell \rho A [N_t]^T [N_t] ds + \int_0^\ell \rho I_d [N_r]^T [N_r] ds \quad (11)$$

$$[G_s] = \int_0^\ell \rho I_p [N_r]^T \begin{bmatrix} 0 & 1 \\ -1 & 0 \end{bmatrix} [N_r] ds \quad (12)$$

$$[K_s] = \int_0^\ell EI [N_r']^T [N_r'] ds + \kappa GA \int_0^\ell \left\{ [N_t]^T [N_t] + [N_r]^T [N_r] + 2[N_t]^T \begin{bmatrix} 0 & -1 \\ 1 & 0 \end{bmatrix} [N_r] \right\} ds \quad (13)$$

Considering the effect of damping on the rotor, the system equation of motion is given as follows:

$$[M]\{\ddot{q}\} + [[C] + \Omega[G]]\{\dot{q}\} + [K]\{q\} = \{F\} \quad (14)$$

where

$$\{q\} = [v_1 \ w_1 \ v_2 \ w_2 \ v_3 \ w_3 \ v_4 \ w_4 \ v_5 \ w_5]^T \quad (15)$$

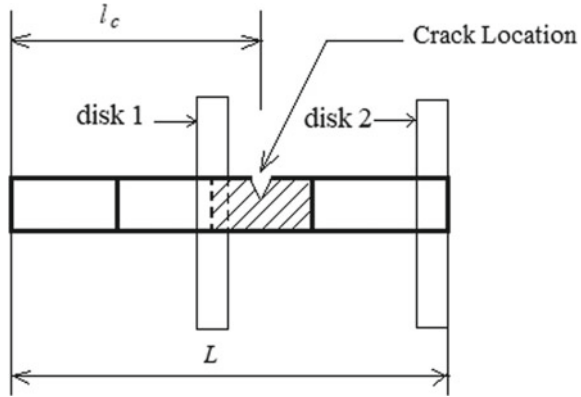
2.6 Crack Model

The transverse crack model leads the parametric inertia or stiffness excitation to the system equation. Due to the parametric inertia, it is required to figure out the effect on the instability regions. Initially, the discrete elements equations of motions of the rotor system are formed. Further, the transverse open crack is considered into account for the current analysis as shown in Fig. 3.

The time-varying stiffness functions of the cracked element are taken as [13],

$$k_{oc}^j(t) = k_{o1}^j + k_{o2}^j \cos(2(\Omega t + \varphi)) \quad (16)$$

Fig. 3 Finite model of the rotor-disk system with open crack



2.7 Final Rotor System Model with Crack

The overall equation of motion of the cracked rotor system is given as,

$$\begin{aligned}
 & [M^S]\{\ddot{q}^S(t)\} - \Omega[G^S]\{\dot{q}^S(t)\} \\
 & + \left([K^S] + [\tilde{K}(t)] \right) \{q^S(t)\} = \{Q^S\}_{4n \times 1}
 \end{aligned}
 \tag{17}$$

where $[M^S]$, $[G^S]$, $[K^S]$, and $[\tilde{K}(t)]$ are the global mass, gyroscopic, stiffness, and cracked elemental matrices having dimensions in $4(n + 1) \times 4(n + 1)$. The constant spin speed (Ω) brings the equation of motion of the system in the time-varying second order periodic differential equation with the open crack frequency of 2Ω .

3 Theoretical Results and Discussions

The rotor-bearing-disk system with crack is distributed as 4 elements and the disk with mass unbalance as given in Fig. 3. The values of the mechanical and physical properties are listed in Table 1. The finite element equations are solved with MATLAB. The equations compute the nodal degrees of freedom by the defined number of elements. Hence, in the beginning stage it calculates the natural frequencies of the system and subsequently gives the Campbell diagram. However, need to give the value of bearing stiffness coefficients manually to avoid further calculations. This procedure helps to verify the system assembly.

The cracked shaft (open crack) equation of motion incorporates the stiffness matrix as constant $(K - K_c)$ in the investigation part. Unbalance mass of $m_u = 10^{-6}$ kg m is considered for the fully opened crack condition at $t = 0$. The result in Fig. 4a shows the unbalance response and critical speed of the rotor-bearing-disk system at

Table 1 Mechanical and physical properties of the shaft elements and rigid disk

Properties	Values	Properties	Values
Density of shaft material (kg/m ³)	7810	MOI of disk, (kg mm ²)	41,750 & 168,100 ($I_{yy} = I_{zz}$)
Young's modulus, E (GPa)	197		83,500 & 336,200 (I_{xx})
Shear modulus, G (GPa)	80	Bearing stiffness coefficients (N/m)	3.503×10^7 ($k_{xx} = k_{yy}$)
Radius of shaft (m)	0.016		-8.756×10^8 ($k_{xx} = k_{yy}$)
Length of shaft (m)	0.526	Bearing clear. (micr.)	20
Radius of disk, (m)	0.156	Mass unbalance, m_u (kg m)	10^{-6}
Mass disk, m_d (kg)	4.4783		

Fig. 4 a UBR of finite system with crack.
b Campbell plot with Ω_{cr} of 1Xhamonic

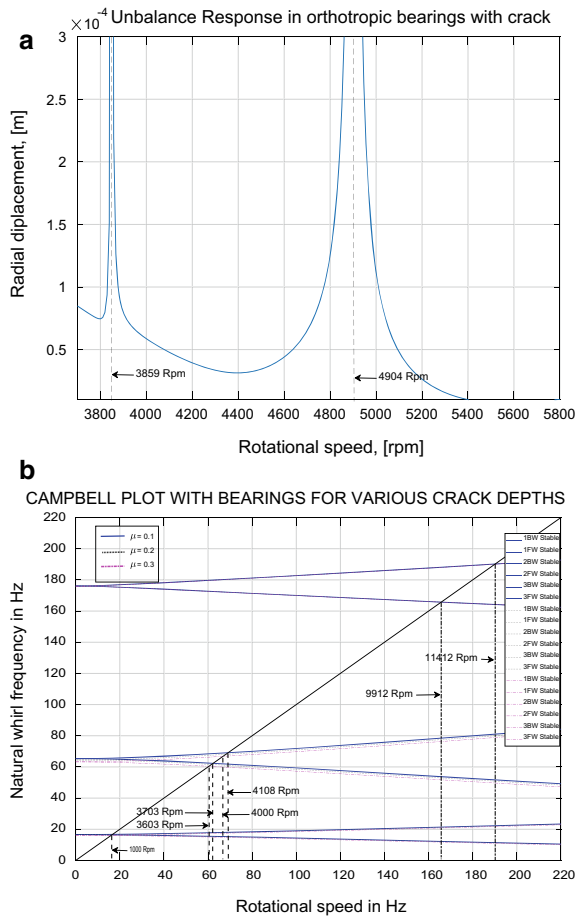


Table 2 List of first six natural frequencies (f_n) with non-dimensional crack depth (μ) at ($L_{\text{crack}} = 0.4235$ m)

Freq. (Hz)	Uncracked (Hz)	μ			Freq. (Hz)	Uncracked (Hz)	μ		
		0.1	0.2	0.3			0.1	0.2	0.3
1st	15.01	14.62	14.39	14.05	4th	63.91	63.31	62.19	61.87
2nd	15.09	14.61	14.40	13.98	5th	170.17	169.94	169.39	169.74
3rd	63.57	63.34	63.18	63.92	6th	170.33	169.86	169.05	169.29

3859 and 4904 rpm with crack. The natural frequencies for various non-dimensional crack depth μ , [14] are listed in Table 2.

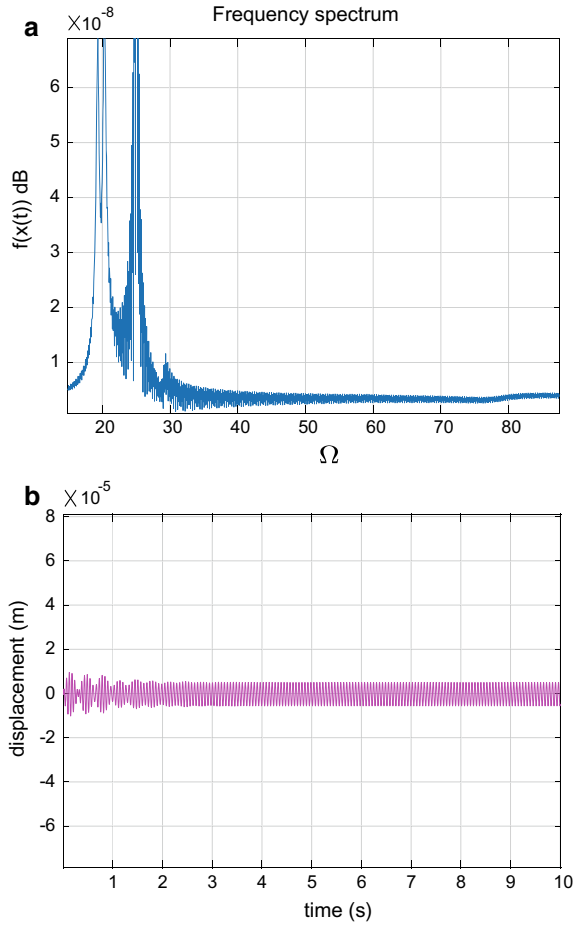
For an open crack at element 3, the natural whirl speeds were plotted for the non-dimensional crack depth $\mu = 0.1, 0.2,$ and 0.3 which shown in Fig. 4b. It clarifies the action of cracked rotor system responds for backward whirl when the crack begins to look at very minimum crack depths, and it can be also understood that the amplitude change with an increase in crack depth values for critical forward and backward whirling speeds. The frequency spectrum of the model with crack influence is plotted in Fig. 5a which shows the disturbed frequencies due to the stiffness of the rotor. For the displacements at disk nodes for both the disk at $\Omega = 1200$ rpm were plotted and shown in Fig. 5b.

The phase portraits for the system with open crack, behave as periodic with a little unstable center at $\Omega = 1200$ rpm which shown in Fig. 6a, b. This effect also can be observed from the disturbed frequency response curves with crack which is shown in Fig. 5a. The viscous damping factors of 0.01 and shear coefficient of 0.65 are considered in the system modeling.

4 Conclusions

This study carries well-organized methods to solve and understand the behavior of the rotor shaft-bearing-disk system with crack. The general solution of the rotor shaft system with open crack has been included in the study to understand the behavior. The outcome from the method which was followed gives the important observations of the natural whirls, cracked unbalance vibration amplitudes, displacements at disk nodes, and phase-plane diagrams. The behavior of the cracked rotor-bearing-disk system for various crack depths with specific speeds was carried. Hence, the approach helps to predict the changes with rotor orbit shapes in specific rotor critical speeds considered at very minimum crack depths.

Fig. 5 **a** Frequency spectrum of the system.
b Displacements at disk 1 & 2 at $\Omega = 1200$ rpm



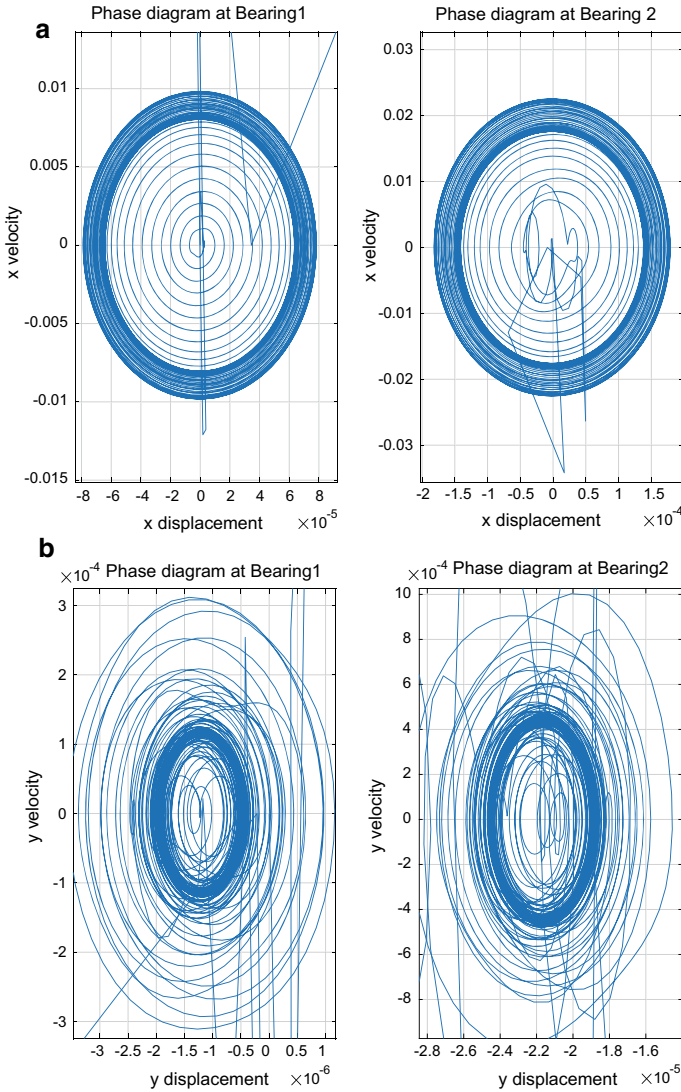


Fig. 6 **a** Phase portraits at disk 1 in $\sim x$ -direction. **b** Phase portraits at disk 2 in $\sim y$ -direction

References

1. Hong SW, Park JH (1999) Dynamic analysis of multi-stepped, distributed parameter rotor-bearing systems. *J Sound Vib* 227(4):769–785
2. Joshi BB, Dange YK (1976) Critical speeds of a flexible rotor with combined distributed parameter and lumped mass technique. *J Sound Vib* 45(3):441–459
3. Lee CW, Jei YG (1988) Modal analysis of continuous rotor-bearing systems. *J Sound Vib* 126(2):345–361

4. Rao BS, Sekhar AS, Majumdar BC (1996) Analysis of rotors considering distributed Bearing stiffness and damping. *Comput Struct* 61:951–955
5. Sekhar AS, Dey JK (2000) Effects of cracks on rotor system instability. *Mech Mach Theory* 35:1657–1674
6. Zhao S, Xu H, Meng G, Zhu J (2005) Stability and response analysis of symmetrical single-disk flexible rotor-bearing system. *Tribol Int* 38:749–756. <https://doi.org/10.1016/j.triboint.2004.11.004>
7. Nelson HD, McVaugh JM (1976) The dynamics of rotor-bearing systems using finite elements. *J Eng Ind*, 593–600
8. Nelson HD (2010) A finite rotating shaft element using Timoshenko beam theory. *J Mech Des* 102:793. <https://doi.org/10.1115/1.3254824>
9. Dimarogonas AD (1996) Vibration of cracked structures: a state of the art review. *Eng Fract Mech* 55:831–857
10. Sekhar AS, Prabhu BS (1994) Transient analysis of a cracked rotor passing through critical speed. *J Sound Vib* 173(3):415–421
11. Rao JS (2009) *Rotor dynamics*. New Age International (P) Limited, New Delhi
12. Genta G (2005) *Dynamics of rotating systems*. Springer, USA
13. Al-shudeifat MA, Butcher EA, Stern CR (2010) General harmonic balance solution of a cracked rotor-bearing-disk system for harmonic and sub-harmonic analysis: analytical and experimental approach. *Int J Eng Sci* 48:921–935. <https://doi.org/10.1016/j.ijengsci.2010.05.012>
14. Sinou JJ, Lees AW (2005) The influence of cracks in rotating shafts. *J Sound Vib* 285:1015–1037. <https://doi.org/10.1016/j.jsv.2004.09.008>

Rotordynamic Design Studies of Medium Thrust Class Twin Spool Engine



R. Siva Srinivas, S. E. Muthu, and Girish K. Degaonkar

Abstract Rotordynamic design studies are an important part of gas turbine design and development since there is a direct influence on the structural integrity, health and fatigue life of rotating as well as static components. Rotordynamic analysis primarily involves the estimation of critical speeds, mode shapes, strain energy distribution, kinetic energy distribution and response to unbalance. The important parameters in design studies include number of bearings, location of bearings, geometric properties of rotor, bearing support design, stiffness and damping in bearing planes. The design procedure is iterative and constraints imposed by the layout should be considered during design modification. In this work, parametric study of various configurations of the rotor-bearing system of a medium thrust class turbofan engine have been presented. The modelling and analysis have been performed in DyRoBeS Rotor software using Timoshenko beam element. The chosen general arrangements are compared against each other to arrive at the optimum configuration from the point of view of overall dynamic behaviour.

Keywords Critical speed · Mode shape · Bearing · Twin spool · Timoshenko beam

Nomenclature

BS Bearing support
FOD Foreign object damage
HPC High-pressure compressor

R. S. Srinivas (✉) · S. E. Muthu · G. K. Degaonkar
Aero Engine Research and Design Centre, Hindustan Aeronautics Limited, Bangalore 560093,
India
e-mail: wydeek@gmail.com

S. E. Muthu
e-mail: esakki.muthu.hal@gmail.com

G. K. Degaonkar
e-mail: girish.degaonkar@hal-india.com

© Springer Nature Singapore Pte Ltd. 2021
J. S. Rao et al. (eds.), *Proceedings of the 6th National Symposium on Rotor Dynamics*, Lecture Notes in Mechanical Engineering,
https://doi.org/10.1007/978-981-15-5701-9_43

HPT	Low-pressure turbine
ISB	Intershaft bearing
Irc	Internal radial clearance
LPT	Low-pressure turbine
LPC	Low-pressure compressor

1 Introduction

A twin spool gas turbine rotor-bearing system using beam, mass and spring elements and performed fan blade-out analysis was modelled in [1]. The time transient response of the system is obtained by solving the system governing equations using new mark- β integration scheme. The same modelling procedure is adopted in the current paper [2]. The twin spool rotor-bearing system of RM-12 engine was modelled using ANSYS, and the results obtained were compared with those obtained from DyRoBeS model in [2]. The rotor-bearing system of a rotor test rig was modelled using Euler–Bernoulli beam elements in [3]. The response of turbofan engine due to FOD events was estimated using wavelet analysis in [4]. The unbalance response characteristics of gas turbine rotor system using transfer matrix method were estimated in [5].

In the present work, preliminary rotordynamic analysis for five different arrangements of twin spool engine rotor-bearing system has been performed using DyRoBeS software. Critical speeds, mode shapes, energy distributions, and response characteristics for all five configurations are shown. As the work is still under progress, actual values of masses of rotors, stiffness and damping parameters of bearings and supports are not given in the paper. The reader has to bear in mind that the results shown in the paper are obtained at some initial stage of design, and therefore, the emphasis of this paper is more on the design procedure than the results tabulated. The rotor-bearing design procedure is essentially iterative due the interdisciplinary nature of gas turbine engine design process. Each configuration is shown to have its own merits and demerits which are discussed in the conclusion.

2 Rotor-Bearing Arrangement of Twin Spool Engine

2.1 Modelling of Rotor-Bearing System

Modelling of rotor system has been performed using 2 node Timoshenko beam elements in DyRoBeS. Discs have been modelled as lumped masses at appropriate nodal locations. Mass and inertial properties of discs have been considered. Stiffness of bearings is modelled using linear constant bearing element. The stiffness and mass of supports and housings are also considered. However, the values are not listed here.

Table 1 Materials of various rotor components

Component	Material	Component	Material
HPC rotor 1–4 stages	Titanium alloy	LPC shaft	Steel alloy
HPC rotor 5th stage	Nickel alloy	LP CT shaft	
HPT rotor	Nickel alloy	HP CT shaft	
LPC rotor 1–3 stages	Titanium alloy	HP bearing shaft	
LPT rotor	Nickel alloy	HP, LP bearing shafts	

The viscous damping provided by external dampers is accounted for by assuming a reasonable damping coefficient for all bearings housed inside bearing support. Intershaft bearing is assumed to have nominal damping coefficient. The material properties for the various rotor elements have been assigned based on Table 1. The models of the five configurations are shown in Fig. 1c–g. Figure 1a, b shows the HP and LP spools of configuration-1. The notations used for various bearing supports in Figs. 4, 5 and 6 are shown in Table 2.

2.2 Merits and Demerits of Various Configurations

Table 3 lists out the salient features of various configurations with the associated advantages and disadvantages in their implementation in the layout.

2.3 Critical Speeds, Mode Shapes and Energy Distribution

Critical speed analysis was performed on configuration-1 to obtain the mode shapes and corresponding energy distributions at each critical speed. The Campbell diagram of the same is shown in Fig. 2. It can be seen that both HP and LP modes are excited throughout the operating range. The distinction between modes is clearer in Fig. 3 where mode shapes of configuration-1 are shown. The Campbell diagrams and mode shapes of other configurations are not shown due to the limit on the paper length. The distribution of energies in rotor and bearing supports varies between each configuration due to the different bearing arrangements. The %SE in LP and HP shafts is shown in Table 4. It can be seen that configurations 1, 2 and 3 have lesser %SE in shafts than configurations 4 and 5 across all the modes. This goes to show the benefit of having intershaft bearing at the turbine end. Figure 4 shows the SE % in bearing supports for various modes for all configurations.

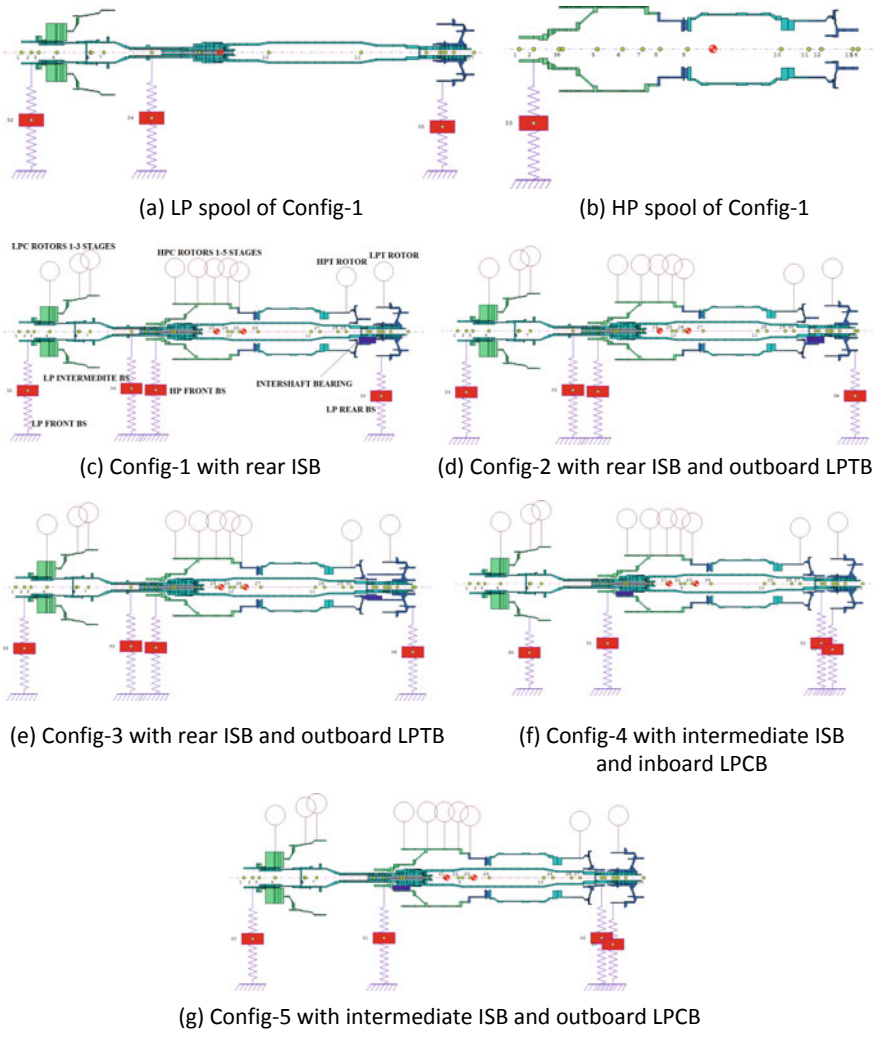


Fig. 1 Various configurations of twin spool rotor-bearing system

Table 2 Bearing support notations

BS-1	LP front bearing support
BS-2	LP intermediate bearing support
BS-3	HP front bearing support
BS-4	LP turbine bearing support

Table 3 Salient features of various rotor-bearing configurations

Configuration	Salient features	Advantages/disadvantages
1	Intershaft bearing at the turbine end; inner race on LP shaft; outer race on HP shaft; outboard LP compressor bearing; intermediate LP shaft bearing	Ease of assembly of Intershaft bearing; needs a separate bearing housing and lubrication system for LP front bearing which adds to weight; conventional lube transfer; <i>irc</i> hardest to control
2	Intershaft bearing at the turbine end; outboard LP compressor bearing; intermediate LP shaft bearing; outboard LP turbine bearing	
3	Intershaft bearing outer race on LP spool and inner race on HP spool	Better <i>irc</i> control, Less wear, Higher stiffness; Intershaft lube transfer
4	Intershaft bearing at midspan with outer race on HP spool and inner race on LP spool; inboard LP front bearing	Common bearing housing for LP and HP turbine bearings; Overhanging LP disc not desirable; Common lubrication to HP, LP and Intershaft front bearings
5	Intershaft bearing at midspan with outer race on HP spool and inner race on LP spool; outboard LP front bearing	Common bearing housing for LP and HP turbine bearings; better LP disc unbalance response; Needs a separate bearing housing and lubrication system for LP front bearing which adds to weight

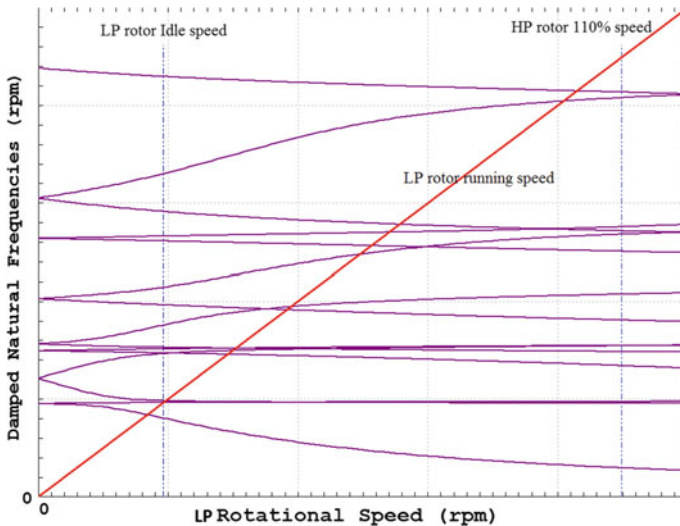


Fig. 2 Campbell diagram of config-1 (LP rotor excitation)

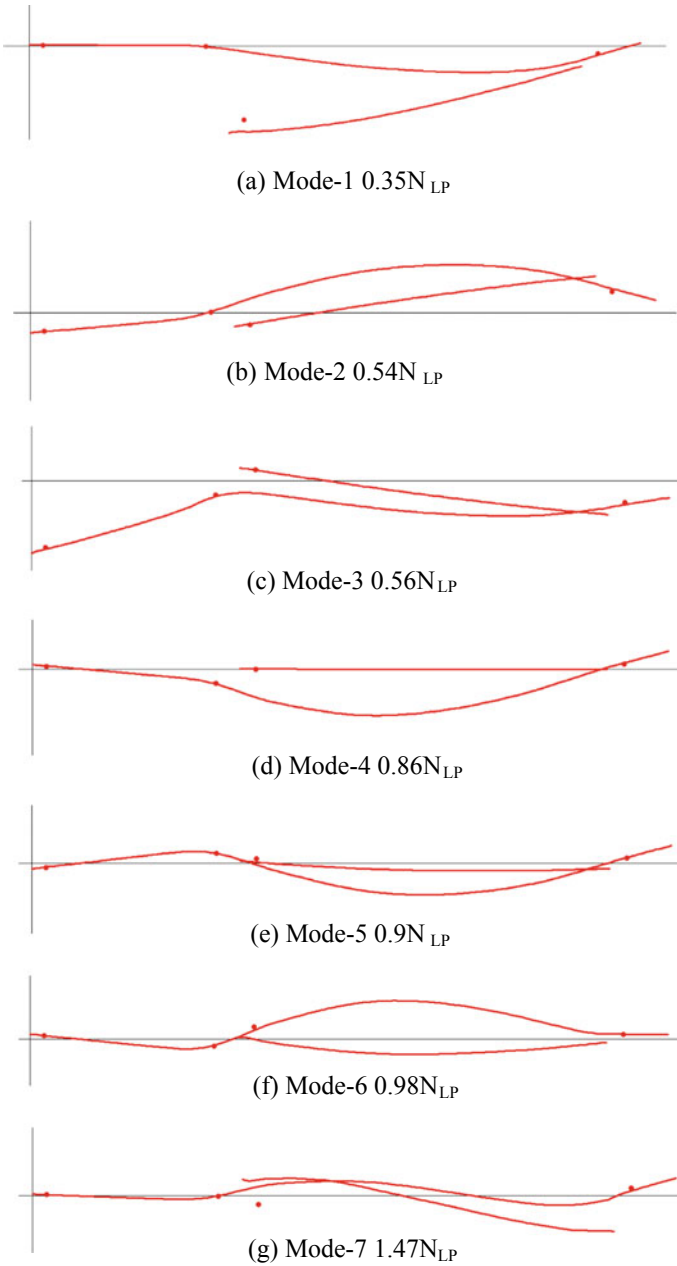


Fig. 3 Mode shapes of config-1 rotor-bearing system

Table 4 Strain energy distribution in LP and HP shafts

% SE		Config-1	Config-2	Config-3	Config-4	Config-5
Mode-1	LP shaft	2	49	39.85	6.3	3
	HP shaft	6	4.4	4.93	5	5
Mode-2	LP shaft	10	23.45	29.54	5.5	14
	HP shaft	2	1.25	0.98	1	0.25
Mode-3	LP shaft	3	3	3	0.83	0.83
	HP shaft	1	1	1	1	1
Mode-4	LP shaft	33	20	15.8	1	1
	HP shaft	1	1	0.12	5.33	5.33
Mode-5	LP shaft	37	14.8	15.3	4.3	3.6
	HP shaft	8	4.3	4.55	33.1	31.15
Mode-6	LP shaft	26	36.5	31.5	79.7	80.6
	HP shaft	26	19.8	23.8	7	1.35
Mode-7	LP shaft	8.1	24	29.8	37	56.2
	HP shaft	20.4	20	18.2	7	12.22

2.4 Response to Unbalance

An in-phase residual unbalance value of 2 cm g is applied at each rotor stage based on the rotor weight and maximum operating speed and G2.5 quality grade of ISO 1940/1 standard. Though the permissible unbalance varies from stage to stage, the highest value of all is chosen and applied at all stages. The synchronous response at discs and bearing supports is estimated. Figure 6 shows the response in config-1 rotor system at the four bearing supports. The KE distribution of bearing supports shown in Fig. 5 is not translated to higher response at the corresponding supports in Fig. 6 due to the fact that unbalance is located at discs. Since Mode 2 and Mode3 are close to each other (refer Fig. 3b, c), the response peaks are indistinguishable in Fig. 8.

Shown in consistent with the KE distribution shown in Fig. 5. Likewise, Fig. 7 shows the KE distribution in all the rotors of both HP and LP stages. The response shown in Fig. 8 follows the pattern shown in Fig. 7.

3 Conclusions

The dynamic characteristics of various rotor-bearing configurations have been studied. The modelling has been performed using 2 node Timoshenko beam elements in DyRoBeS. Discs have been modelled as lumped masses at appropriate nodal locations. LP shaft excited critical speeds have been shown for various configuration-1



Fig. 4 % SE distribution in bearing supports for various configurations

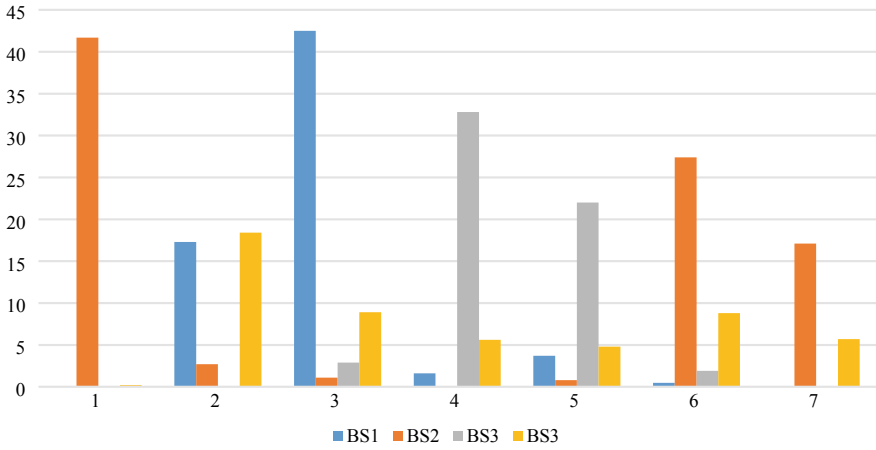


Fig. 5 %KE distribution in bearing supports in Config-1 for various modes

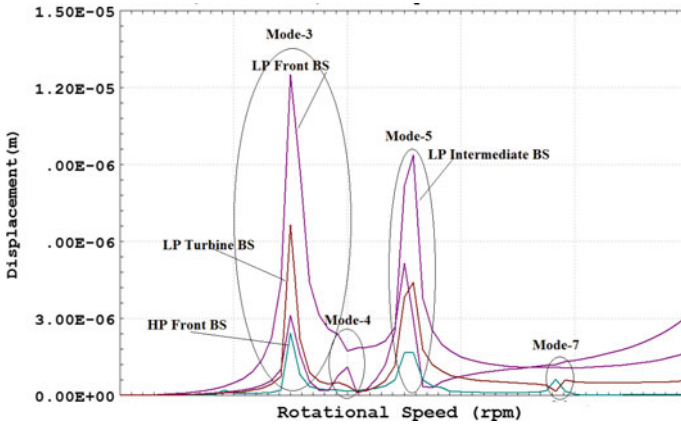


Fig. 6 Unbalance response of bearing supports in Config-1 for various modes

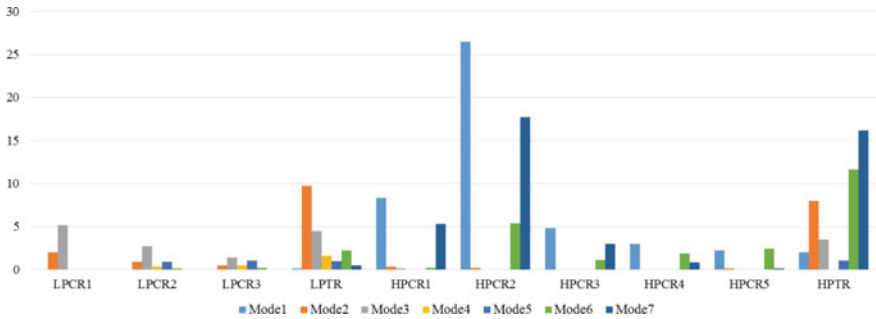


Fig. 7 %KE distribution in rotor stages in Config-1 for various modes

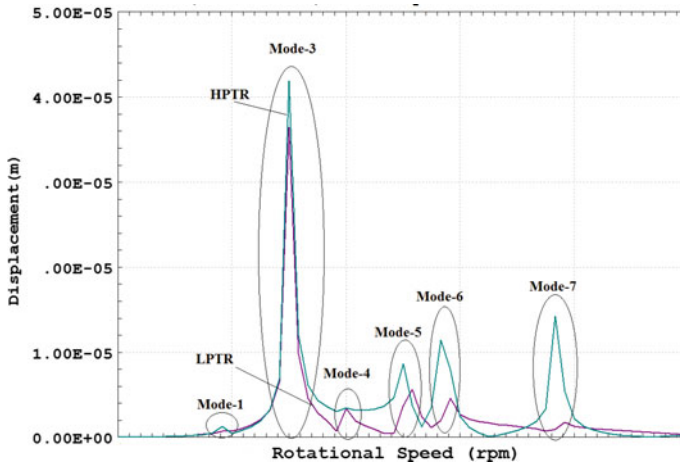


Fig. 8 Unbalance response of HPTR & LPTR in Config-1 for various modes

shown to have its own advantages and disadvantages. The choice of the general arrangement is primarily decided by the placement of critical speeds, energy distribution, and response characteristics. Additionally, rotor/stator weight, lubrication arrangement also influence the final rotor dynamic design. If the intershaft bearing is located at intermediate position, it has to be essentially ball bearing to accommodate roller bearing at the turbine end. The disadvantage in this configuration is that it would be difficult to obtain the axial load acting on the intershaft ball bearing as both the races are rotating. With rear intershaft roller bearing, the LP front bearing would be a ball bearing making the axial load measurement convenient. Also, from the point of view of ease of assembly rear intershaft bearing is preferred. Hence, Configuration-2 is most preferable followed by Configuration-1. If the SE% in LP shaft is large, then positioning intershaft bearing at intermediate location becomes imperative. In such a case, configuration-5 is preferred over configuration-4. The magnitude of unbalance response at various nodal locations along the rotor length depends on the mode shapes excited. This again depends on the axial location, magnitude and phase of unbalance. The paper deals with the preliminary rotordynamic design aspects and does not delve deep into other design aspects such as design of nonlinear dampers, influence of rolling element bearings on the rotordynamic behaviour.

Acknowledgements The authors thank Dr. T. R. Rajanna, Chief Designer, AERDC for his permission to publish this work.

References

1. Yu P, Zhang D, Ma Y, Hong J (2018) Dynamic modelling and vibration characteristics analysis of the aero-engine dual-rotor system with Fan blade out. *Mech Syst Sig Process* 106
2. Nivas DSK (2012) Rotordynamic analysis of RM12 jet engine rotor using ANSYS. MS thesis, Blekinge Institute of Technology, Karlskrona, Sweden
3. Ngo VT, Xie D, Xiong Y, Zhang H, Yang Y (2013) Dynamical analysis of a rig shafting vibration based on finite element. *Front Mech Eng* 8
4. Turso J, Lawrence C, Litt J (2004) Reduced order modelling and wavelet analysis of turbo fan engine structural response due to foreign object damage events. NASA
5. Yang W, Liang M, Wang L, Yuan H (2018) Research on unbalance response characteristics of gas turbine blade-disk rotor system. *J Vibroeng* 20(4)

Rotor Structural Dynamics

Improving Structural Integrity of a Centrifugal Compressor Impeller by Blading Optimization



E. K. Vivek, Lakshya Kumar, R. Senthil Kumaran,
and C. Veera Sesa Kumar

Abstract Three-dimensional blading features of impellers like sweep and lean improve the aerodynamic performance of centrifugal compressors, especially in terms of pressure ratio, stall margin and efficiency. But, these blade geometrical features often impose challenges on mechanical design and structural integrity of the impeller. Modern small gas turbine engines demand high-work input impellers rotating at very high speeds, making the structural design even more difficult. The present study deals with improving the structural integrity of a centrifugal impeller of a compressor stage designed for 42,000 rpm and power input of 1200 kW. The baseline design of the impeller, arrived using an advanced three-dimensional design software, met the aerodynamic performance requirements but failed to satisfy structurally. Higher backward lean present in the blade was found to be contributing to severe bending stresses and deformation. Hence, three different impellers, with modified thickness, lean angle and wrap angle distributions, were designed. These designs were subjected to 3D CFD and FEM analysis. Structural analysis was carried out to study stresses and deformations for all configurations, followed by pre-stressed modal analysis to predict their natural frequencies and corresponding mode shapes. The design with modified wrap angle distribution not only met the aerodynamic requirements but also satisfied structural requirements. This paper elaborates the design evolution of the centrifugal impeller from the baseline design to a more structurally stable one.

E. K. Vivek (✉) · Lakshya Kumar · R. Senthil Kumaran · C. Veera Sesa Kumar
Propulsion Division, CSIR-National Aerospace Laboratories, Bengaluru , Karnataka 560017,
India

e-mail: vivekek@nal.res.in

Lakshya Kumar

e-mail: lakshyakumar@nal.res.in

R. Senthil Kumaran

e-mail: rsk@nal.res.in

C. Veera Sesa Kumar

e-mail: seshakumarch@nal.res.in

Keywords Bending stress · Centrifugal compressor · Deformation · Impeller · Blade lean · Sweep · Wrap

1 Introduction

Modern-day centrifugal compressor designs demand high-pressure ratio, stall margin and efficiency at lowest possible diameters. This aggressive approach leads to use of three-dimensional blading features like sweep and lean for impellers. Though these advanced geometrical features have known to improve aerodynamic performance [1, 2], they pose serious challenges for mechanical design. The blade lean in inducer part of the impeller significantly affects the stresses in the blade [3]. The influence of three-dimensional blading features on the aerodynamic performance is published in abundance. But, the literature covering the effects of blade lean and wrap angles on impeller blade structural aspects such as stresses, deflections and their natural frequencies is scarce.

The present work focusses on improving the structural integrity of a centrifugal impeller of a high-work compressor designed for 42,000 rpm and power input of 1200 kW. The base design of the impeller failed to satisfy structural requirements. Higher level of blade lean was found to be contributing to severe bending stresses and deformation. In the process of minimizing the stresses and deformation, three different modifications were made to the impeller: increased blade root thickness, modified lean angle distribution and modified wrap angle distributions. These design changes were subjected to 3D CFD and FEM analysis.

The design with modified wrap angle distribution met the aerodynamic requirements and also satisfied structural requirements to a large extent by reducing the stresses and deformations to acceptable levels. This paper elaborates the design evolution of the centrifugal impeller from the base design to a more structurally stable one. Related design methods, CFD studies and FEM analysis are also presented here.

2 Centrifugal Compressor

The centrifugal compressor is designed for a small gas turbine application with a pressure ratio of 3.8, mass flow of 5.6 kg and speed of 42,000 rpm. The compressor stage comprises inlet guide vanes (IGVs), impeller, radial diffuser and axial outlet guide vanes (OGVs) with 7, 19, 35 and 37 vanes/blades, respectively. CAD model of the compressor is shown in Fig. 1. The thermodynamic design parameters of the compressor are given in Table 1. Since only the impeller of the compressor is of interest, flow and geometric parameters of the impeller alone are given here. Mean-line flow parameters of the impeller are given in Table 2. Basic geometrical parameters of the impeller are given in Table 3.

Fig. 1 3D CAD model of the centrifugal compressor

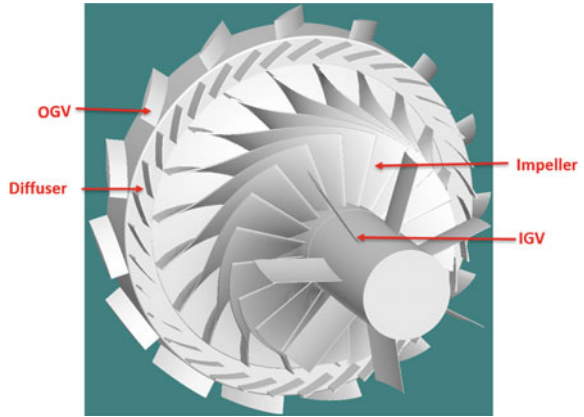


Table 1 Thermodynamic design parameters of the compressor

Inlet total pressure, P_{o1} (kPa)	146.5
Inlet total temperature, T_{o1} (K)	349
Pressure ratio, π	3.8
Mass flow rate, m (kg/s)	5.6
Power required, P (kW)	1162.5
Efficiency, η_{t-t} (%)	79

Table 2 Summary of the mean-line parameters of the impeller

Parameter	Impeller
Mach number, M_{rel}	0.91
Inlet absolute angle, α_{1in} (°)	8.8
Inlet relative angle, β_{1in} (°)	-51.7
Inlet blade speed, U_1 (m/s)	327.8
Exit Mach number, $M_{rel,ex}$	0.59
Exit absolute angle, α_2 (°)	75.7
Exit relative angle, β_2 (°)	-48.8
Exit blade speed, U_2 (m/s)	561.6

Table 3 Geometric parameters of the impeller

Inlet hub radius, r_{1h} (mm)	36.5
Inlet tip radius, r_{1t} (mm)	95
Outlet tip radius, r_{2t} (mm)	124
Hub to tip ratio	0.38
Rotor tip clearance (mm)	0.5

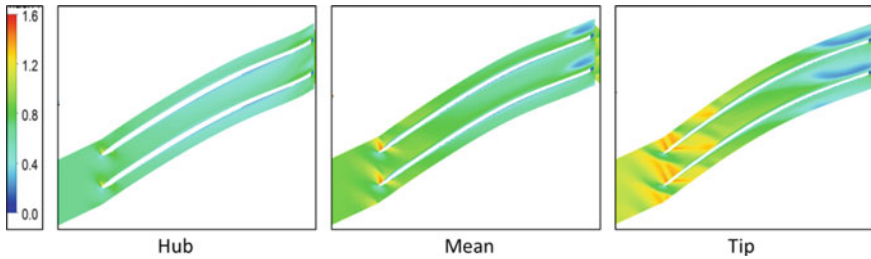


Fig. 2 Relative Mach number contours of the impeller at design condition

Detailed CFD studies were carried out using ANSYS CFX with the full compressor stage at 60, 70, 80, 90 and 100% speeds. The computed Mach number contours of the impeller blade sections at the design condition are shown in Fig. 2. Development of a shock near the leading edge can be seen as Mach number contours are swept from hub to tip. At the tip region, local Mach numbers were close to 1.5. Tip leakage vortex near the trailing edge of the tip section can also be seen. The compressor met the intended performance of 3.8 pressure ratio at 5.6 kg/s mass flow with a decent stall margin of 18%. The impeller, being the only rotating part, was subjected to careful mechanical design and stress analysis.

3 Structural Analysis and Mechanical Design

The centrifugal impeller is designed for a speed of 42,000 rpm. At such high speeds, the disc and the blades experience very high centrifugal loads. In addition to centrifugal loads, stresses resulting from thermal gradients and gas bending loads result in complex stress pattern in the blade and the disc [4]. The tip shock also adds complexity to the mechanical design of the impeller. In this study, only inertial loads were considered. The baseline impeller, which met the basic aerodynamic requirements, was taken for structural analysis. This impeller is referred to as reference impeller. Un-scooped solid model of the impeller is shown in Fig. 3. The impeller disc material was scooped out from either side to reduce weight. Titanium alloy, Ti6Al4V, was selected as the impeller material. Its material properties are mentioned in Table 4. An axial constraint at the hub and a cylindrical constraint at the bore were imposed. Angular velocity of 4398 rad/s was fed. Finite element analysis (FEA) was carried out on full impeller model consisting of 19 blades using ANSYS Workbench software. The stresses and deformations were analysed under full loading conditions. The von Mises stress, total, radial and tangential deformations of the blade were observed to be higher than the acceptable limits. The results are shown in Fig. 4.

When the stresses in the blade exceed material allowable limits, stresses can be reduced by various approaches. Axial and radial dimensions of the impeller can be

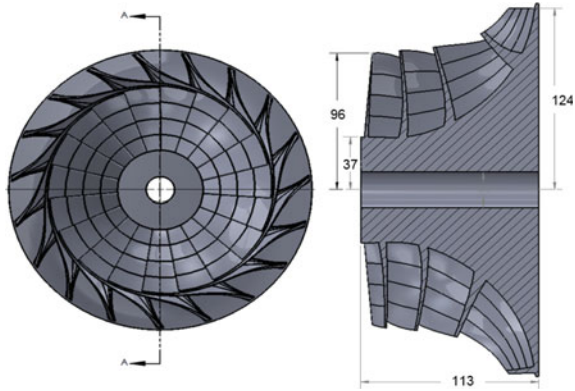
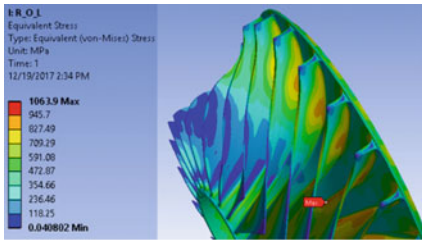


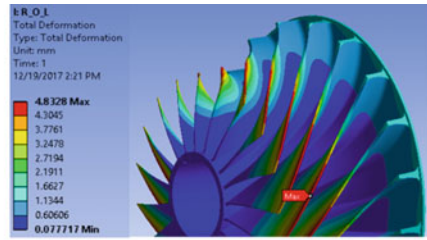
Fig. 3 Impeller CAD model with the bore

Table 4 Material properties of Ti6Al4V

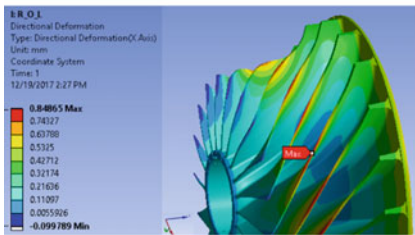
Property	Value
Density, ρ (kg/m ³)	4460
0.2% Proof strength @ RT (MPa)	827
Ultimate tensile strength @ RT (MPa)	896
Young's modulus, E (GPa)	113
Coefficient of thermal expansion, α (m/m K)	9×10^{-6}



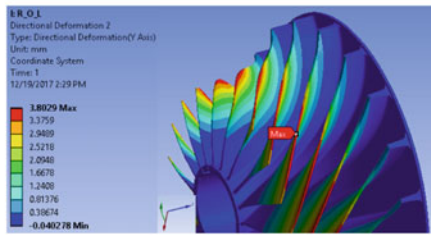
(a) von-Mises stress plot



(b) Total deformation plot



(c) Radial deformation plot



(d) Tangential deformation plot

Fig. 4 FEA results for reference impeller

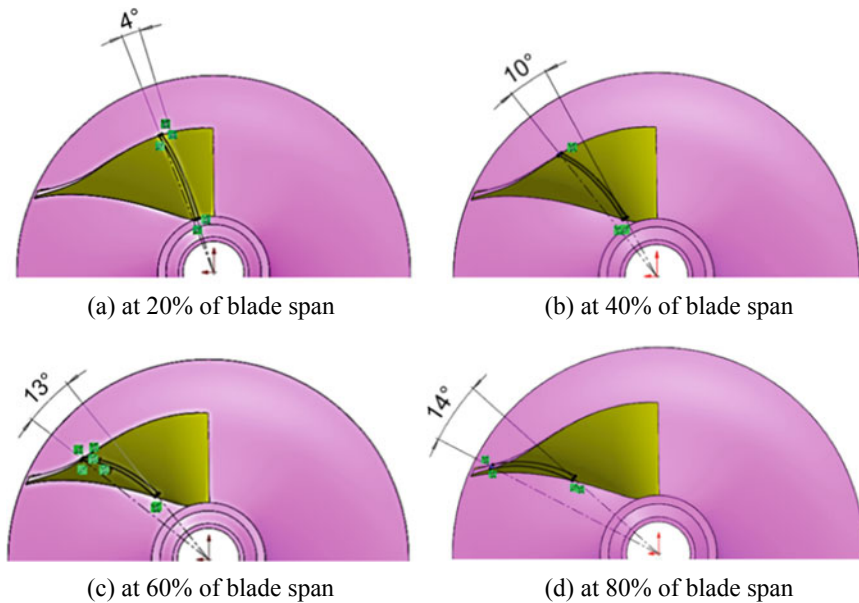


Fig. 5 Blade section lean

varied within allowable limits without affecting pressure ratio and mass flow rate [5]. When the radial dimensions of the impeller cannot be varied due to geometric constraints, the blade root can be thickened to reduce the stresses. Hence, the thickness of the blade was increased to reduce the stresses in the first attempt. The analysis on modified geometry with increased blade root thickness did not show any considerable improvement in blade stresses and deformations. Later, it was observed that the blade was experiencing significant bending which was the main cause for high stresses and deformations. After detailed analysis of blade geometry, the blade section was found to be excessively leaned backward, which can be seen in Fig. 5.

Since the blade mass is not oriented along the radial line (passing through the axis of rotation to the blade centre at hub), the centrifugal forces due to blade self-mass created significant bending moment at the blade root. In order to bring down the blade section lean, two different approaches were considered to modify the blade geometry in the design software. In the first approach, the blade lean angle was increased at exit of the impeller. In the second approach, the wrap angle of the hub curve was reduced at the impeller inducer. Impeller configuration with 23° lean correction at the exit was taken up for finite element analysis. The blade geometry shift is shown in Fig. 6. The results, as shown in Fig. 7, did not indicate any significant reduction in stresses as well as deformations. From the total deformation plot, it can be seen that the blade bending was highest in the region of 20–40% of blade axial span from the inlet and the lean had to be corrected appropriately in that region. Since the lean

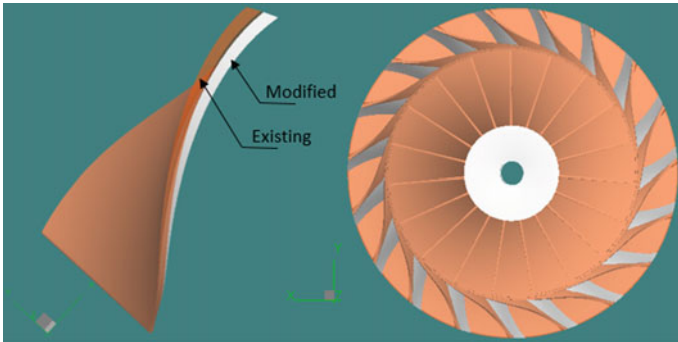
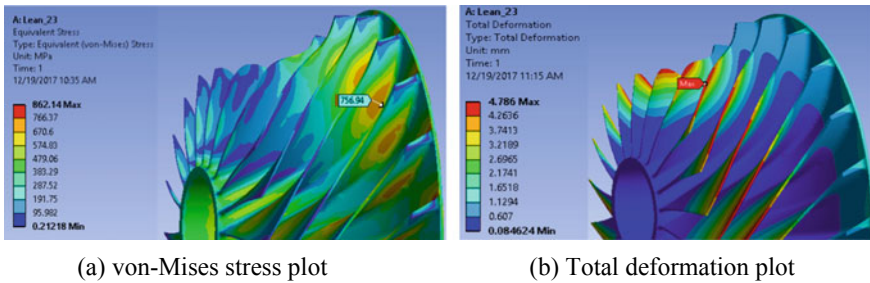


Fig. 6 Blade geometry after lean correction



(a) von-Mises stress plot

(b) Total deformation plot

Fig. 7 FEA results for 23° lean correction model

correction given at the exit was nullified towards the inducer, this approach did not give positive outcome.

The second approach was to correct the wrap angle of blade hub curve by 9° at the impeller inducer, as shown in Fig. 8. It can be seen that the blade hub curve moved

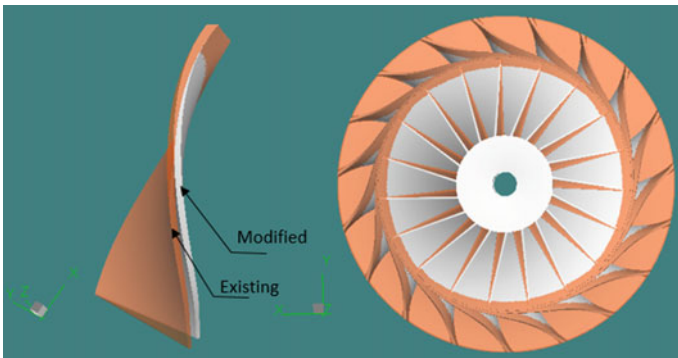


Fig. 8 Blade geometry after wrap angle correction

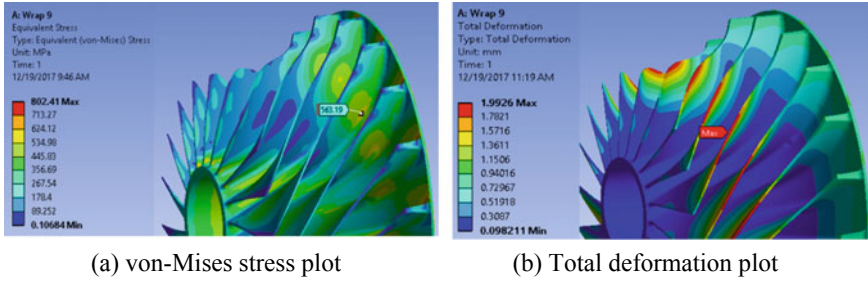


Fig. 9 FEA results for wrap angle correction model

Table 5 Summary of FEA results for various impeller configurations

		Reference impeller	Lean angle correction	Wrap angle correction
von Mises stress in the blade (MPa)		1064	760	563
Radial stress (MPa)	Max @ suction surface	723	668	480
	Min @ pressure surface	-170	-153	102
Total deformation (mm)		4.83	4.79	1.99
Radial deformation (mm)		0.85	0.82	0.49
Tangential deformation (mm)		3.8	3.68	1.53

significantly up to 60% of the blade span reducing the backward lean of the blade considerably. This approach showed significant improvement in both stresses and deformations. The results of this configuration are shown in Fig. 9. The results of all impeller configurations studied are summarized in Table 5. The results obtained with the wrap angle corrected impeller were found to be satisfactory in terms of stress levels and deformation.

4 Modal Analysis of the Impeller

Pre-stress modal analysis was carried out on the reference impeller to study its natural frequencies and their mode shapes. First three natural frequencies were predicted to be 1723, 1734 and 1772 Hz, and the mode shapes are shown in Fig. 10. From Fig. 10, it can be seen that the modes represent nodal diameters 1, 2 and 0, respectively. The frequencies of these modes are significantly higher than the design speed of 700 Hz and do not match with any harmonics of the rotational speed. Hence, the reference impeller did not have resonance issues with probable excitation sources arising from engine operation.

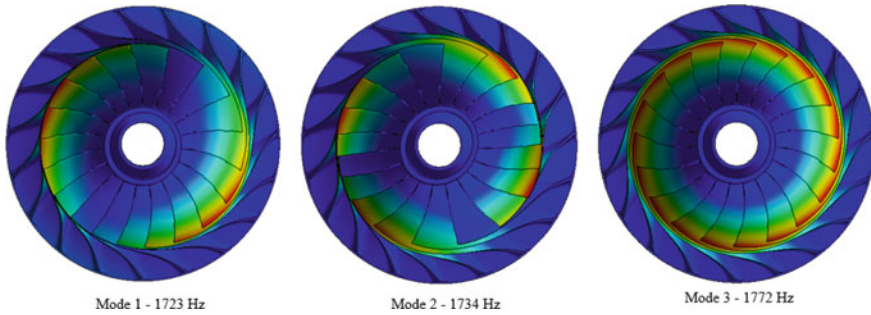


Fig. 10 Mode shapes of reference impeller

Table 6 Natural frequencies of the impeller configurations

Mode no.	Natural frequency (Hz)		
	Reference	Lean corrected	Wrap corrected
1	1723	1722	1655
2	1734	1733	1667
3	1772	1771	1690

The modified versions of reference impeller have also been studied to understand the influence of changes in three-dimensional blading features, i.e. blade lean and wrap. The natural frequencies of first three modes for all three impellers are compared and presented in Table 6. It can be seen that the natural frequencies of the reference impeller and the lean corrected impeller are almost the same. This can be attributed to the nature of the mode shapes. All modes have displacement only in the inducer region of the impeller blade where the blade height is largest and its stiffness is lowest. Since the blade lean correction given at the impeller exit is nullified towards the inducer, its effect on natural frequency also nullified. However, slight reduction in natural frequencies was observed for wrap corrected blade as the wrap correction is given at the inducer part of the blade. Though the natural frequencies of wrap corrected impeller are ~4% lower in comparison with the reference impeller, the variation is marginal and these frequencies also have no resonance with possible excitation frequencies and their harmonics. Hence, the wrap corrected blade met all aerodynamic and structural requirements.

5 Conclusions

A single-stage centrifugal compressor consisting of inlet guide vanes, impeller, diffuser and outlet guide vanes was designed to meet the requirements of 5.6 kg/s mass flow and 3.8 pressure ratio at a speed of 42,000 rpm. Computational analysis confirmed that designed compressor stage met the requirements of mass flow,

pressure ratio and stall margin. Initial structural analysis showed that the impeller blade stresses and deformation were very high. Blade root thickness at the hub of the impeller was increased to reduce the stresses, but no improvement was seen. Later, it was realized that excessive hub to tip lean angle distribution was causing the blade to bend. The lean angle was corrected by 23° near the compressor exit. But, no significant improvement was seen in the stress levels as the correction was nullified towards the region of interest, i.e. 20–40% of blade axial span from inlet. Later, the blade wrap angle was corrected in such a way that the backward lean angle got reduced substantially over the region of interest. This resulted in considerable reduction in stresses and deformations, which were under safe limits. Further, detailed modal analysis was carried out to predict its natural frequencies and corresponding mode shapes. Though there is a marginal drop in natural frequencies, the wrap corrected blade satisfied both aerodynamic and structural requirements.

Acknowledgements The authors would like to express their gratitude to Director, NAL, for giving an opportunity to perform this task. The authors also would like to thank Head and Jt. Head, Propulsion Division, NAL, for their support. The authors are grateful to all the team members for their assistance without which successful completion of this work would not have been possible.

References

1. Oh J, Buckley CW, Agrawal GL (2011) Numerical study on the effects of blade lean on high-pressure centrifugal impeller performance. In: ASME 2011 turbo expo, vol 7: turbomachinery, pp 1957–1969
2. Jagadeeshwar Chary KV, Vijaya Kumar Reddy K, Siva Reddy C (2017) Numerical studies on centrifugal impeller performance with different lean combinations. *Glob J Res Eng D Aerosp Sci* 17(2)
3. Xu C, Amano RS (2012) Empirical design considerations for industrial centrifugal compressors. *Int J Rotating Mach* 2012
4. Zheng X, Ding C (2016) Effect of temperature and pressure on stress of impeller in axial-centrifugal combined compressor. *Adv Mech Eng* 8(6):1–11
5. Muthu E, Dileep S, Mishra R (2012) Optimization of a centrifugal impeller for a small gas turbine engine: a finite element approach. In: ASME 2012 gas turbine India conference, GTINDIA 2012

3D Finite Element Vibrational Analysis of T385 Turbine Rotor BLISK Using SAFE Diagram



Revanna Jai Maruthi , Rajeevalochanam Prathapanayaka ,
and Nanjundaiah Vinod Kumar 

Abstract Integrally bladed rotors (BLISK) are most stressed part of aircraft engines due to high rotational speeds, elevated temperatures and pressures. Turbine blades fail mainly due to fatigue under alternating stresses resulting from vibration of rotor systems. Non-uniform pressure field is experienced by turbine BLISK due to interaction of stator and rotor blades which acts as a source of excitation during turbine operation. The number of stator blades dictates the occurrence of resonance in the rotor BLISK during steady-state operation. Therefore, it is necessary to design a mechanically feasible rotor with respect to stator and verify its modal and harmonic response to ensure its resonance-free operation. Design and development of T385 turbine stage for 1 kN small gas turbine engine are carried out in Propulsion Division, CSIR-NAL. The dynamic behaviour of T385 turbine rotor BLISK is evaluated for vibration reliability. This paper presents vibrational analysis of the T385 turbine rotor BLISK using finite element technique to evaluate critical nodal diameter, critical frequencies and response in engine environment. The turbine speed is 50,500 rpm at the engine design point based on the inlet temperature. Detailed vibration analysis of T385 turbine is carried out using FEA to plot Campbell and SAFE diagrams. The critical nodal diameter extracted from plotted SAFE diagram is 19, which is very well agreeing with Bertini analytical formulae. The Campbell diagram is plotted for T385 turbine at critical nodal diameter of 19. The obtained critical speed from this Campbell diagram is 33,000 rpm, which ensures the rotor is safe in the operating conditions.

Keywords Turbine BLISK · Thermal stress · Centrifugal stress · Vibration · Nodal diameter · SAFE diagram · Campbell diagram · Harmonic response

R. Jai Maruthi (✉) · R. Prathapanayaka · N. Vinod Kumar
Propulsion Division, CSIR-National Aerospace Laboratories, Bengaluru , Karnataka 560017,
India
e-mail: jaimarutinayaka@gmail.com

R. Prathapanayaka
e-mail: prathap@nal.res.in

N. Vinod Kumar
e-mail: nvkumar@nal.res.in

Nomenclature

N	Speed, rpm
M	Mass, kg
C	Damping, N s/mm
K	Stiffness, N/mm
F_n	Frequency, Hz
ω_n	Rotational velocity, rpm
N_B	Number of blades
N_V	Number of vanes
NPF	Nozzle passing frequency, Hz
RSH	Running speed harmonics, Hz
CND	Critical nodal diameter
d_{\max}	Number of nodal diameters
n	Different engine orders
SAFE	Singh's advanced frequency evaluation

1 Introduction

The vibrational analysis is a dynamic parameter to consider while designing a complex rotating system. Dynamic characteristics of rotating components are very crucial in order to overcome from failure. A gas turbine consists of very complex rotating system due to high operating speed and power. The turbine rotor BLISK in a gas turbine engine is very crucial component which is subjected to high centrifugal loads, elevated temperatures and pressures. The vibrational analysis of turbine rotor BLISK should be carried out to avoid resonance condition by extracting all the dynamic characteristics. The dynamic stresses developed while running at high cycle fatigue conditions lead to failure of turbine blade at stress concentration locations. The alternating stresses resultant from vibration lead to failure of turbine rotor component. The dynamic stresses developed during operation depend on natural frequencies, mode shape and excited frequencies with their exciting force shapes. The older traditional analysis shows major interest on analysis of single cantilever beam to get single blade frequencies. The present trend is analysing a whole integrated bladed disc to evaluate frequencies and mode shapes. Integrated bladed rotor is a single component which would give rise to some different dynamic characteristics by producing more frequencies and mode shapes. System at resonance condition behaves nonlinearly, and it gives rise to higher amplitude with the release of higher stored strain energy. The condition of resonance is matching of natural frequency with external excitation frequency. This condition can be analysed with Campbell diagram to get critical speeds and to run a system safely in operating region. The actual resonance condition will occur by not only matching of external and natural frequencies but also matching of shape of these harmonics with normal mode shape of integrated

bladed disc. This is the condition of real resonance which leads to true failure of system. The real resonance condition can be described by a SAFE diagram in which evaluation of critical nodal diameter is necessary to get actual critical speeds.

Singh et al. [1] presented a method to evaluate actual resonance condition called SAFE diagram evaluation. The method will give more information than earlier Campbell diagram. The SAFE diagram compares not only the frequencies of exciting harmonics with natural frequencies of blades, but also the shape of these harmonics with the normal mode shapes of a bladed disc. Examples are also provided to show that the SAFE diagram can pinpoint what interference is likely to cause the largest blade vibration. Singh et al. [2] also presented an analysis of impellers by using interference diagram and observed that fatigue damage due to alternating stresses resultant from vibration of the disc results in higher alternating stresses. The interference diagram is plotted for disc, blade and impeller separately and compared to evaluate overall dynamic characteristics. Bertini et al. [3] derive an equation for nodal diameter evaluation to compare with SAFE diagram. The explanation and application of the SAFE diagram are put forth in whole paper to understand about the dynamics of rotating systems. The analysis of bladed disc by acquaintance frequency modal at quiescent state is described by Lošak and Malenovsky [4]. The full disc model is considered to compare numerical results with analytical results. The investigation of blade failure is done by Choi and Lee [5] during start-up and shutdown condition. Stress analysis and modal analysis with Campbell and interference diagram evaluation are done to predict a failure region. The fatigue failure is the reason for blade failure. A project document by Hassan [6] presents an analysis of turbomachinery blades. FEA results are compared between full bladed disc and sector disc analysis. Both the analysis methods were presented and outlined to get similar frequencies.

Design of T385 turbine stage [7] for 1 kN small gas turbine engine is carried out in Propulsion Division, CSIR-NAL. T385 turbine stage comprises rotor BLISK and NGV (stator) which is designed to produce 385 kW power at design rpm. NGV consists of 19 vanes, and rotor BLISK consists of 50 blades. The design speed is 50,500 rpm at engine conditions for maximum blade temperature. This paper presents the 3D vibrational analysis of T385 turbine rotor BLISK using SAFE diagram. The thermal stress analysis of T385 turbine rotor BLISK is carried out for structural integrity using FEA. The designed BLISK is subjected to pre-stressed modal analysis by considering stress stiffening effects, and thermal and centrifugal loads using FEA. Critical nodal diameter evaluation is presented for real resonance condition by using both SAFE diagram and Bertini analytical formulae. The critical speeds are extracted by Campbell diagram for relevant critical nodal diameter.

2 Brief Review of Concepts

2.1 Modal Analysis

Modal analysis is a technical methodology to study dynamic behaviour of structural systems. Technique is used often and important in a large rotating complex system such as high-speed gas turbines. The method is used to derive frequencies and critical speeds in design stages under steady state condition with or without external vibrational excitations. The eigenvalue (natural frequency) and the accompanying eigenvector (mode shape) of vibrating structure can be presented by using this analysis. The most common method used to perform this kind of analysis is finite element method (FEM). The general form of equation of motion for multi-degree of freedom for all systems is given by Eq. (1) in the eigensystems.

$$[M]\{\ddot{x}\} + [C]\{\dot{x}\} + [K]\{x\} = 0 \quad (1)$$

where $[M]$ is symmetric mass matrix, $[C]$ is symmetric damping matrix, $[K]$ is symmetric stiffness matrix and $\{x\}$ is generalized coordinate vector.

2.2 Mode Shapes

Mode shapes are eigenvectors of any mechanical system, and these will describe the dynamic behaviour of system at each degree of freedom. Complex rotating systems are continuous, and they have infinite degree of freedom. Then, the natural frequencies and mode shapes are also infinite. Each mode shape will give rise to a displacement at particular frequencies, and it also describes about natural shape of structural system. First few modes are very dangerous because they acquire more strain energy to release at the relevant frequencies. Typical mode shapes of the rotor disc are shown in Fig. 1a, b. Combined bending and twisting mode type at nodal diameter 2 for a typical rotor BLISK configuration is shown in Fig. 1a. The umbrella mode with all the blades bending towards one direction for a typical rotor BLISK is shown in Fig. 1b.

Fig. 1 **a** Bending and twisting mode at ND2.
b Umbrella mode

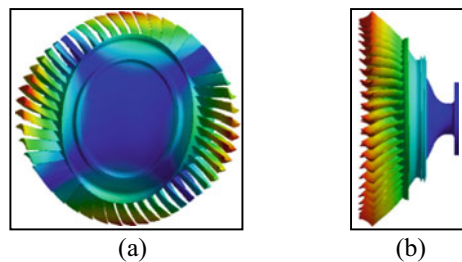
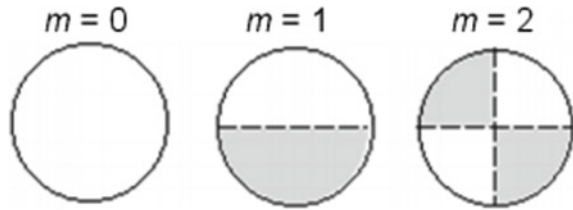


Fig. 2 Different nodal diameters



2.3 Nodal Diameter

Nodal diameter is defined as line of zero displacement position along plane of the disc. The displacement can be in or out of the phase on the displacement line. The number of complete sine waves and zero displacement planes that passes through the circumferential of a disc is also called nodal diameter, and it represents the harmonic content. The turbine disc has several mode shapes, so nodal diameters are indicated as shown in Fig. 2.

Nodal diameter is also the number of distinct harmonics that are formulated to define the vibrating system. Vibration amplitude varies with disc harmonically. Nodal diameter is the other way of representing disc effect by simulating mode shape. Nodal diameter is most useful in cyclic symmetric modal analysis to understand deformation pattern of bladed discs. The stiffness of the disc structure is entirely depending on the number of nodal diameters. Nodal diameter zero indicates that disc does not have any zero displacement planes, and nodal diameter one indicates that disc is having one zero displacement plane as shown in Fig. 2. The number of harmonics is depending on the number of symmetry sections of disc, so nodal diameter for a cyclic symmetric analysis of disc can be calculated as

$$d_{\max} = (N_b/2) + 1, \quad \text{if } N_b \text{ is even} \quad (2)$$

$$d_{\max} = ((N_b + 1)/2), \quad \text{if } N_b \text{ is odd} \quad (3)$$

2.4 Dynamics of BLISK

Since gas turbines operate at higher temperature and high speed, stability of system should be concerned while designing a turbine disc (BLISK) at earlier stages. Vibrations arising from instability lead to failure and less life of the component. Gas turbine rotor discs have to be designed to overcome from resonance conditions by extracting natural frequencies. The external pressure induced on blade due to flow is the root cause for excitations which leads to vibrations. Nozzle passing frequency (NPF) and running speed are the most common source excitations on the turbine rotor disc

with their harmonics of both NPF and running speed. The impact of thermal energy coming through nozzle hits the rotor blades to form nozzle passing frequency. The frequency of NPF depends on the number of stator vanes. A rotor blade impacts with N_v times with stator vanes for a complete revolution of the system; thus, the frequency of the main harmonic component is

$$\Omega_1 = \Omega N_v \quad (4)$$

The main source of excitations are due to unbalance present in the rotor disc which give rise to 1X excitations. The coupling misalignments will give rise to 2X excitations. The aerodynamic excitations produce 0.5X excitation frequencies. These external excitations with NPF plots in Campbell diagram get critical speeds. The cyclic load acting on the blades is determined by the rotation speed combined with the flow distortion produced from a non-uniform inlet or outlet pressure distribution. Running speed harmonics are the multiple frequencies of the rotor running speed. Thus, running speed harmonics can be represented as

$$\text{RSH} = \frac{n * N}{60} \quad (5)$$

Here, $n = 0, 1, 2, 3, 4, 5 \dots n$, representing different engine orders. Nozzle passing frequency can be represented as

$$\text{NPF} = \frac{N_v * N}{60} \quad (6)$$

Here, " N_v " is the number of stator vanes. The wakes behind the stator vanes are considered as the excitation source for the nozzle passing frequency.

2.5 SAFE Diagram

The most common method to evaluate critical speed is Campbell diagram by avoiding resonance condition. Campbell diagram predicts the probable resonance points for rotor disc by plotting all the possible external excitations that matches with natural frequency of the system; thus, resonance may or may not occur. There is a difficulty in avoiding any resonance matching conditions because turbine BLISK poses so many natural frequencies which are close to each other. The drawback of Campbell plot is to differentiate a large number of vibrational modes that are close to natural frequencies in rotor disc. Resonance occurred during the operation by Campbell approach cannot be dangerous in terms of vibration amplitude because of mismatch in external excitation shape with mode shape.

Singh et al. [2] arrived for the condition of real resonance by deriving SAFE diagram, and it compares not only the frequencies of exciting harmonics with natural

frequencies of blades, but also the shape of these harmonics with the normal mode shapes of a bladed disc. Shape matching with frequency matching conditions is the concept of SAFE diagram. Identification of many frequency matchings which are non-critical is ignored in SAFE diagram. Real resonance conditions that are far away from normal resonance conditions are differentiated, and matching shape that fully coincides with each excitation is introduced in SAFE diagram. The forces should be in phase with the displacement to achieve maximum work done when force frequency matches with external excitations of natural modes. This condition leads to a pure resonance by releasing maximum energy with work done on the system to get actual critical speeds. The modes will not have excited to harmonics when force is out of the phase because negative and positive work done by each force will differ. The phase in and phase out of alternative forces combination should be constructive to produce maximum work done than only a condition of pure resonance will occur. Damage of the system occurs when internal energy stored to give rise maximum work done by the system when real resonance occurs. The critical nodal diameter gives rise to a critical mode shape which may cause maximum damage to system.

A typical SAFE diagram generated for the turbine stage having 5 vanes and 43 rotor blades with turbine speed of 40,000 rpm is shown in Fig. 3. The nodal diameters are plotted along x-axis with frequencies along y-axis, and running speed harmonics at each nodal diameter are represented with further reversed along the shape index. The natural mode shapes with nozzle passing frequencies are plotted with relevant nodal diameters. Usually, intersection region between running speed harmonic and nozzle passing frequency gives the critical nodal diameter and critical nodal diameter found to be 5 from typical SAFE diagram. The critical frequencies from Campbell plot are matched with intersection point (NPF and RSH) in SAFE diagram that leads to condition of real resonance. The rotor disc should be designed to operate away from this real resonance condition.

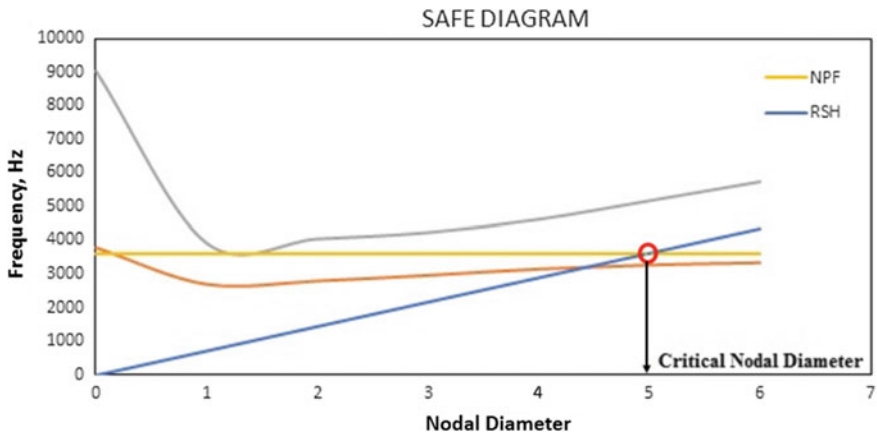


Fig. 3 A typical interference diagram or SAFE diagram

3 Model

The T385 turbine rotor BLISK is designed for structural integrity by thermo-structural analysis [7]. The design speed of the turbine is 50500 rpm. Vibrational analysis is carried out for designed BLISK as shown in Fig. 4.

A cyclic symmetric modal analysis is carried out by generating a single sector of a turbine rotor BLISK. The designed BLISK is subjected to pre-stressed modal analysis by considering stress stiffening effects, and thermal and centrifugal loads using 3D finite element analysis (ANSYS). The frequencies and mode shapes from 3D FEA are plotted in SAFE diagram to get critical nodal diameter. Critical nodal diameter can also be calculated by the analytical formulae given by Bertini [4] for INPF. Bertini [4] derived an analytical expression to determine the critical nodal diameter as given by the following equation:

$$d_m(n) = \left| nN_v - N_B \left[\left(nN_v + \left[\frac{N_B}{2} \right] \right) / N_B \right] \right| \quad (7)$$

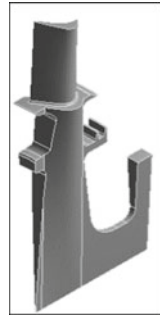
where N_B is the number of blades and N_v is the number of vanes. The critical nodal diameter from SAFE diagram as well as Bertini analytical formulae is compared.

The Campbell diagram is plotted for obtained critical nodal diameter with all the mode shapes and frequencies. The first five engine orders and first NPF are considered to plot in Campbell diagram. The obtained mode shapes are the representation of turbine rotor BLISK behaviour. The obtained critical speeds should not be in the operating region. The operating region of T385 turbine rotor BLISK is around 50,500 rpm. The harmonic response of the BLISK for unbalance is carried out using FE technique to get maximum amplitude at critical interfaces or sealing regions. The response of the system due to any external excitations should be within the permissible limits.

Fig. 4 T385 turbine rotor BLISK



Fig. 5 A single sector of BLISK



4 Finite Element Analysis

4.1 Defining the Model

A single sector of T385 turbine rotor BLISK as shown in Fig. 5 is considered for pre-stressed modal analysis by using FEA. Analysis is carried out for different operating regions from 0 to 60,000 rpm by considering all the load effects. Nickel-based super-alloy Nimonic 90 is used and defined in the FE model. All temperature-dependent properties of Nimonic 90 are considered while defining the model. A cyclic symmetry is applied on both faces of disc to ensure axis symmetry.

4.2 Meshing

Turbine rotor BLISK is subjected to discretization of continuum as shown in Fig. 6. Tetrahedron elements are used to mesh the turbine rotor BLISK. The optimum mesh quality is assigned to rotor system by taking Jacobian and aspect ratios close to 1. The grid dependence study is also performed from coarse mesh to fine mesh. The mesh size of the BLISK is 56,150.

Fig. 6 Meshing of BLISK

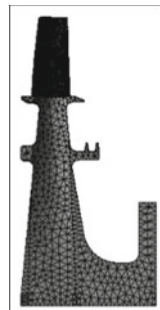


Fig. 7 Thermal constraints

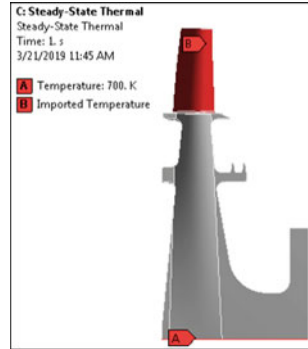
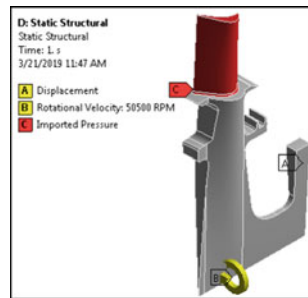


Fig. 8 Boundary conditions



4.3 Boundary Conditions

The relative temperature is mapped on rotor blade with bore temperature as shown in Fig. 7. The thermal stresses arising from thermal analysis with structural loads are applied to turbine BLISK as shown in Fig. 8. The pre-stressed modal analysis is performed by considering equivalent stresses from thermo-structural analysis.

5 Results and Discussion

The total number of nodal diameters for rotor BLISK calculated using Eqs. (2) and (3) is 26. The same equations are used by ANSYS to predict nodal diameters. Frequencies due to different centrifugal loads from each nodal diameter for first six modes are predicted using FEA. Frequencies and mode shapes from 3D FEA are plotted in SAFE diagram to get critical nodal diameter. The obtained critical nodal diameter is 19 from SAFE diagram as shown in Fig. 9. The point of intersection of running speed harmonics (RSH) and nozzle passing frequency (NPF) generally gives critical nodal diameter resulting in full resonance. Critical nodal diameter calculated by the analytical formulae given by Bertini et al. [3] is 19 for 1NPF. Since from both

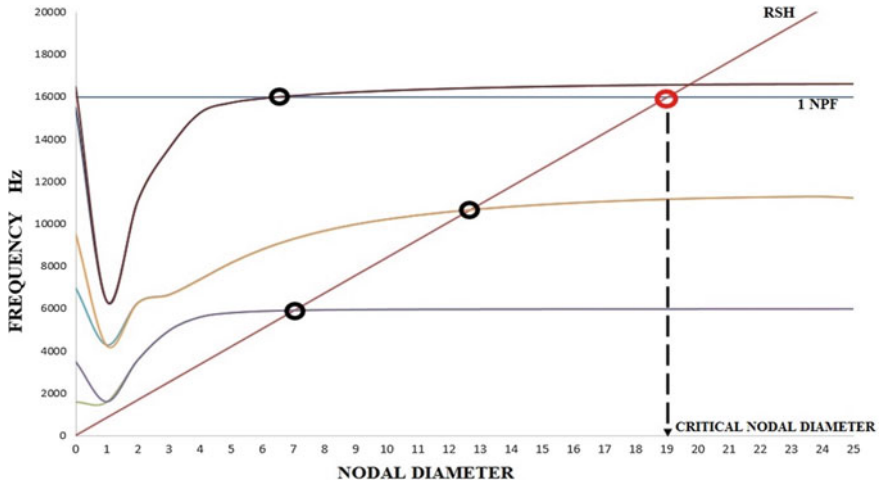


Fig. 9 SAFE diagram

methods the obtained critical nodal diameter is 19, the Campbell diagram is plotted for this nodal diameter.

Thus, first six fundamental vibrational modes are plotted with first five engine orders and first NPF for the turbine rotor BLISK in a Campbell diagram as shown in Fig. 10. The first five engine orders are calculated using Eq. (5) for a range of 0–60,000 rpm. The NPF for a range of 0–60,000 rpm is calculated using Eq. (6) with 19 number of stator blades. Campbell diagram is generated for nodal diameter 19 as suggested by Chromek [8] which is derived from SAFE diagram.

Campbell diagram indicates that all the vibrational modes are above first five engine orders. There are no critical speeds in the operating region since main vibrational modes are not crossing first five engine orders. There is one critical speed, i.e. 33,000 rpm due to NPF in which it is intersecting with first vibrational mode and the

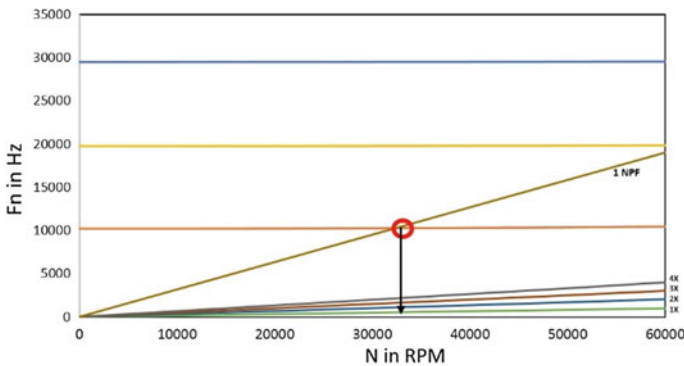
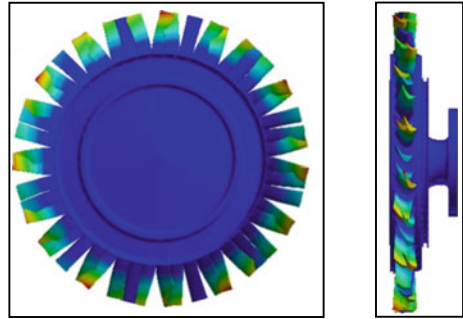


Fig. 10 Campbell diagram for CND 19

Fig. 11 Mode 1 in nodal diameter 19 and only blade bending type



operating range is far away from critical speed. This critical speed is arrived from Campbell for obtained critical nodal diameter 19 is not much effective since higher nodal diameters are having more resistance to deformations. This critical speed may not be effective since first five engine orders are not exciting any modes and NPF may not produce effectiveness in excitations. However, BLISK is a complex system, and care should be taken while operating near 33,000 rpm in engine environment.

First vibrational mode is excited due to NPF to get actual critical speed. The first vibrational mode giving critical speed is only blade bending type as shown in Fig. 11. This mode does not affect since the nodal diameter is high enough to get rigid to give less amplitude in vibrations.

6 Conclusions

3D finite element vibrational analysis of T385 turbine rotor BLISK has been carried out. The frequencies with mode shapes arrived from 3D FEA for 26 nodal diameters are plotted in SAFE diagram. The critical nodal diameter is found to be 19 from SAFE diagram. The critical nodal evaluation from SAFE diagram is compared with Bertini analytical method which is agreeing very well with prediction. From Campbell diagram, it was found that there are no critical speeds due to first five engine order excitations. There is one critical speed around 33,000 rpm excited due to NPF which needs attention during operation even though design operating range is far away from this critical speed. FEA prediction shows that the rotor has sufficient margin from resonance for engine operating conditions.

Acknowledgements The authors acknowledge CSIR support for this project. The authors would like to thank Director, CSIR-NAL, and Head and Joint Head, Propulsion, for their support in carrying out this work. The authors also thank Propulsion Division colleagues for their support and help.

References

1. Singh MP, Vargo JJ, Schiffer DM (1988) Safe diagram—a design and reliability tool for turbine blading. *J Eng Gas Turb Power* 111:601–609
2. Singh MP, Thakur BK, Sullivan WE, Donald G (2003) Resonance identification for impellers. In: Proceedings of the thirty second turbomachinery symposium
3. Bertini L, Monelli BD, Neri P, Santus C, Guglielmo A (2013) Explanation and application of the SAFE diagram. In: Proceedings of the 11th international conference RASD 2013, Pisa, pp 1–15
4. Lošák P, Malenovsky E (2007) Contribution to the dynamic behavior of bladed disks. *Appl Comput Mech* 1:531–540
5. Choi Y-S, Lee K-H (2010) Investigation of blade failure in a gas turbine. *J Mech Sci Technol* 24(10):1969–1974
6. Hassan M (2008) Vibratory analysis of turbomachinery blades. A project document. Rensselaer Polytechnic Institute, Hartford
7. Rajeevalochanam P, Agnimitra Sunkara SN, Mayandi B, Ganesh BB, Chappati VSK, Kumar K (2016) Design of highly loaded turbine stage for small gas turbine engine. In: ASME turbo expo 2016, South Korea
8. Chromek L (2016) Design of the blisk of an aircraft turbojet engine and verification of its resonance free operation. *Appl Comput Mech*

Dynamic Analysis of Thermo-Mechanically Loaded Functionally Graded Disks by an Iterative Variational Method



Priyambada Nayak  and Kashinath Saha 

Abstract The present study focuses on the free vibration behavior of functionally graded (FG) rotating disk under thermal and centrifugal load, up to the limit elastic state of stress. Power law variation across the radial direction is assumed for the material properties of the FG disks. Variational principles are used to obtain the governing equations, and energy principles are used for the analysis method. The solution algorithm is executed by utilizing MATLAB[®] computational simulation software. For various combinations of rotational speed and thermal load up to the limit elastic state as predicted by von Mises criteria, the dynamic characteristics of the FG disk are presented in a non-dimensional plane. Some parametric studies are carried out to explore the impacts of the disk geometries and material gradients on the in-plane natural and forced frequencies of the FG disks.

Keywords Iterative variational method · Functionally graded disk · Thermo-mechanically loaded · Dynamic analysis

1 Introduction

Functionally graded rotating disks with radially varying properties are mostly developed to work under thermo-mechanical loading conditions and are used in wide range of engineering applications, e.g., turbine rotors, grinding wheels, impellers, circular saw blades, etc. There is a significant change in vibration behavior of rotating disks that result from rotation. In mechanical design, the free vibration behavior of FG disks plays a significant role. Hence, a host of research works have focused on them; e.g., Weisensel [1] presented a broad literature review and search of accessible source of numerical results for natural frequency of stationary annular and circular elastic

P. Nayak · K. Saha (✉)
Mechanical Engineering Department, Jadavpur University, Kolkata 700032, India
e-mail: kashinathsaha@gmail.com

P. Nayak
e-mail: priyambada53@gmail.com

plates. Bauer and Eidel [2] computed the natural frequencies of isotropic disks in elastic domain by applying Ritz–Galerkin’s method to build an infinite-dimensional eigenvalue problem. Mazzei [3] used Rayleigh–Ritz method to investigate the natural frequencies of a rotating cantilever FG beam. Ramu and Mohanty [4] performed the vibration behavior of FG rotating plates by utilizing finite element method in high thermal environment. Nayak and Saha [5] evaluated the deformation states and elastic stresses in thermal environment of solid and annular rotating varying thickness disks by a numerical method.

Barasch and Chen [6] used the modified Adam’s method to solve the governing equations for radial eigenfunctions and depicted the natural frequencies by assuming a linear combination of independent solutions. Irie et al. [7] used spline interpolation technique to study the flexural vibration of rotating varying thickness annular disks and distribution of stress. Shahab [8] reported the transverse vibration characteristics of uniform, variable and flexible thickness disks by utilizing the Ritz method and also reported experimental findings by applying the method of holographic interferometry. Tomioka et al. [9] utilized Gram–Schmidt process to generate orthogonal polynomials and Ritz method to investigate the free vibration of a disk blade coupled system. A new higher-order plate theory was proposed by Luo [10] to investigate the asymmetric response of disks, and the large deflection asymmetric mode vibration of the nonlinear solution for rotating disks was proposed [11].

Tornabene [12] analyzed the dynamic characteristics of thick FG annular plates, cylindrical and conical shells based on the FSDT, by utilizing the generalized differential quadrature (GDQ) method. 3D free vibrations of multi-directional graded circular and annular plates were solved by Kermani et al. [13] by utilizing the state space-based differential quadrature method. Nie and Zhong [14] carried out the forced and free vibration of FG circular plate for various boundary conditions by assuming the exponential distribution of the material properties in the thickness direction. Dong [15] investigated the three-dimensional free vibration by utilizing the Chebyshev–Ritz method for FG annular plate with different boundary conditions. Malekzadeh et al. [16] analyzed the free vibration characteristics of FG thick annular plates deployed on the 3D elasticity theory in thermal environment. The material properties were considered to be graded in the thickness direction and temperature dependent. Yang et al. [17] created mesh-free boundary domain integral equation method for the investigation of forced vibration of FG beams assuming exponential distribution for material properties along either longitudinal or transverse direction. The study on rotating annular disk under uniform transverse pressure with out-of-plane free vibration was presented by Das et al. [18]. Vel and Batra [19] proposed three-dimensional analytical solutions for forced and free vibrations of simply supported FG rectangular plates, utilizing Mori-Tanka or the self-consistent scheme to estimate the effective material properties at a point.

In the present study, the vibration behavior of rotating FG disk under the action of centrifugal and thermal load has been investigated numerically by a variational method to derive the governing equations. The radial direction gradation is assumed for the material properties. The solutions are acquired under the assumption of plane stress and up to point of yield limit of the material. The solution algorithm is executed

by utilizing MATLAB[®] computational simulation software. The effects of some parameters such as disk geometries and material gradients on the frequency of the FG disk are investigated. The in-plane modes are only presented to illustrate the free vibration behavior of the disks.

2 Mathematical Formulation

The rotating annular disk with inner radius a and outer radius b is considered to carry out the mathematical formulation, and this generalized formulation is also suitable for solid disk. The problem is modeled under the assumption of plane stress, and the functionally graded material of the disk is presumed to follow a linear stress–strain relationship. The energy method-based formulation is used with suitable variational principles to derive the governing equations. The whole analysis has two parts. In the first part, the static problem of a FG rotating disk subjected to centrifugal load due to rotational speed (ω) is addressed. The corresponding static problem solution parameters are utilized to address the solution of the dynamic problem in the second part. It must be mentioned that the strain and stress measures are based on the original dimensions of the disk geometry and the rotary inertia effect is not considered in the dynamic analysis.

The material property variation of the FG disk is assumed to follow a power law distribution along the radial direction, and for any property (Y) it takes the following form [20]:

$$Y(r) = Y_i \left[1 - \left(\frac{r - a}{b - a} \right)^\beta \right] + Y_o \left(\frac{r - a}{b - a} \right)^\beta \tag{1}$$

where Y_i and Y_o denote the material properties at the inner and outer radii, respectively. However, Poisson’s ratio ν is assumed constant ($= 0.3$) for both the participating materials.

Since the static analysis formulation is necessary for the subsequent dynamic analysis, the governing equation is acquired by using the variational principle $\delta(U + V) = 0$, where the strain energy is U and V is the potential of the external loading of the rotating disk, respectively.

The mathematical expressions of U and V are expressed as

$$U = \frac{\pi}{(1 - \nu^2)} \int_a^b \left\{ \frac{u^2}{r} + 2\nu u \frac{du}{dr} + \left(\frac{du}{dr} \right)^2 \right\} E h dr \tag{2}$$

and

$$V = -2\pi\omega^2 \int_a^b \rho ur^2 h dr - \frac{2\pi(1+\nu)}{(1-\nu^2)} \int_a^b r \left(\frac{u}{r} + \frac{du}{dr} \right) E\alpha \Delta Q h dr, \tag{3}$$

where ΔQ is the change in temperature. The approximation of $u(\xi)$ in Eq. (3) is carried out by a linear combination of sets of orthogonal coordinate functions as $u(\xi) \cong \sum c_i \phi_i$, where the set of orthogonal functions ϕ_i are developed through Gram–Schmidt scheme. The unknown coefficients are c_i corresponding to the n_f number of functions $i = 1, 2, \dots, n_f$. To fulfill the boundary conditions of an annular disk, $\sigma_r|_{(a)} = 0$ and $\sigma_r|_{(b)} = 0$, the necessary start function is stated below:

$$\begin{aligned} \phi_o(r) = & \frac{\rho\omega^2 r(3+\nu)}{8E} \left[(b^2 + a^2)(1-\nu) - \left\{ \frac{(1-\nu^2)r^2}{(3+\nu)} \right\} + b^2 a^2 \frac{(1+\nu)}{r^2} \right] \\ & + \frac{\alpha}{r} \left[(1+\nu) \int_a^r \Delta Q(r) r dr + \frac{(1-\nu^2)r^2 + (1+\nu)a^2}{b^2 - a^2} \int_a^b \Delta Q(r) r dr \right]. \end{aligned} \tag{4}$$

Substituting the expressions given by Eqs. (2) and (3) in the principle of energy $\delta(U + V) = 0$ and utilizing the approximate expressions for displacement field, the governing equation is achieved in the matrix form as $[K]\{c\} = \{f\}$, where the stiffness matrix is $[K]$ and $\{f\}$ is the load vector.

First, the static analysis of the disk under centrifugal loading is carried out and then the displacement field obtained from the static analysis is utilized to carry out the dynamic analysis. In addition, the location of initiation of yielding is found out from the stress field obtained from the static analysis. The point of yield initiation is identified through von Mises yield criterion, i.e., when the von Mises stress $\sigma_{vm} = \sqrt{\sigma_r^2 + \sigma_\theta^2 - \sigma_r \sigma_\theta}$ reaches the value equal to that of the uniaxial yield stress σ_y . The governing equation for the dynamic analysis is derived from Hamilton’s principle, $\delta \left(\int_{\tau_1}^{\tau_2} \zeta d\tau \right) = 0$, where $\zeta = T - (U + V)$ is the Lagrangian and the total kinetic energy is T . The expression of V becomes zero, in the present analysis due to free vibration. The mathematical expression remains similar as stated in Eq. (2) for U , and kinetic energy T is expressed as

$$T = \pi \int_a^b \rho \left(\frac{\partial u}{\partial \tau} \right)^2 h r dr. \tag{5}$$

The dynamic displacement $u(\xi, \tau)$ is presumed to be separable in time and space in the form as $u(\xi, \tau) = \sum_{i=1}^{n_f} c_i \phi_i(\xi) \gamma_i(\tau)$, where the new arrangement of unknown coefficients is c_i and the function obtained through the static analysis is ϕ_i , $\gamma_i(\tau) = e^{i\Omega\tau}$ is the form for the temporal functions where the system natural frequency is represented by Ω and $i = \sqrt{-1}$. For the dynamic analysis, the governing equation

is achieved by substituting the expressions given by Eqs. (2) and (5) in the above stated Hamilton’s principle and utilizing the series form approximation as

$$-\Omega^2[M]\{c\} + [K]\{c\} = 0, \tag{6}$$

where the mass matrix is $[M]$ and the stiffness matrix is $[K]$ same as that of the static problem.

Equation (6) can be transformed into a standard eigenvalue problem. The natural frequencies of the FG disk are determined from the eigenvalues which are obtained numerically by using MATLAB® software. The in-plane mode shapes are plotted by using the displacement fields corresponding to each of the eigenvalues.

3 Results and Discussion

In the present paper, the free vibration behavior of FG rotating disk subjected to centrifugal loading is carried out. The results are presented for the FG disk having the inner and outer radii as $a = 0.2$ m and $b = 1.0$ m, respectively. Y in Eq. (1) is replaced by elasticity modulus (E), coefficient of thermal expansion (α) and density (ρ) of the hollow disk, respectively, to obtain the corresponding variation in material properties. The material at the outer surface is zirconia (ceramic) and inner surface is aluminum (metal), representative material properties of which are listed in Table 1. The variation depends on the gradient parameter (β) describing the change of the volume fraction of two constituents. A graphical representation of the material properties (E , ρ and α) with radial coordinate given by Eq. (1) is shown in Fig. 1a–c for variable gradient parameters, $\beta = 2, 1, 0.5$ and 0.25 . The effect of temperature on the material properties (E , ρ and α) of the aluminum (metal) is considered in the analysis as shown in Fig. 1a–c [21], whereas the material properties at ambient values are considered for the zirconia (ceramic). The yield stress σ_y is assumed as 350 MPa for both the materials. The analysis is carried out for four equal weight disks having different geometries with thickness variations: uniform, taper, exponential and parabolic. The expression of thickness $h(\xi)$ for an exponential disk is given by $h_o \exp[-n(\xi)^k]$ and for a parabolic disk, $h(\xi) = h_o[1 - n(\xi)^k]$. Uniform and taper thickness disks are determined by putting $k = 1$ and $n = 0$ in the form of profile for parabolic variation.

The effect of material gradient parameters on vibration frequencies is shown in Fig. 2a–d for different disk geometries for the first four vibration modes in static condition. It is clear that the vibration frequency decreases with the increase in

Table 1 Material properties

Disk surface	Inner surface	Outer surface
E (GPa)	70	151
α ($10^{-6}/^\circ\text{C}$)	23	10
ρ (kg/m^3)	2700	5700

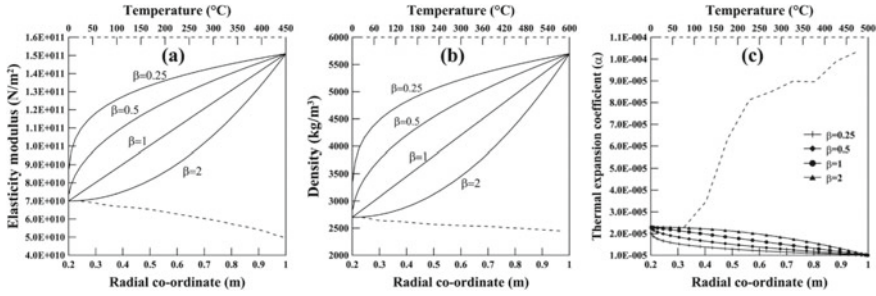


Fig. 1 Variation of **a** elastic modulus (E), **b** density (ρ) and **c** thermal expansion coefficient (α) distributions. Solid lines indicate the variation along the radial direction of the disk for gradient parameters ($\beta = 2, 1, 0.5$ and 0.25), and dotted lines indicate the variation with temperature for aluminum [21]

gradient parameters in general and this is true for all the disk geometries. However, in some cases there is a change in the dynamic behavior after a specific value of gradient parameter, as observed in Fig. 2a for taper disk and in Fig. 2b for second vibration mode of uniform disk. The effect of temperature (ΔQ) = 0–200 °C is also shown in Fig. 2 in dotted lines for $\beta = 1$ for different disk geometries. It is seen that the vibration frequency decreases with increment in temperature for all the modes of vibration.

The effect of rotational speed on loaded frequencies is shown in Fig. 3a–d for $\beta = 2$ for various disk geometries for the first four modes of vibration. The loaded frequencies for various disk geometries are generated up to the limit elastic state, in each of the plots of Fig. 3. From Fig. 3, it is found that the vibration frequency increases with increment in rotational speed for all the vibration modes except for the mode 1 vibration. For the first vibration mode, the vibration frequency decreases with increase in rotational speed.

The mode shape plots for the first four modes of vibration are displayed in Fig. 4a, b for uniform FG disk with $\beta = 0.25$ and $\beta = 2$. It is obvious from the gradation relation in Eq. (1) that with the increment in the value of gradient parameter (β), the disk possesses more flexibility which increases the amplitude of vibration for the similar loading conditions for the prescribed disk geometry.

4 Conclusions and Future Scope of Work

This paper presents the free vibration dynamic behavior of FG rotating disks under centrifugal and thermal loading up to the limit elastic state. The analysis method is deployed on the principles of energy and is approximate in nature. The solution algorithm is executed by utilizing MATLAB® computational simulation software. Various results are furnished to depict the effect of material parameters and loading

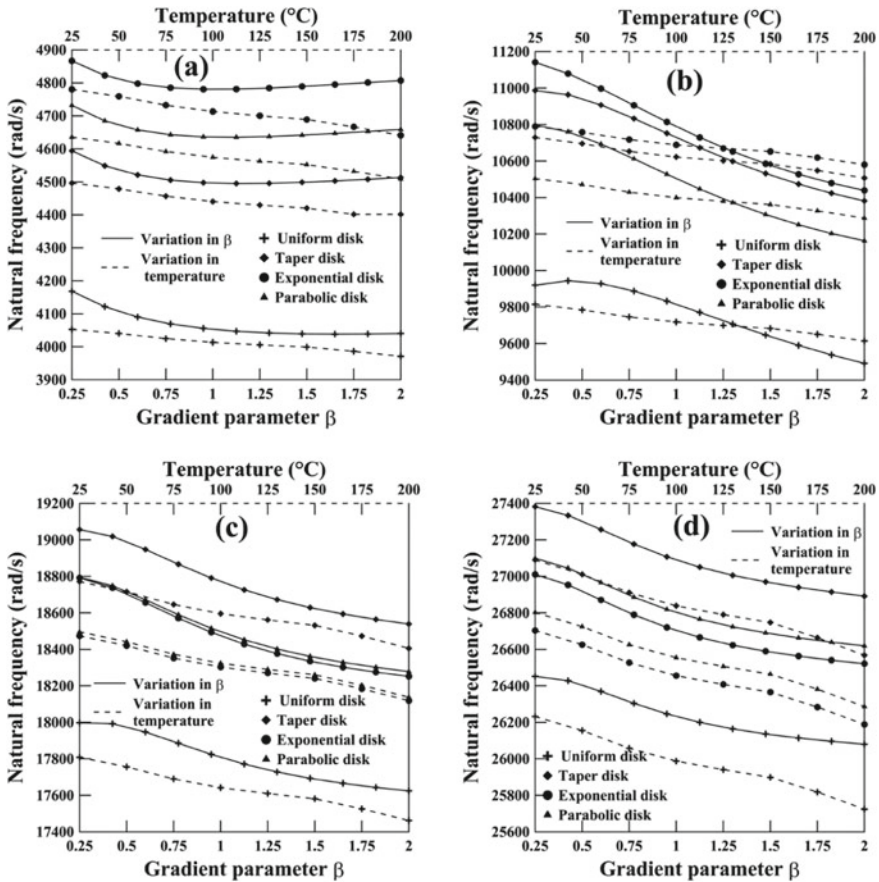


Fig. 2 Variations in natural frequency of FG disk for different geometries in static condition: **a** mode 1, **b** mode 2, **c** mode 3 and **d** mode 4. Solid lines indicate variation in gradient parameter (β) $\Delta Q = 0$, and dotted lines indicate variation in temperature for $\beta = 1$

parameters on the dynamic behavior of FG rotating disks. It is found that the increment in gradient parameters increases the amplitude of vibration for the prescribed disk geometry.

The paper dealt with minimal set of parameter variations, and effect of variation in thermal field could not be touched upon due to restriction in space. However, on top of an elaborate parametric study, future scope of work also includes the following aspects:

- Investigation of the out-of-plane vibration behavior of rotating disks.
- Effect of rotary inertia on the dynamic characteristics of rotating disks.
- Material gradients in both radial and axial directions.

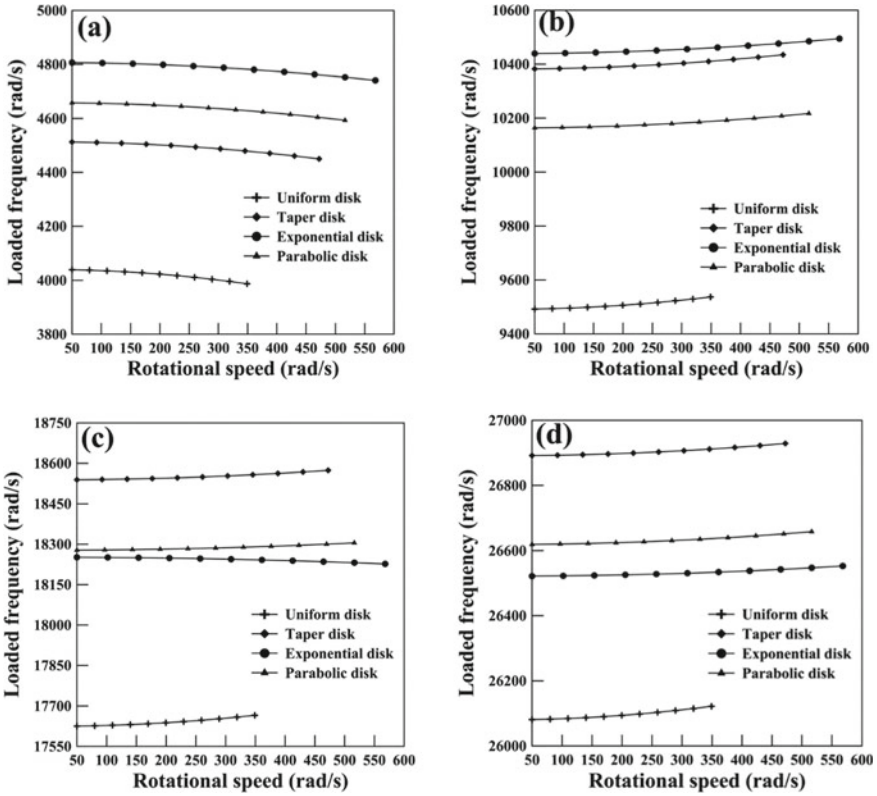


Fig. 3 Loaded frequency versus rotational speed for FG rotating disk of different geometries: a mode 1, b mode 2, c mode 3 and d mode 4

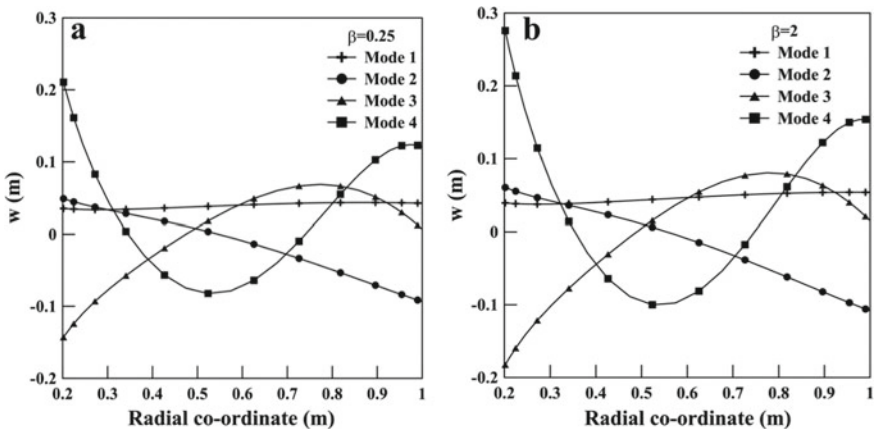


Fig. 4 Mode shapes of FG uniform disk for a $\beta = 0.25$ and b $\beta = 2$

Acknowledgements The first author gratefully acknowledges support from the Council of Scientific and Industrial Research (CSIR) funded by the Government of India for the financial grant.

References

1. Weisensel GN (1989) Natural frequency information for circular and annular plates. *J Sound Vib* 133(1):129–137
2. Bauer HF, Eidel W (2007) Transverse vibration and stability of spinning circular plates of constant thickness and different boundary conditions. *J Sound Vib* 300:877–895
3. Mazzei AJ (2012) On the effect of functionally graded materials on resonances of rotating beams. *Shock Vib* 19:707–718
4. Ramu I, Mohanty SC (2017) Free vibration analysis of rotating plates in high thermal environments using the finite element method. *Int J Acoust Vib* 22:58–67
5. Nayak P, Saha KN (2012) Thermo mechanical analysis and design of rotating disks. In: Emerging trends in science, engineering and technology, proceedings of international conference, INCOSSET 2012. Springer, India, pp 473–484
6. Barasch S, Chen Y (1972) On the vibration of a rotating disk. *J Appl Mech* 39:1143–1144
7. Irie T, Yamada G, Kanda R (1979) Free vibration of rotating non-uniform discs: spline interpolation technique calculations. *J Sound Vib* 66:13–23
8. Shahab AAS (1993) Finite element analysis for the vibration of variable thickness discs. *J Sound Vib* 162:67–88
9. Tomioka T, Kobayashi Y, Yamada G (1996) Analysis of free vibration of rotating disk-blade coupled systems by using artificial springs and orthogonal polynomials. *J Sound Vib* 191:53–73
10. Luo ACJ (2000) An approximate theory for geometrically-nonlinear thin plates. *Int J Solids Struct* 37:7655–7670
11. Luo ACJ, Mote CD (2003) Asymmetric responses of rotating, thin disks experiencing large deflections. *Comput Math Appl* 45:217–228
12. Tornabene F (2009) Free vibration analysis of functionally graded conical, cylindrical shell and annular plate structures with a four-parameter power-law distribution. *Comput Methods Appl Mech Eng* 198(37–40):2911–2935
13. Kermani ID, Ghayour M, Mirdamadi HR (2012) Free vibration analysis of multi-directional functionally graded circular and annular plates. *J Mech Sci Technol* 26(11):3399–3410
14. Nie GJ, Zhong Z (2007) Semi-analytical solution for three-dimensional vibration of functionally graded circular plates. *Comput Methods Appl Mech Eng* 196:4901–4910
15. Dong CY (2008) Three-dimensional free vibration analysis of functionally graded annular plates using the Chebyshev-Ritz method. *Mater Des* 29:1518–1525
16. Malekzadeh P, Shahpari SA, Ziaee HR (2010) Three-dimensional free vibration of thick functionally graded annular plates in thermal environment. *J Sound Vib* 329:425–442
17. Yang Y, Lam CC, Kou KP (2016) Forced vibration analysis of functionally graded beams by the meshfree boundary-domain integral equation method. *Eng Anal Boundary Elem* 72:100–110
18. Das D, Sahoo P, Saha K (2009) Free vibration analysis of a rotating annular disc under uniform pressure loading. *Proc Inst Mech Eng Part C J Mech Eng Sci* 224:615–634
19. Vel SS, Batra RC (2004) Three-dimensional exact solution for the vibration of functionally graded rectangular plates. *J Sound Vib* 272:703–730
20. Peng XL, Li XF (2010) Thermal stress in rotating functionally graded hollow circular disks. *Compos Struct* 92:1896–1904
21. Narender K, Rao ASM, Rao KGK, Krishna NG (2013) Temperature dependence of density and thermal expansion of wrought aluminum alloys 7041, 7075 and 7095 by gamma ray attenuation method. *J Mod Phys* 4:331–336

Stationary and Rotating Frame Instrumentation for Large Scale Rotating Rig



N. Poornima, R. Senthil Kumaran, and Kishor Kumar

Abstract The Large Scale Rotating Rig at NAL is designed to carry out detailed experimental investigations of the flow through compressor and turbine stages. Instrumentation and data acquisition system (DAS) for stationary and rotating frame measurements, pressure distribution measurements across the vane and the blade surface and the flow measurement was developed in-house. This enabled making pressure measurements on the vane surfaces, blade surfaces, platforms and at the vane/blade exit wake flows. There were added challenges in terms of unsteady pressure measurements, transferring of data from rotating frame and condition monitoring of the rig. The DAS is developed using state-of-the-art instruments and is coupled with a GUI data acquisition software developed using LabVIEW to tackle all these challenges. This paper presents elaborated details of the multichannel instrumentation and the DAS.

Keywords Calibration · Data acquisition system · Instrumentation · LabVIEW · Rotating frame measurements · Slip ring

Nomenclature

Symbol	Description
C_x	Axial velocity
fb	Blade pass frequency
U	Blade speed

N. Poornima (✉) · R. Senthil Kumaran · K. Kumar
Propulsion Division, CSIR-National Aerospace Laboratories, Bengaluru, Karnataka 560017, India
e-mail: poorni_n@nal.res.in

R. Senthil Kumaran
e-mail: rsk@nal.res.in

K. Kumar
e-mail: kishorkumar@nal.res.in

5H	5 hole
3H	3 hole
x	Distance in axial direction
Abbreviations	Full Form
CSIR	Council of Scientific and Industrial Research
DAS	Data acquisition system
LSRR	Large Scale Rotating Rig
NAL	National Aerospace Laboratories
P&W	Pratt & Whitney
GUI	Graphical user interface
Pcal	Calibration pressure
Pref	Reference Pressure
Patm	Atmospheric pressure
kS/s/ch	Kilo samples per second per channel

1 Introduction

The Large Scale Rotating Rig (LSRR) installed at CSIR-NAL is an open-circuit suck-down type of turbomachinery rig. The schematic layout of LSRR is shown in Fig. 1. Atmospheric air is drawn through a twelve-foot diameter bell mouth fitted with honeycomb at the inlet to minimize cross flows. The air passes through a series of fine mesh flow straightening screens to the test section. The test section houses a single-stage high work axial flow turbine with 44 nozzle guide vanes (NGV) and 48 rotor blades. At the downstream of the test section, the flow passes through an annular

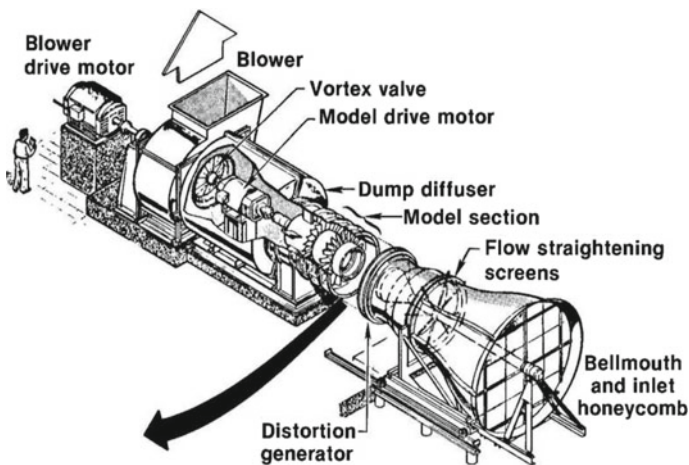


Fig. 1 Schematic layout of LSRR

diffuser into a centrifugal blower and is discharged from the rig. A vortex valve at the blower inlet controls the mass flow rate through the test section. The blower can provide a pressure rise up to 21" H₂O. The rotor is driven by a DC motor system, which is capable of shaft speeds up to 700 rpm. The rotor is driven by a 200 hp DC motor, controlled by a thyristor-based regenerative drive system. Researchers from Pratt & Whitney, USA, have carried out extensive research related to turbine and compressor aerodynamics in the LSRR [1–8].

Mechanical instrumentation for measuring aerodynamic quantities is available in the rig which includes 5-hole pressure probes, 3-hole cobra probes, total pressure probes, thermocouples, static pressure tappings, etc., at various locations in the rig. One 5-hole probe integrated with a 3-hole cobra probe is mounted at the vane exit on the casing, and another such set is mounted at the blade exit on the rotor disk. The vane exit probe combination is used to measure steady-state wake flow total pressure, static pressure, flow velocity and direction in the circumferential plane at any chosen radial location in the stationary frame. The blade exit probe combination is used to make similar measurements at the rotor exit in the rotating frame.

The rig instrumentation also consists of ZOC pressure scanners, static pitot probes, Scanivalve pressure transducers, Scanivalve digital temperature scanner, Scanivalve multiplexers, pneumatic probes, Kulite unsteady pressure sensors, thermocouples, rotor speed sensor, etc.

2 Data Acquisition System of LSRR

The complete DAQ system of LSRR can be divided into four sub-modules as condition monitoring, stationary frame pressure measurement system, rotating frame pressure measurement system and unsteady pressure measurement system.

2.1 Condition Monitoring

Important trim parameters such as inlet total pressure, temperature, rotor speed and axial velocity of the flow are continuously monitored and recorded during the experiments. A number of Kiel probes and thermocouples are distributed circumferentially over the test section to measure the inlet total pressure and temperature. A calibrated pitot-static probe mounted upstream of the stator is used to measure the axial velocity of the flow entering the test section. Speed of the rotor is measured by a magnetic pickup mounted on the shaft. The flow coefficient (C_x/U) is used as the parameter to set the flow condition at the inlet of the test section. The bearing temperatures at various locations of the rig are continuously monitored using thermocouples, while the rig is in operation. The software is programmed to give warning indication if any of the bearing temperatures or the rotor speed crosses the safety limit. The vibration signals are monitored during the initial trial runs after the installation of the rig but

it is not a part of regular experiments. A digital thermocouple scanner, DTS3250, is incorporated for temperature measurement.

The DTS3250 digital thermocouple scanner is a rugged temperature-controlled stand-alone module incorporating 32 thermocouple inputs, a 22 bit A/D converter for each of the input channel, a RAM and a microprocessor. This module is made to communicate via Ethernet. The module is provided with an isothermal block for Uniform Temperature Reference (UTR), with an accuracy of 0.01%. NIST thermocouple tables of standard thermocouples are stored in the RAM. The microprocessor uses these look-up tables to convert mV inputs into engineering units. Temperature can be displayed in °C, °F, °R, K, volts or A/D counts. The total system error of the DTS3250 module for E-, J-, K- and N-type thermocouples is ± 0.2 °C. This module can be controlled with an external or software scan trigger. All the scan and calibration variables are configured by the user through the software, which includes the sampling speed, number of frames per scan, number of averages per frame, etc. More details about this module are available in [9].

2.2 Stationary Frame Measurement System

The stationary frame measurement involves vane surface pressure measurement using ZOC miniature pressure scanners and vane exit wake flow measurement using the calibrated 5-hole/3-hole probe combination, controlled by a 3-axis stepper motor-based probe traverse mechanism. Figure 2 shows the block schematic of the stationary frame measurement system.

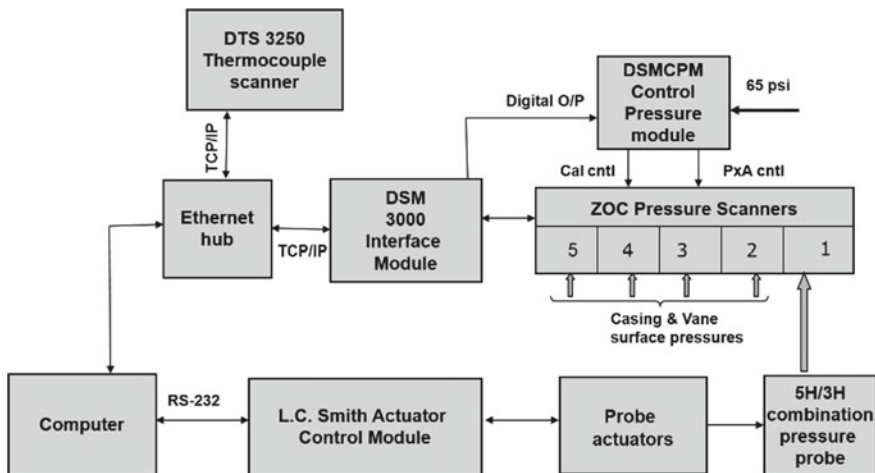


Fig. 2 Block schematic of stationary frame measurement system

Vane surface and platform pressures are measured from the pressure tappings using four 64 port ZOC pressure scanners (ZOC33/64Px) of range ± 1 psid. The pressure scanners are interfaced with a stand-alone module, DSM 3000. Each ZOC33/64Px module contains 64 sensors in eight sensor packs. Each pack contains eight sensors, a calibration valve, an excitation board and a high-speed multiplexer. The channel to be recorded is selected by a 6-bit binary address. The pneumatic inputs consist of pressure input ports (P_x inputs), control pressure ports (P_x A Ctl, CAL Ctl), calibration input and reference input. A control pressure of 65 psi is used to switch the pressure scanner to different modes of operation, namely calibrate, operate and isolate. The switching action is controlled by a control pressure module, DSM CPM 3000. Complete details of ZOC33/64Px module are available in [10]. The DSM 3000 interface module allows the ZOC pressure scanners to be used in an Ethernet system. The DSM can accept 8 ZOC modules. The DSM has individual 16-bit A/D converter, for each ZOC module.

The digital outputs of the DSM control the operation of the control pressure module. The DSM contains many configuration variables which are set up appropriately for it to function properly. The configuration variables dictate the DSM about the number of channels to be included in the scan, number of samples to acquire, output engineering unit, etc. Complete details of these configuration variables and commands are given in [10]. The data acquisition software is developed using National Instruments LabVIEW to acquire 250 channels of pressures from the stationary frame. The software incorporates a GUI-based front panel as shown in Fig. 3 for the user to interact with the data acquisition system and monitor the rig parameters.

While the program is executed, the vane surface pressures are measured through the ZOC pressure scanner. The trim parameters such as C_x/U , speed, inlet total pressure, inlet total temperature and the bearing temperatures are displayed. The user has the option to define the name of the output file, number of acquisitions and the interval. The averaged data is recorded in a user-defined file.

The vane exit wake flow measurement involves mapping of the flow parameters with the help of a calibrated combined 5-hole/cobra 3-hole pressure probe. Measurements are carried out in the stationary frame by traversing these probes in the circumferential plane at chosen radial location across two vane pitches (approximately 18°). The probes are moved and paused over a number of points at regular intervals for measuring flow variables during the circumferential traverse. Aerodynamic parameters such as total pressure coefficient, dynamic pressure, flow directions (yaw and pitch components) and flow velocities can be deduced using the probe pressures measured during the traverse. The probe actuators with gears are used to displace the probes in the radial/circumferential directions. While a ball bearing rod (BBR) actuator is used for the radial and yaw movements, a third motion actuator is used for the circumferential motion. The actuators are equipped with stepper motor drives for moving the probe and also fitted with potentiometers for obtaining the position feedback. Limit switches are provided to define the safe operational range. The actuator control unit used to operate the probe works as a stand-alone unit, or it can interface with the computer through the RS-232 port. A snapshot of the front panel of the vane

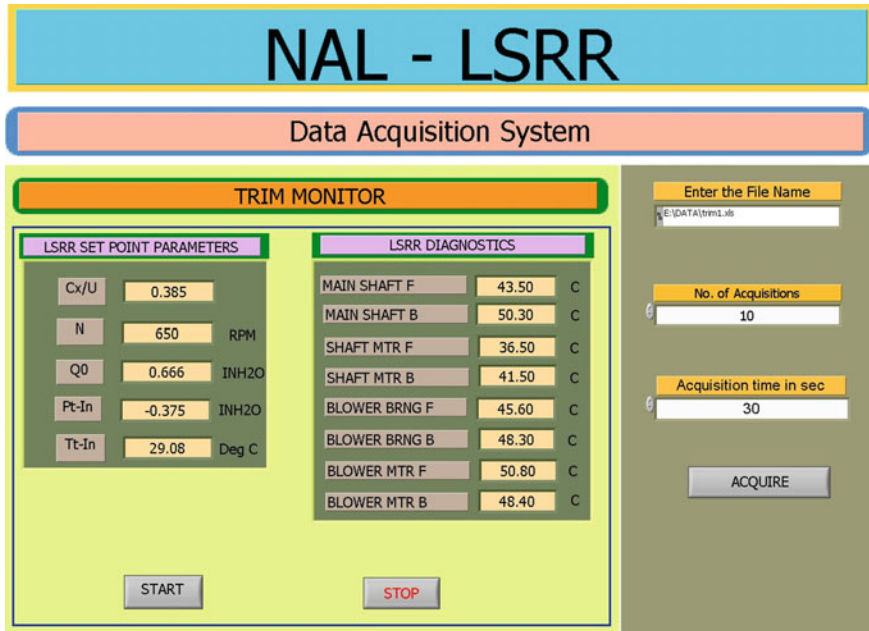


Fig. 3 Front panel of vane surface pressure measurement

exit flow measurement system is shown in Fig. 4. The user is prompted to enter the input and output data file paths. The input data file contains the radial, yaw and the set of pitch-wise locations for the probe traverse.

When the program is executed, the probe positions are read from the predefined file. The radial location is set first; the yaw angle is set next, and the circumferential traverse commences. At each circumferential location, the pressures from 5-hole and 3-hole probes are measured by the ZOC pressure scanner. The data is acquired over a period of 10 s, and the averaged data is written to the user-defined output file with the radial and yaw positions of the probe. A typical vane surface pressure data measured is plotted in terms of velocity ratio and compared with P&W data in Fig. 5. A typical vane exit total pressure coefficient distribution measured using the 5-hole probe is compared with P&W data in Fig. 6.

2.3 Rotating Frame Measurement System

The rotating frame pressure measurement comprises:

- Rotor exit flow measurement/rotating frame probe traverse measurement.
- Blade surface pressure measurement.
- Calibration of rotating pressure transducers.

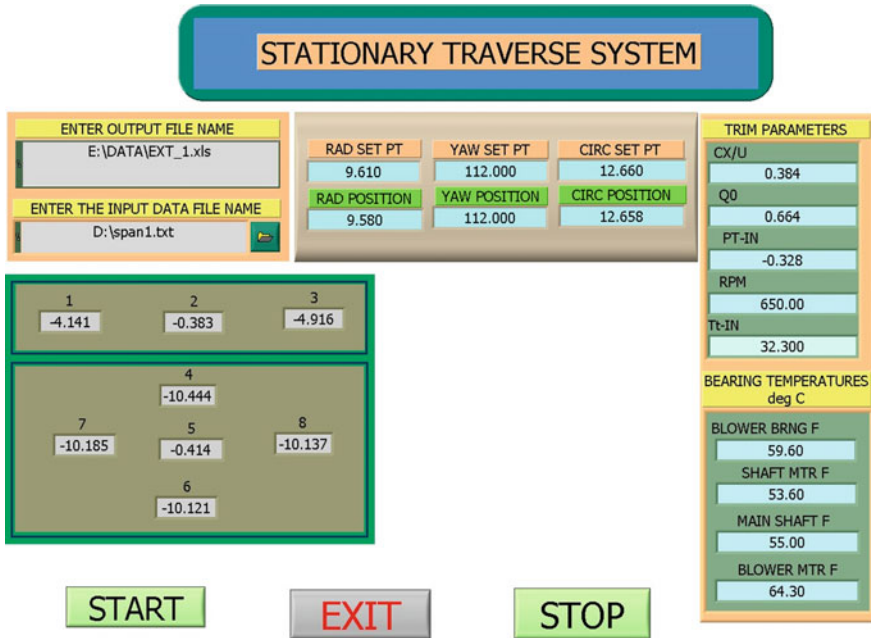


Fig. 4 Front panel of vane exit flow measurement

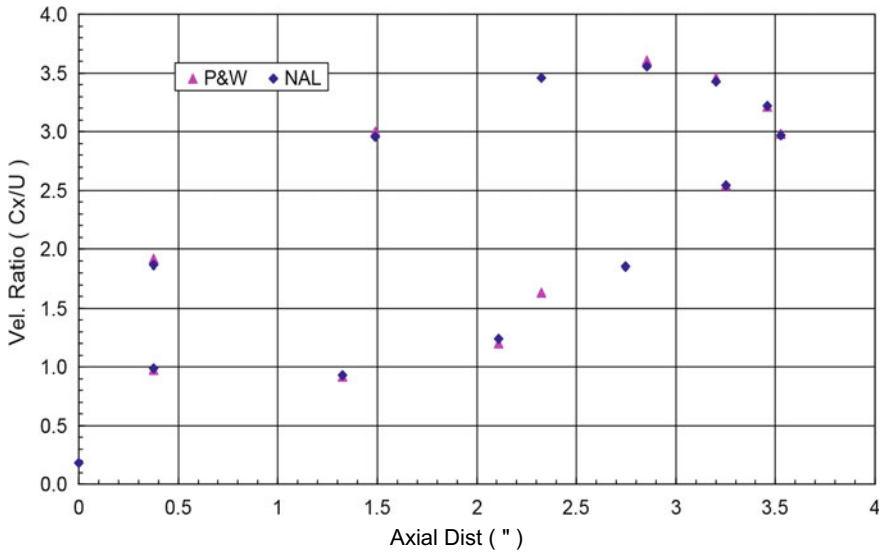


Fig. 5 Typical plot of vane surface velocity distribution

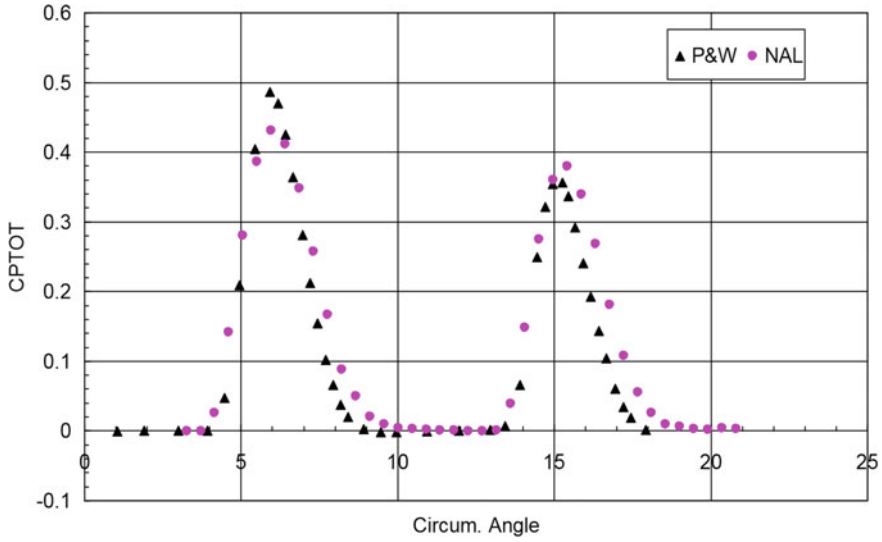


Fig. 6 Typical plot of vane exit total pressure coefficient distribution

The block schematic of rotating frame measurement system is shown in Fig. 7.

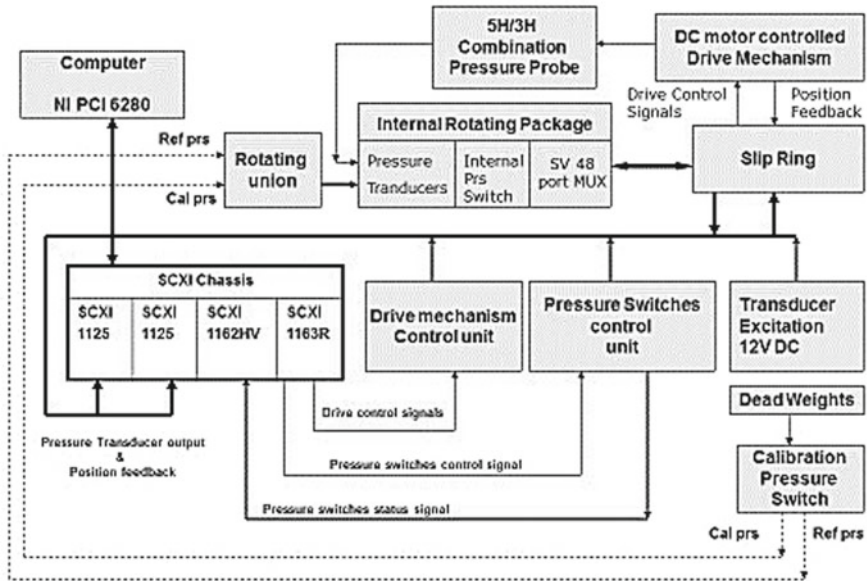


Fig. 7 Block schematic of rotating frame measurement system

2.3.1 Rotor Exit Flow Measurement/Rotating Frame Traverse Measurement

The rotor exit flow measurement involves mapping of blade exit wake flow field using a rotating calibrated 5-hole/3-hole pressure probe combination with a 3-axis traverse mechanism. Figure 8 shows the schematic of the probe.

The traverse mechanism consists of three 26 V DC motors for 3-axis movement of the probe. Feedbacks from individual potentiometers are provided for all the three drives to know the position of the probe. An input voltage of 5 V is fed to the potentiometer. Each drive has two limit switches to avoid the movement of the probe beyond a set limit in both directions. Traverses are made at different radial locations across one blade pitch (7.5°) using 30 uniformly spaced pitch-wise locations. The internal rotating package mounted inside the hollow rotor shaft consists of five 1 psi differential pressure transducers (named SV, Y1, Y2, P1, P2), a 48 port Scanivalve pressure multiplexer (SV MUX), a fluid switch stepper and 3 Scanivalve wafer switches. A regulated excitation voltage of 12 V is fed to the transducers. The input voltage to the motor, pressure switches, potentiometers and internal transducers are fed through slip ring. The output voltage of the transducers and the feedback from the potentiometers are passed through the slip ring to the data acquisition system. The fluid switch position determines the mode of operation of the transducers. There are four modes, namely calibration mode, zero mode, 5-hole probe measurement mode and 3-hole probe measurement mode as mentioned in Table 1. The fluid switch stepper is set to position '0' for calibrating the transducers, position '1' for acquiring the initial value of the transducers (CAL and REF ports of the transducers are both connected to PREF), position '2' for measuring the 5-hole probe pressures and position '3' for measuring the 3-hole probe pressures.

The data transfer through the slip ring created huge deterioration of the signals due to impedance mismatch and noise. To overcome this issue, several onboard signal conditioners are placed over the rotating shaft to condition the low-level signals before they are fed to the slip ring. A sample chart indicating the offset signal of a rotating transducer acquired over time is shown in Fig. 9. It is seen that the transducer

Fig. 8 Schematic of 5-hole/3-hole pressure probes

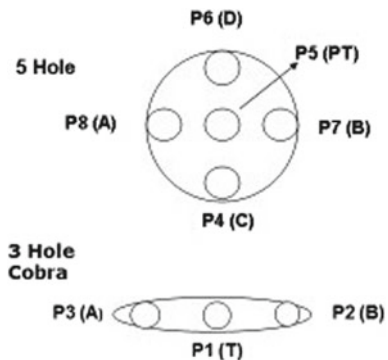


Table 1 Operating modes of rotating transducers

SV MUX position	1	0	1	1
Fluid switch stepper position	0	1	2	3
Mode	Calibration	Zero	5-Hole	3-Hole
SV	Pcal-Pref	Pref-Pref	P5-Pref	P1-Pref
Y1	Pcal-Pref	Pref-Pref	P8-P7	P3-P2
Y2	Pcal-Pref	Pref-Pref	P8-P5	P3-P1
P1	Pcal-Pref	Pref-Pref	P6-P4	Pcal-Pref
P2	Pcal-Pref	Pref-Pref	P6-P5	Pcal-Pref

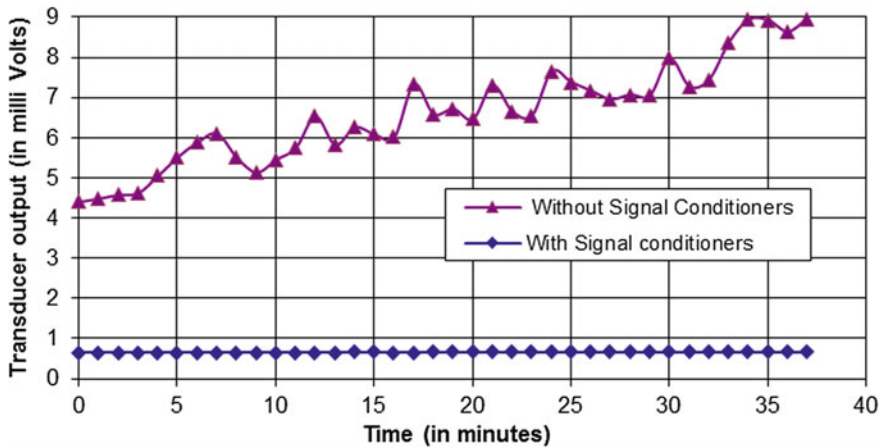


Fig. 9 Rotating transducer output signal transferred via slip ring

offset signal has huge drift and unstable without signal conditioners but it is true and stable after incorporating the signal conditioners.

The data acquisition system for rotating frame measurement is built using **NI PCI 6280 18-bit card** with the following signal conditioning modules. More details of the card and signal conditioning modules are available in [11].

1. SCXI 1125

Two SCXI 1125 analog input signal conditioning modules are used to read the five transducers’ output and the three potentiometer feedback values. The analog inputs of the SCXI 1125 consist of eight programmable isolation amplifiers. Each channel can be programmed independently for input ranges from ± 2.5 mV to ± 5 V. Each channel has a low-pass filter that can be configured for 4 Hz or 10 kHz.

2. SCXI 1163R

The SCXI 1163R optically isolated solid-state relay module is used to control the drive system and the pressure switches. The SCXI 1163R contains 32 normally

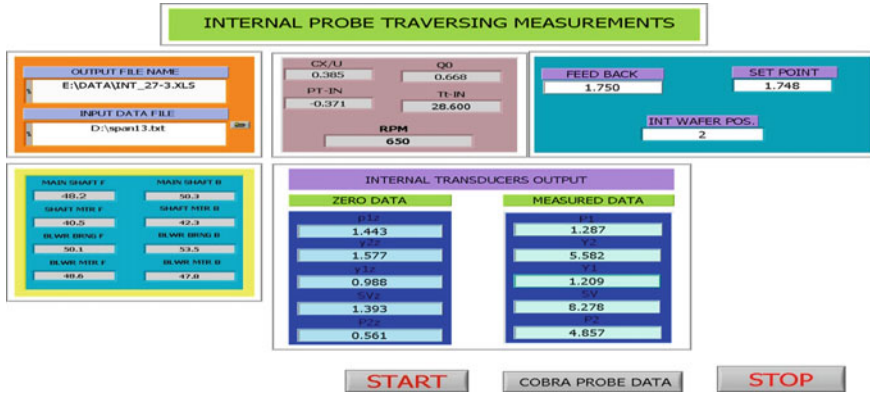


Fig. 10 Front panel of rotor exit flow measurement system

open or Form A solid-state relays arranged in eight banks of four relays with one common pole for each bank. It can switch high-voltage loads, up to 240 V AC/DC and up to 200 mA.

3. **SCXI 1162HV**

The SCXI 1162HV optically isolated digital input module is used to know the status of the Scanivalve multiplexer and the wafer switches. The SCXI 1162HV has 32 channels of optically—isolated digital inputs, arranged into eight isolated banks of four input lines each.

The front panel of the rotor exit wake flow measurement software is shown in Fig. 10. The flow condition is set based on the C_x/U value. The user is prompted to enter the input and output data file paths. The input file contains a list of predefined locations for the probe traverse. At each pitch-wise location, the yaw stepper is switched to acquire the transducer initial offset followed by the probe data (either 5H or 3H or both, as instructed by the user) and the data is recorded in the user-defined output file.

2.3.2 Blade Surface Pressure Measurement

The pressure distribution on the rotor blade surface is measured using the 48 port Scanivalve mechanical multiplexer in the internal rotating package. The pressure tubes from the instrumented blades are connected to the multiplexer. The multiplexer is first set to the 'Home' position and later stepped through all the 48 ports. At each position, the pressure is sensed by the SV pressure transducer in the internal package. The output of the transducer is sensed by one of the channels of SCXI 1125 and recorded in a file. Later the voltage outputs are translated into engineering units using the calibration coefficients of the transducers. The Scanivalve multiplexer is connected as shown below:

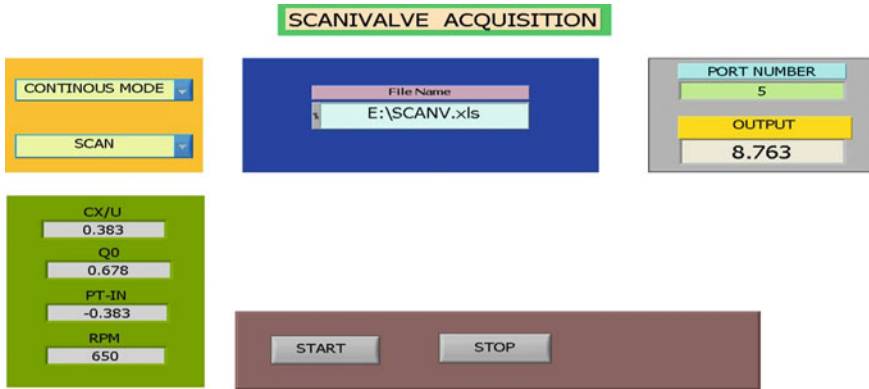


Fig. 11 Front panel of blade surface pressure measurement

1. Port '0' for transducer initial offset check.
2. Port '1' for calibration and 5-hole/3-hole probe total pressure measurement.
3. Ports '2' to '47' for blade pressure distribution measurements.

The front panel of blade pressure distribution measurement system is shown in Fig. 11. The user has option to select either the continuous mode or the single-step mode. In the continuous mode, the multiplexer steps through all the 48 ports starting from the 'Home' position. At each position, the data is averaged over a period of 10 s and the averaged data is written to a file. In the single-step mode, the multiplexer is stepped only when the 'NEXT' button is pressed.

2.3.3 Calibration of the Rotating Pressure Transducers

The internal transducers are calibrated in rotation by giving different calibration pressures from four 'dead weight testers.' The pressures from the dead weight testers are transmitted to the transducers using nitrogen gas. The calibration fluid is transferred to the rotating frame through a specially designed rotating union. The dead weight testers are set for calibration pressures of 8" H₂O, 15" H₂O, 22" H₂O and 27" H₂O. The outputs of the dead weights are connected to the calibration pressure switch, which is a two-sided six-port wafer switch. A five-point calibration is carried out by moving the calibration switch through position '0' to position '5' to get various combinations of calibration pressures while maintaining the reference pressure constant. Figure 12 shows the calibration switch plumbing. Table 2 shows the calibration pressure for various positions of the calibration switch. These pressures are read accurately ahead of the rotating union using two ports of the ZOC pressure scanner.

The calibration pressure value and the corresponding outputs of the transducers are recorded to a file. A linear curve fit is obtained by plotting the transducer output against the differential calibration pressures. The calibration data and the linear curve fit for one of the rotating pressure transducers are shown in Fig. 13. A typical rotor

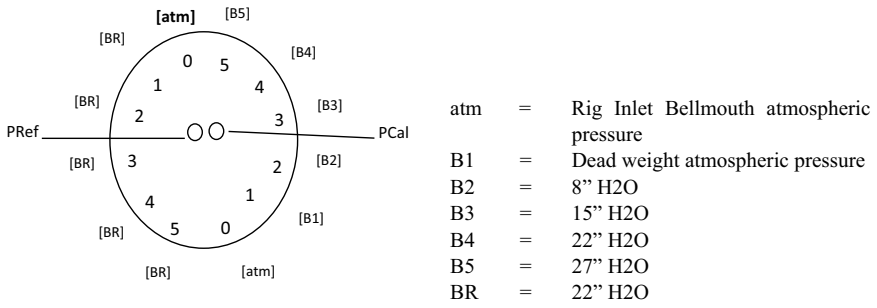


Fig. 12 Plumbing layout of the calibration pressure switch

Table 2 Calibration pressures for various positions of wafer switch

Calibration wafer position	CAL ("H2O)	REF ("H2O)	ΔP (CAL-REF)
0	Atm prs	Atm prs	0
1	0	22	-22
2	8	22	-14
3	15	22	-7
4	22	22	0
5	27	22	+5

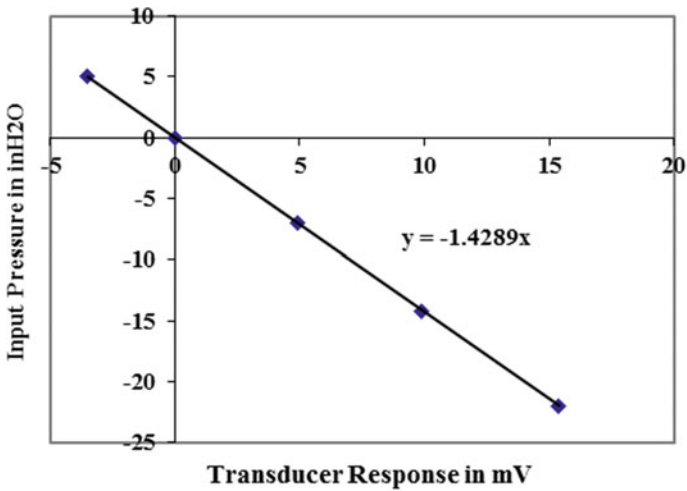


Fig. 13 Typical calibration chart of a rotating pressure transducer

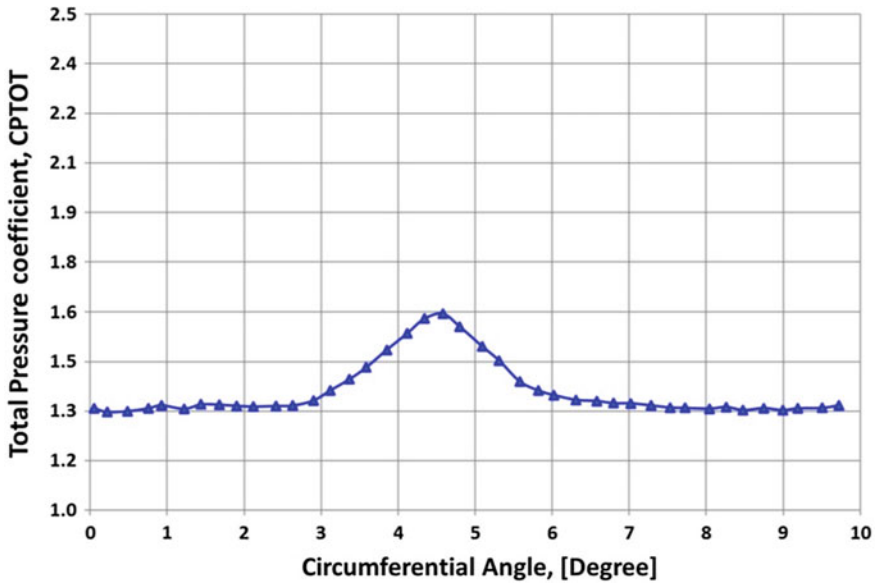


Fig. 14 Typical rotor blade exit total pressure coefficient variation

blade exit total pressure coefficient distribution in the wake flow measured using the rotating 5-hole probe and DAS is shown in Fig. 14.

2.4 Unsteady Pressure Measurement System

The rig is fitted with high response pressure transducers on the curved casing surface of the blade outer air seal segments to study the unsteady effects in turbine tip clearance flows. Five Kulite high-response miniature pressure transducers of range 5 psid are positioned at five different axial locations relative to the blade tip footprint as shown in Fig. 15. The low-level output signals of the pressure transducers are conditioned using AD524 instrumentation amplifiers. The pressure transducers are calibrated after being installed in the rig. The data is acquired using NI PCI 6143 16-bit simultaneous sampling multifunction data acquisition card. An optical pickup is used to trigger the phase-locked data acquisition. The data is acquired at a rate of 10 kS/s/ch. Typically, 50 ensembles were recorded and the ensemble averaged data is used for calculating the unsteady pressure coefficient. A typical plot displaying the unsteady pressure variation at one of the axial locations is shown in Fig. 16. A detailed tip leakage flow study was carried out in LSRR using this unsteady pressure measurement system and is published in [12].

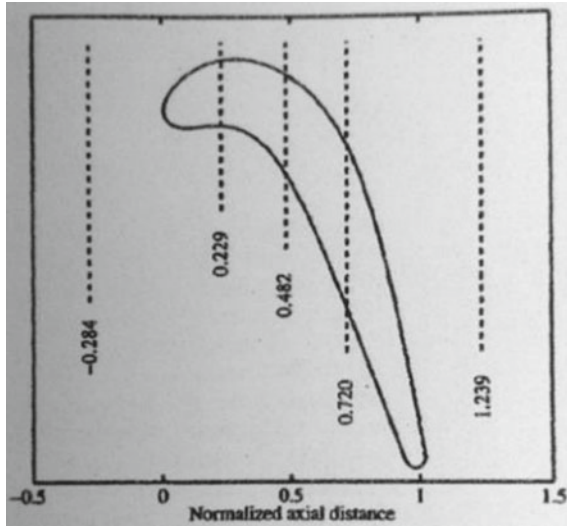


Fig. 15 Axial locations of unsteady pressure ports

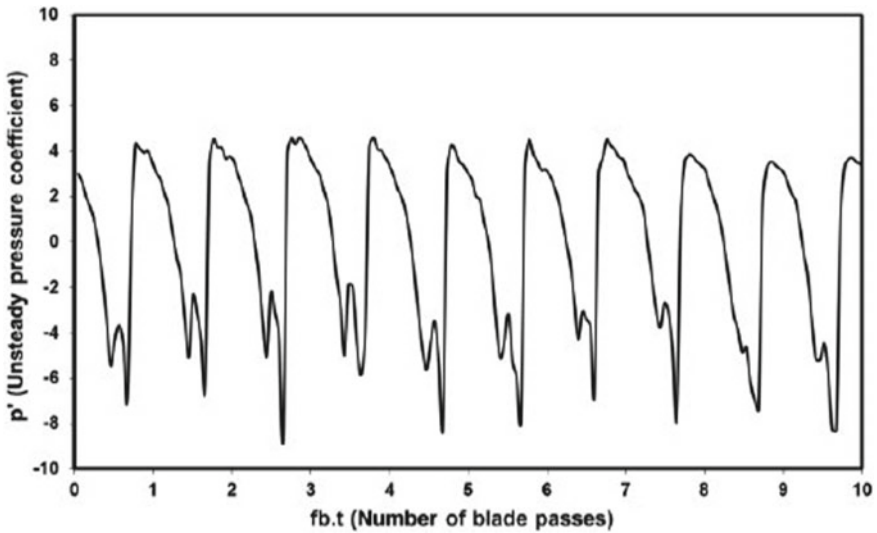


Fig. 16 Unsteady pressure variation at one of the axial locations

3 Conclusions

The old data acquisition system of the Large Scale Rotating Rig was successfully replaced with state-of-the-art devices. The data acquisition system includes advanced National Instruments hardware for stationary and rotating frame measurements with

inbuilt signal conditioners. Hence, the complicated bulky amplifiers and filters are no longer required. New LabVIEW-based data acquisition software has been developed indigenously and tested with the rig. With the upgradation of the data acquisition system, the run time has reduced significantly and quality of the data has improved considerably. Satisfactory benchmark data have been obtained from the rig using the new look DAS and have been validated with the P&W data. Fast response pressure sensors have been installed on the rotor casing at the blade footprint, and unsteady pressure measurements have been carried out to study the tip leakage flows.

Acknowledgements The authors would like to express their gratitude to Director, NAL and M/S. Pratt & Whitney, USA, for giving an opportunity to perform this task. The authors would like to thank Head and Jt. Head, Propulsion Division, NAL, for their support. The authors would like to thank Dr. Anil Prasad and Mr. Joel Wagner, Pratt & Whitney, USA, for their useful inputs in setting up the instrumentation for the Large Scale Rotating Rig. The authors are grateful to all the team members for their assiduous assistance without which successful completion of this work would not have been possible.

References

1. Dring RP, Joslyn HD (1981) Measurement of turbine rotor blade flows. *ASME J Eng Power* 103:400–405
2. Joslyn D, Dring R (1992) Three-dimensional flow in an axial turbine: part 2—profile attenuation. *ASME J Turbomach* 114:71–78
3. Dring RP, Joslyn HD (1987) Throughflow analysis of a multistage compressor operating at near-stall conditions. *ASME J Turbomach* 109:483–491
4. Joslyn D, Dring R (1992) Three-dimensional flow in an axial turbine: part 1—aerodynamic mechanisms. *ASME J Turbomach* 114:61–70
5. Joslyn HD, Dring RP (1985) Axial compressor stator aerodynamics. *ASME J Eng Gas Turb Power* 107:485–493
6. Stauter RC, Dring RP, Carta FO (1991) Temporally and spatially resolved flow in a two-stage axial compressor: part 1—experiment. *ASME J Turbomach* 113
7. Dring RP, Joslyn HD, Hardin LW (1982) An investigation of axial compressor rotor aerodynamics. *ASME J Eng Power* 104:84–96
8. Joslyn HD, Dring RP (1989) Multi-stage compressor airfoil aerodynamics: part II—airfoil boundary layer analysis. *AIAA* 86:1744
9. DTS3250/32Tx thermocouple scanner instruction and service manual. <http://scanivalve.com/media/27939/dts3250v419.pdf>
10. ZOC 33/64Px and ZOC 33/64PxX2 electronic pressure scanning module instruction and service manual. http://www.scanivalve.com/media/28028/zoc33_1603.pdf
11. www.ni.com
12. Senthil Kumaran R, Kumar K, Poornima N (2017) Experimental study of unsteady pressure fluctuations due to tip leakage flows in an axial flow turbine. In: *GTINDIA2017 – 4868*, ASME GT India conference, Bangalore

Performance of Bolted Joint Modelling Using Master Element



G. Vamsi Krishna, C. Viswanath, and Ashok Kumar Pandey 

Abstract Energy dissipation at the interfaces of the mechanical joints is the primary source of damping in many rotor dynamics structures as well as built-up structures. In the majority of structures, micro- and macro-slips at the interfaces are the mechanisms for energy dissipation. Modelling of the dissipation using detailed finite element (FE) of the joint interfaces is computationally very expensive. Consequently, it places severe restrictions in the application of detailed FE methods to real-life structures for capturing energy dissipation at joints. In the present work, a reduced-order Masing's model is adopted to model overlapping joint interfaces. The dynamic contact of the overlapping interface is captured using coupled normal and tangential Masing's contact rate forms in commercial FE software through the user-defined subroutine. Masing's parameters are established from the detailed FE model of isolated bolt structure. It is found that the reduced-order modelling is well suitable for capturing dissipation energies without the need for the detailed finite element methods.

Keywords Bolted joint · Reduced-order modelling · Masing's model

1 Introduction

Many built-up structures such as components of aero-engine rotors, non-rotating missiles, etc., in which the components are held together through bolted joints. Since these structures are subjected to many different types of loads such as cyclic torque, axial load combined with variable rotating bending moment, gyroscopic moment, etc., which may lead to dissipation as well as loosening of bolted joints. Such mechanisms may lead to energy losses at the joints and change in stiffness [1]. Therefore,

G. Vamsi Krishna

Advanced Systems Laboratory, Defence Research and Development Organization, Hyderabad, Telangana 500058, India

G. Vamsi Krishna · C. Viswanath · A. K. Pandey (✉)

Department of Mechanical and Aerospace Engineering, Indian Institute of Technology Hyderabad, Kandi, Telangana 502285, India

e-mail: ashok@iith.ac.in

© Springer Nature Singapore Pte Ltd. 2021

J. S. Rao et al. (eds.), *Proceedings of the 6th National Symposium*

on Rotor Dynamics, Lecture Notes in Mechanical Engineering,

https://doi.org/10.1007/978-981-15-5701-9_48

an accurate prediction of damping and stiffness in structural joints are necessary to capture the dynamics of structures. In this paper, we discuss the energy dissipation of bolted joint under axial loading condition which is prevalent in rotor blades in the form of cantilever under dynamic condition. To achieve our aim, we discuss the performance of a master element based on Masing's model to capture energy losses at the joint, which, in turn, can be also used to capture energy losses in structures with many bolted joints, thus minimising the computational effort.

Modelling of energy dissipation phenomenon requires models for friction. Several models of friction of varying complexity are proposed in the literature starting from simple quasi-static friction model such as Coulomb's model to more complex dynamic friction models [2, 3]. A thorough review of friction modelling on friction-induced vibration is given by Ibrahim [4, 5]. Friction energy dissipation at interfaces is a highly localised and nonlinear process. Furthermore, when coupled with the dynamic contact processes at interfaces, it becomes a challenging phenomenon to be represented in an analytical expression. Finite element method with the discretisation of frictional interfaces has the potential to address dynamic contact happening at interfaces. Chen and Deng [6], Lee et al. [7] and Oldfield et al. [8] successfully employed detailed finite element models with ultrafine discretisation at frictional interfaces for understanding and characterising the nonlinear damping behaviour of different structural joint configurations. They employed the Coulomb friction model at contact interfaces in which friction coefficient was the only parameter used to describe contact conditions. Though the method was demonstrated to be flexible and reliable, it requires ultrafine mesh at joint interfaces to capture the micro-slip. Additionally, time step size for simulation also needs to be reduced to satisfy stability requirements. With this limitation, the dynamic analysis of engineering structures with multiple joints using detailed FE methods is computationally prohibitive. Integration of reduced-order models into FEM helps in capturing the nonlinear nature of joint mechanics. It is achieved by employing elements with sizes natural to the scale of the structures.

In the present work, a new method of reduced-order model implementation based on Masing's model [9, 10] is developed using contact elements in a commercial FE software package, ANSYS [11], through a user-defined subroutine. The idea of the present work is to capture the dissipation effects at overlapping interfaces with considerably less computational cost by employing contact element-based reduced-order model. In the bolted overlapped structure, not the entire interface is under the macro-slip regime, but only pockets of the region would exist in the interface which operates in the macro-slip regime as the amplitude of vibration increases. Hence, Masing's reduced-order contact model is chosen for implementation which has the ability to simulate both micro- and macro-slip effects.

2 Finite Element Modelling Procedure

In order to compare the influence of master element, we first demonstrate the finite element modelling of bolted joint based on Coulomb model to capture the micro- and macro-slip using ANSYS. Using this model, we demonstrate the procedure to generate the hysteresis loop under the effect of pre-tightening and tangential load.

2.1 Modelling and Analysis of an Isolated Joint

The FE models consist of an isolated bolted joint having *M10* bolt and nut (8.8 class) of standard dimensions connecting two steel plates (AISI 1040) of size of 30 mm × 30 mm with 6.5-mm thickness as shown in Fig. 1a. The bottom face of the bottom plate is fixed. One of the side faces of the top plate is loaded with the cyclic varying load as shown in the inset of Fig. 1a. Plates are held together with bolt pretension. The interfaces are modelled using the contact elements to complete the model. In order to capture the micro-slip effectively, the radial divisions on the face of the plate around bolt/nut are adjusted to refine the element size around bolt hole as shown in Fig. 1b. Subsequently, the mesh is swiped along the thickness to activate *SOLSH190* 8-noded linear solid-shell element—for meshing both the plates. These elements have extra degrees of freedom to account for bending modes. Solid-shell is especially employed when the solid body is meshed with only one layer of the element in a direction, and the deformation is dominated by bending which is the case when these developed implementation procedures are used for dynamic analysis of structure with overlapping interfaces. For bolt and nut, mapped face meshing with two layers of pinch elements is introduced in a radial direction along the shaft and meshed with *SOLID186* 20-noded quadratic 3D elements.

For calculation of dissipation effects at the underside of bolt and nut with plates, 3D models of bolt and nut are employed. *CONTA174* and *TARGE170* contact elements

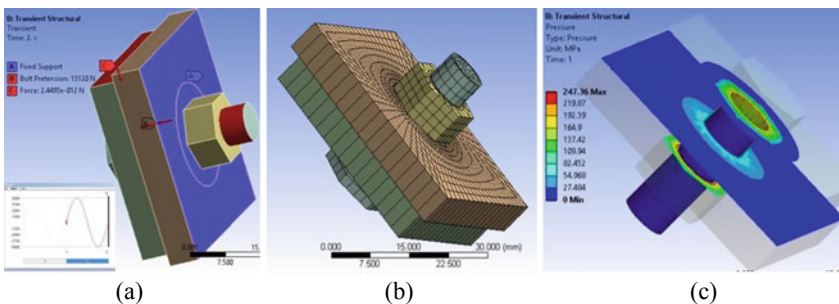


Fig. 1 a A solid model and b discretised model of an isolated joint, and c pressure distribution at contact interfaces under static preload

are introduced at all the contact interfaces, namely contact interface of the top and bottom plates; top plate and underside of the bolt; bottom plate and underside of the nut; and bolt and nut interface. Frictional contact with 0.2 coefficient of friction is defined for all the contact interfaces except at bolt and nut interface. Augmented Lagrange contact formulation is defined with the contact detection method at Gauss points on contact surface, and behaviour is set as symmetric. Bolt pretension is defined using bolt pretension element. For creating bolt pretension effects, bonded contact is defined between bolt and nut using multi-point constraint (MPC) contact formulation. The analysis is carried out for a bolt pretension of 21.2 kN corresponding to pre-torques of 34 Nm. The average axial tensile stress on the bolt shank caused by the pre-torque is 586.0 MPa which is below the yield stress (600 MPa) of the bolt material. The bottom surface of the bottom block is fixed, and the side surface of the top block is loaded with a sinusoidal varying force of 5 kN magnitude (one complete cycle of loading in 1 s time; starting with 0 kN magnitude at 1 s and ending again with 0 kN magnitude at the end of 2 s) along global *Y*-direction which is sufficient to ensure macro-slip at the interface for given applied pretension and coefficient of friction.

2.2 Generation of Hysteresis Curve

In order to generate hysteresis loop and isolated joint, we divide the loading into two steps; first, a bolt pretension of 21.2 kN is applied as the static load in step-1, and a cyclic tangential load of 5 kN is applied as the time-varying load in step-2. Figure 1c shows the pressure distribution over an annular area over which effect of pre-tightening torque is shown. It shows that the pressure is maximum around the bolt hole and diminishes radially outwards. Since the annular area around the bolt hole at the interface up to which contact pressure is felt is contained within the block area of isolated joint, the isolated joint can fully capture the hysteretic energy loss around the single bolt. Hence, the generated parameters from this model can be employed for damping characteristic estimation of mechanical joint with multiple bolts as long as the distance between bolts is high enough to ensure non-interference of contact pressure distribution of adjacent bolts of the joint. Except for very thick plates, the standard practice of employing two times the bolt diameter spacing between adjacent bolt centres would ensure the non-interference of contact pressure distribution due to bolt torque. Figure 2a shows that accumulated slip is maximum at the end of the annular area along the *y*-direction at the end of load step-2. Figure 2c shows the evolution of contact status with external load. At the beginning of load step-2, i.e. at time 1.0 s, contact state distribution is symmetric with sticking around a bolt hole and sliding at the outer peripheral area, and open beyond the sliding outer peripheral area. As load increases sinusoidally, at time 1.05 s, sliding area extends and sticking area diminishes along the load direction. The effect is more pronounced at 1.1 s. At the peak of the external load, i.e. at time 1.25 s, complete area at the plate interface is sliding, indicating the ability of load applied to capture the plastic state

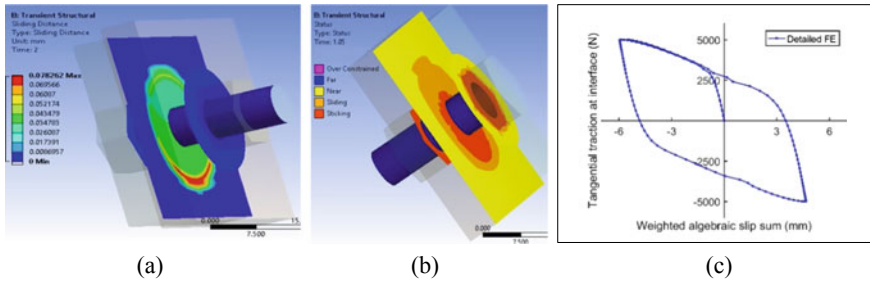


Fig. 2 **a** Slip accumulation at the end of sinusoidal load, **b** a typical contact interfaces at a given instant during ramping up of sinusoidal loading; and **c** hysteresis loop generated from FE model under preload of 21.2 kN and cyclic tangential load of 5 kN

of the hysteresis curve as well. Repeating the process for each load set, an average algebraic sliding distance (algebraic sliding at each of the nodes of the contact element is averaged) along the tangential load direction, at each of the contact elements, is extracted. The weighing of averaged algebraic sliding at each of the elements is carried out by multiplying with respective element contact area to make the results independent of mesh discretisation. Summing of the weighted sliding distance of all the elements is carried for each load set result. Weighted algebraic sum sliding in the direction of tangential load obtained in each load set is plotted against the tangential load magnitude during each load set for one full sinusoidal loading cycle. Figure 2c shows the hysteresis curve obtained through a weighted average of algebraic sliding versus the tangential traction of 5 kN (sinusoidal) and bolt preload of 21.2 kN.

3 Reduced-Order Model Based on Masing’s Model

Masing’s model [9] consists of a combination of Jenkins elements in parallel with a spring. A Jenkins element is a spring and slider (Coulomb element) in series. A slider element has two states—stick and slip. In its sticking state, it provides a resistive force equal and opposite to the input force to the element. When the input force exceeds the friction capacity of the Jenkins element, then the element enters into its sliding state. The model can be generalised by taking several Jenkins elements in parallel with a spring to model the energy dissipation due to both micro- and macro-slips. The hysteresis curve of Masing’s model is piecewise linear exhibiting corners and converges for an increasing number of Jenkins elements towards smooth lancet shape. Now, we describe the implementation of Masing’s model using FEM.

3.1 Implementation of Masing's Model in FEM

In this subsection, the implementation of Masing's contact laws using *userinter* subroutines in ANSYS is outlined. ANSYS overlays the contact and target elements on contacting parent components at the interface, following the same element discretisation as that of parent components. Since these contact elements are 2D, the traction vector in corresponding contact and target elements describes interface stresses and is given by Eq. (1).

$$\{t\}^{\text{bottom}} = \{t_{T_x} t_{T_y} t_n\}^T, \{t\}^{\text{top}} = \{t_{T_x} t_{T_y} t_n\}^T, \{t\} = \{t\}^{\text{top}} = -\{t\}^{\text{bottom}} \quad (1)$$

In contact mechanics, the relative displacement field of contacting surfaces is of interest and is given by Eq. (2):

$$\Delta u = \{u\}^{\text{top}} - \{u\}^{\text{bottom}} \quad (2)$$

The constitutive relation between the contact tractions and the relative displacement field is implemented at the interface using Eq. (3):

$$\{t\} = [C]\{\Delta u\} \quad (3)$$

Userinter is a user-defined subroutine which allows users to write custom interface laws. In the present analysis, Masing's contact is modelled by implementing the tangential and normal contact laws mentioned in [9, 10]. Additionally, user-defined traction–separation relations and pressure–penetration relations are also coded in it. It also updates history variables and computes consistent tangent matrix at each of the integration points. *Userinter* receives following input arguments from ANSYS: element number, element integration point number, the key options of contact formulation, real constants (pinball region, penetration tolerance factor, normal penalty stiffness factor, etc.), number of friction stress components, normal and tangential penalty stiffness, contact status, current time value, time increment over current sub-step, slip increment in current sub-step, accumulated slip from previous sub-step, current normal pressure, frictional stress from previous sub-step [11]. The user-defined frictional properties and user-defined material properties are input through *tbddata* command. Masing's parameters $c_1, c_3, g_0, k_\infty, k_n, n, \mu$ are given as input to *userinter* using *tbddata* command. NSVR (no. of integration points \times no. of state variables per integration point) command is used to tell about the number of additional state variables to be used. Using these input arguments, subroutine calculates pressure and traction along tangential directions in current sub-step. It also updates internal variables and computes consistent material tangent modulus required for Newton–Raphson iterations. *Userinter* is accessed for the contact elements by invoking with inter-command with *tbopt = user*.

Since traction–separation relations in rate form cannot be coded, for linearising the rate-dependent tangential contact laws, time integration of rate equation is done

using the forward Euler method as follows. Time integration of tangential contact law along 'u' direction is shown below [9, 10]:

$$\dot{t}_{Tx} = k_{\infty} \Delta \dot{u} + \dot{\vartheta}_{Tx}; \quad \dot{\vartheta}_{Tx} = k_1 \Delta \dot{u} \left[1 - s \left(\frac{\sqrt{\vartheta_{Tx}^2 + \vartheta_{Ty}^2}}{\vartheta_{max}} \right)^n \right] \quad (4)$$

where s is given by $s = \frac{1}{2} [1 + \text{sgn}(\Delta \dot{u} \vartheta_{Tx} + \Delta \dot{v} \vartheta_{Ty})]$ which is calculated from ϑ_{Tx} , ϑ_{Ty} , $\Delta \dot{u}$, $\Delta \dot{v}$ known from previous iteration.

$$\Delta t_{Tx} = k_{\infty} (\Delta u - \Delta u') + k_1 (\Delta u - \Delta u') (1 - sc) \quad (5)$$

$$\text{where } c = \left(\frac{\sqrt{\vartheta_{Tx}^2 + \vartheta_{Ty}^2}}{\vartheta_{max}} \right)^n \quad (6)$$

where

$$\Delta t_{Tx} = m (\Delta u - \Delta u') \quad \text{and} \quad m = k_{\infty} + k_1 - k_1 sc \quad (7)$$

In numerical modelling of the frictional interface using Masing's model based on the above discussion, the following three significant aspects have to be considered. First, if the value of ' $c > 1$ ', then take ' $c = 1$ '; second, the bolt hole and bolt need not be explicitly modelled to avoid duplication of stiffness due to bolt when macro-slip starts; third, bolt preload has to be applied as uniformly distributed pressure on the interface.

3.2 Influence of Mesh Discretisation on Masing's Model Performance

In this section, the influence of numerical parameters such as the mesh size, loading and time-stepping is analysed on the performance of Masing's model. Since Masing's equations are implemented with Euler's forward discretisation, it is sensitive to time step size. For time step of < 0.01 s, convergence is observed for given numerical parameters. The minimum time step requirement is checked to hold good for all the possible mesh sizes (10–0.5 mm). Detailed FE analysis is carried out with the ultrafine mesh discretisation and Coulomb friction at the interface as shown in Fig. 1b, while the reduced-order modelling is carried out with coarse mesh with Masing's normal and tangential contact law at the interface as shown in Fig. 3a. Figure 3b shows the hysteresis curve comparison of detailed FE to the different mesh sizes modelled using Masing's equations [2, 3, 9] with Masing's parameter values of k_0

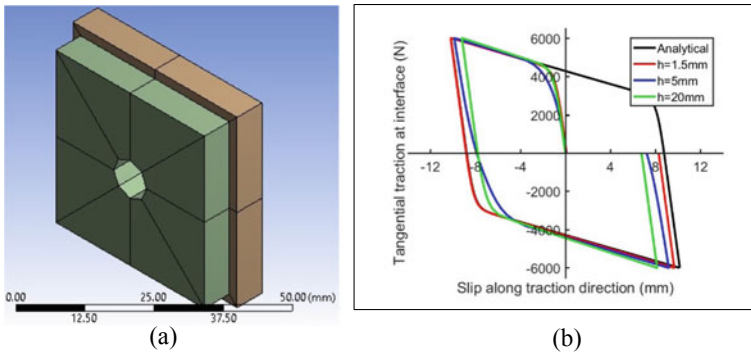


Fig. 3 **a** An FE model with coarse mesh and Masing's model at the interface, **b** mesh dependency on hysteresis curve obtained using the FE model with Masing's contact law at the interface

$= 4270 \text{ N/mm}^2$, $k_\infty = 170 \text{ N/mm}^2$ and $n = 3$ with uniform load of 21.2 kN on the top surface of the top plate and 6 kN force tangentially applied on the side face of the top plate. It is also observed that even though the overall shape of the hysteresis curves of different mesh sizes modelled with Masing's interface laws at the interface is relatively similar, the area enclosed by the curves is off by a maximum of $\sim 15\%$. Single element model is more accurately representing the hysteresis curve obtained from detailed FE methods. The average slopes in the elastic and plastic region for different element sizes are slightly off from analytical Masing's parameters used for modelling the interface. Average elastic stiffness being lesser than k_0 parameter and average plastic stiffness being more than k_∞ parameter lead to decrease in area with a decrease in element size. Since reduced-order modelling is meant to work with a coarser mesh, Masing's parameters k_0 and k_∞ are to be adjusted accordingly to compensate for the variable pressure distribution due to discretisation effects. Hysteresis loop comparison with adjusted Masing's parameters is shown, and the area enclosed by the curves differs by $<0.2\%$ from analytical estimates. The adjusted Masing's parameters once identified for particular mesh size, holds good all load cases. The same is demonstrated in Fig. 4a, b corresponding to 10 kN preload and 1.5 kN tangential load, and 3.5 kN preload and 1 kN tangential load, respectively. In both the cases, same adjusted Masing's parameters as listed in Table 1 are used.

Finally, the formulation based on Masing's model can be used to ease the computation of in-built structures with bolted joints. Now, we demonstrate the accuracy of computing dissipation in a bolted joint.

3.3 Energy Dissipation in a Lap Joint with Multiple Bolts

In this section, we apply the above procedures to compute modal damping ratio in a lap joint with multiple bolts as shown in Fig. 5a. To perform the analysis, we take

Finally, we state that the master element developed based on Masing's model works well and the same procedure can be applied to develop master element based on other bolted joint models.

4 Conclusions

In this paper, we present procedure to develop a master element based on Masing's model to capture energy dissipation in a bolted joint. To meet the objective, we solve Masing's traction–separation contact equations numerically to generate traction–separation hysteresis curve. Subsequently, we perform detailed FE analysis of specific isolated bolted joint configuration subjected to harmonic tangential loads to obtain hysteresis curves first with Coulomb friction model and then with Masing's model-based finite element. It is found that the results obtained with Coulomb model (detailed FE procedure) under very fine mesh are compared with that obtained using Masing's model under coarse mesh. Finally, we state that the master element based on Masing's model presented in the paper can be used model bolted joints in various in-built structures.

Acknowledgements The project is partially supported by AR&DB, India, with project number 1824.

References

1. Kuratani F, Hirai T, Koide K, Kido I (2013) Damping in jointed friction plates with partially overlapping interfaces. In: RASID 2013, 11th international conference
2. Beards CF (1992) Damping in structural joints. *Shock Vib Dig* 24:3–7
3. Ahmadian H, Jalali H (2007) Identification of bolted lap joints parameters in assembled structures. *Mech Syst Sig Process* 21:1041–1050
4. Ibrahim RA (1994) Friction-induced vibration, chatter, squeal, and chaos—part I: mechanics of contact and friction. *ASME Appl Mech Rev* 47(7):209–226
5. Ibrahim RA (1994) Friction-induced vibration, chatter, squeal, and chaos—Part II: dynamics and modeling. *ASME Appl Mech Rev* 47(7):227–253
6. Chen W, Deng X (1999) A finite element analysis of friction damping in a slip joint, DETC99/VIB-8189. In: Proceedings of 1999 ASME design engineering technical conferences, Las Vegas
7. Lee S-Y, Ko K-H, Lee JM (2000) Analysis of dynamic characteristics of structural joints using stiffness influence coefficients. *KSME Int J* 14:1319–1327
8. Oldfield MJ, Ouyang H, Mottershead JE (2005) Simplified models of bolted joints under harmonic loading. *Comput Struct* 84:25–33
9. Masing G (1923) Zur Heynschen Theorie der Verfestigung der Metalle durch verborgene elastische Spannungen. *Wissenschaftliche Veröffentlichungen aus dem Siemens-Konzern* 3:231–239

10. Segalman DJ (2006) Modeling contact friction in structural dynamics. *Struct. Control Health Monit* 13:430–453
11. ANSYS (2017) A mechanical APDL, programmer's reference, guide to user-programmable features, SAS IP, INC